CREEP OF SERVICE-AGED WELDS

by

Wei Sun, *BSc MSc*

Thesis submitted to the University of Nottingham for the degree of Doctor of Philosophy

MAY 1996

CONTENTS

ABSTRACT

The creep behaviour of welds in service-aged pipes are studied. The aims of the research have been achieved using analytical, numerical and experimental approaches to the relevant subjects. Several features of the work are presented: (i) a systematic parametric study of the creep of two-material test specimens including a stress singularity analysis, (ii) an impression creep testing method using a rectangular indenter, which can be applied to study the creep properties in welds, and (iii) methods used for damage constitutive equation generation involving FE-damage modelling of the rupture tests of cross-weld specimens.

General observations on the creep of two-material structures have been made using analytical solutions derived from four simple structures. The effects of geometries and relative creep properties on the creep stress or strain-rate distributions have been investigated using the finite element approach with idealised, two-material, axisymmetric models. The stress variations have been extensively studied on the centre-line and in the singularity regions of the models.

An impression creep testing technique with a "long" rectangular indenter has been developed for the study of the creep properties in the narrow zones within weldments. The effect of varying the geometric test parameters has been fully analysed. The application and the possible advantages of the technique for determining the creep properties in welded components have been highlighted.

Experimental testing has been performed for the purpose of verifying the impression creep testing technique and to provide the creep and rupture information required for the generation of creep and damage parameters for the exposed materials. The results obtained have further validated the applicability of the impression creep testing technique.

Creep continuum damage investigations have been performed in order to generate the material parameters in a continuum damage constitutive equation and to model practical weldments. The methods used for material data generation have been established. The failure analysis and prediction for the service-aged welded pipes using steady-state analysis, damage modelling and extrapolation technique have been addressed.

ACKNOWLEDGEMENTS

The duration of my PhD research has given me the opportunity to meet many people who have been directly or indirectly involved in the completion of my work. Their efforts have been crucially fruitful and deservedly appreciated.

Firstly, I would like to express my deepest gratitude and appreciation to my supervisors Professor T H Hyde and Dr A A Becker for their invaluable scientific guidance, encouragement, support and care in the preparation of this thesis and throughout the period of my study in Nottingham.

I am also sincerely grateful to Dr J A Williams for his helpful advice, assistance and contribution to this work through many informative and beneficial discussions. Thanks and gratitude are also due to Mr B Russell-Smith for his imaginative and indispensable contribution throughout the period of my experimental work, to Mr R Pickard, Mr A Higgins and other staff for their skilful technical support, and to Miss J Bray for her efficient and kind secretarial assistance.

My recognition must go to PowerGen and Nuclear Electric for their financial support of this work, to the CVCP for offering me an ORS Award, and to Dr D J Allen (PowerGen), Dr R A Ainsworth (Nuclear Electric) and Mr J K Hepworth (PowerGen) for their involvement in this project. I am also thankful to the China State Education Commission who provided funding and made it possible for me to spend one year at the University of Nottingham as a visiting scholar when I had the honour of working with Professor T H Hyde and Professor H Fessler.

I would like to show my gratitude to the staff of the Department of Mechanical Engineering, George Green Library, Cripps Computer Centre and the Faculty of Engineering, at the University of Nottingham, for their assistance during the period of this study.

Finally, the friendly and sincere scientific and social interaction with my friend and colleague Dr A H Yaghi has added an element of pleasure to my stay at the University of Nottingham, which has been enhanced by the friendliness and pleasantness of all my colleagues there.

NOMENCLATURE

A, A_A, A_B, A_C	constants in creep constitutive equations
A_1, A_2	areas of bars
b	beam width or initial indentation depth
b_1, b_2	beam dimensions
B, B_1, B_2	constants in creep constitutive equations
BM	base material
d	beam depth, specimen diameter or indenter width (or diameter)
d_1, d_2	beam dimensions
D	reference multiplier
E	Young's Modulus
f, g	indenter position parameters
G_{eq}, G_x	factors in linear stress equations (functions of x)
H, H_1, H_2	heights of indentation specimens
HAZ	heat-affected zone
K_{eq}, K_x	factors in linear stress equations (functions of x)
K_{ij}	stress singularity parameter related to σ_{ij}
K_{rr}, $K_{\theta\theta}$, $K_{r\theta}$, K_{eq}	stress singularity parameters related to σ_{rr}, $\sigma_{\theta\theta}$, $\sigma_{r\theta}$ and σ_{eq}, respectively
$\hat{K}_{rr}, \hat{K}_{\theta\theta}, \hat{K}_{r\theta}, \hat{K}_{eq}$	maximum values of K_{rr}, $K_{\theta\theta}$, $K_{r\theta}$, and K_{eq}, respectively
$\dot{K}, \dot{K}_{ss}$	curvature rate and steady-state curvature rate

l_1, l_2	lengths of bars
L, Le	length and gauge length
m	constant in creep constitutive equations
M	bending moment or damage parameter
n	stress exponent in creep constitutive equation
N_{ij}	stress singularity parameter related to σ_{ij}
N_{rr}, $N_{\theta\theta}$, $N_{r\theta}$, N_{eq}	stress singularity parameters related to σ_{rr}, $\sigma_{\theta\theta}$, $\sigma_{r\theta}$ and σ_{eq}, respectively
$\overline{N}_{ij}$, $\overline{N}_{eq}$	averaged values of N_{ij} and N_{eq}
p, p_a, p_i, p_1	pressure, axial pressure, internal pressure and interface pressure
P, P_L	load and limit load
Q	activation energy
r	radial position
r*	radial distance of singularity zone
R	gas constant
R_1, R_i, R_o	interface, inside and outside radii of cylindrical components
R_{MS}, R_{TS}	rupture time ratios
S_{ij}	deviatoric stress ($=\sigma_{ij} - \delta_{ij}\sigma_{kk} / 3$)
t	creep time
t_f, t_{fss}	failure time and the failure time predicted by steady-state creep analysis
$\dot{u}(r)$	radial displacement rate at radius r
w	width of material type A
W, W_A, W_B, W_C	widths of indentation specimens

WM	weld metal
x	axial position
α	stress scaling factor or damage parameter
α_R	reference value of scaling factor α
β	non-dimensionalised reference multiplier
β_o	β value at b = 0
η	reference parameter related to mean indenter pressure
η_o	η value at b = 0
δ_{ij}	Kronecker delta (= 1 for i = j, and = 0 for i ≠ j)
Δ, Δ_{el}, Δ_i, Δ_r	deformation (displacement, curvature, rotation or strain), initial elastic deformation, initial deformation and deformation due to redistribution, respectively
$\dot{\Delta}_{ss}$	steady-state displacement-rate
ε, ε_{ij}	strain and strain tensor
$\dot{\varepsilon}^c$, $\dot{\varepsilon}^c_{ss}$	creep strain rate and steady-state creep strain rate
ε_θ, ε_a (or ε_x), ε_r, ε_{eq}	hoop, axial, radial and equivalent strains
$\dot{\varepsilon}_\theta, \dot{\varepsilon}_a$ (or$\dot{\varepsilon}_x$), $\dot{\varepsilon}_r, \dot{\varepsilon}_{eq}$	hoop, axial, radial and equivalent strain rates
ν	Poissons' ratio
σ, σ_{ij}, σ_{nom}	stress, stress components and nominal stress
σ_1, σ_2	stresses in bar 1 and bar 2
σ_r, σ_{rss}	rupture stress and steady-state rupture stress
σ_{rr}, $\sigma_{\theta\theta}$, $\tau_{r\theta}$	stress components in singularity analysis
σ_Y, σ_R	yielding stress and reference stress

$\sigma_x(y)$, $\sigma_x^1(y)$, $\sigma_x^2(y)$	bending stresses at distance y from the neutral axis
σ_θ, σ_a (or σ_x), σ_r, σ_{eq}	hoop, axial, radial and equivalent stresses
σ_{eff}	effective stress ($=\left(\frac{3}{2}S_{ij}S_{ij}\right)^{1/2}$)
$\hat{\sigma}$	maximum principal stress
$\hat{\sigma}_r, \hat{\sigma}_{rss}$	peak rupture stress and steady-state peak rupture stress
$\hat{\sigma}_x, \hat{\sigma}_{eq}$	maximum or peak axial and equivalent stresses
Φ/Φ_o	notched bar geometric ratio
θ	angular position
ω, $\dot{\omega}$	damage and damage rate
χ, ϕ	damage parameters

CHAPTER I

INTRODUCTION

Creep is the time-dependent deformation of a material under a stress which is lower than the yield point (Power [1986]). Whilst creep can occur over the whole temperature range, with engineering metals and alloys creep is generally only of practical importance at high temperature. The phenomenon of creep is the source of many problems in engineering design. Foremost amongst these is the need for the generation of methods to predict whether components operating in the creep range will safely function for the life required (Penny and Marriott [1992]).

Welds are an essential feature of large-scale plants for pressurised piping and vessels as, for example, in electric power generation, chemical installations and the oil and gas industries. Welded joints usually are used to join component parts of the assembly, which often operate at elevated temperature for long periods of time, i.e. they operate under predominantly creep conditions. Indeed, the performance of welds is often the life limiting factor in many components and structures, particularly under service conditions where creep failure may occur. Yet, in general, design codes do not specially identify welds as an important parameter (Evans and Wilshire [1985]). For example, present UK and European design codes do not include a high temperature allowance for welds. In design terms, welds are normally accounted for simply by postulating a "weld-efficiency factor". In many cases, this merely involves down-rating

the allowed stress calculated for a homogeneous component and by stipulating that the ductility of any part of the weldment should be adequate for the application envisaged.

The long-term integrity of high temperature engineering structures is of considerable economic importance, particularly in electricity power generation plants, where failure can lead to expensive plant outages. In practice the majority of problems associated with high temperature components are caused by or associated with cracking in weldments. Experience suggests that the life of the components and the plant as a whole may be governed by the behaviour of welds which are locally inhomogeneous in structure and properties. During service, components are often subjected to combinations of cyclic and steady loading periods at elevated temperature. Such service histories can induce defects in these components or cause pre-existing defects to propagate. These problems primarily arise because the welded zone is a region of inhomogeneity. One feature of these kinds of failure is that the rupture of the components is associated with time-dependent accumulation of damage (e.g. Lee and Muddle [1986]).

The prediction of the behaviour of welds is difficult not only because of the complex microstructure and therefore properties involved, but also because of the wide range of weld geometries usually found in practice. During the welding of low-alloy ferritic steels, which are widely used in power generation plants and other high temperature plants, regions of the steel component immediately adjacent to the fusion boundary are heated rapidly to temperatures which approach the melting temperature of the weld metal and then cooled by conduction at rates determined by heat flow considerations.

In the parent material the region where the microstructure is modified by the welding process is termed the heat-affected zone (HAZ). Since the peak temperature attained and the subsequent cooling rates decrease from the fusion interface, the welding process leads to a variety of non-equilibrium microstructures in the HAZ of low-alloy ferritic steels.

From the above, it can be appreciated that the prediction of the performance of weldments in high temperature plants is considerably more complicated than the problems associated with homogeneous structures. Essentially, the failure characteristics of weldments under elevated temperature creep conditions can be determined by large-scale testing of individual components or by laboratory testing of suitably designed so called "cross-weld" test specimens. Because of the cost and time required for full-scale or large-scale testing, the creep testing of cross-weld specimens is usually preferable. It should be noted that the creep data from the cross-weld specimen tests are difficult to interpret to use to describe the creep behaviour of practical welded structures or components; one of the reasons is the lack of knowledge of the effect of specimen geometries.

The prediction of the deformation of and stress variations within welds due to creep is not a straightforward task. This is due to many reasons such as the uncertainty of the mathematical models used to describe the material behaviour and the need to extrapolate the relatively short term experimental data to real component life times. Detailed information of stress and strain distribution cannot be derived by analytical methods except for very simplified structures with simple geometries. In the case of

complex structures, closed-form analytical solutions from which the creep deformation and stress can be predicted do not exist. For this reason, numerical simulation techniques are often adopted.

So far, many numerical methods, such as the finite element (FE) method, finite difference method and boundary element method (BE), have made it possible to model very complicated components (Becker et al [1994]). For the modelling of weldments, the finite element method is the most used tool. Standard commercial FE packages, such as ABAQUS [1994] and PAFEC [1974][1984], have been extensively used for steady-state creep analysis. Since standard FE packages do not currently include the capability of damage analysis, creep rupture modelling has to be performed by specialised non-commercial packages. Reliable creep and damage material properties, which are usually obtained from experimental testing, should be determined before costly and time-consuming creep damage analyses are carried out.

Service experience suggests that the welds in a structure are the weakest parts and failure usually occurs within or near the HAZ of the weldments. This indicates that, for modelling purposes, the generation of the proper material constitutive equations which correctly describe the creep and damage behaviour of all of the material zones is essential. Material properties of parent and weld metals can be generated by using the information of single material uniaxial tests incorporated within the FE modelling of uniaxial creep rupture tests of notched specimens (Hyde et al [1996]). The generation of HAZ material properties is much more complicated. For a virgin weldment, it may be possible to obtain the HAZ material properties form tests using thermally simulated

HAZ material. However, in the case of service-aged material, since the material behaviour may have been changed significantly during long-term service at elevated temperature, the exact thermal simulation of such material is nearly impossible. For this reason, the impression creep testing technique, which can be used to obtain the creep properties of a relatively small volume of material, has been developed (e.g. Hyde et al [1993]). Using the primary and secondary creep properties of the HAZ material, determined from impression tests, it is possible to determine the damage parameters for the HAZ material by modelling the behaviour of rupture tests performed on uniaxial cross-weld specimens.

The impression creep testing technique is a modified hot hardness testing method which involves the application of a steady load to a flat-ended indenter, placed on the surface of a material, at elevated temperature. Creep allows the indenter to push its way into the surface of the material. The displacement-time record from such a test is related to the creep properties of a relatively small volume of material in the immediate vicinity of the indenter. With the aid of a mechanics-based approach, using the reference stress method, the conversion factors (reference parameters), which are used to convert the impression creep behaviour to that of an equivalent uniaxial creep test, can be obtained.

The work to be introduced in this thesis will cover some aspects of the topics described above. The subject of the study is a service-aged weldment which was removed from the main steam pipe line of a power generation plant, after 174,800 hour service, at nominally 568° C, steam pressure 16.55 MPa, OD (outer diameter) 355.6

mm, and wall thickness 63.5 mm. Compared with the study of a virgin weldment, the research work on the service-exposed material is more difficult because of the uncertainty of the material properties after long-term operation and the lack of information available on such materials. However, the methods used for this study, in general, are similar to those used for the new materials. Although the work introduced in this thesis has included some metallurgical aspects, the study mainly focuses on the mechanical aspect of the creep analysis of welded components.

Chapter II of the thesis contains a literature review which is divided into three main parts. The first one (Section 2.2) gives a brief review on some general topics encountered in the study of creep in welds, such as the metallurgical and mechanical behaviour, the failure mechanisms of weldments and the methods used in research. In the latter sections, several specific subjects which are closely linked to the current research work are introduced. Section 2.3 presents a detailed review of the main aspects of the creep analysis of cross-weld specimens, while Section 2.4 provides a general description of the impression creep testing technique. Finally, a brief introduction on creep continuum damage analysis is given in Section 2.5.

Chapter III mainly deals with the creep analysis of two-material components. In order to understand the general behaviour of two-material components, Section 3.2 introduces the theoretical solutions and analyses for the creep stress distributions in four, simple, two-material structures, for which the closed-form solutions can be derived. The general observation on the creep of two-material structures and the applicability of simple design rules, established for single-material structures, to two-

material structures, are discussed. Sections 3.3 and 3.4 present the results of a parametric study of an axisymmetric, idealised, two-material, creep test specimen, using the finite element method; the influence of specimen geometry and material properties were investigated. The stress or strain-rate distributions on the centre-line of the specimen and the application of a simple interpolation technique are first covered and then stress singularity behaviour at the free surface of the specimen is dealt with. The physical significance and the implication of the singularity results obtained for practical situations are described.

In Chapter IV an impression creep testing technique, specially developed for the study of welds, is fully analysed. The results of a theoretical and finite element investigation of the impression creep test method, using a long rectangular indenter under plane strain conditions, rather than the conventional cylindrical indenter, are discussed. The application of the impression creep testing technique, for determining the creep properties of the various zones within welds, is considered. The finite element method is used to obtain the accurate (creep) or approximate (elasto-plastic limit load) reference stress solutions for the rectangular indenter, placed at different positions in the parent material, HAZ and weld metal. The effect of varying the geometric test parameters is reported. The possible advantages of the technique for determining some of the important creep properties in welded structures are identified.

Chapter V of the thesis introduces the experimental aspects of this research. Firstly, the objectives of the experimental work, together with a fully defined test program, are given. Then, the test materials and the specimens preparation, as well as the

experimental procedures, are described in details. A full set of the test results is presented in a later section. Based on these results, further verification of the impression creep testing technique, with a rectangular indenter, is achieved. Finally, several discussion points such as the validity of the experimental results and the generation of the creep properties for the tested weldment materials as well as the examination of the fracture surfaces of the tested cross-weld specimens are addressed. It should be mentioned that in order to shorten the duration of the experimental work the temperature used in the creep tests of this study is higher than the practical operation temperature in plants.

In Chapter VI the methods used for the generation of creep damage constitutive equations for the aged parent, weld and HAZ materials are introduced and a full set of damage constants for the aged materials is presented. The FE continuum damage failure modelling for single-material notched bars and cross-weld notched and waisted creep test specimens was performed for this purpose. The effect of the damage parameters on the rupture lives of the test specimens was studied and the procedure for the damage parameter generation has been fully described.

Chapter VII introduces the steady-state stress analysis and its application for the practical notched and waisted creep test specimens used in this work. The steady-state stress distributions in single-material and cross-weld notched and waisted specimens were investigated using the realistic dimensions and material properties, and the tri-axiality of the notched and waisted specimens was identified. By defining a steady-state effective failure stress, it has been shown that an approximate method for failure

life prediction can be employed. The applicability of the approximate method was confirmed by comparing the steady-state results and damage modelling results. On this basis, further applications of the steady-state rupture stress analysis were recommended.

In Chapter VIII the investigation of the failure prediction for the practical service-aged weldment is introduced. The FE creep continuum damage failure modelling for the aged weldment was performed, using the realistic dimensions, loading and material properties obtained at 640° C. For comparison purposes, the steady-state analysis was also conducted, which was found to be conservative. Since the test temperature used in this research is higher than the real temperature in plants, a simplified extrapolation technique was used to estimate the failure life of the aged weldment at the practical operating temperature of 568° C.

Chapter IX presents a general discussion and main conclusions of the current research, which aims to summarise the methodology used in this study and to emphasise the advantages and applications of the work. In Section 9.3, the main features of this work which mainly covers the steady-state parametric analysis, impression creep test technique, experimental testing for the aged materials and the creep continuum damage investigation, etc. were highlighted. Several specific topics such as steady-state failure prediction, Type IV failure of the aged weldment and the failure life extrapolation were discussed. The limitations of the current research methods were also addressed. In Section 9.3, the general conclusions of this study were summarised.

Finally, in Chapter X of this thesis future work based on the current research is recommended.

CHAPTER II

LITERATURE REVIEW

2.1 INTRODUCTION

Welded joints are among the most important construction elements in power generation plants; it is estimated that there are over 40,000 to 50,000 weldments for a 300-MW unit (Kussmaul [1993]). Safe and reliable service of welds at elevated temperature is, therefore, of crucial importance for the performance of power and other plants. For this reason, research work on the creep behaviour of welds has been carried out extensively.

The welding process introduces a feature of material inhomogeneity. During service at elevated temperature, the materials in different zones of a weldment exhibit different creep behaviour, which usually causes a reduction in the structure's integrity. In fact, the service performance of high temperature welded structures depends greatly on the material joining efficiency. Therefore, on this basis, the prediction of the performance and the prediction of the failure mechanism of the weldments are more difficult than the problem associated with homogeneous components.

A large number of creep failures have been found to be located in the weldments and therefore the creep behaviour and material properties of the weldments are of particular interest in order to assess residual life and improve design principles. The complexity of the creep properties in a weldment requires that methods for creep testing of a weldment and interpretation of the resulting test data have to be devised before predictions of creep in welded components can be modelled. In this context, the most common way to determine creep data from weldments is the uniaxial cross-weld creep test. For the purpose of interpreting the test data, an understanding of the stress distribution in cross-weld specimens and the influence of different factors which could affect the stress distribution is of great importance.

In order to study the creep properties of weldments, the impression creep testing technique , which has been used in the work, can be employed. Based on a mechanics-based approach using the reference stress method, the technique can be applied to determine the creep properties in the narrow zones, for example, the HAZ, which occurs in weldments.

The work to be described in this thesis deals with the creep behaviour of welds in service-aged pipes. This Chapter contains a literature review in which previous research work in the field is introduced, aiming to demonstrate the main problems associated with the creep analysis of welds and the ways in which they are tackled at present.

In the first section of this Chapter, some general topics such as the metallurgical and failure behaviours of the weldments under high temperature conditions, and the research methods used to investigate them, are discussed briefly. The later sections include several specific topics, namely, the creep analysis of the cross-weld specimens, the impression creep testing technique and creep damage analysis, which are closely related to the current work described in this thesis.

2.2 CREEP ANALYSIS OF WELDS

2.2.1 Introduction

This section deals with the effects of the welding process on the creep properties of the welded components. The performance and failure mechanisms of welded joints under creep conditions will be discussed. The research work carried out to cope with the problems arising due to creep of welded structures will be reviewed briefly.

There are many publications concerned with investigations of the effect of the welding process on the welded components, mechanical and creep properties and performance during service at elevated temperature. One of the most comprehensive accounts has been documented by Price and Williams [1982], in which 127 papers were reviewed, in an attempt to present a clear picture of the problems associated with welding and the performance of welds in the creep range. In this section, only those aspects of the

problems which are directly related to the current research work will be highlighted; any further detailed information can be easily obtained from the extensive literature available in this field.

2.2.2 Metallurgical and Mechanical Features of Weldments

Welded components differ from forged and cast structures. During welding, a hot weld metal is deposited onto a relatively cool parent material. The first weld bead laid generates a temperature gradient in the parent material which can be represented, at a particular time, as a series of isotherms centred on the weld bead. The extent and magnitude of the isotherms is determined by the heat input, thermal properties of the materials, and time, amongst other parameters (Williams [1982-2]). The material local to the weld bead is subjected to a heating and cooling cycle and the resulting structure in this region, defined as the heat affected zone, HAZ, will be controlled by the peak temperature, time at that temperature, cooling rate, the material and its metallurgical state. This is illustrated in Fig. 2.1(a) for a ferritic 1/2Cr1/2Mo1/4V steel welded with 1/2Cr1Mo weld metal. The Figure shows a schematic representation of the variation in grain size produced by a typical thermal cycle. In addition, various transformation products may be formed during the cooling cycle. Subsequent weld beads subject the weld metal, HAZ and parent material to further heating and cooling cycles leading to further modification of the metallurgical structure, see Fig. 2.1(b). Thus, the important characteristic of a weld is that it is inhomogeneous and shows a repetitive, definable distribution of metallurgical structures, each of which has different deformation, failure strain and stress rupture behaviour. The magnitude of any structure and property

difference depends primarily on the particular parent material considered and the welding conditions.

One of the detrimental effects of the welding process is the residual stresses generated due to the differences in the thermal material properties of various parts of the weldment and the different cooling rates according to the location of the fusion zone and the heat source. Phase transformation on cooling when accompanied by volume change (shrinking) also causes residual stresses to build up in the joint. For a welded pipe, these stresses, when measured at room temperature, will have a characteristic macroscopic distribution, typically a high hoop stress in the weld metal and high axial stresses in the weld metal/parent metal interface. Post weld heat treatment, PWHT, needs to be applied to welded joints in an attempt to relieve (i.e. smooth out these local peak stresses) the residual stresses, to decrease the general stress level and, in addition, to temper the microstructure.

The mechanical properties of the welded material are significantly changed after welding. Generally, the UTS (ultimate tensile stress), the yield stress and the ductility are substantially changed due to welding. The values for these properties vary at different locations within a weld, in the parent material, at various locations in the HAZ and in the weld metal, for austenitic and ferritic austenitic welds (Price and Williams [1982]). Creep properties, e.g. minimum creep strain rate, creep ductility and creep rupture times, also vary. Many test results have shown that (Parker [1995]) the mismatch in the creep strain-rate between parent and weld metals can be higher than 5 times. The HAZ also exhibits different creep and creep rupture properties. As

compared with the parent metal, the coarse grain HAZ (see Fig. 2.1) generally has a smaller creep strain-rate and higher creep rupture strength and better ductility. The welding process also affects the creep crack growth-rate at high temperature, when it can be very fast in brittle regions, as may be the case in the weld metal, whereas it may be relatively slow in parent metal, where ductility is retained.

Any failure analysis on the creep of weldments must take these special features, described in this section, into account where necessary and only an examination of actual failures can determine their importance.

2.2.3. Weldment Performance and the Failure Mechanisms

Service experience suggests that whilst the majority of high energy components operating in electricity-generating plants exhibit satisfactory performance, problems have been identified with the presence of weldments (Price and Williams [1982]). For the piping systems of these plants low alloy steels are frequently used. These steels are selected since they offer the necessary creep strength at optimal cost. A number of different alloys have been developed based on chromium/molybdenum steels, however, much existing high energy piping in the UK is fabricated from 1/2Cr1/2Mo1/4V steel. This alloy derives its excellent creep strength from a dispersion of vanadium carbide precipitates. Experience shows that although satisfactory operation can normally be achieved in the component parent metal, long-term failures have been documented in weldment heat affected zones (HAZ) (Toft and Yeldman [1972]). These failures are associated with either a region of high strength microstructure with low ductility, i.e.

reheat cracking, or low strength microstructure with high ductility, i.e. the so called Type IV cracking.

Recent evidence suggests that a broad range of steels are susceptible to long term cracking where relatively low ductility failures occur within the HAZ. Damage of this type has been reported in 1/2Cr1/2Mo1/4V (Gooch and Kimmins [1987]), 1Cr1/2Mo (Wu et al [1992]) and many others. The fact that similar damage has been observed in different steels used in various plants world-wide has resulted in this cracking being given an international designation of Type IV (Schuller et al [1974]). The form of damage developed in Type IV cracking is illustrated by consideration of a 1/4Cr1/2Mo component which operated for approximately 88,000 hours at normally 538° C and 44.6 MPa (Westwood et al [1990]). In this situation a major macroscopic defect developed at the edge of the HAZ adjacent to the base material. Detailed examination revealed that extensive grain boundary damage was associated with the main defect.

The performance of a welded structure is highly affected by the circumstances described in Section 2.2.2. Unexpectedly, failures do not always occur at the location where the weakest material is, as a result of the redistribution of stresses and strains according to the strength of the weldment (Price and Williams [1982]). The creep rupture or failure primarily depends on the strength and ductility of various material zones and the interaction effects between them.

All the creep failures of weldments are associated with the formation of cracks which are related to poor welding practices, inadequate post weld heat treatment, PWHT,

and material compositions as well as creep damage accumulated in service. The cracking that has been experienced in welded components has been classified (Schuller et al [1974]), as shown in Fig. 2.2. This classification relates only to the location and orientation of cracking in a weldment and not necessarily to the cracking mechanism involved.

In Fig. 2.2, Type I cracking represents the failure mode of a homogeneous component. Transverse weld material cracking, i.e. Type II cracking, is similar, being due to an interaction of residual welding stresses with low ductility regions in the weld metal. It is primarily a consequence of inadequate PWHT, and the time for microcracks to occur is usually 25,000 to 40,000 hours. The mechanism can be thought of as an early stage cavity nucleation which is followed by link up and macroscopic cracking over an extended period, under the pressure and residual stresses in service.

Circumferential heat affected zone cracking, i.e. Type III cracking, is mainly due to the interaction of welding residual stresses with the brittle, coarse grained bainite in the ferritic HAZ. It can be detected after PWHT and at an early stage in service life.

Type IV cracking occurs as a result of the interaction of system stresses, predominantly axial or bending, with the soft overtempered region near the HAZ in ferritic alloys. The circumferential cracking in the HAZ immediately adjacent to the parent material can be observed after service times of about 50,000 to 80,000 hours. The mechanism of failure is again creep cavitation, leading to macroscopic growth and failure.

The Type IV cracking in CrMoV weldments forms in the low temperature part of the HAZ, i.e. intercritical/tempered regions where the properties are reduced below those of the parent and high temperature HAZ. This position, where the damage and cracks form, is weaker in creep strength and probably has a higher local ductility, although the full properties have not been unambiguously defined, particularly the ductility. Thus in very general terms, this form of cracking will occur in the low temperature regions of the HAZ where creep properties are lower than those for the adjacent parent and high temperature HAZ regions.

2.2.4 Study of Creep of Welded Structures

From the above description it is clear that many problems exist when a welded component operates in the creep condition. This has made the problem of creep of weldments a field of interest for many researchers. Extensive research work has been carried out on the subjects of weldment creep involving the welding technology, simulation of the weldment performance, assessment of the remaining life and the design methods of weldments. A large number of papers have been published on these subjects, for example, welding processes and residual stress (Masubuchi [1981]), post weld heat treatments (Prager and Leyda [1988]), stress distributions (Parker [1988]), metallurgical studies (Senior [1990]), crack initiation and growth (Dole [1991]), weldment assessment strategy (Coleman and Miller [1994]), weldment strength and design (Corum [1990] and Samuelson et al [1992]), and creep continuum damage analysis (Hall and Hayhurst [1991]).

The finite element method is a useful tool for the purpose of modelling the creep performance of weldments. Walters and Cockcroft [1972] were possibly the first to use the finite element method in analysing the creep of weldments; weldments were considered as a combination of only two materials. Coleman et al [1985] incorporated a three-material model and used a parametric approach to cover a wide range of weld/parent metal creep properties. The published FE analyses also cover the creep behaviour of cross-weld test specimens (Storesund et al [1992]), which is one of the main topics of the present thesis and will be discussed in detail later.

Another aspect of the study of creep in welds is the experimental creep testing. In theory, it seems to be possible to predict component life analytically, using stress analysis together with material data and an appropriate damage model. In practice, limitation of numerical analysis in the creep range and current uncertainties in multi-axial material data, preclude rigorous assessments for all but the simplest situations. For this reason, laboratory creep testing of welded components is often desirable. However, full scale components tests are very costly, and in most cases, uniaxial cross-weld testing is adopted as an alternative, using specimens cut from the welded structure (e.g. Chilton et al [1984]). In some cases, thermally simulated materials/specimens can be used (Cane [1981]).

2.3 CREEP ANALYSIS OF CROSS-WELD SPECIMENS

2.3.1 Introduction

Methods for assessing the creep performance of welded joints have been studied by many researchers. The techniques have ranged from an examination of simple uniaxial creep rupture data on all weld metal or all parent material to cross-weld specimens containing a complete section of the weldment, in addition to modelling welded tube tests.

The most common way to determine creep data from weldments is uniaxial cross-weld testing of weld metal, parent metal and cross-weld test specimens from the weldment. Creep curves, creep rupture data and the failure position can be obtained from cross-weld specimen testing.

A uniaxially loaded cross-weld specimen may have a complex tri-axial stress state due to the differences of material properties of the various constituents of the weldment. Although some analytical work has been carried out based on simple models (e.g. Williams [1982-1] and Nicol [1985]), there is still a lack of detailed understanding of the creep behaviour of the cross-weld specimens, and hence it is difficult to apply the results to practical situations. To evaluate the stress/strain distribution in cross-weld specimens, the finite element method is an effective tool. Strictly speaking, the cross-weld specimen cannot be considered as an axisymmetric structure when weld angles are present. However, both numerical and analytical analyses (Storesund et al [1992]) have indicated that the influence of the weld angle is not significant on the stress state

and the total strain of the specimen. Hence, in many cases it is appropriate to model the specimen using a two-dimensional axisymmetric analysis.

In order to interpret the data obtained from uniaxial cross-weld specimens for a practical welded structure, geometrical effects of cross-weld specimens have been considered (Storesund and Tu [1995]). Also, the problem of the stress singularity which may exist at the free surface of the specimen due to the material dissimilarity needs to be understood since the existence of such a singularity point may affect the integral strength of the specimen.

Creep testing of cross-weld specimens has been widely used. The data obtained can be used to assess the detrimental effects of welds on the life of elevated temperature components, such as those used in power plants. Interpretation of the test results still remains a difficult task since there may be interactions effect among the different parts of the weldment.

In this section, the above aspects of the creep analysis of the cross-weld specimens will be briefly reviewed.

2.3.2 Analytical Work

Very few publications have been found on the theoretical study of cross-weld creep test specimens. Williams [1982-1] developed a simplified approach to examine the creep behaviour of a two-material axisymmetric specimen with a soft weld, using the

limit load reference stress method. Later, a special theoretical investigation which used a refined plate theory, i.e. Cosserat plate theory (Green et al [1968]), was used to obtain the strains accumulating in steady-state creep for butt-welded joints (Nicol [1985]). The weldments were modelled by a semi-infinite plate of thickness h. The cross-section of the plate was subjected, at infinity, to a constant tensile force, see Fig. 2.3. Appropriate constitutive equations were developed for the plate theory which correspond to standard uniaxial and three-dimensional equations. In particular, Norton's Law, $\dot{\varepsilon}^c = A\sigma^n$, was adopted. Three assumptions were made for the simplification of the problem:

i) the model is a plane strain problem;

ii) no bending on the centre surface of the plate occurs with time t; and

iii) the stress index, n, was taken to be the same for all zones.

The work on this theoretical method was initially carried out by Nicol [1985], who studied the plane strain creep problem for a thin plate with parent material and weld material only (see Fig. 2.3(a)). The creep strain rates were obtained for different creep strength ratios of the two materials, the stress indices and the size of weld zone. Hawks [1989] and Craine and Hawks [1993] developed the model by firstly including the narrow type IV region and HAZ (see Fig. 2.3(b)) and secondly investigating how the relative sizes of all the regions influenced the strain rates. Newman [1993] and Craine and Newman [1991][1992][1996] further developed the method by incorporating a simple version of the Kachanov-Rabotnov damage equation (Rabotnov [1969]) into the model to study the rupture time and the position of rupture for the plate with a butt weld or a V-shaped weld under tensile loading (see Fig. 2.3(c)).

The results of this theoretical approach reveal that in a weldment the interaction effects are extremely important, i.e. the strain rate at a position in a region not only depends on the properties of the region but can be significantly affected by those of the other regions.

2.3.3 Experimental Investigations and Finite Element Analyses

Creep testing of cross-weld specimens are used to obtain data which can be used to assess the detrimental effects of welds on the life of elevated temperature components. Experimental work has been conducted by some researchers, involving such aspects as the failure mechanisms (e.g. Ivarsson and Sandstrom [1980]), deformation and strain localisation (e.g. Parker and Straford [1995]) and the effects of geometry of the cross-weld specimens (e.g. Henry and Eills [1990] and Storesund et al [1995]). Uniaxial round bar specimens have been popularly adopted. Other shape specimens, such as rectangular or square cross-section specimens and plate specimens have also been used (e.g. Muramatsu et al [1992] and Endo and Sakon [1980]). In many cases, these laboratory tests can provide reasonable evaluations of fracture behaviour, i.e. the damage developed is considered representative of that obtained in service. In a recent work by Parker et al [1995], the fracture process in typical ex-service 2-1/4Cr1Mo-1/2Cr1/2Mo1/4V weldment was investigated. The specimens were examined both macroscopically and microscopically after failure. Their results have shown that the deformation was concentrated in the fine grained intercritical region of the HAZ of the weldments.

The finite element method has often been used to model creep tests and to study the detailed stress and strain distributions in cross-weld specimens The weldment can usually be assumed to consist of three constituents, i.e. parent metal, HAZ and weld metal. In some cases, the HAZ was divided into two zones, namely, a coarse grain zone and a fine grain zone (e.g. Roode et al [1980] and Storesund et al [1992]), or more zones (Kussmaul et al [1993]). The material properties and dimensions of metallurgical zones of cross-weld specimens must be carefully determined for the FE analysis in order to obtain the most reliable results. Details of the finite element analysis work can be found in some relevant publications.

2.3.4 Effect of Specimen Geometry

One of the most important problems associated with the creep testing of cross-weld specimens is the fact that the results obtained with specimens cut from welded components do not necessarily describe the actual behaviour of the structure. For specimens consisting of a nominally homogeneous material with no anisotropy, the test results will be affected by the following factors: the gauge length, the cross-sectional area of the specimen and the shape of grips. However, in an inhomogeneous specimen, such as a cross-weld specimen, there is also the effect of restraint at the inhomogeneous interfaces.

The geometrical effects of cross-weld specimens have been studied (Storetund and Tu [1995]), but very few publications which are closely related to this subject can be

found. Williams [1982-1] generated a simple analytical model of an axisymmetric tensile specimen consisting of parent and weld metals only, where the weld material was weaker than the parent metal. The model was based on the limit load approach to define a reference stress which could be used in the creep regime. The effect of weld width to specimen diameter ratio on the stress rupture behaviour of cross-weld specimens was examined. In later analytical work on cross-weld plate models by Nicol [1985], Hawks [1989], Newman [1993] and Craine and Newman [1996], the effect of various material zone lengths has been used to determine the interaction behaviour of strain accumulation and rupture of the specimens. However, a full understanding of the influence of the dimensions of a cross-weld specimen cannot be obtained from the results of simple analytical models.

Experimental work and finite element investigation of the geometrical effects of cross-weld specimens have been performed by a number of researchers (see, for example, Muramatsu et al [1992]). Horton and Lai [1980] used cross-weld specimens cut from Type 316 weld metal butt-welded plate to perform uniaxial rupture testing. The specimens were of 5 mm and 12 mm diameter round bars, cut transversely and longitudinally and tested at 625° C and an initial stress of 186.2 MPa. The results were found to be extensively scattered for all 5 mm diameter specimen tests, and no significant improvement or difference was observed from the results of thicker specimens. However, other experimental results clearly indicated that life increased with increasing diameter. Ellis and Brosche [1993] performed rupture tests of cross-weld specimens of conventional size (6.4 mm gauge diameter) and large rectangular bars (50.8 mm × 25.4 mm). The results show that the large specimen creep-rupture

time was approximately 2.5 times greater than that for the conventional size of rupture specimens. This is probably due in part to an oxidation effect previously observed in small specimens caused by the smaller section thickness and testing in air.

Computational investigations using the finite element method to study the geometrical effects can also be found in several publications (e.g. Storesund and Tu [1992]). Kussmaul et al [1993] conducted FE calculations taking into account the creep properties of parent, weld and HAZ (being divided into three sub-zones) materials with the intention of explaining the different rupture times of small and large scale specimens exhibited in their experimental work for a dissimilar weldment of 12%Cr/1%CrMoV. They used axisymmetric models for the small scale round bar specimens and plane strain and plane stress flat specimens. The results show that for the same test duration, the maximum values of axial and equivalent stresses are higher in the small scale specimens than those in the large scale ones. The reason for this is a slower stress and strain redistribution in the large scale specimens due to higher constraint, which finally leads to their longer rupture times.

Muramatsu et al [1992] used three-dimensional FE meshes to study the size and shape effects of welded joint specimens, in order to clarify whether specimens cut from welded joints can produce the creep behaviour of actual components. The effect of grip shape and gauge length were considered and the relationships between cross-sectional areas and strains in different sectional specimens were investigated. They concluded that considerably different creep strain behaviour can be obtained due to different shape of grip, shape and size of the cross-section and position of the weld

metal within the specimen, even if the same nominal stress is applied. They also mentioned that in some cases, even the use of a very large specimen is not sufficient to reproduce the creep behaviour of actual components, although the size influence on the creep life was not covered.

In a later publication, Storesund and Tu [1995] used axisymmetric methods to study the influence of the diameter of the specimen and fraction of each constituent (coarse grain HAZ, fine grain HAZ and weld metal). The creep properties were evaluated for the different zones of the specimen, to simulate a 1Cr1/2Mo weldment. They found that there is a significant life enhancement with increasing diameter and that for some weldments the cross-weld specimen of a large diameter may have a creep strength comparable with that of a pure parent metal or weld metal specimen. They also indicated that the location of the maximum stress enhancement in the specimen can be altered when the diameter is changed. Changing the HAZ width also influences the creep life of the specimen, whereas the change of weld width in a practical range does not show such an influence.

2.3.5 Interfacial Stress Singularities

For a structure or component consisting of more than one material it has been widely accepted that at the corners, between bonded-edge (interface) and free-edge, a stress singularity region exists. The singularity behaviour usually depends on the material properties, the geometry and the boundary conditions of the structure for a specified type of applied load (mechanical or thermal).

The singularity problem of a two-material structure sustaining elastic or elastic-plastic deformation has been studied using analytical methods (e.g. Rudge [1993]). Generally, the theoretical study assumes that a power law for the stress singular field can be applied, i.e.

$$\sigma_{ij} \propto r^N \quad (N < 0) \tag{2.1}$$

where σ_{ij} are the stress components and r is the distance from the singular point. The singularity behaviour of two-edge bonded elastic wedges of different material and different wedge angle has been extensively studied by Bogy [1971], who showed that different types of solution are possible for stress and displacement at the intersection between the free edge and the bonded edge of the two materials. Lan and Delale [1988] studied the plastic stress variation in a two material plane strain model for different material ratios and angular positions. They indicated that their solution would be applicable to the corresponding power-law creep situation if displacements and strains were interpreted as their time rates instead. However, the range of properties for which power-law solutions are available is limited and these solutions are strictly applicable to plane strain situations only.

There have been no published reports so far which provide either theoretical or numerical analysis of the singularity problem in multi-material creep structures. The stress singularity feature in a cross-weld specimen needs to be studied in order to determine whether it significantly influences the behaviour of a weld. For this purpose, a parametric study of the stress singularity behaviour of a two-material, axisymmetric

creep test specimen has been conducted, the results of which will be described in Chapter III.

The existence of a stress singularity in a welded structure has been described by Ryder [1990]. The singularity is dependent on the difference in material properties and the angle made by the weld interface with the free surface. One of the reasons which demonstrates the existence of the singularity is that when an inelastic finite element analysis is performed, extremely high local stress/strain concentration will usually be predicted even in a joint which is known to have lasted in service for over 30 years.

2.4 IMPRESSION CREEP TECHNIQUE

2.4.1 Introduction

Impression creep testing (e.g. Chu and Li [1977]) is the name given to the technique in which a flat-ended indenter is placed on the flat surface of a material, at elevated temperature, and is subjected to a steady load, as illustrated in Fig. 2.4. Initial deflection takes place when the load is first applied, which may be elastic or elastic-plastic, followed by time-dependent creep deformation. The displacement vs time record from such a test is related to the creep properties of a relatively small volume of material in the immediate vicinity of the indenter. The creep test, if performed to obtain the material creep properties, usually requires the deformation (indenter depth)

obtained to be very small, so that after the test, only a shallow impression on the test material surface is left; hence the name "impression creep".

Since conventional creep testing requires many specimens to establish stress and temperature effects, the hot indentation hardness test is sometimes used as a substitute. Various ways have been proposed to relate the creep rate to the time-dependent hardness, but none seemed to work well until flat end indenters were adopted. The reason is simple: when the hardness decreases with time, the stress also decreases, and no steady-state can be achieved (Chu and Li [1977]). There were early attempts to make indentations using flat-ended indenters but these attempts were limited to hardness testing only. The impression creep technique was first used by Chu and Li [1977] and was proposed as an alternative method for obtaining creep properties, instead of the conventional method. Previous work by Li and others [1977-1980] noted that:

(i) Impression depth versus time curves are similar to those of conventional, uniaxial creep tests, having primary and secondary regions. However, tertiary creep is not exhibited by impression creep test data.

(ii) The steady-state indentation rate has the same stress and temperature dependence as conventional, uniaxial creep data, with the same "stress exponent".

(iii) The steady-state indentation rate of the punch, at the same stress level, is proportional to the diameter of the indenter.

Most authors (e.g. Chu et al [1977], Gibbs [1983] and Yu et al [1985]) have effectively used a trial-and-error approach to correlate the impression creep data with conventional uniaxial creep data. This requires conversion factors to be obtained which relate the average indenter pressure, p, to the equivalent uniaxial stress level, σ, and the steady-state impression depth rates, $\dot{\Delta}^c_{ss}$, to the equivalent uniaxial steady-state strain rates, $\dot{\varepsilon}^c_{ss}$, i.e.,

$$\sigma = \eta \times p \tag{2.2}$$

and

$$\dot{\varepsilon}^c_{ss} = \dot{\Delta}^c_{ss} / \beta d \tag{2.3}$$

where β and η are experimentally determined constants and d is the indenter diameter. Table 2.1 summarises the values of β and η obtained by several researchers, from which it can be seen that there is a general agreement that β and η values of about 1.0 and 0.3, respectively, are applicable to most of the materials tested. Gibbs [1985] states that β and η are geometric correction factors, whereas other researchers (Yu et al [1986] and Tasnadi et al [1988]) describe them as material constants.

Based on the above work, Hyde et al [1993] developed a mechanics-based approach using the finite element method to clarify the nature of η and β factors in Equs. (2.2) and (2.3); the values of η and β of 0.296 and 0.755, respectively, were obtained from a two-dimensional, single material, axisymmetric model. For the purpose of studying the creep properties in welds, in this work, a new impression creep testing technique, using rectangular indenters and two-dimensional plane strain models, was developed and

used to investigate the multi-material indentation behaviour and the size effect of the specimens.

Table 2.1 Summary of η and β factors obtained from experimental tests

Reference	Material	Test temp. (° C)	Stress exponent n	η	β
Chu & Li 1977	Succinonitrite (single crystal)	37	4	0.303	1.0
Chu & Li 1979	βTin (single crystal)	60-203	4-5	0.256-0.357	1.0
Yu & Li 1977	LiF (single crystal)	----	----	0.1493	2.6
Gibbs 1983	Al 99.999%	300-400	6.1	0.415-0.416	1.0
Yu et al * 1985	1018 steel	----	----	0.345	0.67
	Al	----	----	0.287	1.0
	Cu	----	----	0.347	1.0
	Ni	----	----	0.345	0.625
Tasnadi et al *1988	Al 90.74% alloy	----	----	0.303-0.333	1.0

* The results are based on elastic-plastic tests, not creep tests.

2.4.2 The Reference Stress Method

On first loading of a component at elevated temperature, an initial deformation at a point of interest, Δ_i, is produced; Δ_i may be a strain, displacement or rotation. This deformation will depend on the component dimensions and the initial multi-axial stress-strain (elastic or elastic-plastic) behaviour of the material. At elevated temperature, if the load is held constant, the material will creep, stress redistribution will occur and further creep deformation will take place. For materials obeying a Norton (power law) creep constitutive equation,

$$\dot{\varepsilon}^c = B\sigma^n \tag{2.4}$$

the stress distribution will approach a steady state and the displacement rate will approach a steady-state value, $\dot{\Delta}_{ss}$. Therefore, the total deflection, Δ, at time t is given by:

$$\Delta = \Delta_i + \dot{\Delta}_{ss} t + \Delta_r \tag{2.5}$$

where Δ_i is the initial (elastic + plastic) component of a deformation and Δ_r is the component of deformation associated with stress redistribution, which is usually small compared with initial and steady-state creep deformations (Penny and Marriott [1971]) (see Fig. 2.5).

For some components, it is possible to obtain analytical expressions for $\dot{\Delta}_{ss}$ (e.g. Anderson et al [1963] and Johnsson [1973]). These show that the general form of the solution is:

$$\dot{\Delta}_{ss} = f_1(n)\, f_2(\text{dimension})\, B\sigma_{nom}^{\ n} \tag{2.6}$$

where f_1 (n) is a function of the stress index, n, of Equ. (2.4), f_2 (dimensions) is a function of the component dimensions and σ_{nom} is a conveniently determined nominal stress for the component and loading.

By introducing an appropriate scaling factor, α, for the nominal stress, Equ. (2.6) can be rewritten as:

$$\dot{\Delta}_{ss} = \frac{f_1(n)}{\alpha^n} f_2(\text{dimension})\, B(\alpha\sigma_{nom})^n \tag{2.7}$$

Choosing α (= α_R) so that $f_1(n)/(\alpha_R)^n$ is independent (or approximately independent) of n, then Equ. (2.7) can be further simplified, i.e.

$$\dot{\Delta}_{ss} \approx D\dot{\varepsilon}^c(\sigma_R) \qquad (2.8)$$

where D is the so-called reference multiplier [D = $(f_1(n)/(\alpha_R)^n)f_2$ (dimensions)] and $\dot{\varepsilon}_c$ (α_R) is the creep strain rate obtained from a uniaxial creep test at the so-called reference stress, σ_R (= $\alpha_R\sigma_{nom}$).

If an analytical solution can be obtained, substituting two values of n in the expression $f_1(n)/\alpha^n$ and equating the two resulting expressions allow the value of α_R to be determined. Hence, σ_R (= $\alpha_R\sigma_{nom}$) and D can be obtained. This approach was proposed by MacKenzie [1968]. However, analytical solutions only exist for a small number of relatively simple components and loading. Therefore, computational methods (Sim [1970][1971] and Sim and Penny [1971]) and approximate methods based on limit load solutions (Penny and Marriott [1971] and Sim [1968]) have been devised.

If computed (e.g. finite element) solutions to a creep problem are obtained using several n values, but keeping all other material properties, loading and component dimensions the same, then σ_R can be obtained (Sim [1970][1971] and Sim and Penny [1971]). This is done by taking several values of α, normalising the steady-state value of displacement rate, $\dot{\Delta}_{ss}$, with respect to $B(\alpha\sigma_{nom})^n$ and hence finding the value of α which renders $[\dot{\Delta}_{ss} / (B(\alpha\sigma_{nom})^n)]$ independent of n. This process is most easily visualised by plotting log $[\dot{\Delta}_{ss} / (B(\alpha\sigma_{nom})^n)]$ for various values of α against n, as

illustrated in Fig. 2.6. It can be seen that the straight lines produced, using all of the α values, have the same intercept on the log $[\dot{\Delta}_{ss} / (B(\alpha\sigma_{nom})^n)]$ axis. This intercept is equal to the logarithm of the reference multiplier, D.

Using the similarity between elastic and elastic-perfectly-plastic stress distributions with creep solutions having n = 1 and n = ∞, Sim [1968] was able to devise an approximate method for determining reference stresses based on elastic and limit load solutions. Sim [1968] showed that:

$$\sigma_R \approx \frac{P}{P_L}\sigma_Y \qquad (2.9)$$

and

$$D \approx \frac{\Delta_i^{el}}{(\sigma_R / E)} \qquad (2.10)$$

where P_L is the limit load for a component with a yield stress, σ_Y, and Δ_i^{el} is the initial (elastic) deflection for the same component with a Young's modulus, E (a Poisson's ratio, ν, of 0.5 should also be used to maintain similarity with the multi-axial creep constitutive equations).

The reference stress method has been successfully used in the analysis and design of components operating in the creep range (e.g. Goodall [1990] and Boyle [1983]). However, until now the method has only been applied to components or structures made of a single material, and the physical basis of the method for such cases is well understood. Although a clear physical basis for applying the reference stress method to two or more material components has not been established, results obtained by

Hyde et al [1996] show that the technique can be used to obtain reasonably good predictions for two-material components.

2.4.3 Impression Creep Testing of Welds

Impression creep tests have been performed by a number of researchers. Most publications state that impression creep testing is a new method for obtaining creep properties, which has advantages over conventional methods. However, only a few of the researchers noted that the impression creep testing technique could be of practical value in obtaining the creep properties in the various regions (parent material, HAZ and weld metal) of a weldment (Gibbs [1983], Gibbs et al [1985, 1990] and Lisin et al [1989]). Gibbs [1983] and Gibbs et al [1985] studied the relative creep properties within a welded joint and found that the technique is very useful in evaluating the position dependence of the creep properties. For the particular weld investigated by Gibbs, he showed that the minimum creep resistance occurs in the HAZ near the fusion line.

Detailed review of the impression creep testing can be found in some relevant publications (for example, Yehia [1994]).

2.5 CREEP CONTINUUM DAMAGE STUDY OF WELDMEMTS

2.5.1 Introduction

Structural components operating at high temperature often suffer from creep damage, which results from metallurgical inhomogeniety or the nucleation and coalescence of micro-cavities. Creep deformation and/or creep rupture is often the main cause of failure of these components. To assess the safe lifetime of such components, it is important to accurately predict the extent of creep damage and creep rupture life.

Over recent years, significant progress has been made in the development of design procedures in the creep ranges (see, for example, Penny and Marriott [1971], Kraus [1980] and Hayhurst et al [1975, 1984]). Much of the research work has been directed towards the determination of the life of components, under given loading conditions, at elevated temperature.

Creep damage localisation in weldments has been observed in both engineering practice and laboratory simulation. Experience shows that many component failures arise as the result of localised damage in welds. On this basis, an understanding of creep continuum damage, or creep failure behaviour, may provide guidance for the design of welded components in the future.

2.5.2 Damage Equations

A conventional way to describe tertiary creep is to use Kachanov's damage equation [1960]. Kachanov introduced the damage parameter, ω, the value of which is equal to

zero for no damage and unity for rupture or failure. The damage parameter was meant to represent the internal cavitation and rupture of the material. The effect of the damage parameter, ω, on stress is to magnify it by a factor of $1/(1 - \omega)$ due to a loss in load bearing cross-section. Thus, the modified uniaxial stress-strain equation becomes:

$$\dot{\varepsilon}^c = A\left(\frac{\sigma}{1-\omega}\right)^n t^m \tag{2.11}$$

where the rate of damage increase, $\dot{\omega}$, is

$$\dot{\omega} = B\frac{\sigma^\chi}{(1-\omega)^\phi} t^m \tag{2.12}$$

where B, χ and ϕ are material constants, which can be determined from experimental creep rupture data. A multi-axial creep equation can be written in terms of the von-Mises equivalent stress, σ_{eq}, and the deviatoric stress, S_{ij}, as follows (Kraus [1980]):

$$\dot{\varepsilon}_{ij}^c = \frac{3}{2}A\left[\frac{\sigma_{eq}}{1-\omega}\right]^{n-1}\frac{S_{ij}}{1-\omega} t^m \tag{2.13}$$

where the rate of change of damage parameter, $\dot{\omega}$, can be expressed in terms of a "rupture stress", σ_r, i.e.:

$$\dot{\omega} = B\frac{\sigma_r^\chi}{(1-\omega)^\phi} t^m \tag{2.14}$$

The rupture stress, σ_r, is often assumed to be a function of the maximum principal stress, $\hat{\sigma}$, and the equivalent stress, σ_{eq}, as follows:

$$\sigma_r = \alpha\hat{\sigma} + (1-\alpha)\sigma_{eq} \tag{2.15}$$

where α is a multi-axial rupture parameter ($0 \le \alpha \le 1$), which can be determined by bi-axial material testing (Hayhurst [1972]).

2.5.3 Damage Analysis of Weldments

Although some analytical work (for example Newman [1993]) has incorporated a damage parameter in the models used to represent a weldment, the first paper that presented a thorough study of the creep damage in a weldment was published by Hall and Hayhurst [1991]. In their work, the physical mechanism model of the weldment was defined and then a mathematical creep continuum damage model, suitable for FE numerical calculations, was created. Stress and strain redistributions as well as details of localised damage within the pipe weldment were obtained and the failure life of the weldment was estimated. By comparing the calculated results with the data from a full size pressure vessel weldment test, they concluded that the numerical predictions were reliable provided that the material characterisation was carried out correctly and that the constitutive equations which control the evolution of creep strain and damage could represent the dominant physical mechanisms present.

More recently, other work which involved finite element damage analysis of welds was carried out (e.g. Tu et al [1993, 1994]), for the purpose of studying the creep strength of welds. For the weldment in a 1/2Cr1/2Mo1/4V pipe which they modelled, it was found that the damage caused severe strain concentration in the weld metal (Tu et al [1994]). Although the individual weld metal exhibited higher creep strength, the damage occurred preferentially in the weld metal as a result of stress redistribution. They concluded that under normal operating conditions, the creep lifetime could be reduced by a factor of 3 due to the presence of a weld.

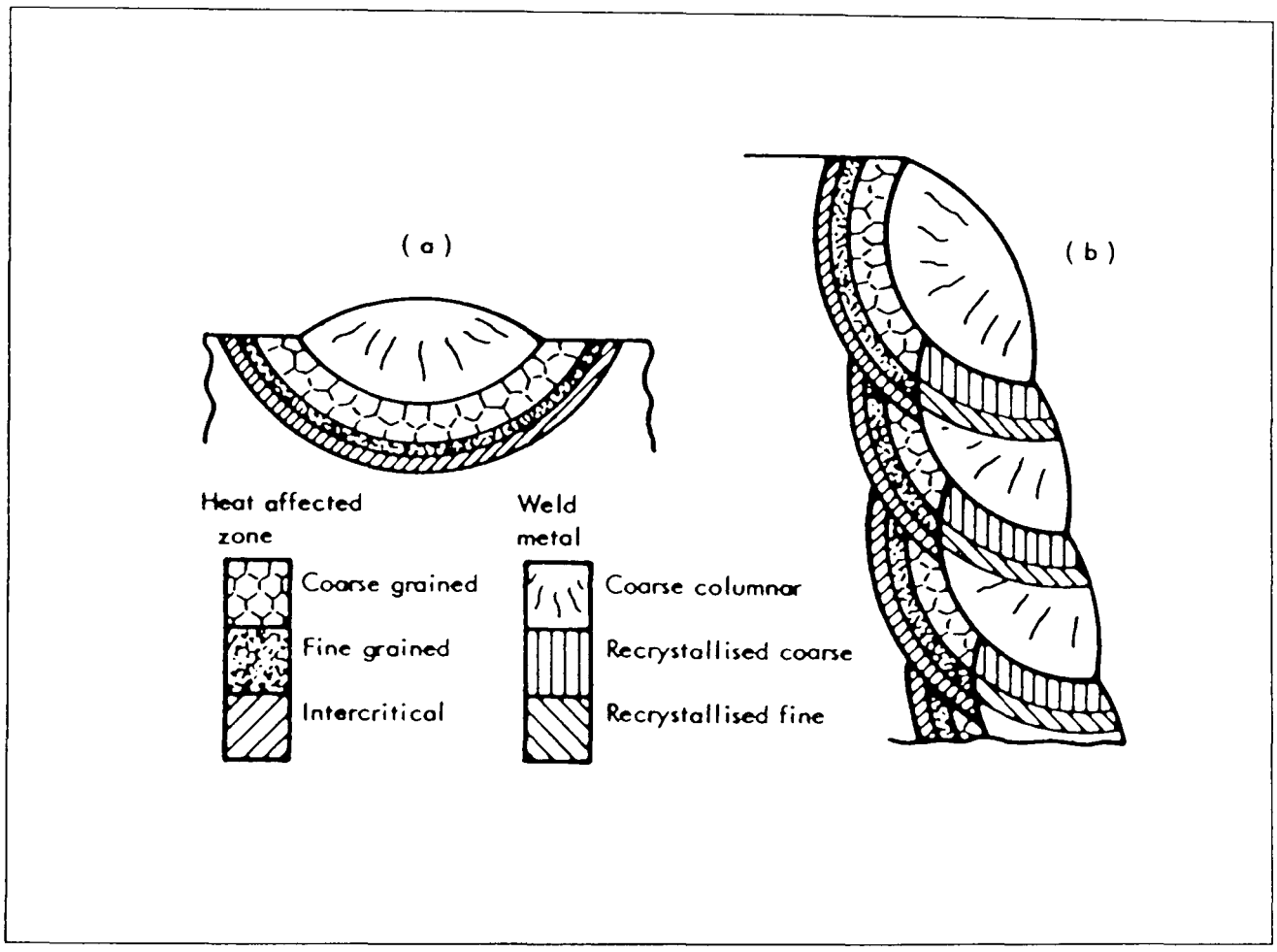

Fig. 2.1 Schematic representation of the microstructure in (a) single bead and (b) multiple bead weldments (Williams [1982-2]).

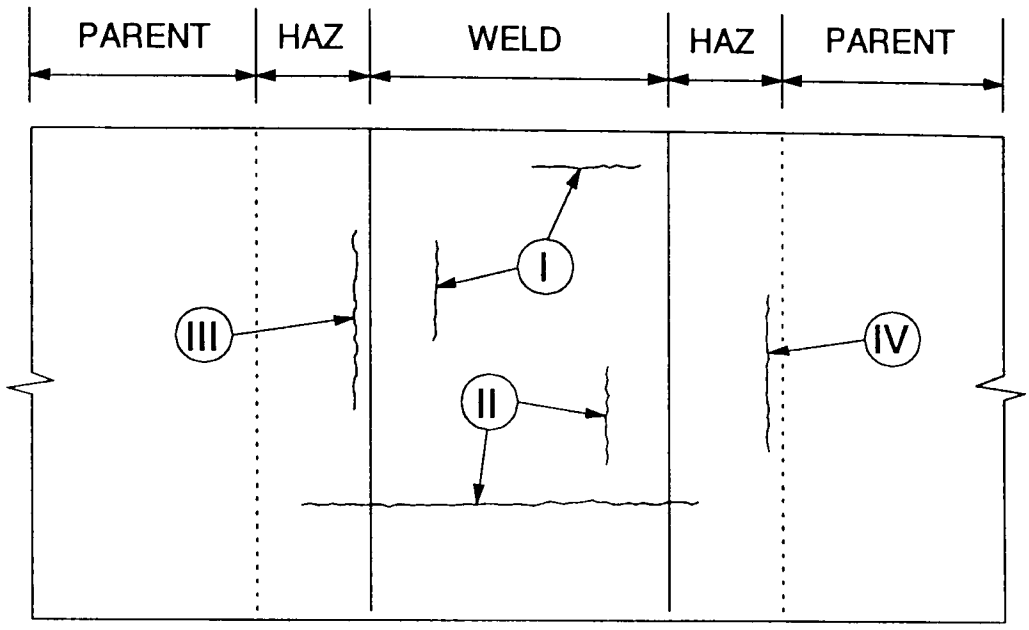

(a) plane view

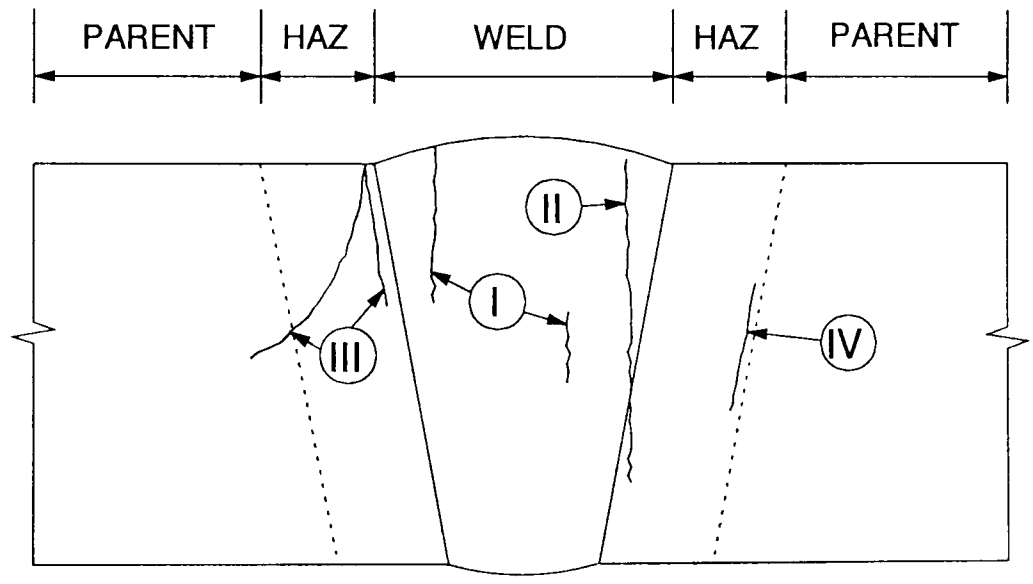

(b) cross section

Fig. 2.2 Classification of cracking in weldments (Schuller et al [1974]).

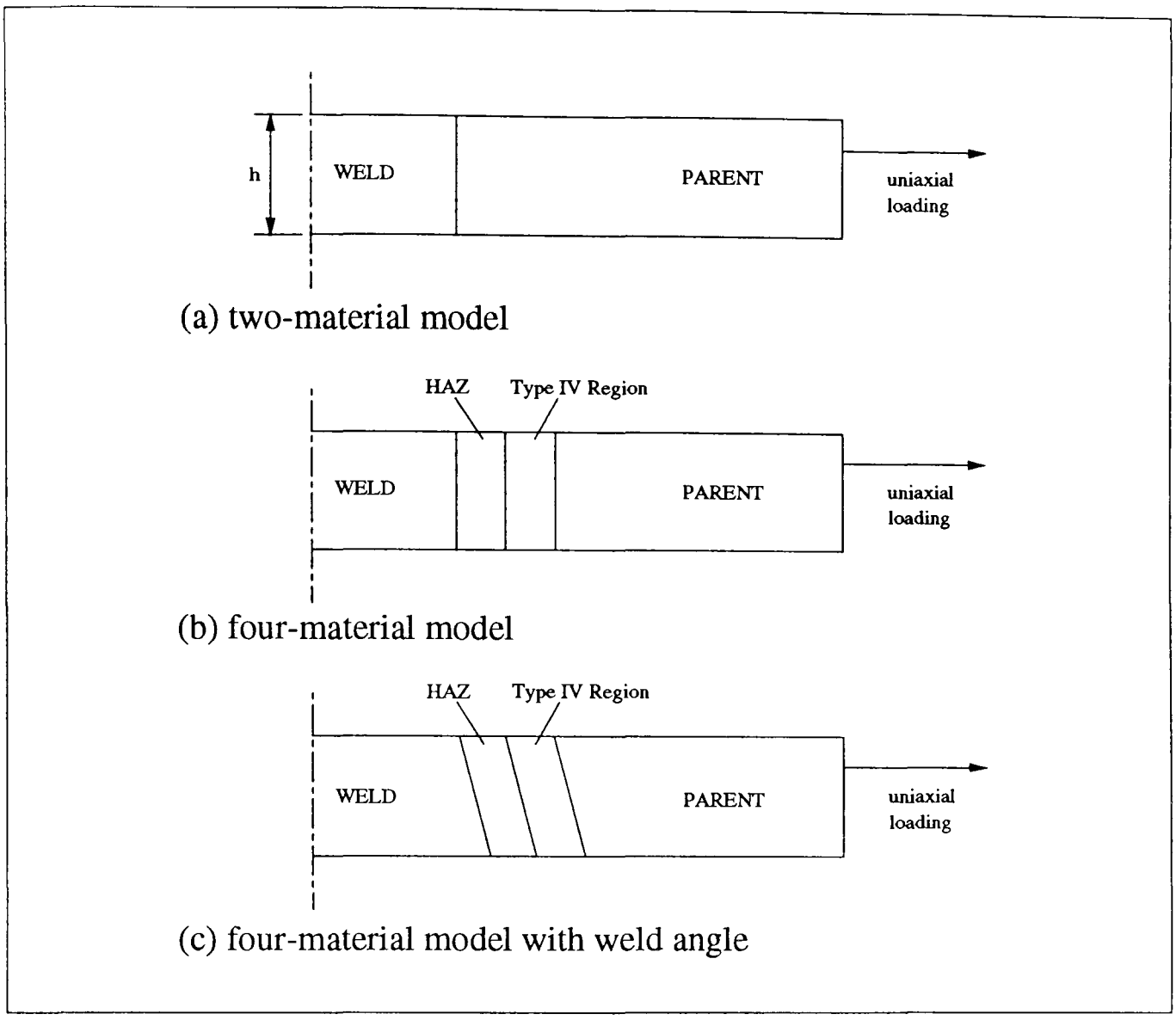

Fig. 2.3 Plane strain analytical models of cross-weld specimen.

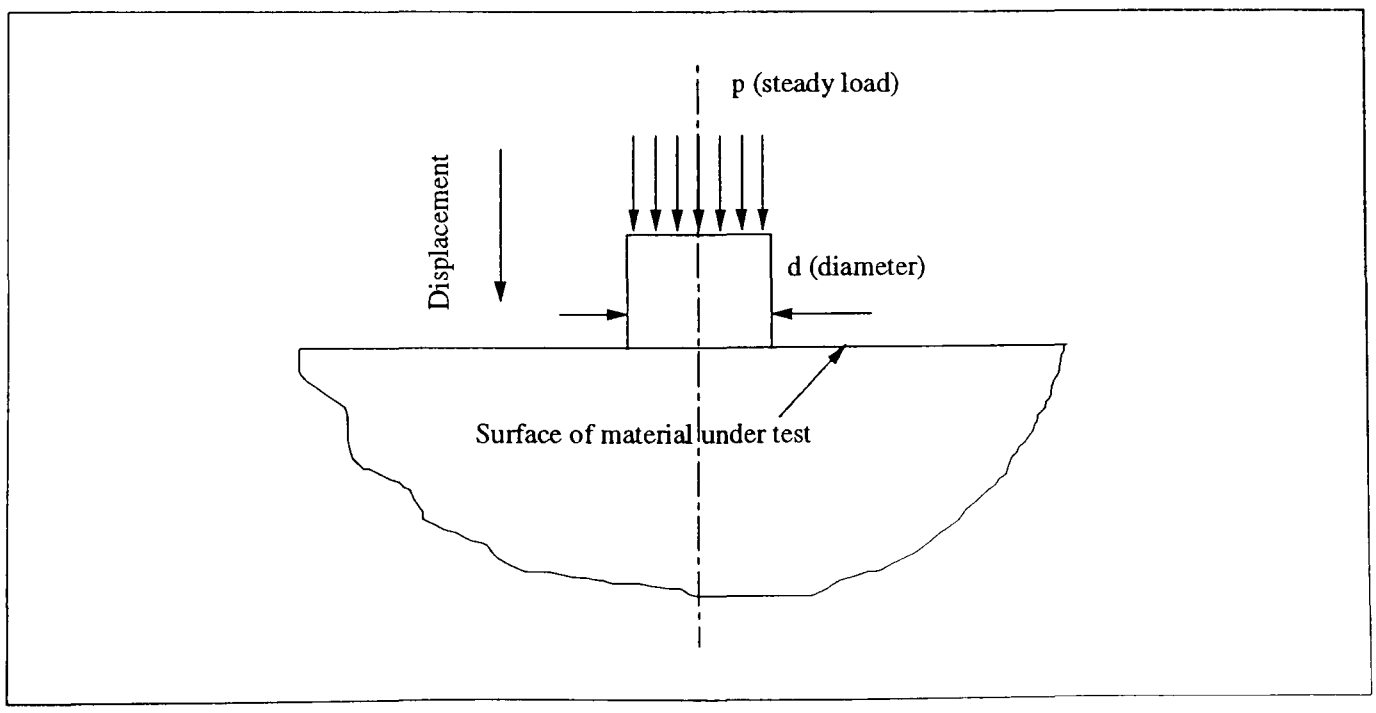

Fig. 2.4 Schematic diagram of an impression test.

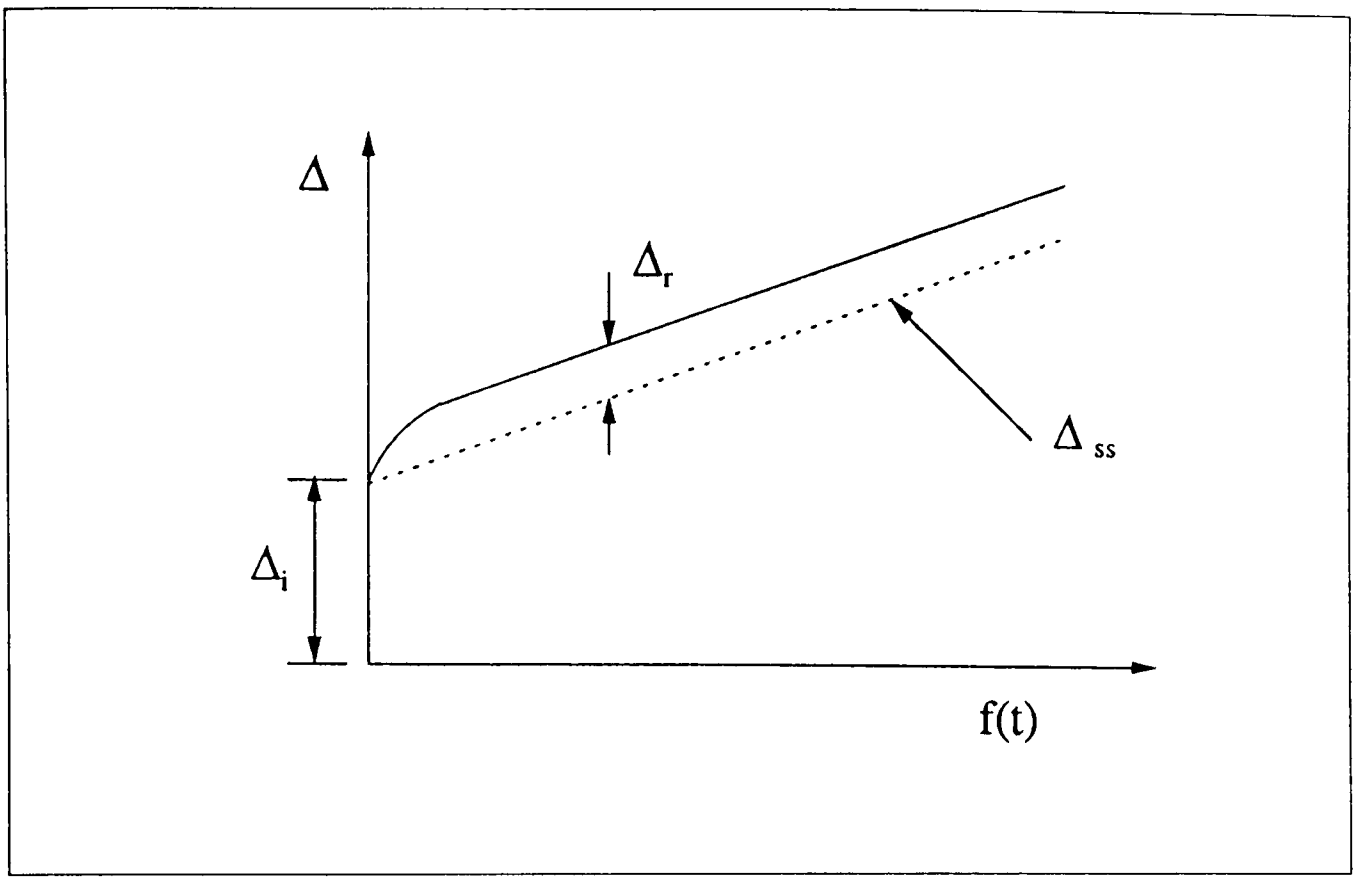

Fig. 2.5 Schematic diagram showing the contribution of deformation.

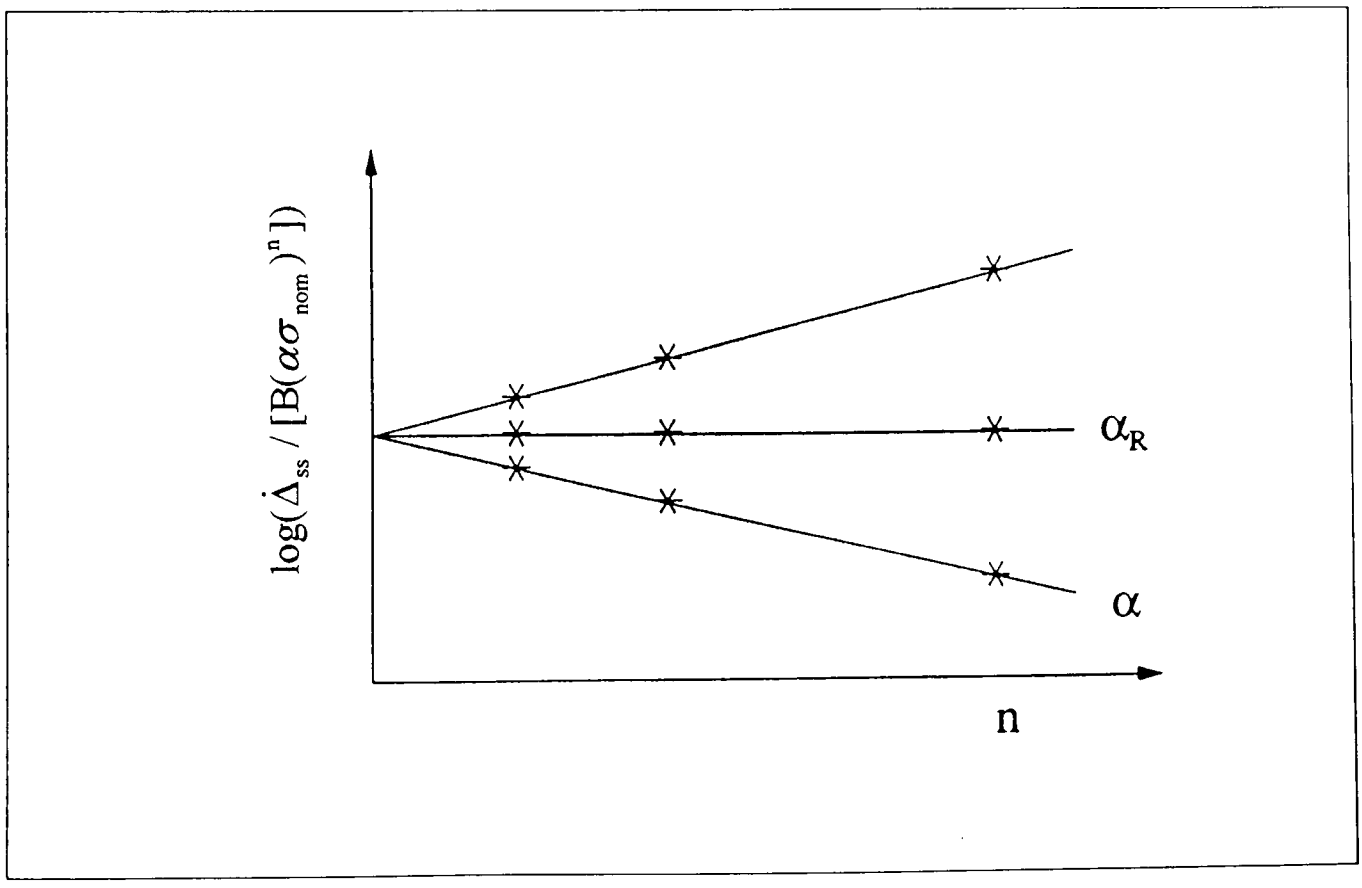

Fig. 2.6 Schematic diagram illustrating the method used to obtain reference parameters from FE-analysis.

CHAPTER III

STEADY-STATE CREEP ANALYSIS OF TWO-MATERIAL STRUCTURES AND TEST SPECIMENS

3.1 INTRODUCTION

A weld is an inhomogeneous structure. The weld metal can have different physical, mechanical and creep properties from those of the parent metal. In addition, the very act of welding changes the metallurgical properties of the metals in a heat affected zone (HAZ) around the weld.

When such an inhomogeneous structure is subjected to realistic loading at elevated temperature, the resulting deformation and cracking distribution can be very complex. Detailed theoretical analysis of welds is difficult because welded zones tend to have highly irregular shapes. However, one of the basic problems is the effect of different creep properties and the sizes of HAZ's. Although considerable work has been carried out on this subject, there is still a lack of detailed understanding of the stress and strain distributions within the welded structures under creep conditions. Therefore, it is difficult to apply the information, from the available results, to actual weld situations.

Creep testing of cross-weld specimens is frequently used to obtain data which can be used to assess the detrimental effects of welds on the life of elevated temperature components. In order to have a better understanding of the creep behaviour of cross-weld specimens, the creep stress distributions in some typical two-material structures, and idealised axisymmetric specimens, were investigated in detail using both analytical and numerical methods.

The research work to be described in this Chapter is considered in three main sections. The first one (Section 3.2) mainly deals with the general characteristics of the creep stress variations, based on the results from four typical two-material structures, using analytical solutions. Results obtained using these solutions can be used to assess the applicability of simple design rules, established for single-material structures, to two-material components and structures. Based on this analysis, some general observations on the creep stress distributions in two-material structures are made.

Section 3.3 introduces the stress distributions on the centre line of an idealised, axisymmetric, two-material, creep test specimens. Finite element creep analyses were performed using models with various geometrical and material property ratios. Using the results obtained, it has been shown that a simple interpolation technique can be used to obtain the stress/strain-rate distribution of any geometry and relative creep properties.

In Section 3.4 the more specific problem of the stress singularity behaviour at the free surface of the same idealised, two-material, axisymmetric specimen is described. Using

the finite element method, the stress singularity parameters for different geometries and creep properties and the effect of angular position were fully studied. The physical significance and the implications of the results for practical situations are discussed.

3.2 OBSERVATIONS ON THE CREEP OF ONE-MATERIAL AND TWO-MATERIAL STRUCTURES

3.2.1 Introduction

For single-material structures with simple geometric shapes and loading modes, closed form analytical solutions can be obtained for the stress distributions and deformations (e.g. Anderson et al [1963], MacKenzie [1968], Sim [1970], Johnsson [1973] and Boyle and Spence [1983]). For more complex geometries and loading situations, computational methods (e.g. the finite element method) can be used to obtain stress distributions and deformations (e.g. Sim [1970][1971] and Sim and Penny [1971]). Also, for single-material structures, simple design rules, based on the reference stress method (e.g. Anderson et al [1963] and Sim [1970]) and on the approximately linear variation of the stress at a point in a structure with 1/n, have been developed (Goodall [1990]), where n is the stress exponent in the material creep constitutive equation ($\dot{\varepsilon}^c = B\sigma^n$).

By comparison with the single-material case, relatively little information is available for predicting the behaviour of structures which consist of more than one creeping material.

An example of a situation in which more than one creeping material exists is that of a weld; the creep properties of the base, weld and heat-affected zone (HAZ) materials may all be different. Therefore the existence of the weld may significantly affect the local stress and strain distributions, increase the rate of damage accumulation and cause creep cracks to initiate and grow. Also, the simple design rules for single-material structures are not directly applicable to structures with more than one material.

The main purpose of the work introduced in this section is to present the analytical solutions for four simple two-material structures, i.e. a two-bar structure (Fig. 3.2.1(a)), two beams in bending (Figs. 3.2.1(d) and 3.2.1(e)) and a thick cylinder (Fig. 3.2.1(g)). These solutions are then used to assess the applicability of the approximately linear variations of stress with 1/n and reference stress methods, developed for single-material structures, to two-material situations. For comparison, the results obtained for the corresponding single-material cases are also presented.

In this work only the stress distributions of the structures investigated are presented. The corresponding deformation behaviour investigated using a reference stress approach can be found in Hyde et al [1996].

3.2.2 Single-Material Structures

(1) Two-bar structure

The steady-state creep behaviour (i.e. when stress redistribution is effectively completed) of the two-bar structure shown in Fig. 3.2.1(a) is fully defined by the load-point displacement rate, $\dot{\Delta}_{ss}$, and the stresses, σ_1 and σ_2, in the two bars.

From the equilibrium (i.e., $\sigma_1 A_1 + \sigma_2 A_2 = P$), compatibility (i.e. $\varepsilon_1 = \Delta/l_1$ and $\varepsilon_2 = \Delta/l_2$) and material creep behaviour (i.e. $\dot{\varepsilon}^c = B\sigma^n$, taking both bars to be made of the same material) equations, it can be shown that in the steady-state

$$\dot{\Delta}_{ss} = \left[\frac{1 + \frac{A_2}{A_1}}{1 + \frac{A_2}{A_1}\left(\frac{l_1}{l_2}\right)^{\frac{1}{n}}} \right]^n l_1 B(\sigma_{nom})^n \qquad (3.2.1)$$

$$\sigma_1 = \frac{\left(1 + \frac{A_2}{A_1}\right)\sigma_{nom}}{\left(1 + \frac{A_2}{A_1}\left(\frac{l_1}{l_2}\right)^{\frac{1}{n}}\right)} \qquad (3.2.2(a))$$

$$\text{and} \quad \sigma_2 = \frac{\left(1 + \frac{A_1}{A_2}\right)\sigma_{nom}}{\left(1 + \frac{A_1}{A_2}\left(\frac{l_2}{l_1}\right)^{\frac{1}{n}}\right)} \qquad (3.2.2(b))$$

where $\sigma_{nom} = P/(A_1 + A_2)$.

Using equations (3.2.2(a)) and (3.2.2(b)) it can be seen that if $l_2 > l_1$, then $\sigma_1 > \sigma_{nom}$ and $\sigma_2 < \sigma_{nom}$. Also, as $n \rightarrow \infty$, then $\sigma_1 = \sigma_2 = \sigma_{nom}$. Taking the case of $l_2 > l_1$, the variations of σ_1 (the greater of the two stresses) with 1/n were obtained, for a range of l_1/l_2 and A_2/A_1 values, shown in Figs. 3.2.2. From Figs. 3.2.2 it can be seen that the variation of stress with 1/n is in general non-linear. The degree of non-linearity depends on the l_1/l_2 and A_2/A_1

ratios. However, for fairly wide ranges of A_2/A_1 and l_1/l_2 the relationship can be represented reasonably well by straight lines. However, as $l_1/l_2 \rightarrow 0$, the linearity becomes poor. The case of $l_1/l_2 \rightarrow 0$ is not a practical two-bar case because, as equation (3.2.1) indicates, when $l_1 \rightarrow 0$ then $\dot{\Delta}_{ss} \rightarrow 0$ and the structure does not creep. These results indicate that although the stress varies approximately linearly with 1/n for a wide range of geometries, the approximately linear relationship breaks down for highly constrained situations (i.e. when $l_1 << l_2$).

(2) Beams in bending

The steady-state creep behaviour of the rectangular cross-sectional beam and the I-sectioned beam, shown in Figs. 3.2.1(b) and 3.2.1(c) are fully defined by the rate of change of curvature, $\dot{K}_{ss}$, and the variation of bending stress, $\sigma_x(y)$, with position y on the cross-section.

For the rectangular cross-sectioned beam, the equilibrium (i.e., $M = 2b \int_0^{d/2} y\, \sigma_x(y)\, dy$), compatibility (i.e. $\dot{\varepsilon}_x(y) = \dot{K}y$) and material creep behaviour (i.e. $\dot{\varepsilon}^c = B\sigma^n$) equations can be used to show that in the steady-state

$$\dot{K}_{ss} = \left(1 + \frac{1}{2n}\right)^n \frac{2}{d} B(\sigma_{nom})^n \qquad (3.2.3)$$

$$\sigma_x(y) = \left(1 + \frac{1}{2n}\right)\left(\frac{2y}{d}\right)^{\frac{1}{n}} \sigma_{nom} \qquad (3.2.4)$$

where $\sigma_{nom} = 4M/bd^2$.

A similar analysis for the I-sectioned beam, shown in Fig. 3.2.1(c), leads to

$$\dot{K}_{ss} = \frac{\left(1 + \frac{1}{2n}\right)^n}{\left(1-\left(1 - \frac{b_1}{b_2}\right)\left(\frac{d_1}{d_2}\right)^{2+\frac{1}{n}}\right)} \cdot \frac{2}{d_2}.B(\sigma_{nom})^n \qquad (3.2.5)$$

and $$\sigma_x(y) = \frac{\left(1 + \frac{1}{2n}\right)}{\left(1-\left(1 - \frac{b_1}{b_2}\right)\left(\frac{d_1}{d_2}\right)^{2+\frac{1}{n}}\right)} \cdot \left(\frac{2y}{d_2}\right)^{\frac{1}{n}} \sigma_{nom} \qquad (3.2.6)$$

where $\sigma_{nom} = 4M/b_2d_2^2$.

For the rectangular cross-sectioned beam, the normalised maximum stress, $\hat{\sigma}_x/\sigma_{nom}$, which occurs at the surface, varies exactly linearly with 1/n, i.e., $\hat{\sigma}_x/\sigma_{nom} = 1 + 1/2n$. However, it should be noted that the bending stresses at other positions (i.e. $y < d/2$) do not vary exactly linearly with 1/n. The deviations from linearity, as indicated in Fig. 3.2.3 (for $y < d/2$), are not large and are most significant for the lowest values of y, which correspond to the low stress values and are hence of least significance.

Unlike the rectangular cross-sectioned beam, the maximum stress for the I-section beam does not vary exactly linearly with 1/n; in this case

$$\frac{\hat{\sigma}_x}{\sigma_{nom}} = \frac{\left(1 + \frac{1}{2n}\right)}{\left(1-\left(1 - \frac{b_1}{b_2}\right)\left(\frac{d_1}{d_2}\right)^{2+\frac{1}{n}}\right)} \qquad (3.2.7)$$

However, for particular values of b_1/b_2 and d_1/d_2 it is found that the variation of $\hat{\sigma}_x/\sigma_{nom}$ with 1/n is practically linear. Fig. 3.2.4 shows the variations of σ_x/σ_{nom} with 1/n for b_1/b_2 = 0.2 and d_1/d_2 = 0.8, at various $2y/d_2$ values, which indicate that practically linear variations occur except at the lowest stress positions. These results are typical of those obtained with any b_1/b_2 and d_1/d_2 ratios.

(3) Internally pressurised, closed-ended thick cylinder

The steady-state creep behaviour of the internally pressurised thick cylinder shown in Fig. 3.2.1(f) is fully defined by the variation of the radial displacement rate, $\dot{u}(r)$, and the variations of the hoop, axial and radial stresses ($\sigma_\theta(r)$, $\sigma_a(r)$ and $\sigma_r(r)$) with radial position r.

From the equilibrium (i.e. $d\sigma_r/dr = (\sigma_\theta - \sigma_r)/r$), compatibility (i.e. $d\dot{\varepsilon}_\theta / dr = (\dot{\varepsilon}_r - \dot{\varepsilon}_\theta)/r$) and multi-axial material creep behaviour (i.e., $\dot{\varepsilon}_{ij} = 3\,B\,(\sigma_{eff})^{n-1}\,S_{ij}/2$, where $\sigma_{eff} = (1.5\,S_{ij}\,S_{ij})^{0.5}$ and S_{ij} is the deviatoric stress) equations, together with the boundary conditions (i.e. $\sigma_r = -p$ at $r = R_i$ and $\sigma_r = 0$ at $r = R_o$), it can be shown that in the steady-state

$$\dot{u}(r) = \left(\frac{\sqrt{3}}{2}\right)^{n+1}\left(\frac{2}{n}\right)^{n}\frac{1}{\left((R_o/R_i)^{\frac{2}{n}}-1\right)^{n}}\frac{R_o^2}{r}\,B\,p^n \qquad (3.2.8)$$

$$\begin{Bmatrix}\sigma_\theta(r)\\ \sigma_a(r)\\ \sigma_r(r)\end{Bmatrix} = \frac{p}{\left((R_o/R_i)^{\frac{2}{n}}-1\right)}\begin{Bmatrix}1+\left(\frac{2-n}{n}\right)\left(\frac{R_o}{r}\right)^{\frac{2}{n}}\\ 1+\left(\frac{1-n}{n}\right)\left(\frac{R_o}{r}\right)^{\frac{2}{n}}\\ 1-\left(\frac{R_o}{r}\right)^{\frac{2}{n}}\end{Bmatrix} \qquad (3.2.9)$$

Also, the variation of the effective stress, $\sigma_{eff}(r)$, with radial position, in the steady-state is given by

$$\sigma_{eff}(r) = \frac{\sqrt{3}}{n}\left(\frac{R_o}{r}\right)^{\frac{2}{n}} \frac{p}{\left((R_o/R_i)^{\frac{2}{n}} - 1\right)} \qquad (3.2.10)$$

Figs. 3.2.5(a) and 3.2.5(b) show the variations of σ_θ and σ_{eff} with radial position, for a thick cylinder having $R_o/R_i = 2$, for a range of values of n. From Fig. 3.2.5 it can be seen that for $n < 2$ the maximum hoop stress occurs at the bore of the cylinder, but for $n > 2$ the maximum hoop stress occurs at the outer surface of the cylinder. As $n \rightarrow \infty$, l'Hopitals rule can be used, with equation (3.2.10), to show that σ_{eff} becomes independent of r, having a value of $\sqrt{3}p/(2\ln(R_o/R_i))$. Using equations (3.2.9), the variations of hoop stress with 1/n were obtained at various radial positions, for $R_o/R_i = 2$ and 4, as shown in Fig. 3.2.6(a) and 3.2.6(b), respectively. For $R_o/R_i = 2$ it can be seen that the stresses vary practically linearly with 1/n but the deviations from linear behaviour are more pronounced with the higher values of R_o/R_i. Similar variations of stress with 1/n can also be obtained for the other stress components (equations (3.2.9)) and for other radius ratios, R_o/R_i.

From Fig. 3.2.6 it can also be seen that at certain combinations of n and R_o/R_i it is possible to have negative hoop stresses near the bore of the cylinder. The combinations of n and R_o/R_i resulting in negative hoop stresses can be obtained from equation (3.2.9), i.e. they occur when $1 + (2 - n)(R_o/R_i)^{2/n}/n < 0$. Similarly, it is also possible to have negative axial stresses for some combinations of n and R_o/R_i.

3.2.3 Two-Material Structures

(a) Material behaviour

In two-material structures (or structures comprising of more than two materials such as welds), the creep properties can often be reasonably represented by Norton creep laws, i.e. $\dot{\varepsilon}^c = B\sigma^n$. For many engineering materials in their practical stress ranges, the stress exponents, n, are in the range 2 to 8 and are usually close to 4. Also, the stress exponents of materials being joined are often about the same (e.g. Hall and Hayhurst [1991]). However, there can be large variations in the B-values for the different materials being joined. For these reasons, and in order to simplify the analyses of two-material structures, it will be assumed that the n-values are the same for the two materials but that the B-values can be different.

(b) Two-bar structure

As in the single-material case, the steady-state creep behaviour of a two-bar structure, consisting of two materials (material 1 and material 2), shown in Fig. 3.2.1(a), is fully defined by the load-point displacement, $\dot{\Delta}_{ss}$, and the stresses, σ_1 and σ_2, in the two bars.

Using the equilibrium (i.e. $\sigma_1 A_1 + \sigma_2 A_2 = P$), compatibility (i.e. $\dot{\varepsilon}_1 = \dot{\Delta} / l_1$ and $\dot{\varepsilon}_2 = \dot{\Delta} / l_2$) and material creep behaviour (i.e. $\dot{\varepsilon}^c = B_1 \sigma^n$ for bar 1 and $\dot{\varepsilon}^c = B_2 \sigma^n$ for bar 2) equations, it can be shown that in the steady-state,

$$\dot{\Delta}_{ss} = \left[\frac{1 + \frac{A_2}{A_1}}{1 + \frac{A_2}{A_1}\left(\frac{B_1 l_1}{B_2 l_2}\right)^{\frac{1}{n}}} \right]^n l_1 \, B_1 (\sigma_{nom})^n \qquad (3.2.11)$$

$$\sigma_1 = \frac{\left(1 + \frac{A_2}{A_1}\right) \sigma_{nom}}{1 + \frac{A_2}{A_1}\left(\frac{B_1}{B_2}\frac{l_1}{l_2}\right)^{\frac{1}{n}}} \qquad (3.2.12(a))$$

and $$\sigma_2 = \frac{\left(1 + \frac{A_1}{A_2}\right) \sigma_{nom}}{1 + \frac{A_1}{A_2}\left(\frac{B_2}{B_1}\frac{l_2}{l_1}\right)^{\frac{1}{n}}} \qquad (3.2.12(b))$$

where $\sigma_{nom} = P/(A_1 + A_2)$.

By comparing equations (3.2.11) and (3.2.12) with equations (3.2.1) and (3.2.2), respectively, it can be seen that in the equations for the two-material structure the quantities $B_1 l_1$ and $B_2 l_2$ simply replace l_1 and l_2, respectively, in the equations for the corresponding single material structure. Hence the behaviour of the single-material, two-bar structure, as depicted in Fig. 3.2.2, can also be used to describe the behaviour of the two-material, two-bar structure simply by replacing $B_1 l_1$ for l_1 and $B_2 l_2$ for l_2. As with the single-material, two-bar structure, the situation in which $B_1 l_1 \rightarrow 0$ is not a practical two-bar case, because under these conditions $\dot{\Delta}_{ss} \rightarrow 0$, i.e. the structure would not be creeping. Therefore, it can be inferred that for a wide range of geometries the stresses vary approximately linearly with 1/n. However, the approximately linear relationship breaks down in situations when $B_1 l_1 << B_2 l_2$.

(c) Beams in bending

Two examples of rectangular cross-sectioned, two-material beams in bending are shown in Figs. 3.2.1(d) and 3.2.1(e); these are referred to as case 1 and case 2, respectively. In case 1 (Fig. 3.2.1(d)) the division of the beam is such that each of the materials spans the full depth of the beam but only occupies part of the breadth of the beam. In case 2 (Fig. 3.2.1(e)) each of the materials occupies the full breadth of the beam but only part of the depth of the beam.

i) Case 1

The steady-state creep behaviour is fully defined by the rate of change of curvature, $\dot{K}_{ss}$, and the variations of bending stress, $\sigma_x^{(1)}(y)$ and $\sigma_x^{(2)}(y)$, with position y, on the cross-section, of the parts of the beam made from materials 1 and 2, respectively.

From the equilibrium (i.e. $M = 2b_1 \int_0^{d/2} y\sigma_x^{(1)}(y)\,dy + 2(b_2 - b_1)\int_0^{d/2} \sigma_x^{(2)}(y)\,dy$), compatibility (i.e. $\dot{\varepsilon}_x(y) = \dot{K}y$) and material creep behaviour (i.e. $\dot{\varepsilon}^c = B_1\,\sigma^n$ for material 1 and $\dot{\varepsilon}^c = B_2\,\sigma^n$ for material 2) equations, it can be shown that in the steady-state

$$\dot{K}_{ss} = \frac{\left(1 + \frac{1}{2n}\right)^n}{\left(1 + \frac{b_1}{b_2}\left(\left(\frac{B_2}{B_1}\right)^{\frac{1}{n}} - 1\right)\right)^n} \cdot \frac{2}{d} \cdot B_2\,(\sigma_{nom})^n \qquad (3.2.13)$$

$$\sigma_x^{(1)}(y) = \frac{\left(1 + \frac{1}{2n}\right)}{\left(\frac{b_1}{b_2} + \left(1 - \frac{b_1}{b_2}\right)\left(\frac{B_1}{B_2}\right)^{\frac{1}{n}}\right)} \cdot \left(\frac{2y}{d}\right)^{\frac{1}{n}} \cdot \sigma_{nom} \qquad (3.2.14(a))$$

$$\text{and} \quad \sigma_x^{(2)}(y) = \frac{\left(1 + \frac{1}{2n}\right)}{\left(1 + \frac{b_1}{b_2}\left(\left(\frac{B_2}{B_1}\right)^{\frac{1}{n}} - 1\right)\right)} \cdot \left(\frac{2y}{d}\right)^{\frac{1}{n}} \sigma_{nom} \qquad (3.2.14(b))$$

where $\sigma_{nom} = 4M/b_2d^2$.

From equations (3.2.14(a)) and (3.2.14(b)) it can be seen that as $n \rightarrow \infty$, both $\sigma_x^{(1)}$ and $\sigma_x^{(2)}$ become independent of y and equal to σ_{nom}, irrespective of the b_1/b_2 and B_2/B_1 ratios. This is the same as the single-material stress distribution as $n \rightarrow \infty$ (see equation (3.2.4)). It can also be seen from equations (3.2.14(a)) and (3.2.14(b)) that $\sigma_x^{(1)}/\sigma_x^{(2)} = (B_2/B_1)^{1/n}$, and if $B_1 > B_2$ then $\sigma_x^{(2)} > \sigma_x^{(1)}$, at any value of $y > 0$, and if $B_1 < B_2$ then $\sigma_x^{(1)} > \sigma_x^{(2)}$, at any value of $y > 0$. Fig. 3.2.7 illustrates the form of the stress distributions in the two parts of the beam with different stress exponents, n, for the example of $b_1/b_2 = 0.5$ and $B_2/B_1 = 5$. From Fig. 3.2.7 it can be seen that for the material 2 part of the beam the stresses generally increase as n increases, whereas for the material 1 part of the beam the stresses for low 2y/d values increase but those for high 2y/d values decrease. For a number of combinations of b_1/b_2 and two B_2/B_1 ratios, the variations of the maximum bending stresses with 1/n are shown in Fig. 3.2.8(a) and 3.2.8(b) (for the combinations chosen the maximum stress occurs in material 1, i.e. $B_2/B_1 > 1$). It can be seen that when the most creep resistant material occupies the largest volume (e.g. $b_1/b_2 = 0.9$) the maximum stress varies approximately

linearly with 1/n irrespective of the B_2/B_1 ratio ($1 < B_2/B_1 < 100$). When both materials occupy similar volumes (i.e. $b_1/b_2 = 0.4$ to 0.6) the maximum stress varies approximately linearly for $B_2/B_1 = 10$; whereas for $B_2/B_1 = 100$, a linear relationship is not so accurate. When the most creep resistant material occupies the smallest volume (e.g. $b_1/b_2 = 0.1$), a reasonable linear relationship only exists for values of B_2/B_1 close to unity.

ii) Case 2

As with Case 1, the steady-state creep behaviour is fully defined by the rate of change of curvature, $\dot{K}_{ss}$, and the variations of bending stress, $\sigma_x^{(1)}(y)$ and $\sigma_x^{(2)}(y)$, with position y, on the cross-section (Fig. 3.2.1(e)), for the parts of the beam made from materials 1 and 2, respectively.

From the equilibrium (i.e. $M = 2b \left(\int_b^{d1/2} y\, \sigma_x^{(1)}(y)\, dy + \int_{d1/2}^{d2/2} y\, \sigma_x^{(2)}(y)\, dy\right)$), compatibility (i.e. $\dot{\varepsilon}_x(y) = \dot{K}y$) and material creep behaviour (i.e. $\dot{\varepsilon}^c = B_1 \sigma^n$ for material 1 and $\dot{\varepsilon}^c = B_2 \sigma^n$ for material 2) equations, it can be shown that in the steady-state

$$\dot{K}_{ss} = \frac{\left(1 + \frac{1}{2n}\right)^n}{\left(1 + \left(\frac{d_1}{d_2}\right)^{2+\frac{1}{n}} \left(\left(\frac{B_2}{B_1}\right)^{\frac{1}{n}} - 1\right)\right)^n} \cdot \frac{2}{d_2} \cdot B_2 \, (\sigma_{nom})^n \qquad (3.2.15)$$

$$\sigma_x^{(1)}(y) = \frac{\left(1 + \frac{1}{2n}\right)}{\left(\frac{B_1}{B_2}\right)^{\frac{1}{n}} \left(1 + \left(\frac{d_1}{d_2}\right)^{2+\frac{1}{n}} \left(\left(\frac{B_2}{B_1}\right)^{\frac{1}{n}} - 1\right)\right)} \cdot \left(\frac{2y}{d_2}\right)^{\frac{1}{n}} \sigma_{nom} \qquad (3.2.16(a))$$

$$\sigma_x^{(2)}(y) = \frac{\left(1 + \frac{1}{2n}\right)}{\left(1 + \left(\frac{d_1}{d_2}\right)^{2+\frac{1}{n}}\left(\left(\frac{B_2}{B_1}\right)^{\frac{1}{n}} - 1\right)\right)} \cdot \left(\frac{2y}{d_2}\right)^{\frac{1}{n}} \sigma_{nom} \qquad (3.2.16(b))$$

where $\sigma_{nom} = 4M/bd_2^2$.

From equations (3.2.16(a)) and (3.2.16(b)) it can be seen that as $n \rightarrow \infty$, both $\sigma_x^{(1)}$ and $\sigma_x^{(2)}$ become independent of y, irrespective of the d_1/d_2 and B_2/B_1 ratios. This is the same as the single-material stress distribution as $n \rightarrow \infty$ (see equation (3.2.4)) and case 1 of the two-material beam (see equation (3.2.14(a)) and (3.2.14(b))).

Typical variations of the maximum stress with 1/n (this may be in either material 1 or material 2) are shown in Figs. 3.2.9(a) to (d), for a range of B_1/B_2 values ($0.01 < B_1/B_2 < 100$) and d_1/d_2 values ($0.1 < d_1/d_2 < 0.9$). When the highest stress is at the interface in material 1 (e.g. Figs. 3.2.9(a) and 3.2.9(b)), reasonably linear variations of maximum stress with 1/n are obtained for the higher d_1/d_2 ratios for $B_1/B_2 = 0.01$. For $B_1/B_2 = 0.1$, the intermediate values of d_1/d_2 result in the most non-linear results. When the highest stress is in material 2 (e.g. Figs. 3.2.9(c) and 3.2.9(d)), the deviations from linearity are more pronounced as B_1/B_2 is increased and d_1/d_2 is increased. This indicates that as the volume of material 2 is decreased and/or its relative creep resistance is increased the deviation from linearity becomes more pronounced.

iv) Internally pressurised, closed-ended thick cylinder

As in the case of the single-material thick cylinder, the behaviour of the two-material cylinder (Fig. 3.2.1(g)) is fully defined by the variation of the radial displacement rate, $\dot{u}(r)$, and the variations of the hoop, axial and radial stresses ($\sigma_\theta(r)$, $\sigma_a(r)$ and $\sigma_r(r)$) with radial position, r.

From the equilibrium (i.e. $d\sigma_r/dr = (\sigma_\theta - \sigma_r)/r$), compatibility (i.e. $d\dot{\varepsilon}_\theta/dr = (\dot{\varepsilon}_r - \dot{\varepsilon}_\theta)/r$) and material creep behaviour (i.e. $\dot{\varepsilon}_{ij} = 3B_1 (\sigma_{eff})^{n-1} S_{ij}/2$ for material 1 and $\dot{\varepsilon}_{ij} = 3B_2 (\sigma_{eff})^{n-1} S_{ij}/2$ for material 2) equations, together with the boundary conditions (i.e. $\sigma_r = -p$ at $r = R_i$, $\sigma_r = 0$ at $r = R_o$ and $\dot{u}$ is the same for materials 1 and 2 at the interface radius, R_1), it can be shown that in the steady-state

$$\dot{u}(r) = \left(\frac{\sqrt{3}}{2}\right)^{n+1} \left(\frac{2}{n}\right)^{n} \frac{1}{\left((R_1/R_i)^{\frac{2}{n}} - 1\right)^{n}} \frac{R_1^2}{r} B_1 (p - p_1)^n \qquad (3.2.17)$$

$$\begin{Bmatrix} \sigma_\theta(r) \\ \sigma_a(r) \\ \sigma_r(r) \end{Bmatrix} = \frac{p}{\left(1-(R_i/R_1)^{\frac{2}{n}}\right)} \begin{Bmatrix} \left(1-\frac{p_1}{p}\right)\left(1+\left(\frac{2-n}{n}\right)\left(\frac{R_i}{r}\right)^{\frac{2}{n}}\right)\left(1-(R_i/R_1)^{\frac{2}{n}}\right) \\ \left(1-\frac{p_1}{p}\right)\left(1+\left(\frac{1-n}{n}\right)\left(\frac{R_i}{r}\right)^{\frac{2}{n}}\right)\left(1-(R_i/R_1)^{\frac{2}{n}}\right) \\ \left(1-\frac{p_1}{p}\right)\left(1-\left(\frac{R_i}{r}\right)^{\frac{2}{n}}\right)-\left(1-(R_i/R_1)^{\frac{2}{n}}\right) \end{Bmatrix} \qquad (3.2.18)$$

for material 1 and

$$\dot{u}(r) = \left(\frac{\sqrt{3}}{2}\right)^{h+1} \left(\frac{2}{n}\right)^{n} \frac{1}{\left((R_o/R_1)^{\frac{2}{n}} - 1\right)^{n}} \frac{R_o^2}{r} B_2 \; p_1^n \qquad (3.2.19)$$

$$\begin{Bmatrix}\sigma_\theta(r)\\ \sigma_a(r)\\ \sigma_r(r)\end{Bmatrix} = \frac{p_1}{\left((R_o/R_1)^{\frac{2}{n}}-1\right)}\begin{Bmatrix}1+\left(\frac{2-n}{n}\right)\left(\frac{R_o}{r}\right)^{\frac{2}{n}}\\ 1+\left(\frac{1-n}{n}\right)\left(\frac{R_o}{r}\right)^{\frac{2}{n}}\\ 1-\left(\frac{R_o}{r}\right)^{\frac{2}{n}}\end{Bmatrix} \qquad (3.2.20)$$

for material 2, where p_1, which is the interface pressure, is given by

$$p_1 = \frac{p}{\left[1+\left(\frac{B_2}{B_1}\right)^{\frac{1}{n}}\left[\frac{(R_1/R_i)^{\frac{2}{n}}-1}{1-(R_1/R_o)^{\frac{2}{n}}}\right]\right]} \qquad (3.2.21)$$

Also, the variations of the effective stress, $\sigma_{eff}(r)$, with radial position are given by

$$\sigma_{eff}(r) = \frac{\sqrt{3}}{n}\left(\frac{R_i}{r}\right)^{\frac{2}{n}} p \frac{\left(B_2/B_1\right)^{\frac{1}{n}}\left[\left(R_1/R_i\right)^{\frac{2}{n}}-1\right]}{\left[1-\left(R_i/R_1\right)^{\frac{2}{n}}\right]\left[1-\left(R_1/R_o\right)^{\frac{2}{n}}+\left(B_2/B_1\right)^{\frac{1}{n}}\left[\left(R_1/R_i\right)^{\frac{2}{n}}-1\right]\right]}$$

(3.2.22)

for material 1 and

$$\sigma_{eff}(r) = \frac{\sqrt{3}}{n}\left(\frac{R_o}{r}\right)^{\frac{2}{n}} \frac{p_1}{\left((R_o/R_1)^{\frac{2}{n}}-1\right)} \qquad (3.2.23)$$

for material 2.

From equations (3.2.22) and (3.2.23), using l'Hopitals rule, it can be shown that as $n \to \infty$, σ_{eff} in both cylinders becomes independent of radial position and is the same in both cylinders, irrespective of the B_2/B_1 ratio, having a value of $\sqrt{3}\ p/[2 \ln (R_o/R_i)]$ which is the same as that in a single-material cylinder having the same overall dimensions and internal

pressure. Therefore, a two-material thick cylinder under internal pressure, with the same creep stress exponent, n, for both materials, will have the same distribution of effective stress, σ_{eff}, when $n \rightarrow \infty$, as that for a single-material cylinder as $n \rightarrow \infty$. Hence, the similarity of the limit load equivalent stress distribution to the stress distribution for a single-material structure, as $n \rightarrow \infty$, is also applicable to two-material structures as $n \rightarrow \infty$.

Typical variations of the σ_{eff}/p (at the inside radius, at the interface between the two materials and at the outer radius) with 1/n, for $R_o/R_i = 1.5$ and T_2/T_1 ratios of 0.1 and 10, where $T_2/T_1 = (R_o - R_1)/(R_1 - R_i)$, are shown in Figs. 3.2.10(a) - (f); these are typical examples of the behaviour for other T_2/T_1 ratios in the range $0.1 < T_2/T_1 < 10$. The variations of σ_θ/p with 1/n are similar to the corresponding σ_{eff}/p versus 1/n variations. When T_2/T_1 is relatively small (e.g. $T_2/T_1 = 0.1$, see Figs. 3.2.10(a) - (c)), the stresses in material 2 are relatively uniform and are greater than those in material 1 when $B_2 < B_1$, i.e. when material 2 is more creep resistant. When T_2/T_1 is relatively large (e.g. $T_2/T_1 = 10$, see Figs. 3.2.10(d) - (f)), the stresses in material 1 are relatively uniform and are greater than those in material 2 when $B_2 > B_1$, i.e. when material 1 is more creep resistant. Figs. 3.2.10(a) - (f) indicate that in the important, highest stress regions of the two-material cylinder the variations of the effective stress with 1/n can be reasonably accurately represented by straight lines, especially for values of B_2/B_1 near unity.

3.2.4 General Behaviour of One and Two-Material Structures

(a) Single-material

From the similarities of some of the results of the above analyses of the three examples of single material structures, it is possible to make some general observations:

The variation of the stress at a point in a component with 1/n can often be accurately represented by a linear relationship. This is particularly the case for the peak stress position in a structure. This linear relationship was observed for a number of creep situations and has been used to assist with the development of design codes for high temperature applications (e.g. Goodall (editor) [1990]). The fact that the stress distributions for $n = 1$ and $n = \infty$ are analogous to the elastic and limit-load stress distributions allows approximate peak stresses to be obtained from a knowledge of the peak elastic stress, $\hat{\sigma}^e$, and the limit load, P_L, for a structure, i.e.

$$\hat{\sigma} \approx \frac{P}{P_L}\,\sigma_Y + \frac{1}{n}\left(\hat{\sigma}^e - \frac{P}{P_L}\,\sigma_Y\right) \qquad (3.2.24)$$

However, it should be noted that there are situations in which the linear approximation is not sufficiently accurate (e.g. when $l_1/l_2 \approx 0$ for the two-bar structure, or $R_o/R_i >> 1$ for the internally pressurised thick cylinder). Hence, care should be taken when using this approach for estimating the peak stress under stationary state stress conditions.

(b) Two-material

Although the behaviour of two-material structures is more complex than that of single-material structures, by making the simplifying assumption that the stress exponents, n, for the two parts of the structure are the same, it is possible to make some general observations:

(i) As $n \rightarrow \infty$, the stress distribution within a two-material structure, for any B_1/B_2 ratio, is the same as that for a single-material structure, as $n \rightarrow \infty$, having the same overall dimensions.

(ii) The peak stress position can be in either of the two materials and depends on the relative dimensions of the two parts of the structure and on the B_1/B_2 ratio. However, for wide ranges of dimensions and B_1/B_2 ratio, the peak stress seems to vary approximately linearly with 1/n. Therefore, the peak stationary-state stress can be estimated using equation (3.2.24). In this case, P_L is the limit load for the equivalent single material structure with a yield stress of σ_y and a peak elastic stress of $\hat{\sigma}^e$ is the elastically calculated peak stress with the two materials having Young's moduli of E_1 and E_2, such that $E_1/E_2 = B_2/B_1$ ($\nu = 0.5$ should be used for the elastic solutions). However, it should be noted that the ranges of dimensions for linear behaviour are more restricted than those in the corresponding single-material structures. Hence, even greater care should be taken when using this approach for estimating the peak stress.

(iii) Since the stress states for $n \rightarrow \infty$ for single-material and two-material structures are the same, the stress distribution in a creeping structure, with an infinite value of n, can be represented by a similar (i.e. having the same overall dimensions) single-material structure at collapse even if the creeping structure is a two-material structure.

Analytical solutions are presented for the deformations of and stresses in two-bar structures, beams in bending and thick cylinders, under creep conditions. Single-material

and two-material cases were investigated. Results obtained using these solutions were used to assess the applicability of reference stress and other simple design rules, established for single-material structures, to two-material components and structures. In this thesis only the stress distributions of the structures studied are presented. The corresponding deformation behaviour can be found in the relevant Reference (Hyde et al [1996]).

3.3 A METHOD FOR ESTIMATING THE STRESS DISTRIBUTIONS ON THE CENTRE LINE OF AXISYMMETRIC TWO-MATERIAL CREEP TEST SPECIMENS

3.3.1 Introduction

A schematic diagram of a typical weld is shown in Fig. 3.3.1; it generally consists of base metal (BM), weld metal (WM) and heat affected zones (HAZ). Creep testing of cross-weld specimens, see Fig. 3.3.2, provides data which can be used to assess the detrimental effects of welds on the life of elevated temperature components (Nicol and Williams [1985] and Etienne and Heerings [1993]). However, the information obtained from cross-weld creep tests is difficult to directly apply to the life assessment of welded components. One of the main problems associated with the application of the data is the specimen size effect which is observed.

The results of many attempts to determine the stress and strain distributions in cross-weld specimens have been published (e.g. Storesund et al [1992]). However, it is difficult to generalise the results of these analyses in order to predict the stress state in a cross-weld specimen from a knowledge of the creep properties of the constituent parts. In this section, a method which allows the stationary state stress and hence strain-rate distributions to be quickly obtained from a knowledge of the creep properties of the constituent materials, is presented. To simplify the presentation of the method, the idealised, two-material specimen, shown in Fig 3.3.3, is used.

The general behaviour of the specimen (Fig. 3.3.3) is characterised by the stress and strain-rate distributions on the centre-line. Hence only the results for the centre line are presented in this section. The stress singularities which may exist near the specimen surface (position S in Fig. 3.3.3) where the material boundaries occur, will be discussed in Section 3.4.

Finite element creep analyses have been performed for an axisymmetric two-material specimen. Stationary-state stress and strain-rate results were obtained for various geometries and relative material properties. Using these results, it has been shown that a simple interpolation technique can be used to obtain the stress distributions of any geometry and relative creep properties.

3.3.2 Problem Definition and Finite Element Analysis

The idealised, axisymmetric specimen is assumed to consist of two materials, defined as material types A and B in Fig. 3.3.3; material type A is between two pieces of material type B. Both materials are assumed to obey power-law creep, i.e.

$$\dot{\varepsilon} = A\ \sigma^n \qquad (3.3.1(a))$$

for material A, and

$$\dot{\varepsilon} = B\ \sigma^n \qquad (3.3.1(b))$$

for material B. It can be seen that the stress exponent, n, is assumed to be the same for both materials; this is the case for many practical weld situations (e.g. Storesund et al [1992]). However, the constants A and B are different so that if A > B, material B is more creep resistant than material A and vice-versa.

The axial load (σ_{nom}) is applied remotely from material A so that the geometry can be fully defined by the diameter, d, and the axial length, w, of the zone occupied by material A.

Stress and strain-rate distributions along the centre-line of the specimen, i.e. r = 0 (see Figs. 3.3.3), and in the vicinity of the singularity point, S (see Fig. 3.3.3), were investigated in detail. A typical finite element mesh used to obtain general stress and strain-rate distributions is shown in Fig. 3.3.4; it consists of eight-noded, axisymmetric, isoparametric elements. Various mesh refinements were used to establish the accuracy of the results obtained, on the basis of the differences in stresses between one mesh and another and the magnitudes of the stress discontinuities at element boundaries. It should be noted that discontinuities in stress actually occur in some stress components on the interface between materials A and B, as indicated in Appendix I in which the relationships between stress and strain-rate on the centre line are given. The investigation of the stress singularities which

occur at position S, shown in Fig. 3.3.3, requires a much more refined mesh in this region. This will be described in Section 3.4.

Finite element creep calculations, using the ABAQUS [1994] finite element software system, were continued until a stationary-state stress distribution was achieved. The achievement of a stationary-state was established by checking the stress distribution along the centre line at different time increments, using the FEMVIEW [1992] post processing facilities. It should be noted that when $A/B << 1$ the stresses near the centre of the specimen approach the stationary-state very slowly. However, since the stresses at these positions are relatively low, small errors in these results are not considered to be significant.

3.3.3 Stress Variation on the Centre Line and the Effects of Material Properties and Specimen Geometries

(a) General behaviour

Normalised, stationary-state stress contours for a situation in which $w/d = 1$, $n = 4$ and $A/B = 10$ are shown in Fig. 3.3.5. These results were obtained with the mesh shown in Fig. 3.3.4, and hence the stresses in the vicinity of point S (Fig. 3.3.3) are not accurate.

It is evident from Fig. 3.3.5 that the two extremes of stress state occur on the centre-line (i.e. $r = 0$) and on the specimen surface (i.e. $r = d/2$). Therefore, the rest of the results presented in this section will be restricted to the variations of stress with x for $r = 0$.

(b) Centre-line stress and strain-rate distributions

i) Effect of n

The centre-line (r = 0) variations of σ_x/σ_{nom}, σ_r/σ_{nom} (= $\sigma_\theta/\sigma_{nom}$) and σ_{eq}/σ_{nom} with x, for a range of n-values, with w/d = 1 and for A/B = 0.1 and 10, are shown in Figs. 3.3.6(a) and 3.3.6(b). As expected, the σ_x/σ_{nom} stress is continuous across the interface, but the σ_r/σ_{nom} and σ_{eq}/σ_{nom} distributions are discontinuous. Although closed-form solutions for the stresses and strain-rates cannot be obtained, the ratio of the σ_{eq} values on either side of the interface can be determined; this ratio is given by equation (A1.11), see Appendix I. The finite element σ_{eq} ratios were found to be very close to the theoretical ratios, being generally well within 1%.

From Figs. 3.3.6(a) and 3.3.6(b) it can be seen that as $n \rightarrow \infty$, σ_{eq} becomes independent of x and equal to σ_{nom}, which is the same stress distribution as would be obtained for A = B, i.e. for a single-material specimen. Uniform σ_{eq} distributions, independent of the A/B value, were also obtained for a number of simple, two-material components for which analytical solutions can be obtained (Hyde et al [1996]).

When material A is more creep resistant than material B (i.e. A/B < 1) the maximum centre-line axial stress, $\hat{\sigma}_x$, in material A occurs at the interface (x = w/2), whereas the maximum centre-line axial stress, $\hat{\sigma}_x$, in material B occurs away from the interface (x > w/2). Under the same conditions, i.e. A/B < 1, the maximum centre-line equivalent stress,

$\hat{\sigma}_{eq}$, in materials A and B occurs at the interface (x = w/2) and away from the interface (x > w/2), respectively. When material A is less creep resistant than material B (i.e. A/B > 1), the maximum centre-line axial stress, $\hat{\sigma}_x$, occurs at the centre of material A (i.e. x = 0) and away from the interface for material B (i.e. x > w/2); the magnitude of the maximum centre-line axial stress in material B is close to nominal stress, σ_{nom}. Also, when A/B > 1, the maximum centre-line equivalent stress, $\hat{\sigma}_{eq}$, occurs at the centre of material A (i.e. x = 0) and at the interface for material B (i.e. x = w/2). The σ_r (= σ_θ) distributions are also discontinuous at x = w/2 but the stress magnitudes at any x-value are generally significantly less than those of σ_x and σ_{eq}. The variations of $\hat{\sigma}_x$ /σ_{nom} and $\hat{\sigma}_{eq}$ /σ_{nom} with 1/n, for various A/B values, with w/d = 1, are shown in Fig. 3.3.7. It can be seen that under most circumstances, for a practical range of n-values (e.g. 4 < n < 10), the data shown in Fig. 3.3.7 can be closely approximated by straight line fits. Reasonably accurate linear fits to the variations of stress with 1/n were also obtained at other positions on the centre-line and for other geometries (0.2 < w/d < 3.0). Similar behaviour has also been observed for other two-material structures (Hyde et al [1996]). The straight line fits to the data can be characterised by two quantities, K and G (i.e. σ /σ_{nom} = K + G/n).

ii) Effect of A/B

The centre-line (r = 0) variations of σ_x/σ_{nom}, σ_r/σ_{nom} (= $\sigma_\theta/\sigma_{nom}$) and σ_{eq}/σ_{nom} with x, for a range of A/B values, with w/d = 1 and n = 4, are shown in Fig. 3.3.8.

It can be seen (Fig. 3.3.8(a)) that maxima in σ_x/σ_{nom} curves occur at the centre of material A (i.e. at x = 0) for A/B > 1 and away from the interface in material B (i.e. x > w/2) when A/B < 1. The variations of these maxima in σ_x/σ_{nom} with A/B are shown in Fig. 9 for a range of w/d values. The maxima in σ_x/σ_{nom} in material A are fairly strongly dependent on w/d, particularly for the higher A/B values, whereas the maxima in σ_x/σ_{nom} in material B are weakly dependent on w/d and to a lesser extent they are relatively weakly dependent on A/B.

Maxima in σ_{eq}/σ_{nom} occur in the same places as those in σ_x/σ_{nom} (Fig. 3.3.7(b)). In addition to these maxima, the discontinuities in σ_{eq} at the interface between materials A and B result in high stresses in material A at x = w/2 (at the interface) when A/B < 1 and high stresses in material B at x = w/2 (at the interface) when A/B > 1. The variations of the maxima and high interface values of σ_{eq} with A/B are shown in Figs. 3.3.10 for a range of w/d values. From Fig. 3.3.10(a) it can be seen that the maxima in σ_{eq}/σ_{nom} for material A (at x = 0) when A/B > 1 are strongly dependent on w/d, particularly for small w/d and high A/B values. However, these maxima are less than unity indicating that if material A is less creep resistant than material B, then there is a beneficial reduction in the equivalent stress even though the corresponding maximum axial stress increases with A/B (Fig. 3.3.9(a)). Fig 3.3.10(d) shows that the maxima in σ_{eq}/σ_{nom} for material B (x > w/2) are practically independent of both w/d and A/B, the value being only slightly greater than unity. The high equivalent stresses at the interface (x = w/2) in both materials A and B (Figs. 3.3.10(b) and 3.3.10(c)) are strongly dependent upon A/B but for w/d > 0.4 they are relatively independent of w/d. However, Fig. 3.3.10(c) indicates that as w/d becomes small (i.e. 0.2 or less) the equivalent stress at the interface becomes very sensitive to the w/d value.

iii) Effect of w/d

The centre-line (r = 0) variations of σ_x/σ_{nom}, σ_r/σ_{nom} (= $\sigma_\theta/\sigma_{nom}$) and σ_{eq}/σ_{nom} with x, for a range of w/d values, with n = 4, and for A/B = 0.01 or 100 are shown in Figs. 3.3.11(a) and 3.3.11(b).

The variations in σ_x/σ_{nom} with 2x/w, for n = 4, shown in Figs. 3.3.11(a)I and 3.3.11(b)I show that maxima occur in material A (at x = 0) when A/B > 1 and in material B (at x > w/2) when A/B < 1. The variations of these maxima in σ_x/σ_{nom}, with w/d, are shown in Figs. 3.3.12 for a range of A/B values. The maximum stress in material A, when A/B > 1 (at x = 0), is sensitive to w/d, particularly for low w/d values and high A/B values, see Fig. 3.3.12(a). However, the maximum stress in material B, when A/B < 1 (x > w/2), is relatively insensitive to w/d for all A/B values and is also practically independent of A/B for A/B < 0.01, see Fig. 3.3.12(b).

From Fig. 3.3.11(a)III it can be seen that when A/B < 1 the highest centre-line equivalent stress in material A occurs at the interface (i.e. x = w/2) and the highest centre-line equivalent stress in material B occurs away from the interface (i.e. x > w/2). When A/B > 1, Fig. 3.3.11(b)III shows that the highest centre-line, equivalent stress in material A occurs at the centre of material A (i.e. x = 0) and the highest centre-line, equivalent stress in material B occurs at the interface (i.e. x = w/2). The variations of the $\hat{\sigma}_{eq}/\sigma_{nom}$ with w/d, for n = 4 and a range of A/B values, are shown in Figs. 3.3.13. When A/B > 1, $\hat{\sigma}_{eq}/\sigma_{nom}$ in material A (at x = 0) is less than 1 for w/d < 0.6 but is greater than 1 for w/d > 0.6.

However, when w/d > 0.6 the $\hat{\sigma}_{eq}/\sigma_{nom}$ value is relatively insensitive to both w/d and A/B (Fig. 3.3.13(a)). Also when A/B > 1, $\hat{\sigma}_{eq}/\sigma_{nom}$ in material B (at x = w/2) can be seen to be relatively insensitive to w/d (see Fig. 3.3.13(b)) but is sensitive to A/B. When A/B < 1, $\hat{\sigma}_{eq}/\sigma_{nom}$ in material A (at x = w/2) is relatively insensitive to w/d, except at low w/d values, but is sensitive to A/B. However, when A/B < 1, $\hat{\sigma}_{eq}/\sigma_{nom}$ in material B (x > w/2) is practically independent of both w/d and A/B.

From Figs. 3.3.11(a)II and 3.3.11(b)II it can be seen that significant tensile radial (and hoop) stresses occur on the centre line (r = 0) in material A when w/d is small and A/B > 1 and that significant compressive radial (and hoop) stresses occur on the centre line (r = 0) in material A when w/d is small and A/B < 1. The variation in the ratio of the hydrostatic stress component, $(\sigma_r + \sigma_\theta + \sigma_x)/3$, to the equivalent stress, σ_{eq}, at x = 0 and r = 0, for n = 4, with w/d is shown in Fig. 3.3.14, for a range of A/B values. It can be seen that for A/B > 1 and w/d < 0.6 this ratio may be significantly greater than unity.

3.3.4 Estimating Centre-line Stress and Strain-Rate Distributions

In section 3.3.3 it was shown that over practical ranges of the stress exponent, n, the axial and equivalent stresses at a point on the centre-line, $\sigma_x(x)$ and $\sigma_{eq}(x)$, vary approximately linearly with 1/n, such that

$$\sigma_{eq}(x)/\sigma_{nom} \approx K_{eq}(x) + G_{eq}(x)/n \qquad (3.3.2(a))$$

and

$$\sigma_x(x)/\sigma_{nom} \approx K_x(x) + G_x(x)/n \qquad (3.3.2(b))$$

On the centre-line, $\sigma_r(x) = \sigma_\theta(x) = \sigma_x(x) - \sigma_{eq}(x)$, hence if $\sigma_x(x)$ and $\sigma_{eq}(x)$ are determined then $\sigma_r(x)$ and $\sigma_\theta(x)$ can be easily obtained.

Examples of the variations of K_x, G_x, K_{eq} and G_{eq} with 2x/w for w/d = 0.2, 1.0 and 3.0 are shown in Figs. 3.3.15(a)-(c), for a range of A/B values. Using Fig. 3.3.15 and similar results for other w/d values, the $\sigma_x(x)/\sigma_{nom}$ and $\sigma_{eq}(x)/\sigma_{nom}$ distributions can be determined from any particular n-value. If results for the w/d and A/B values of interest are not available then results for the w/d and A/B values spanning the values of interest can be determined and interpolated to obtain the required values. Figs. 3.3.9 and 3.3.10 show that linear interpolation of the σ_x/σ_{nom} and σ_{eq}/σ_{nom} versus log (A/B) will give reasonably accurate stresses over one decade. Also, as Figs. 3.3.12 and 3.3.13 show, linear interpolation between two w/d values, spanning the required value will give reasonably accurate results. It should be noted that for combinations of high A/B with low w/d the linear assumption is less accurate.

Results show that when w/d is very large (≈ 3.0) the stress variations along the centre line become symmetrical about the interface. This indicates that from values of w/d > 3.0, the stress variations across the interface should be the same as those of w/d = 3.0.

Having determined the σ_x/σ_{nom} and σ_{eq}/σ_{nom} distributions, then the σ_r/σ_{nom} and $\sigma_\theta/\sigma_{nom}$ distributions can be obtained (equations A1.2 and A1.3). Also, using the material constants, A, B and n, for the two materials, the effective strain-rates can be determined (i.e. $\dot{\varepsilon}_{eff} = A\ \sigma_{eff}^n$ for material A and $\dot{\varepsilon}_{eff} = B\ \sigma_{eff}^n$ for material B) at any position, x, and hence $\dot{\varepsilon}_x, \dot{\varepsilon}_r$ and $\dot{\varepsilon}_\theta$ can be obtained (equations A1.4 and A1.5).

3.3.5 Conclusions

Although cross-weld specimens (Fig. 3.3.2) and the idealised two-material components (Fig. 3.3.3) for which results are presented in this section, are geometrically simple, the stress distributions within them are very complex. The stress distributions are strongly dependent upon the geometry (w/d) and the relative creep properties (A/B) and the stress exponent (n). However, on the centre line (r = 0) of the specimen, the complete stationary-state stress and strain-rate distributions can be determined from a knowledge of the axial and equivalent stress distributions (see Appendix I).

The axial stress on the centre line is continuous but the radial, hoop and equivalent stresses are discontinuous at x = w/2. As $n \rightarrow \infty$, the equivalent stress becomes independent of position and A/B; this is similar to the behaviour observed with the other two-material components (Hyde et al [1996]).

Over relatively large ranges of stress exponent the stresses (σ_x and σ_{eq}) were found to vary linearly, to a close approximation, with 1/n; see Figs. 3.3.7 (note that the stress axes in Fig. 3.3.7 are not drawn starting zeros, which exaggerates any small non-linearities which may exist). In general, the differences between the actual stresses and those from straight line fits to the plots of stress versus 1/n are within 2%. These good approximations to linear behaviour, taken together with the smooth variations of stress with log (A/B), see Fig. 3.3.10, allow accurate interpolation of results to obtain the centre-line stress distributions for any material properties (n and A/B) for a particular w/d. Hence the sensitivity of the

behaviour of the two-material specimen (Fig. 3.3.3) to material and geometric variables can be easily assessed from the results presented. In particular, variations of maximum principal stress, effective stress and hydrostatic stress with position, x, can be determined; these quantities affect the failure times for the specimens. Stresses determined can also be used to determine the strains, which when used in conjunction with the stress-state can be used to obtain failure ductilities; again this may be useful in determining the failure times for the specimen.

Using the parametric study described above, the effect of geometric and material property ratios on the minimum test gauge length of the specimen can be determined. It has been found that the minimum gauge length depends on the geometry only, i.e. w/d values, and is independent of n and A/B (see Figs. 3.3.6 and 3.3.8). Fig. 3.3.16 presents an example of the variation of the minimum gauge length against w/d on a logarithm scale.

3.4 STRESS SINGULARITIES AT THE FREE SURFACE OF AN AXISYMMETRIC TWO-MATERIAL CREEP TEST SPECIMEN

3.4.1 Introduction

Creep tests of cross-weld specimens, see Fig. 3.3.2, are used to obtain data which can be used to assess the detrimental effects of welds on the life of elevated temperature components, such as those used in power and chemical plants. However, due to a lack of

detailed understanding of the stress and strain distributions within cross-weld specimens under creep conditions, it is difficult to apply the information obtained from these tests to actual weld situations. A method for estimating the stress distributions on the centre-line of axisymmetric two-material creep test specimens has been described in Section 3.3. In this section, the stress singularity which occurs at the free surface, in the vicinity of the interface, of an axisymmetric, two-material, creep test specimen is described. As in Section 3.3, an idealised, two-material specimen, shown in Fig. 3.4.1, is used for this purpose.

The stress and strain singularities at dissimilar material interfaces have been the subject of a number of papers (e.g. Bogy [1968], Dundurs [1969], England [1971] and Kelly et al [1992]). Most of the previous work relates to the singularities caused by dissimilar elastic material properties (Young's moduli and Poisson's ratios) under the plane strain conditions. The effect of the wedge angles between the interface and free surfaces, on the nature of the singularities, has been included in these investigations. Differences in the plastic flow resistance for bi-material wedges can also cause stress and strain singularities (e.g. Lau and Delale [1988] and Rudge [1993]). Power-law hardening material behaviour models were assumed and plane strain solutions were obtained. Lau and Delale [1988] also pointed out that their solutions would be applicable to the corresponding power-law creep situation if displacements and strains were interpreted as their time rates instead. However, the range of properties for which power-law solutions are available is limited and these solutions are strictly applicable to plane strain situations only. In this section the effects of the geometric variable, w/d (Fig. 3.4.1), and the relative creep properties of the two materials (A and B in Fig. 3.4.1), on the stress singularity under axisymmetric conditions are reported, and the physical significance of the singularity is discussed.

The nature of the singularity which occurs at the surface of an axisymmetric two-material creep test specimen has been investigated. It was found that the stress state in the vicinity of the singularity is of the form $\sigma_{ij} = \sigma_{nom} K_{ij} (r/d)^{-N}$. The exponent N was found to be practically the same for all angular positions and stress components, for given n and A/B values, and does not depend on the geometry (i.e. w/d). The functions K_{ij} define the variations of the stresses with angular position, θ; these were found to depend upon w/d as well as n and A/B. The implications of the results for practical situations are also discussed.

3.4.2 Problem Definition

The idealised, axisymmetric specimen is assumed to consist of two materials, defined as material types A and B in Fig. 3.4.1(a). Both materials are assumed to obey power-law creep, i.e.,

$$\dot{\varepsilon} = A\sigma^n \qquad (3.4.1(a))$$

for material A, and

$$\dot{\varepsilon} = B\sigma^n \qquad (3.4.1(b))$$

for material B.

The stress exponent, n, is assumed to be the same for both materials; this is a reasonable assumption for many practical weld situations (e.g. Hall and Hayhurst [1991]). The relative creep properties are therefore conveniently characterised by the ratio A/B.

The axial load is applied remotely from material A so that the geometry can be fully defined by the diameter, d, and the axial length, w, of the zone occupied by material A. The stress state is defined in terms of the r, θ co-ordinate system, as shown in Fig. 3.4.1(b). The expressions of the stress components and the method used to obtain the singularity parameters are given in Appendix II. A typical finite element mesh used to obtain the stress distributions in the vicinity of the singularity point S (Fig. 3.4.1) is shown in Fig. 3.4.2; it consists of six-noded and eight-noded, isoparametric elements. Various mesh refinements were used to establish the accuracy of the results obtained, on the basis of the differences in stress between one mesh and another and the magnitudes of the stress discontinuities at element boundaries.

Finite element calculations, using the ABAQUS [1994] finite element software system, were continued until a stationary-state stress distribution was achieved. The achievement of a stationary-state was established by checking the stress distribution along the interface at different time increments, using the FEMVIEW [1992] post processing facility.

3.4.3 Singularity Parameters K and N and the Effects of Creep Properties and Specimen Geometries

(a) Typical behaviour

Typical variations of the normalised stationary-state stress components (i.e. σ_{rr}/σ_{nom}, $\sigma_{\theta\theta}/\sigma_{nom}$ and $\tau_{r\theta}/\sigma_{nom}$) and the normalised equivalent stress (σ_{eq}/σ_{nom}) with the normalised radial position, r/d, for a range of angular positions, θ, are shown in Figs. 3.4.3 and 3.4.4 (r

and θ are defined in Fig. 3.4.1(b)). These results were obtained for w/d = 0.5 and n = 2 with A/B = 0.1 (Fig. 3.4.3) and A/B = 10 (Fig. 3.4.4). It can be seen that, in general, as r $\rightarrow$ 0, the stresses increase rapidly. The variations of stress with radial position are singular and it is assumed that the stresses can be represented by an equation of the form:

$$\sigma_{ij} / \sigma_{nom} = K_{ij}(r/d)^{-N_{ij}} \qquad (3.4.2(a))$$

and

$$\sigma_{eq} / \sigma_{nom} = K_{eq}(r/d)^{-N_{eq}} \qquad (3.4.2(b))$$

where the N_{ij} and N_{eq} are positive exponents and the K_{ij} and K_{eq}, which are functions of θ, describe the variations of the stresses with θ. Equations (3.4.2) can be seen to be valid from the linear relationships between log (σ/σ_{nom}) and log (r/d) which are obtained, as shown in Figs. 3.4.5 and 3.4.6; the gradients of these straight lines are equal to $-N_{ij}$ and $-N_{eq}$ and the K_{ij} and K_{eq} values are obtained from the intercepts on the log (σ_{ij}/σ_{nom}) and log (σ_{eq}/σ_{nom}) when log (r/d) = 0.

(b) Effects of n and A/B for w/d = 1

The variations of N_{ij} and N_{eq} with θ, for n = 1, 2, 4 and 8, with A/B = 0.1 and 10 are shown in Figs. 3.4.7 and 3.4.8. It can be seen that for each n-value, the N_{ij} and N_{eq} values appear to be only weakly dependent on θ. Also, the N_{ij} and N_{eq} values for each stress component and for the equivalent stress are practically the same. The N_{ij} values reduce with increasing n-value such that as n $\rightarrow \infty$ then N_{ij} and $N_{eq} \rightarrow 0$. The variations of the average N_{ij} and N_{eq} with 1/n for a range of A/B values, for w/d = 1, are shown in Fig. 3.4.9.

The variations of K_{ij} and K_{eq} with θ, for n = 1, 2, 4 and 8, with A/B = 0.1 and 10, are shown in Figs. 3.4.10 and 3.4.11. It can be seen that $K_{\theta\theta}$ and $K_{r\theta}$ are continuous functions whereas K_{rr} and K_{eq} are discontinuous at the interface ($\theta = 0^o$). Also, $K_{\theta\theta}$ appears to be continuous in slope as well as magnitude, at $\theta = 0^o$, but $K_{r\theta}$ is only continuous in magnitude. For a given A/B value, the general forms of each of the K_{ij} vs θ and K_{eq} vs θ plots are similar for all n values with the absolute magnitudes of the K_{ij} and K_{eq} values being dependent on n. Also, as Fig. 3.4.12 shows, the variations of K_{ij} and K_{eq} with θ (for A/B = 0.01, 0.1,10 and 100, with n = 2) are strongly dependent on A/B.

The maximum K_{rr} value occurs at the surface of material A (i.e. $\theta = 90^o$) when A/B < 1 and at the surface of material B (i.e. $\theta = -90^o$) when A/B > 1. The variation of the maximum value of K_{rr}, i.e. $\hat{K}_{rr}$, with 1/n, for w/d = 1, is shown in Fig. 3.4.13(a). It can be seen that $\hat{K}_{rr}$ increases as A/B increases above unity or decreases below unity and is greatest when n $\approx$ 8 (NB. results for higher n-values were not obtained). The $\hat{K}_{rr}$ results for a given A/B ratio are the same as those for the same B/A ratio (see Fig. 3.4.13(a)).

The maximum $K_{\theta\theta}$ value occurs at $\theta \approx 15^o$ (i.e. in material A) when A/B > 1 and at $\theta \approx -15^o$ (i.e. in material B) when A/B < 1. The $\hat{K}_{\theta\theta}$ values also appear to be greatest when n $\approx$ 8 (Fig. 3.4.13(b)). Variations of $|\hat{K}_{r\theta}|$ and $\hat{K}_{eq}$ with 1/n, for w/d = 1, are shown in Figs. 3.4.13(c) and 3.4.13(d). The $|\hat{K}_{r\theta}|$ values which occur at $\theta \approx 30^o$ for A/B < 1 and at $\theta \approx -30^o$ for A/B > 1, are less than unity (except for $n = \infty$ and for A/B = 1) and reduce with increasing 1/n for a given A/B value. The $\hat{K}_{eq}$ values are similar to the corresponding $\hat{K}_{rr}$

values. However, the $\hat{K}_{eq}$ values at the interface (i.e. $\theta = 0°$) are practically the same as the values at $\theta = -90°$ for $A/B > 1$.

(c) Effect of w/d

By comparing the K_{ij} and K_{eq} distributions for w/d = 1 (Fig. 3.4.12) with those for w/d = 0.5 (Fig. 3.4.14) and 0.1 (Fig. 3.4.15), it can be seen that the results for w/d = 0.5 and 1.0 are practically the same, but the w/d = 0.1 results are significantly different. This indicates that the w/d = 0.5 and 1.0 results are effectively applicable to remote conditions, i.e. the singularities at one of the interfaces are unaffected by the existence of the other interface. Hence, the w/d = 0.5 or 1.0 results are applicable for any w/d value greater than 0.5. However, when $A/B < 1$, the K_{ij} and K_{eq} distributions for w/d = 0.1, 0.5 and 1.0 are all practically the same. Hence, the results for w/d = 0.1, 0.5 and 1.0 are effectively applicable to remote conditions for $w/d > 0.1$ provided $A/B < 1$.

(d) General forms of the singularity equation

When w/d = 0.1, the K_{ij} and K_{eq} variations with θ, for $A/B > 1$, are different from those with w/d = 0.5 or 1.0. However, the average N_{ij} and N_{eq} values for a particular A/B value, are practically independent of w/d, as shown in Fig. 3.4.16. This indicates that the general forms of equations 3.4.2 are as follows:

$$\sigma_{ij} \;/\; \sigma_{nom} = K_{ij}\,(n,\ A/B,\ w/d)\,(r/d)^{-N(n,\ A/B)} \qquad (3.4.3(a))$$

and

$$\sigma_{eq} \;/\; \sigma_{nom} = K_{eq}\,(n,\ A/B,\ w/d)\,(r/d)^{-N(n,\ A/B)} \qquad (3.4.3(b))$$

However, when A/B ≤ 1 for w/d ≥ 0.1, or when A/B > 1 for w/d > 0.5, then

$$\sigma_{ij} / \sigma_{nom} = K_{ij}(n, A/B)(r/d)^{-N(n, A/B)} \qquad (3.4.4(a))$$

and

$$\sigma_{eq} / \sigma_{nom} = K_{eq}(n, A/B)(r/d)^{-N(n, A/B)} \qquad (3.4.4(b))$$

It should be noted that the exponent, N, in equations 3.4.3 and 3.4.4 is practically the same for any stress component and for the equivalent stress, when the n and A/B values are the same, (i.e., $N_{rr}(n, A/B) = N_{\theta\theta}(n, A/B) = N_{r\theta}(n, A/B) = N_{eq}(n, A/B)$).

3.4.4 Physical Significance of Stress Singularity

In reality the interfaces between weld material and HAZ material and between base material and HAZ material will not be as distinct as those represented by the idealised models analysed in this section. Hence there may be a gradual variation of creep properties across a small interface zone between the weld material and HAZ material and between the base material and the HAZ material. Also, on a small scale, the material cannot be regarded as a continuum, as represented by the creep constitutive equations (e.g. equations (3.4.1)). Hence, if the "singularity zone" is not significantly larger than metallurgical features such as the grain size etc., and larger than the interface zone width, then the calculated singularity will have no physical significance.

If the "singularity zone" is defined as the radial distance, r*, from the singularity point S, inside which the equivalent stress is greater than 2 × σ_{nom}, then the conditions under which the singularity is physically significant can be estimated. In Section 3.3, which presents the centre-line stresses, the σ_{eq}/σ_{nom} values are generally significantly less than 2 and hence

using $\sigma_{eq}/\sigma_{nom} = 2$ to obtain r* seems reasonable. Table 3.4.1 gives r*/d values for n = 1 to 8 and A/B = 0.01 (or 100) and 0.1 (or 10). If r*/d > 0.01, then it is likely that the singularity would have physical significance for practical specimen diameters (typically 7 to 20 mm). Hence the results in Table 3.4.1 indicate that for n values greater than about 4, the singularity is unlikely to have physical significance except for the A/B >> 100 (or << 0.01).

Table 3.4.1 r/d values for various n and A/B values*

(r is defined as the radial position at which $\sigma_{eq}/\sigma_{nom} = 2$)*

A/B n	1	2	4	8
0.01(100)	0.1234	0.1028	0.0276	1.0066×10^{-4}
0.1(10)	0.0364	0.0201	4.0898×10^{-5}	4.2595×10^{-22}

3.4.5 Conclusions

The stress singularity in the vicinity of the surface at the interface of an axisymmetric two-material creep test specimen was found to be of the form $\sigma_{ij} = \sigma_{nom} K_{ij} (r/d)^{-N}$ (and $\sigma_{eq} = \sigma_{nom} K_{eq} (r/d)^{-N}$). The exponent N was found to be practically the same for all stress components and for the equivalent stress and it was found to be independent of angular position, θ. The N value was found to be dependent upon the material creep constants, i.e. n and A/B, but was not a function of geometry, i.e. w/d. The K_{ij} and K_{eq} functions, which describe the variations of stress with angular position, θ, were found to be functions of n, A/B and w/d. However, for w/d > 0.5, K_{ij} and K_{eq} are independent of w/d.

For practical purposes, the singularity is unlikely to be important for n-values greater than about 4, unless A/B is very large (>>100) or very small (<<0.01).

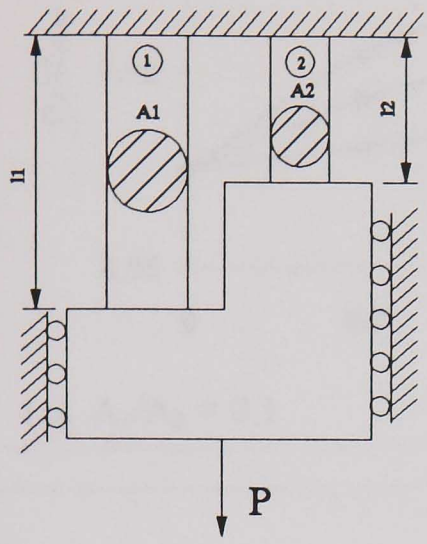

(a) two-bar struture

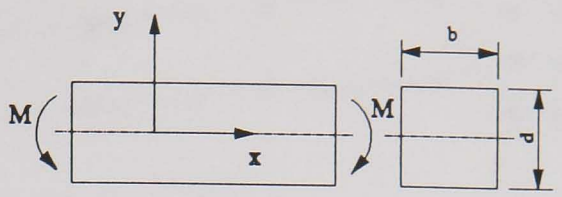

(b) rectangular cross-sectioned beam subjected to pure bending

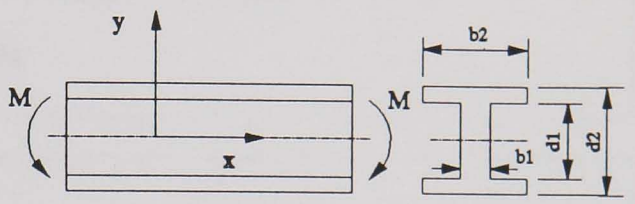

(c) I-sectioned beam subjected to pure bending

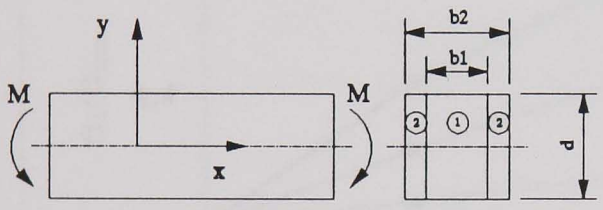

(d) two-material beam subjected to pure bending(case 1)

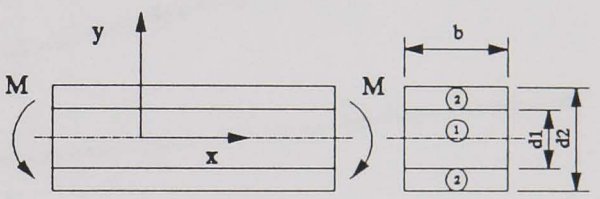

(e) two-material beam subjected to pure bending(case 2)

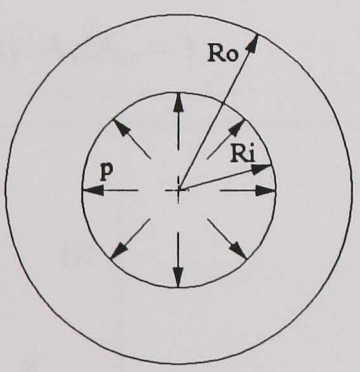

(f) thick cylinder subjected to internal pressure

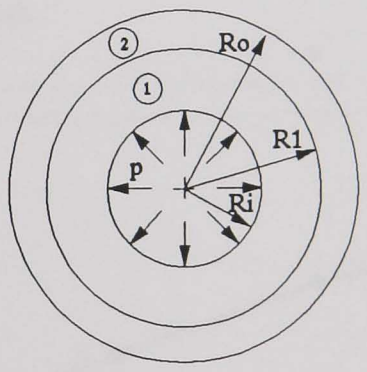

(g) two-material thick cylinder subjected to internal pressure

Fig. 3.2.1 Dimensions of the structures used.

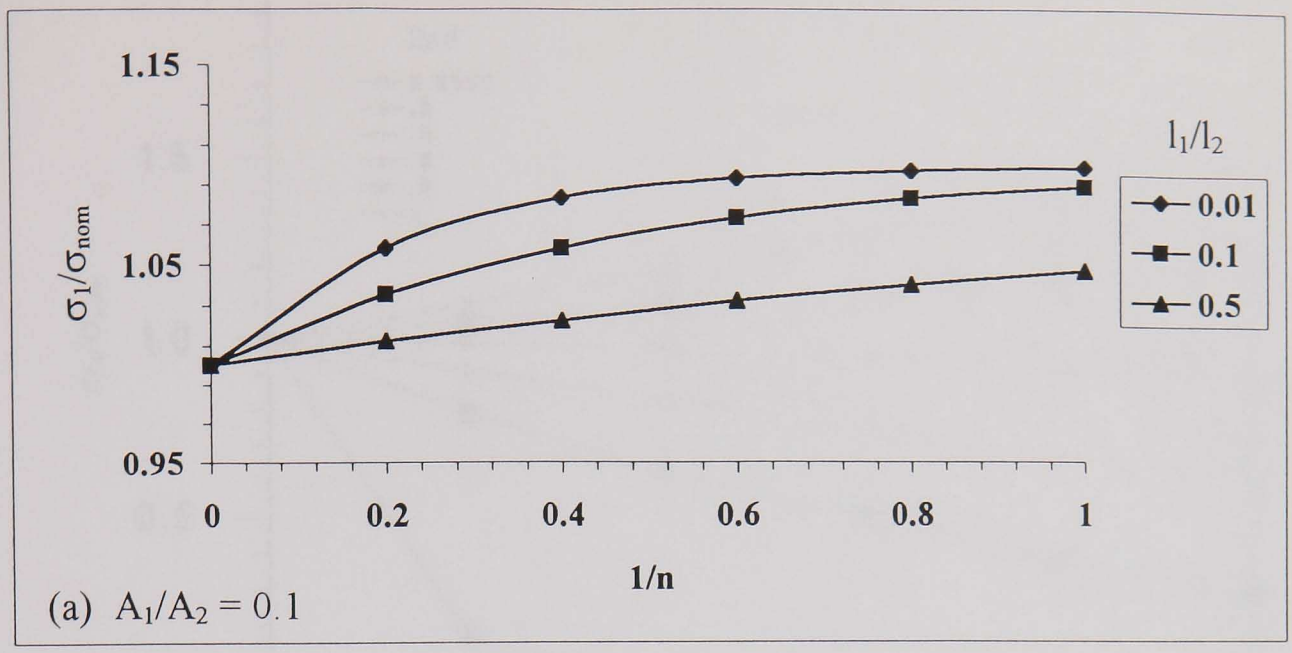

(a) $A_1/A_2 = 0.1$

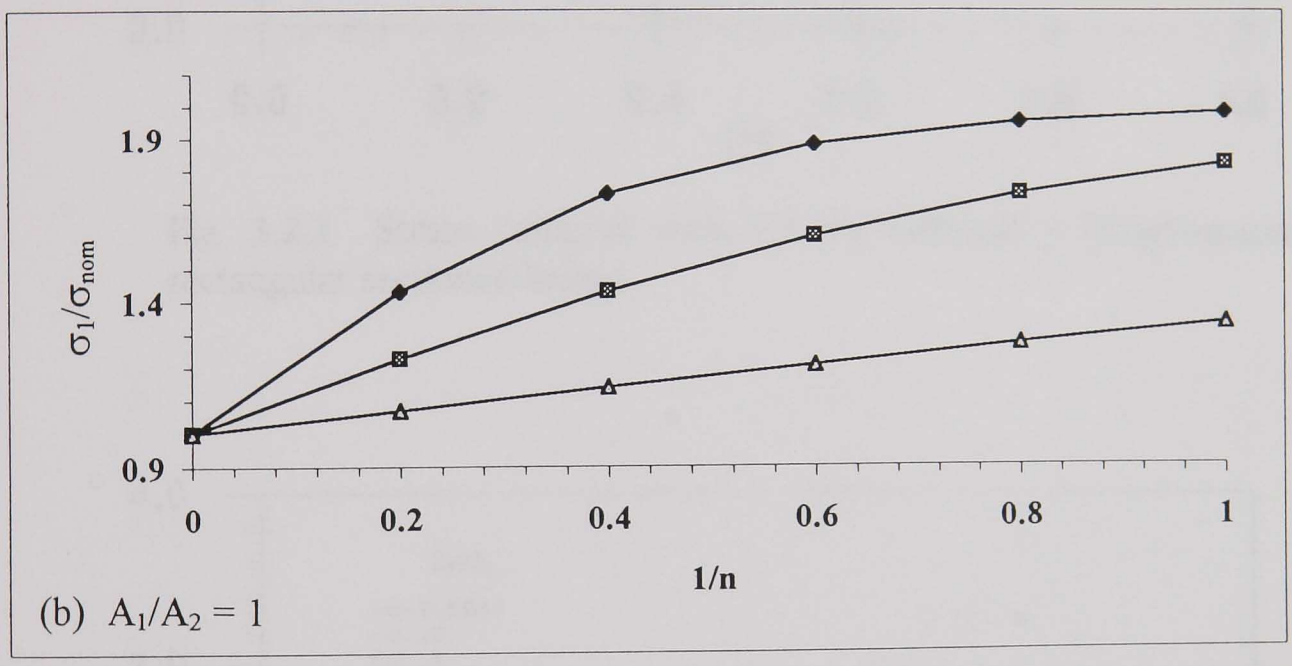

(b) $A_1/A_2 = 1$

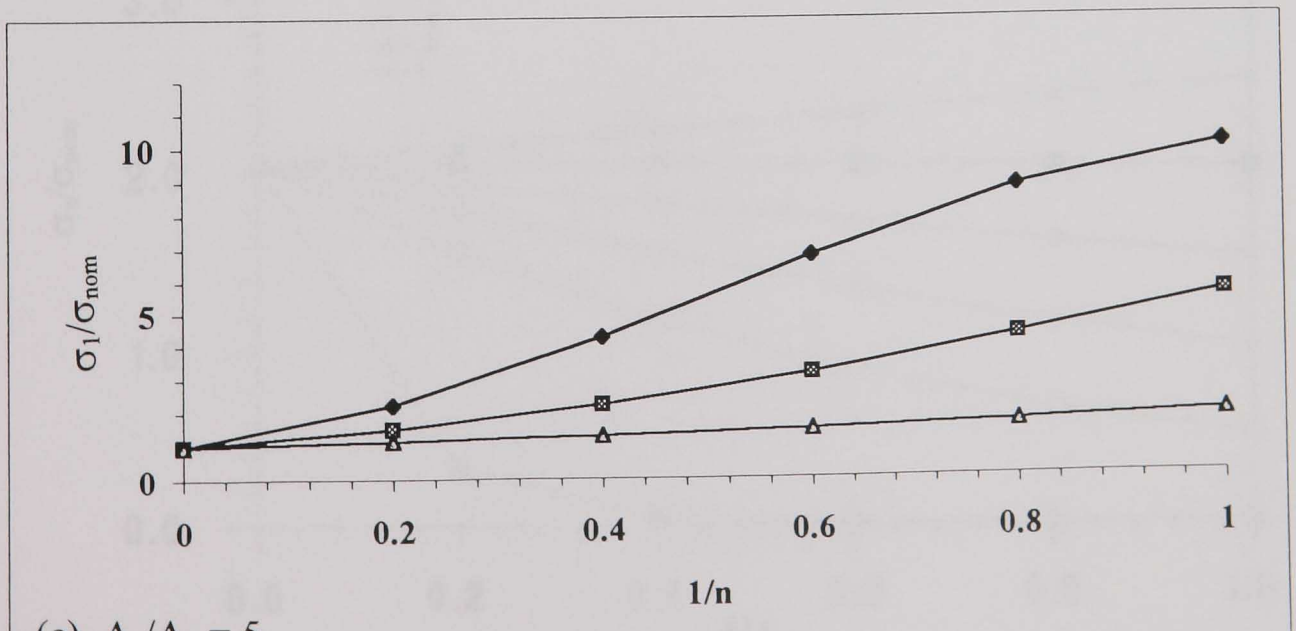

(c) $A_1/A_2 = 5$

Fig. 3.2.2 σ_1 in single-material two-bar structure against 1/n with different l_1/l_2 ($\sigma_1 > \sigma_2$ in this case).

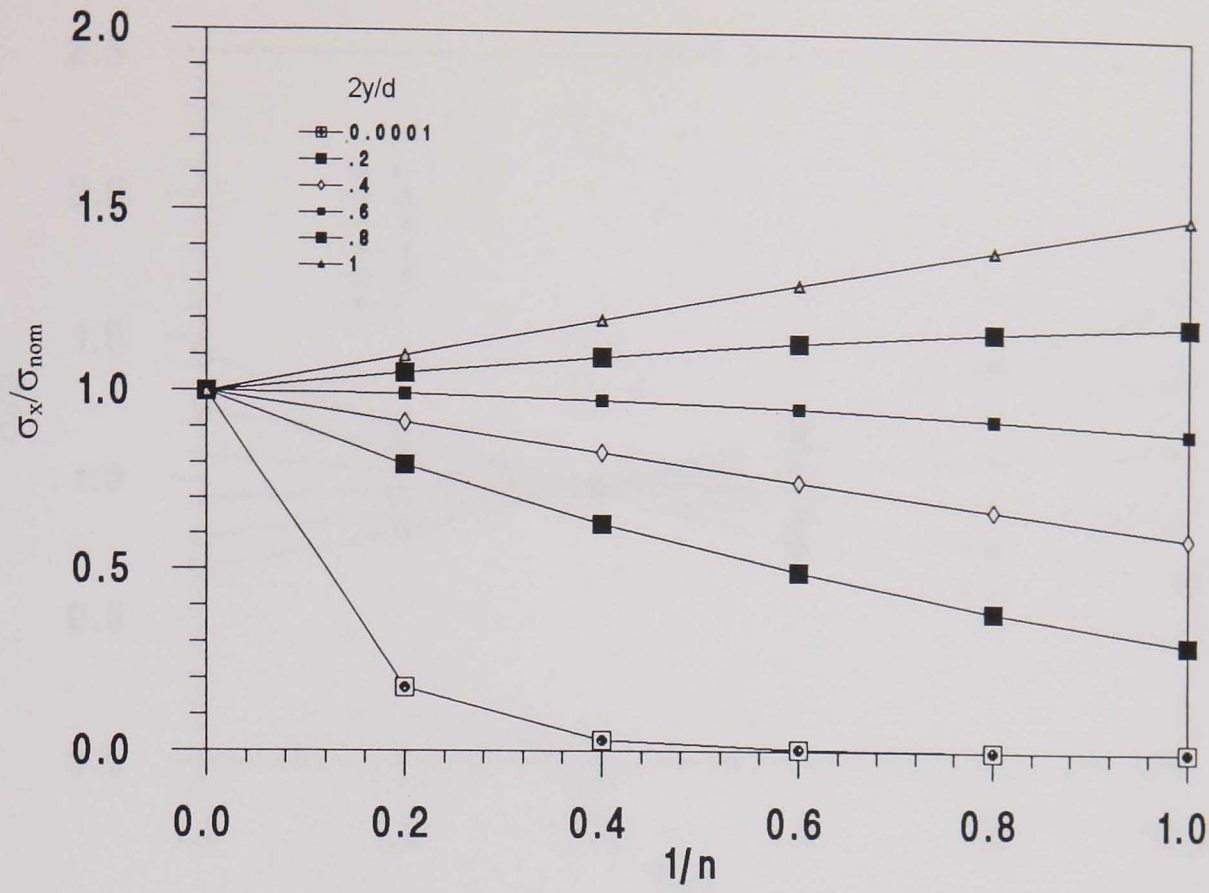

Fig. 3.2.3 Stress variation with 1/n for different y (single-material rectangular sectioned beam).

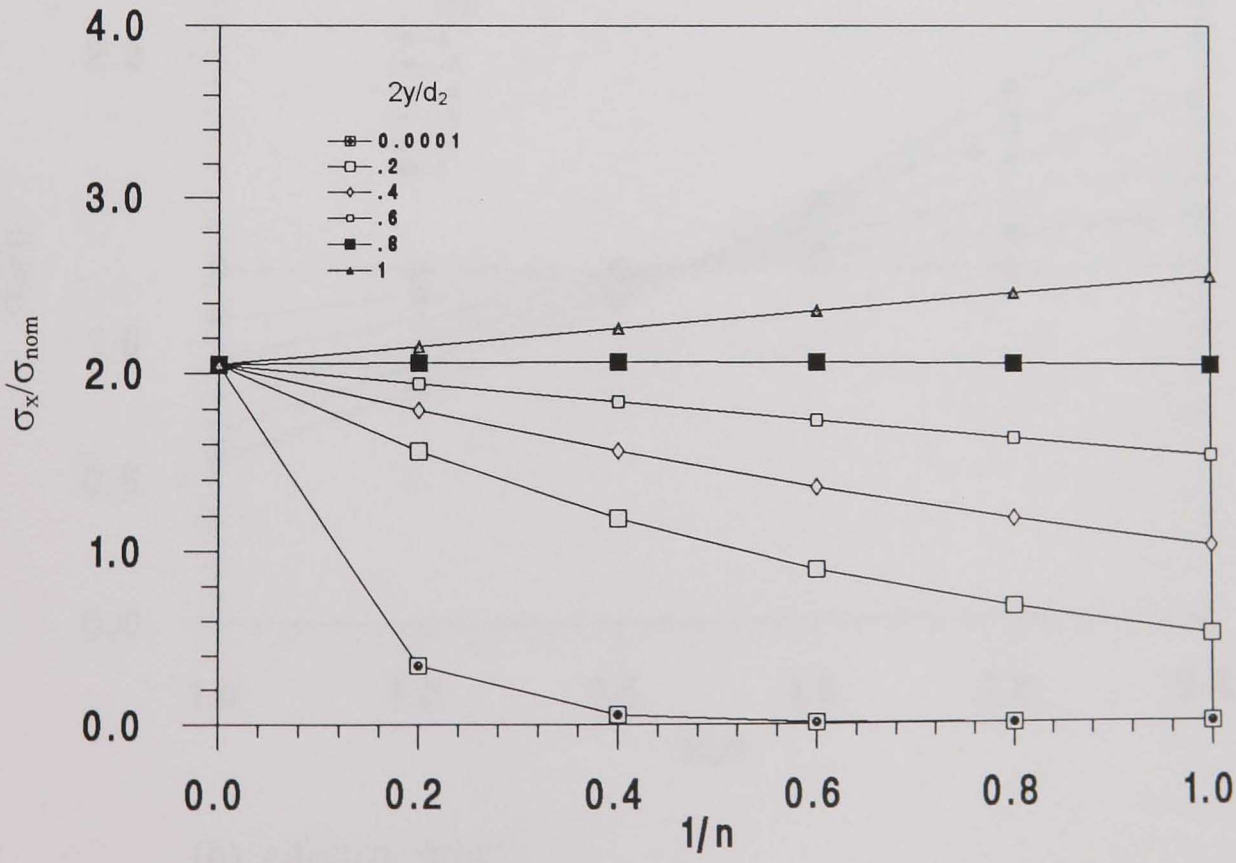

Fig. 3.2.4 Stress variation with 1/n for different y (single-material I-sectioned beam, $b_1/b_2 = 0.2$, $d_1/d_2 = 0.8$).

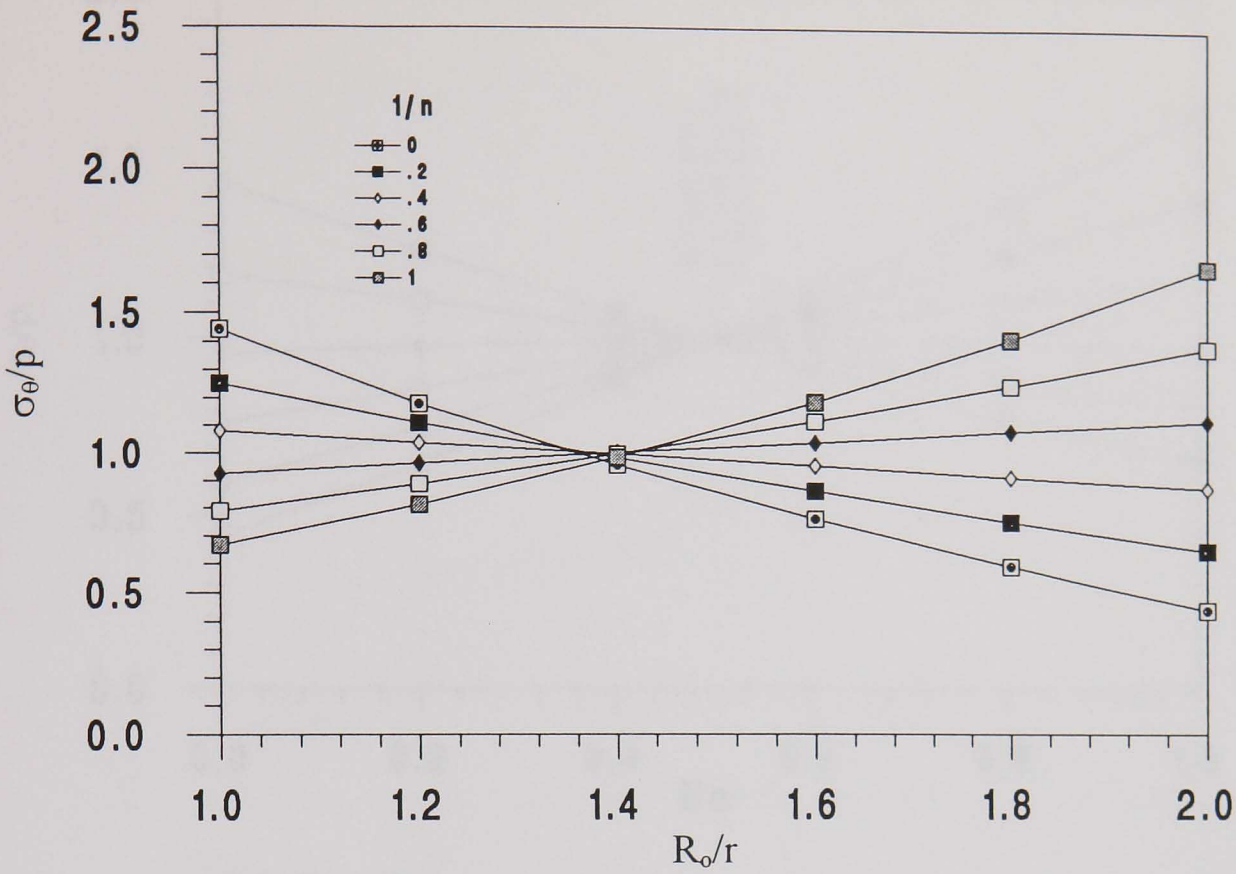

(a) hoop stress

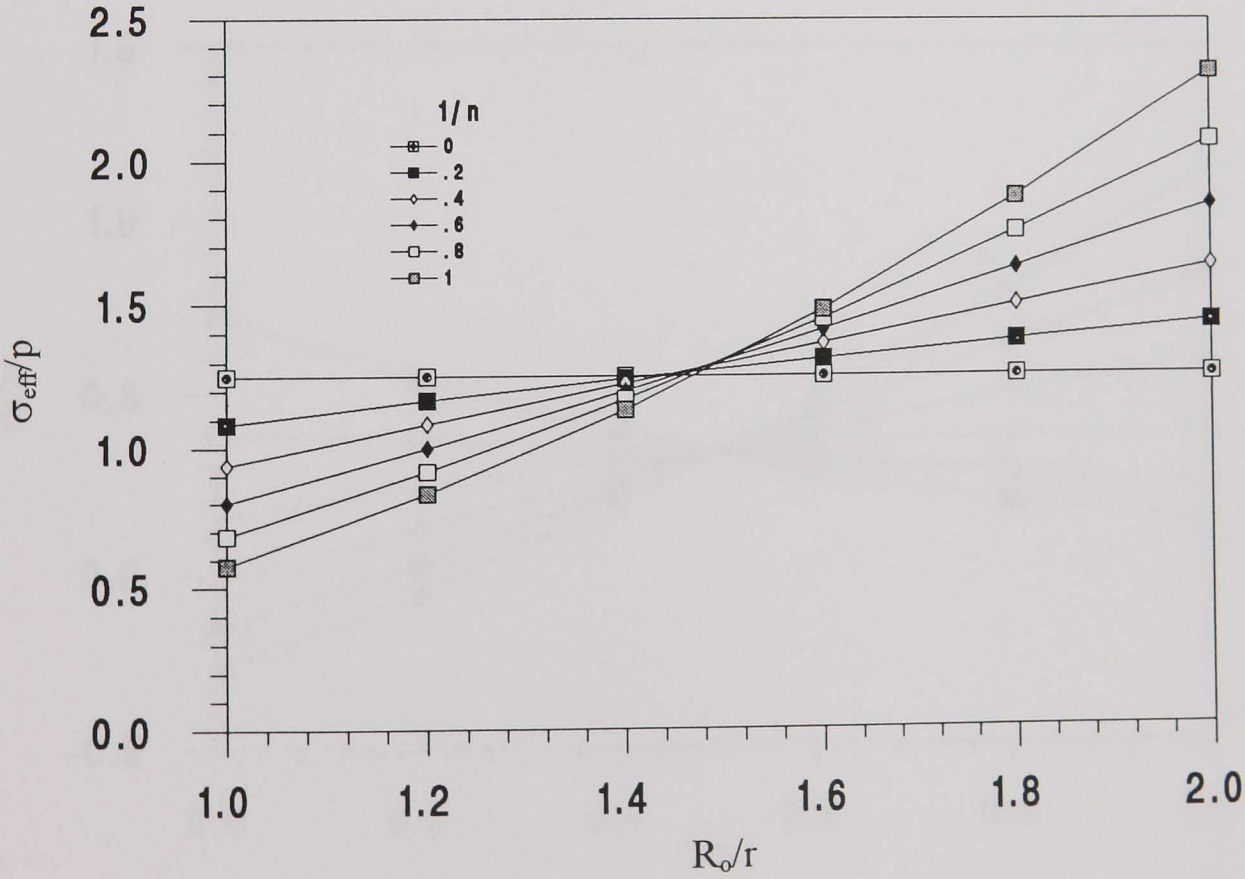

(b) effective stress

Fig. 3.2.5 Stress vatiation against r with different n (single-material thick cylinder, $R_o/R_i = 2$).

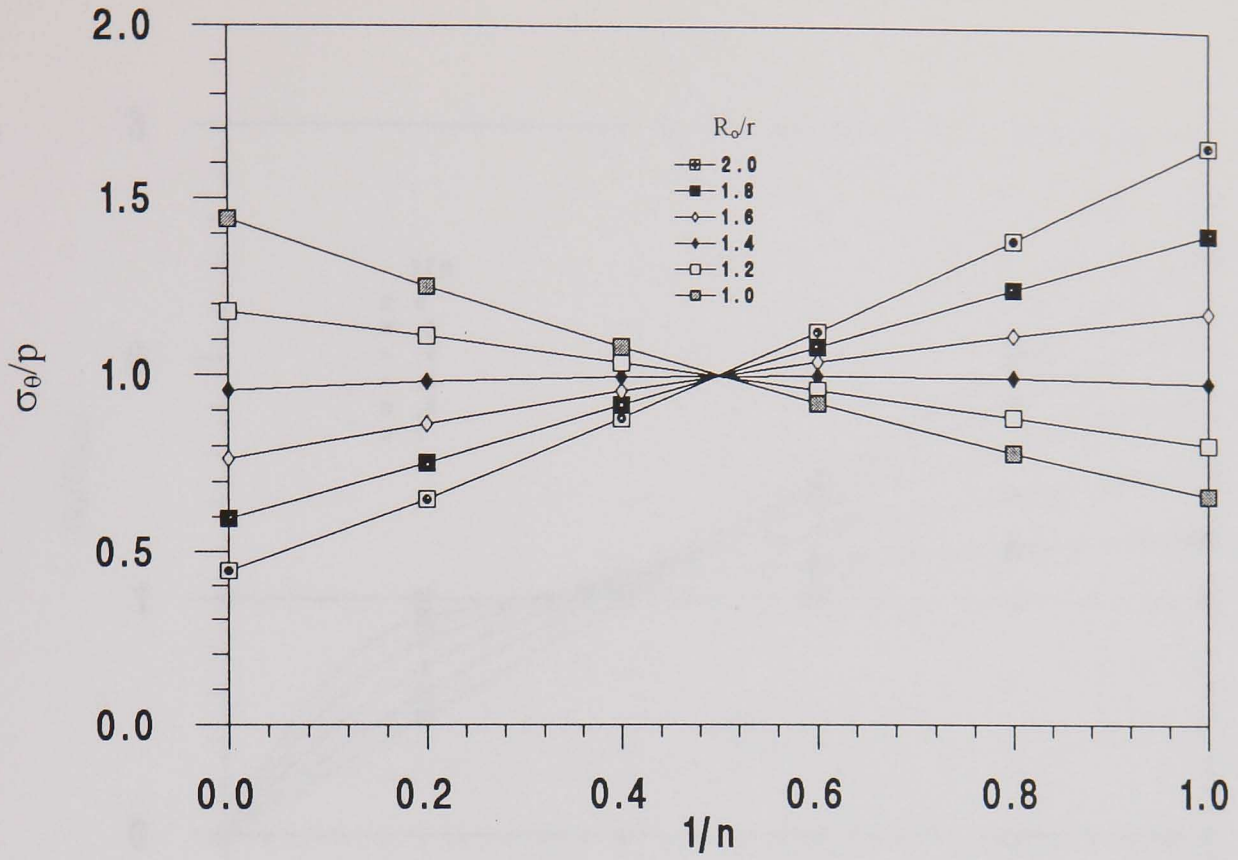

(a) $R_o/R_i = 2$

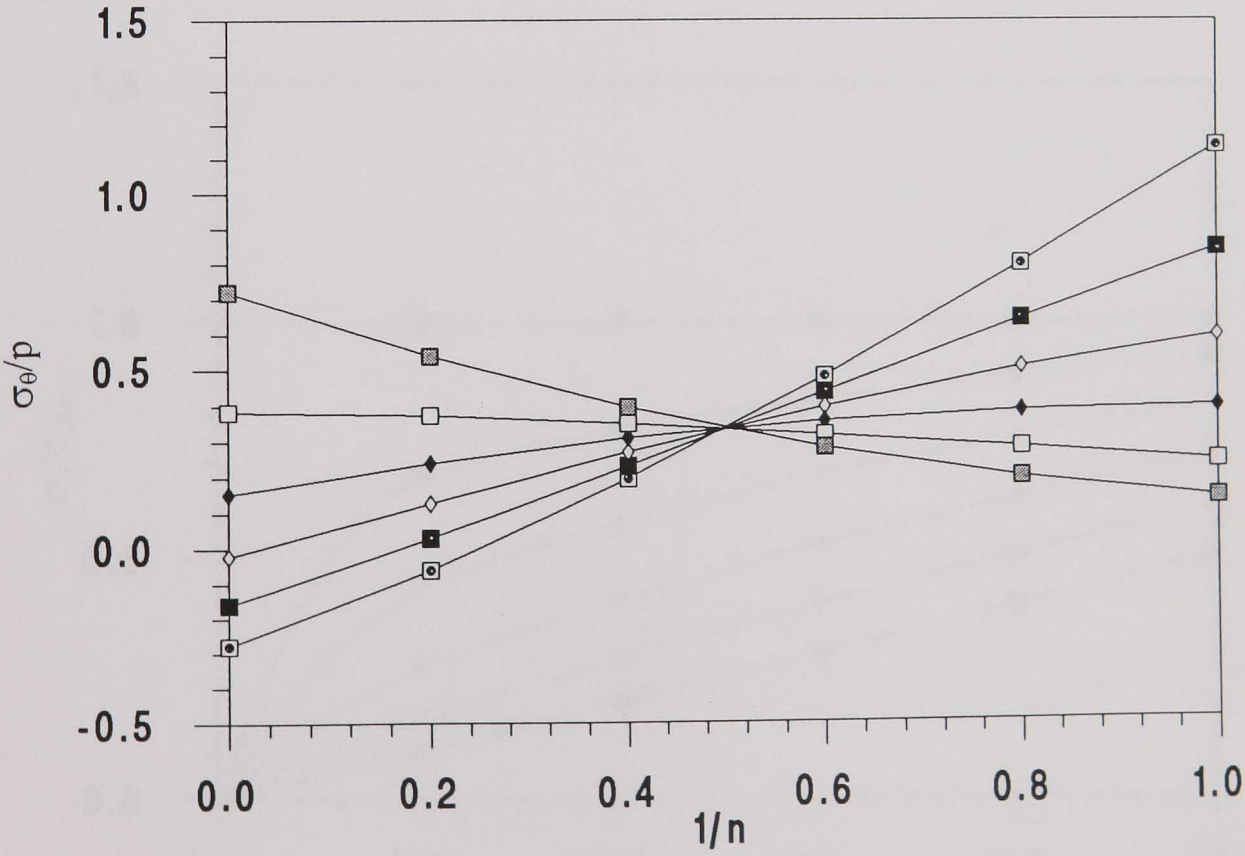

(b) $R_o/R_i = 4$

Fig. 3.2.6 Hoop stress variation with 1/n for different r (single-material thick cylinder).

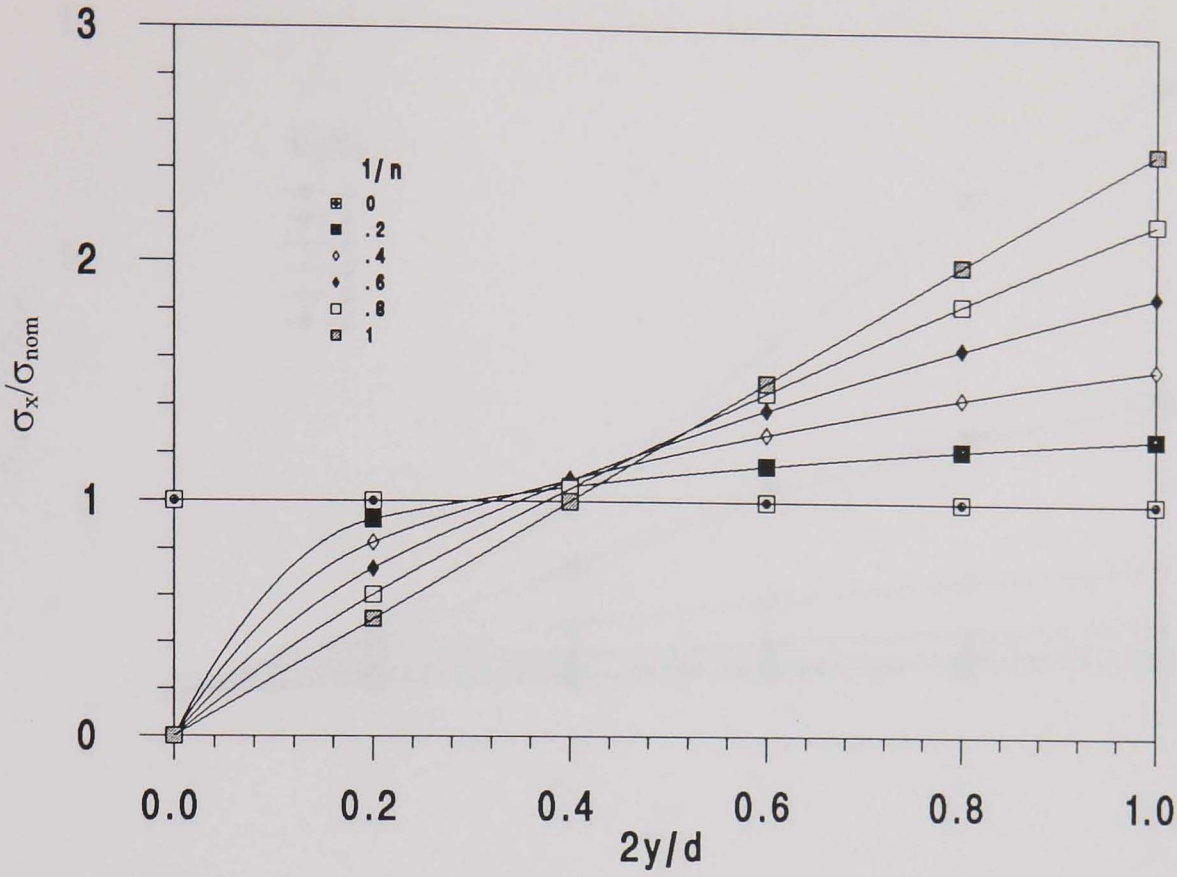

(a) stress in material 1

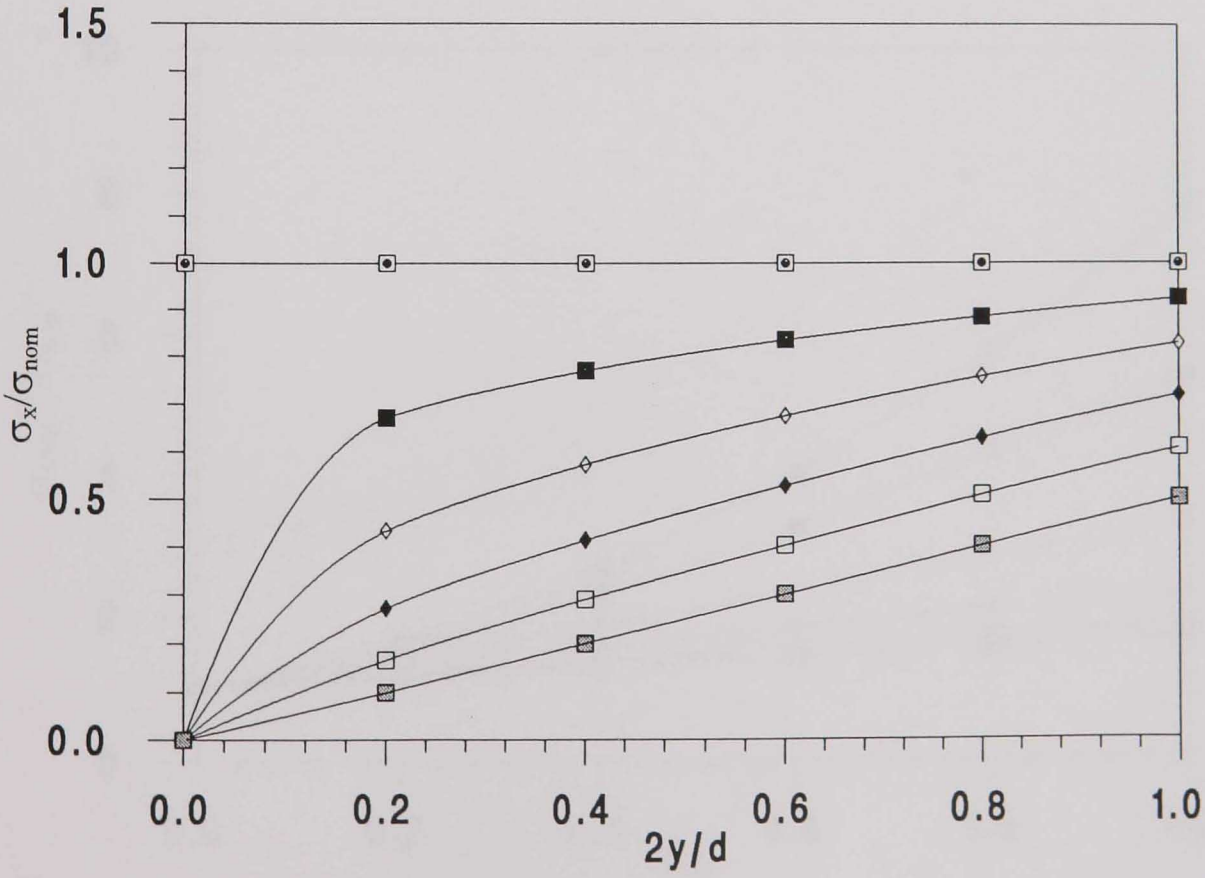

(b) stress in material 2

Fig. 3.2.7 Stress variation with y for different n (two-material beam, case(1), $B_2/B_1 = 5$, $b_1/b_2 = 0.5$).

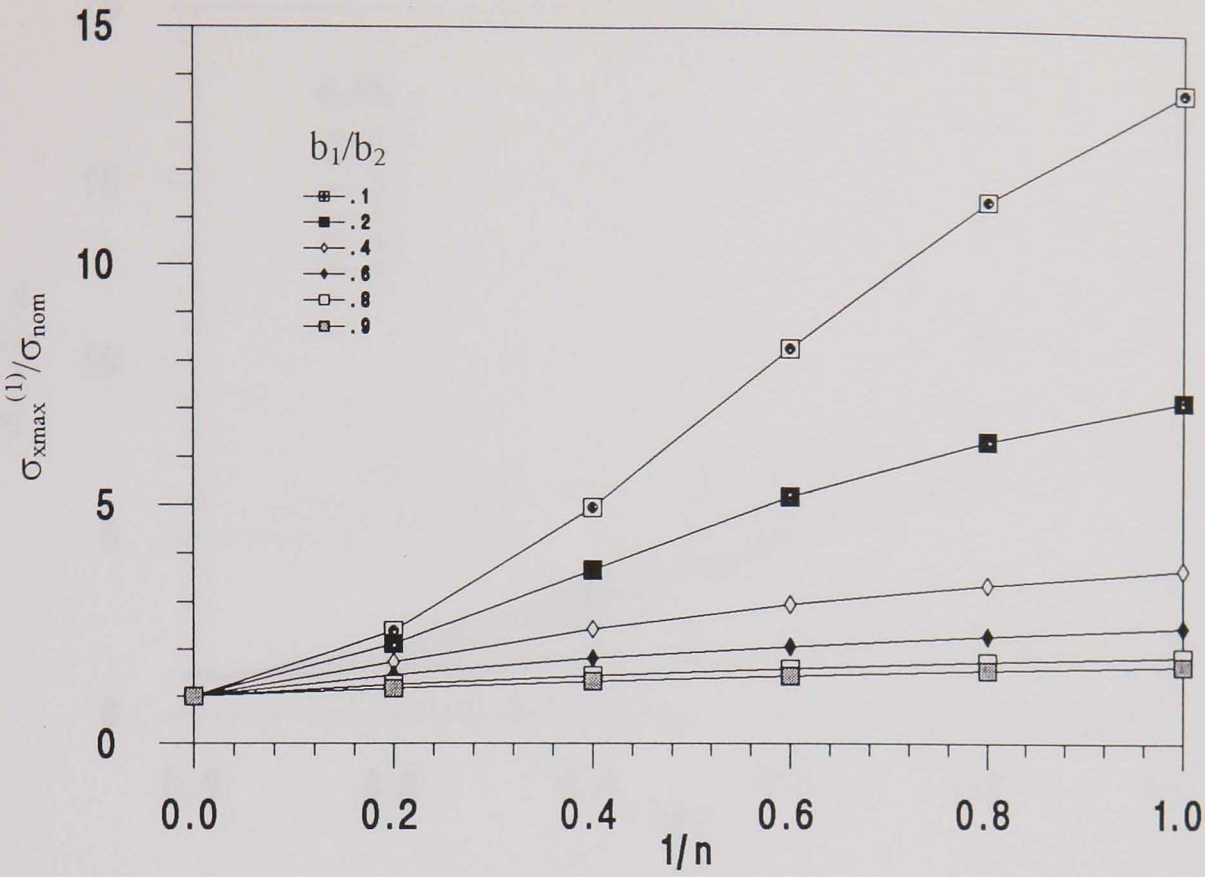

(a) $B_1/B_2 = 0.01$

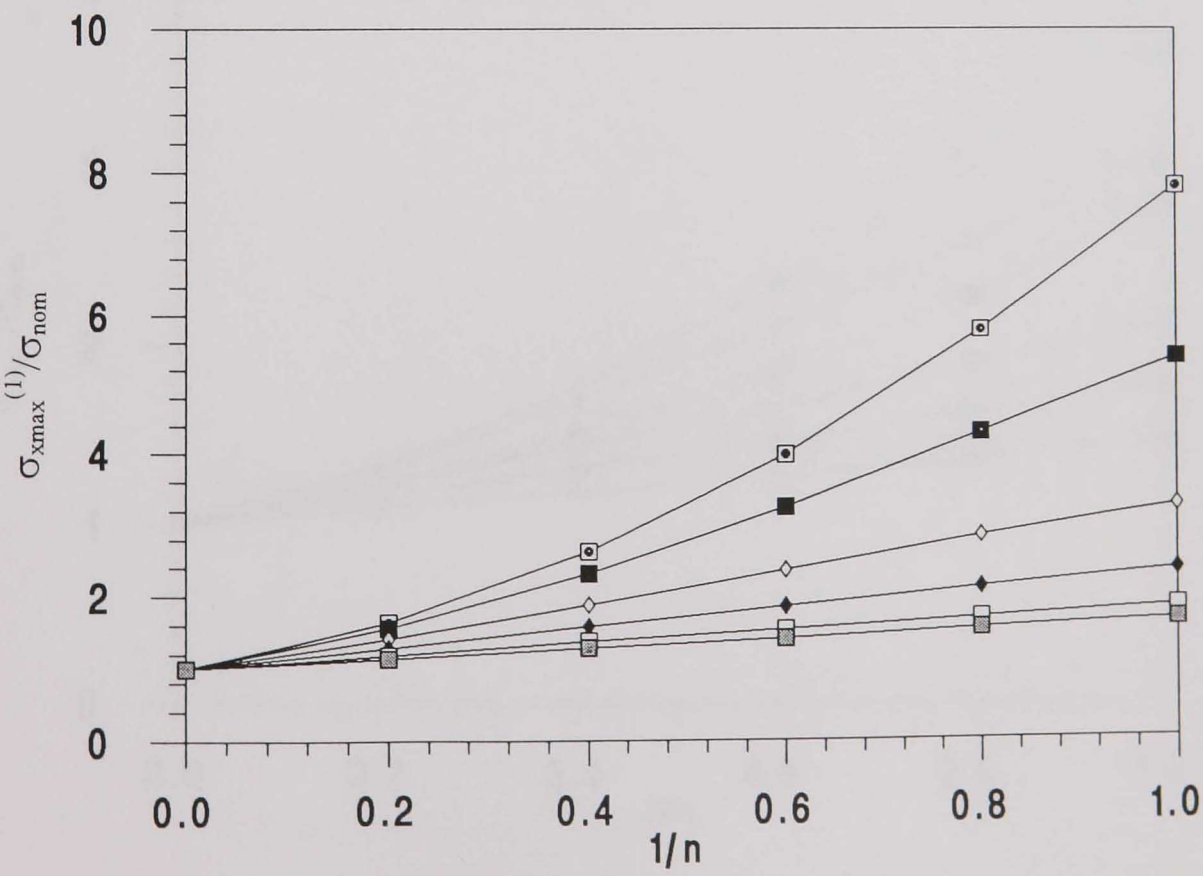

(b) $B_1/B_2 = 0.1$

Fig. 3.2.8 Stress variation with 1/n for different b_1/b_2 (two-material beam, case(1)).

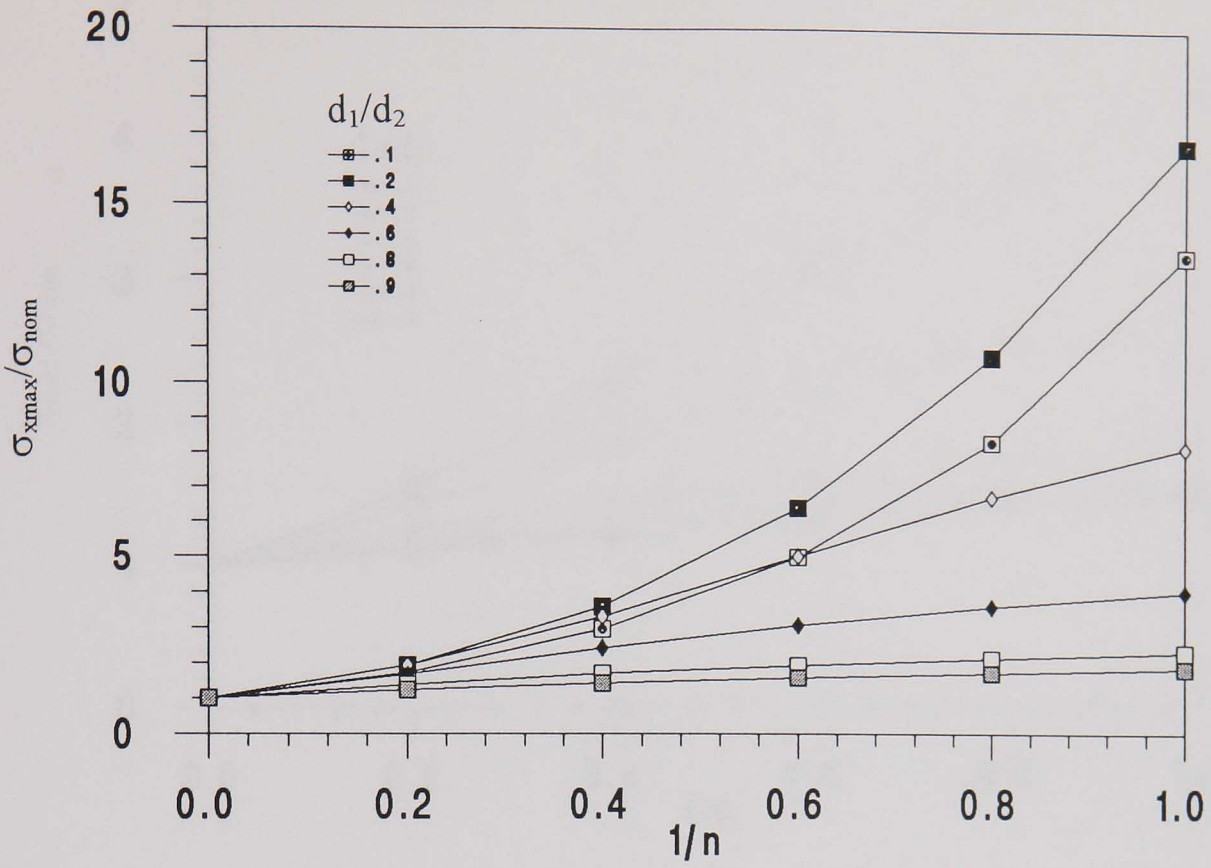

3.2.9(a) material 1, $B_1/B_2 = 0.01$

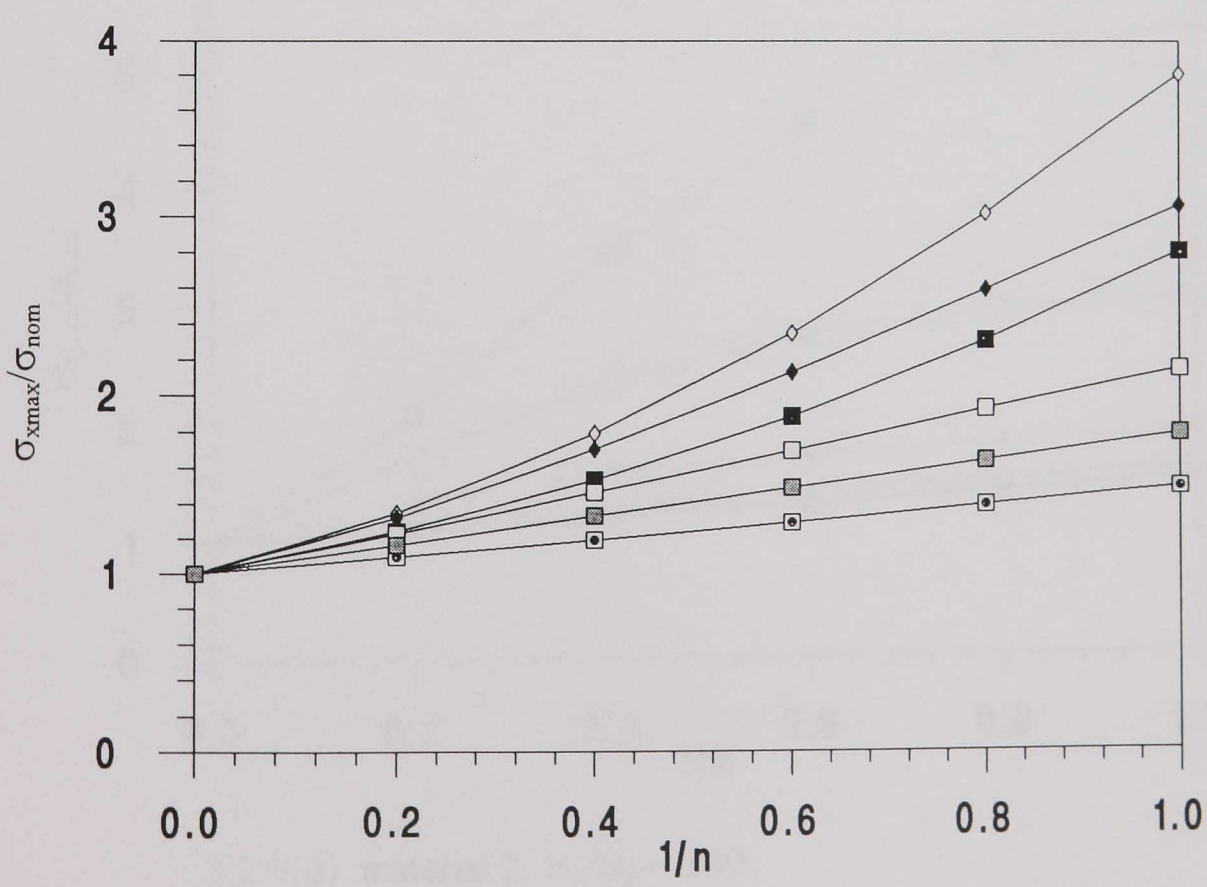

3.2.9(b) material 1, $B_1/B_2 = 0.1$

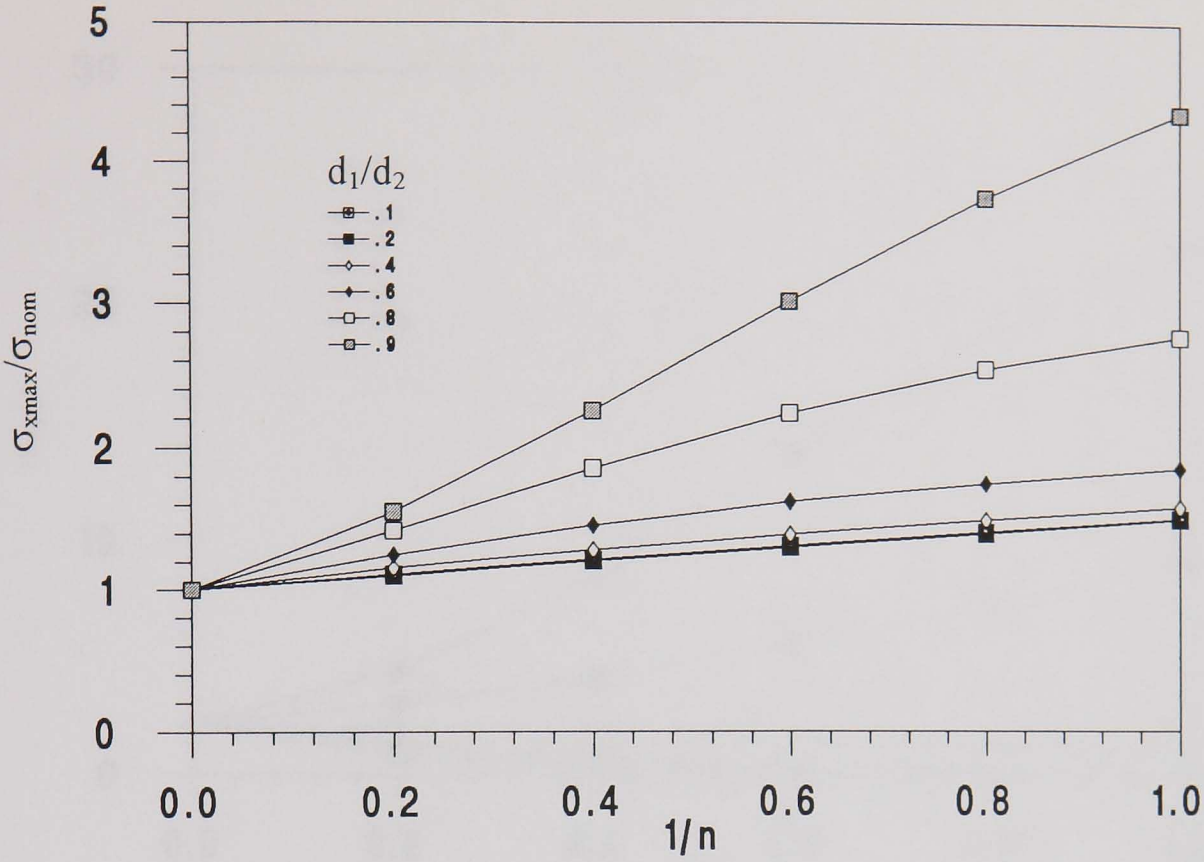

3.2.9(c) material 2, $B_1/B_2 = 10$

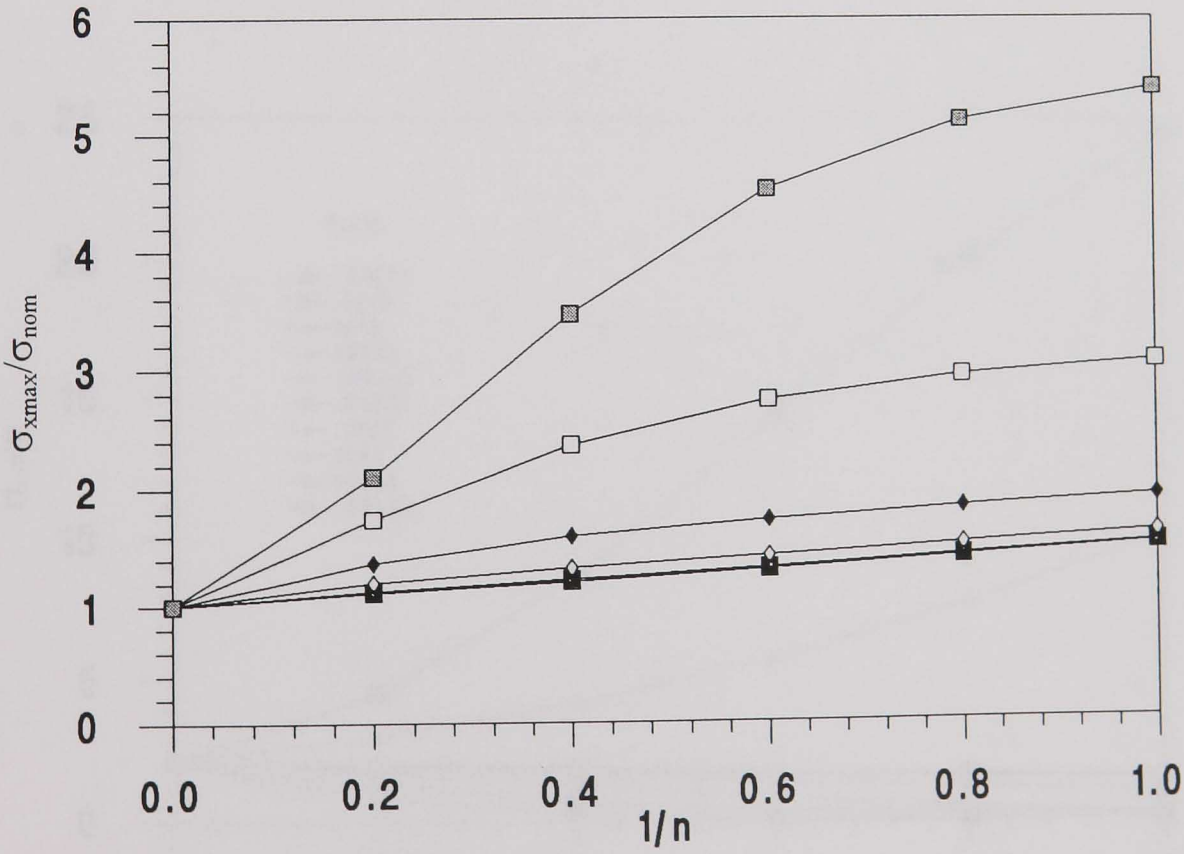

3.2.9(d) material 2, $B_1/B_2 = 100$

Fig. 3.2.9 Stress variation with 1/n for different d_1/d_2 (two-material beam, case(2)).

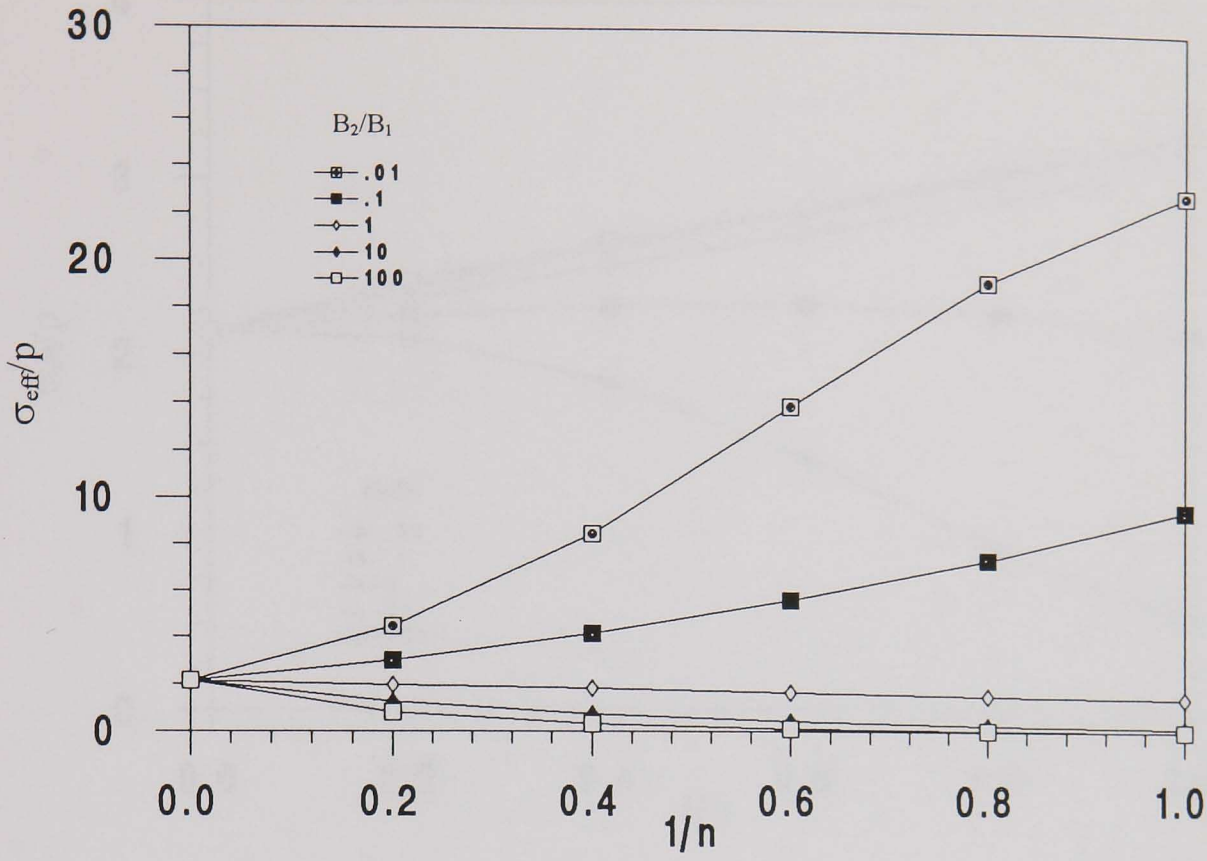

3.2.10(a) $T_2/T_1 = 0.1$, $r = R_o$

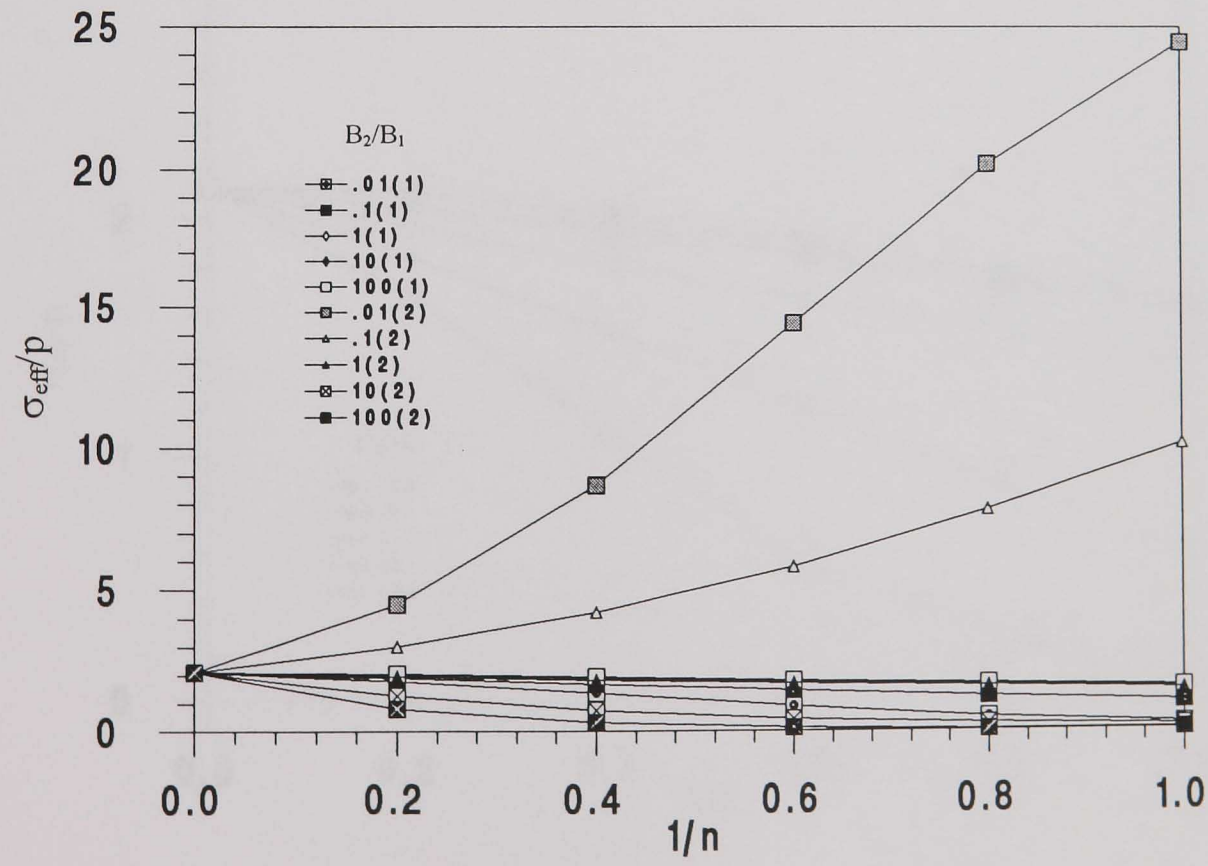

3.2.10(b) $T_2/T_1 = 0.1$, $r = R_1$

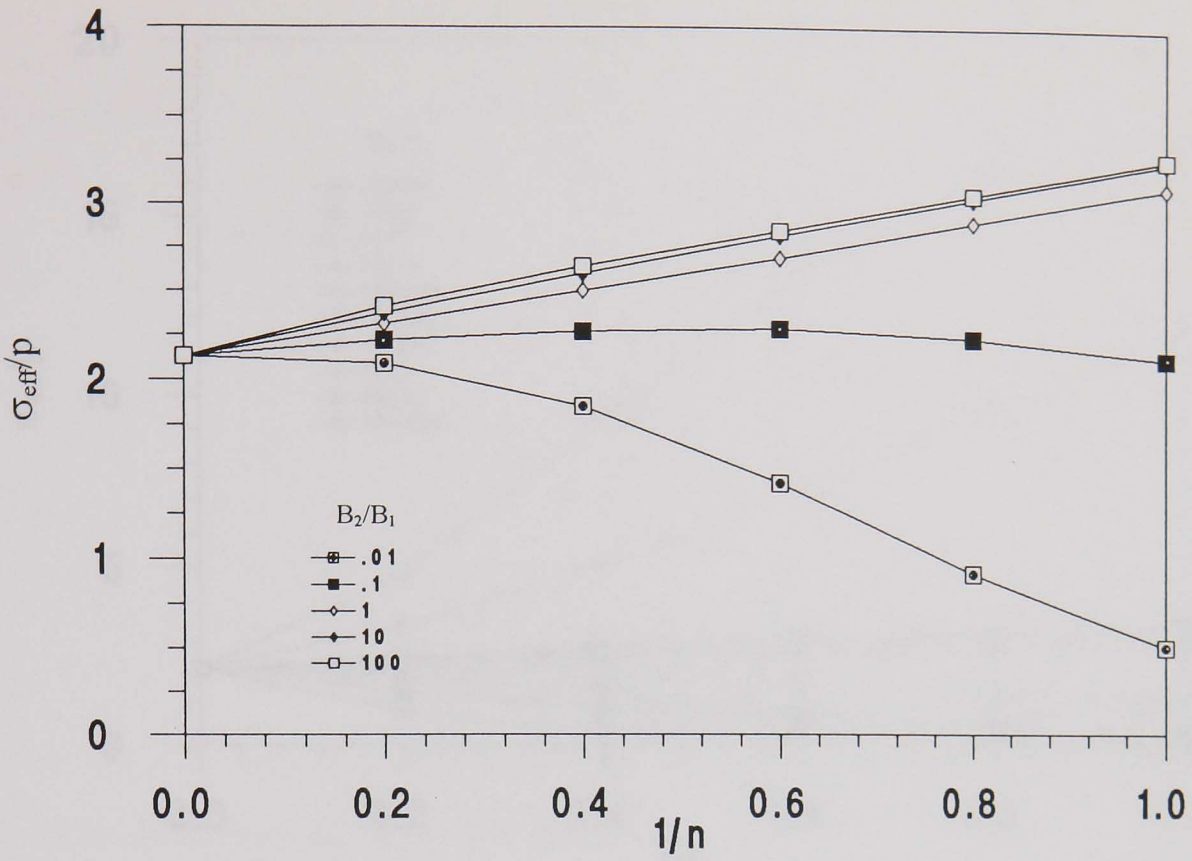

3.2.10(c) $T_2/T_1 = 0.1$, $r = R_i$

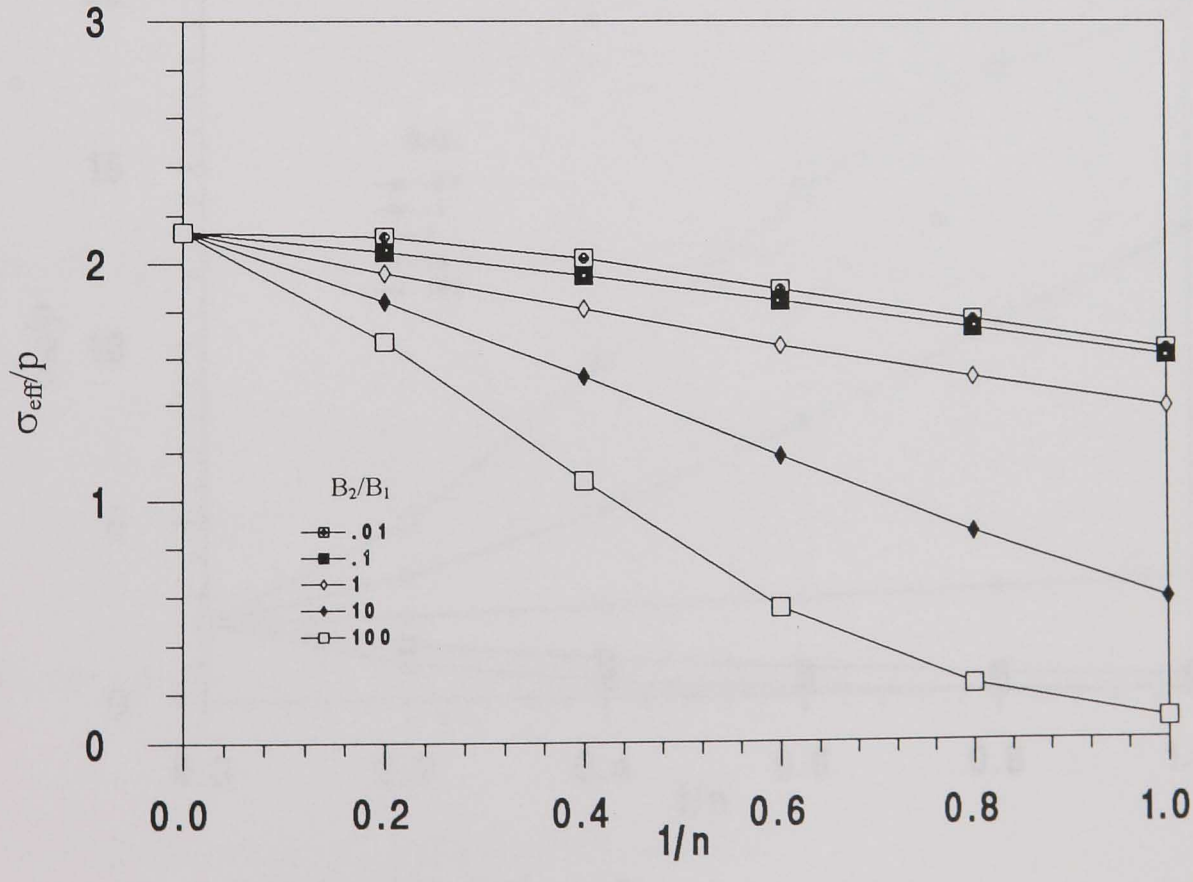

3.2.10(d) $T_2/T_1 = 10$, $r = R_o$

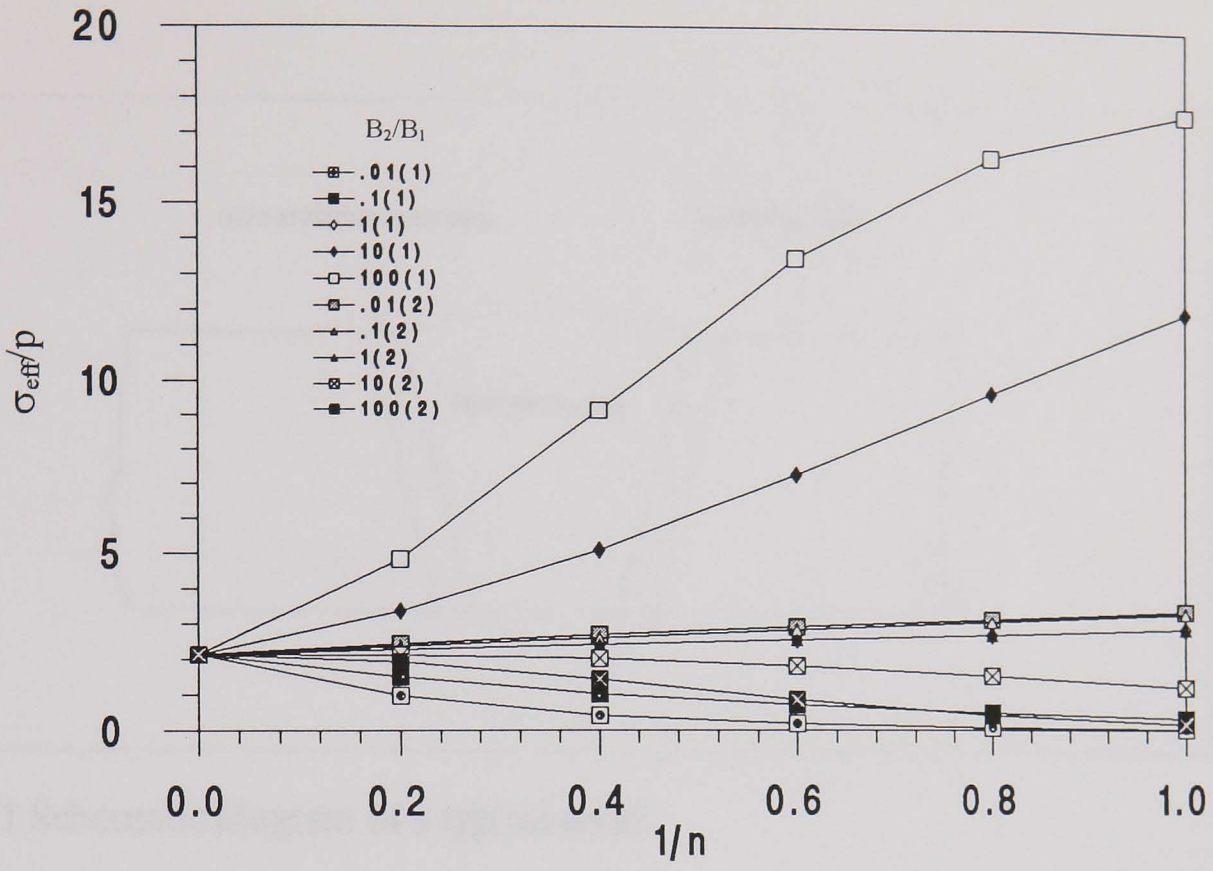

3.2.10(e) $T_2/T_1 = 10$, $r = R_1$

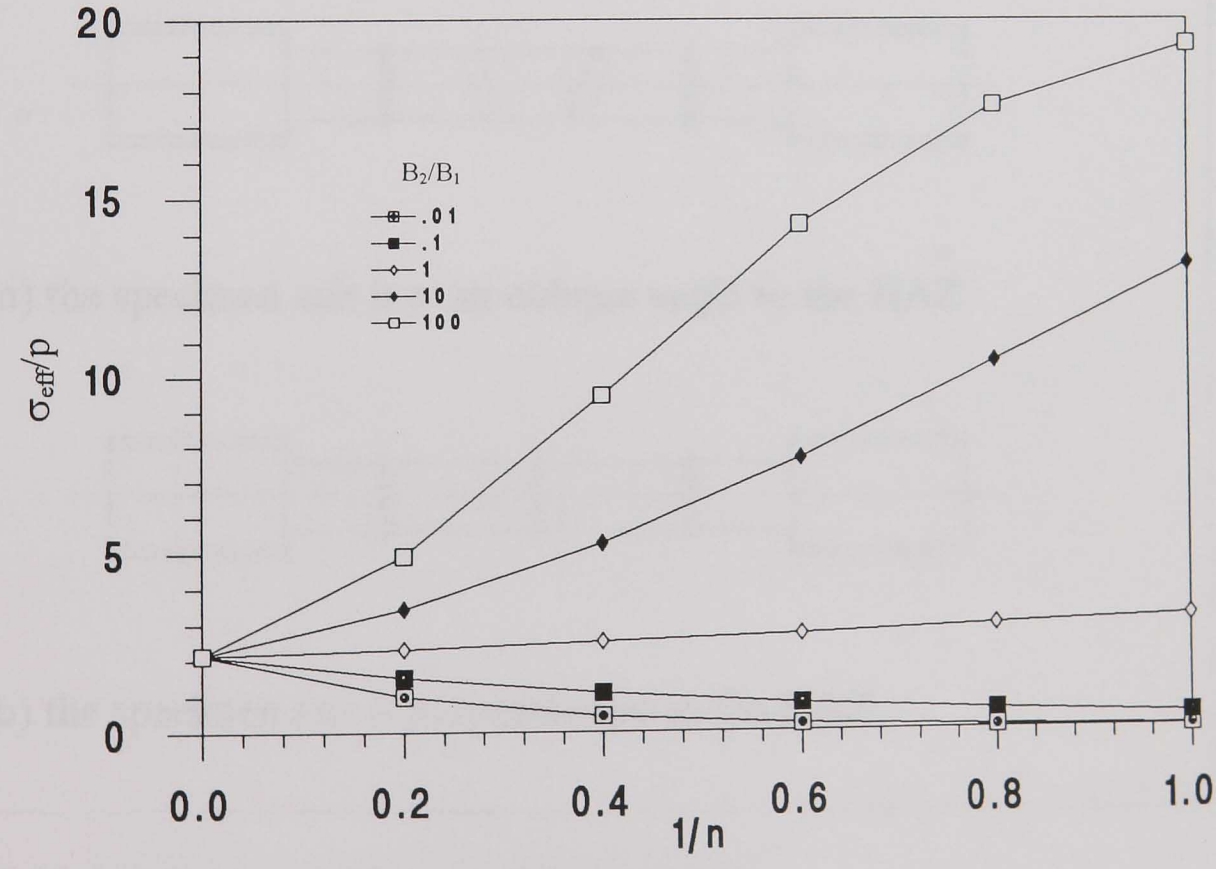

3.2.10(f) $T_2/T_1 = 10$, $r = R_i$

Fig. 3.2.10 Variation of effective stress with 1/n for different B_2/B_1 (two-material thick cylinder, $R_o/R_i = 1.5$, $T_2/T_1 = (R_o-R_1)/(R_1-R_i)$).

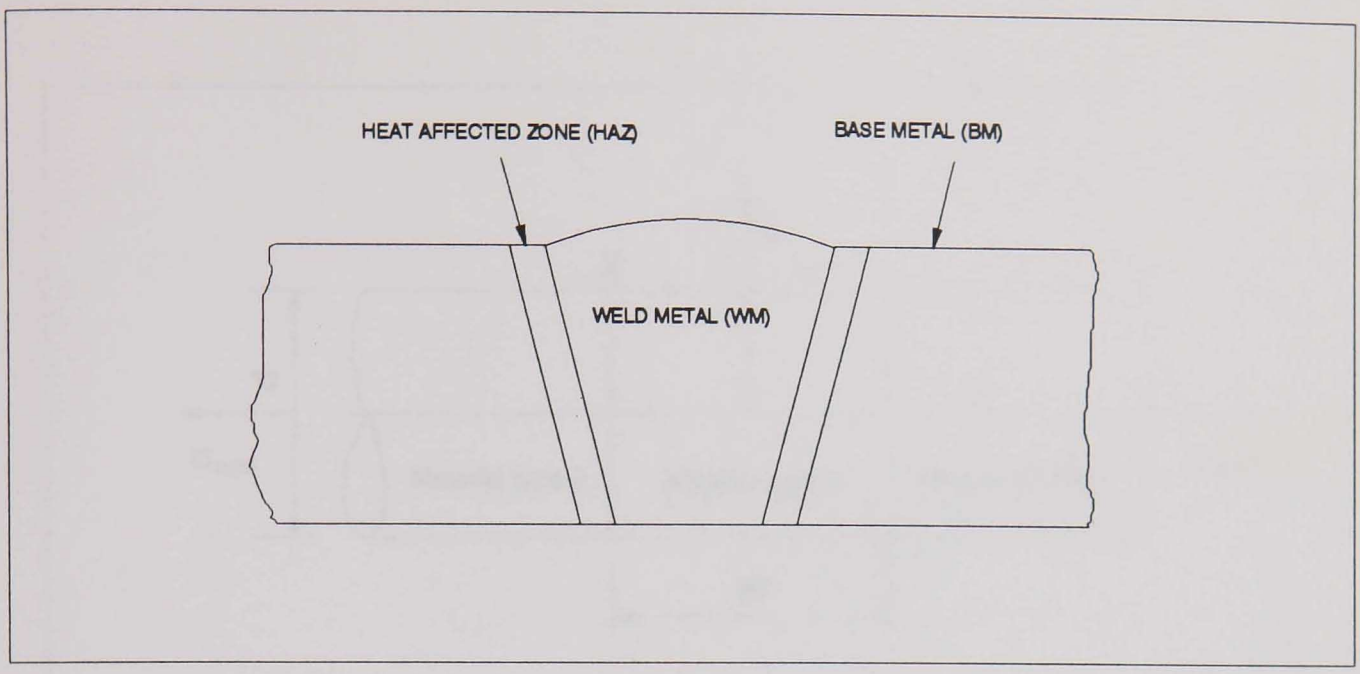

Fig. 3.3.1 Schematic diagram of a typical weld.

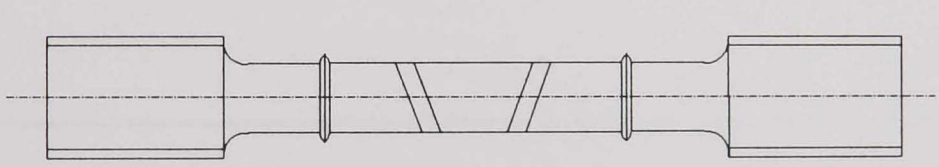

(a) the specimen axis is at an oblique angle to the HAZ

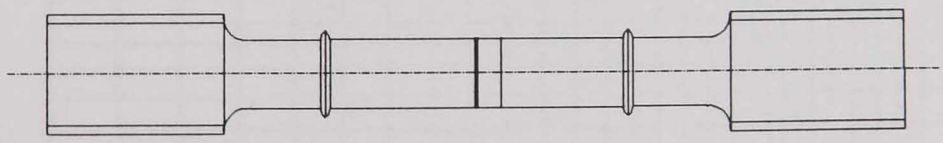

(b) the specimen axis is perpendicular to the HAZ

Fig. 3.3.2 Uniaxial cross-weld creep test specimens.

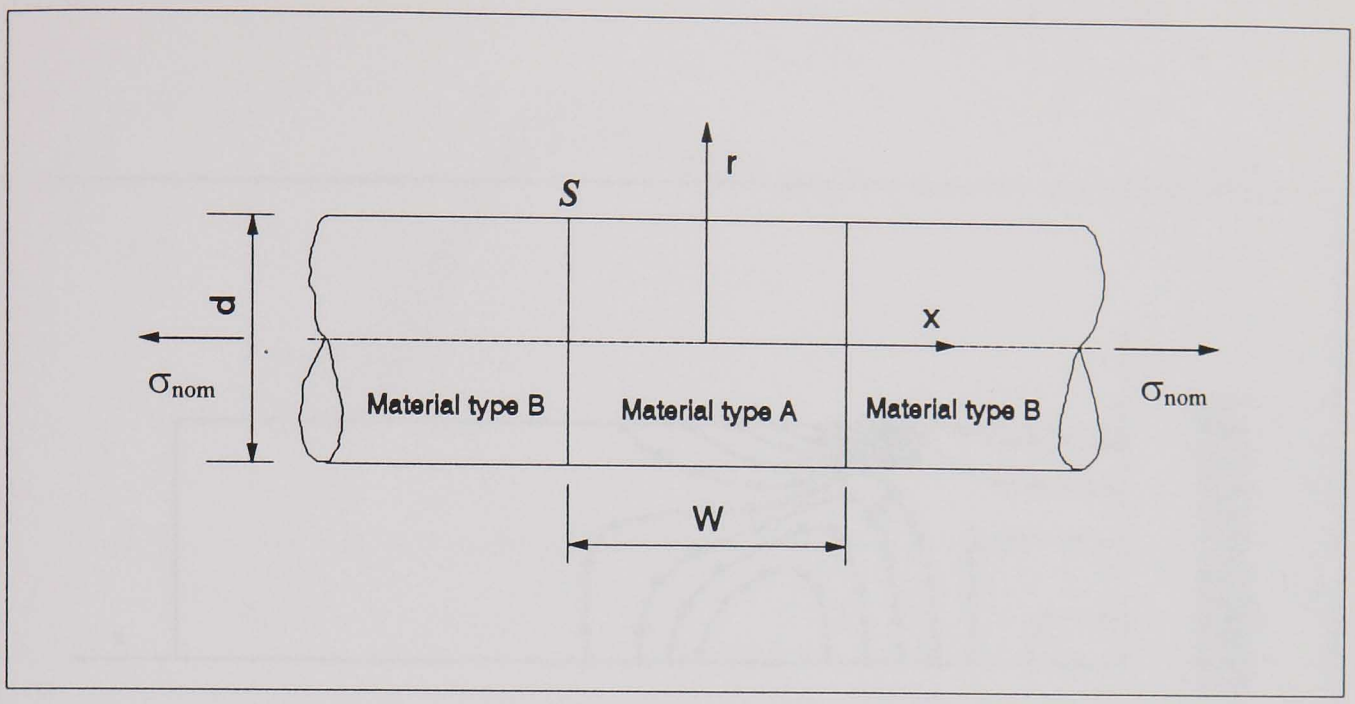

Fig. 3.3.3 Idealised cross-weld specimen.

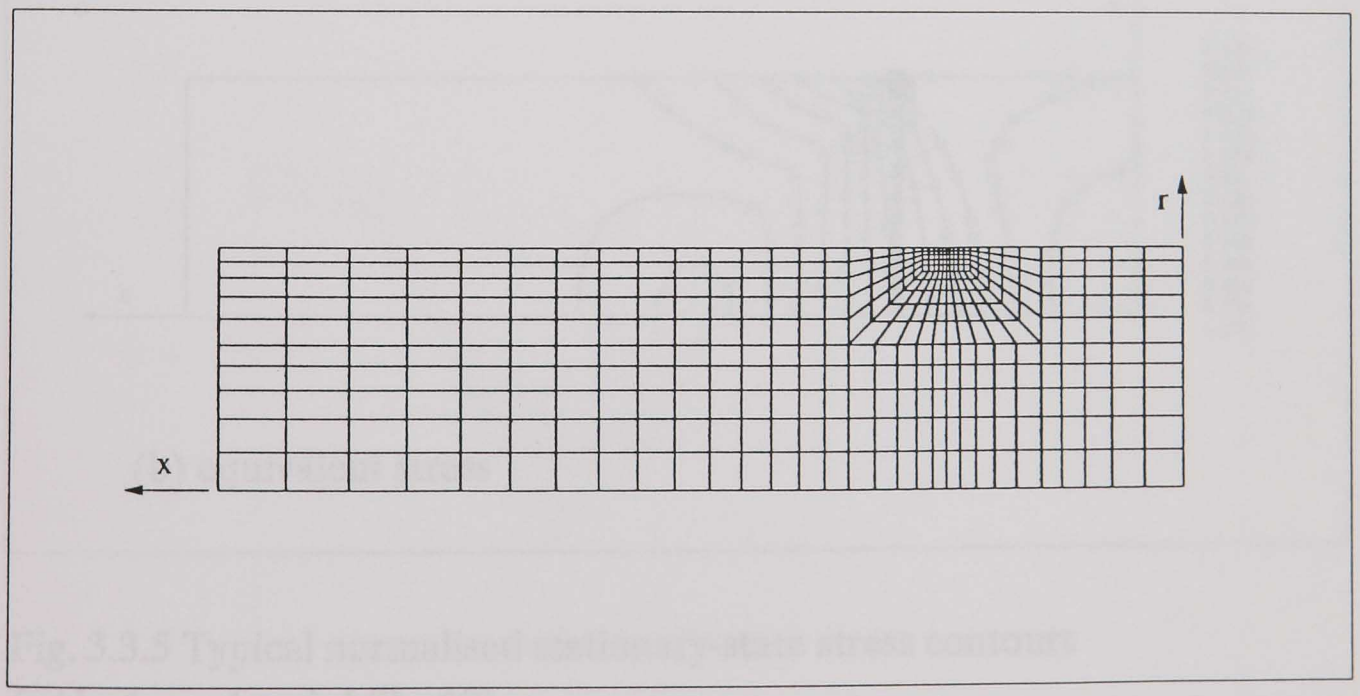

Fig. 3.3.4 A typical mesh for FE analysis (w/d=1).

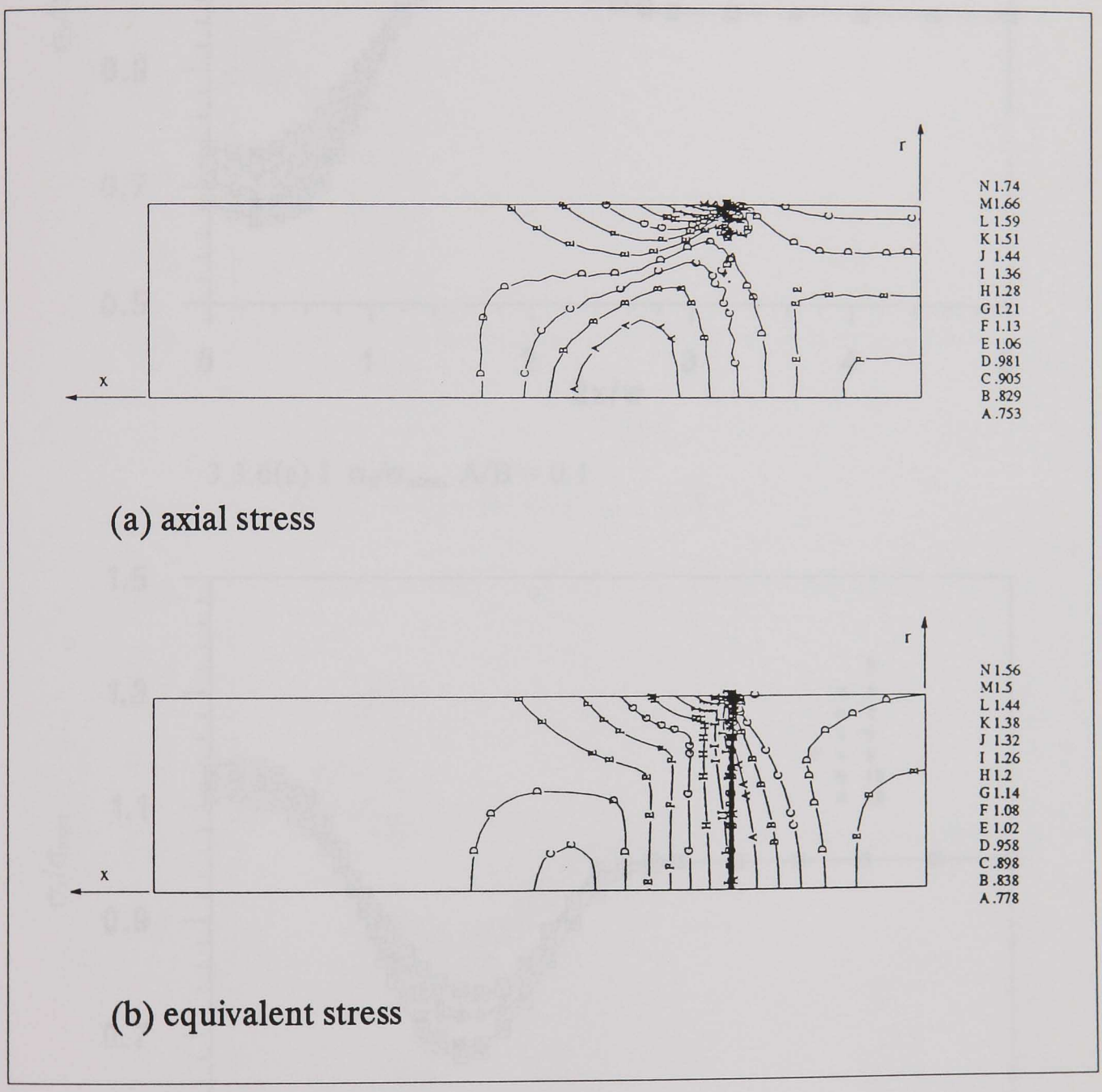

Fig. 3.3.5 Typical normalised stationary-state stress contours (w/d=1, n=4 and A/B=10).

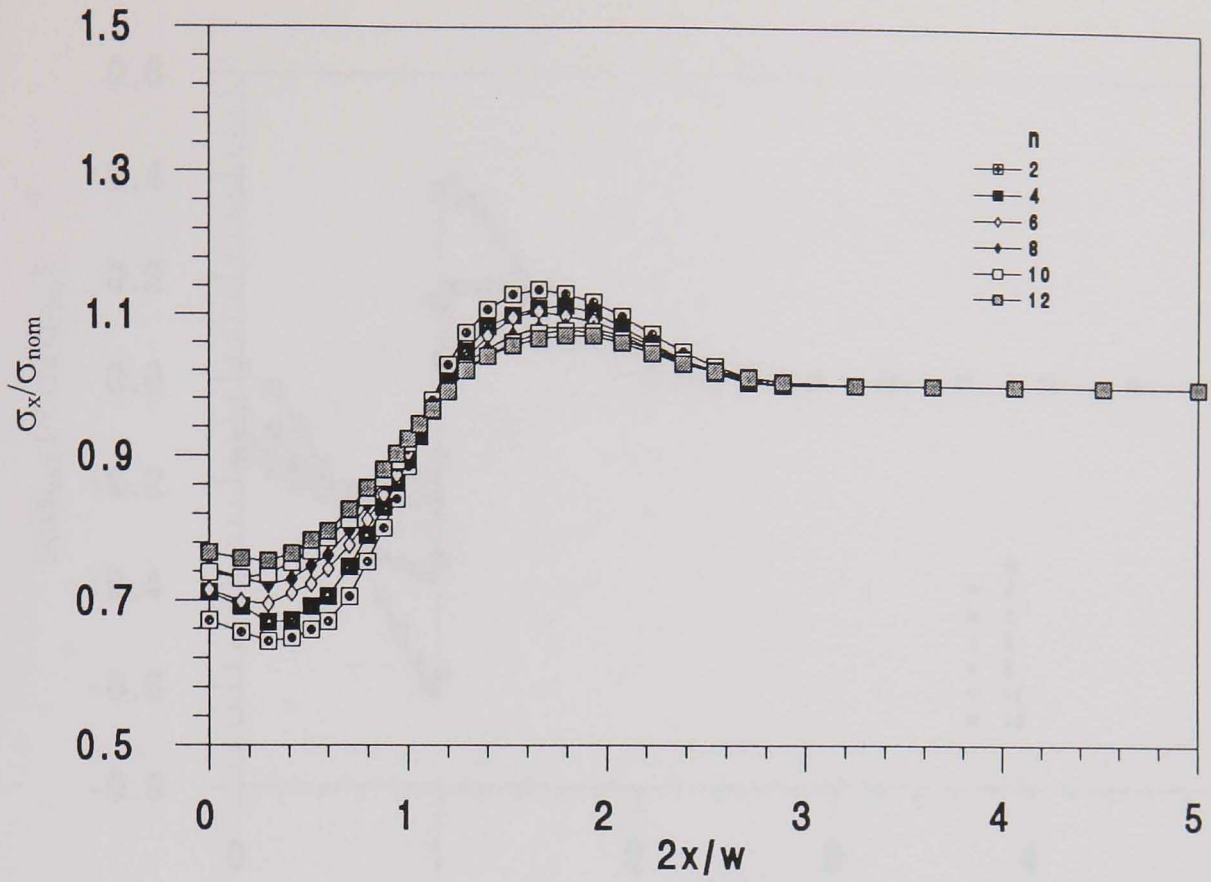

3.3.6(a) I σ_x/σ_{nom}, A/B = 0.1

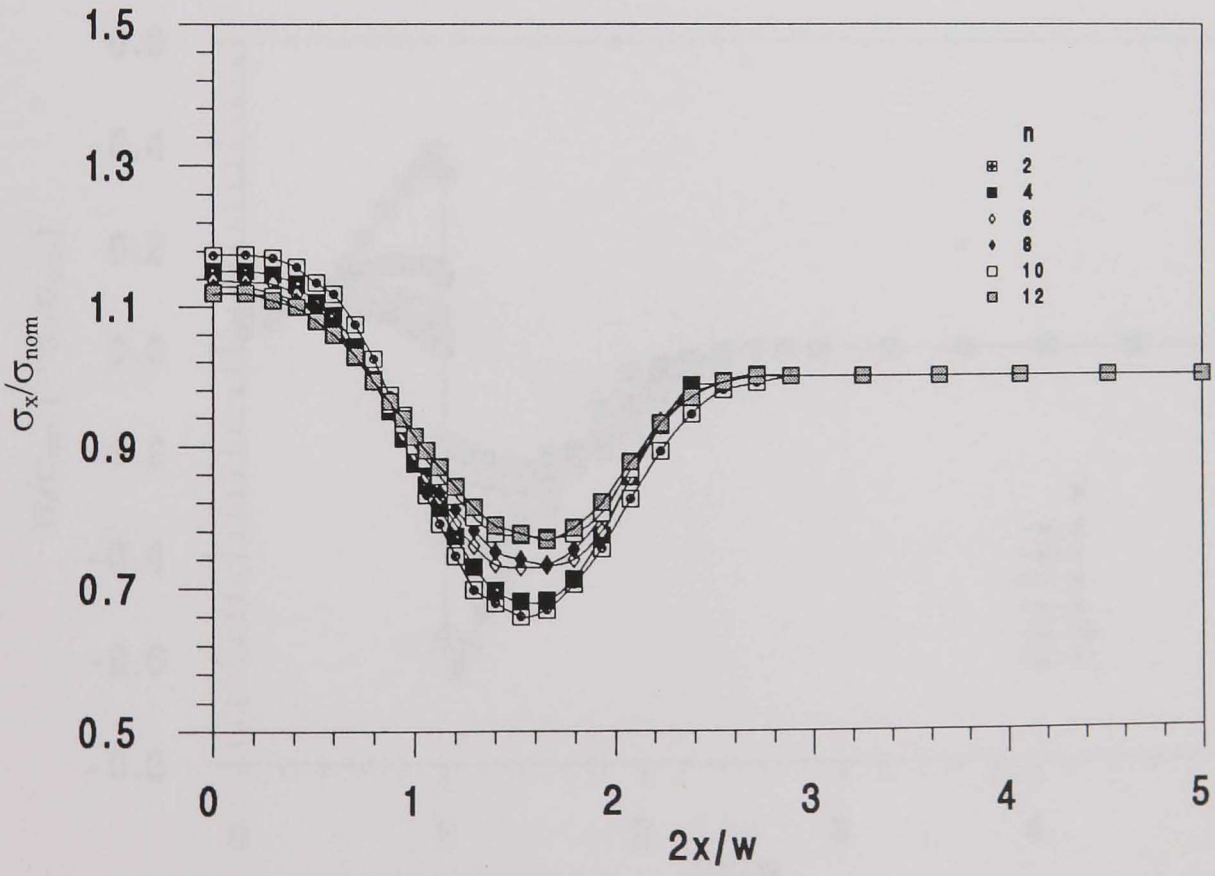

3.3.6(b) I σ_x/σ_{nom}, A/B = 10

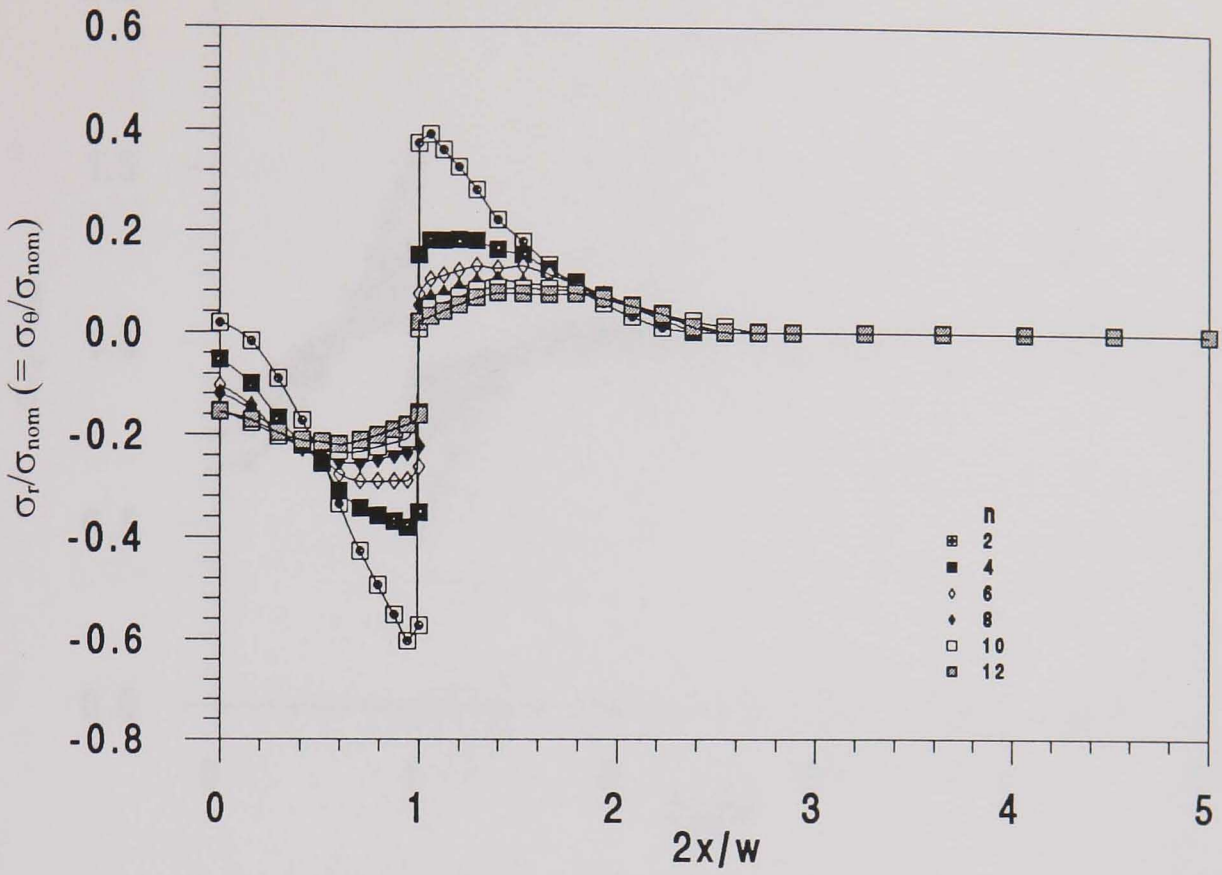

3.3.6(a) II σ_r/σ_{nom} (or $\sigma_\theta/\sigma_{nom}$), A/B = 0.1

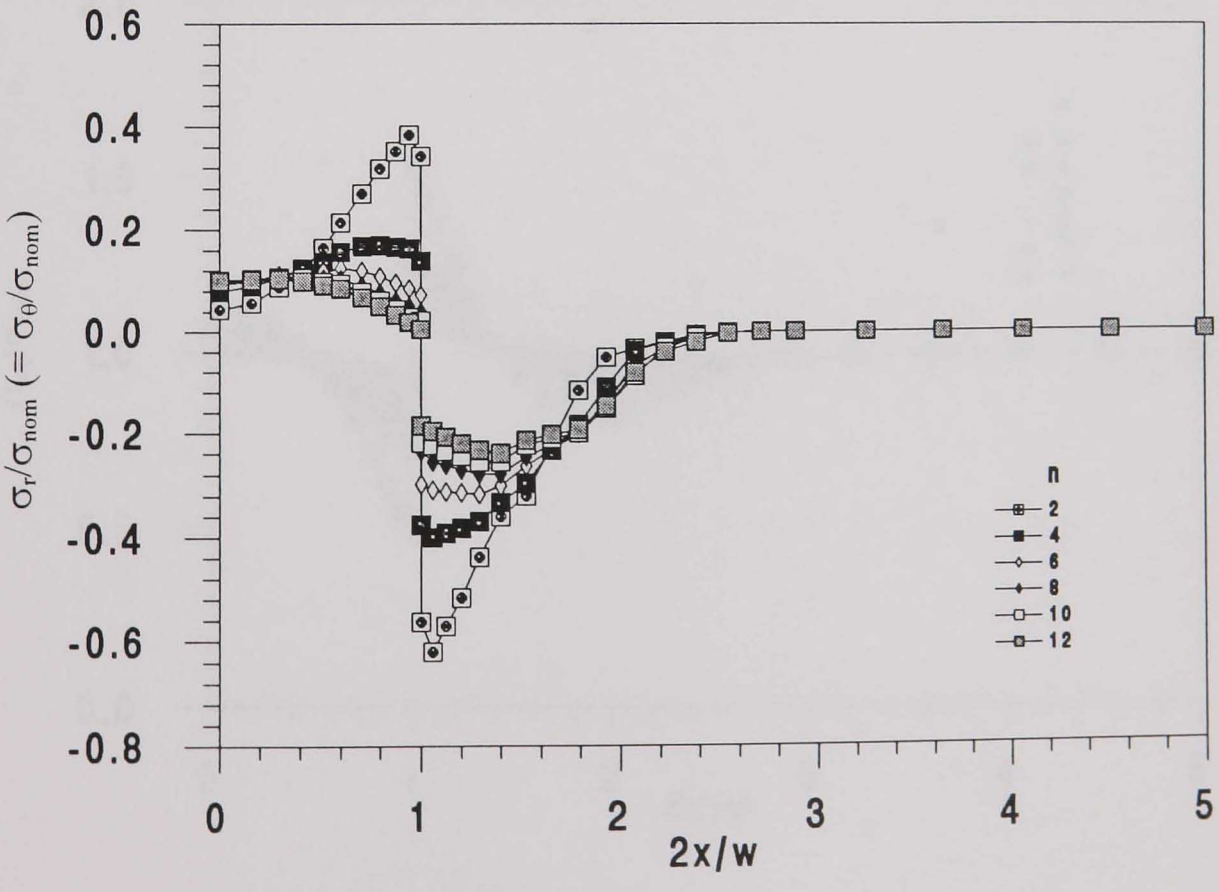

3.3.6(b) II σ_r/σ_{nom} (or $\sigma_\theta/\sigma_{nom}$), A/B = 10

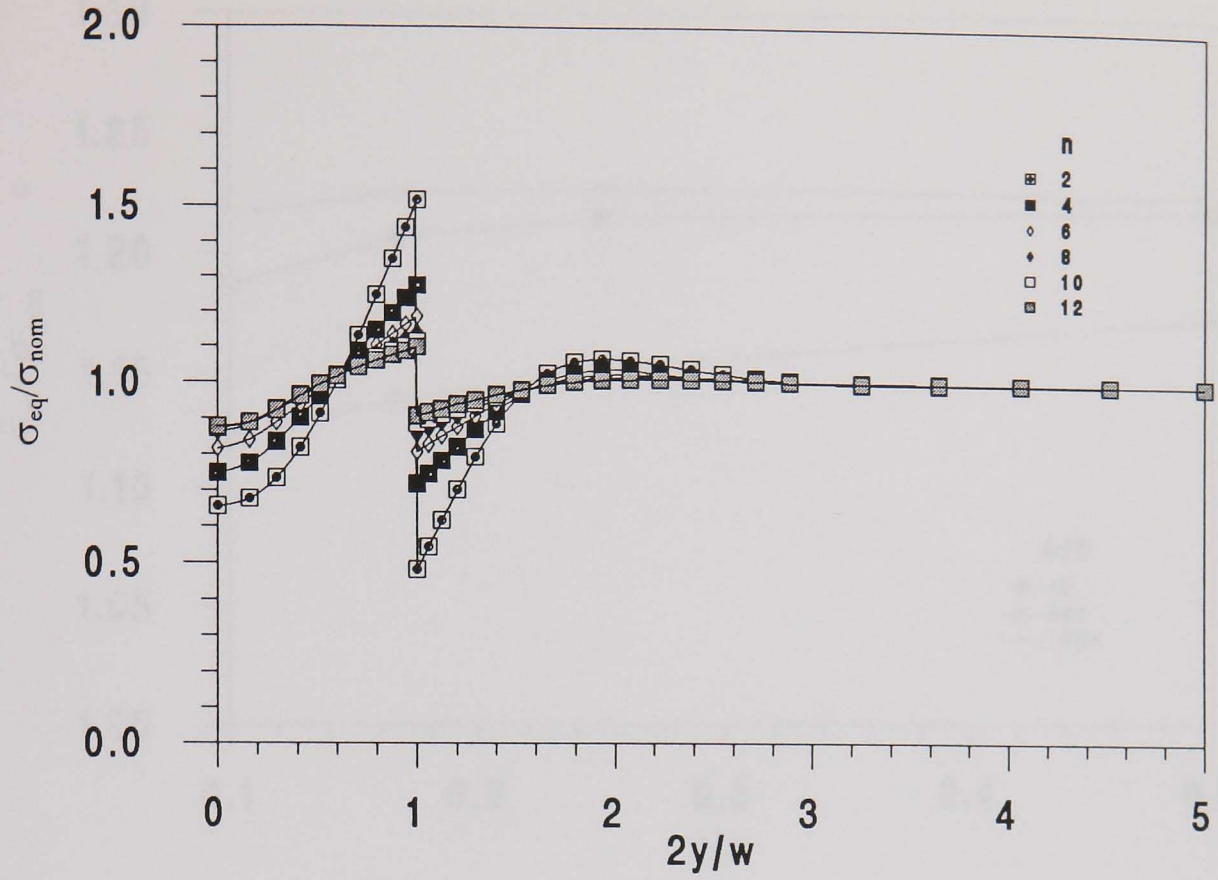

3.3.6(a) III σ_{eq}/σ_{nom}, A/B = 0.1

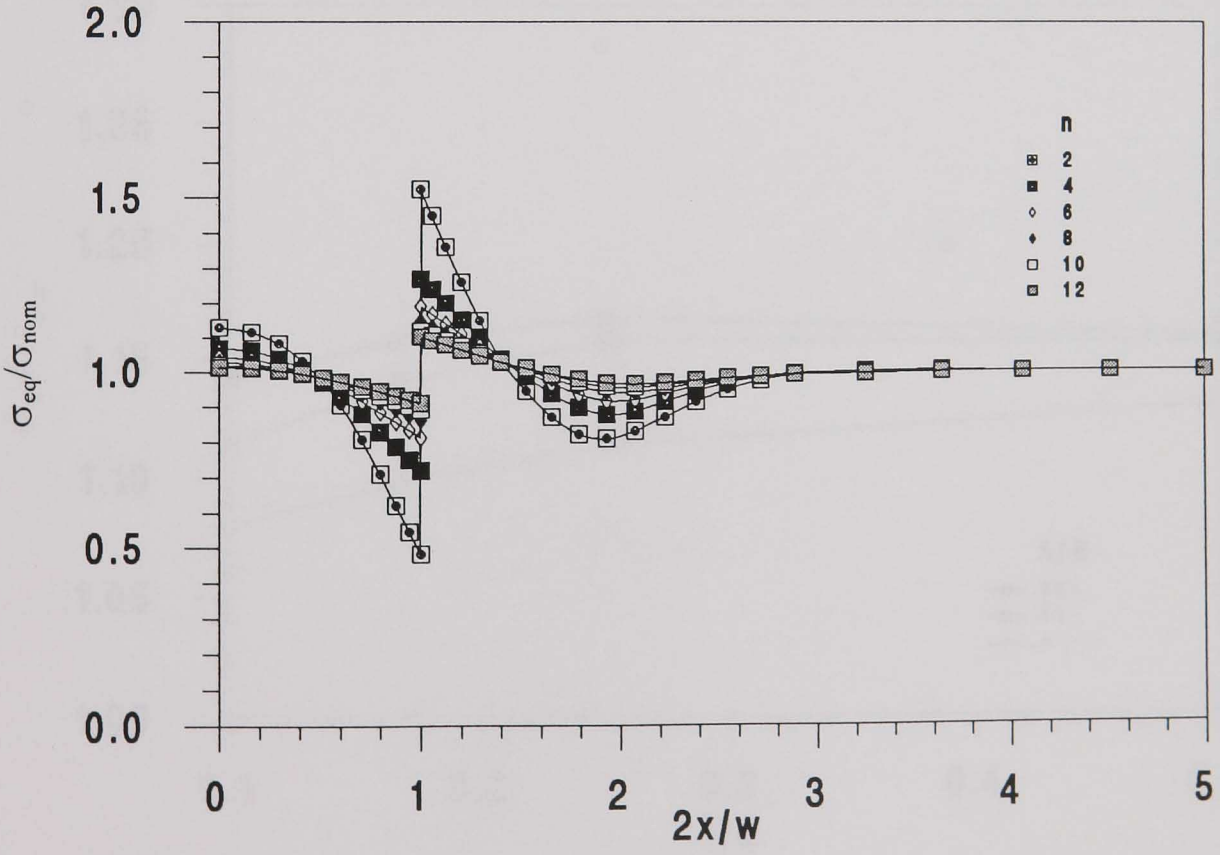

3.3.6(b) III σ_{eq}/σ_{nom}, A/B = 10

Fig. 3.3.6 Effect of n on the centre-line (r = 0) variations of σ_x/σ_{nom}, σ_r/σ_{nom} (= $\sigma_\theta/\sigma_{nom}$) and σ_{eq}/σ_{nom} with 2x/w, for w/d = 1.

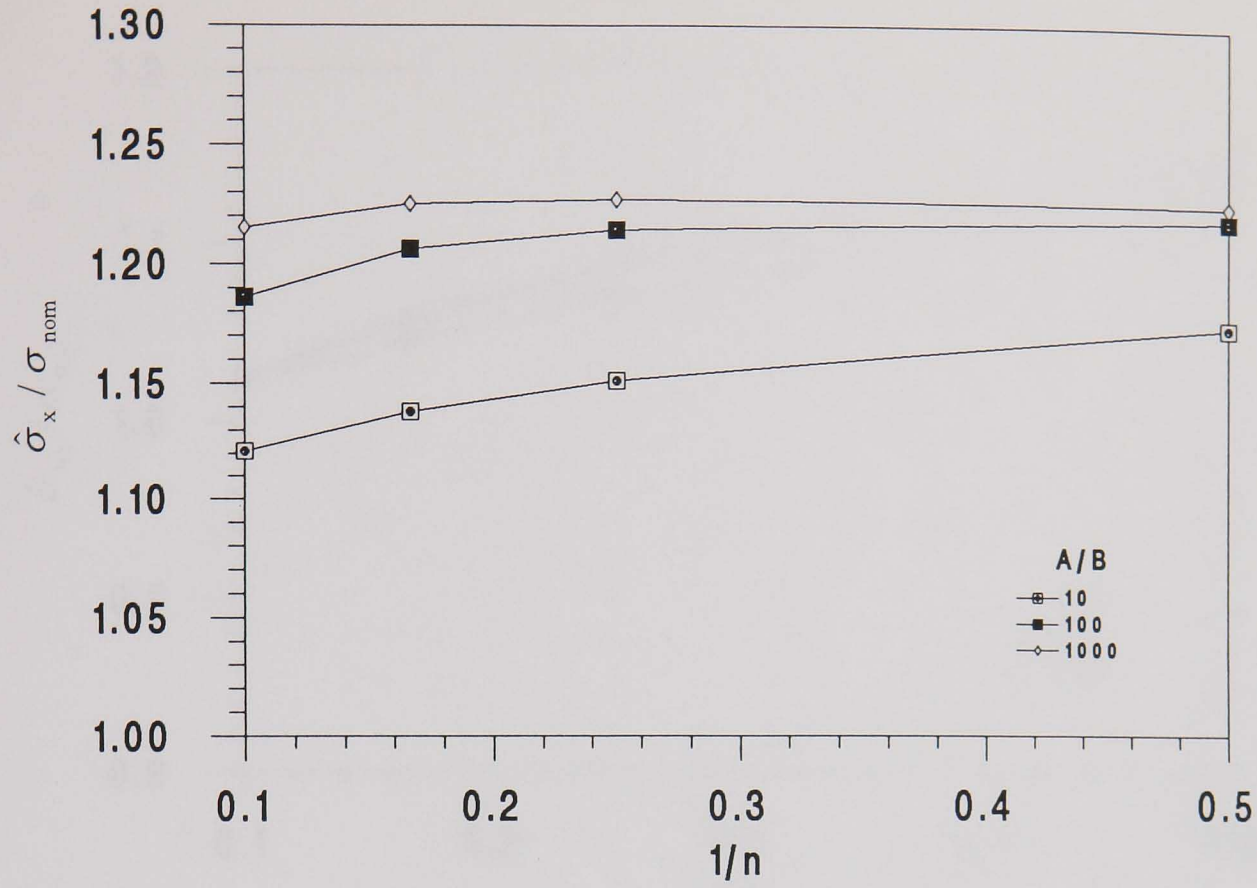

3.3.7(a) I $\hat{\sigma}_x / \sigma_{nom}$, x = 0, A/B > 1, material A

3.3.7(a) II $\hat{\sigma}_x / \sigma_{nom}$, x > w/2, A/B < 1, material B

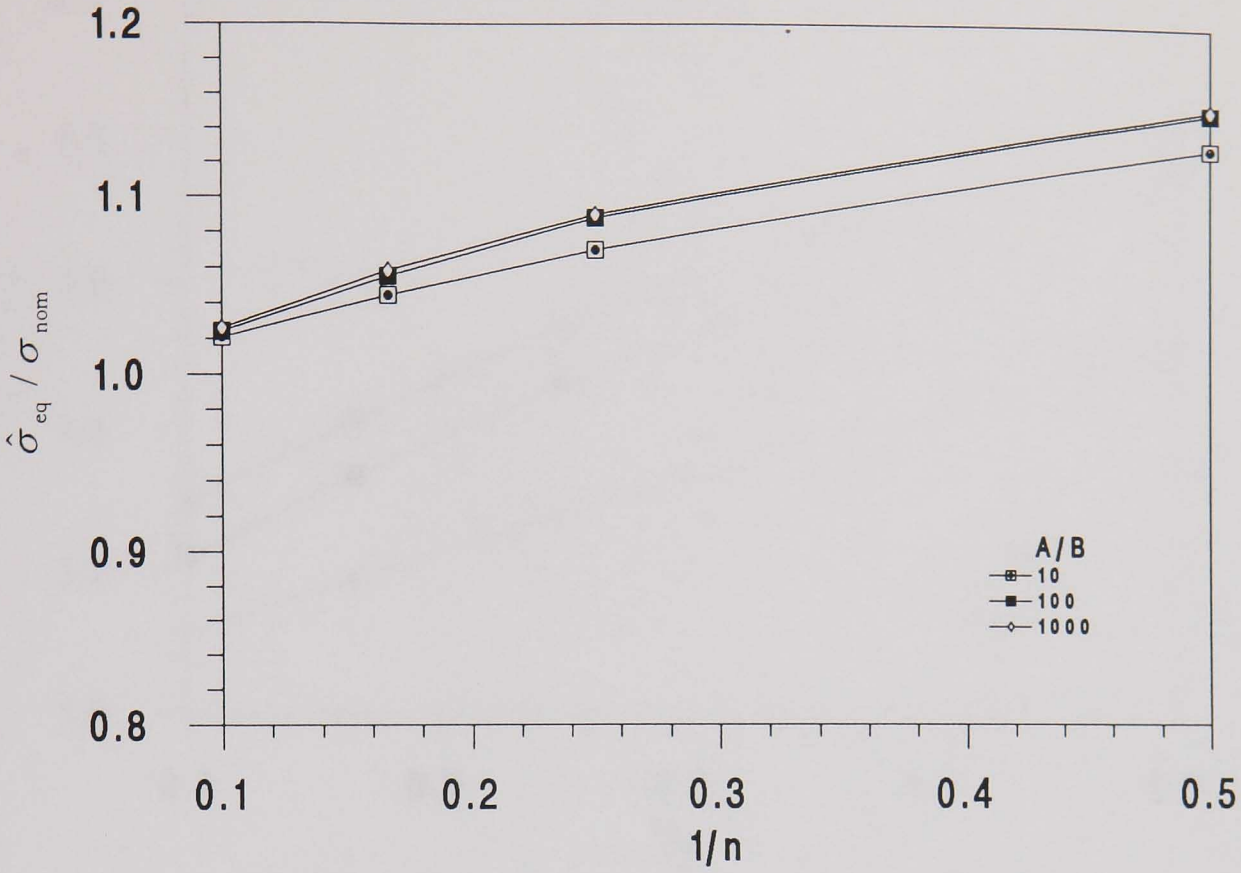

3.3.7(b) I $\hat{\sigma}_{eq} / \sigma_{nom}$, x = 0, A/B > 1, material A

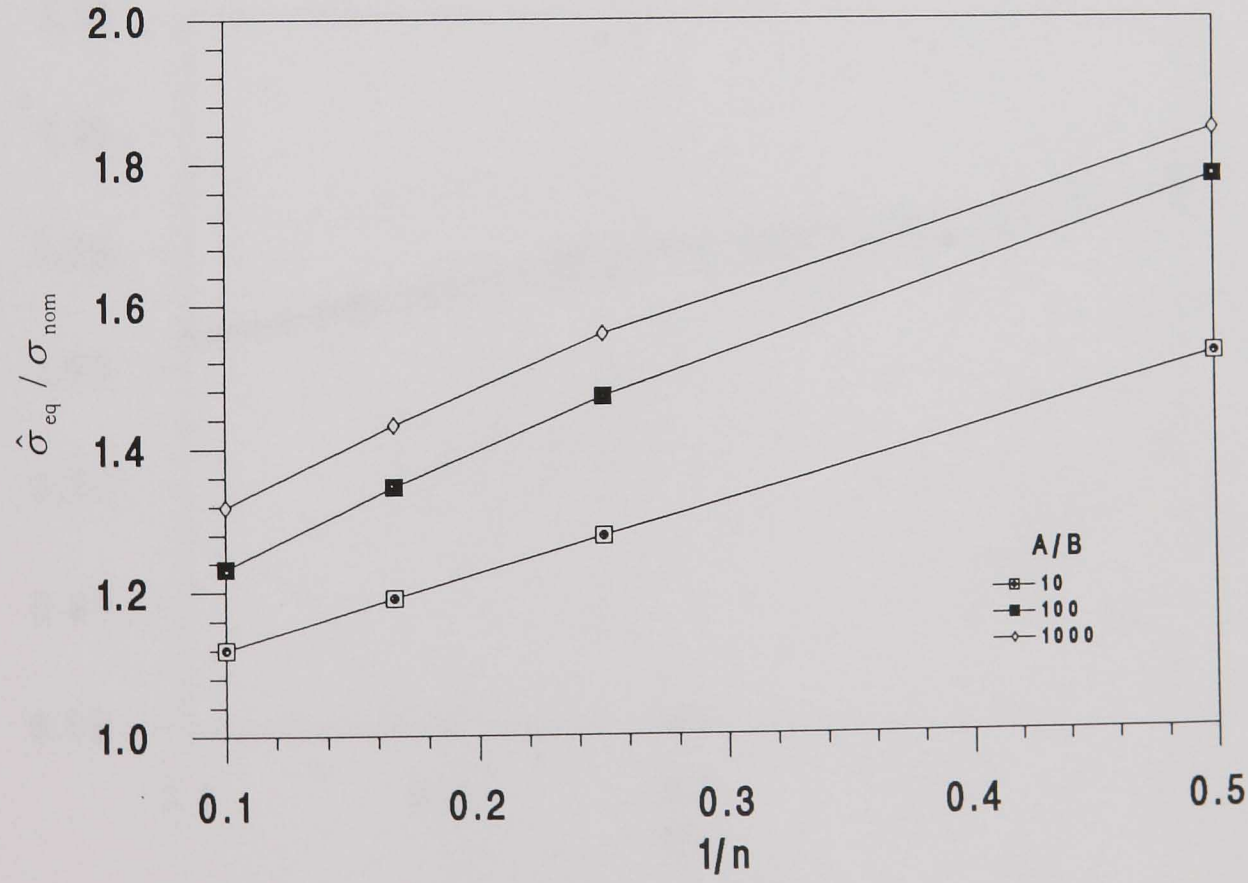

3.3.7(b) II $\hat{\sigma}_{eq} / \sigma_{nom}$, x = w/2, A/B > 1, material B

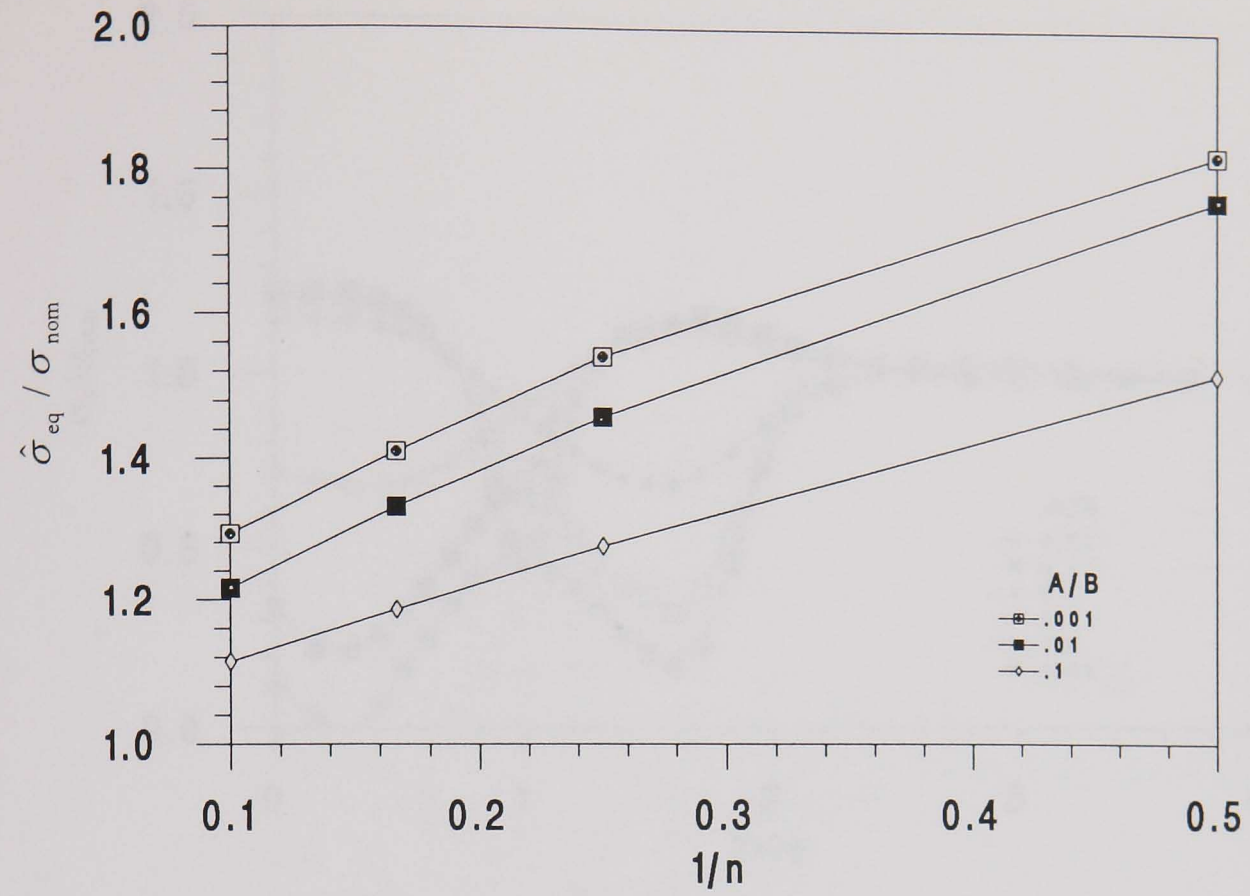

3.3.7(b) III $\hat{\sigma}_{eq} / \sigma_{nom}$, x = w/2, A/B < 1, material A

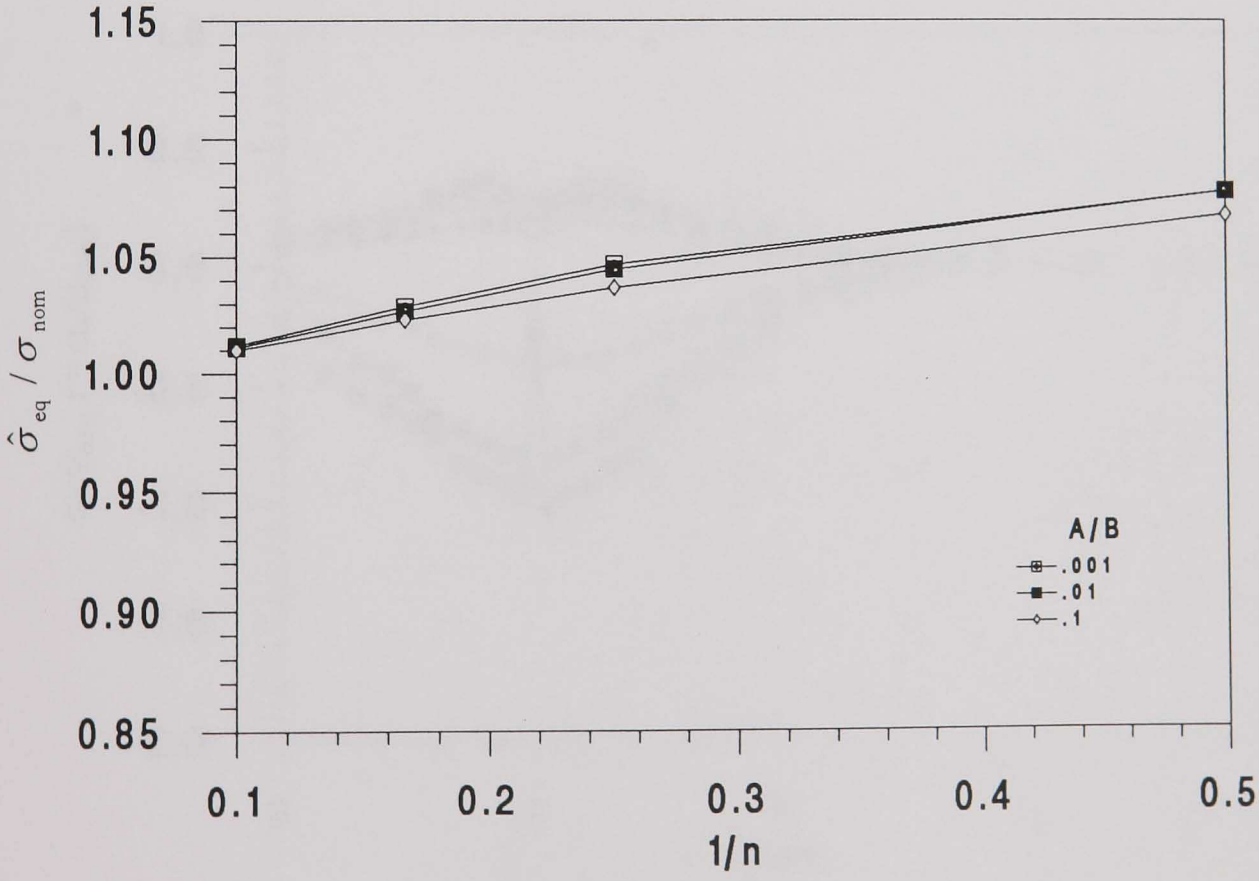

3.3.7(b) IV $\hat{\sigma}_{eq} / \sigma_{nom}$, x > w/2, A/B < 1, material B

Fig. 3.3.7 Variations of $\hat{\sigma}_{x} / \sigma_{nom}$ and $\hat{\sigma}_{eq} / \sigma_{nom}$ with 1/n for a range of A/B values (0.001 < A/B < 1000) with w/d = 1.

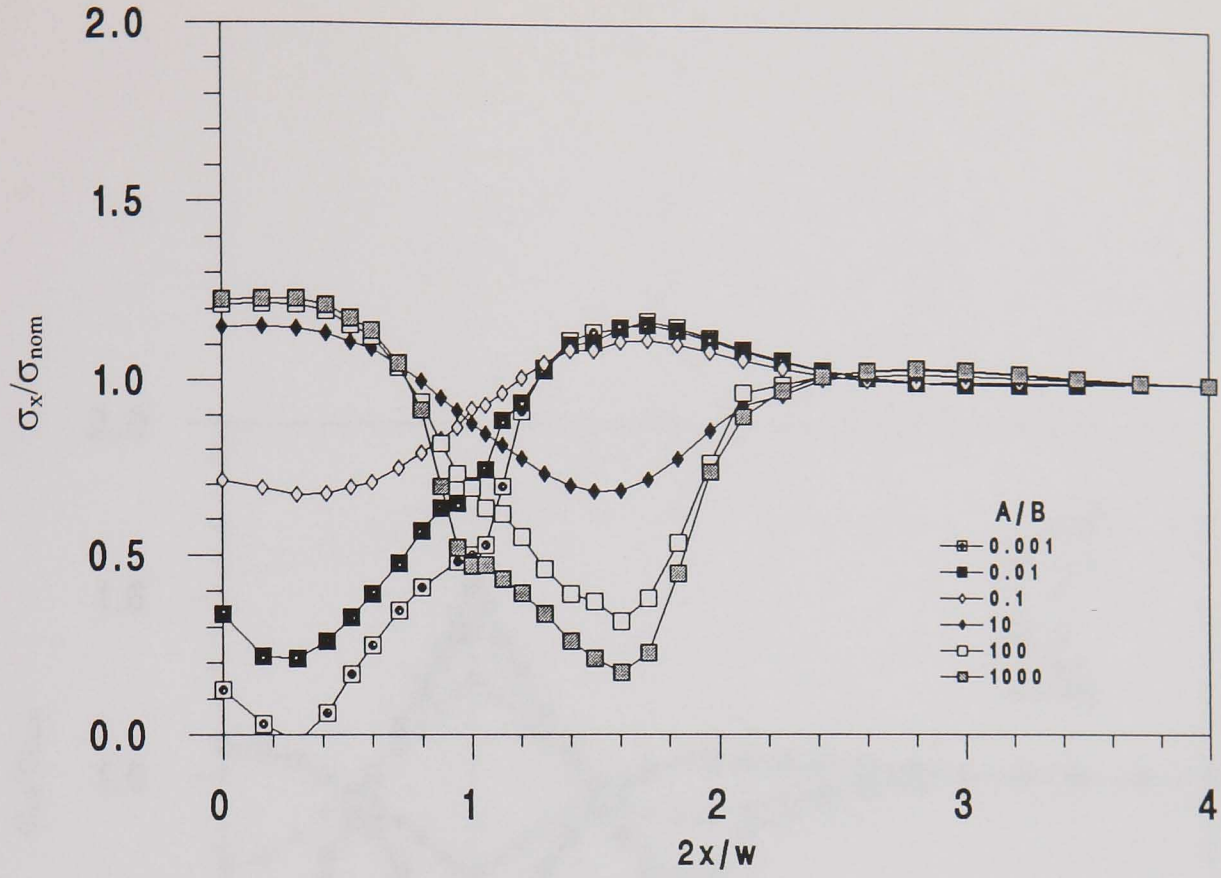

3.3.8(a) σ_x/σ_{nom}

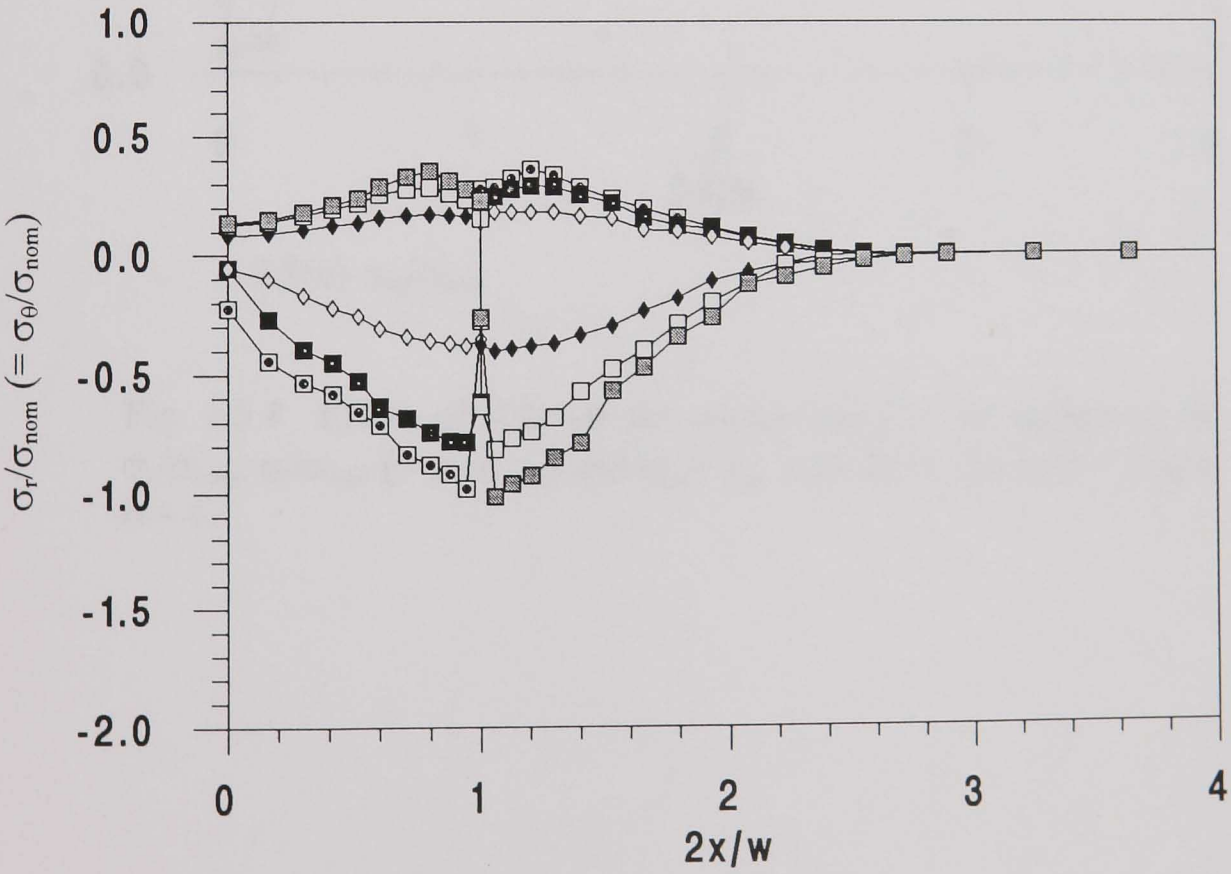

3.3.8(b) σ_r/σ_{nom} (= $\sigma_\theta/\sigma_{nom}$)

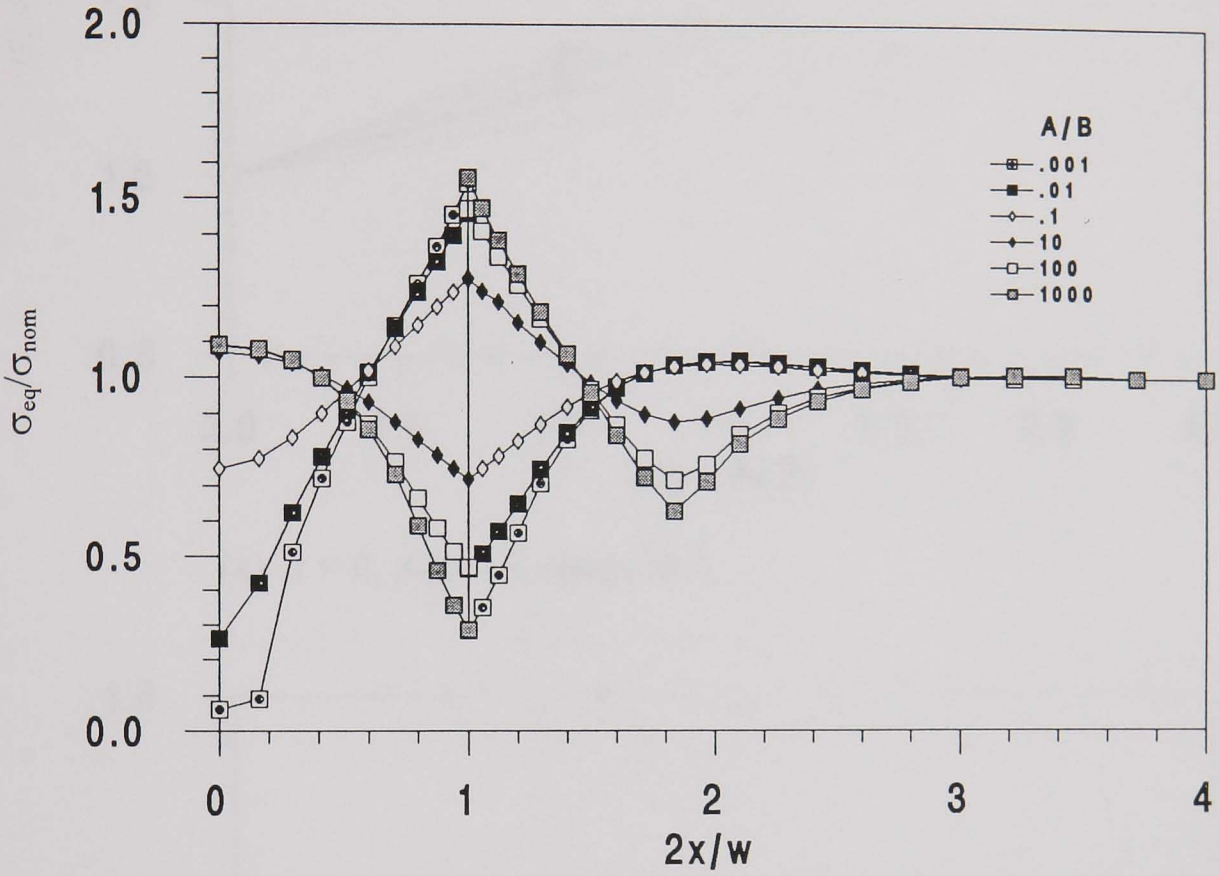

3.3.8(c) σ_{eq}/σ_{nom}

Fig. 3.3.8 Effect of A/B on the centre-line (r = 0) variations of σ_x/σ_{nom}, σ_r/σ_{nom} (= $\sigma_\theta/\sigma_{nom}$) and σ_{eq}/σ_{nom} with 2x/w, for w/d = 1 and n = 4.

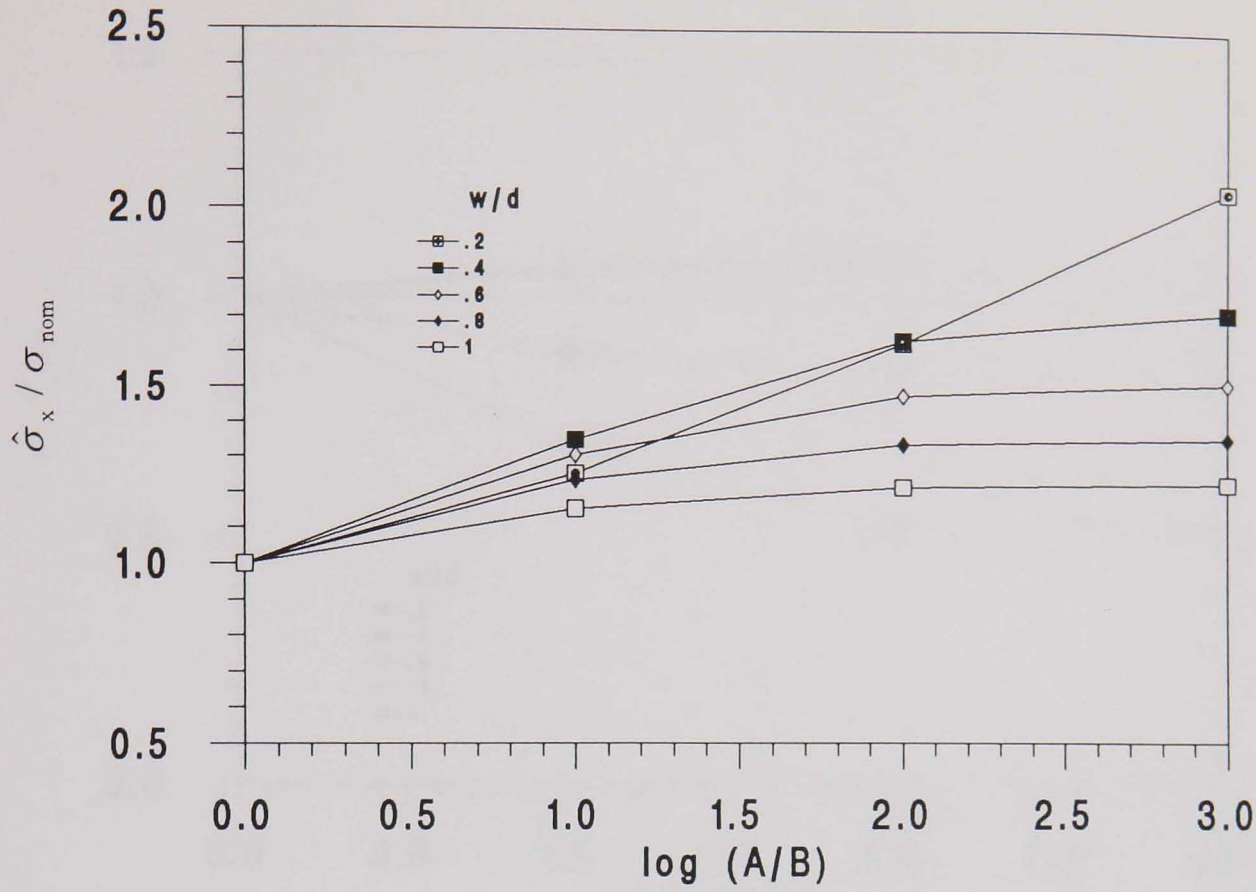

(a) x = 0, A/B > 1, material A

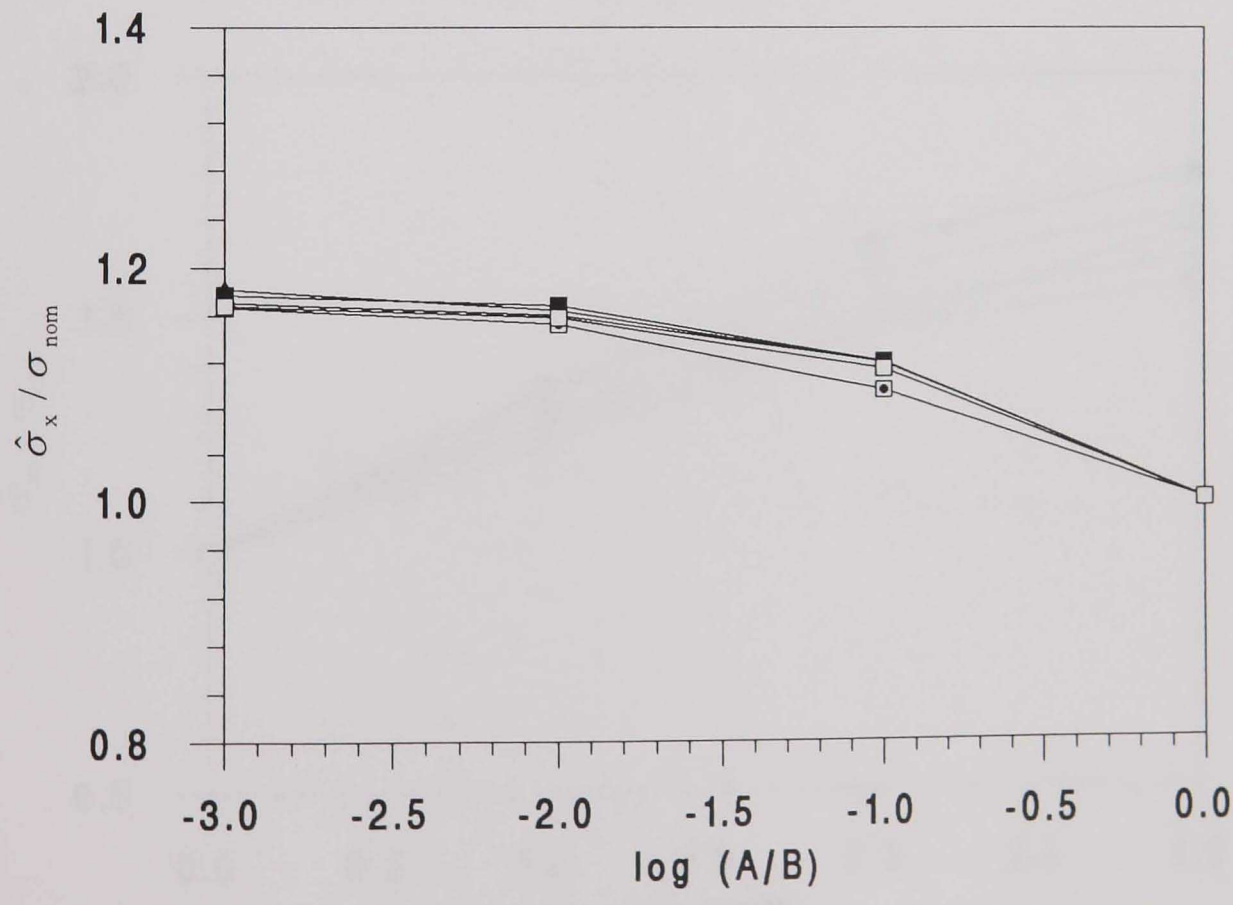

(b) x > w/2, A/B < 1, material B

Fig. 3.3.9 Effect of w/d on the centre-line (r = 0) variations of $\hat{\sigma}_x / \sigma_{nom}$ with log (A/B) for n = 4.

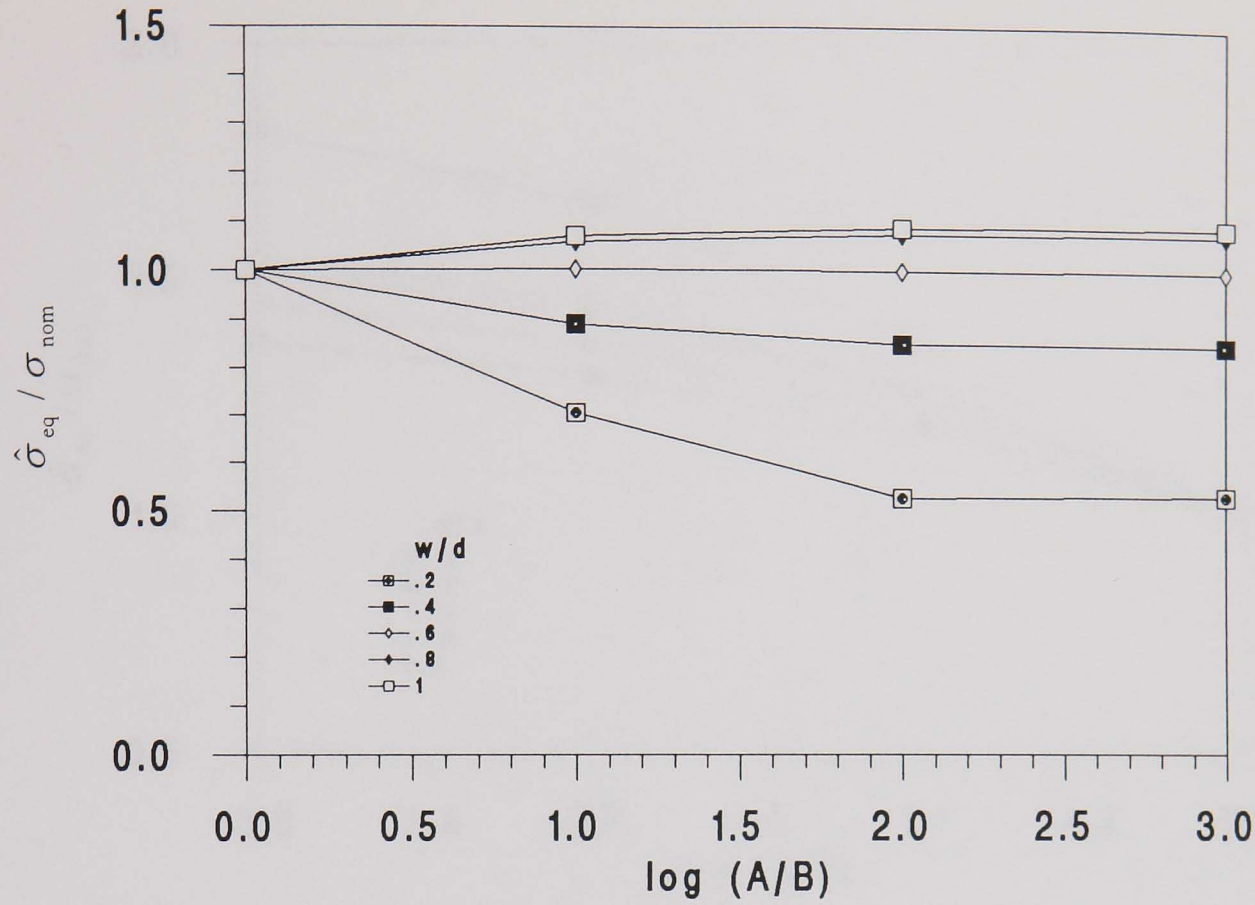

3.3.10(a) x = 0, A/B > 1, material A

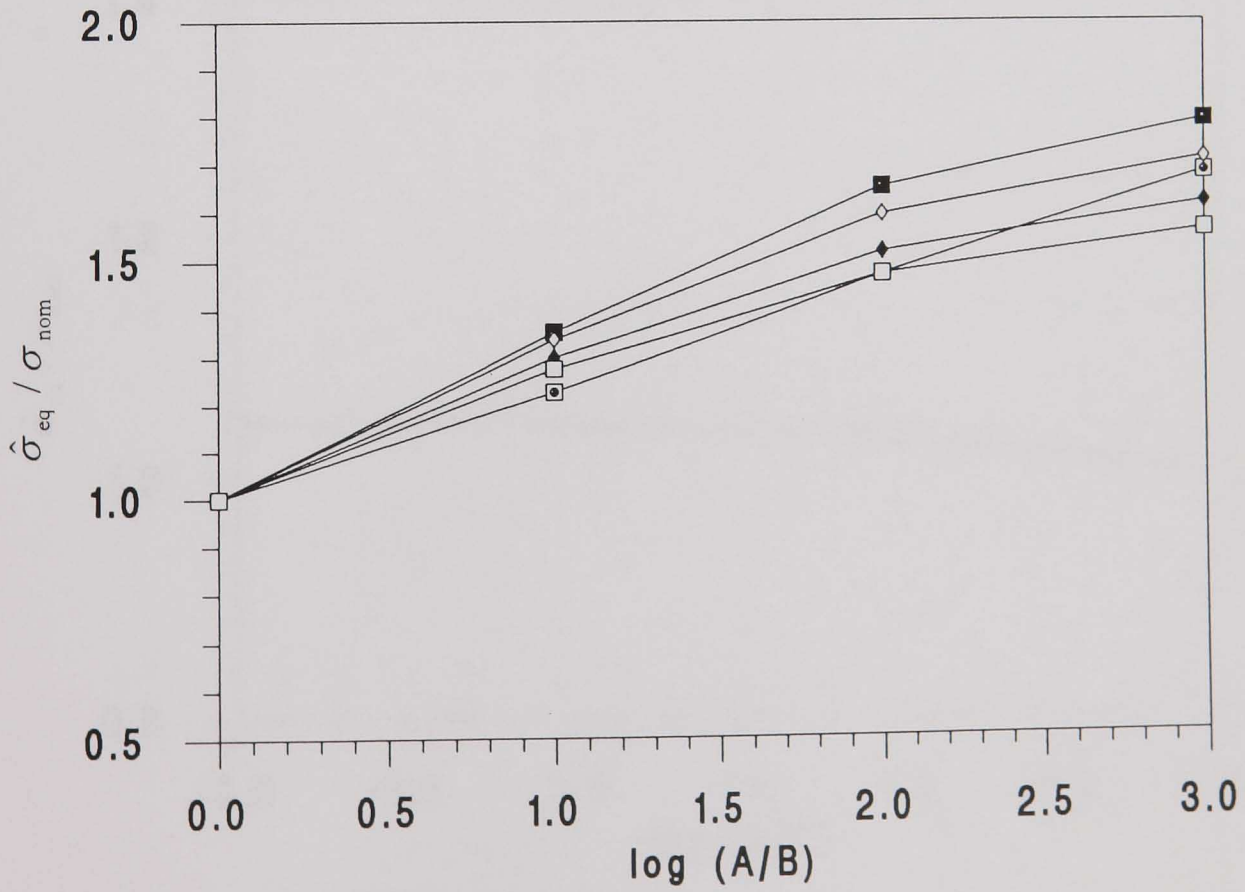

3.3.10(b) x = w/2, A/B > 1, material B

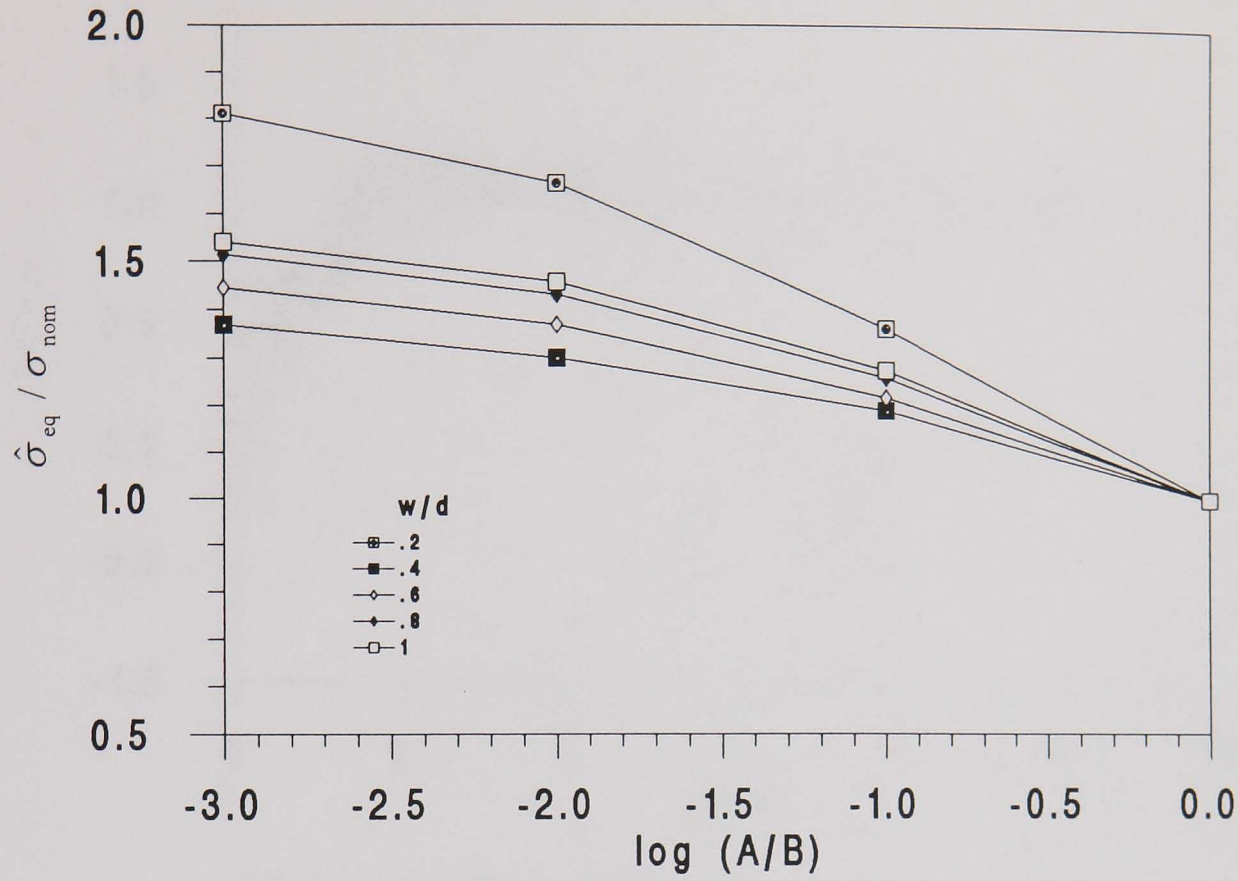

3.3.10(c) x = w/2, A/B < 1, material A

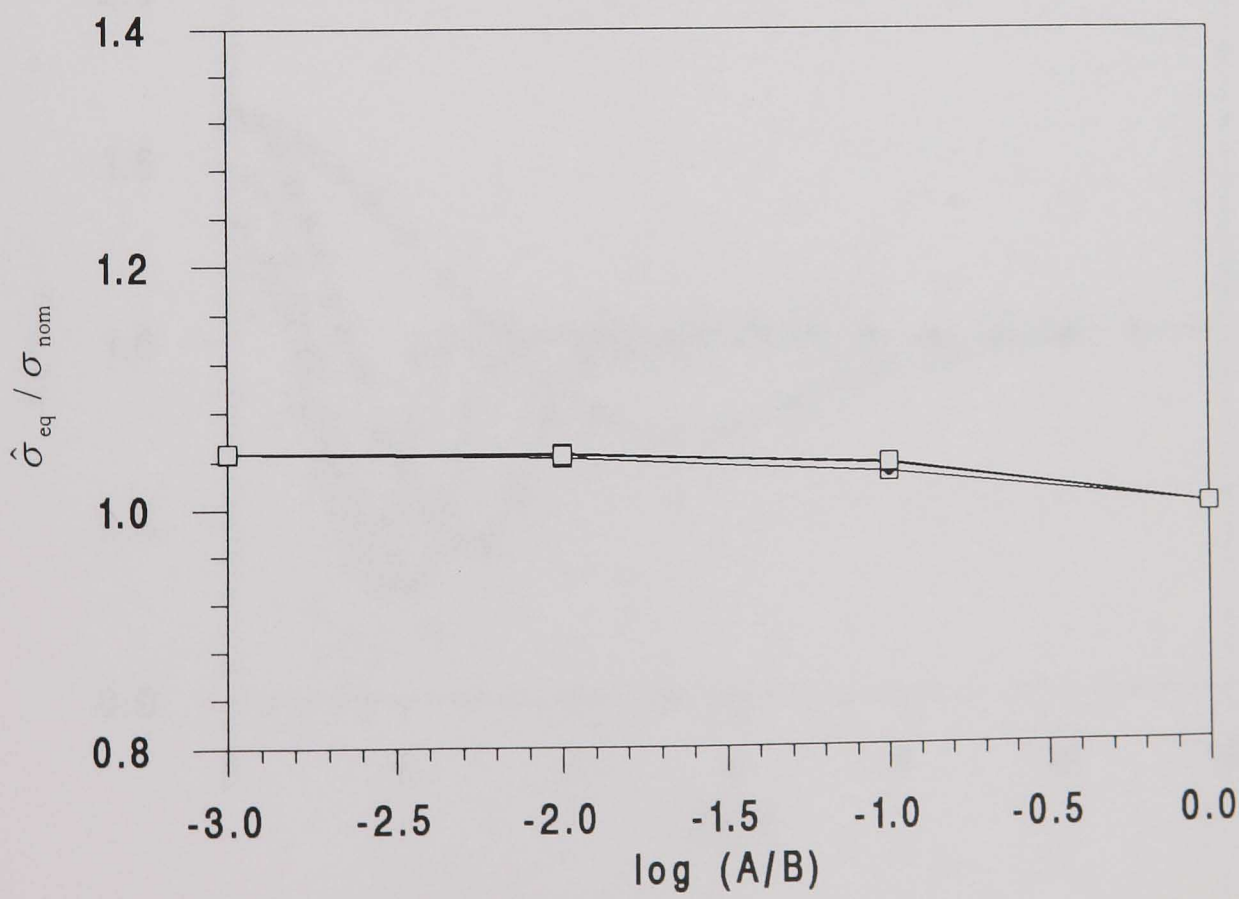

3.3.10(d) x > w/2, A/B < 1, material B

Fig. 3.3.10 Effect of w/d on the centre-line (r = 0) variations of $\hat{\sigma}_{eq} / \sigma_{nom}$ with log (A/B) for n = 4.

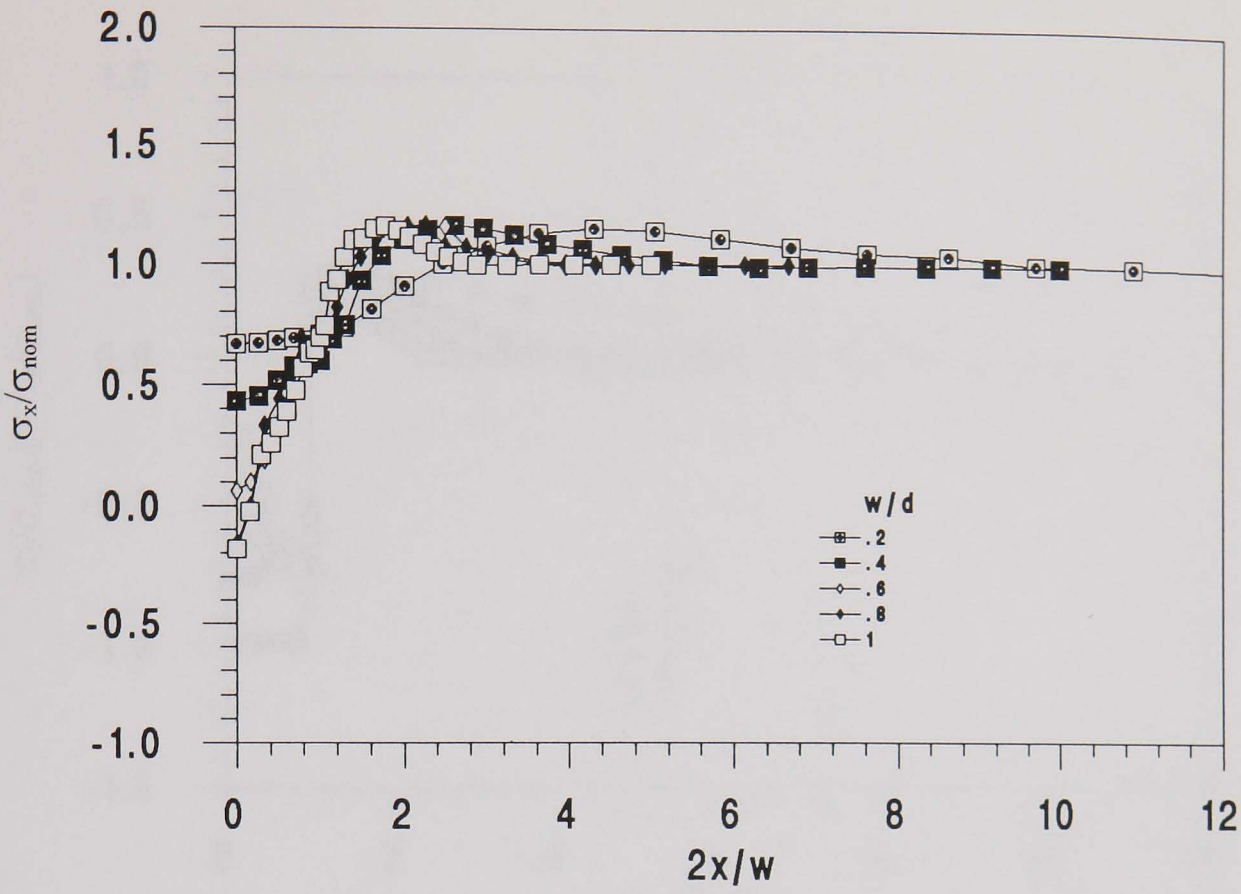

3.3.11(a) I σ_x/σ_{nom}, A/B = 0.01

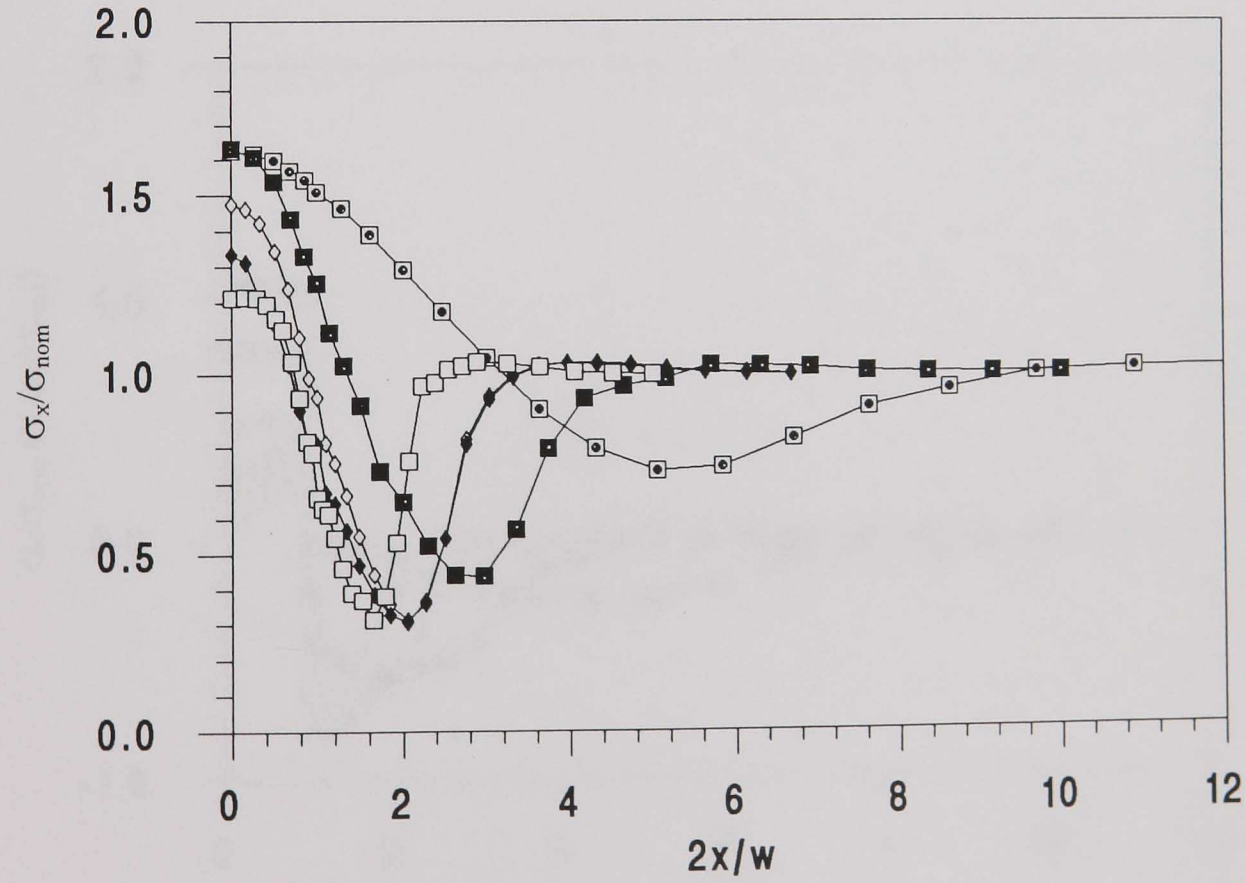

3.3.11(b) I σ_x/σ_{nom}, A/B = 100

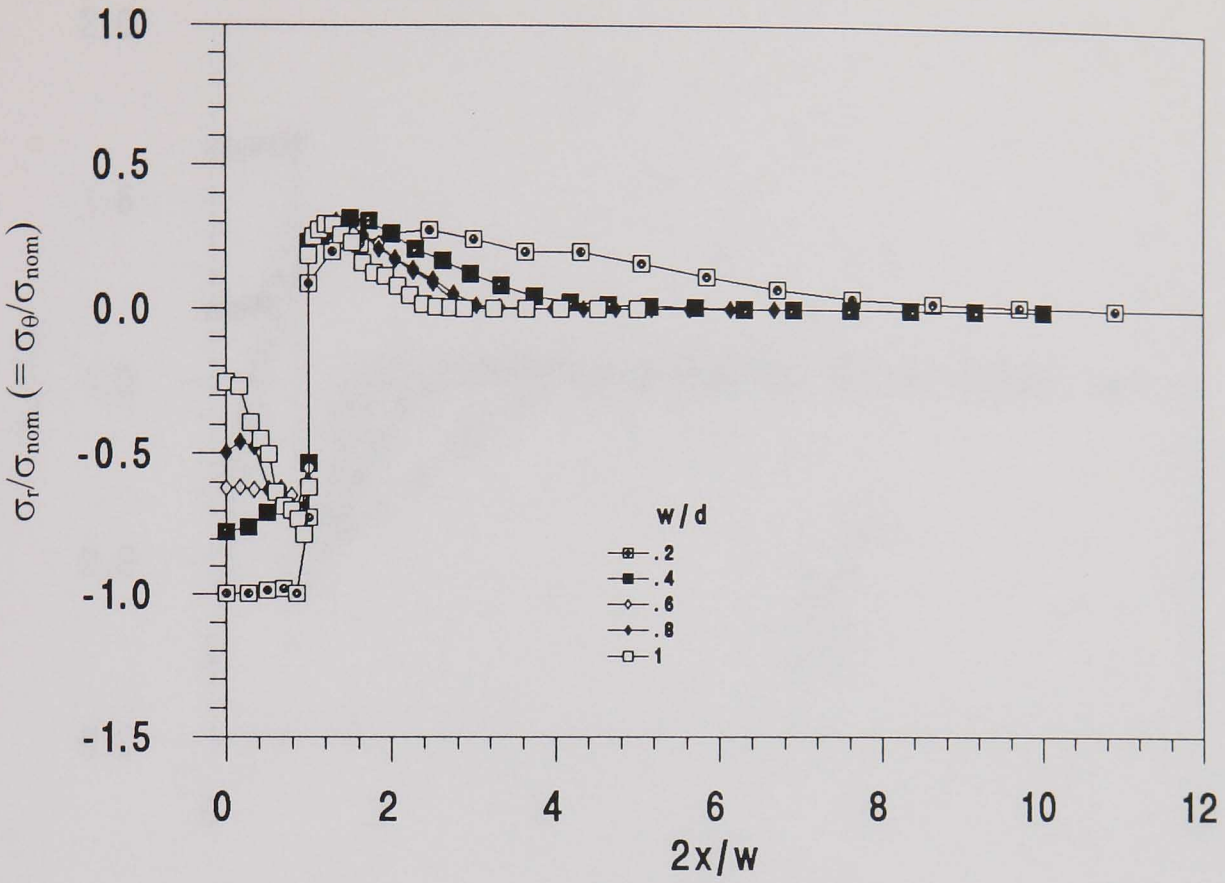

3.3.11(a) II σ_r/σ_{nom} ($= \sigma_\theta/\sigma_{nom}$), A/B = 0.01

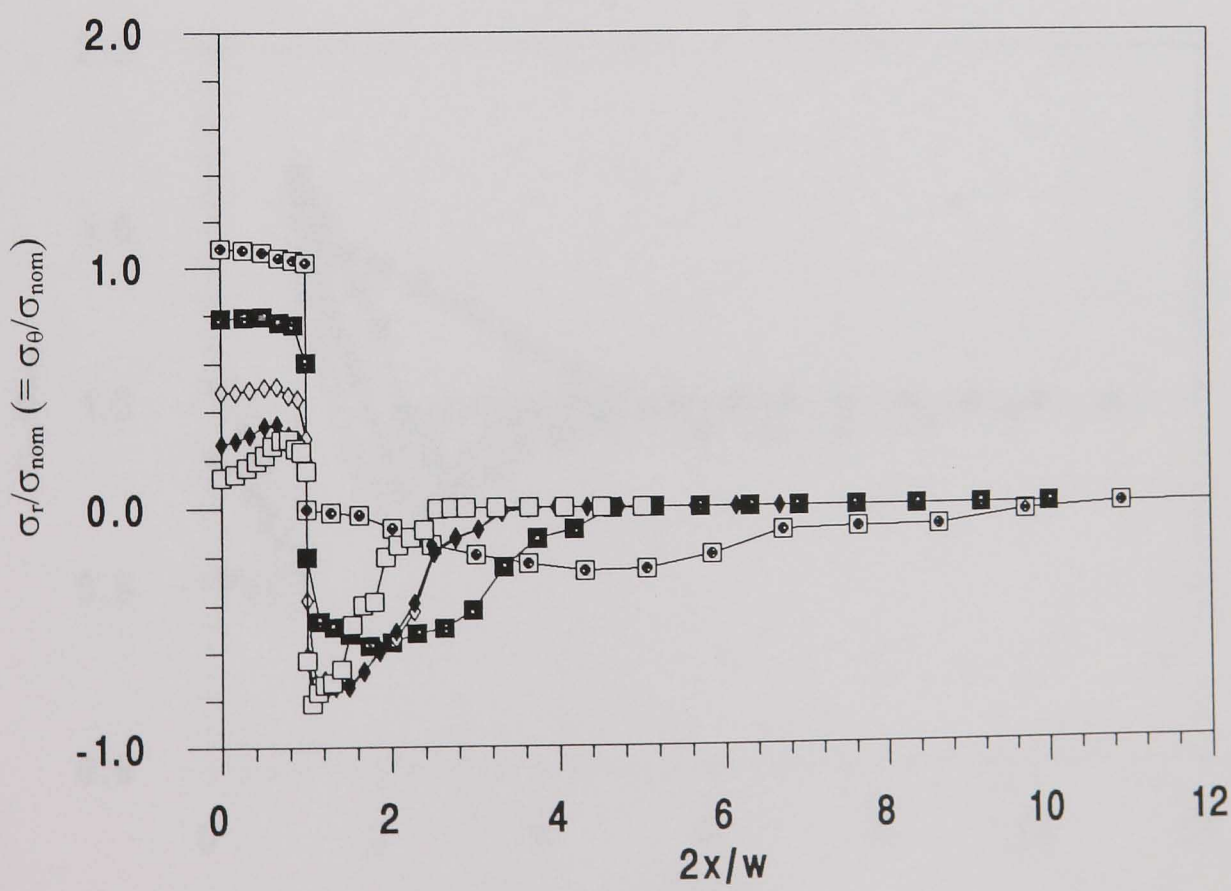

3.3.11(b) II σ_r/σ_{nom} ($= \sigma_\theta/\sigma_{nom}$), A/B = 100

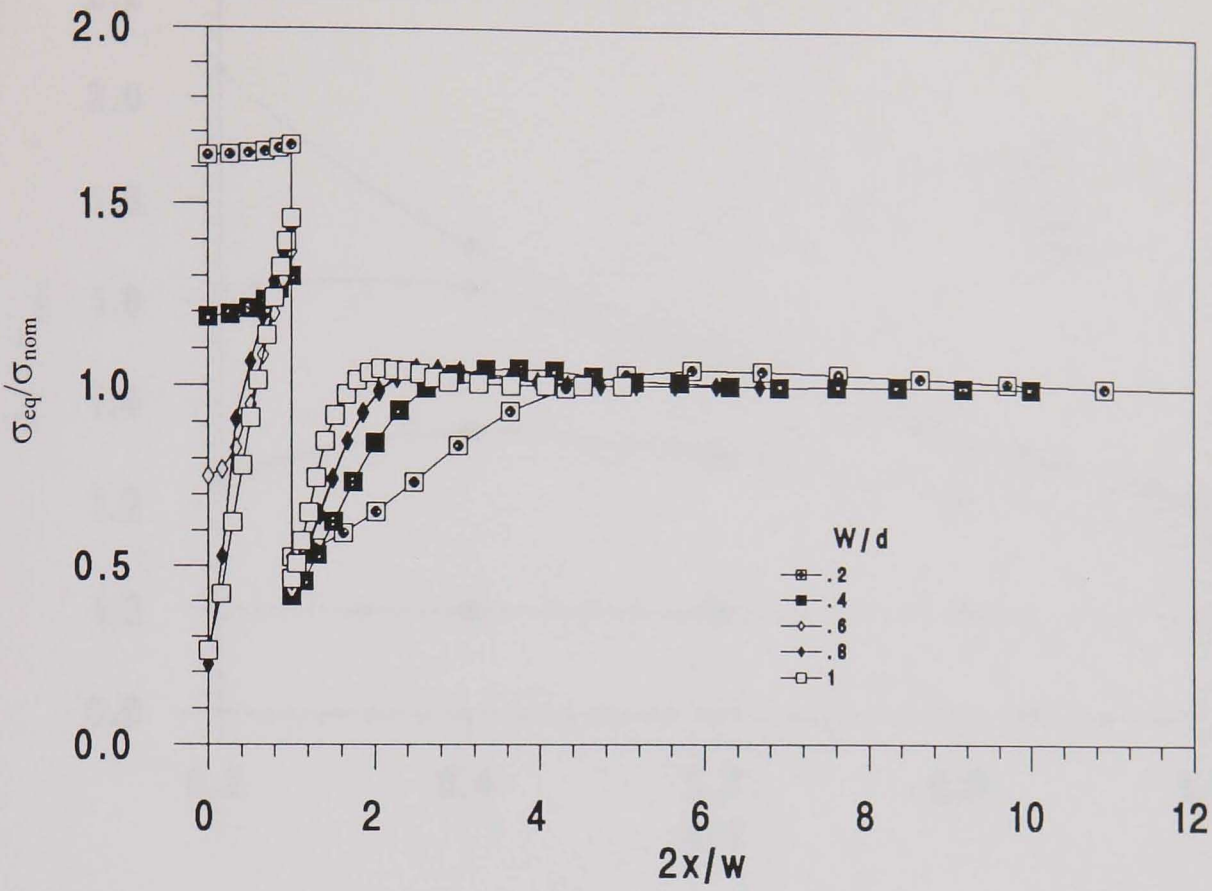

3.3.11(a) III σ_{eq}/σ_{nom}, A/B = 0.01

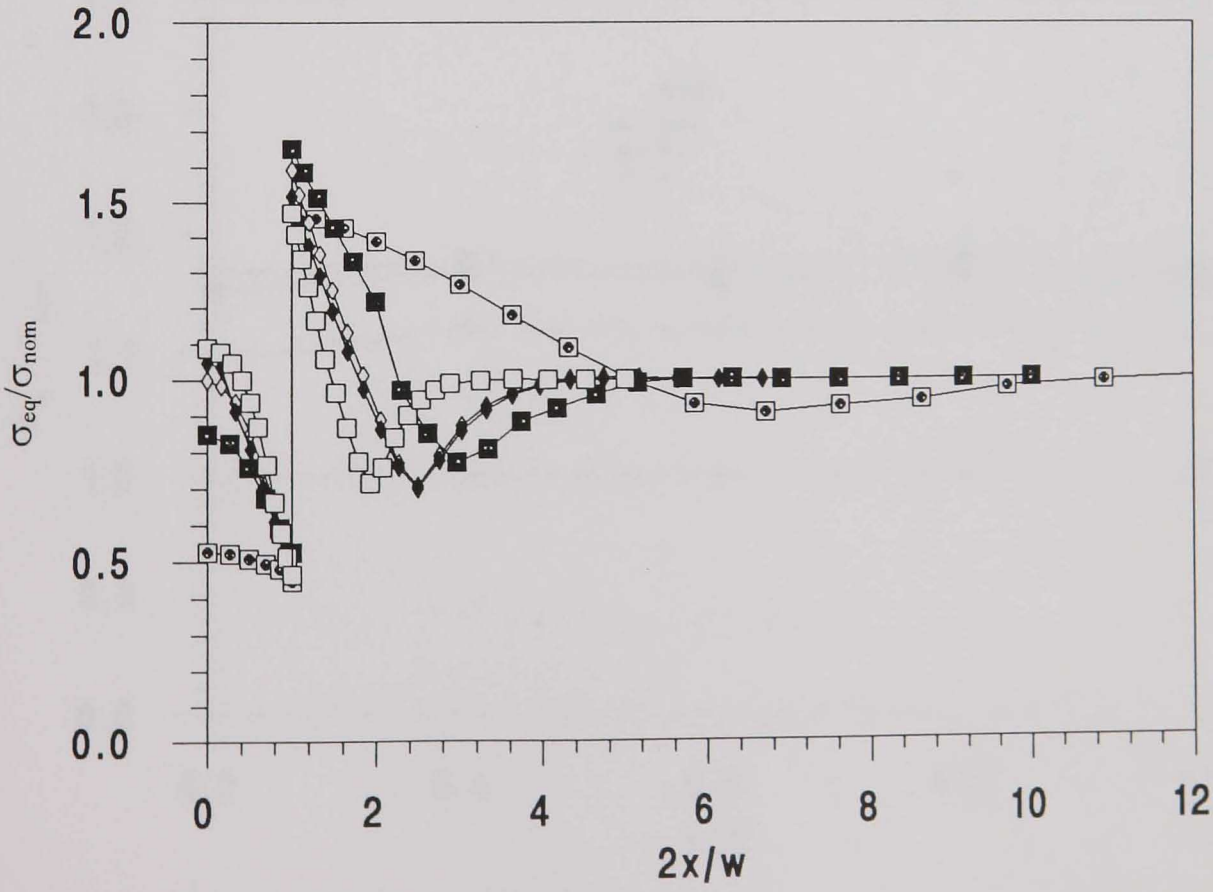

3.3.11(b) III σ_{eq}/σ_{nom}, A/B = 100

Fig. 3.3.11 Effect of w/d on the centre-line (r = 0) variations of σ_x/σ_{nom}, σ_r/σ_{nom} (= $\sigma_\theta/\sigma_{nom}$) and σ_{eq}/σ_{nom} with 2x/w, for n = 4.

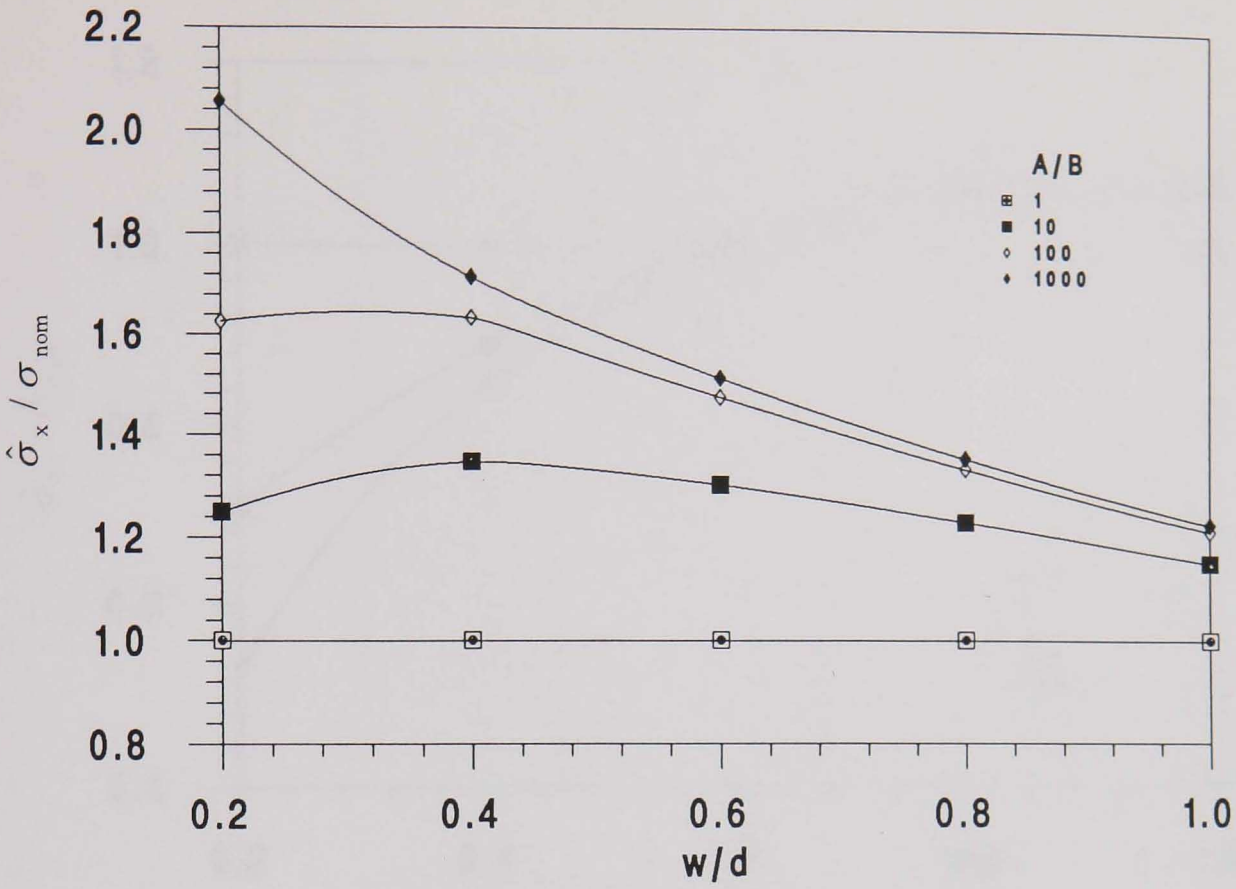

(a) x = 0, A/B > 1, material A

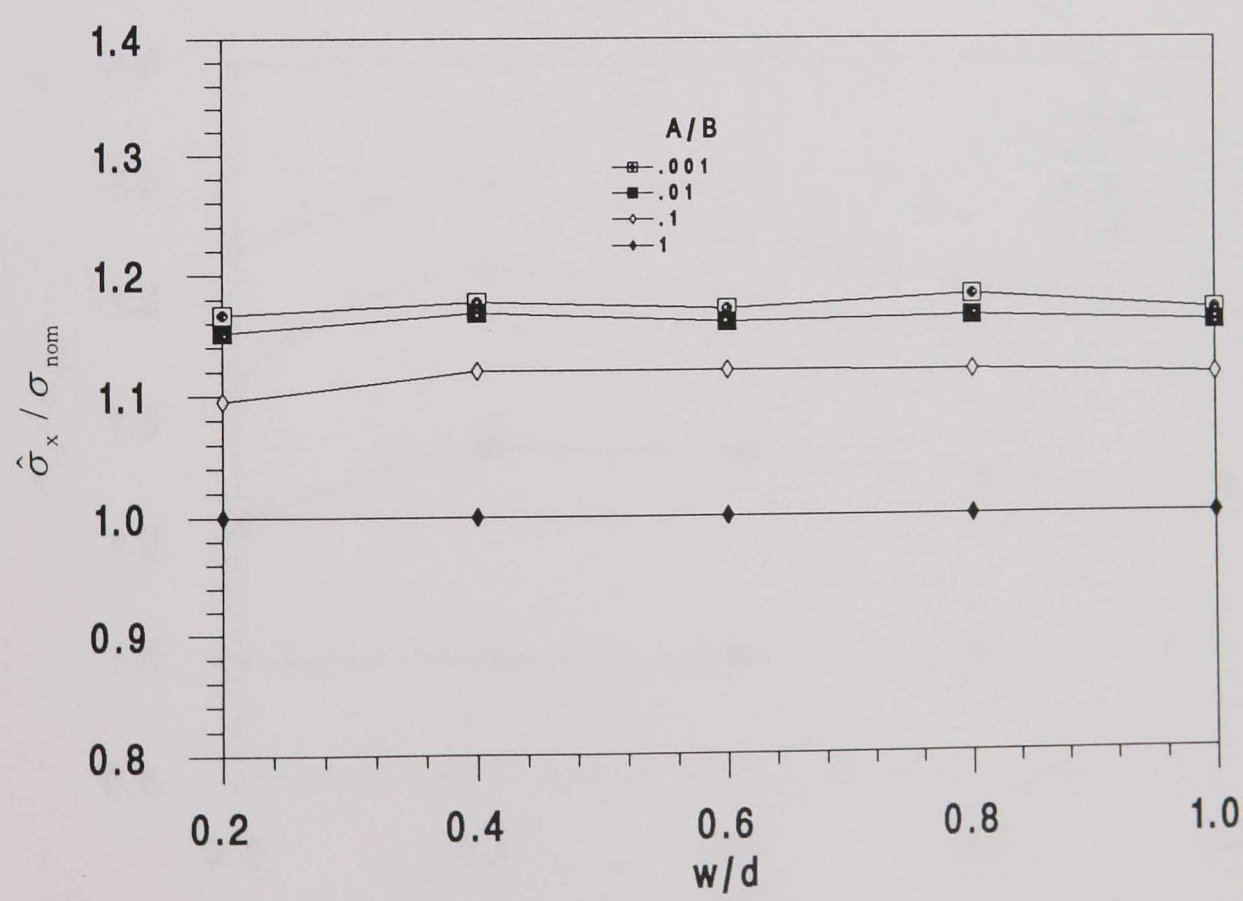

(b) x > w/2, A/B < 1, material B

Fig. 3.3.12 Effect of A/B on the centre-line (r = 0) variations of $\hat{\sigma}_x / \sigma_{nom}$ with w/d, for n = 4.

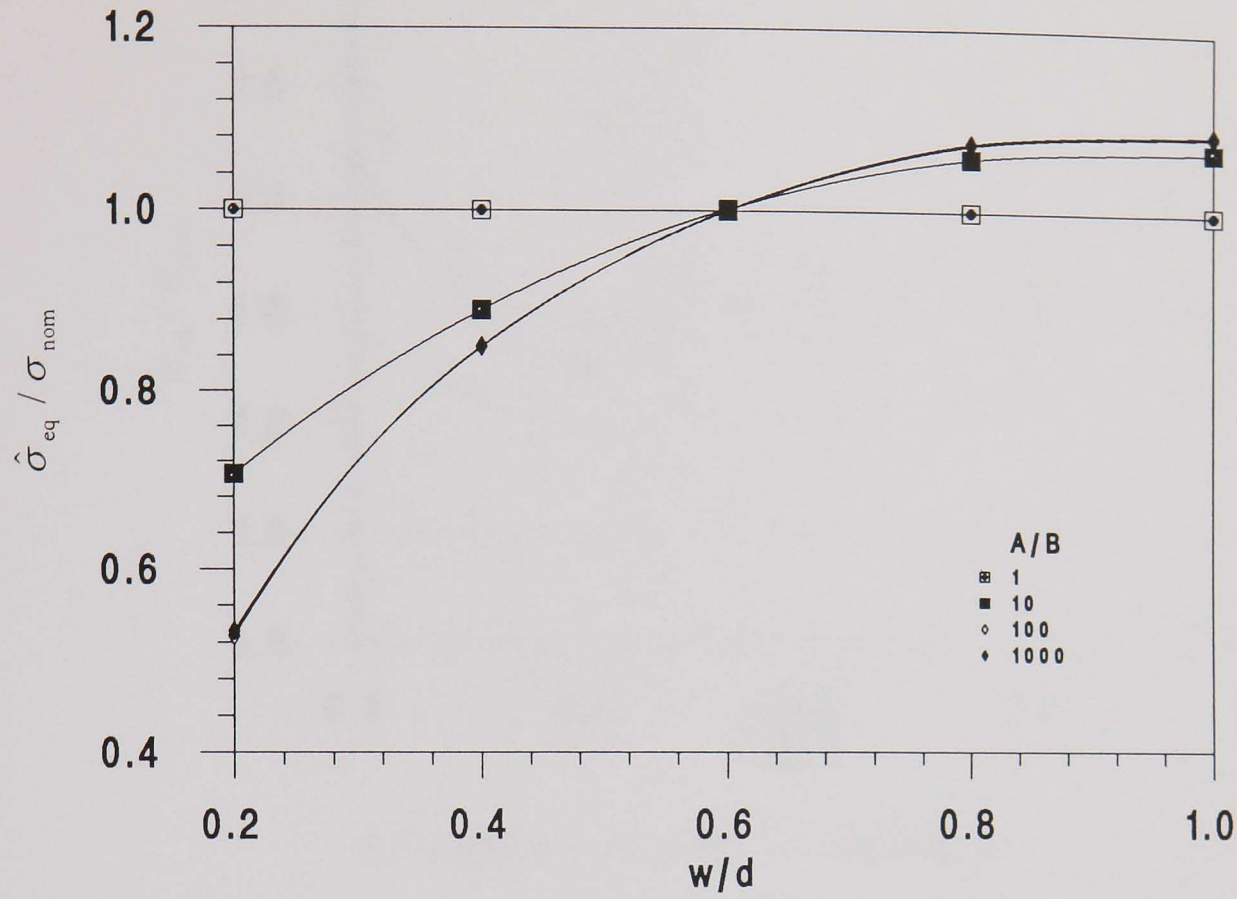

3.3.13(a) x = 0, A/B > 1, material A

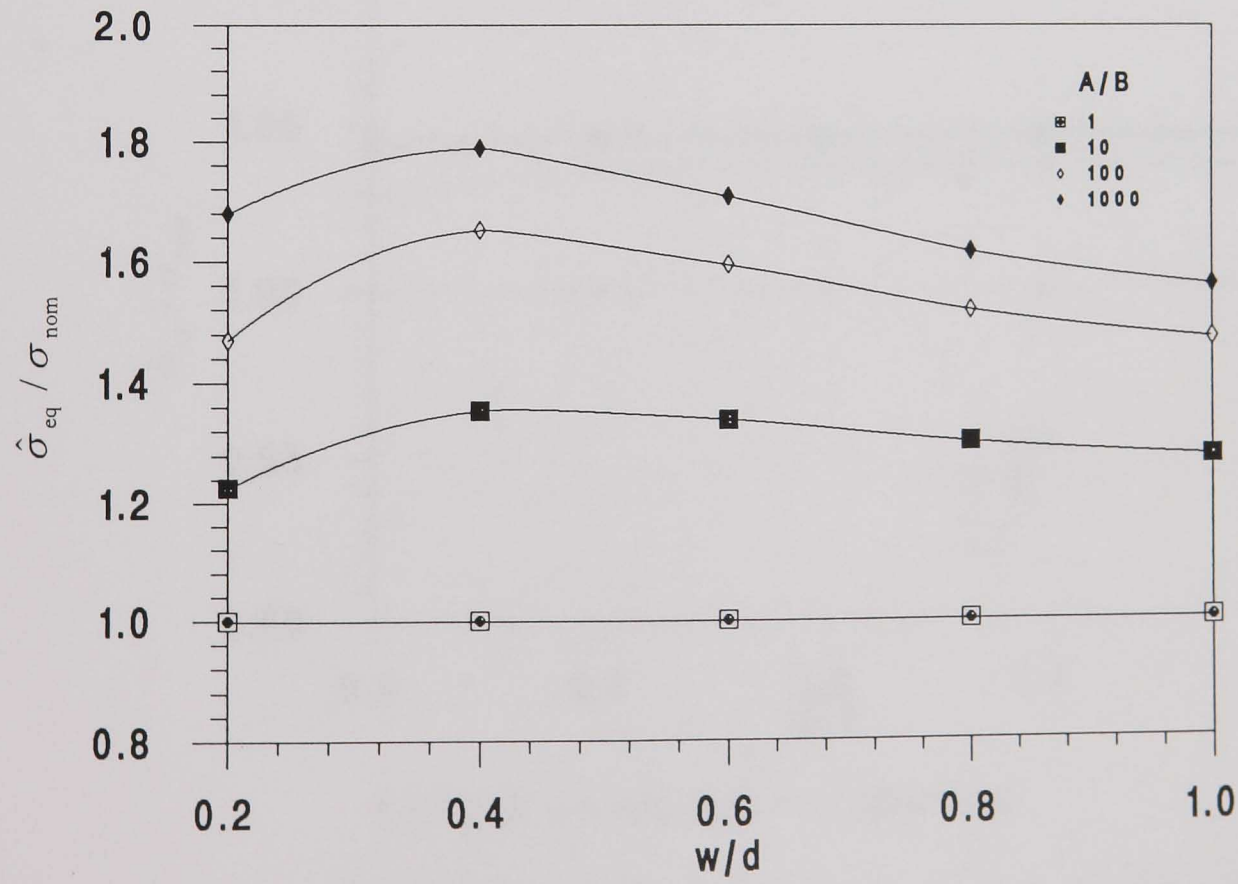

3.3.13(b) x = w/2, A/B > 1, material B

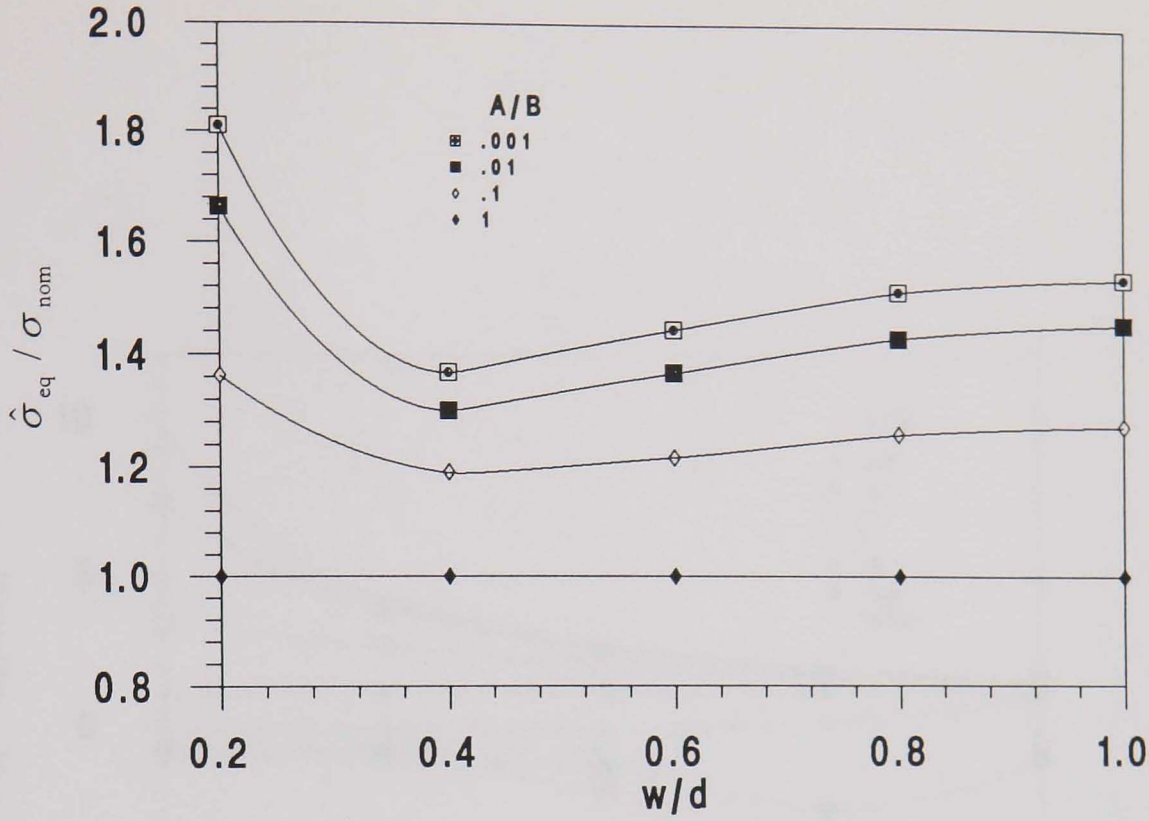

3.3.13(c) x = w/2, A/B < 1, material A

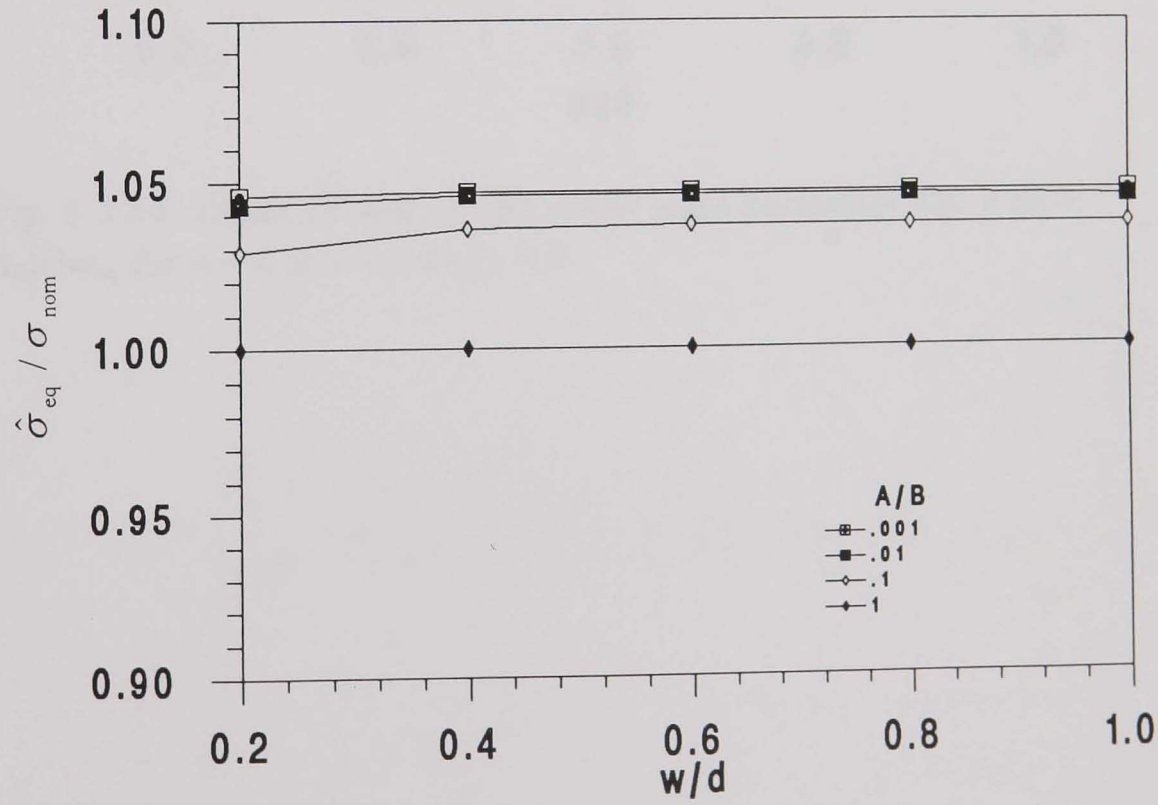

3.3.13(d) x > w/2, A/B < 1, material B

Fig. 3.3.13 Effect of A/B on the centre-line (r = 0) variations of $\hat{\sigma}_{eq} / \sigma_{nom}$ with w/d, for n = 4.

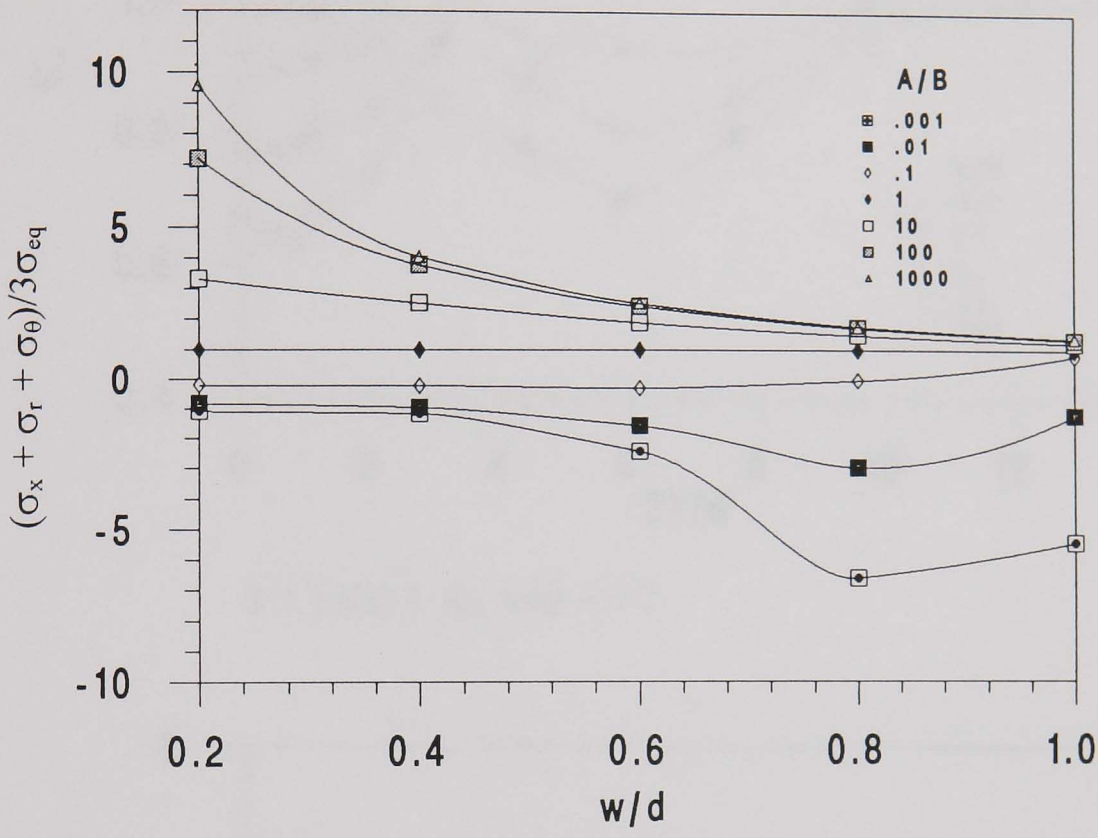

Fig. 3.3.14 Effect of w/d on the stress state parameter $(\sigma_x + \sigma_r + \sigma_\theta)/3\sigma_{eq}$ for n = 4 at x = 0 and r = 0.

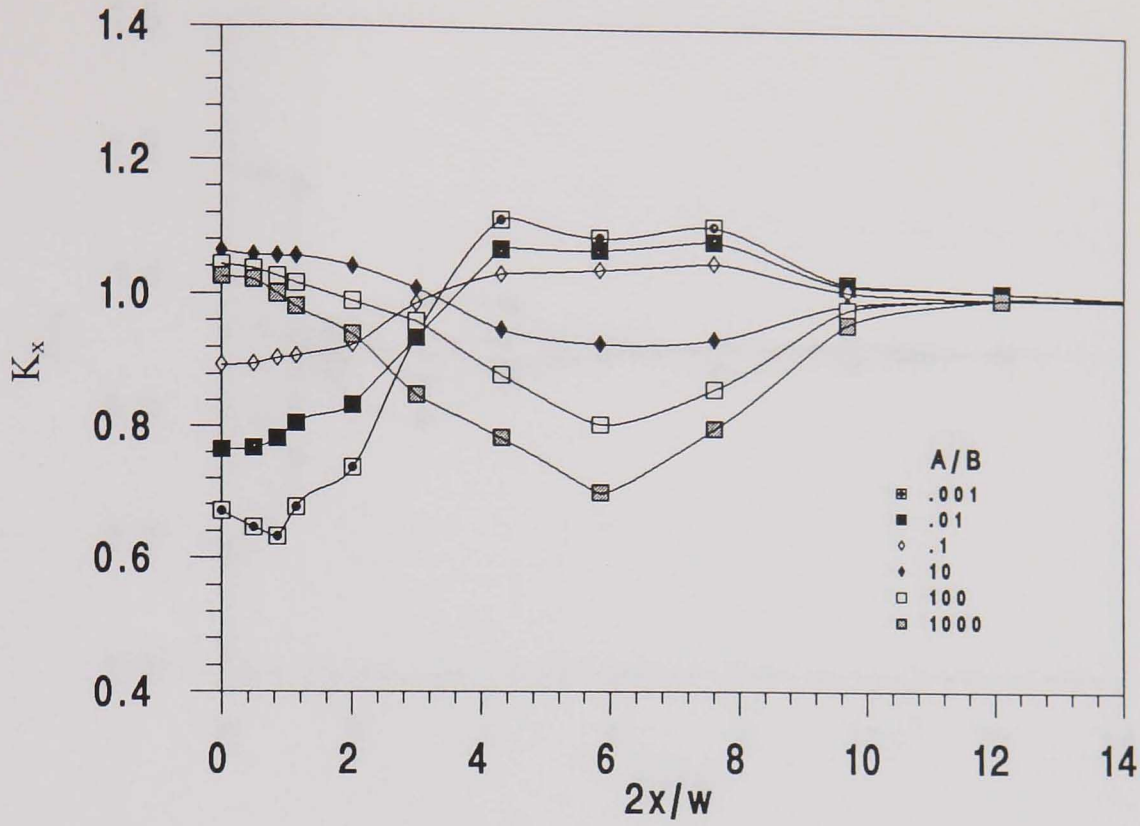

3.3.15(a) I K_x, w/d = 0.2

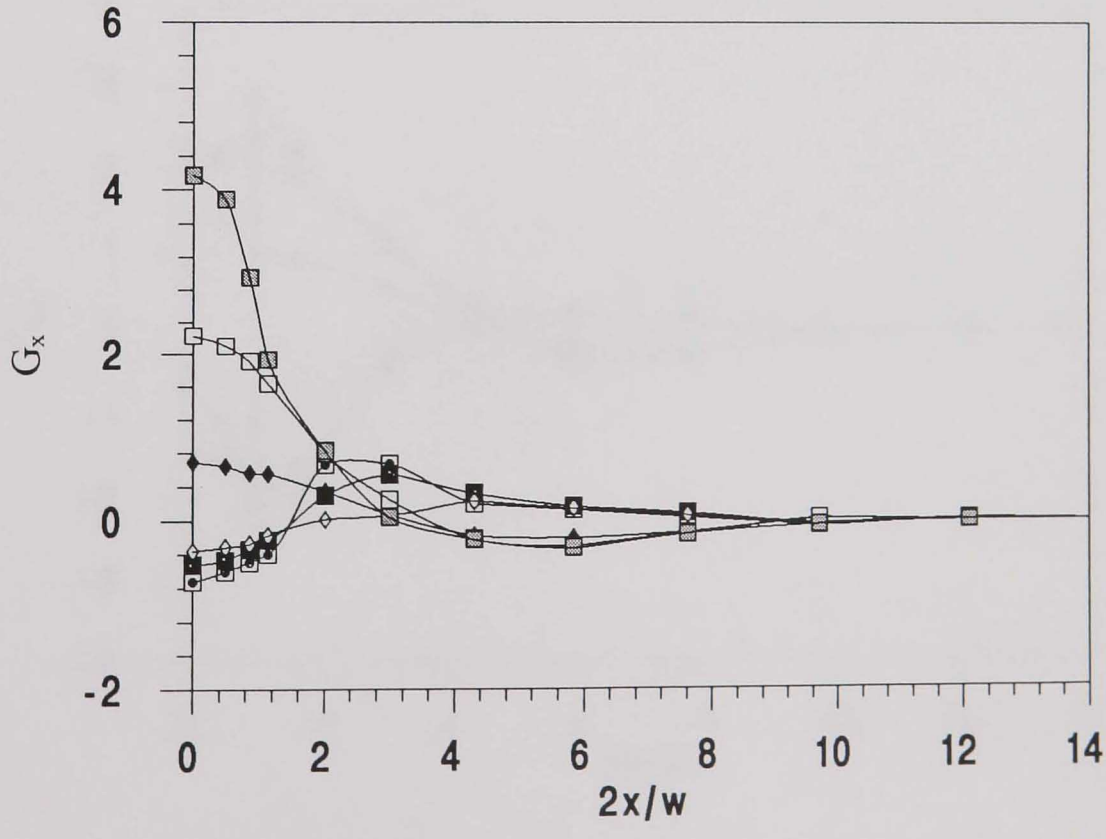

3.3.15(a) II G_x, w/d = 0.2

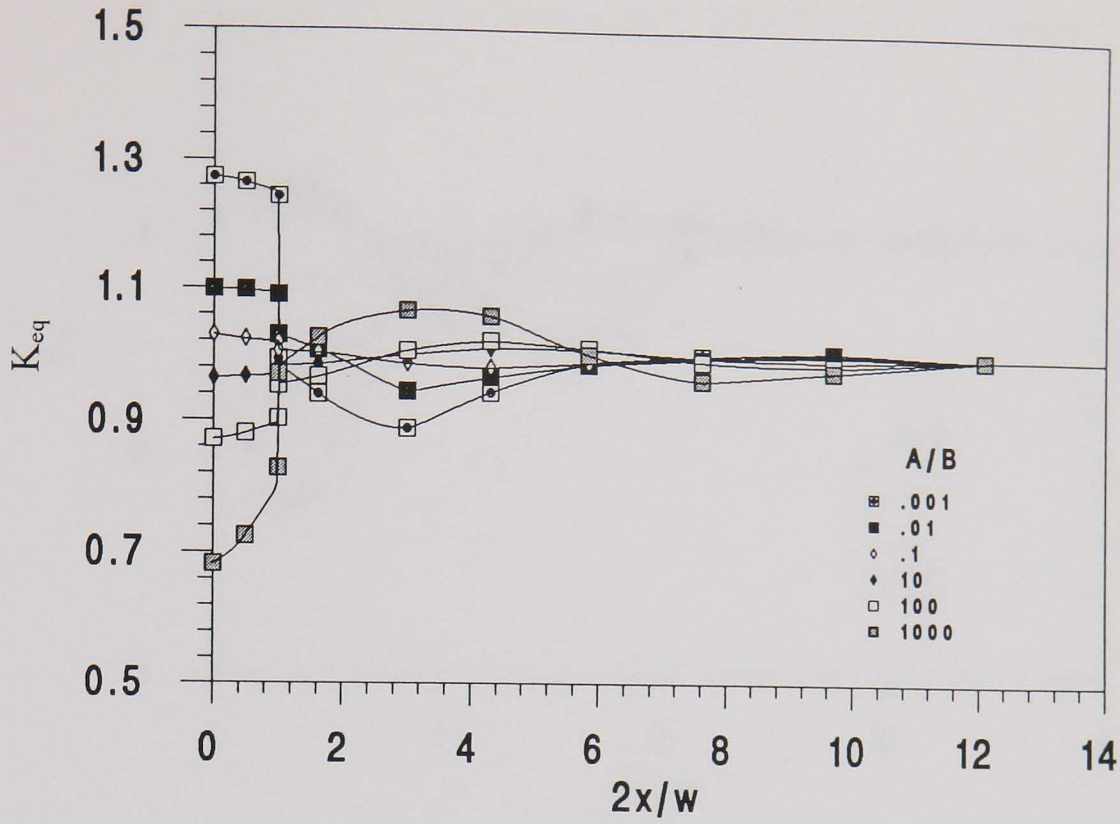

3.3.15(a) III K_{eq}, w/d = 0.2

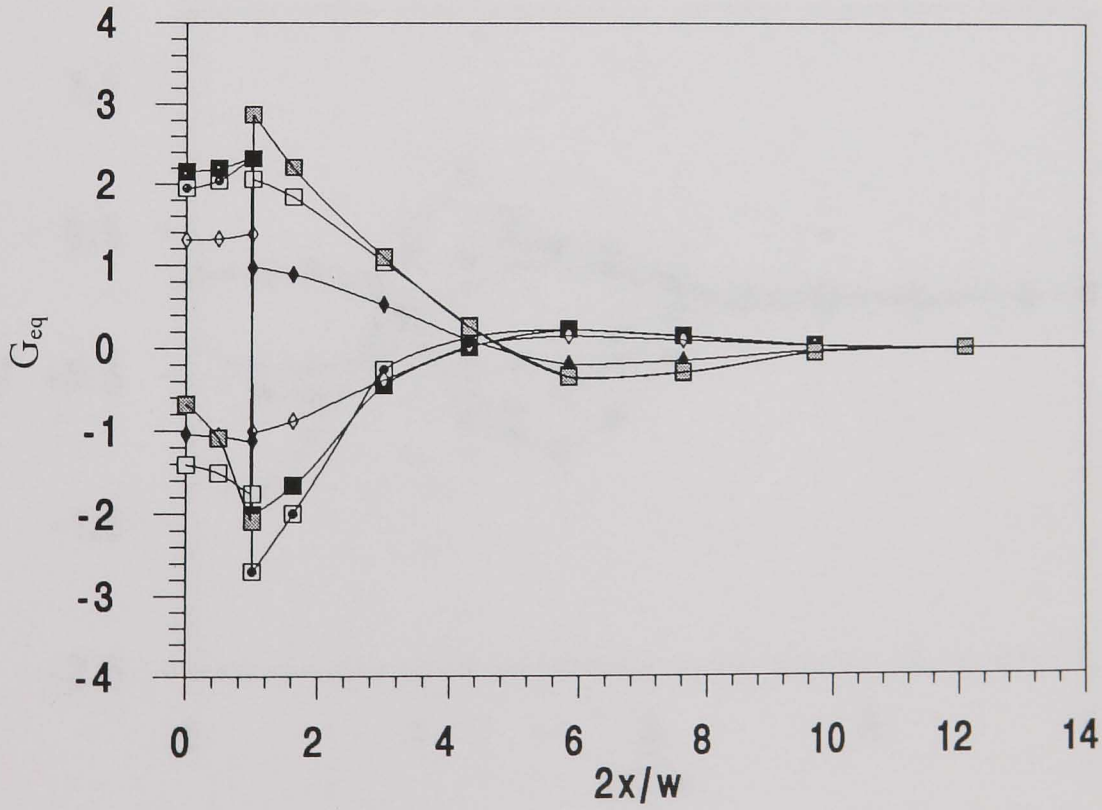

3.3.15(a) IV G_{eq}, w/d = 0.2

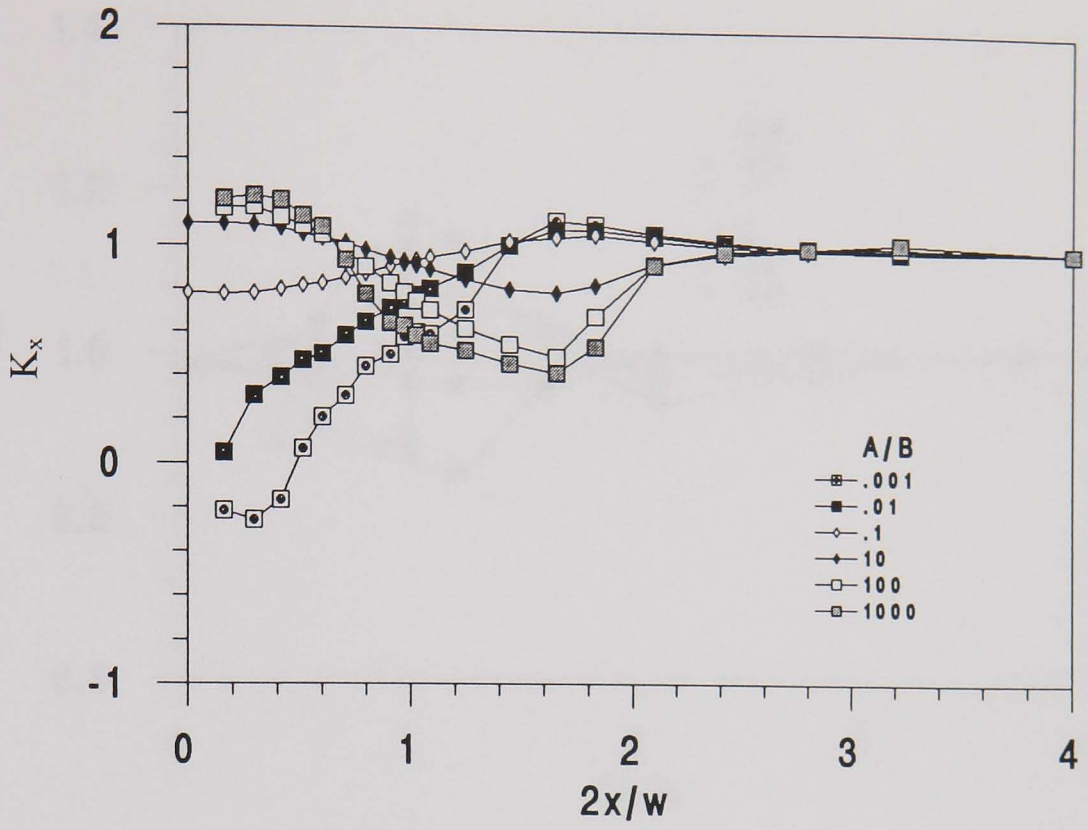

3.3.15(b) I K_x, w/d = 1

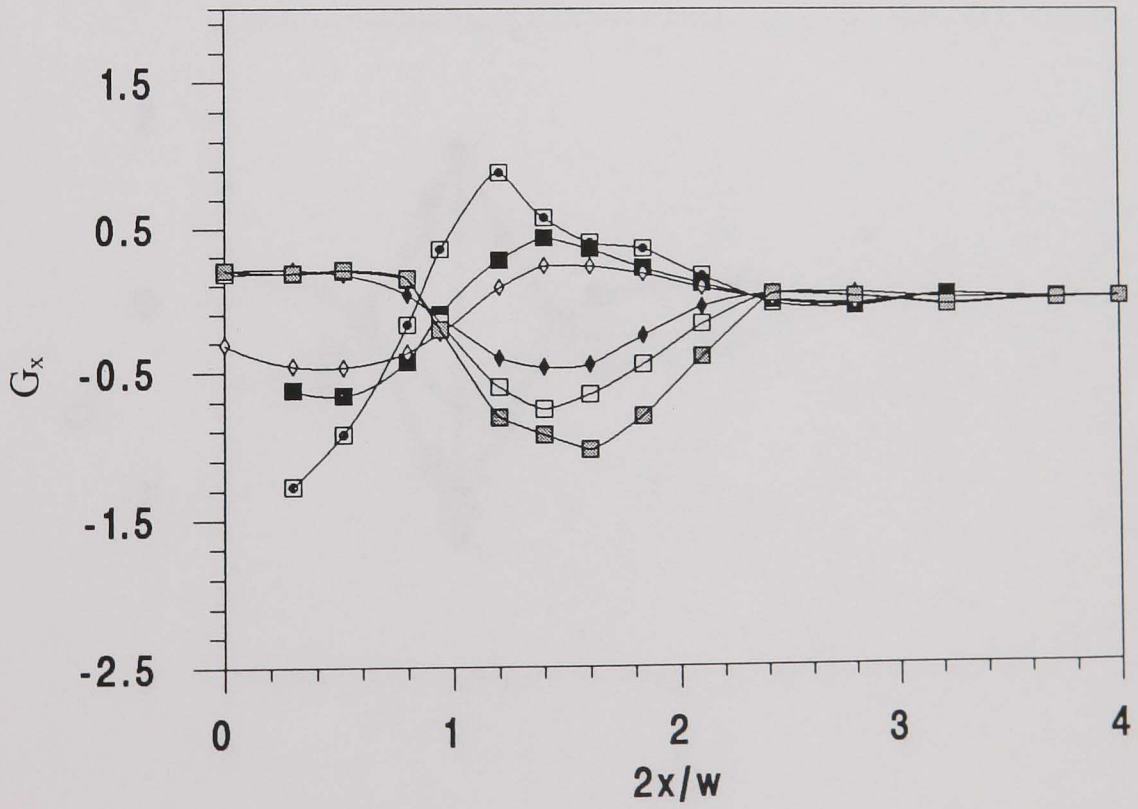

3.3.15(b) II G_x, w/d = 1

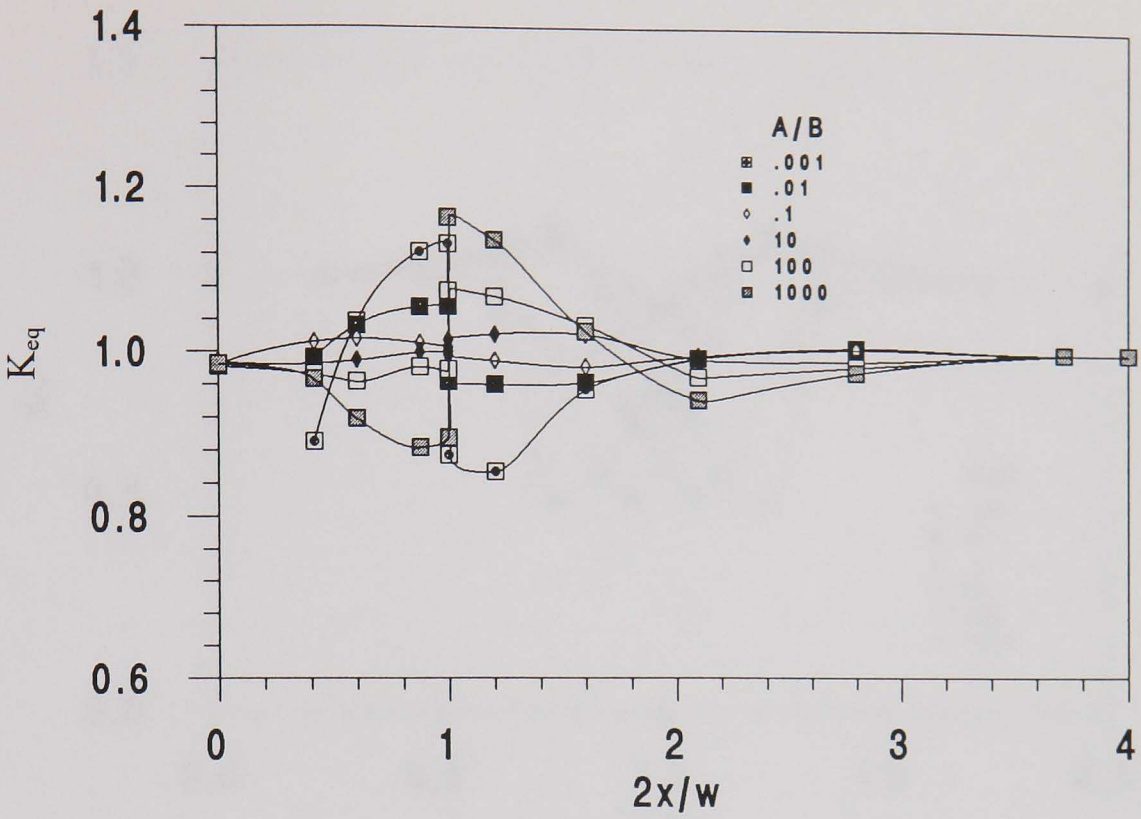

3.3.15(b) III K_{eq}, w/d = 1

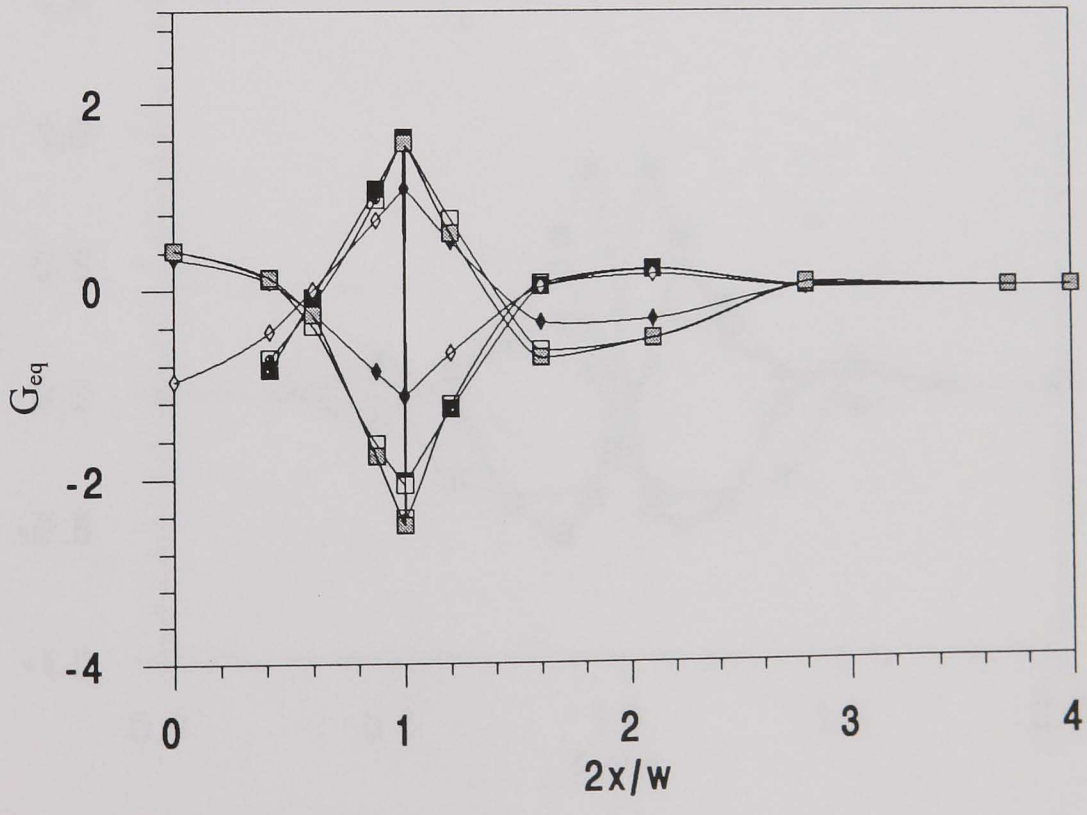

3.3.15(b) IV G_{eq}, w/d = 1

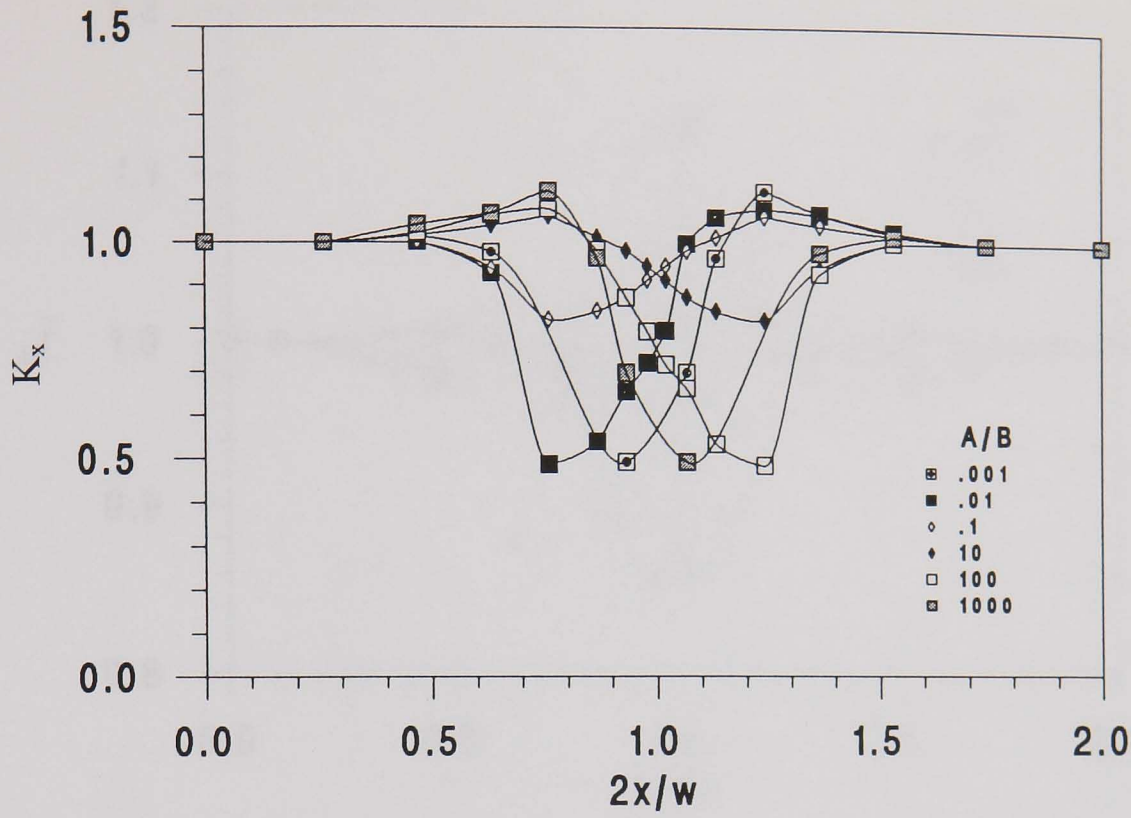

3.3.15(c) I K_x, w/d = 3

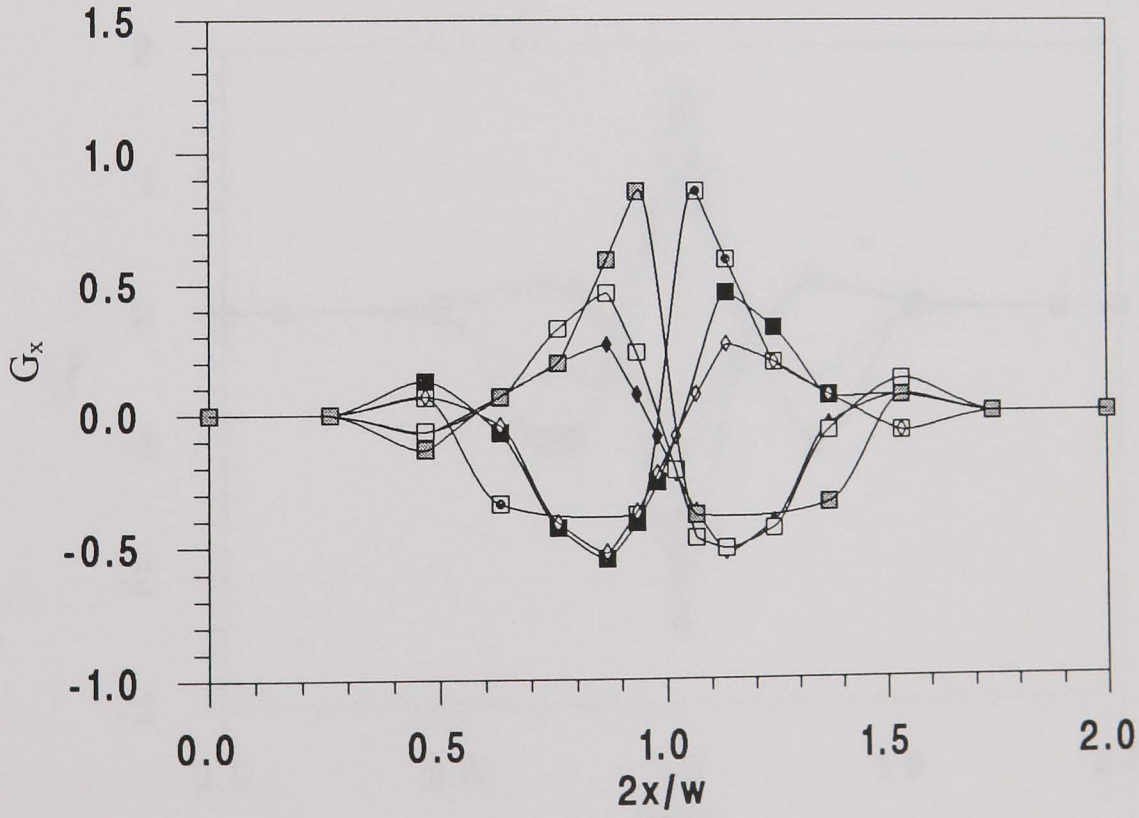

3.3.15(c) II G_x, w/d = 3

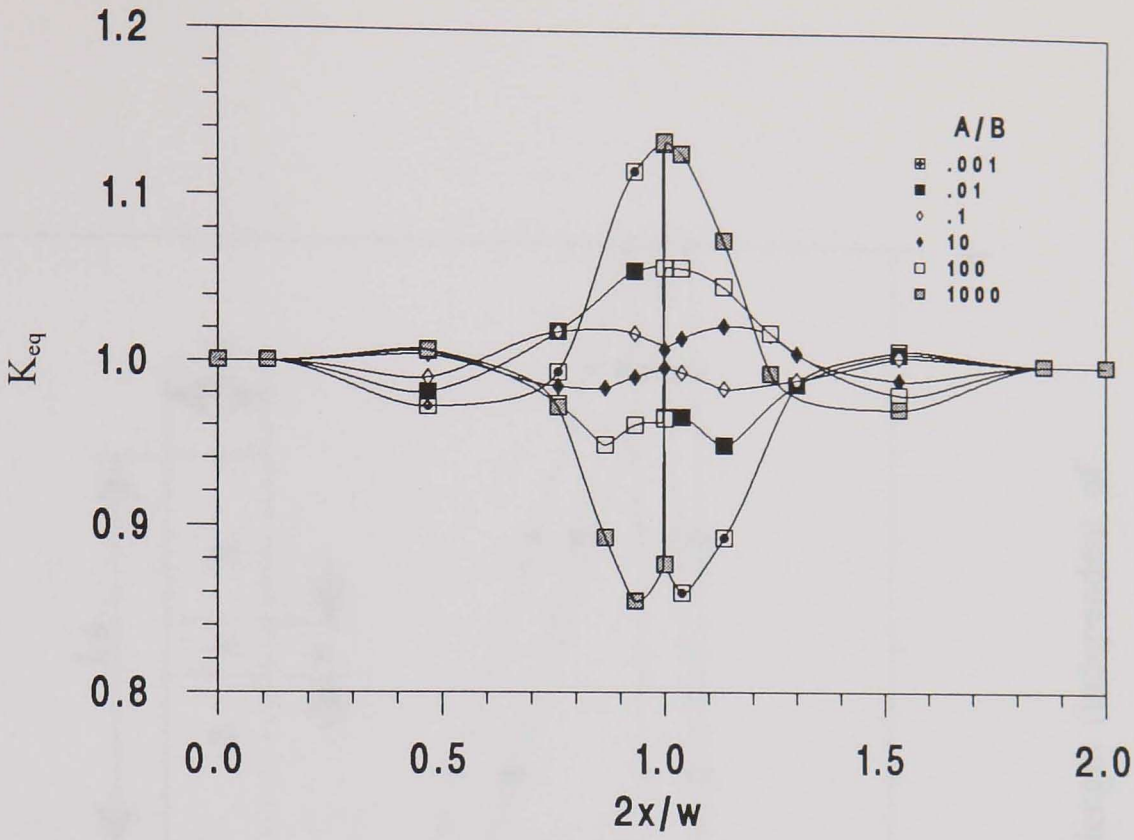

3.3.15(c) III K_{eq}, w/d = 3

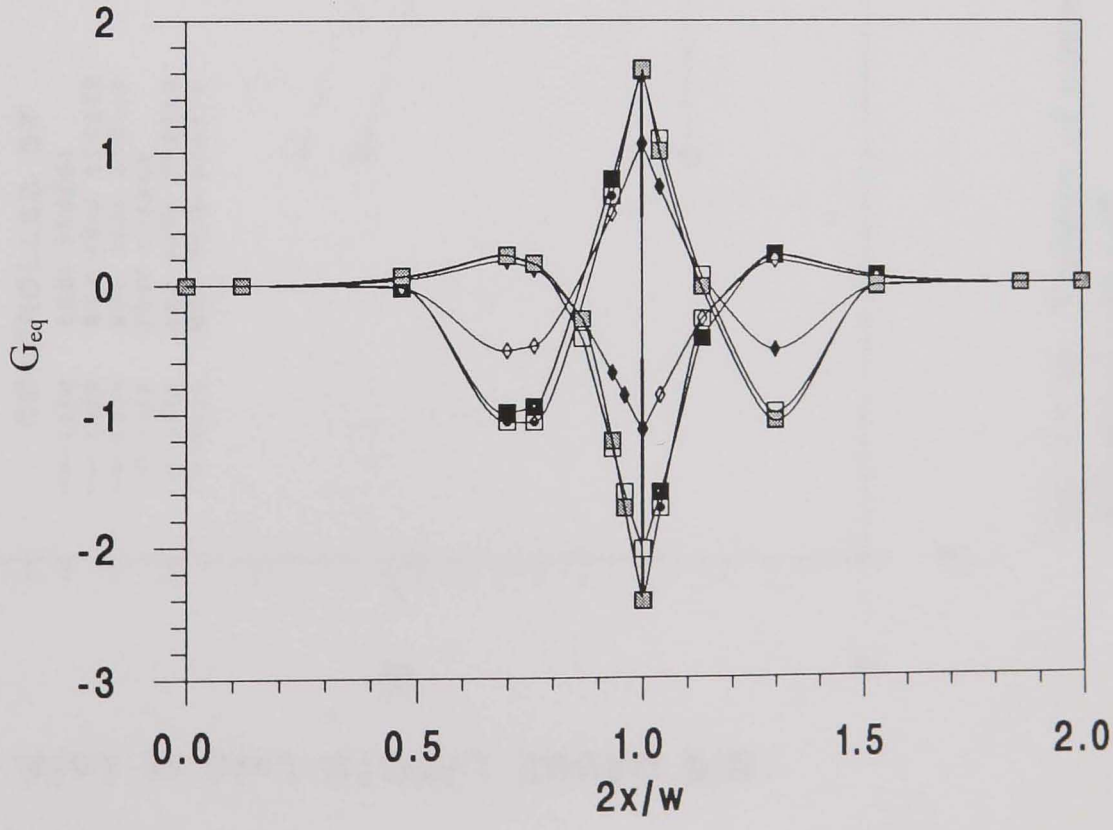

3.3.15(c) IV G_{eq}, w/d = 3

Fig. 3.3.15 Centre-line (r = 0) variations of K_x, G_x, K_{eq} and G_{eq} with 2x/w for a range of A/B.

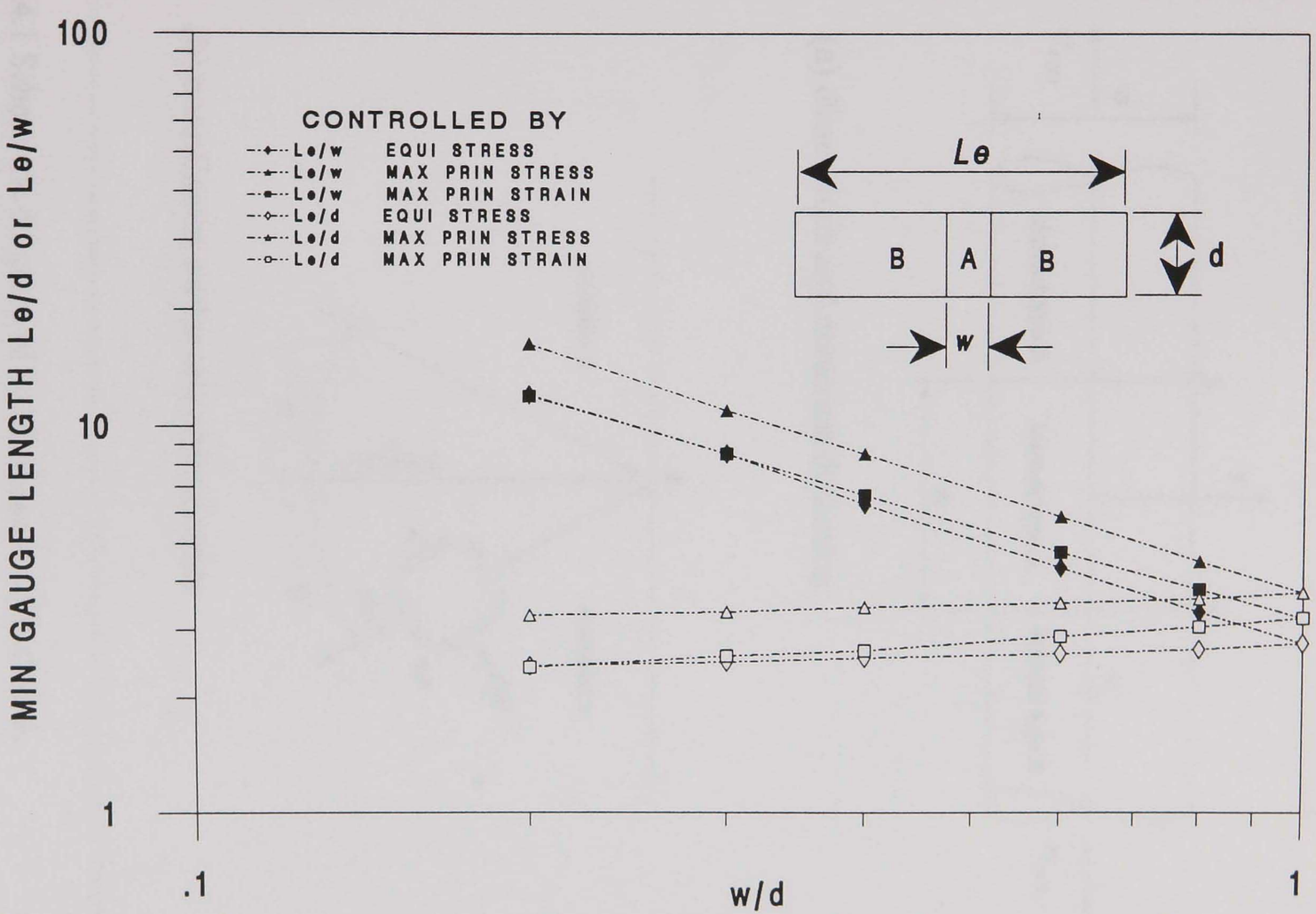

Fig. 3.3.16 Variation of minimum gauge length (independent of A/B and n) with w/d.

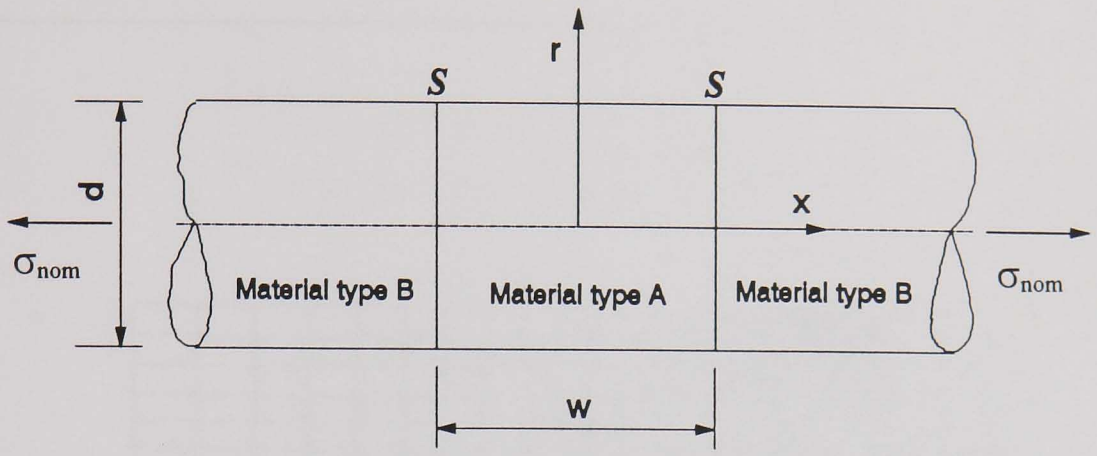

(a) dimensions and materials definition

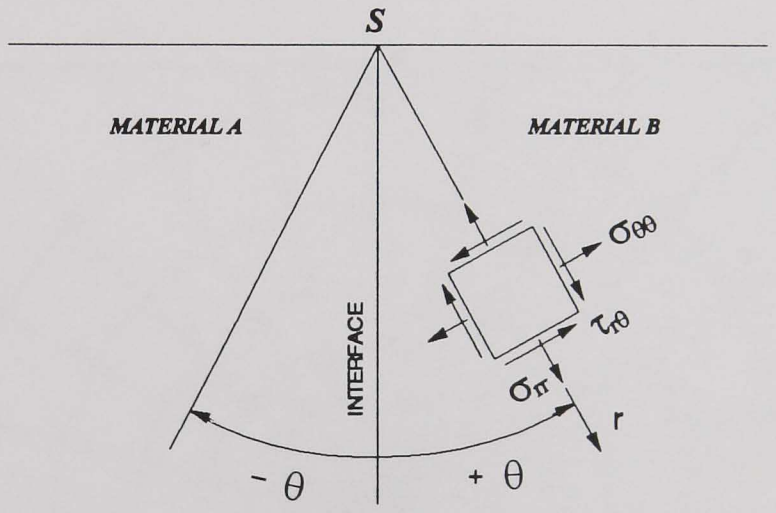

(b) coordinates and stress components

Fig. 3.4.1 Schematic diagram of an idealised, two-material, cross-weld specimen.

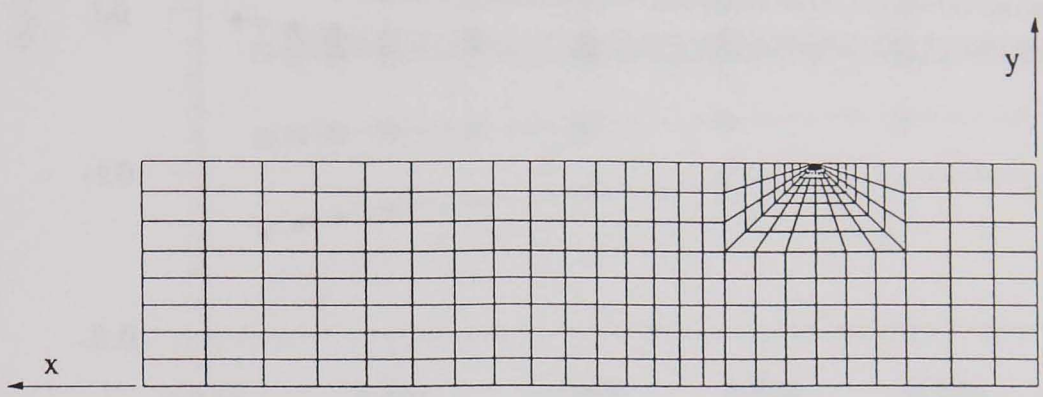

(a) general mesh

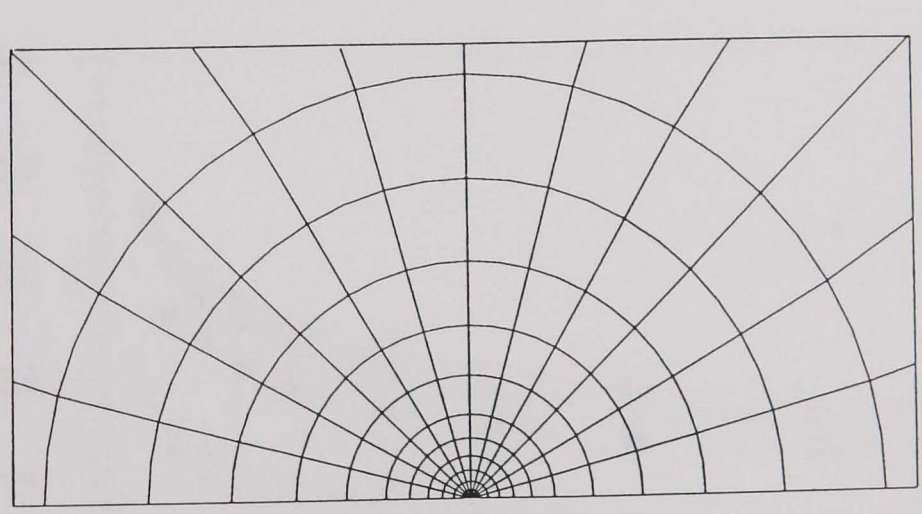

(b) mesh details in the vicinity of the singularity S

Fig. 3.4.2 A typical finite element mesh.

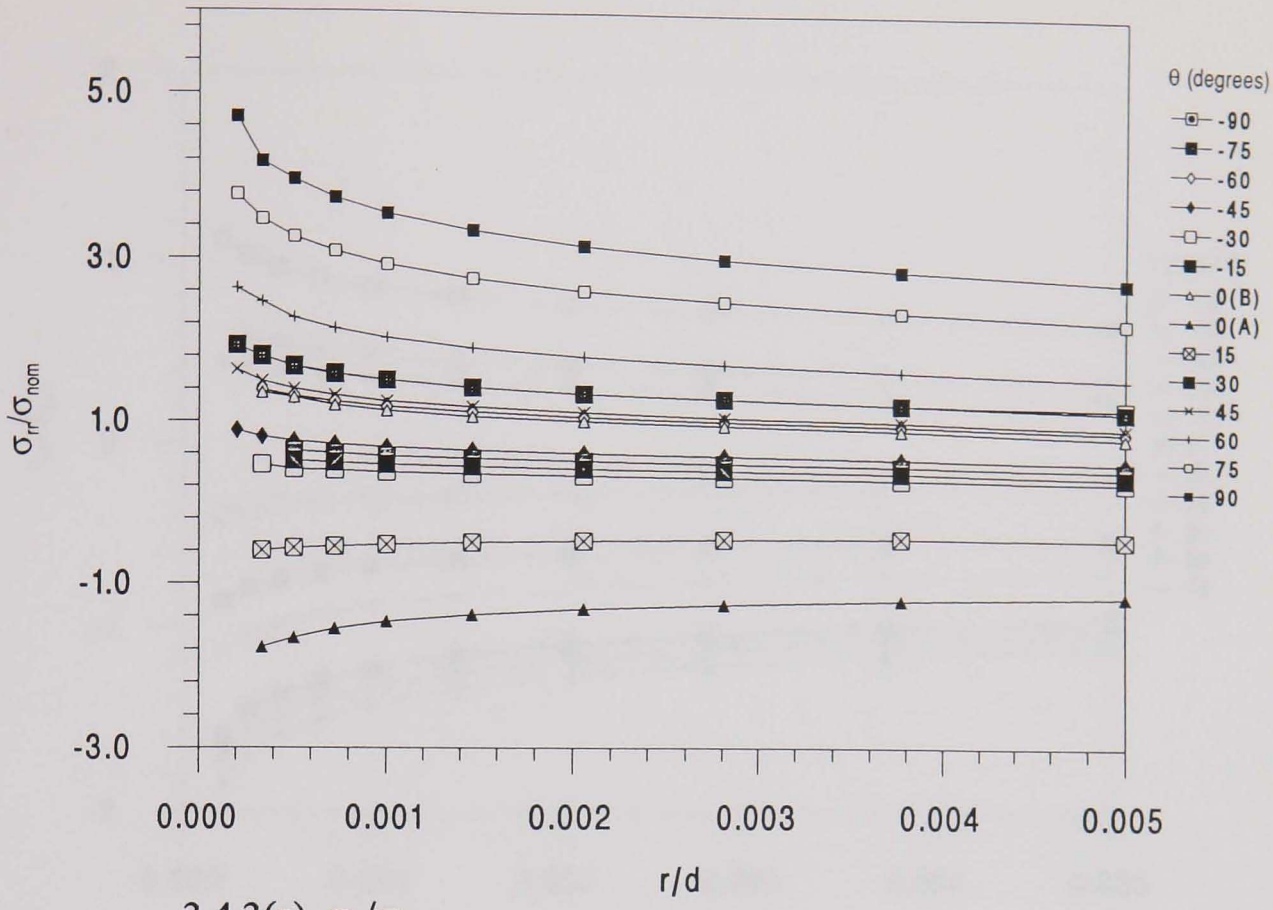

3.4.3(a) σ_{rr}/σ_{nom}

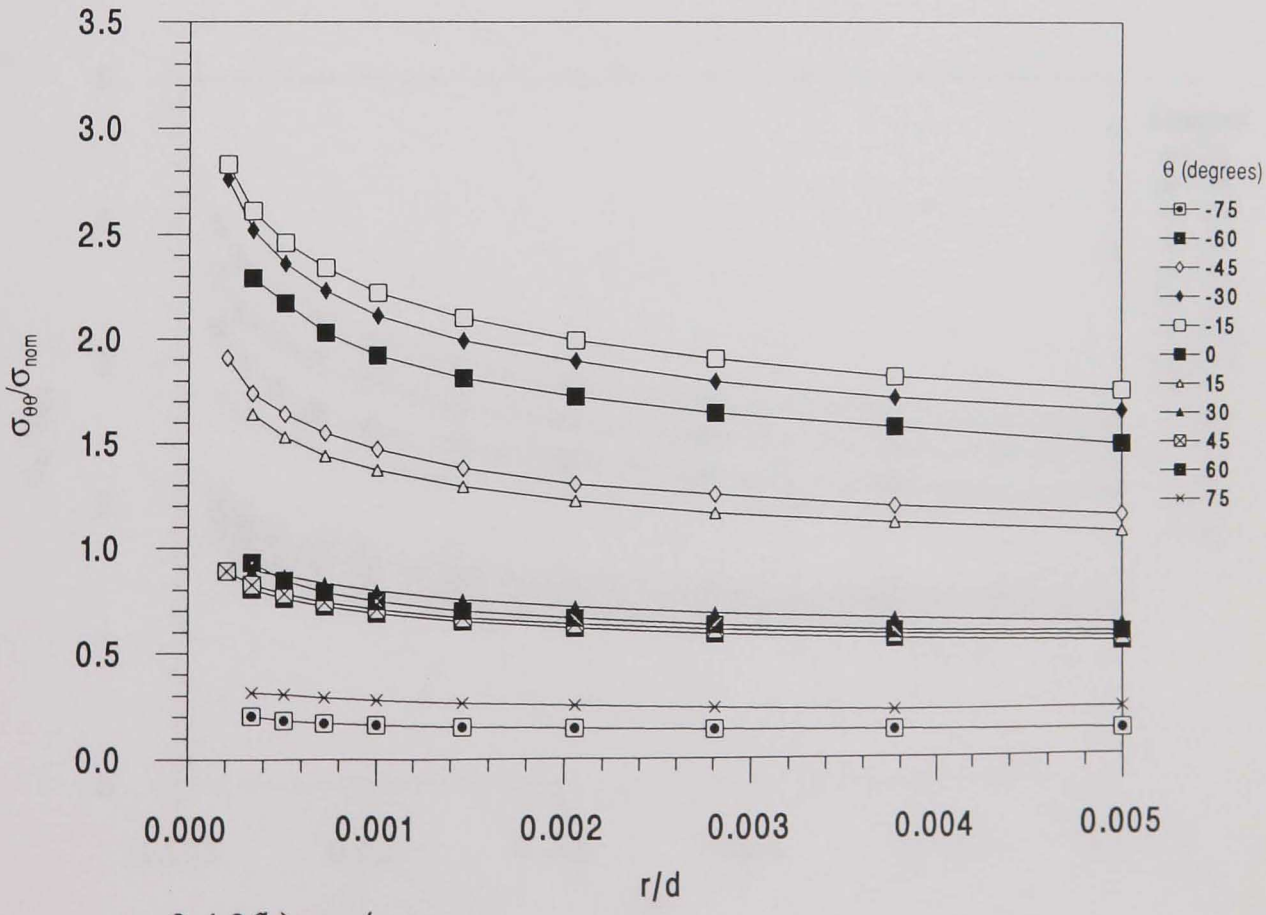

3.4.3(b) $\sigma_{\theta\theta}/\sigma_{nom}$

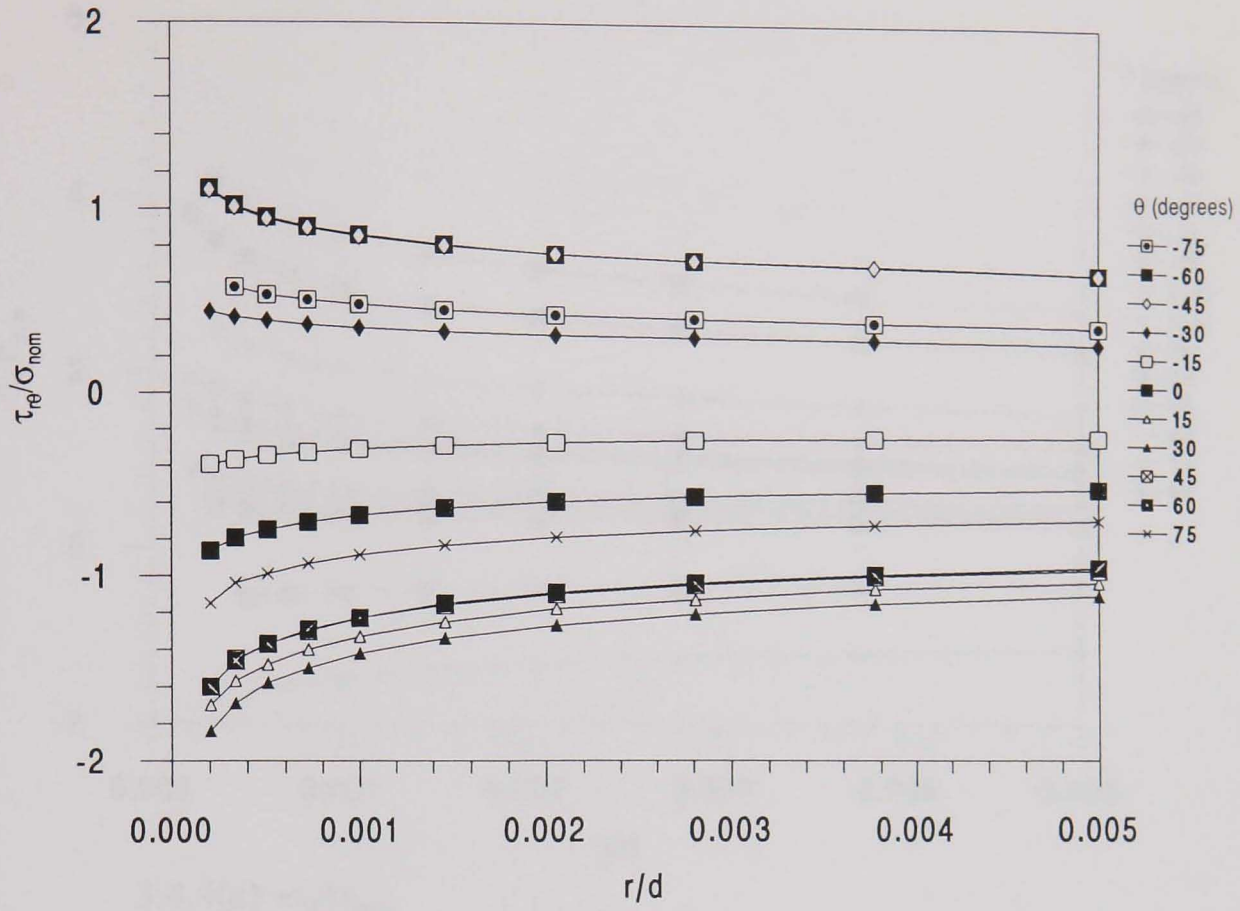

3.4.3(c) $\tau_{r\theta}/\sigma_{nom}$

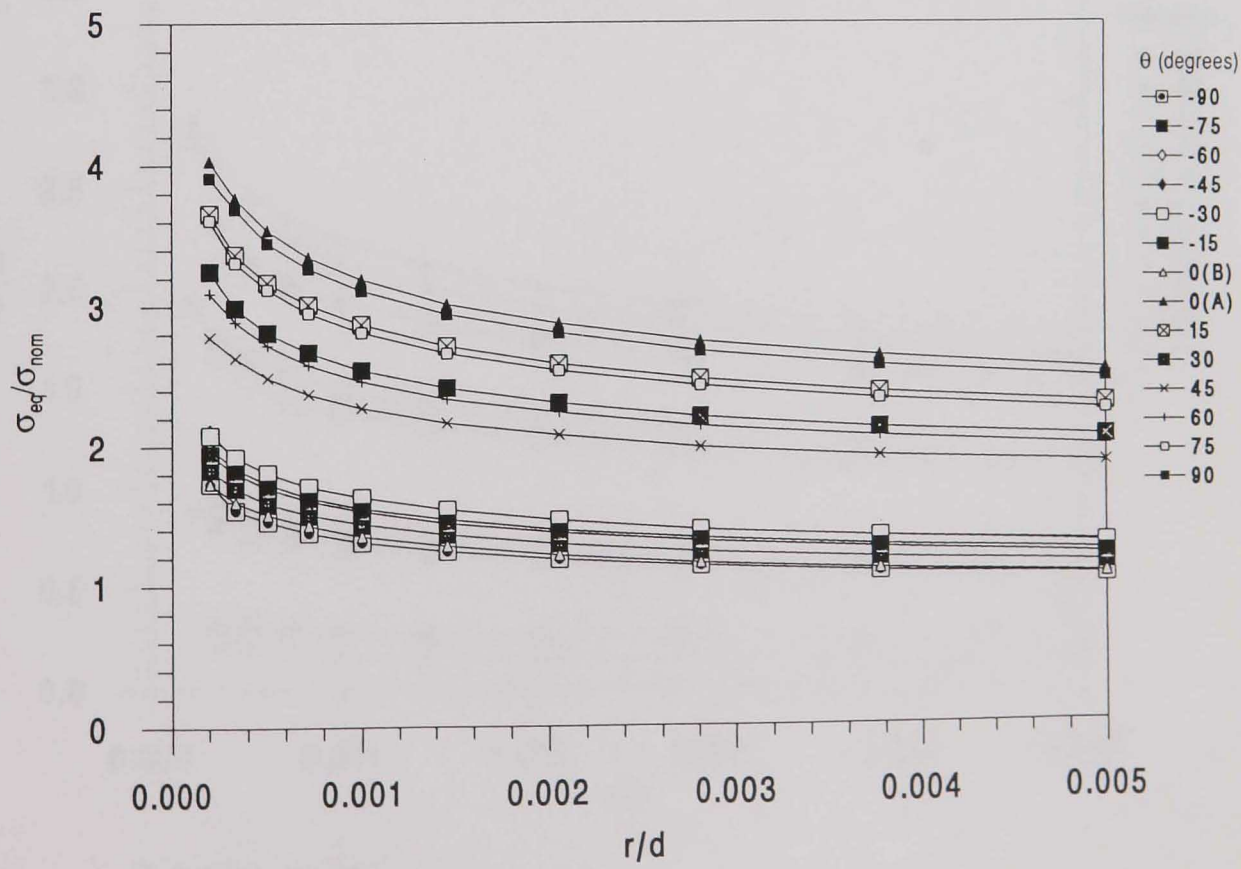

3.4.3(d) σ_{eq}/σ_{nom}

Fig. 3.4.3 Variations of stresses with r/d for a range of angular positions θ; w/d = 0.5, n = 2 and A/B = 0.1.

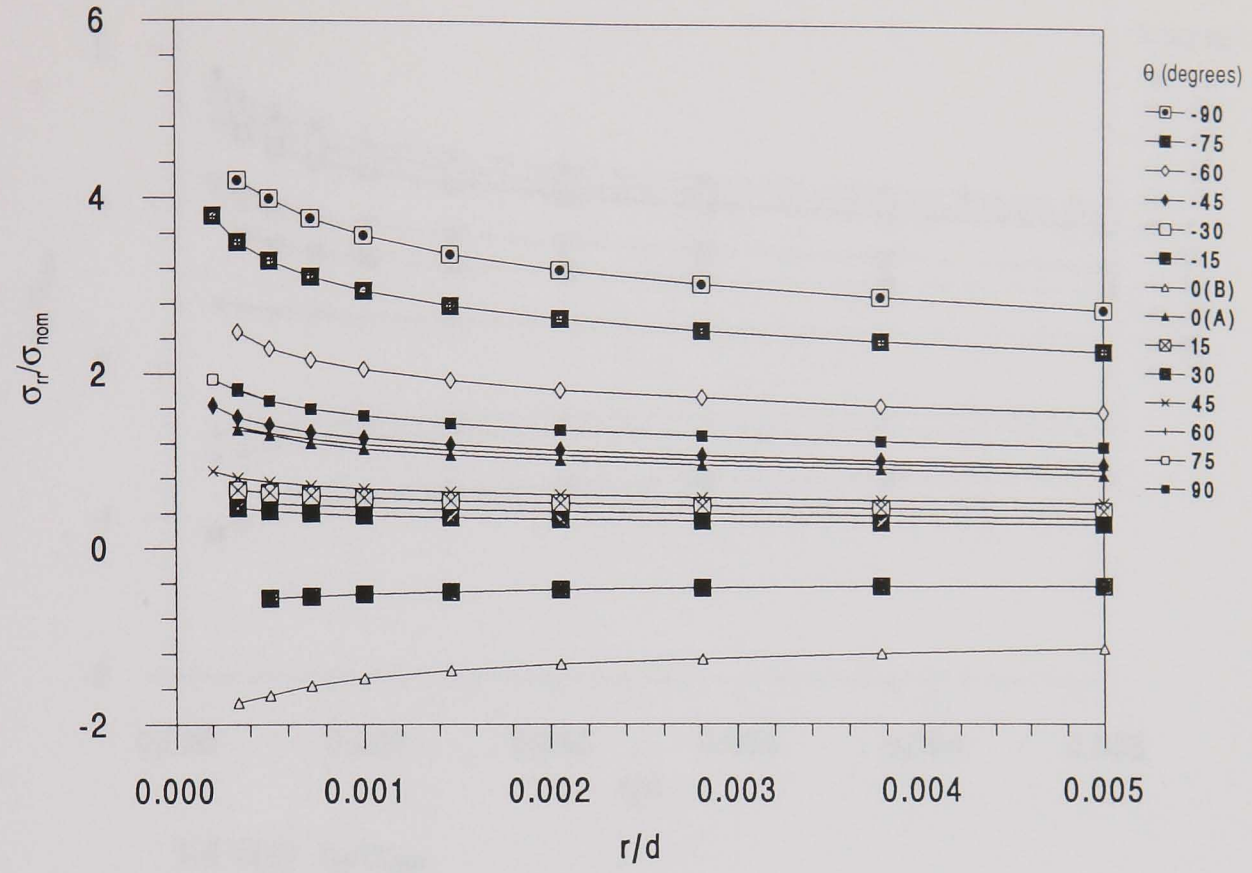

3.4.4(a) σ_{rr}/σ_{nom}

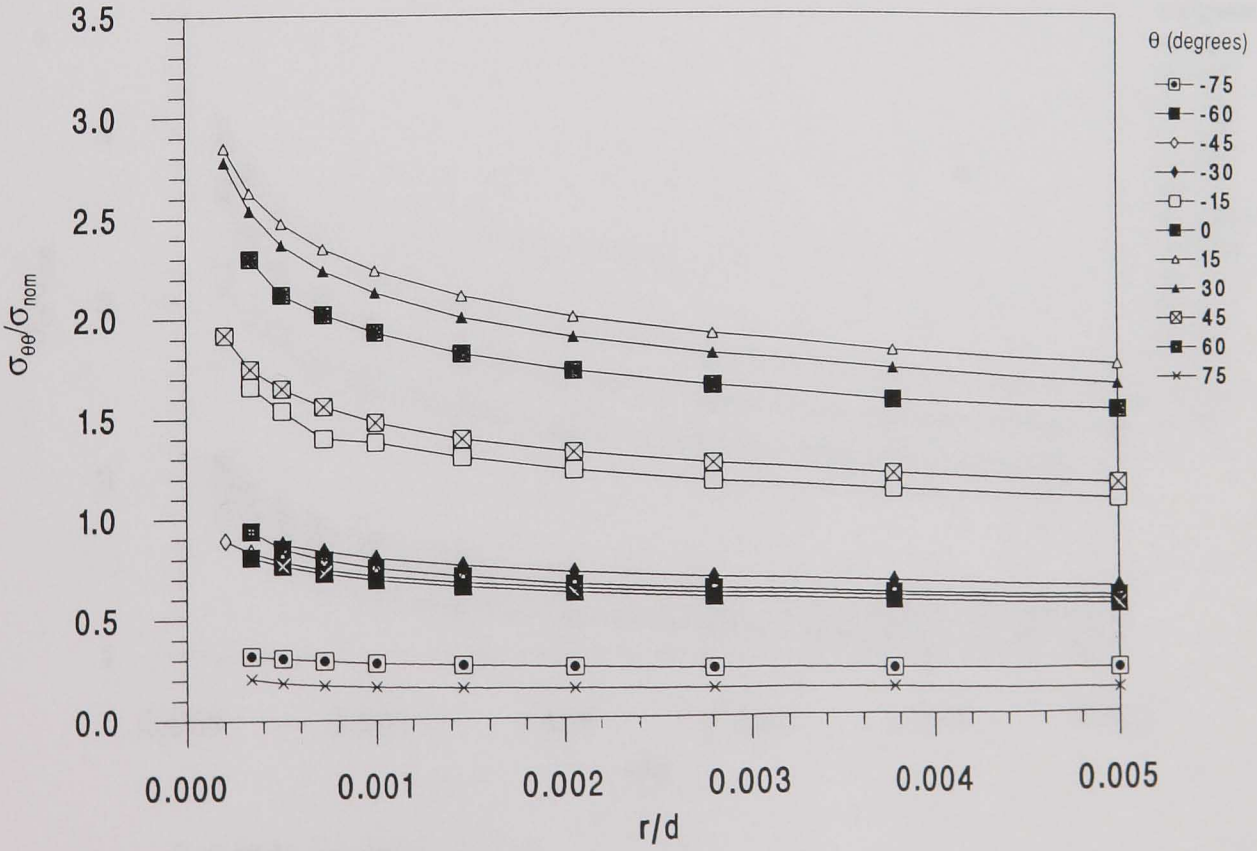

3.4.4(b) $\sigma_{\theta\theta}/\sigma_{nom}$

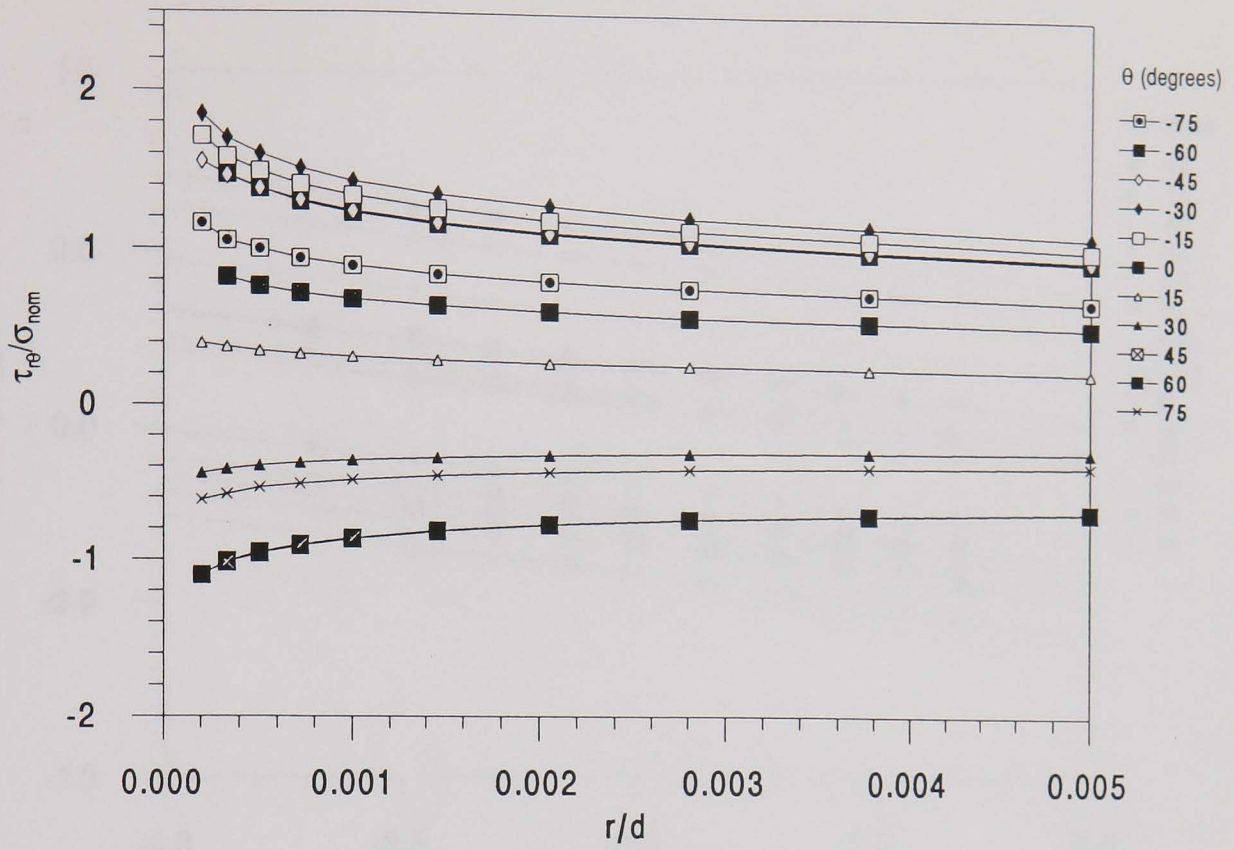

3.4.4(c) $\tau_{r\theta}/\sigma_{nom}$

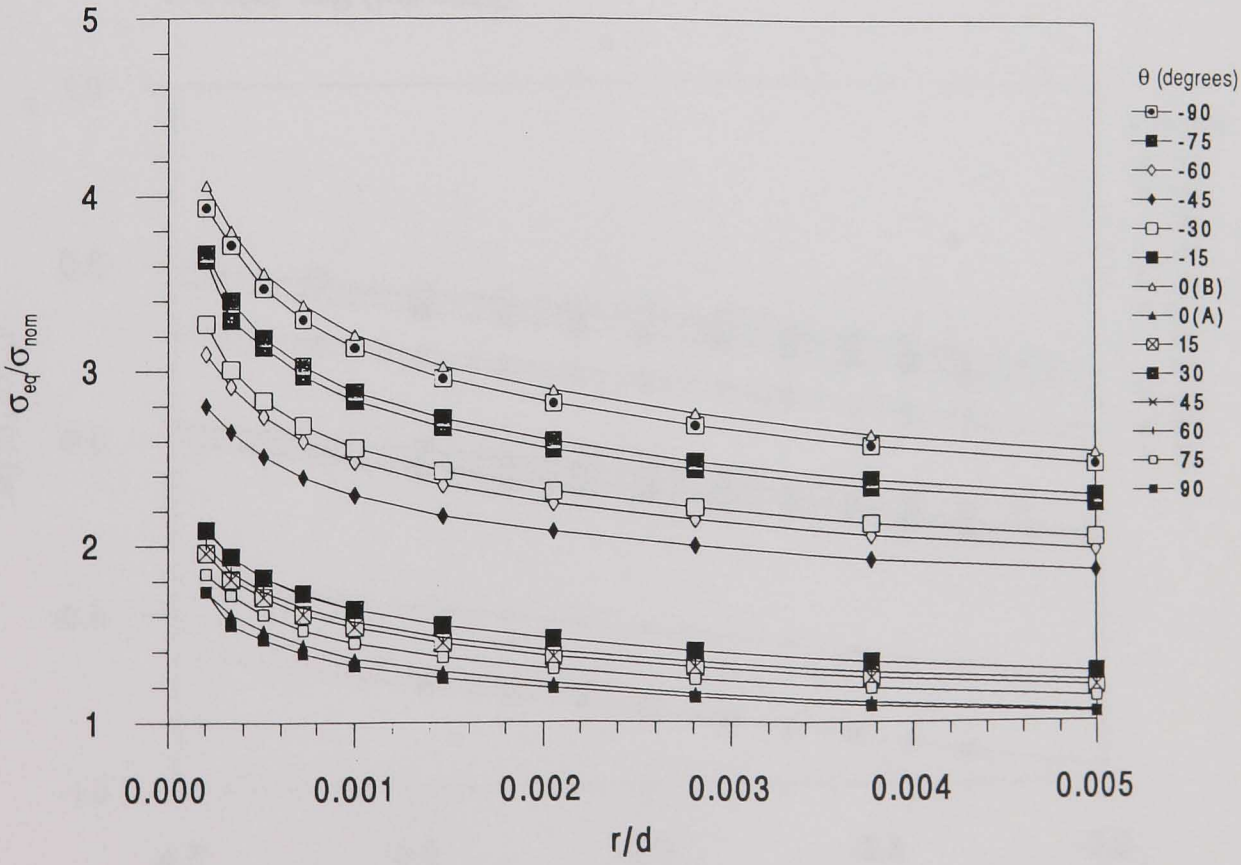

3.4.4(d) σ_{eq}/σ_{nom}

Fig. 3.4.4 Variations of stresses with r/d for a range of angular positions θ; w/d = 0.5, n = 2 and A/B = 10.

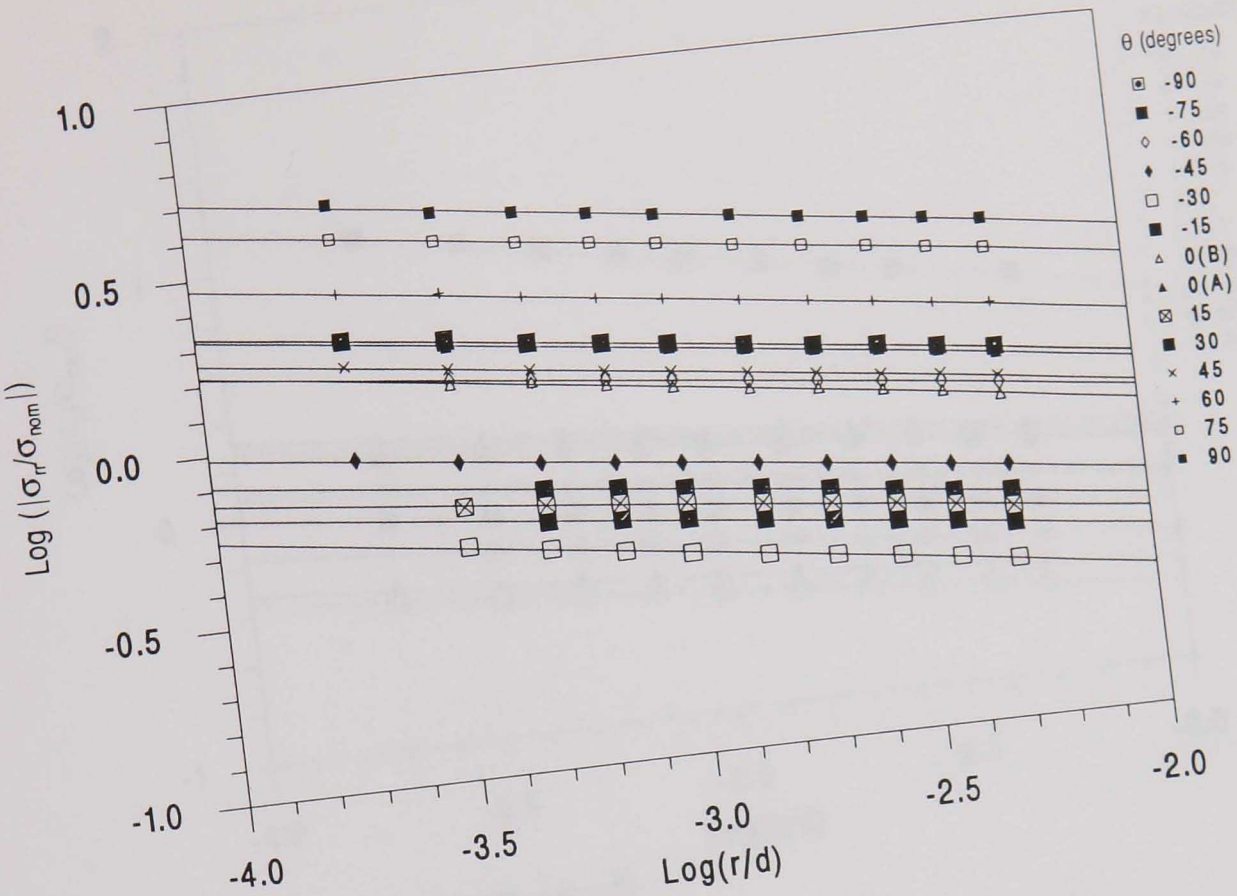

3.4.5(a) log ($|\sigma_{rr}/\sigma_{nom}|$)

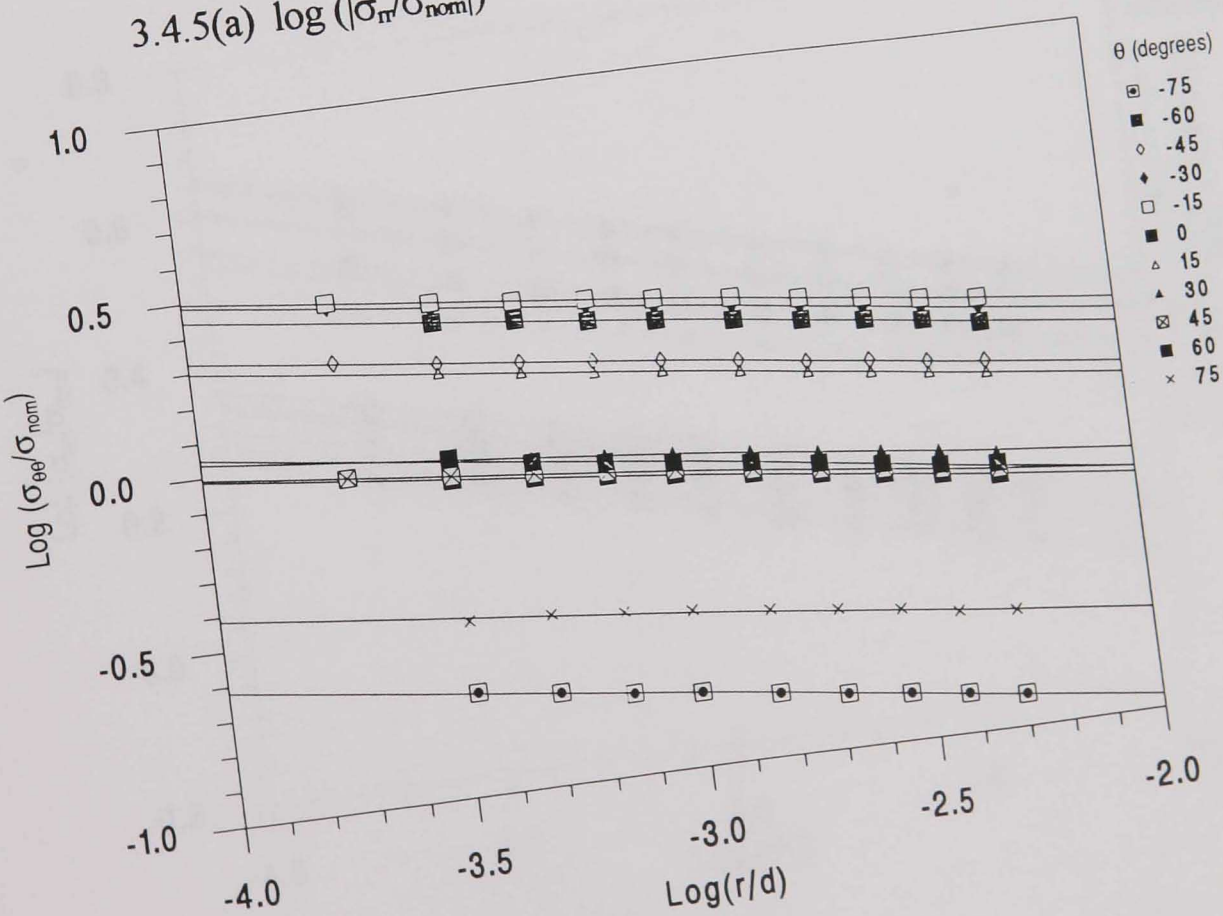

3.4.5(b) log ($\sigma_{\theta\theta}/\sigma_{nom}$)

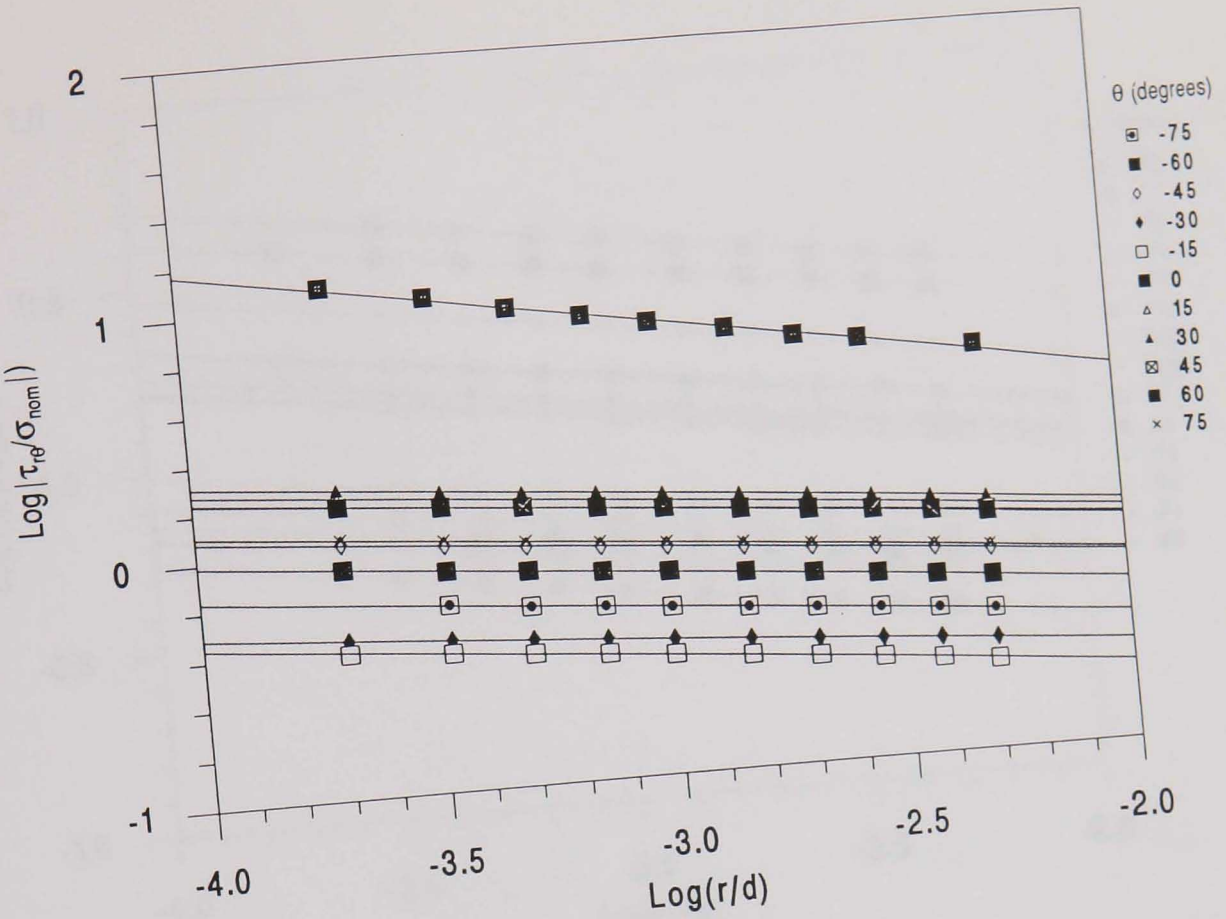

3.4.5(c) log ($|\tau_{r\theta}/\sigma_{nom}|$)

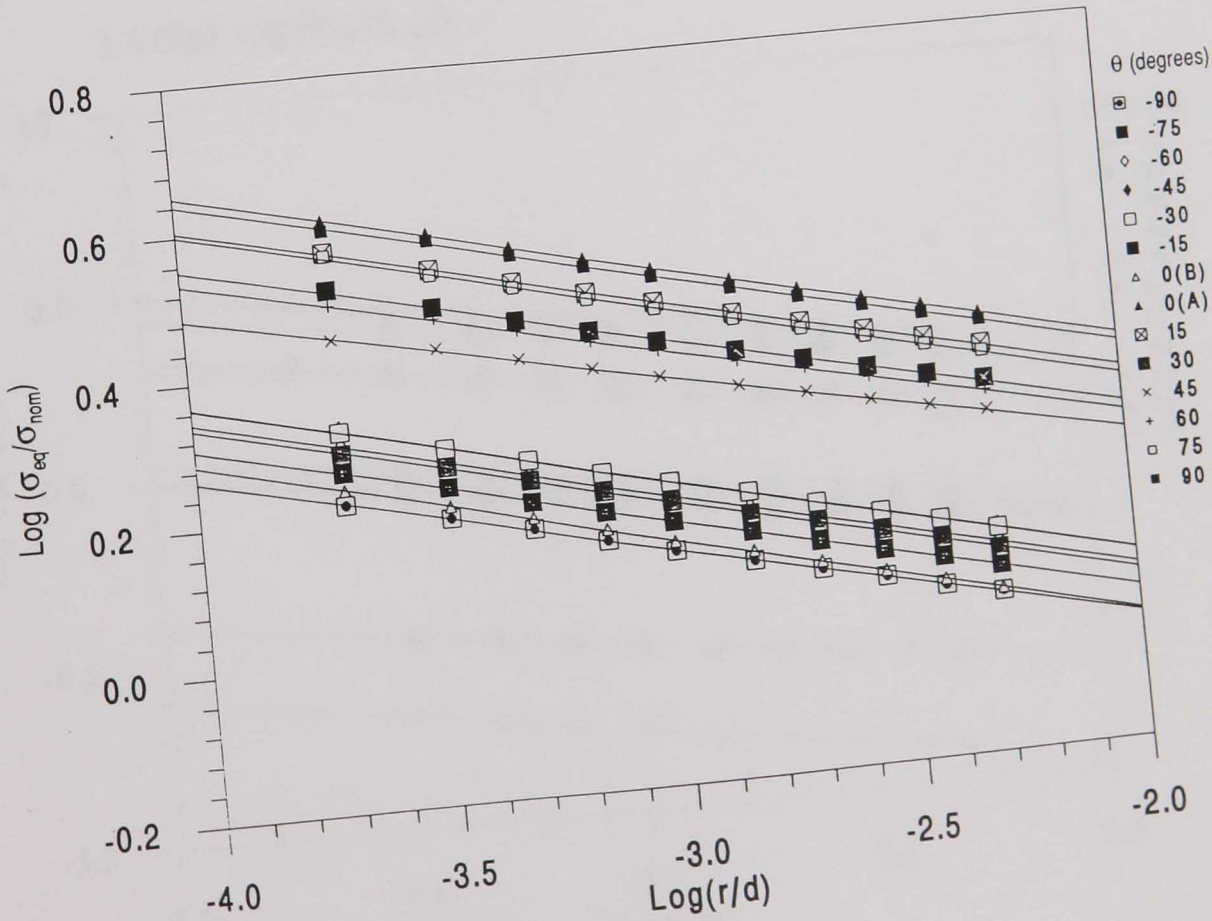

6(d)

3.4.5(d) log (σ_{eq}/σ_{nom})

Fig. 3.4.5 Variations of log (σ/σ_{nom}) with log (r/d) for a range of angular positions θ; w/d = 1.0, n = 2 and A/B = 0.1.

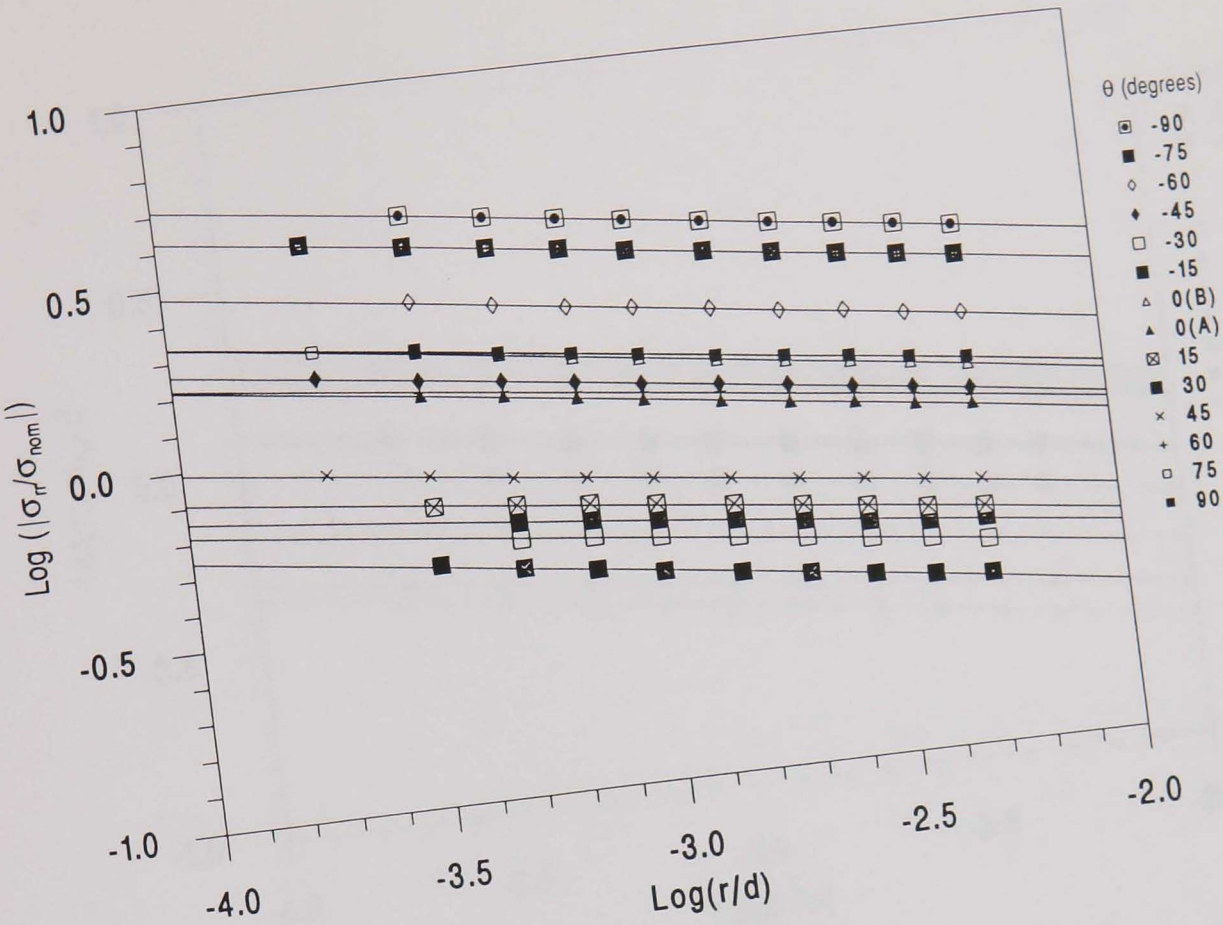

3.4.6(a) log ($|\sigma_{rr}/\sigma_{nom}|$)

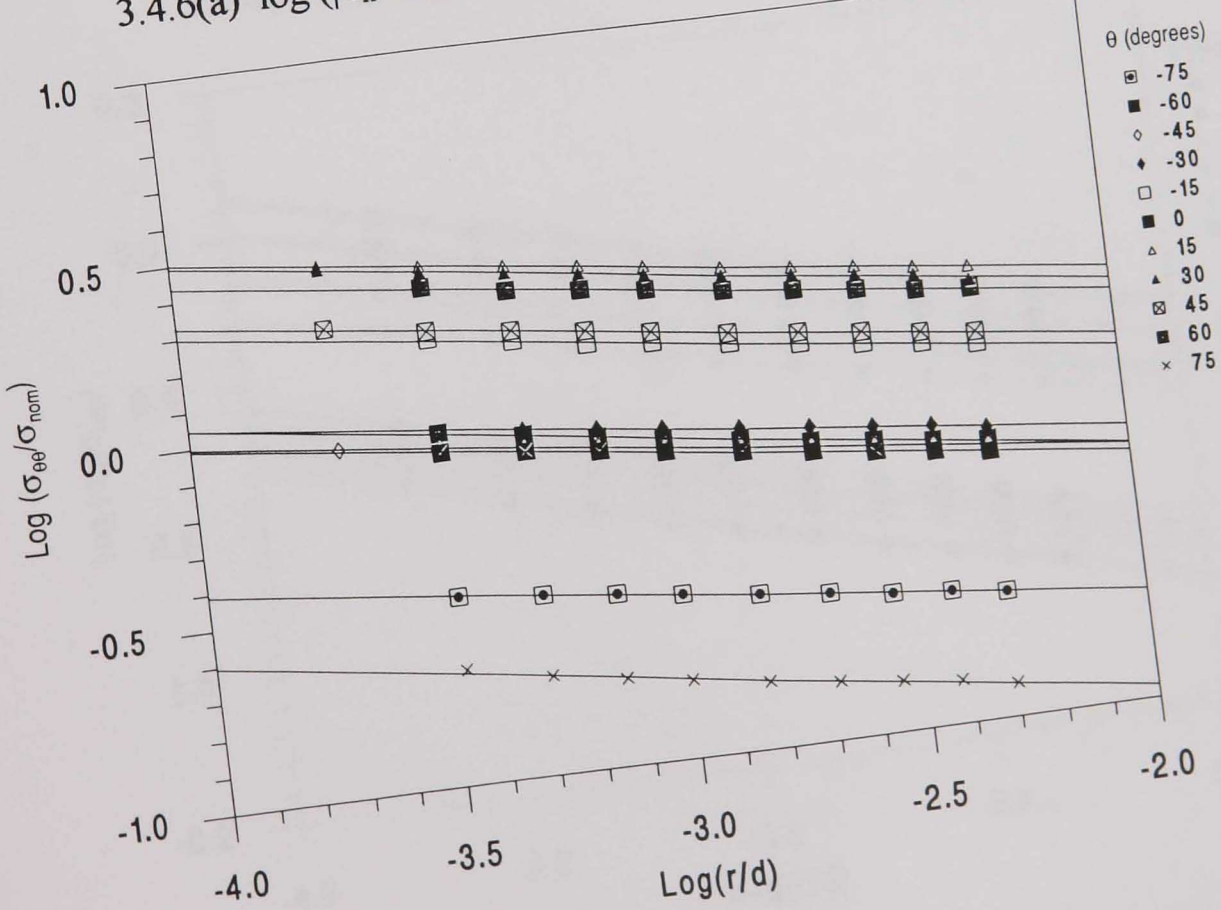

3.4.6(b) log ($\sigma_{\theta\theta}/\sigma_{nom}$)

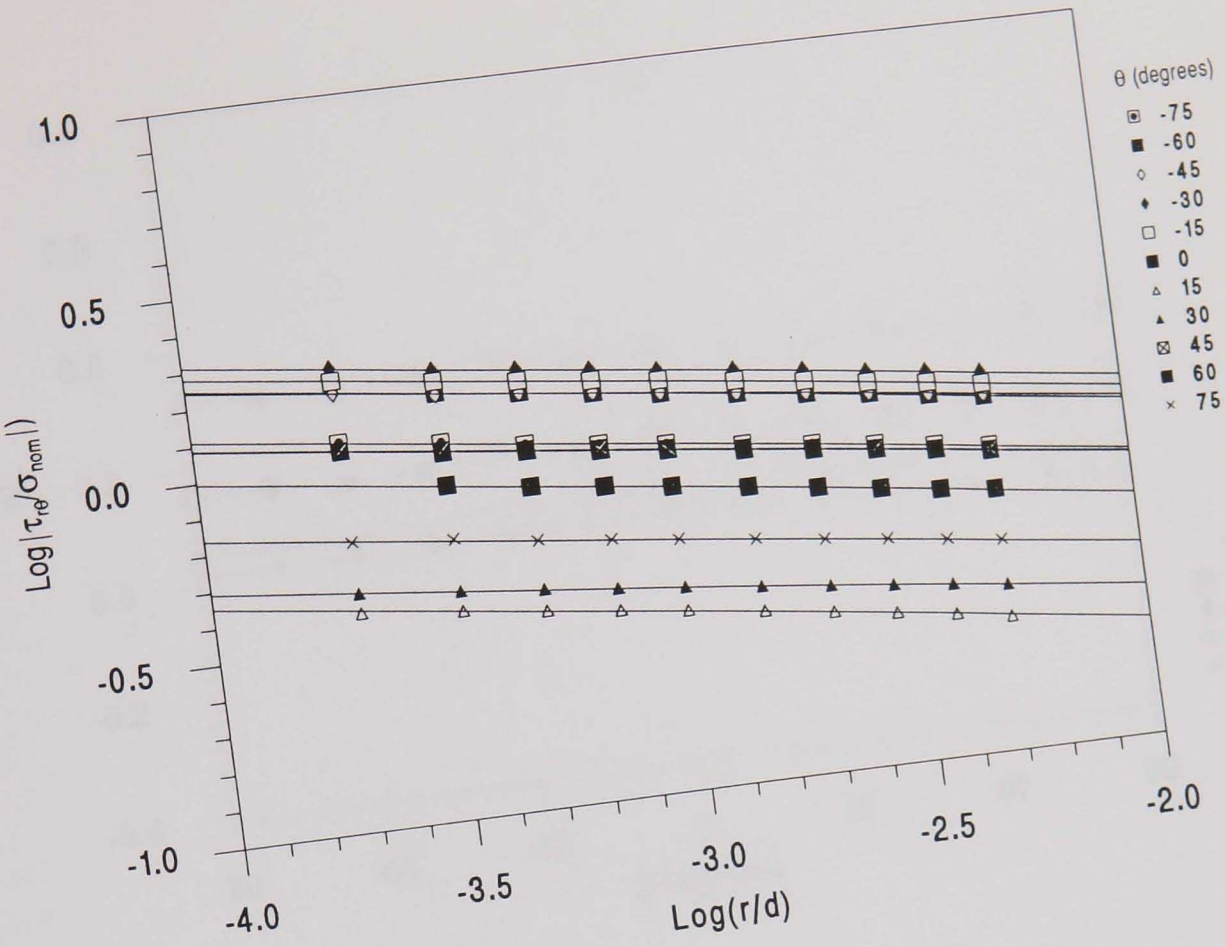

3.4.6(c) log ($|\tau_{r\theta}/\sigma_{nom}|$)

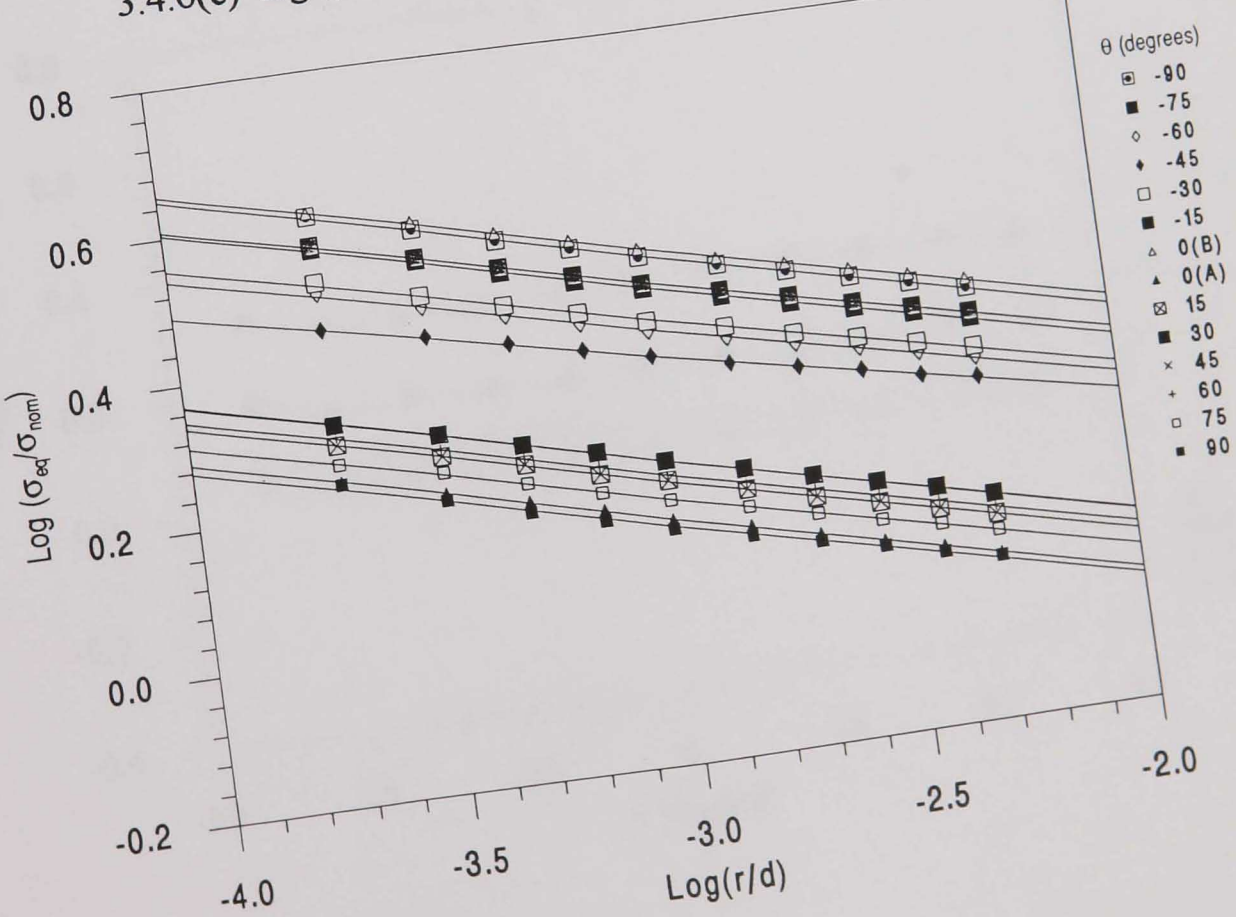

3.4.6(d) log (σ_{eq}/σ_{nom})

Fig. 3.4.6 Variations of log (σ/σ_{nom}) with log (r/d) for a range of angular positions θ; w/d = 1.0, n = 2 and A/B = 10.

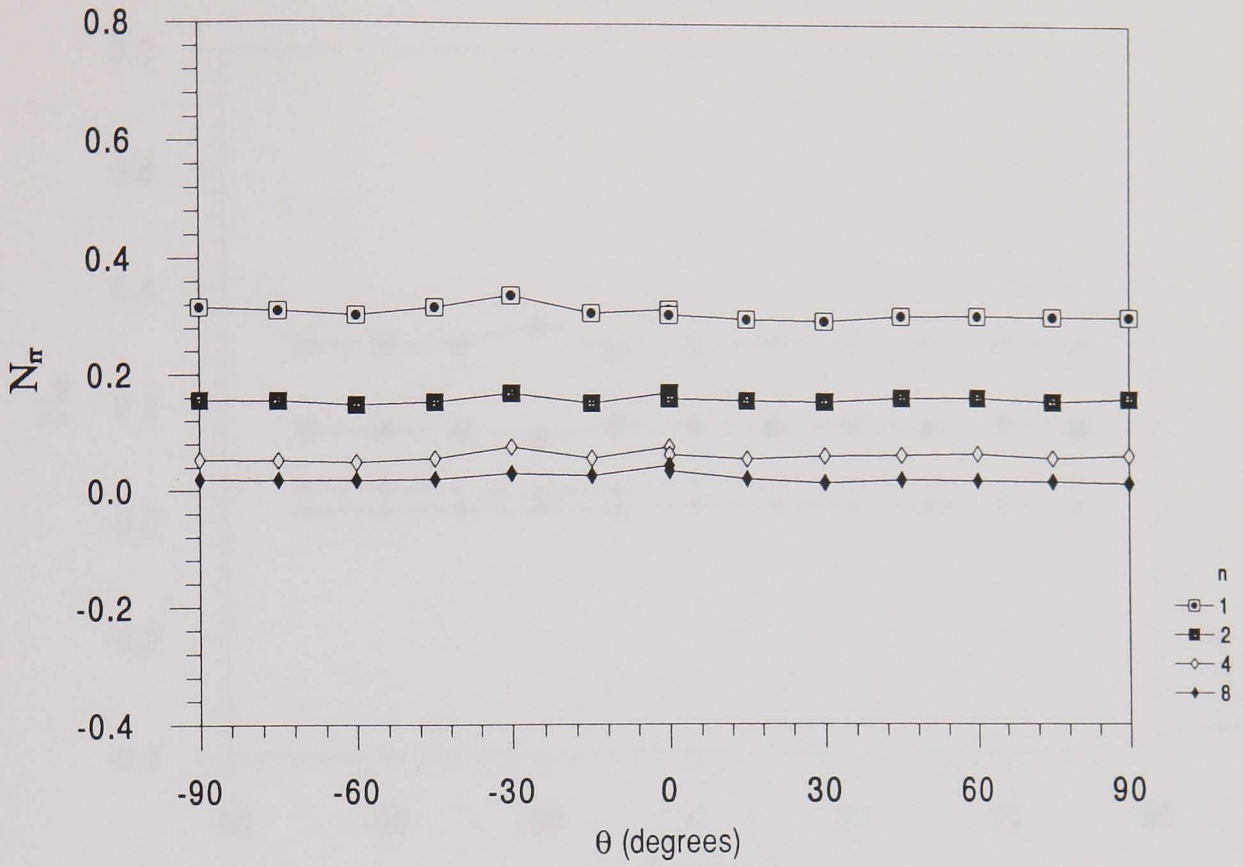

3.4.7(a) N_{rr}

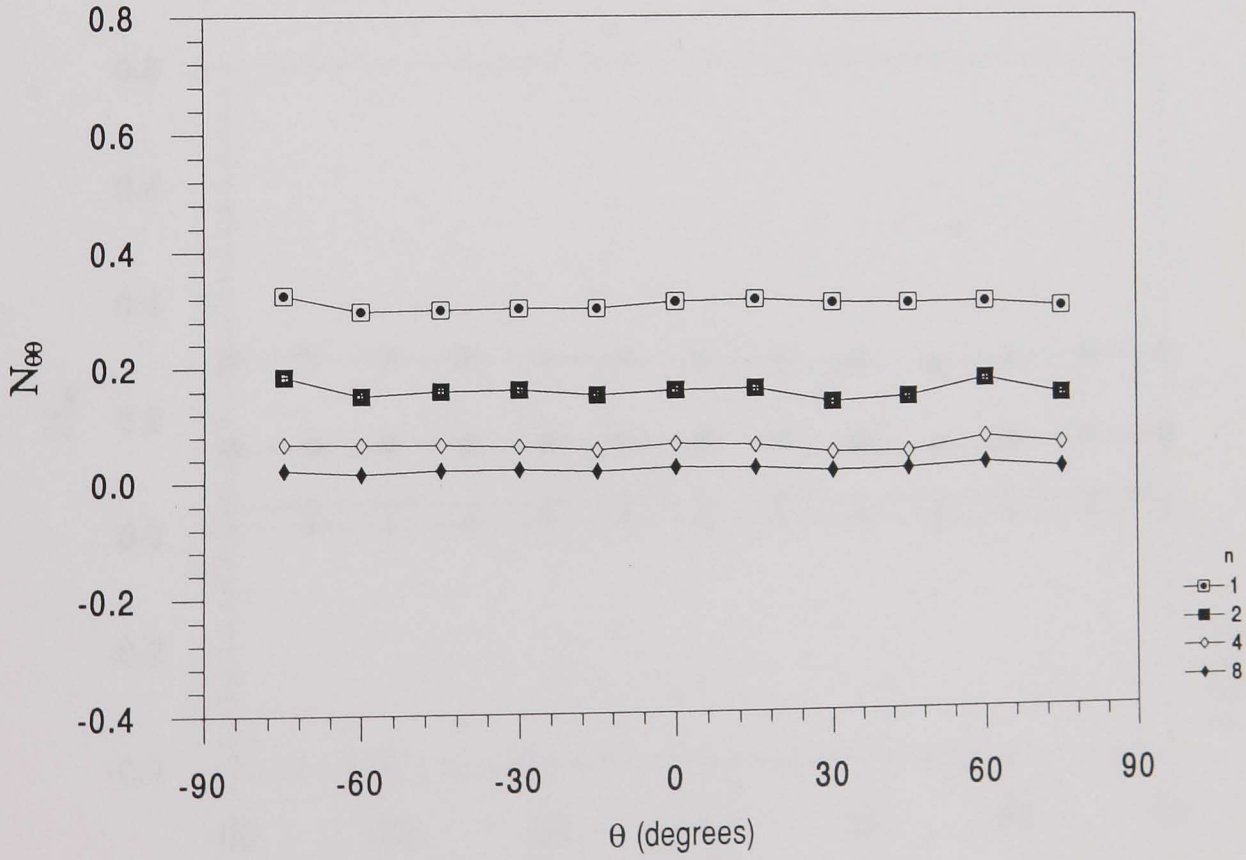

3.4.7(b) $N_{\theta\theta}$

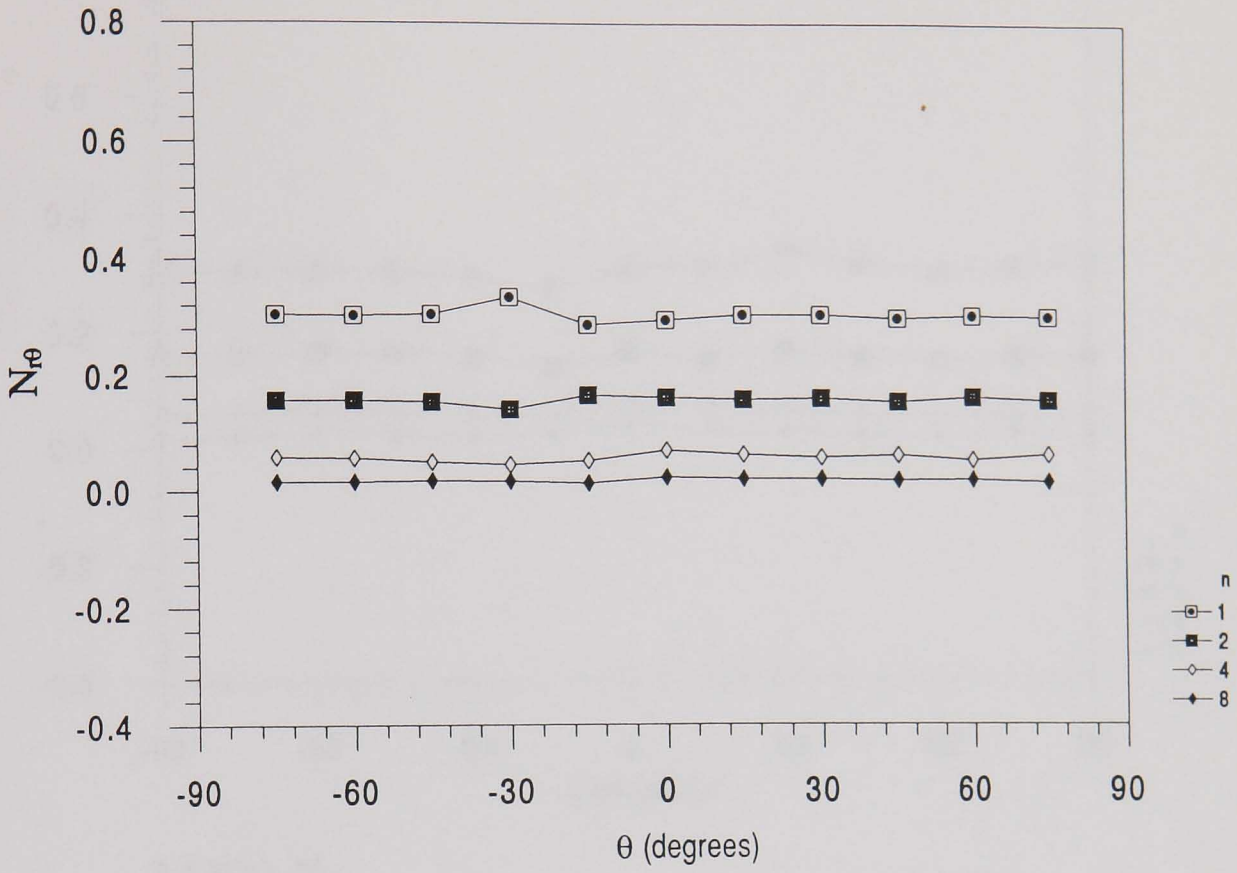

3.4.7(c) $N_{r\theta}$

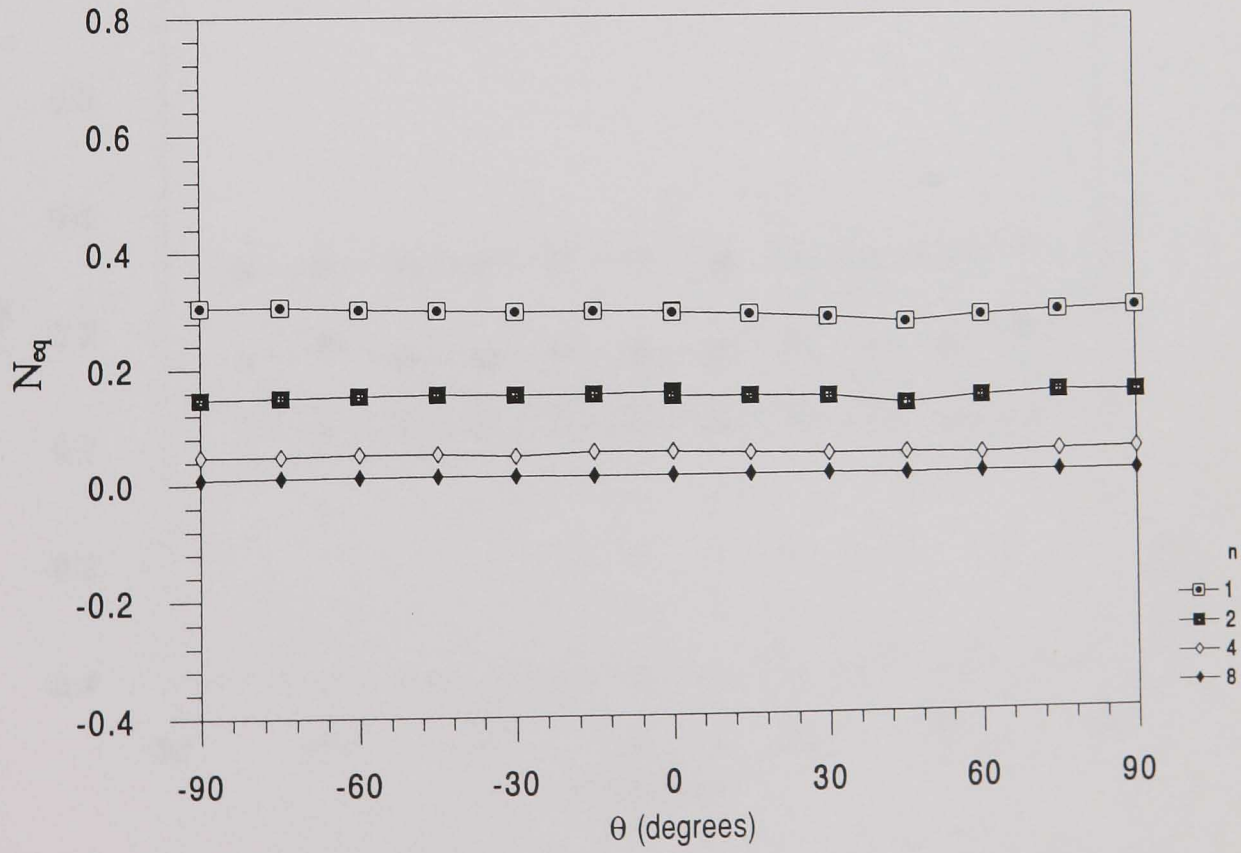

3.4.7(d) $N_{\theta q}$

Fig. 3.4.7 Variations of N_{ij} and $N_{\theta q}$ with θ for a range of n values with w/d = 1 and A/B = 0.1.

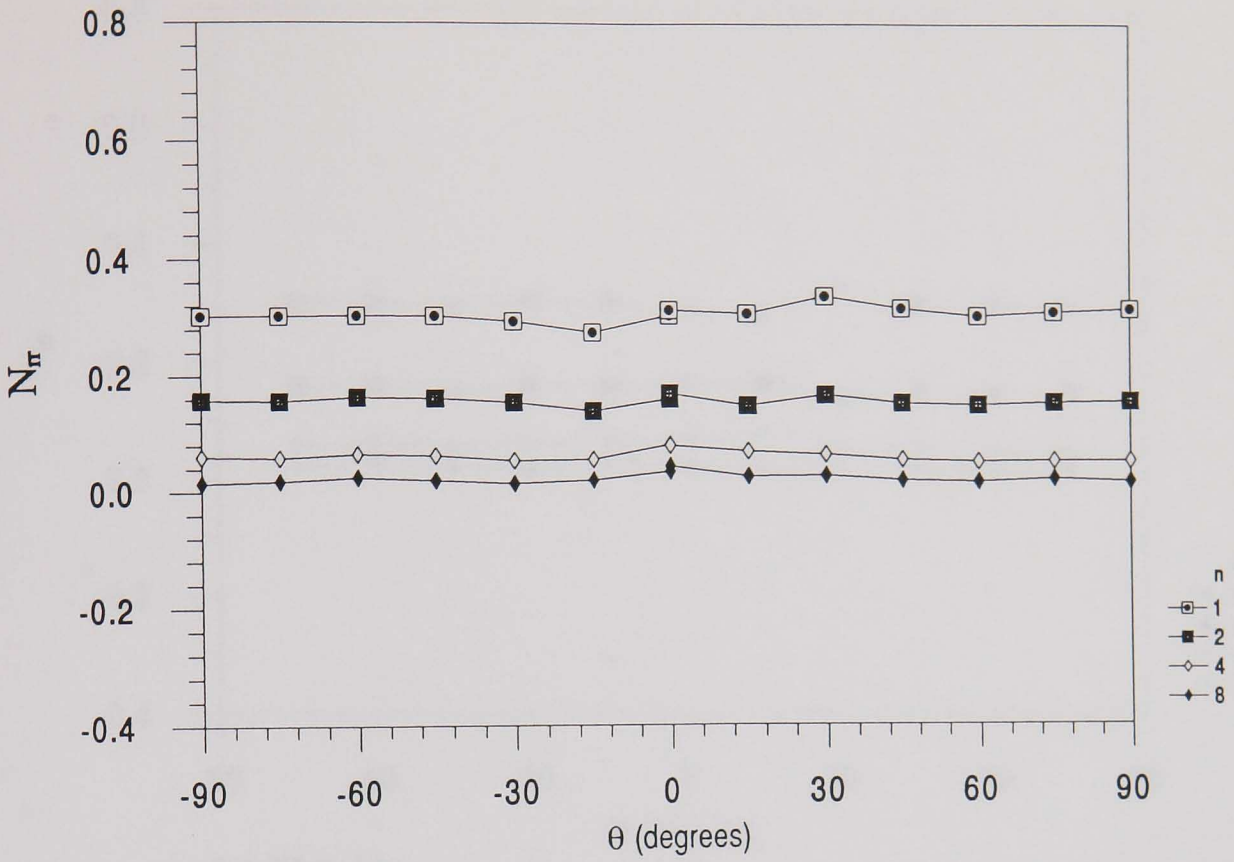

3.4.8(a) N_{rr}

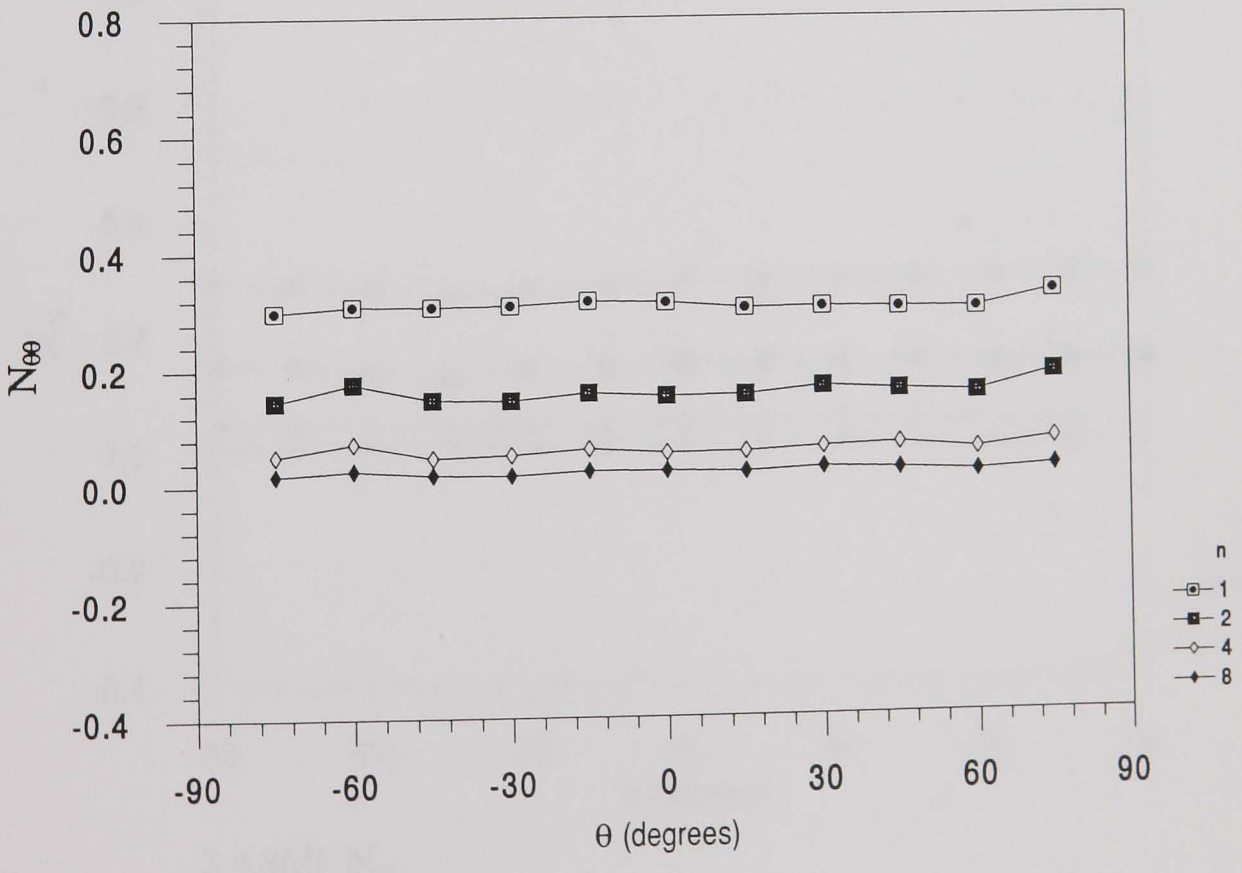

3.4.8(b) $N_{\theta\theta}$

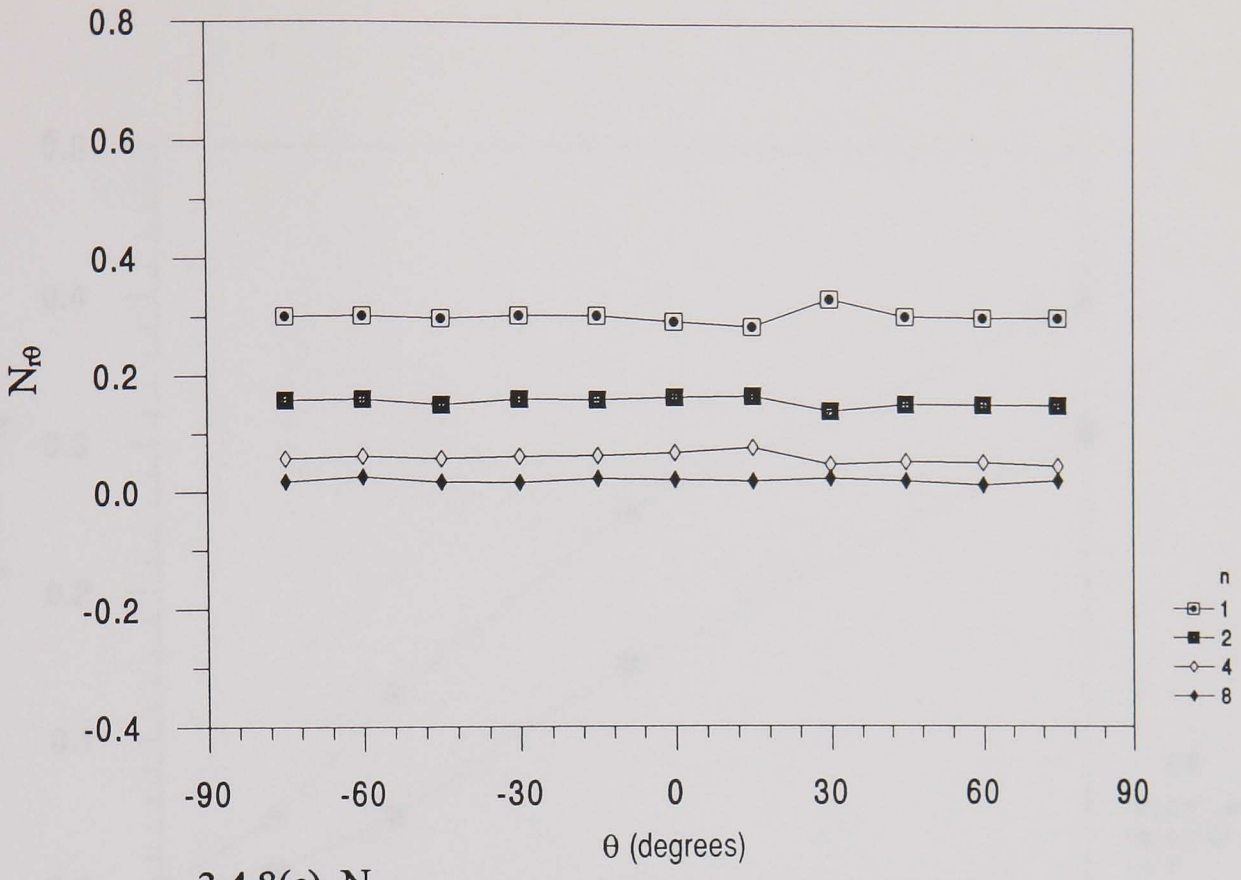

3.4.8(c) $N_{r\theta}$

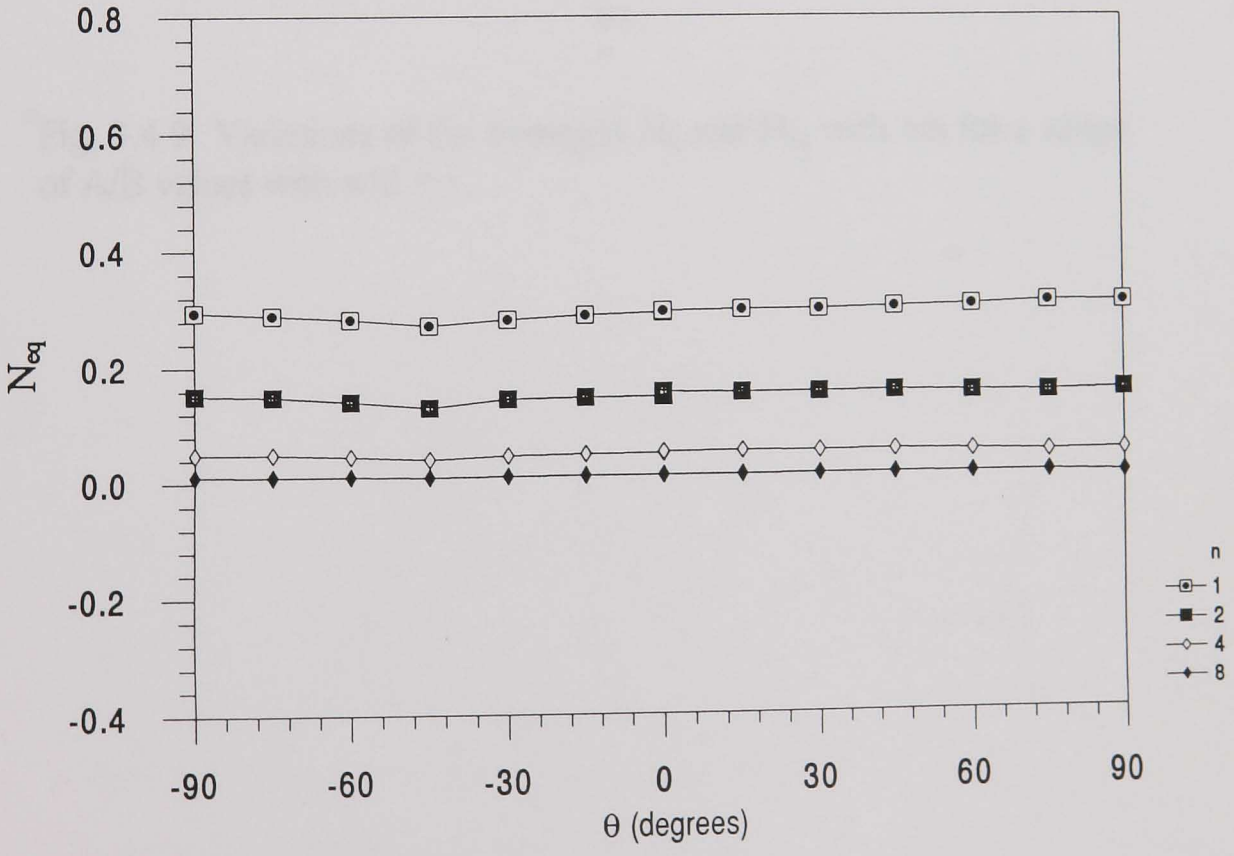

3.4.8(d) N_{eq}

Fig. 3.4.8 Variations of N_{ij} and N_{eq} with θ for a range of n values with w/d = 1 and A/B = 10.

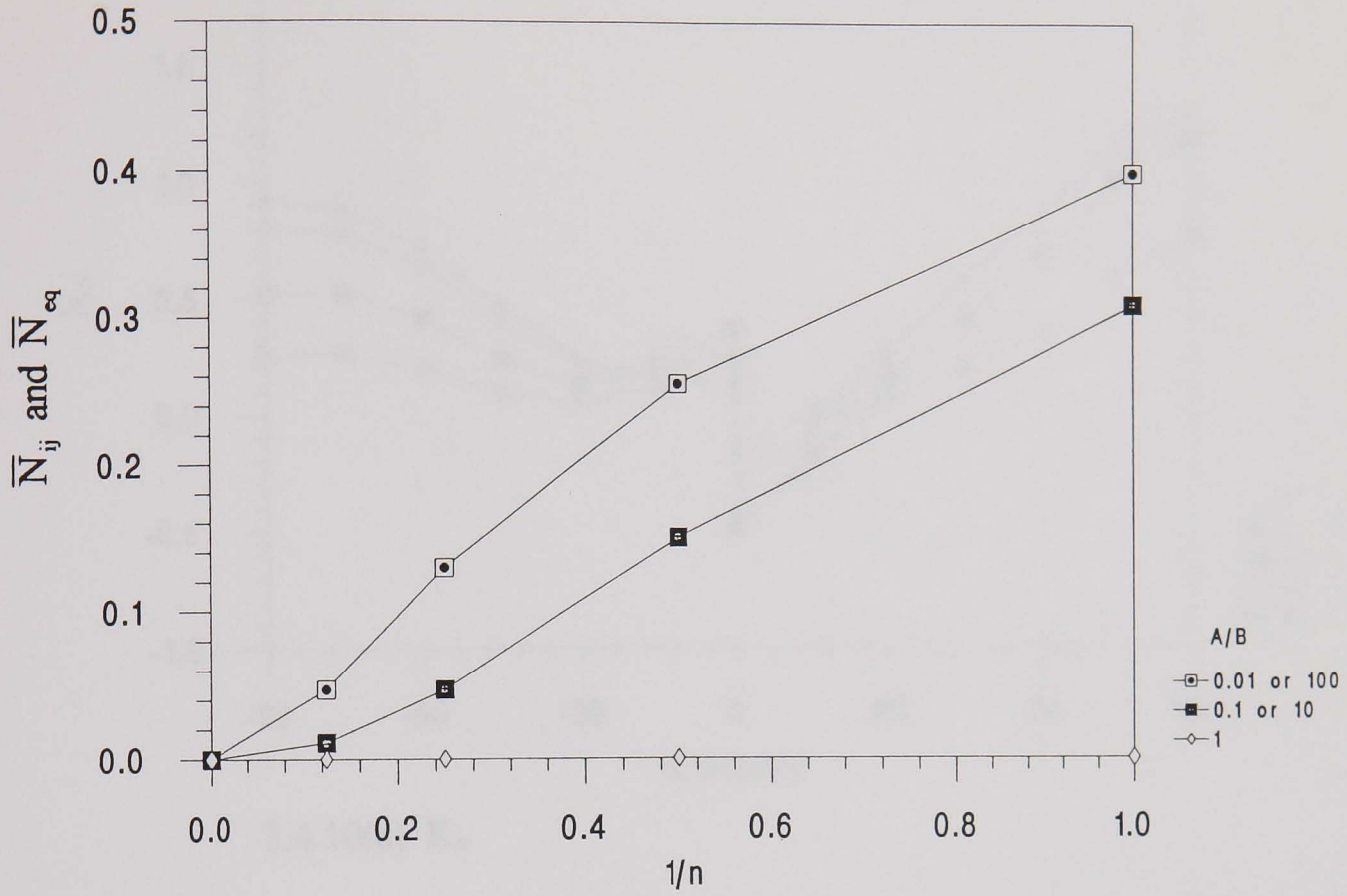

Fig. 3.4.9 Variations of the averaged N_{ij} and N_{eq} with 1/n for a range of A/B values with w/d = 1.

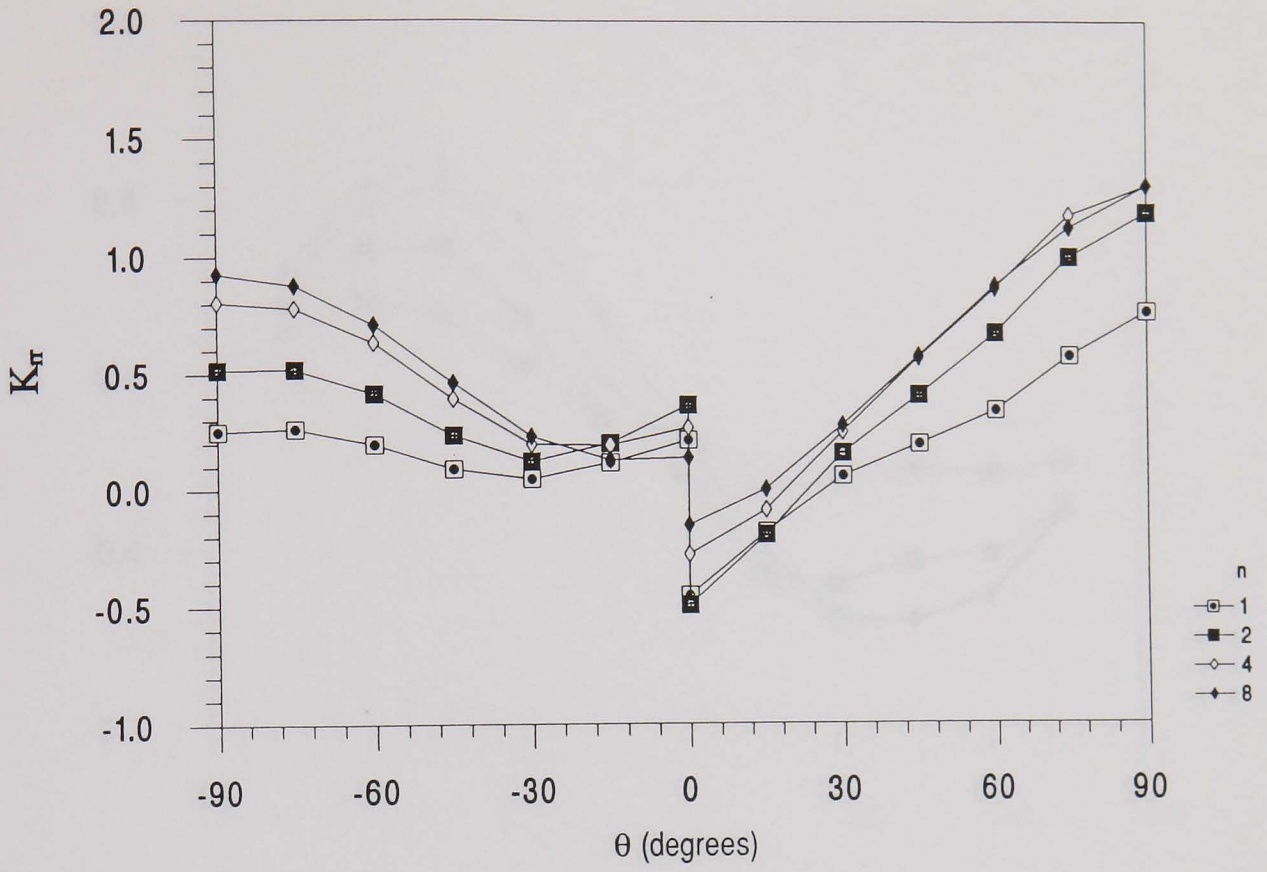

3.4.10(a) K_{rr}

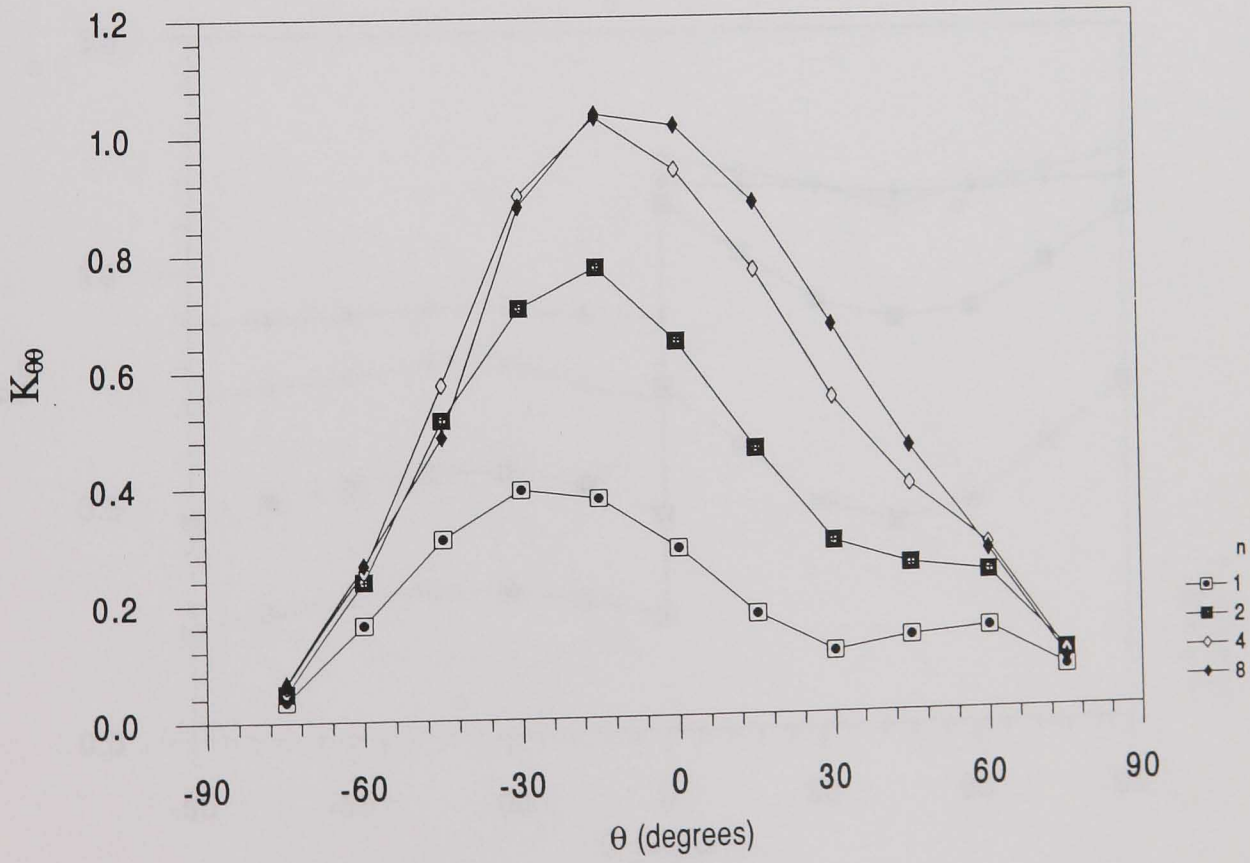

3.4.10(b) $K_{\theta\theta}$

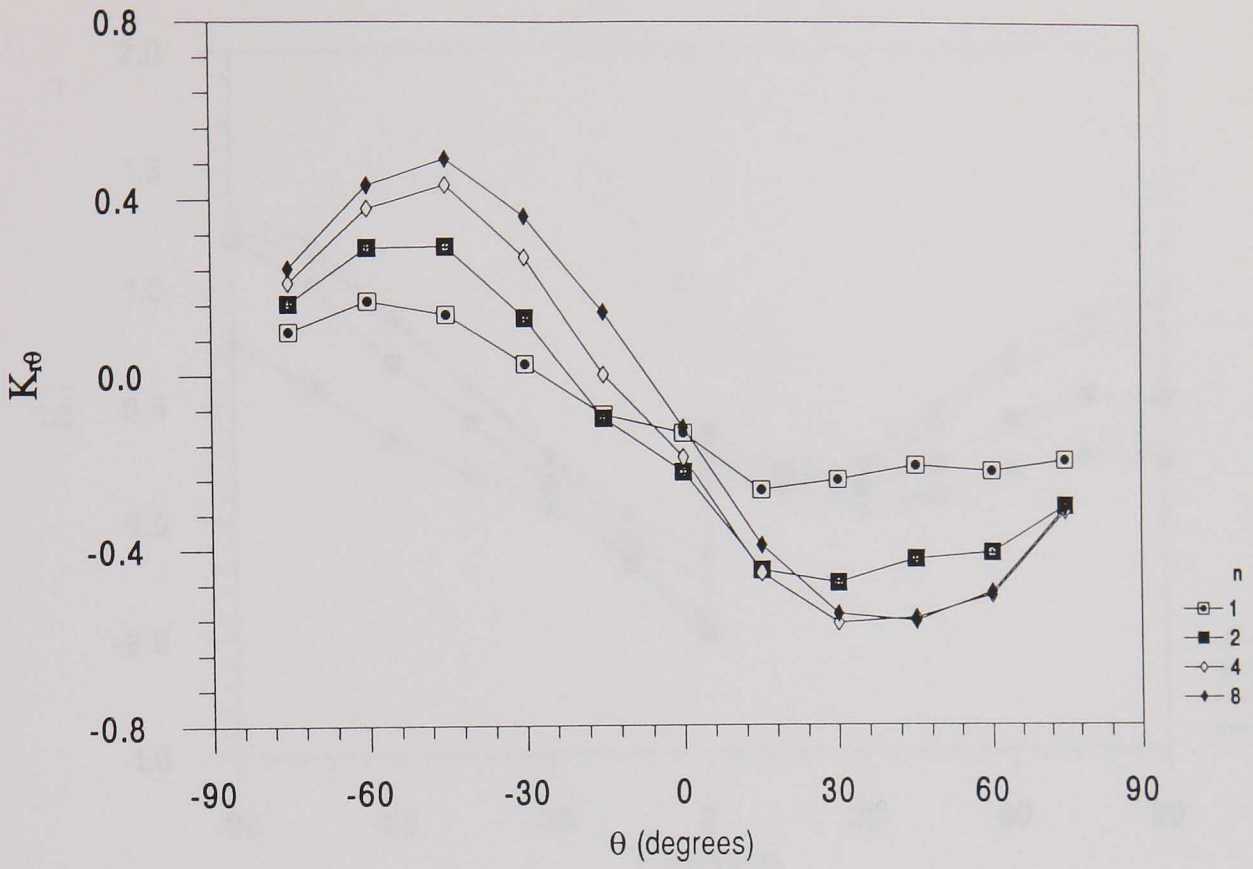

3.4.10(c) $K_{r\theta}$

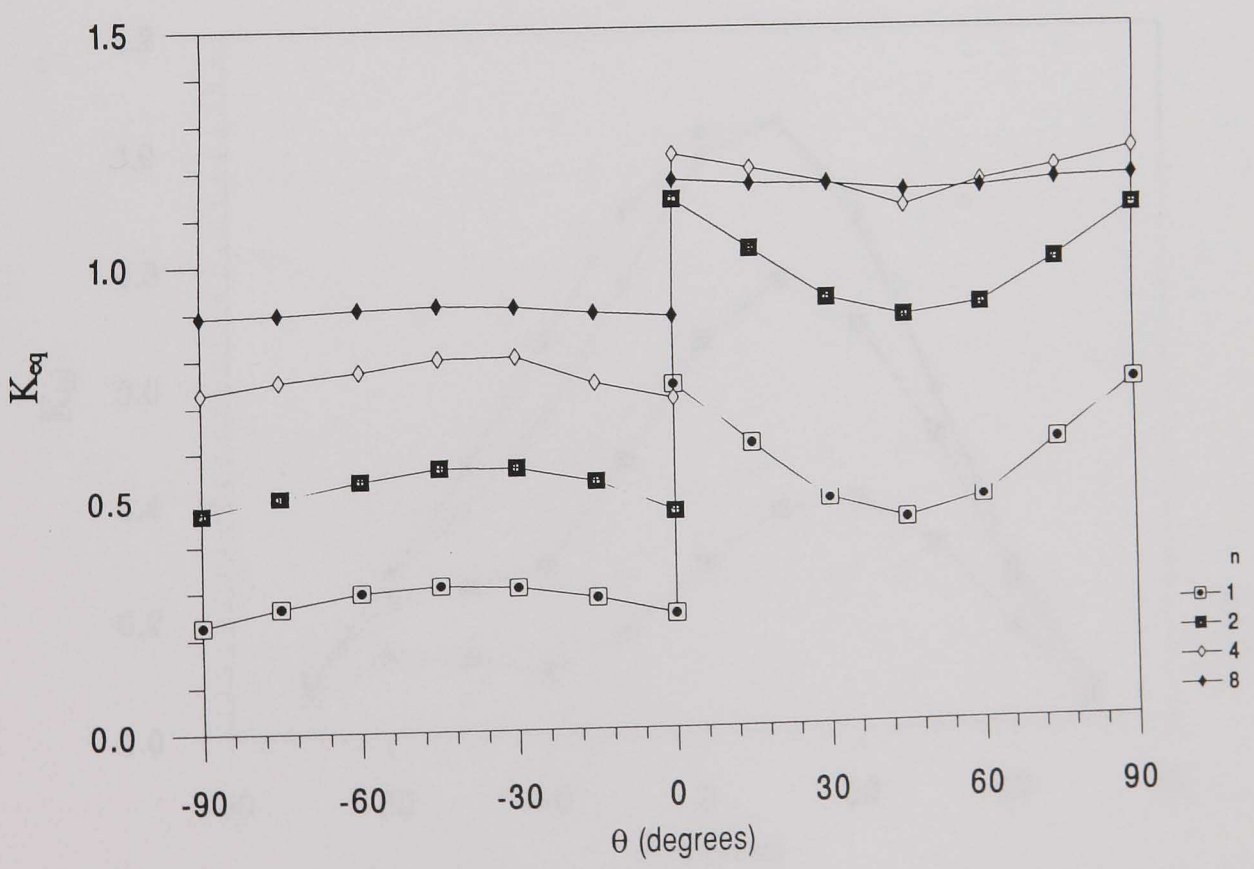

3.4.10(d) K_{eq}

Fig. 3.4.10 Variations of K_{ij} and K_{eq} with θ for a range of n values with w/d = 1 and A/B = 0.1.

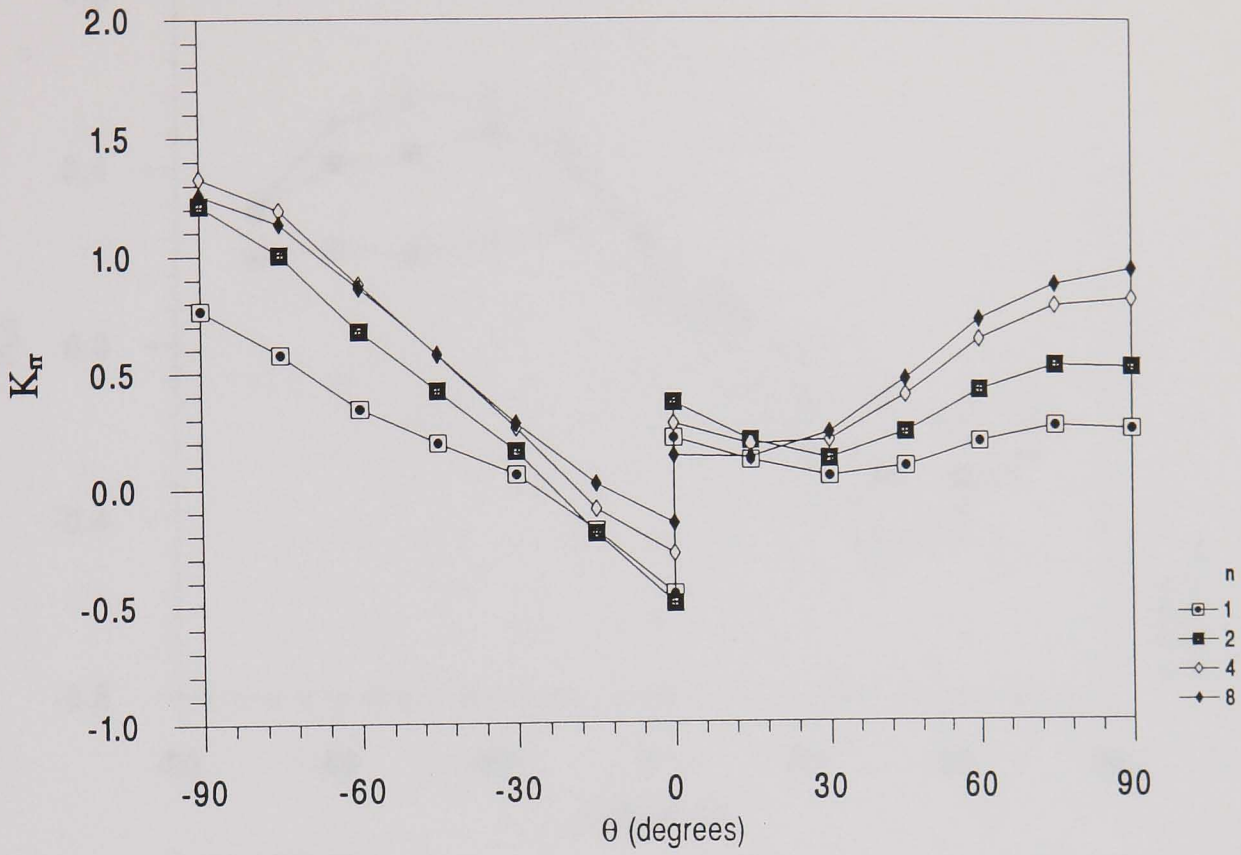

3.4.11(a) K_{rr}

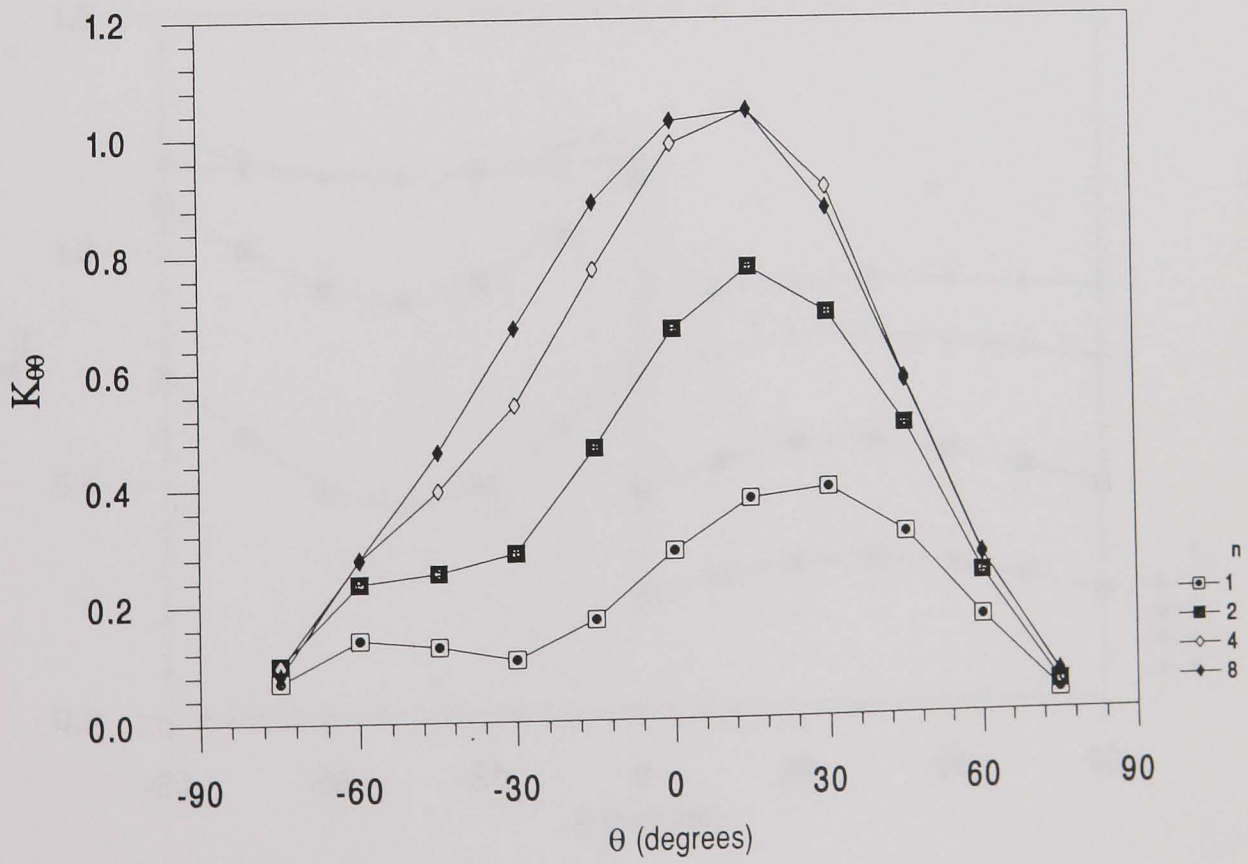

3.4.11(b) $K_{\theta\theta}$

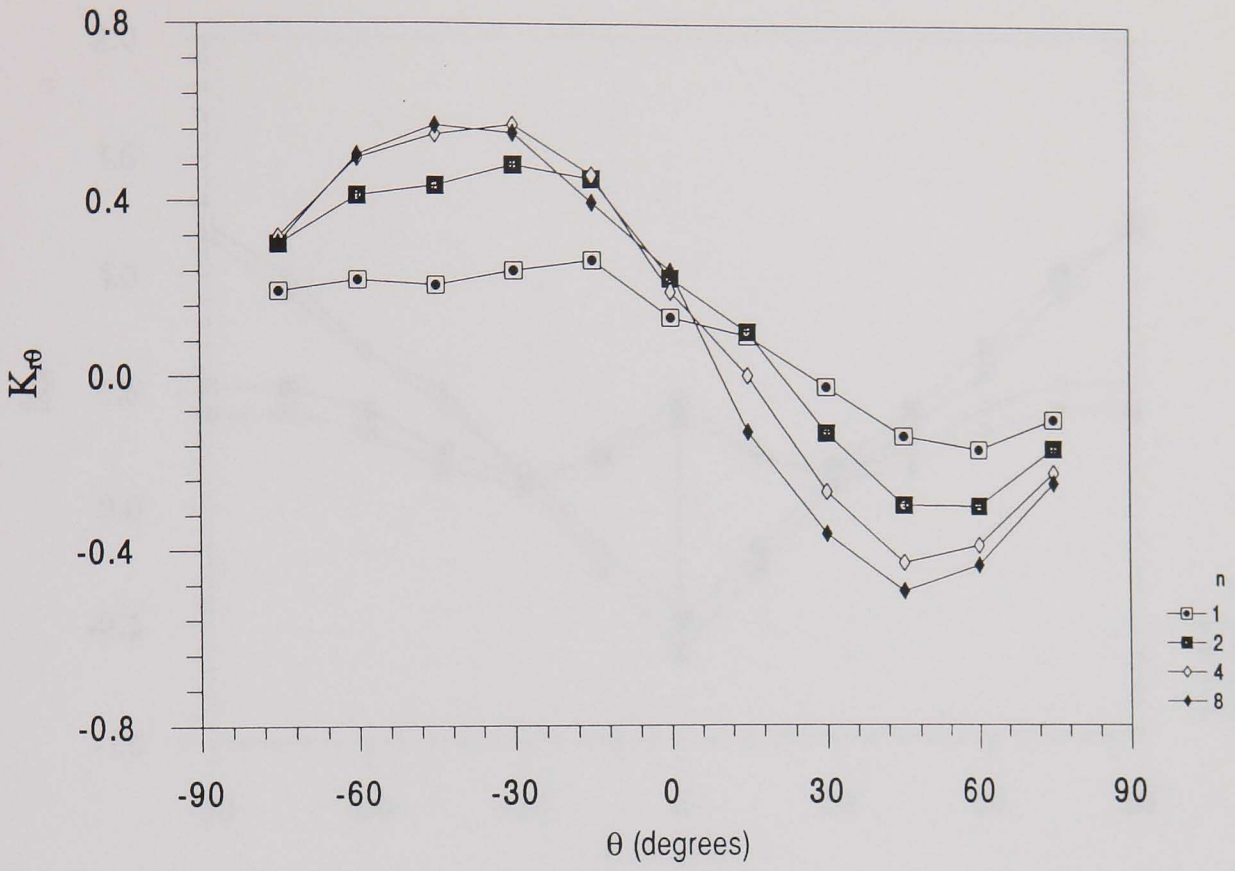

3.4.11(c) $K_{r\theta}$

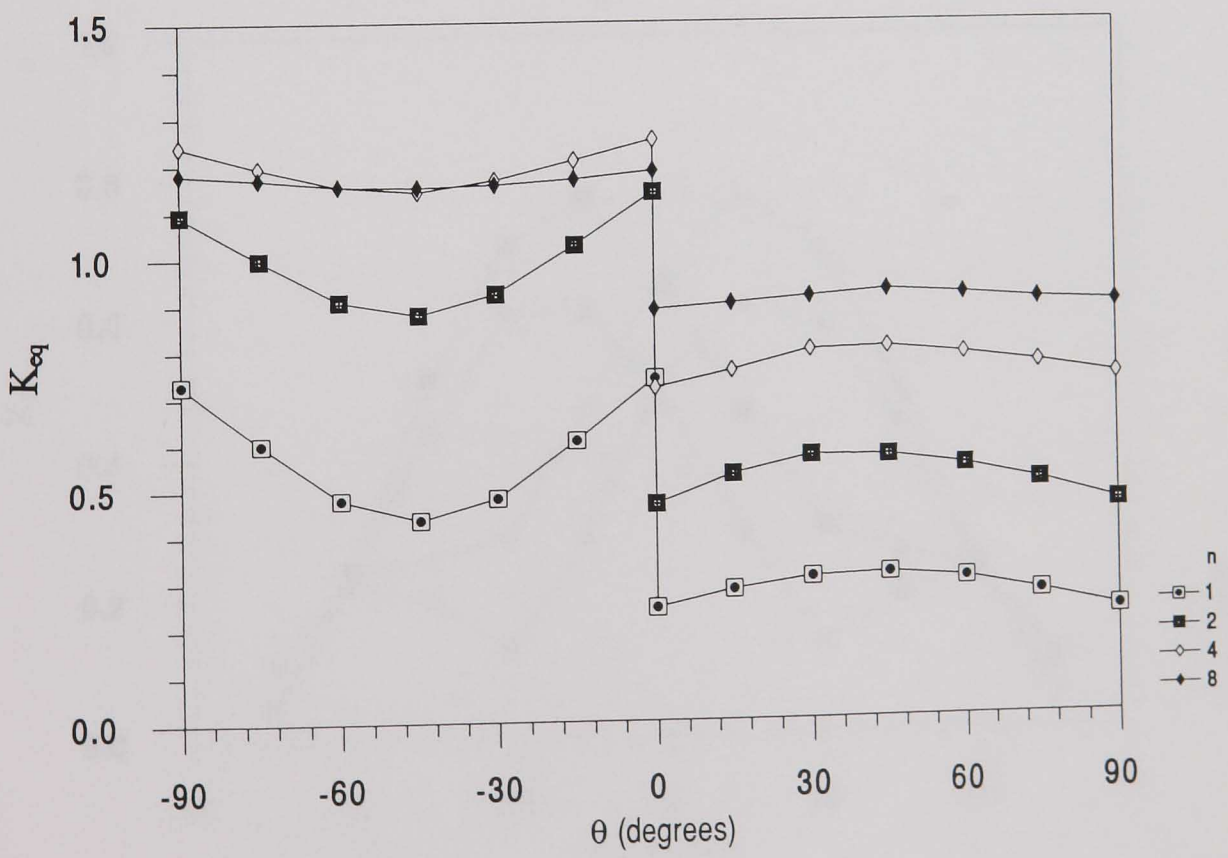

3.4.11(d) K_{eq}

Fig. 3.4.11 Variations of K_{ij} and K_{eq} with θ for a range of n values with w/d = 1 and A/B = 10.

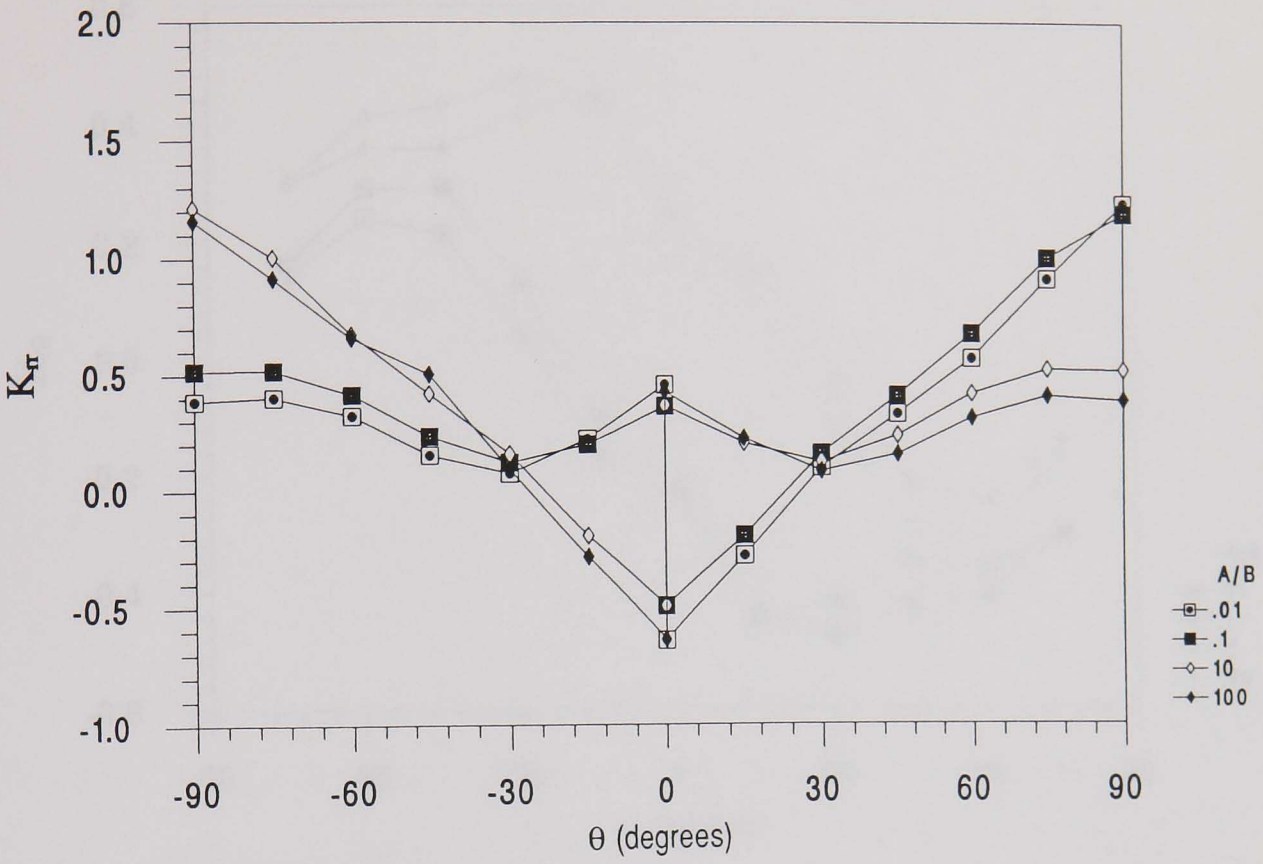

3.4.12(a) K_{rr}

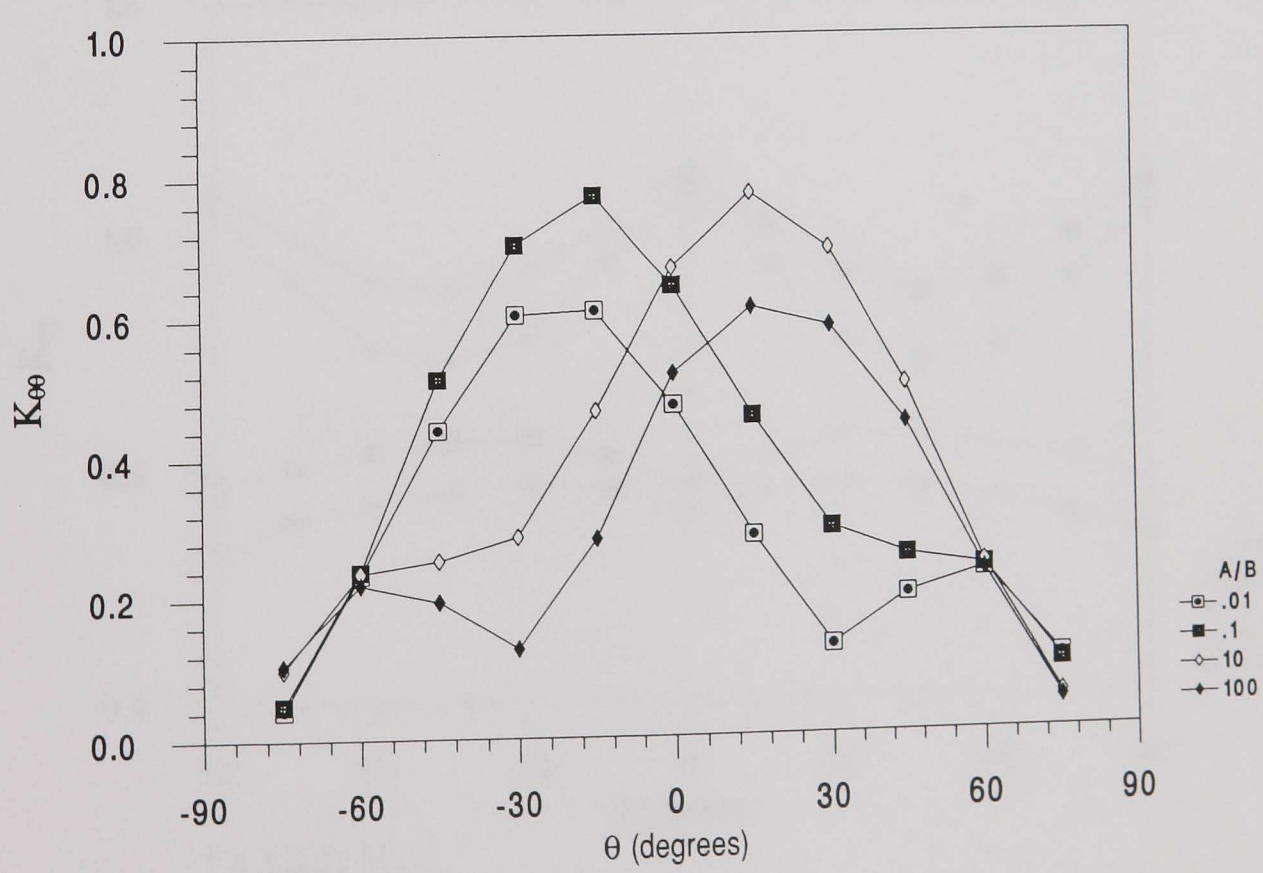

3.4.12(b) $K_{\theta\theta}$

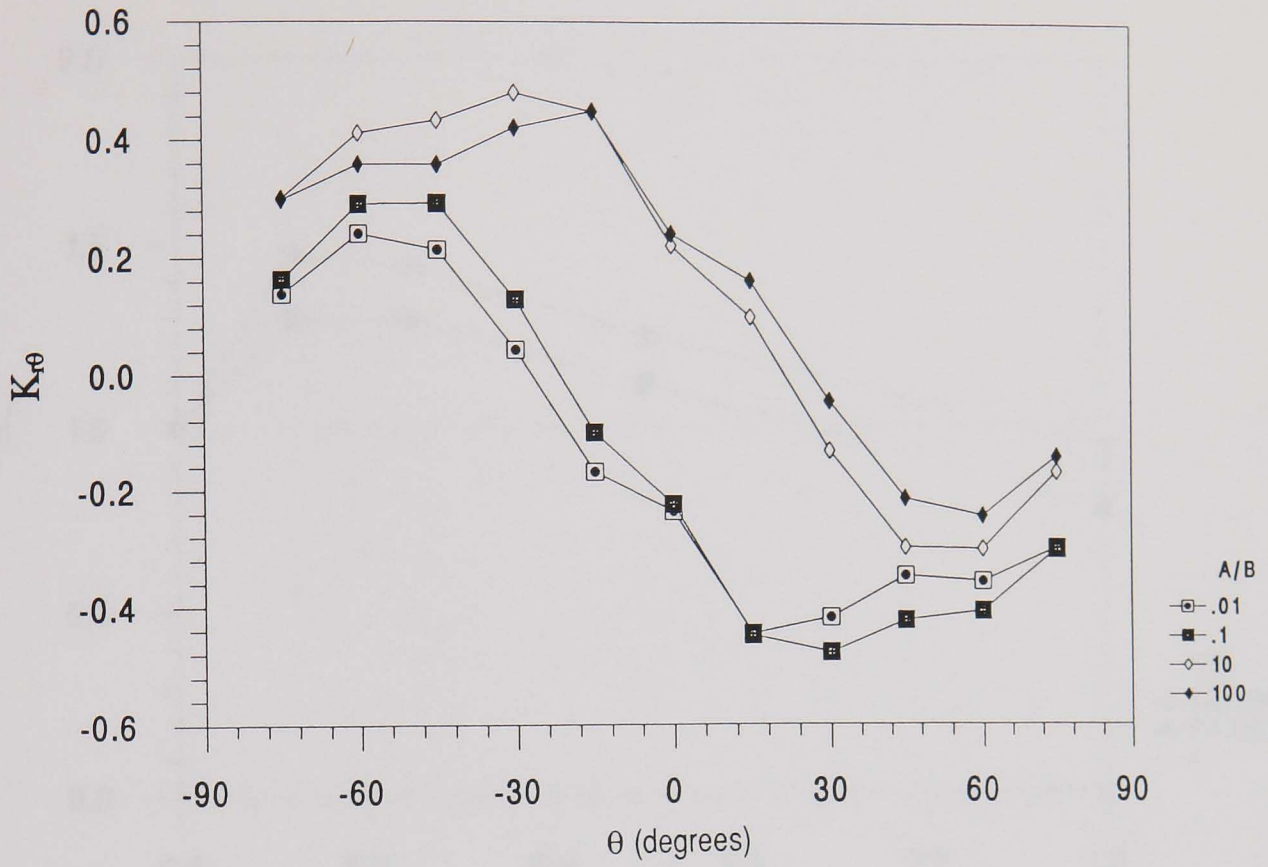

3.4.12(c) $K_{r\theta}$

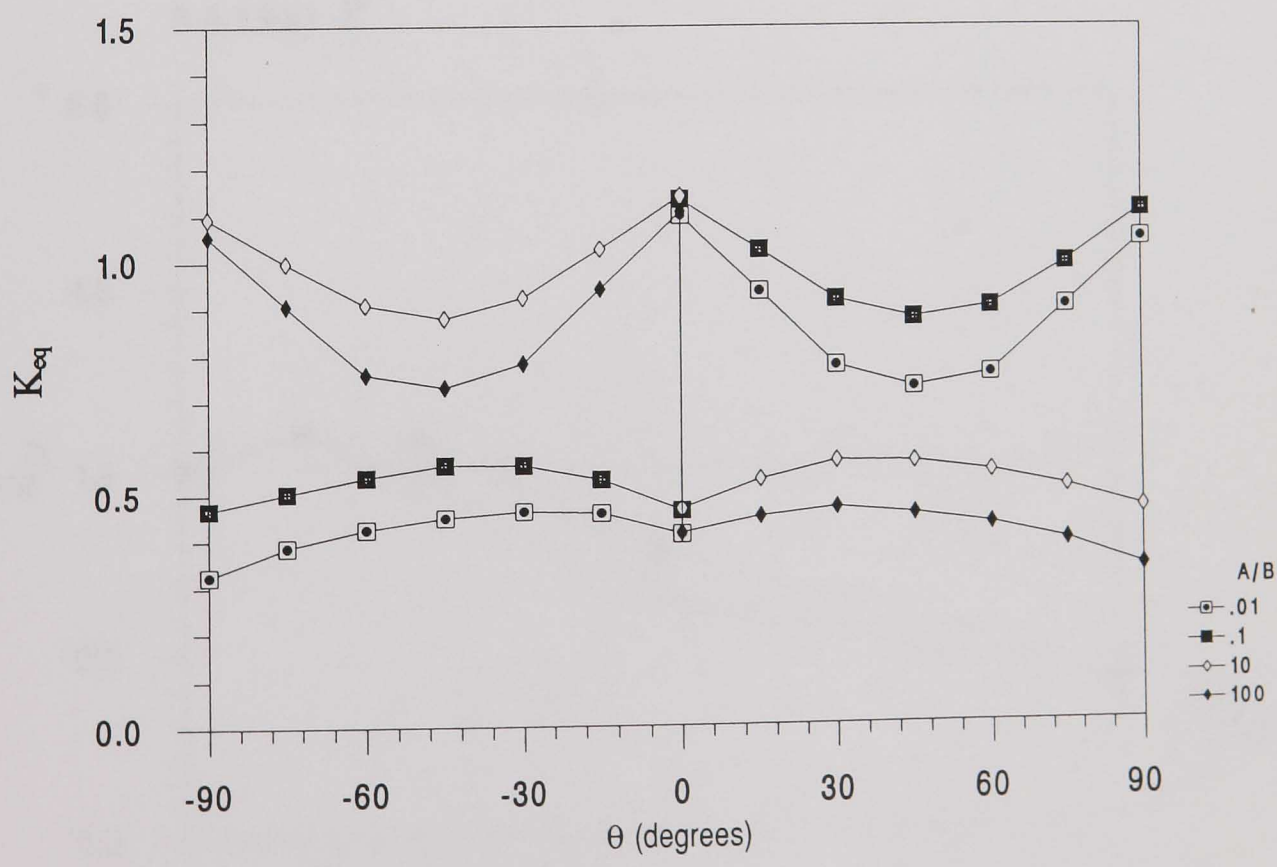

3.4.12(d) $K_{\sigma q}$

Fig. 3.4.12 Variations of K_{ij} and $K_{\sigma q}$ with θ for a range of A/B values with n = 2 and w/d = 1.0.

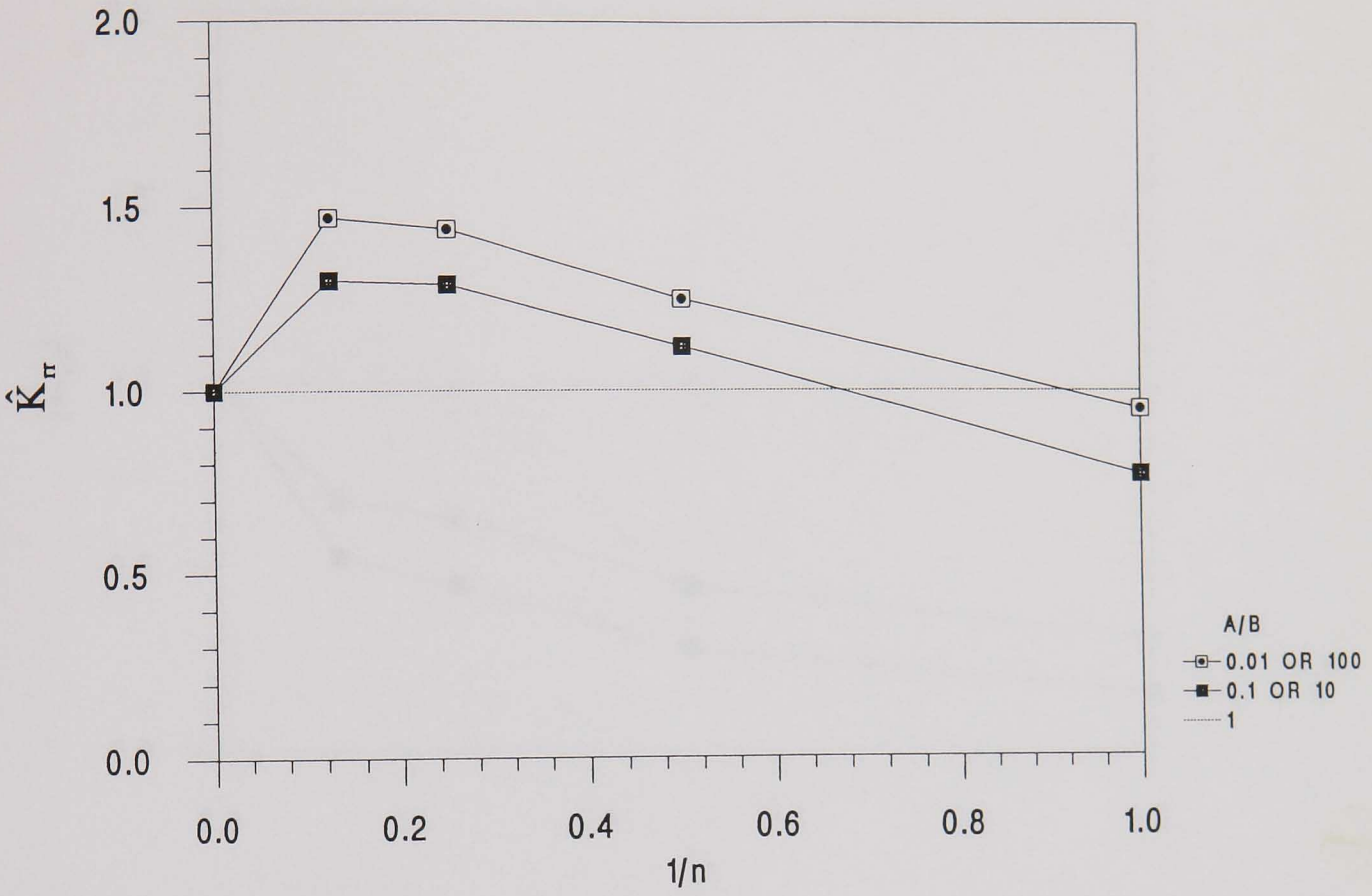

3.4.13(a) $\hat{K}_{\pi}$

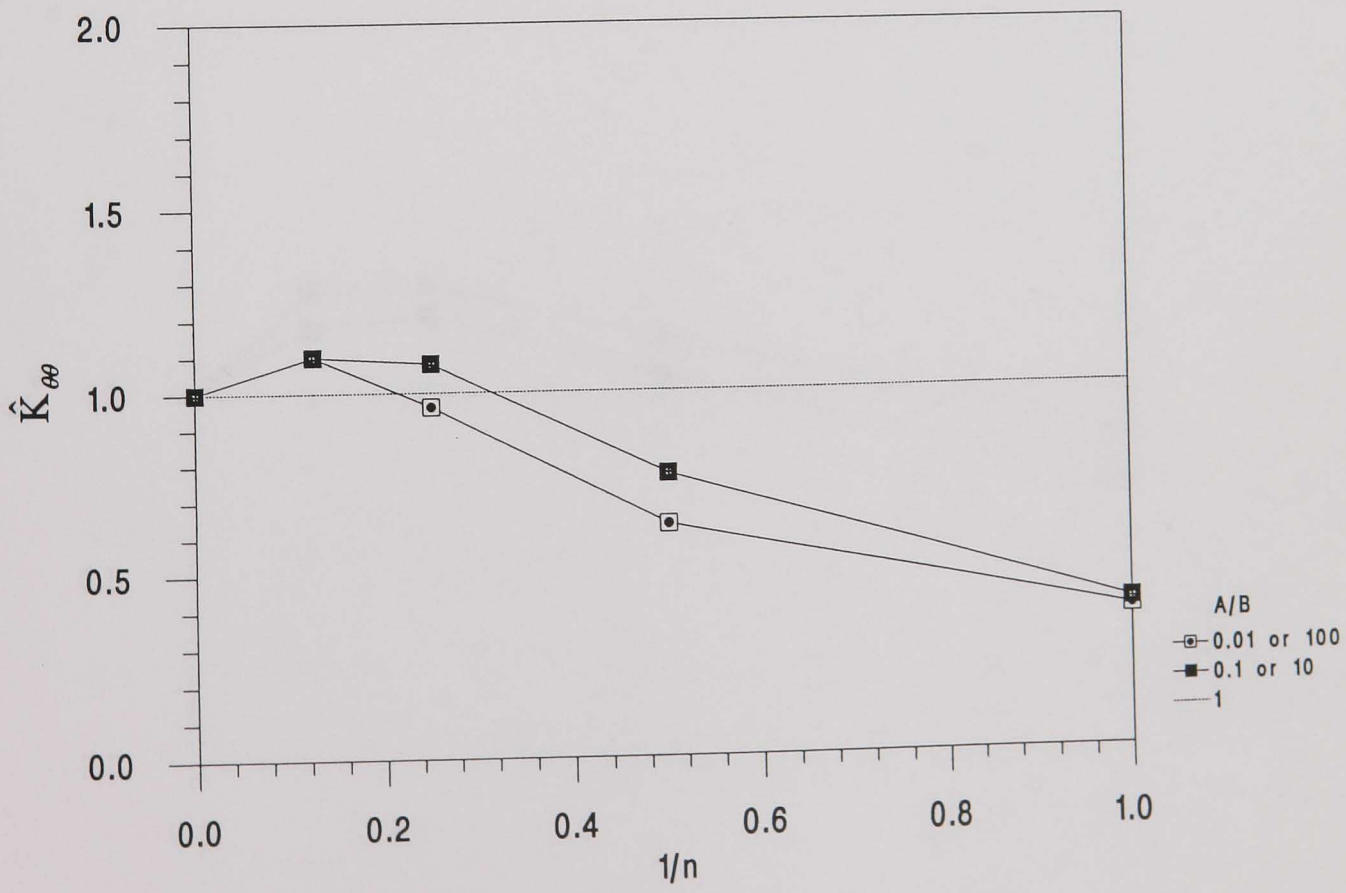

3.4.13(b) $\hat{K}_{\theta\theta}$

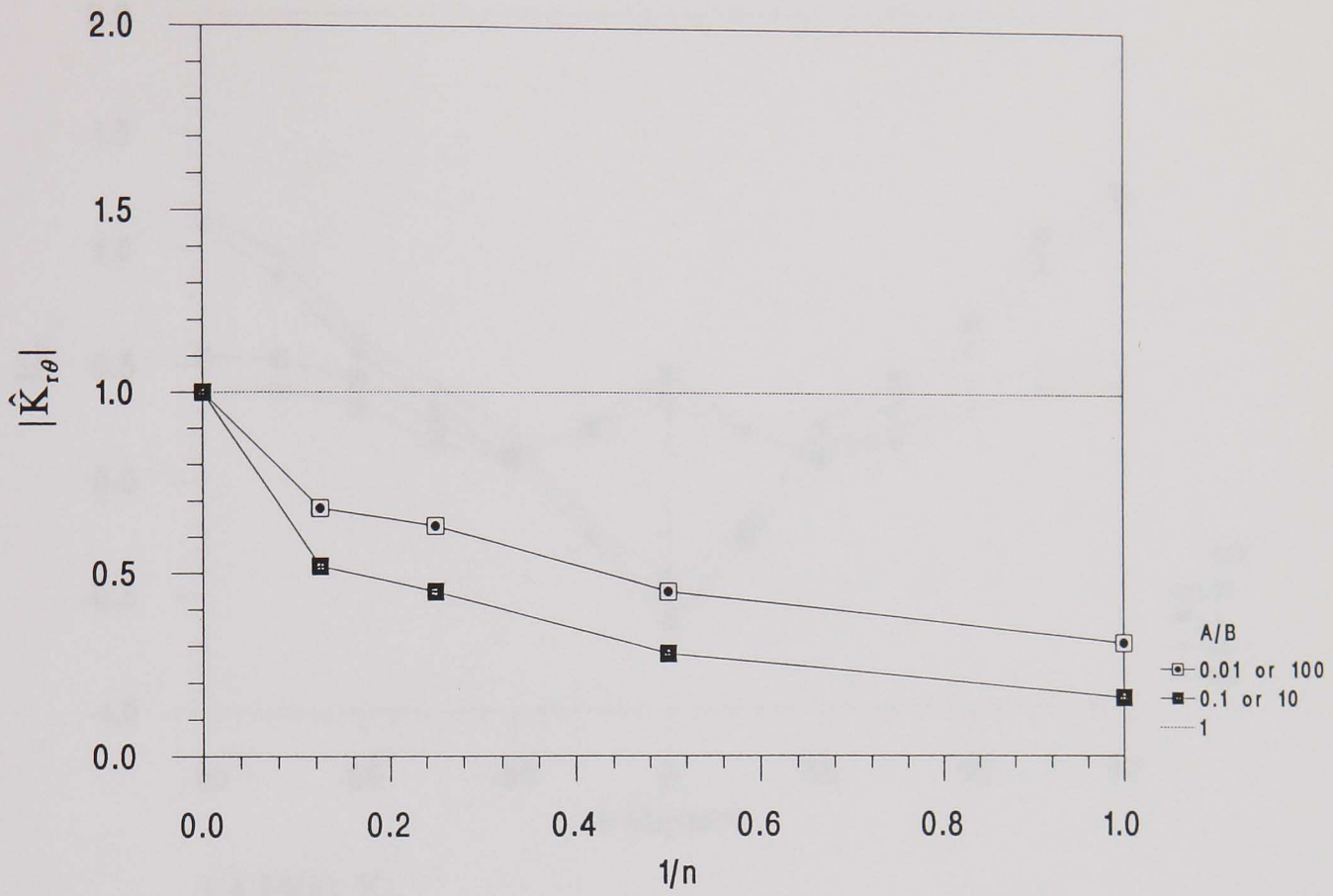

3.4.13(c) $|\hat{K}_{r\theta}|$

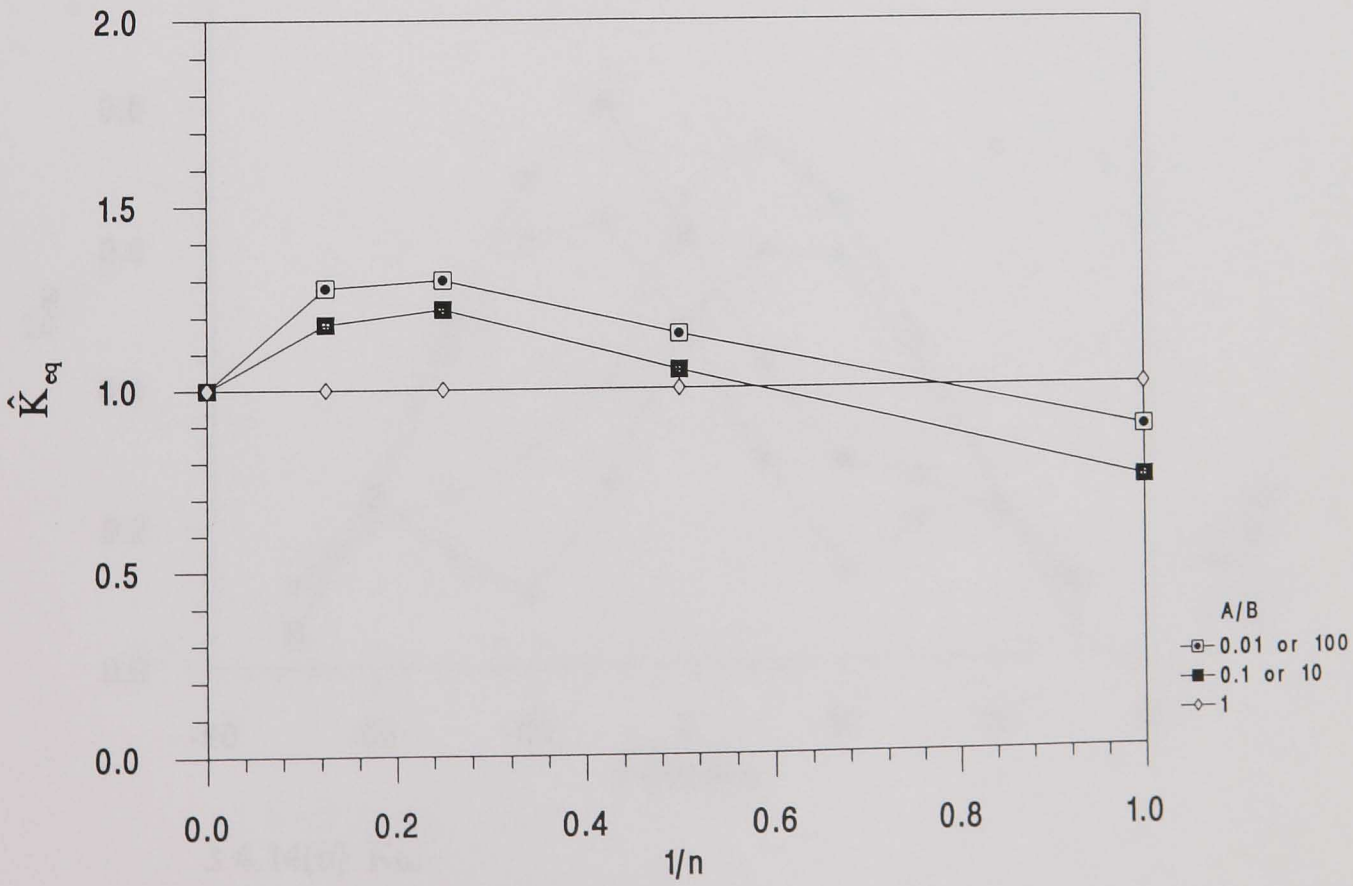

3.4.13(d) $\hat{K}_{eq}$

Fig. 3.4.13 Variations of $\hat{K}_{ij}$ and $\hat{K}_{eq}$ with 1/n for a range of A/B values with w/d = 1.

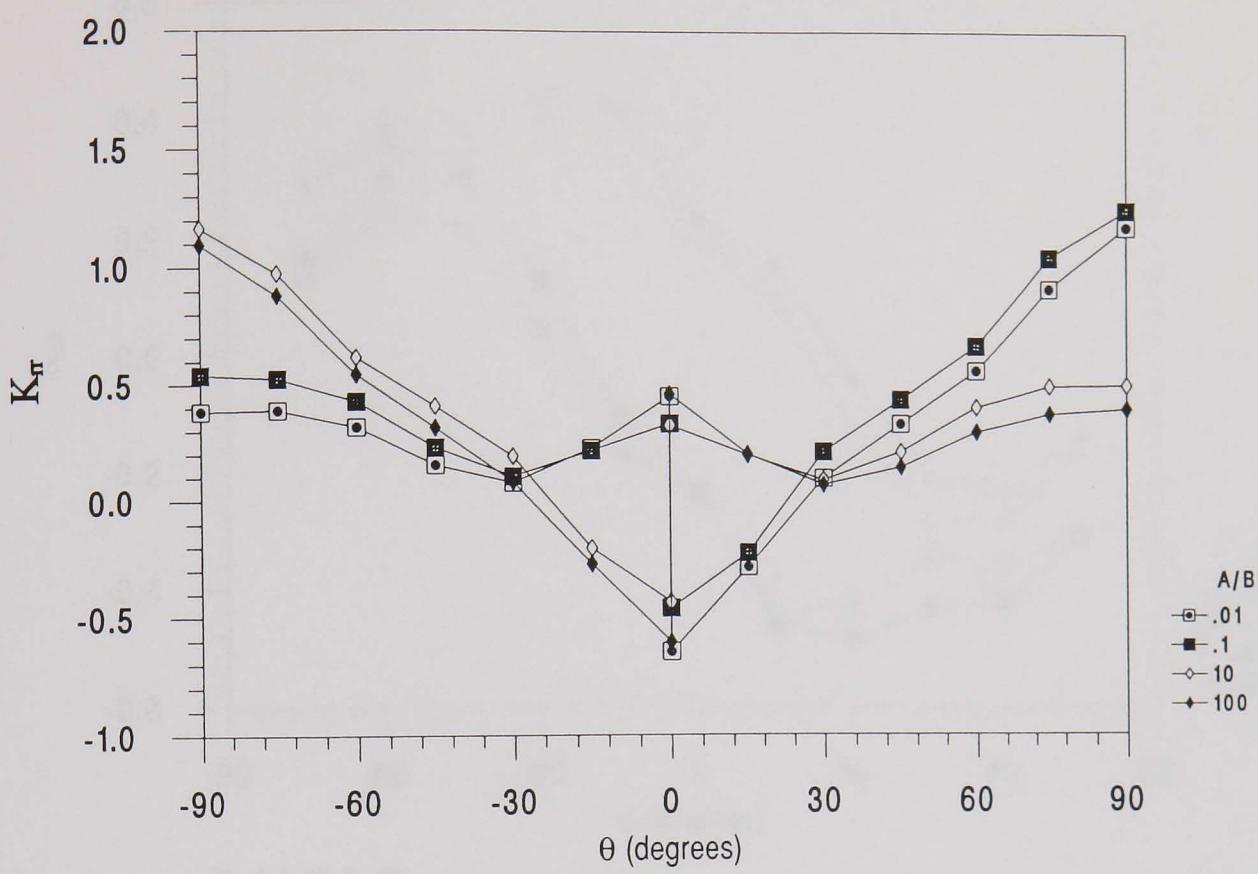

3.4.14(a) $K_{r\theta}$

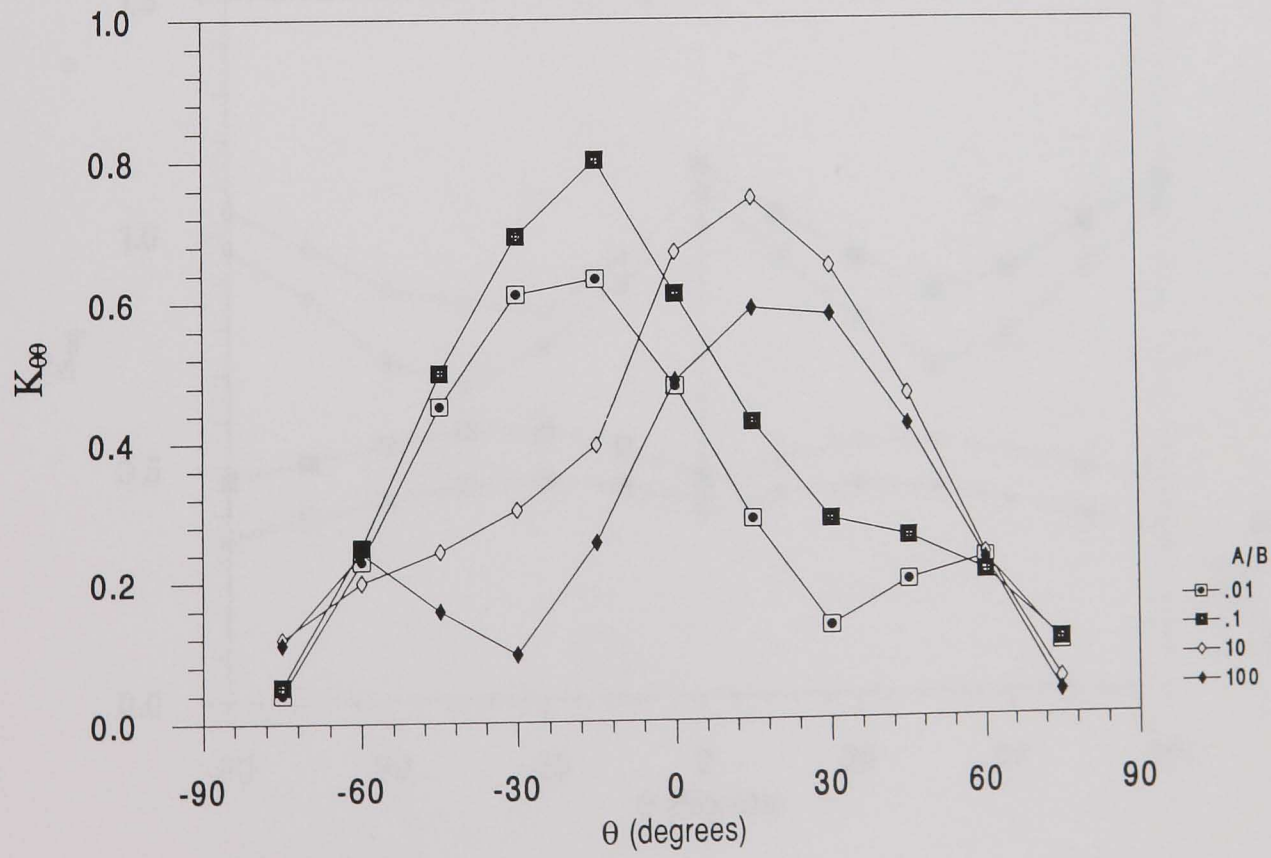

3.4.14(b) $K_{\theta\theta}$

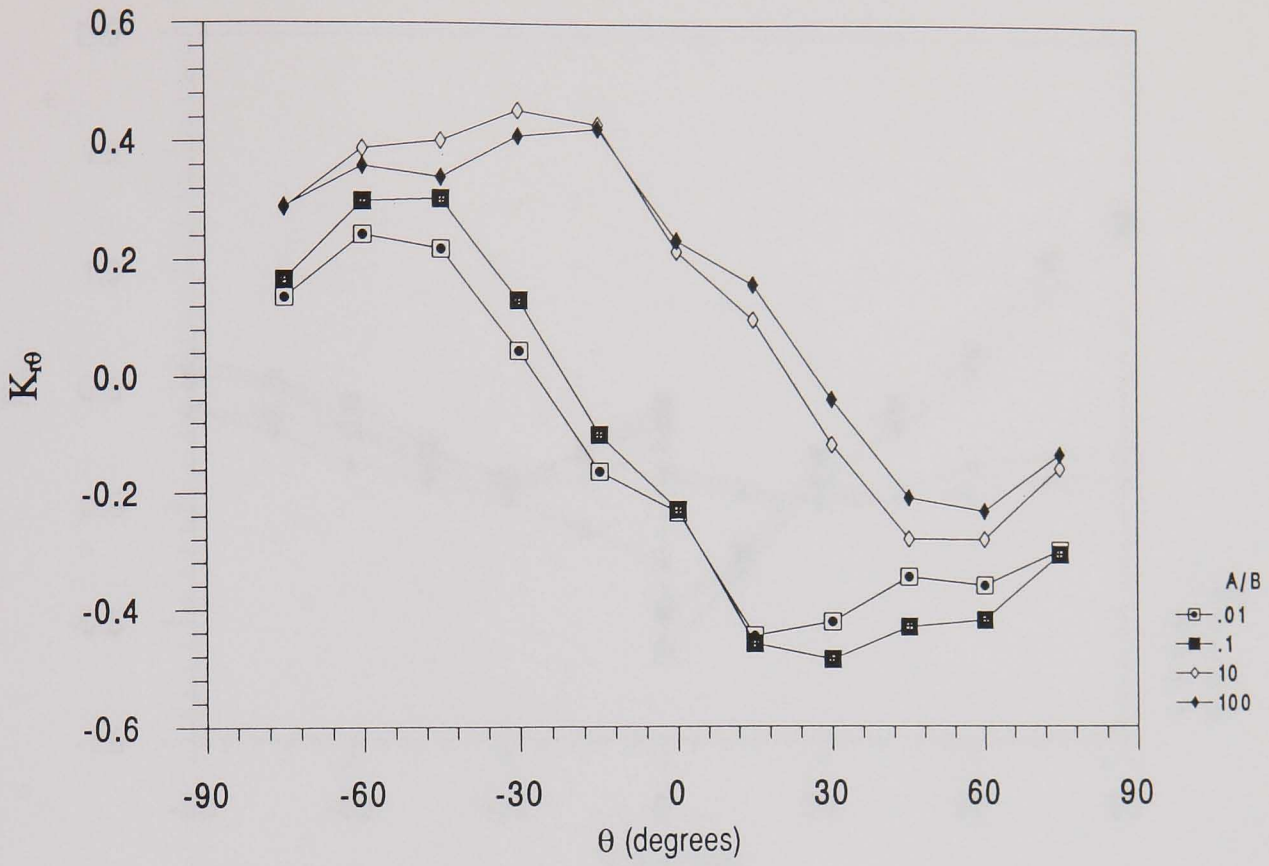

3.4.14(c) $K_{r\theta}$

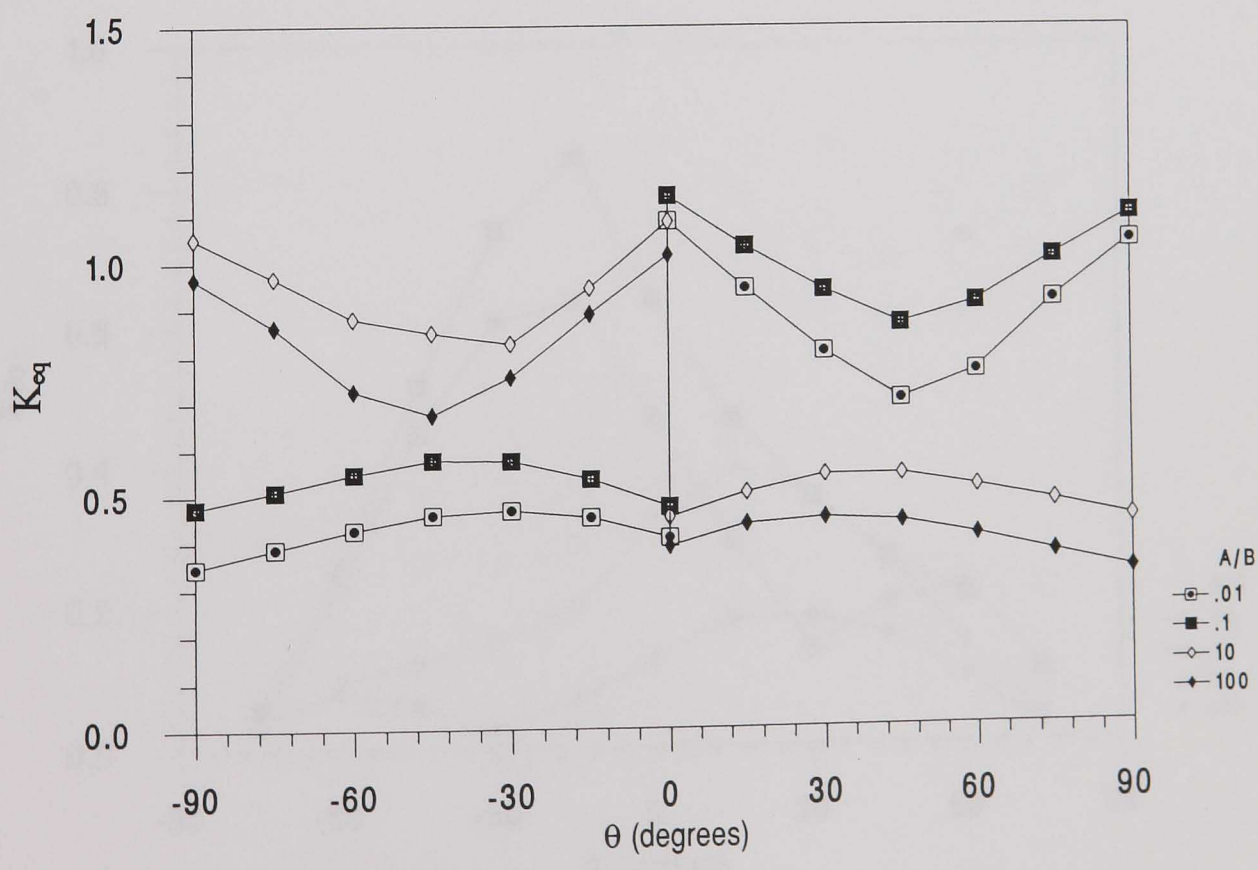

3.4.14(d) $K_{\theta q}$

Fig. 3.4.14 Variations of K_{ij} and $K_{\theta q}$ with θ for a range of A/B values with n = 2 and w/d = 0.5.

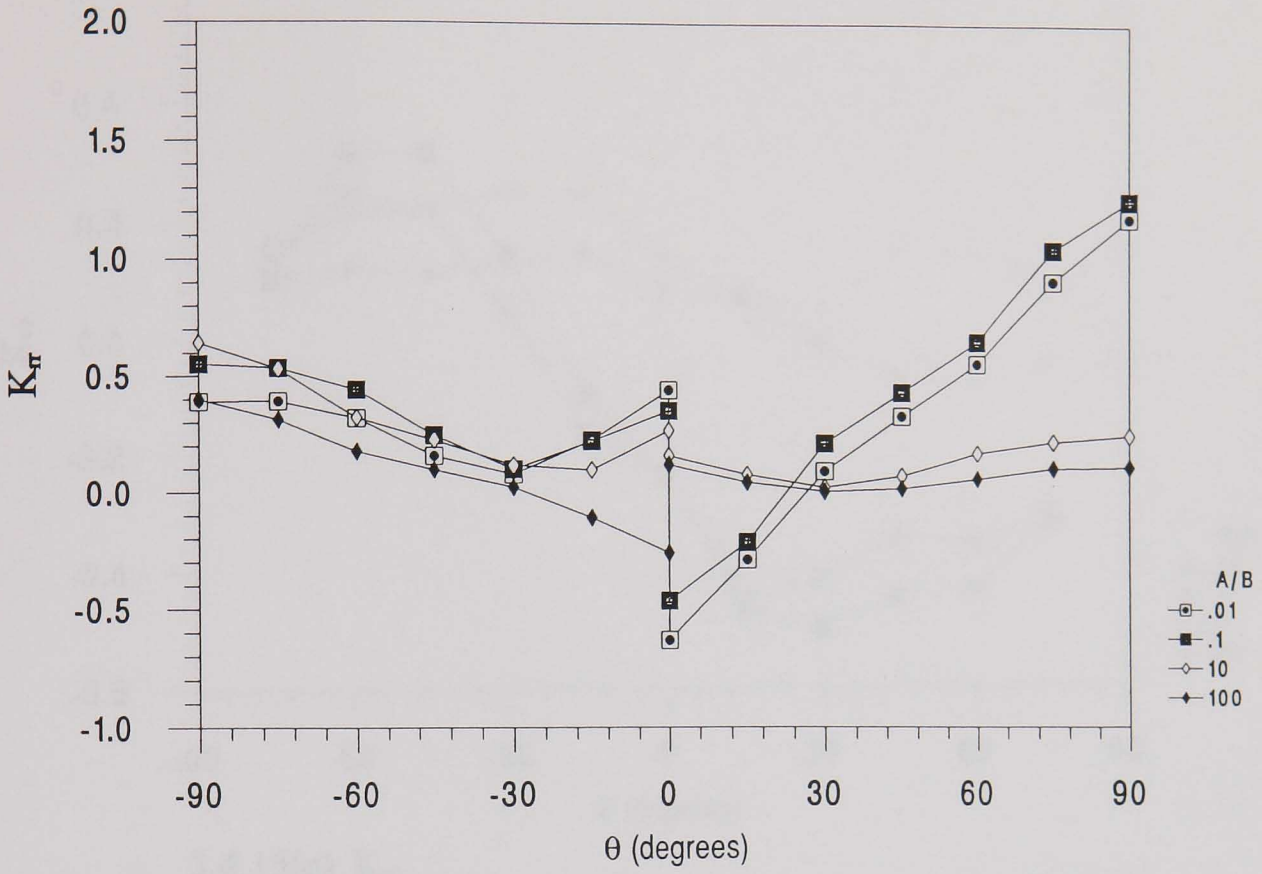

3.4.15(a) K_{rr}

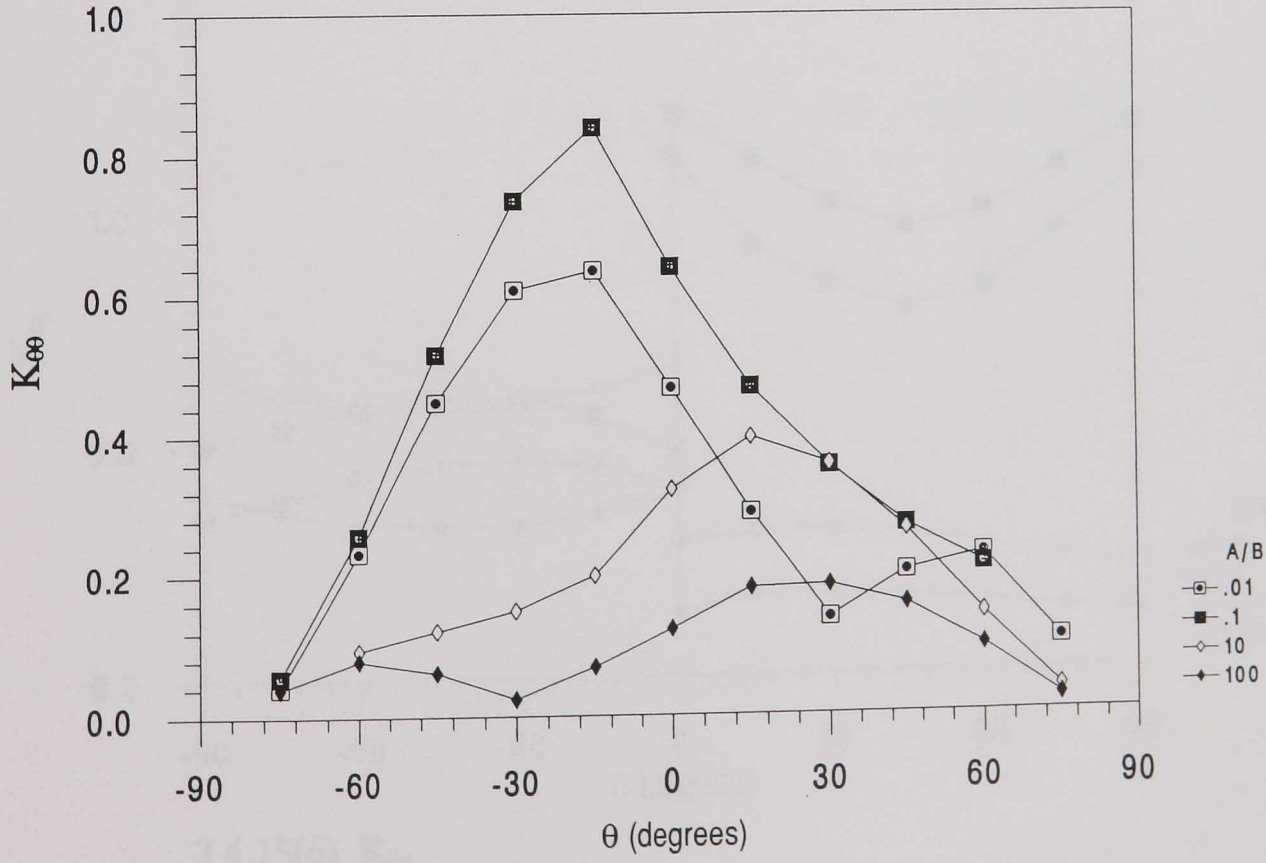

3.4.15(b) $K_{\theta\theta}$

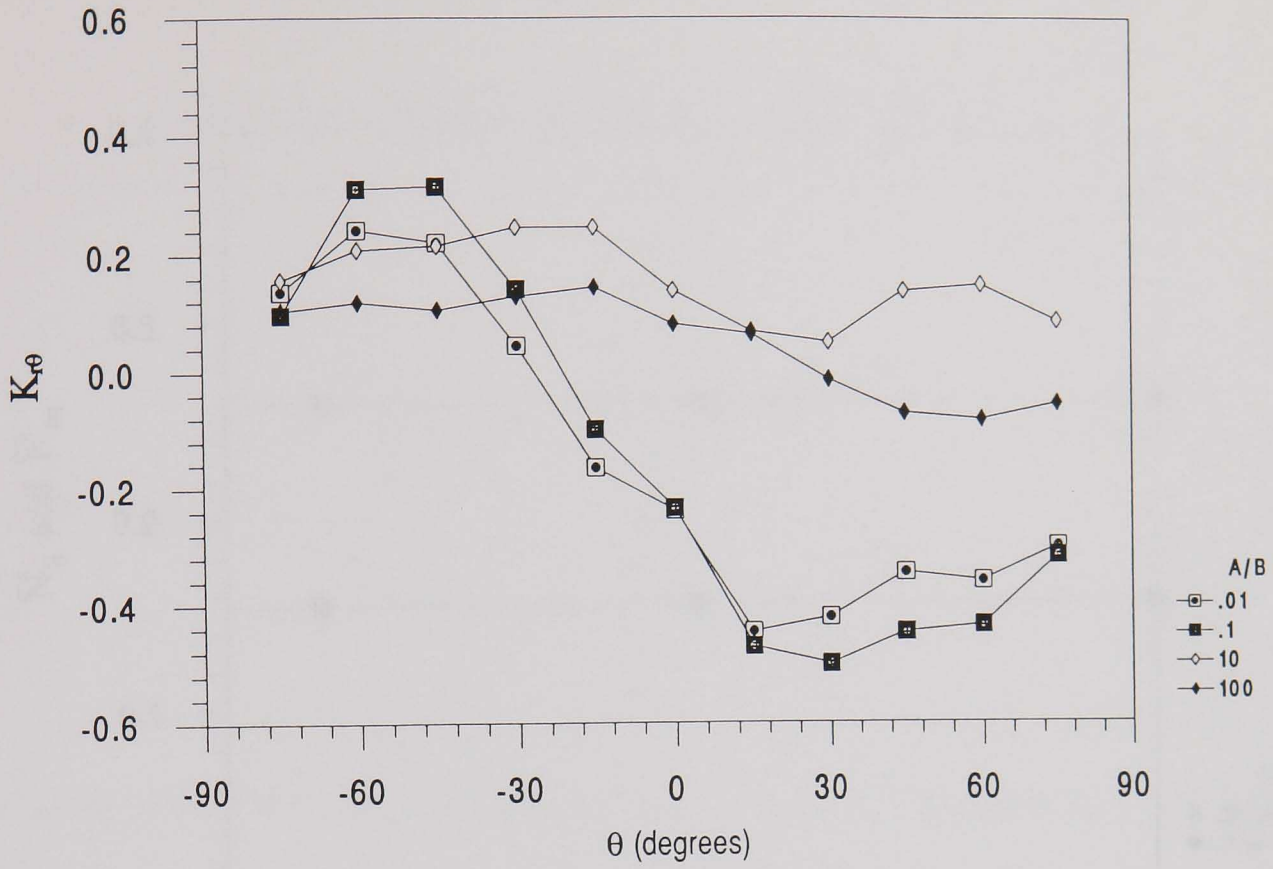

3.4.15(c) $K_{r\theta}$

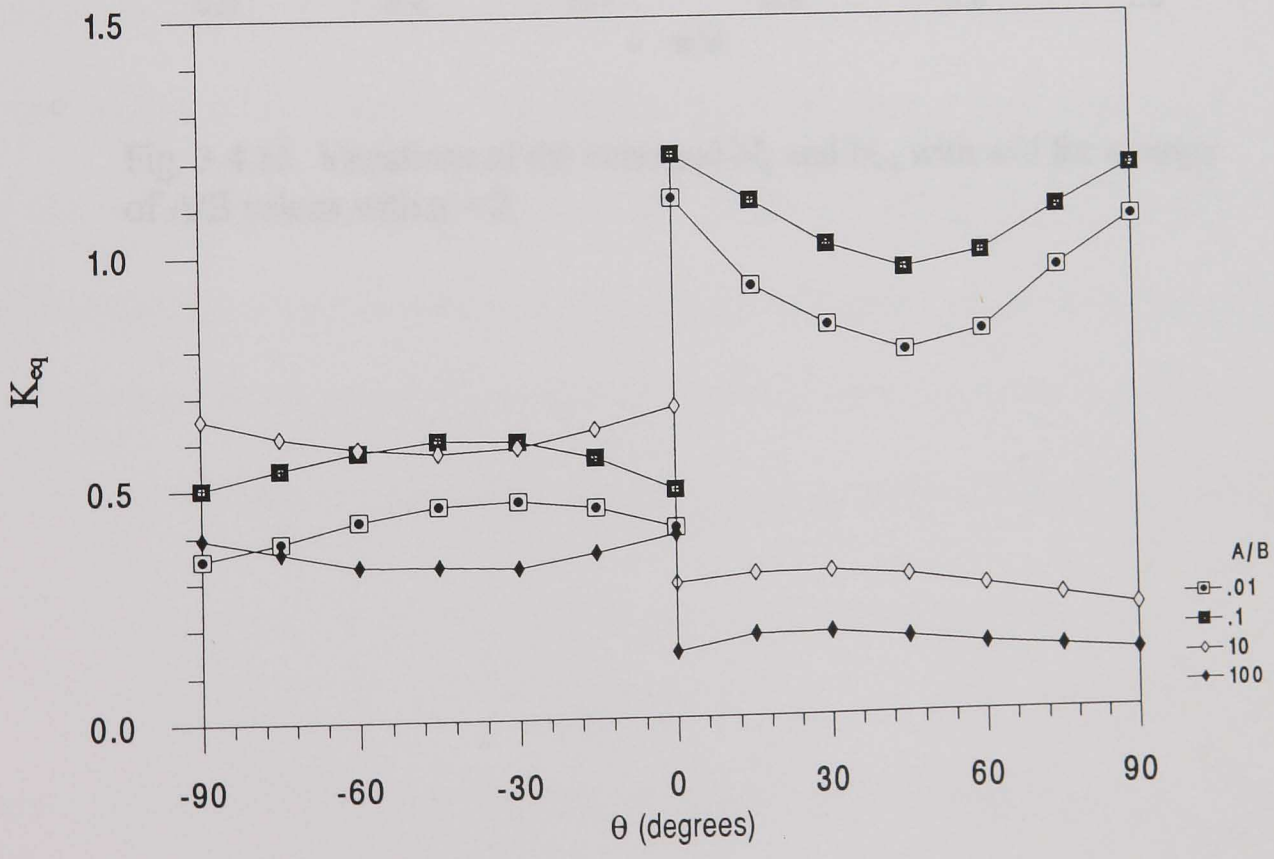

3.4.15(d) K_{eq}

Fig. 3.4.15 Variations of K_{ij} and K_{eq} with θ for a range of A/B values with n = 2 and w/d = 0.1.

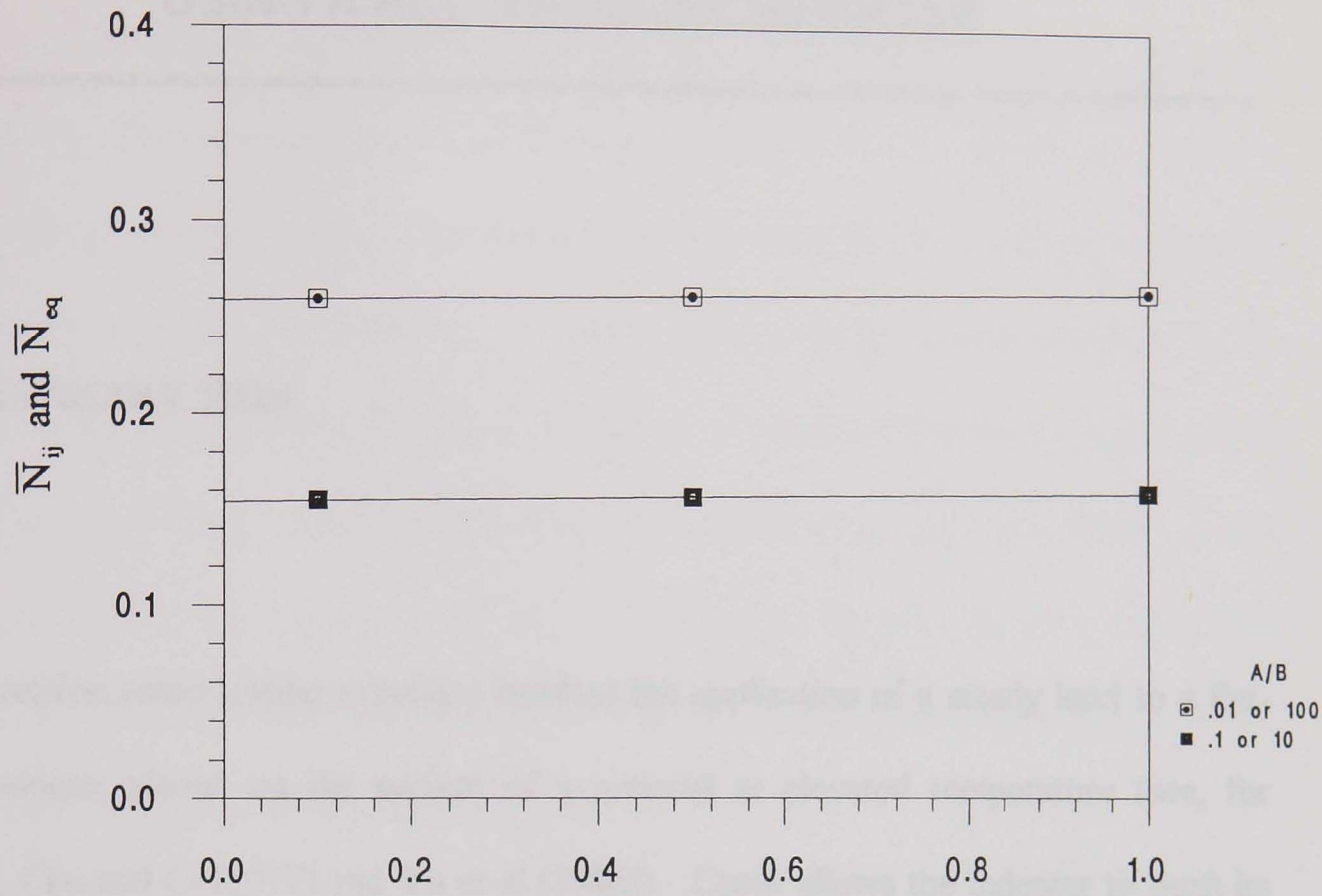

Fig. 3.4.16 Variations of the averaged N_{ij} and N_{eq} with w/d for a range of A/B values with n = 2.

CHAPTER IV

ANALYSIS OF IMPRESSION CREEP TEST METHOD USING A RECTANGULAR INDENTER

4.1 INTRODUCTION

The impression creep testing technique involves the application of a steady load to a flat-ended indenter placed on the surface of a material at elevated temperature (see, for example, Chu and Li [1977] and Yu et al [1986]). Creep allows the indenter to push its way into the surface of the material. The displacement-time record from such a test is related to the creep properties of a relatively small volume of material in the immediate vicinity of the indenter. Usually the indenter is cylindrical (diameter = d), and for this type of indenter it has been shown (e.g. Hyde et al [1993]) that the reference stress approach can be used to convert the mean pressure under the indenter, p, to the corresponding uniaxial stress, σ, i.e.

$$\sigma = \eta p \tag{4.1}$$

and to convert the creep displacement, Δ^c, to the corresponding uniaxial creep strain, ε^c, i.e.

$$\varepsilon^c = \frac{\Delta^c}{\beta d} \tag{4.2}$$

where η and β are the reference parameters. The η and β values have been shown to be 0.296 and 0.755, respectively, for a cylindrical indenter (Hyde et al [1993]).

One particularly attractive application of the impression creep testing technique is in determining the creep properties at positions where variations of creep properties exist, such as in the base, heat-affected zone (HAZ) and weld metal of a fusion joint. However, care must be taken to ensure that the contact area between the indenter and the test material is large enough compared to metallurgical features (e.g., grain size) to ensure that characteristic properties are obtained. For this reason, a long, rectangular indenter, as indicated in Fig. 4.1, rather than a cylindrical indenter, is used in the present investigation. As well as the obvious benefit of increasing the contact area, there is a benefit in the resultant increase in the required load levels. A rectangular indenter can be used in weld situations because significant variations in the properties only occur in one direction, i.e. perpendicular to the fusion line (Fig. 4.2).

Creep properties for the base material and weld metal can be obtained by testing conventional uniaxial creep specimens. Within the HAZ, there may be more than one metallurgical structure, with different creep properties related to each of these zones in which the different metallurgical structures exist. However, by polishing and etching, each distinct zone can be clearly identified and hence the indenter can be positioned at an optimum position within the appropriate zone. For the present purposes, it will be assumed that only three distinct zones exist, i.e. base material, HAZ and weld metal. However, the results obtained can also be used if there are more than three distinct metallurgical zones.

It should be noted that as in the cases where a cylindrical indenter is used, only the primary and steady-state creep properties can be obtained using a rectangular indenter. Tertiary

creep, internal damage which is created in a conventional tensile creep test, and detailed multi-axial stress behaviour are not obtained from impression creep tests. These aspects of the creep behaviour in welds are of significant importance and also need to be determined before a full assessment of the weld behaviour can be performed. However, an understanding of the primary and steady-state creep behaviour of the various materials within a weld is of paramount importance to the understanding of the stress and strain fields that exist within welds. Further work has been carried out on the development of methods which will allow the tertiary creep, internal damage and multi-axial stress behaviour, of the various materials within welds, to be determined. The results of this work will be presented in Chapter VI of this thesis.

If the HAZ material is to be impression creep tested, using a rectangular indenter, specimens can be removed from the weldment and conveniently loaded in the local x, y or z direction (see Fig. 4.2), as indicated in Fig. 4.3. For x-direction loading (Fig. 4.3(a)) the specimen consists of HAZ and either the weld or base material. For y-direction and z-direction loading the specimens may consist of HAZ and/or weld and base materials. It should be noted that if the HAZ was wide enough it may be possible to obtain specimens consisting entirely of HAZ material. However, in general, this is unlikely to be the case. In all three cases, the indenter width, d, is intended to be small compared to its length and hence the deformation can be closely approximated by plane-strain conditions. The three loading cases can therefore be represented by four basic problem types, as shown in Fig. 4.4. Material A is the material for which the creep properties are required.

The main objective of this work is to determine the effects of the various geometric parameters, such as d, H, W, etc., and of the relative creep resistance of materials A, B and C on the reference parameters η and β. Hence, the practical situations under which impression creep testing can produce accurate creep data for HAZ regions are identified. Therefore, recommendations for performing this type of test are given.

4.2 DETERMINATION OF THE REFERENCE PARAMETERS

The method of determining the reference parameters, η and β, has been fully described by Hyde et al [1993]. Therefore, only a brief outline will be given here. Two approaches can be adopted, one based on a series of finite element creep calculations, the other using limit load (elasto-plastic) solutions.

For the purpose of determining the η and β values using finite element creep calculations, the material is assumed to creep according to a Norton (power-law) creep behaviour law, i.e.

$$\dot{\varepsilon}^c = A\sigma^n \tag{4.3}$$

Also, for the cases in which more than one material is involved, the stress exponents, n, are assumed to be the same for all of the materials. Steady-state displacement rates, $\dot{\Delta}_{ss}$, were obtained for a range of n-values, keeping all other material constants, the load level, and the geometry, the same. The displacement rates were then normalised with respect to a stress multiplier, α^n, and the value of α which caused the $\dot{\Delta}_{ss}/[A(\alpha\sigma_{nom})^n]$ values to be practically

independent of n was determined; this value of α is the reference parameter η in equation (4.1). A computational optimisation procedure was used to obtain the α-value which fits the $\dot{\Delta}_{ss}/[A(\alpha\sigma_{nom})^n]$ data most accurately. The equivalent uniaxial strain rate, $\dot{\varepsilon}_{ss}$, can be determined by substituting the reference stress, ηp, into equation (4.3). The β-value is then obtained by using the steady-state indentation deformation rate, $\dot{\Delta}_{ss}$, i.e.

$$\beta = \frac{\dot{\Delta}_{ss}}{d\,\dot{\varepsilon}_{ss}} = \frac{\dot{\Delta}_{ss}}{dA\,(\eta p)^n} \qquad (4.4)$$

A series of calculations of this type is required to determine the η and β values for every geometry and relative creep properties, i.e., relative A-values in equation (4.3).

By using the similarity between elastic and elastic-perfectly-plastic stress distributions with creep solutions having n = 1 and n = ∞, Sim [1968][1970][1971] showed that approximate reference parameters can be obtained on the basis of elastic and limit-load solutions, i.e. for the present application,

$$\eta = \frac{\sigma_y}{P_L} \qquad (4.5)$$

and

$$\beta = \frac{E\,\Delta^{el}}{d\,\eta p} \qquad (4.6)$$

where P_L is the limit load corresponding to a yield stress of σ_y and Δ^{el} is the elastic deflection corresponding to a Young's modulus of E. Again, elastic and limit load solutions are required for each geometry.

4.3 FINITE ELEMENT ANALYSES

The ABAQUS [1994] finite element code was used to perform all the finite element analyses shown in the next section. Eight-noded, isoparametric, quadratic, plane strain elements with 2 x 2 (reduced) integration points were used. In order to check mesh convergence, a series of runs with different mesh refinements were performed using the creep and elasto-plastic routines in the program. An optimum degree of mesh refinement was established, similar to that shown in Fig. 4.5 for both creep and limit load (elasto-plastic) analysis.

Since the indenter material is assumed rigid, the contact conditions are simulated by prescribing a uniform vertical displacement over the contact nodes and preventing them from moving horizontally, i.e. no slip condition at the contact surface.

For the limit load analysis, the Riks algorithm was implemented. This algorithm is used by the ABAQUS code with an automatic load incrementation procedure to produce a reliable solution to non-linear static equilibrium problems in which unstable behaviour may occur, for example when the load or displacement may decrease during the incremental/iterative numerical solution. Further details on the Riks algorithm and other non-linear solution algorithms can be found in Crisfield [1981] and Powell and Simons [1981]. A typical applied mean pressure versus deformation curve is shown in Fig. 4.6. The finite element solution for the limit load agrees with the corresponding analytical solution (Johnson and Mellor [1962]) to within 2%.

For the creep analysis, steady state solutions for the deformation rate were obtained and plotted against the reciprocal of time , as shown in Fig. 4.7 for a typical case. The intercept on the deformation rate axis represents the steady state solution (i.e. as $t \rightarrow \infty$). In order to arrive at the values of η, several finite element creep analyses were performed for a wide range of n values until steady state conditions were reached. By plotting the logarithm of the normalised creep displacement rate against the value of n, as shown in Fig. 4.8 for a typical case, the value of the stress multiplier α producing a horizontal line (i.e. independent of n) is the reference value, i.e. η in equation (4.1). Furthermore, the reference multiplier from equation (4.4) can also be obtained from this plot from the intercept on the vertical axis. The above procedure of obtaining the value of η has been automated by using a numerical algorithm which is presented in Appendix III.

4.4 RESULTS

4.4.1 Single Material

The geometry for this situation is shown in Fig. 4.4(a). The variations of η with W/d for a range of H/d values ($2.5 \leq H/d \leq 10$), obtained from the accurate (creep) and approximate (limit load) analyses, are given in Fig. 4.9(a). The approximate η-values are larger than the corresponding accurate η-values and the discrepancy between them is greater for the higher H/d situations. For a particular value of H/d, both the accurate and approximate results indicate that above a certain W/d value, η is independent of W/d. Also, the value of W/d

for which η is independent of W/d increases as H/d is increased. In general, the η-values reduce with increasing H/d. An alternative presentation of the same data is given in Fig. 4.10(a), from which it can be seen that provided W/H is greater than about 2 the η-value is independent of W/H, although the value does depend on H/d. From the information provided in Figs. 4.9(a) and 4.10(a) the η-value for any specific specimen geometry can be easily determined.

The variations of β with W/d and with W/H for a range of values of H/d ($2.5 \leq H/d \leq 10$) are given in Fig. 4.9(b) and 4.10(b), respectively. The approximate β-values are higher than the corresponding accurate β-values. The discrepancy between the approximate and accurate β-values increases as H/d is increased. As with the η-values, above a certain W/d value, for a given H/d, β is independent of W/d. In general, the β-values increase with increasing H/d. Also, as indicated by Fig. 4.10(b), provided W/H is greater than about 2, the β-value, for a particular H/d, is independent of W/H. Therefore, Figs. 4.9(b) and 4.10(b) can be used to obtain the β-value for any specific specimen geometry.

It is recommended that for single material impression creep tests, using a rectangular indenter, the geometry should be chosen such that $W/H \geq 2$. Also, any convenient H/d value can be chosen, but η and β become less sensitive to the actual geometry as H/d is increased.

4.4.2 Two Materials in Series

The geometry for this situation is shown in Fig. 4.4(b). Compared to the single material situation, an additional geometric variable is introduced, i.e., H_A and H_B instead of just H, as well as different creep constants, A_A and A_B, for the two materials. The creep stress exponent, n, in equation (4.3), is taken to be the same for the two materials, but the effect of changing the relative magnitudes of the constant A (equation 4.3) was investigated. Results were obtained for $0.001 \leq A_A/A_B \leq 1000$ with $0.667 \leq H_A/H_B \leq 1.5$. This covers the range of A across the weld in practical cases. Also, on the basis of the results obtained for a single material (Section 4.4.1), the overall geometry was fixed to be W/H = 2 and H/d = 5, where $H_A + H_B = H$. It should be noted that W/H = 2 results in $W/H_A \geq 2$, and H/d = 5 results in $H_A/d \leq 5$.

The variations of η with H_A/H_B for a range of values of A_A/A_B ($0.001 \leq A_A/A_B \leq 1000$) are given in Fig. 4.11(a). An alternative representation of the same data is given in Fig. 4.12(a), in which the variation of η with log (A_A/A_B), for a range of values of H_A/H_B ($0.667 \leq H_A/H_B \leq 1.5$), is presented. It is evident, from Figs. 4.11(a) and 4.12(a), that provided $A_A/A_B \geq 1$ then η is practically independent of A_A/A_B and of H_A/H_B (with W/H = 2 and H/d = 5). Therefore, provided that $A_A/A_B \geq 1$, the η-value for a single material case can be used. Similarly, Figs. 4.11(b) and 4.12(b), which show the variations of β with H_A/H_B and A_A/A_B, respectively, indicate that for $A_A/A_B \geq 1$ the β-values for a single material can be used. When $A_A/A_B \leq 1$, the β-value is sensitive to A_A/A_B. From a practical point of view, these results indicate that it is not necessary to know the exact depth of the HAZ material, when a specimen of this type is removed from a weld, in order to obtain the HAZ properties, provided the substrate material is more creep resistant than the HAZ material. Also, if the HAZ consists of two or more zones with different creep properties, it should be

possible to obtain the creep properties of the least creep resistant zone using this type of specimen.

4.4.3 Two Materials Side-by-Side

The geometry for this situation is shown in Fig. 4.4(c). Compared with the single material situation, two additional geometric variables are introduced; the proximity of the indenter to the interface, f, and W_A and W_B are required instead of just W. The creep stress exponent, n, in equation (4.3), is taken to be the same for the two materials, but the effect of changing the relative magnitudes of the constant A (equation (4.3)) was investigated. Results were obtained for $0.01 \leq A_A/A_B \leq 100$, with $0.5 \leq f/d \leq 2$. Also, on the basis of the results obtained for a single material (Section 4.4.1) the overall geometry was fixed at W/H = 2 and H/d = 15. It should be noted that any H/d value greater than about 5 could be chosen without any significant effect on the results being expected.

The variations of η and β with f/d for a range of A_A/A_B values ($0.01 \leq A_A/A_B \leq 100$) are given in Figs. 4.13(a) and 4.13(b), respectively. From Fig. 4.13(a) it can be seen that the η-value is practically independent of both the A_A/A_B and f/d values. However, Fig. 4.13(b) shows that the β-value may be significantly affected by both the A_A/A_B value and the indenter position, f/d. As f/d is increased the dependence on both A_A/A_B and f/d is reduced. From a practical point of view, provided $A_A/A_B \geq 1$ and $f/d \geq 1$, a β-value obtained for the single material would be reasonably accurate (within 12%) and the f/d value would have an insignificant effect.

4.4.4 Three Materials Side-by-Side

The geometry for this situation is shown in Fig. 4.4(d). Compared with the single material situation, three additional geometric variables are introduced, i.e. the proximity of the indenter to one of the interfaces, g, and W_A, W_B and W_C being required instead of just W. The creep exponent, n, in equation (4.3) is taken to be the same for all three materials, but the effect of changing the relative magnitude of the constant A (equation (4.3)) was investigated. In order to reduce the number of variables, it was also assumed that $A_B/A_C = 1$. Results were obtained for $0.001 \leq A_A/A_B \leq 1000$ with $3 \leq W_A/d \leq 6$ and $0.667 \leq 2g/W_A \leq 1.00$. On the basis of the results obtained for the single material (Section 4.4.1) and two materials which are side-by-side (Section 4.4.3), W/H = 2 (where $W = W_A + W_B + W_C$) and $W_B = W_C = 2W_A$, were chosen for the calculations. The overall dimensions were selected, taking into account a practical weld situation; the HAZ in a weld in general is unlikely to have a width greater than about 3 mm and a 0.5 mm indenter width was considered to be the smallest of practical use. Also, since the boundaries between the HAZ and the adjacent zones are unlikely to be straight and parallel, the sensitivity of the values of η and β to the exact ratios of W_A/d and $2g/W_A$ (the centralisation parameter) was considered to be of primary importance.

The variations of η and β with A_A/A_B for $W_A/d = 3$ and 6 and $0.667 \leq 2g/W_A \leq 1.0$ are given in Figs. 4.14(a) and 4.14(b), respectively. It can be seen that there is a systematic variation in the η and β values with A_A/A_B and that the specific values depend on W_A/d. However, for the range of $2g/W_A$ investigated, the η and β values are insensitive to the exact value of $2g/W_A$. From a practical point of view, this indicates that exact

centralisation of the indenter is not critical and that slightly curved and non-parallel interfaces will not significantly affect the result.

The effect of W_A/d on the η and β values is illustrated in Figs. 4.15(a) and 4.15(b), respectively, where it is shown that when $A_A/A_B \geq 1$, the η and β values are practically independent of A_A/A_B. In addition, since W_A could be determined with reasonable precision, accurate η and β values could also be determined, particularly for situations in which $A_A/A_B \geq 1$.

4.5 ADVANTAGES OF RECTANGULAR INDENTERS

Compared with cylindrical indenters, rectangular indenters possess the following attractive features:

(1) Much higher loading levels can be used on the indenters if the width of the indenter is equal to the diameter of a corresponding cylindrical indenter because the contact area of a rectangular indenter is significantly larger. This is particularly significant when small capacity test machines are not available and it is necessary to apply low stress levels.

(2) Care must be taken to ensure that the contact area between the indenter and the test material is large enough compared to metallurgical features (e.g., grain size) to

ensure that characteristic properties are obtained. By using a rectangular indenter, greater accuracy, in this respect, can be achieved. This is particularly important for the HAZ material, where the homogenous behaviour may be significantly poorer than that of the parent and weld materials.

(3) Finite element numerical simulation can be greatly simplified. Plane-strain two-dimensional models can be used to perform FE-calculation, instead of three-dimensional models which would have to be used for multi-zone problems with cylindrical indenters (see Fig. 4.16).

(4) The effect of the indenter depth on the η and β parameters can be significantly reduced. This can be demonstrated by using the results of finite element simulations with different initial indenter depths, b, see Fig. 4.17. The $b = 0$ case corresponds to the situation in which the indenter depth is ignored. Figs. 4.18 and 4.19 show the effects of b on the reference parameters, η and β, respectively, for both plane strain (rectangular indenter) and axisymmetric (cylindrical indenter) models of a single material with $W/d = 2H/d = 10$. The results indicate that the variations of η and β with b are very small using the rectangular indenter, less than 5% even when $b/d = 0.2$, whereas the errors are over 15% using the cylindrical indenter for the same case. Experimental results show that, for all of the parent, weld and HAZ material tests performed on the exposed pipe material under the highest loading level (1.75 kN, see Table 5.2), the maximum b/d value was found to be < 0.2 at the end of the test (the creep time is long enough for obtaining the steady-state strain rate by fitting the time-displacement curves). This shows that

the reference parameters, η and β, obtained from the FE-calculations with b/d = 0, are applicable to the practical impression creep tests.

4.6 DISCUSSION AND CONCLUSIONS

Experimental creep data have been produced using the indentation creep technique for a number of single material specimens (Chu et al [1979], Gibbs [1983], Yu et al [1985] and Tasandi et al [1988]). These tests have all been performed using circular indenters. It has been shown that the reference stress technique can be used to convert the results from indentation creep tests to corresponding uniaxial creep test data. Because the area of contact between the indenter and the specimen may be quite small, care must be taken to ensure that the indenter diameter is significantly greater than the dimensions of characteristic metallurgical features (e.g., grain size, etc.). If this is not possible, a rectangular indenter (Fig. 4.1) could be used in some cases; the author is not aware of any impression creep tests in which the use of rectangular indenters have been reported. One of the purposes of this work is to establish the reference parameters, η and β, which will allow the results of indentation creep tests, using rectangular indenters, to be converted to corresponding uniaxial creep data. In general, the η and β values are functions of both W/d and H/d (see Fig. 4.4(a)). However, if $W/H \geq 2$ and $W/d \geq 10$ the η and β values are insensitive to the values of W/H and W/d. Fig. 4.20 is a schematic diagram which shows the general effect of the specimen geometry on the reference parameters for the single material case.

The indentation creep technique has the potential of allowing the creep properties of the various regions within the HAZ of a weld to be determined. Since the creep properties only vary, significantly, in a direction perpendicular to the fusion line (see Fig. 4.2), this is an appropriate case for the use of a rectangular indenter. Specimens can be machined from welds and subsequently polished and etched to determine the boundaries between the HAZ region and the adjacent materials. The possible loading directions and specimen configuration include those shown in Figs. 4.2 to 4.4. In practical weld situations, in general, the HAZ is unlikely to be more than about 3 mm wide and the indenter width would not be less than about 0.5 mm. Therefore, remote boundary conditions cannot easily be achieved and so the practical effects of various geometric variables and differences in material properties need to be understood. This is especially important because boundaries will not necessarily be straight and/or parallel.

Considering the two-material configuration shown in Fig. 4.4(b), which is an idealisation of that shown in Fig. 4.3(a), it is unlikely that H_A and H_B will be constant, i.e. the interface will be curved. However, Figs. 4.11(a) and 4.11(b) indicate that the reference parameters to be used, η and β, would not be strongly affected if the H_A/H_B value was only known to an accuracy of about $\pm 10\%$; this is particularly true for the η value and for both η and β when $H_A/H_B \geq 1$. Also, if material A, i.e. the material to which the indenter is being applied, is less creep resistant than material B (i.e. $A_A/A_B > 1$), the reference parameters are insensitive to the precise properties of material B.

The specimen configurations indicated by Figs. 4.4(c) and 4.4(d), which are idealisations of that shown in Fig. 4.3(c), were investigated to see whether they offer any advantages over the configuration indicated in Fig. 4.4(b). If the creep properties vary across the HAZ then these configurations (Figs. 4.4(c) and 4.4(d)) are advantageous because the indenter can be easily placed at the appropriate position within the HAZ. Figs. 4.12(a) and 4.13(a) indicate that the position of the indenter relative to the interface is not critical. This also indicates that if there is a significant variation of creep properties close to the boundary, this will not significantly affect the accuracy of the results obtained.

In general, owing to the geometric effect of the plane strain model, before starting a specific indentation test, finite element calculation should be performed, using dimensions identical to those of the actual specimen in order to obtain reliable reference parameters for the test. The indentation direction (one of the three possible directions) and the cutting of the specimen from the weld should be carefully determined by studying the detailed micro-structure within the welds. Since the single-material case can provide the most accurate results, it is suggested that the single-material impression creep specimens are preferable in the impression creep tests, as long as the application of this simplest case is possible.

This study has highlighted the advantages of using a rectangular indenter, rather than the conventional circular indenter, in impression creep testing. The reference stress approach can be used to obtain reference parameters, η and β, which are used to convert the impression creep test data into the corresponding uniaxial creep data. The finite element method was used to perform accurate (creep) or approximate (limit load) calculations to obtain the reference parameters. Several positions of the rectangular indenter were

investigated. The analysis featured a large number of specimen geometric parameters, such as the width of the heat affected zone, depth of the specimen, relative width of indenter to the material zone tested, etc., as well as the effect of changing the relative creep resistances of the material. The material stress index, n, was taken to be the same for the base material, heat affected zone and weld metal. Specific recommendations were made regarding the specimen geometric parameters and the orientation of the rectangular indenter.

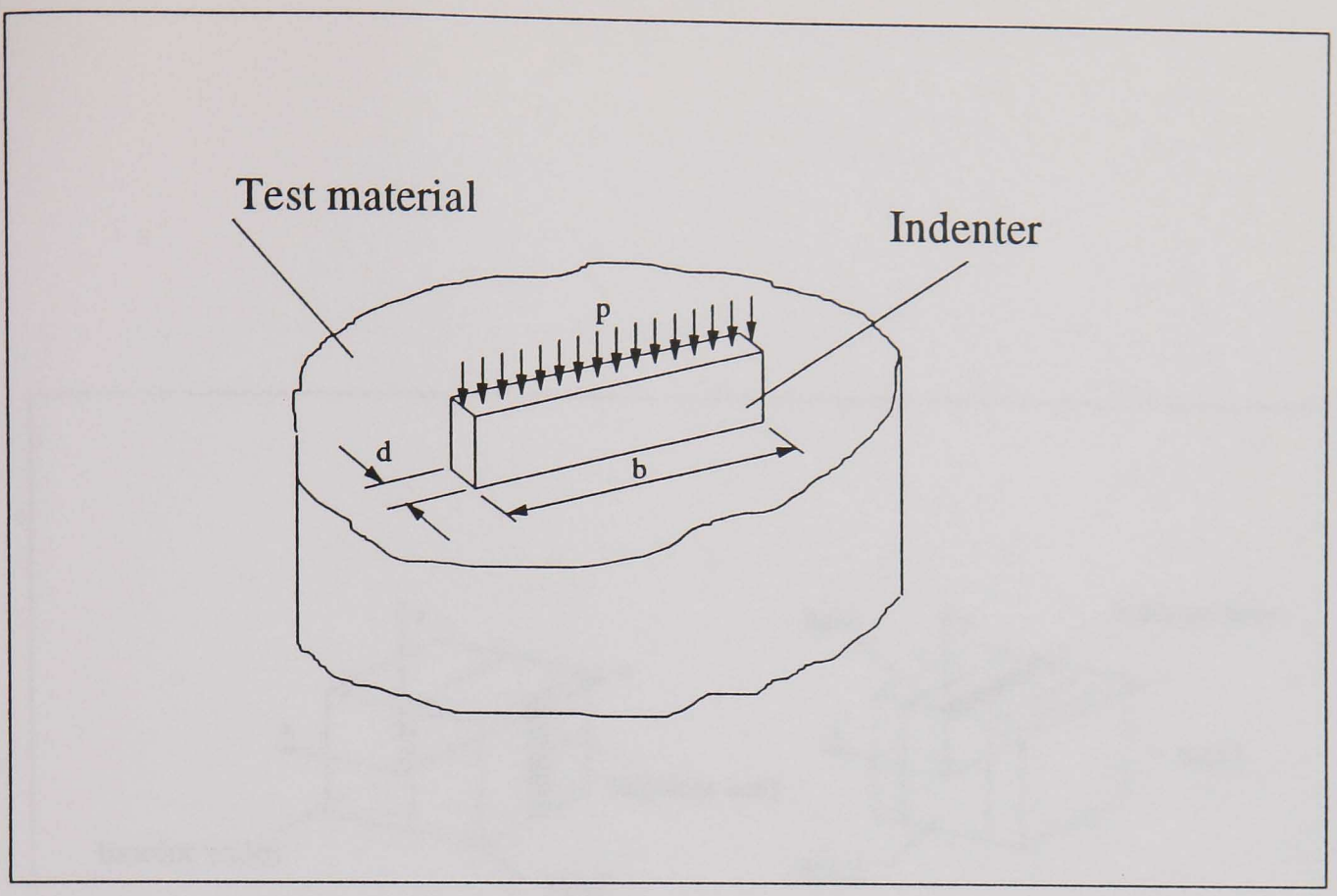

Fig. 4.1 A rectangular indenter.

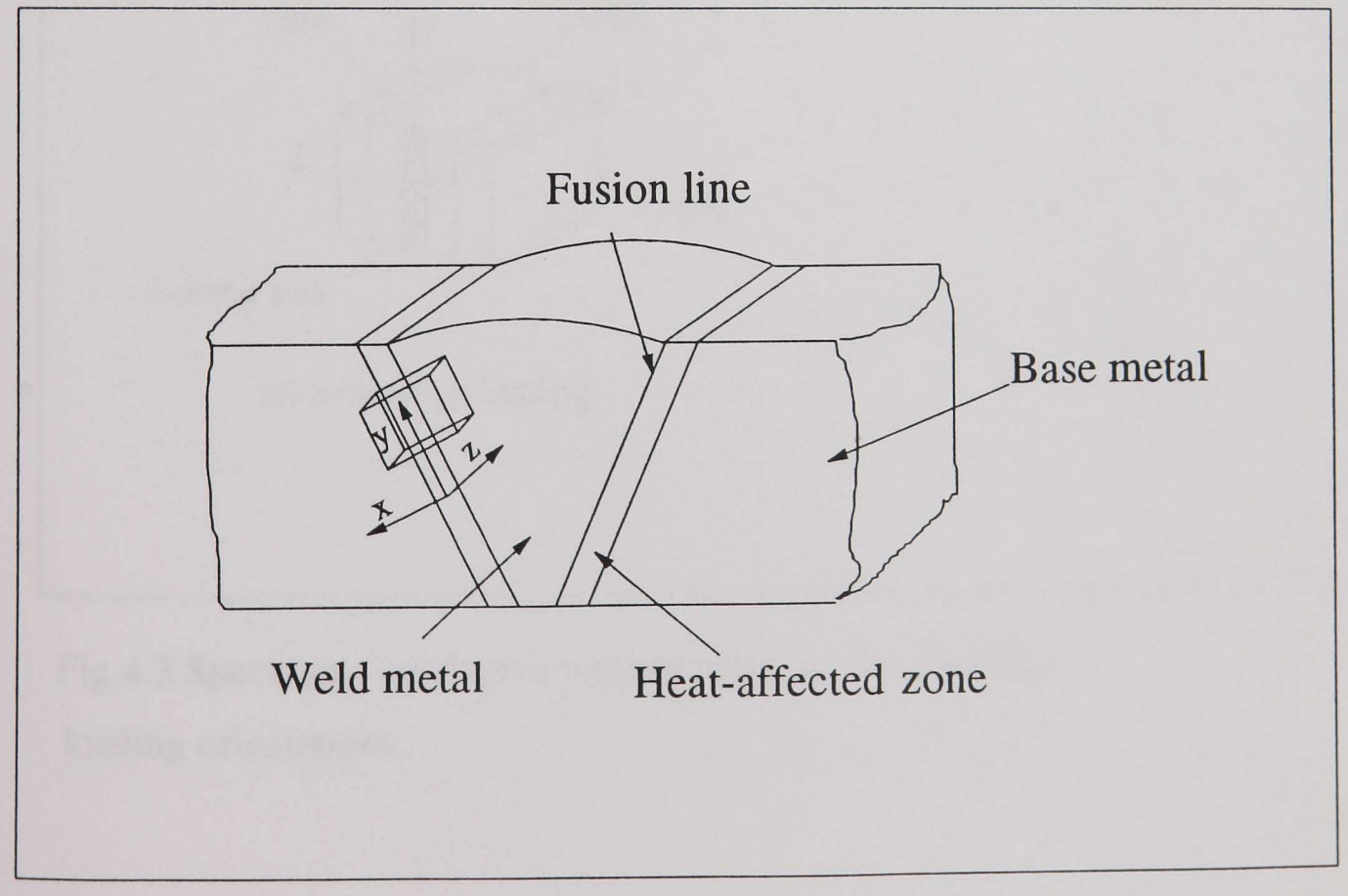

Fig. 4.2 A schematic diagram showing base material, HAZ and weld metal (x direction is perpendicular to the fusion line).

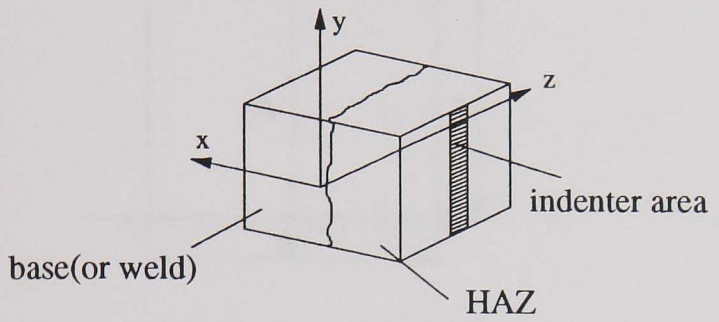

(a) x-direction loading

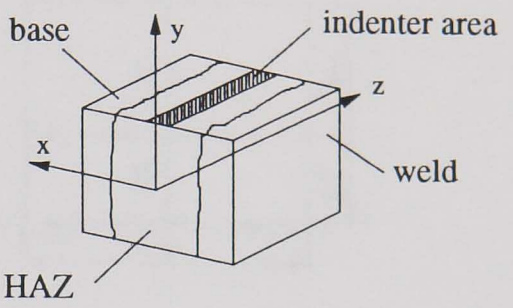

(b) y-direction loading

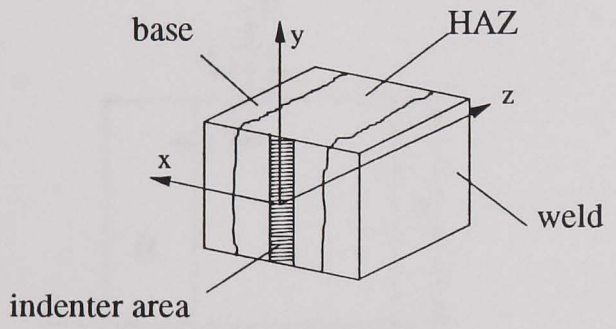

(c) z-direction loading

Fig.4.3 Specimens cut from a welded joint and the possible loading orientations.

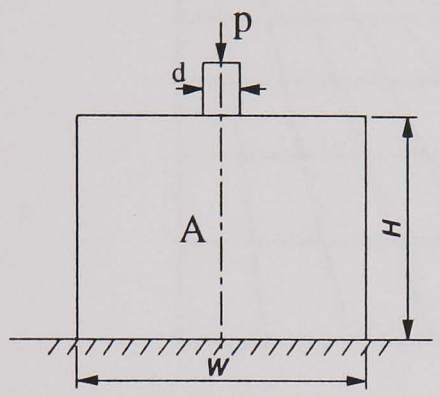

(a) single material

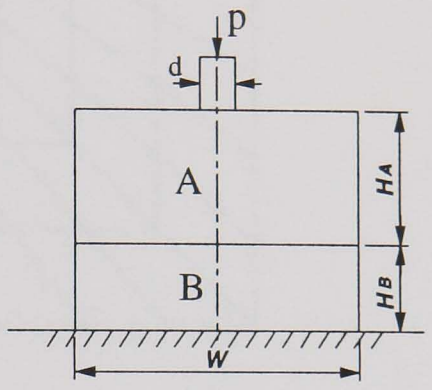

(b) two materials in series

(c) two materials side-by-side

(d) three materials side-by-side

Fig.4.4 Four load configurations and geometric prameters.

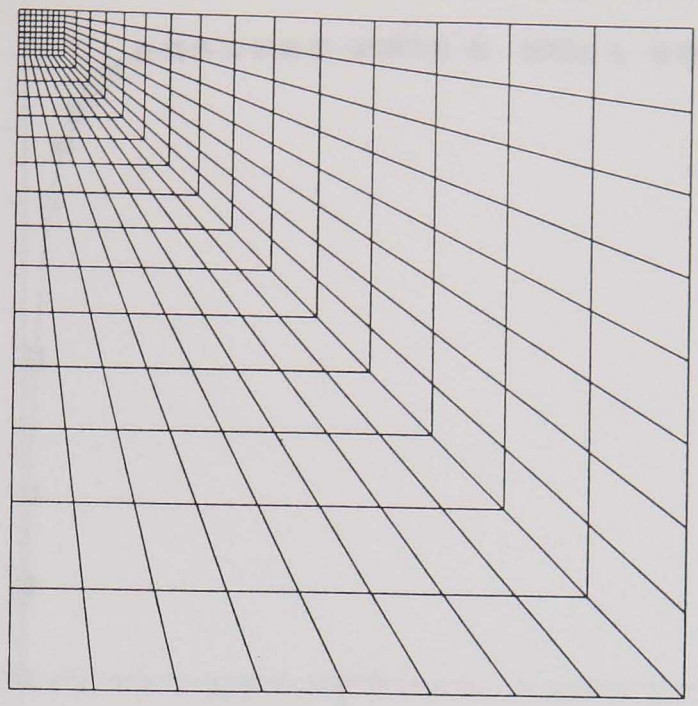

(a) for single-material model

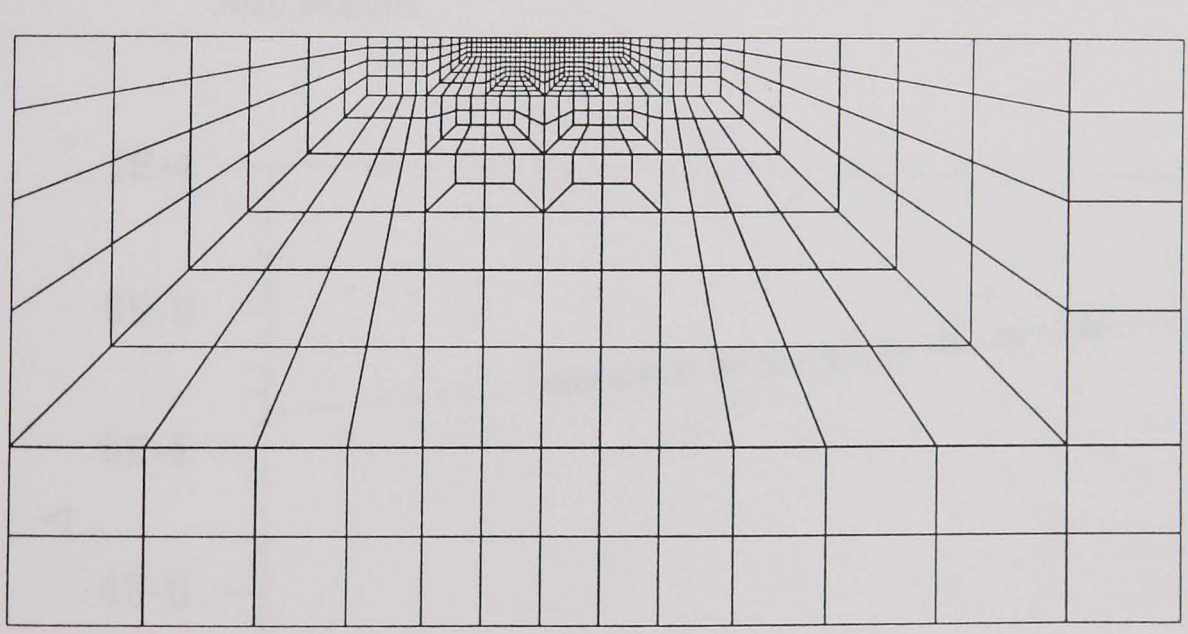

(b) for multi-material model

Fig. 4.5 Typical FE meshes used for creep and limit load analysis.

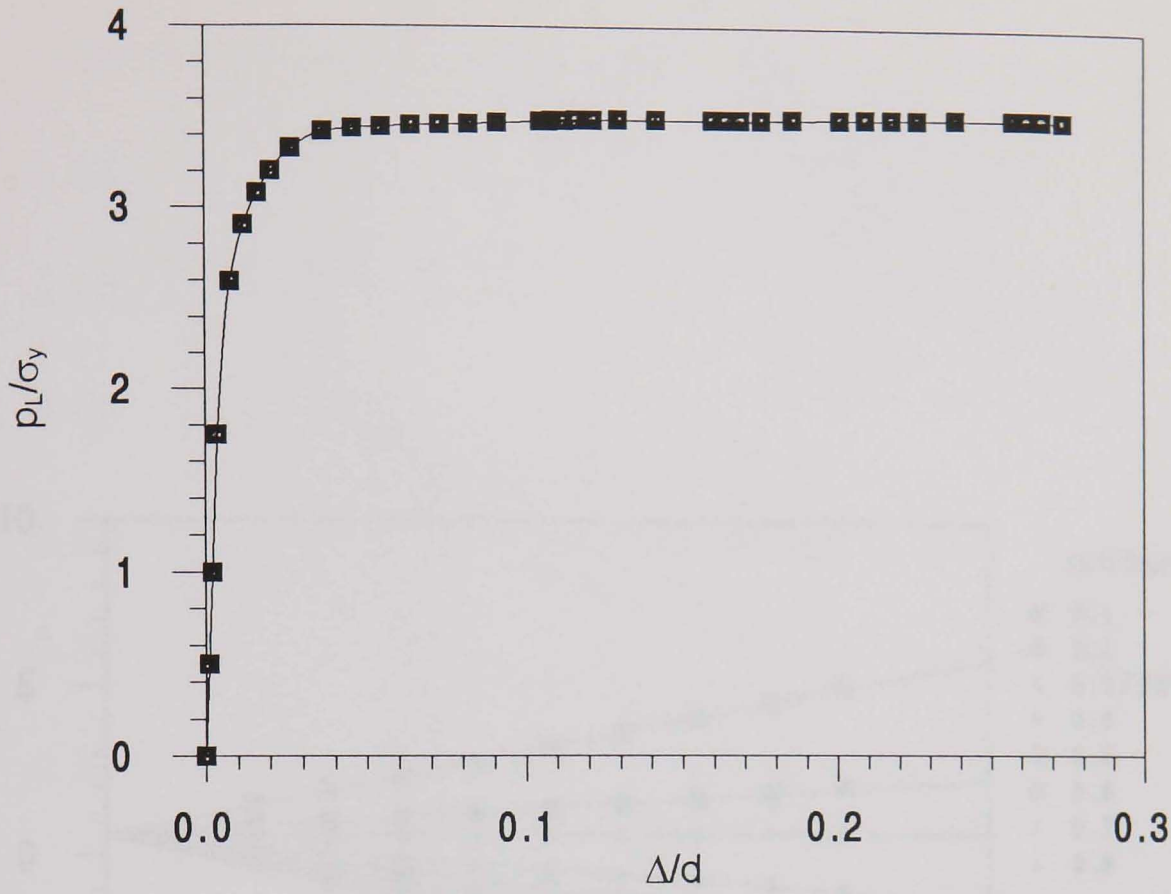

Fig. 4.6 Typical stress-displacement curve obtained from the limit load analysis.

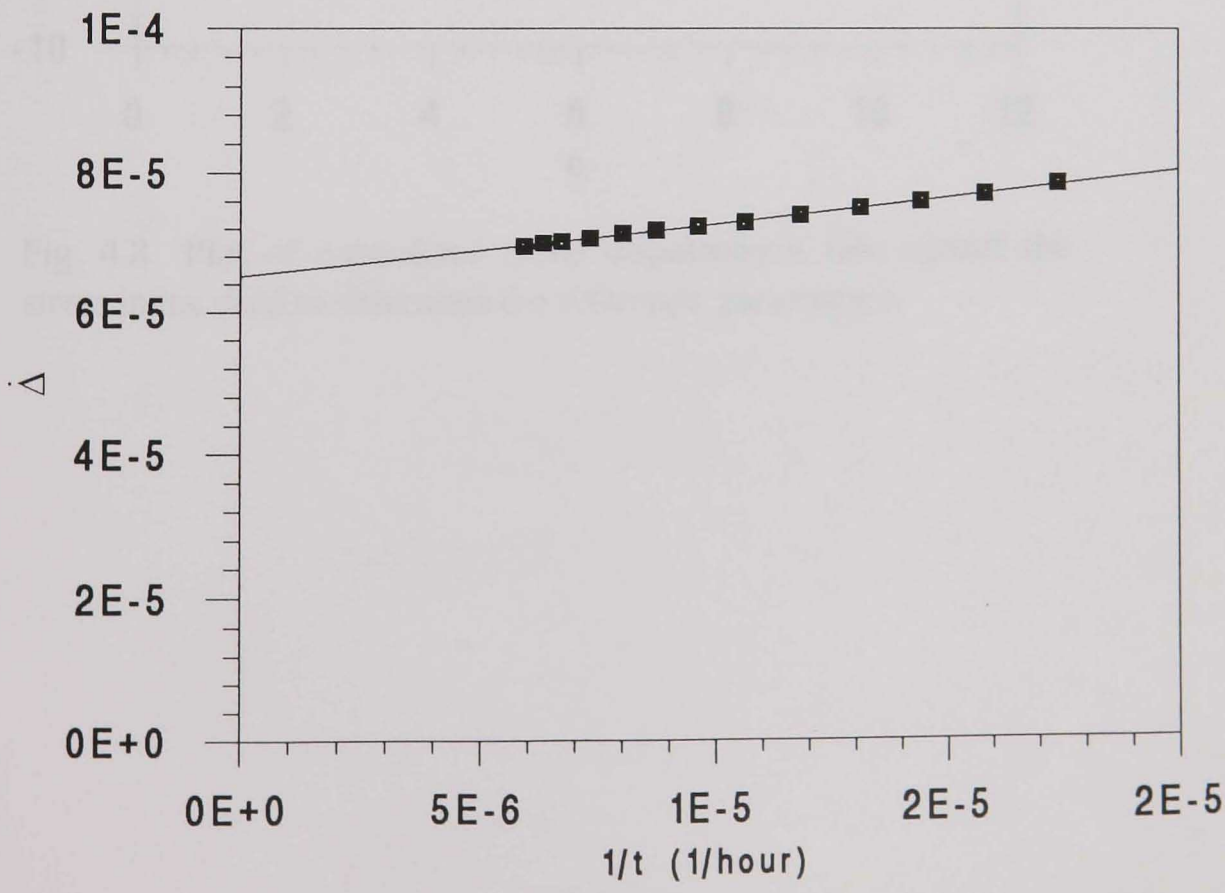

Fig. 4.7 Plot of creep displacement rate against the reciprocal of time used to obtain steady state creep values.

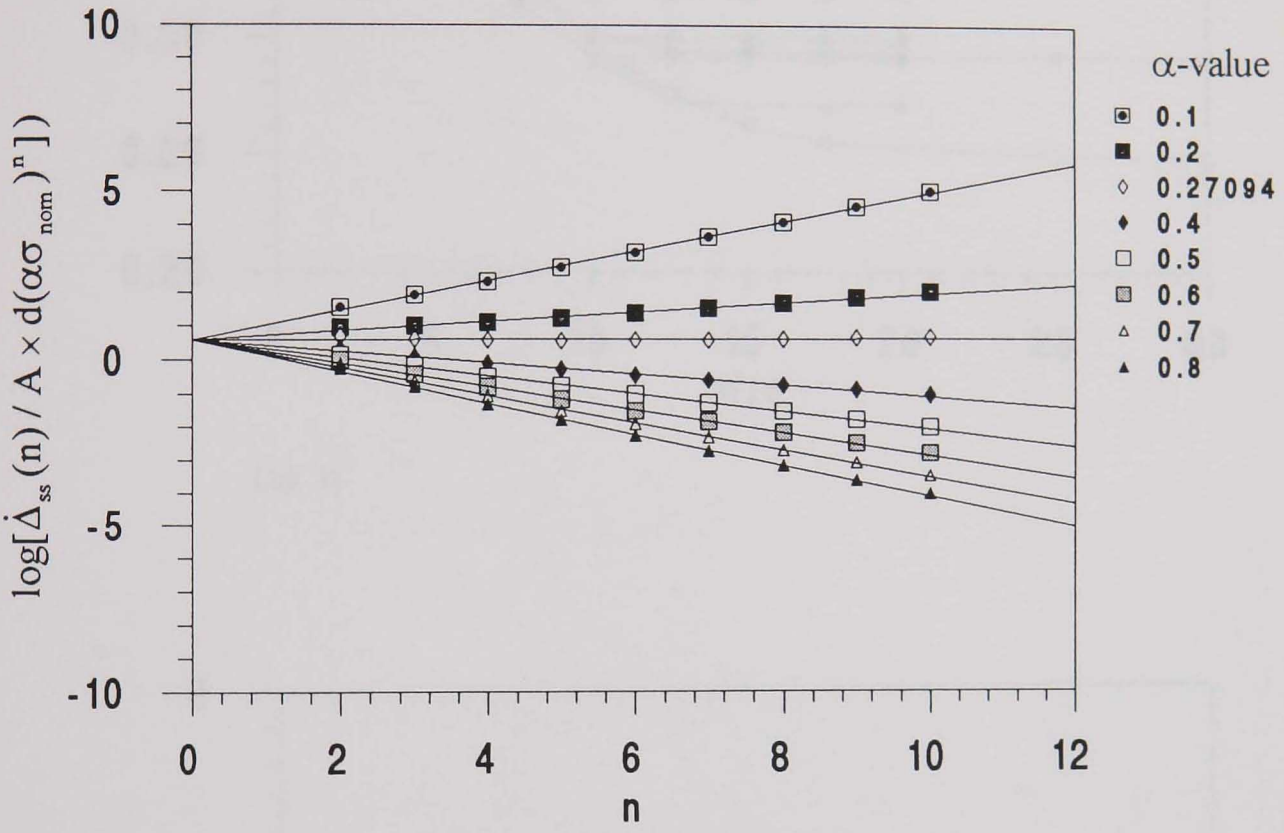

Fig. 4.8 Plot of normalised creep displacement rate against the stress index used to determine the reference parameters.

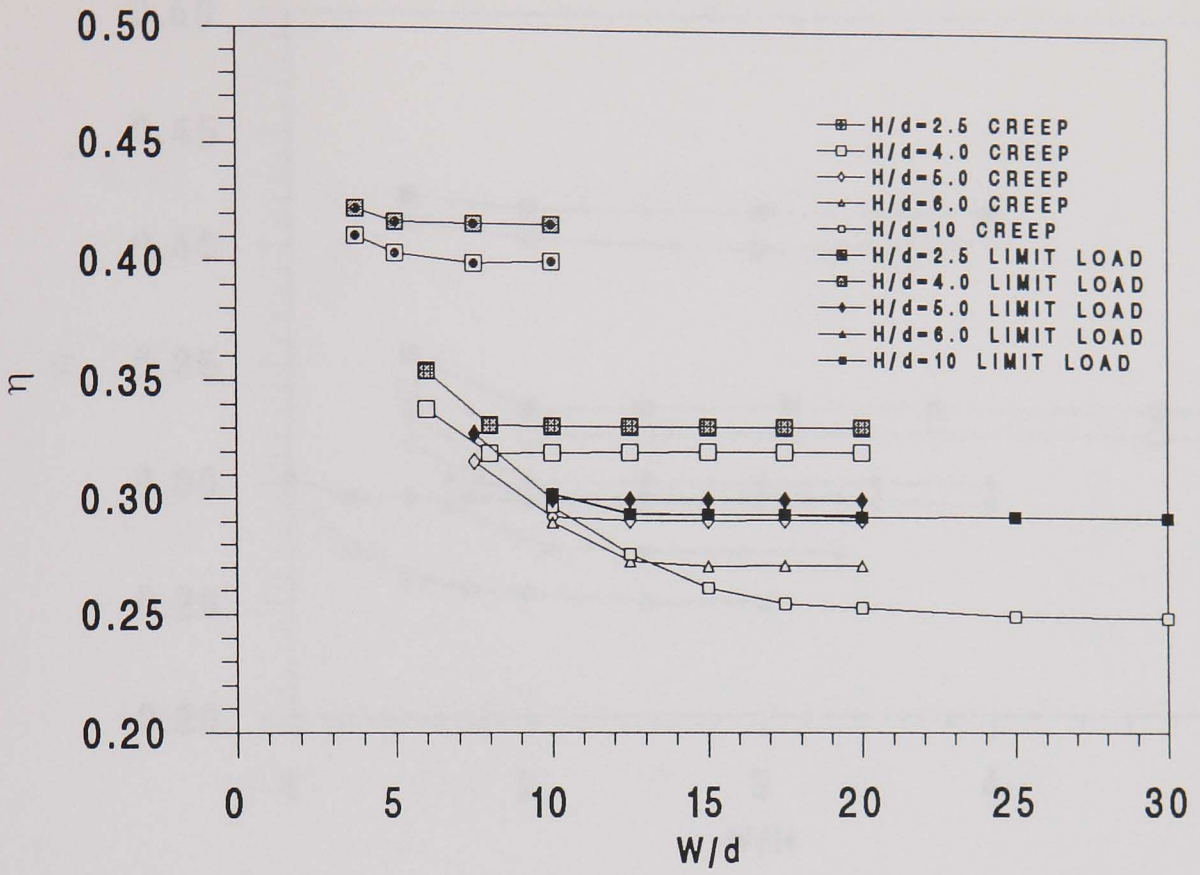

(a) η

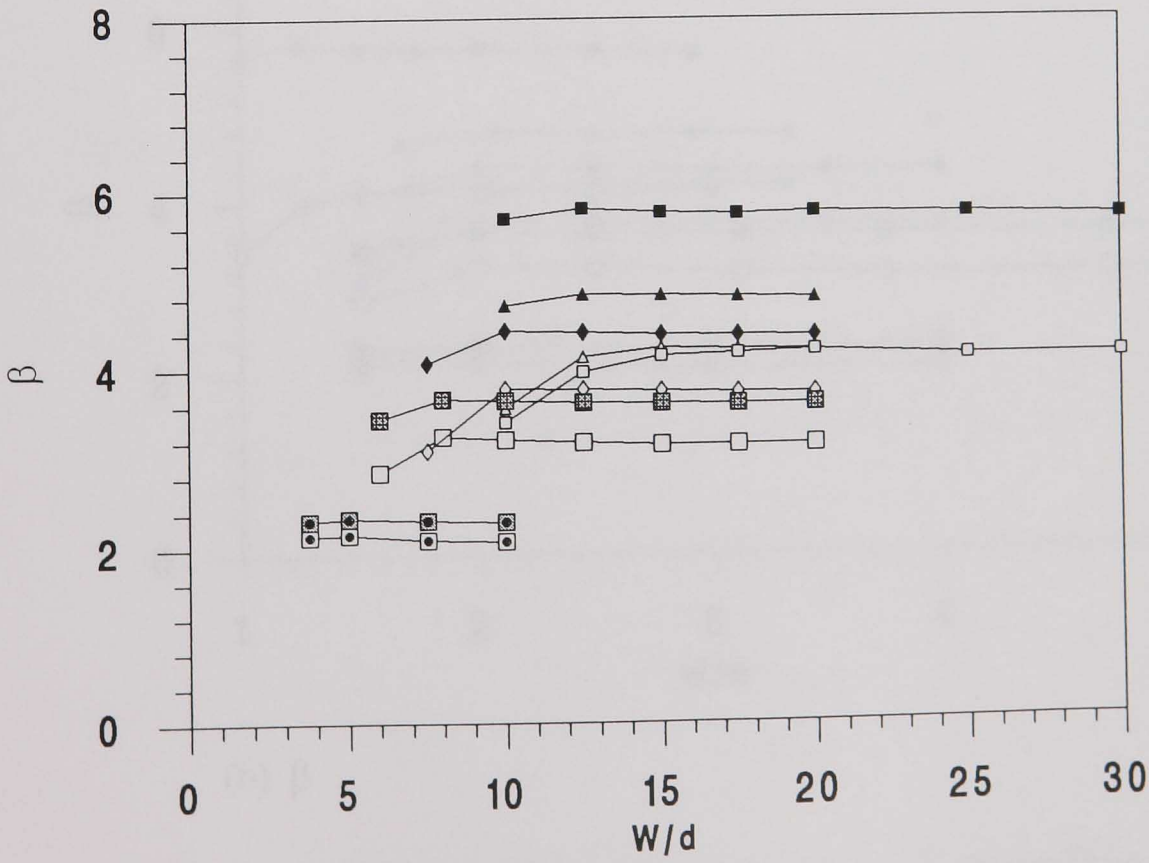

(b) β

Fig. 4.9 Variation of the reference parameters with W/d for the single material case.

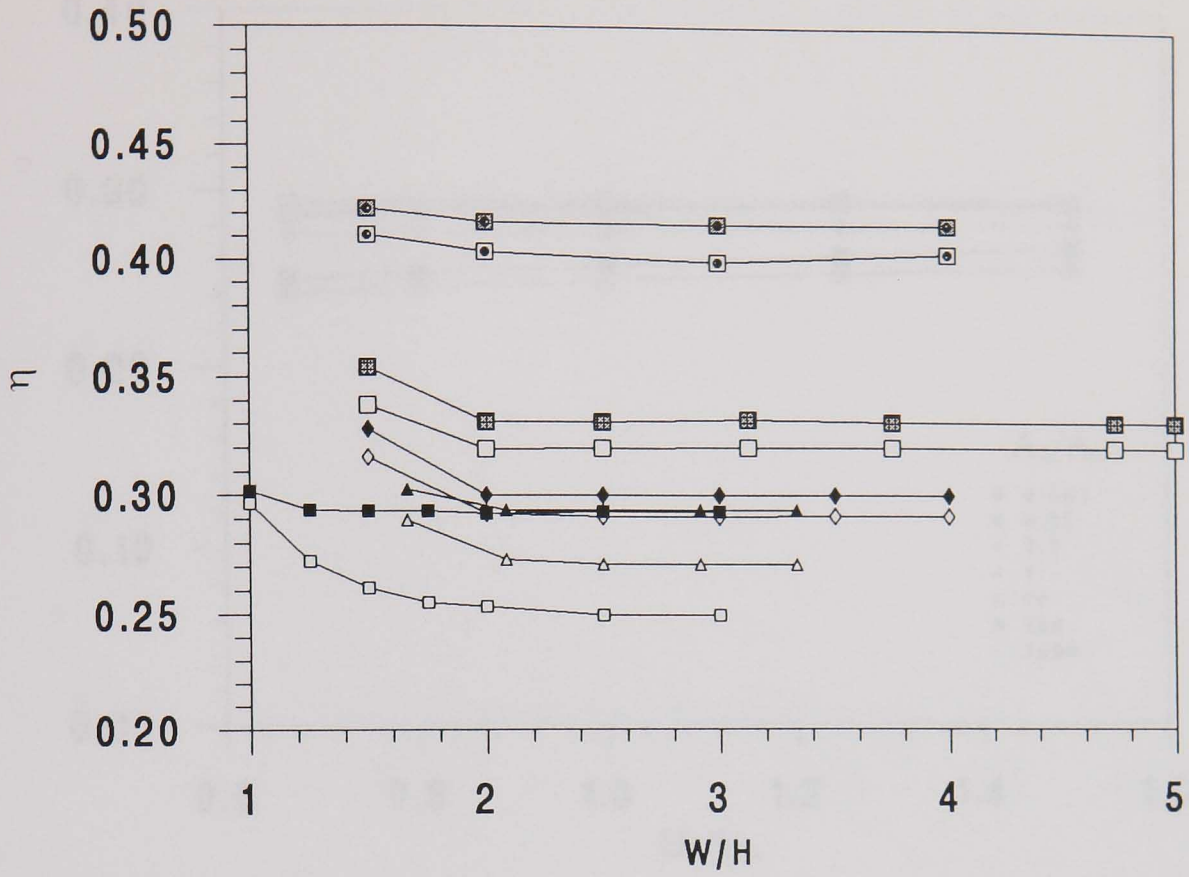

(a) η

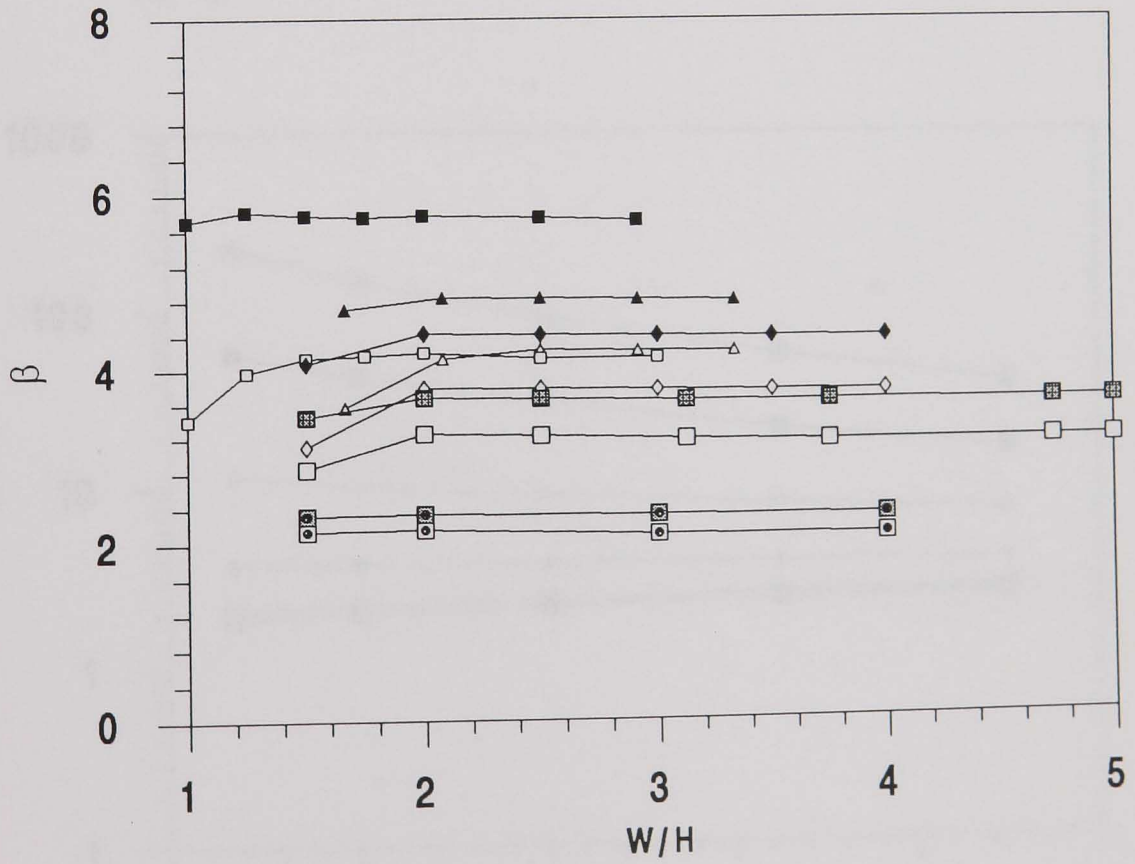

(b) β

Fig. 4.10 Variation of the reference parameters with W/H for the single material case (same keys as used in Fig. 4.9).

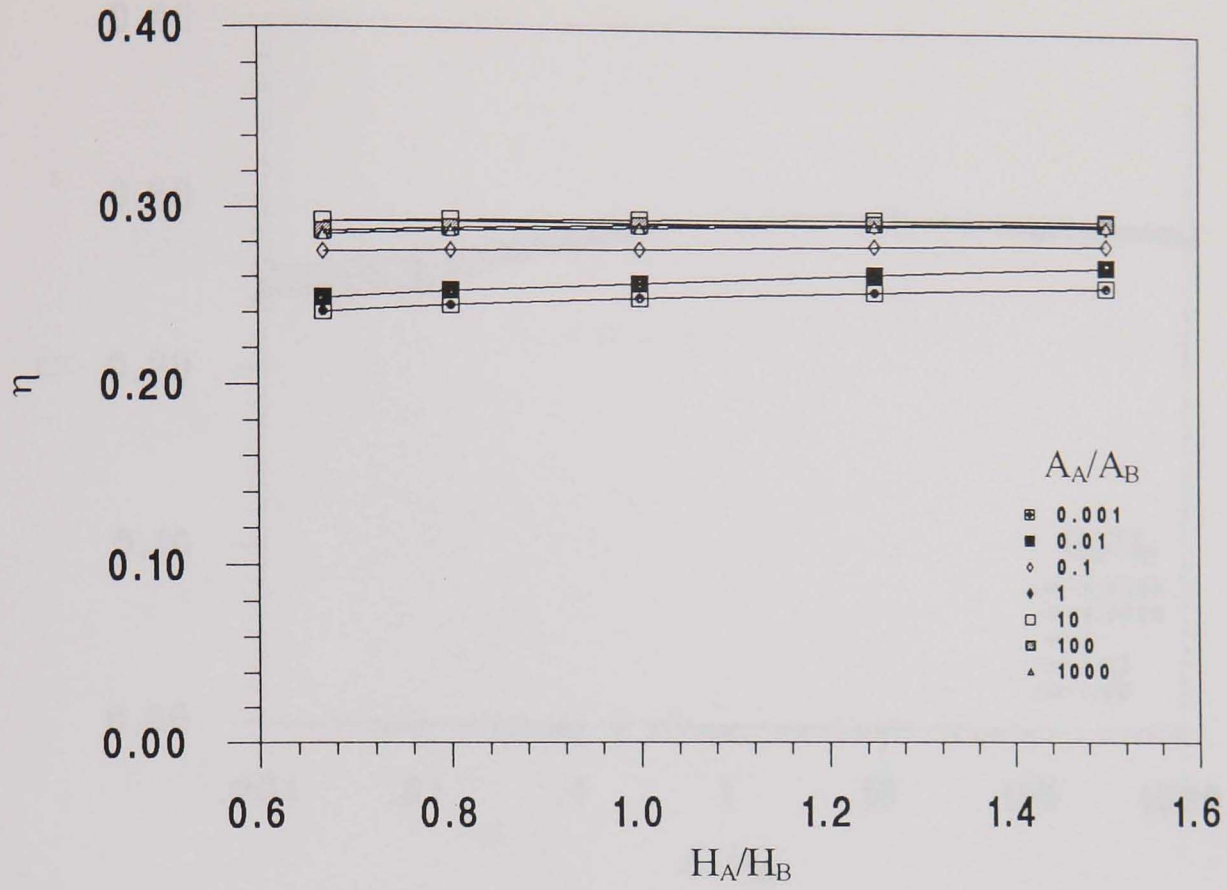

(a) η

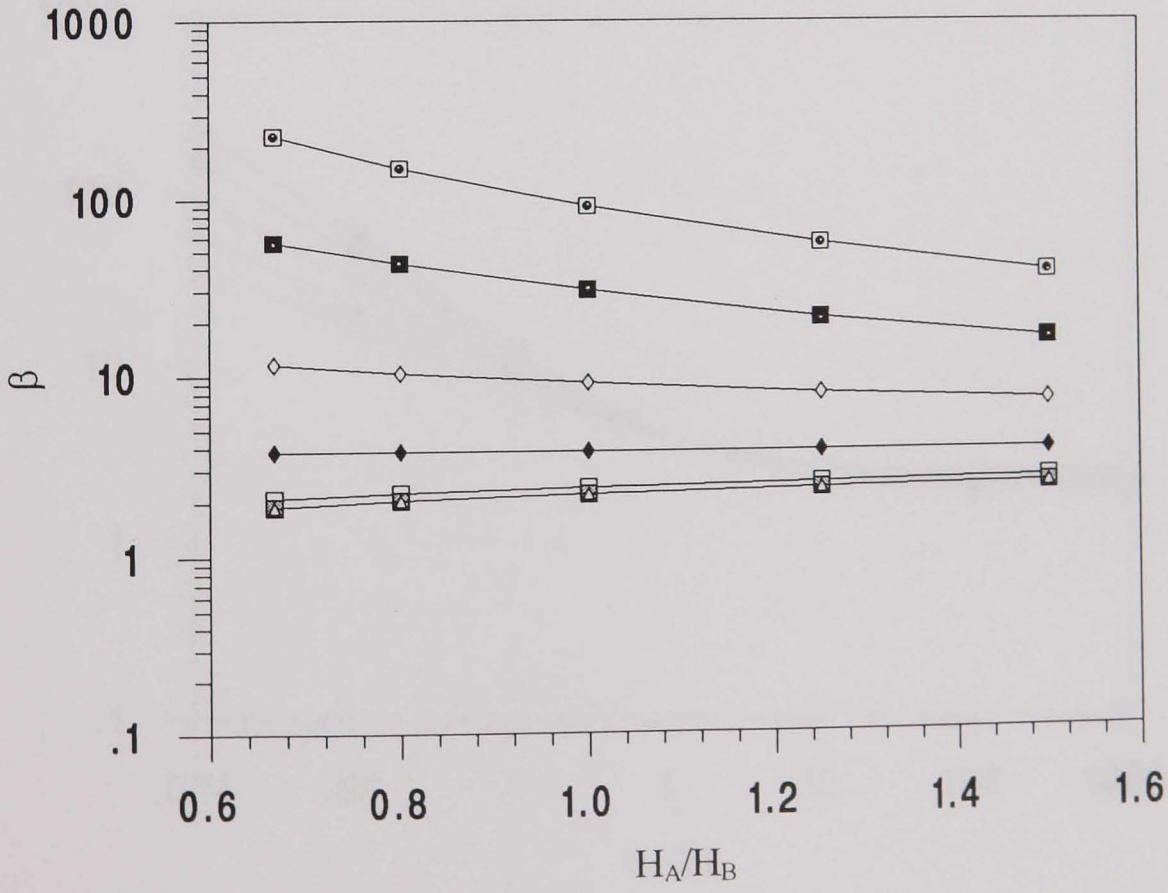

(b) β

Fig. 4.11 Variation of the reference parameters with H_A/H_B for the two materials (in series) case.

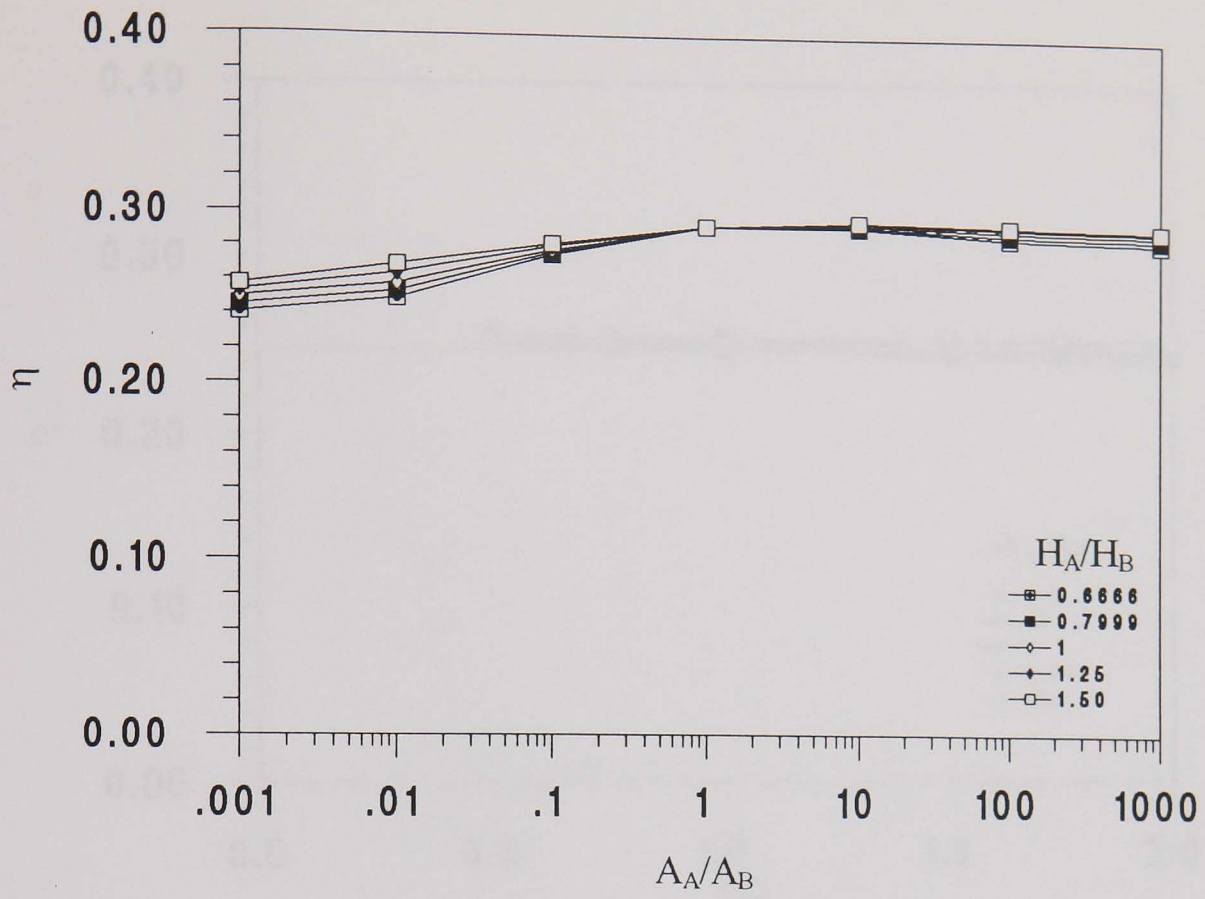

(a) η

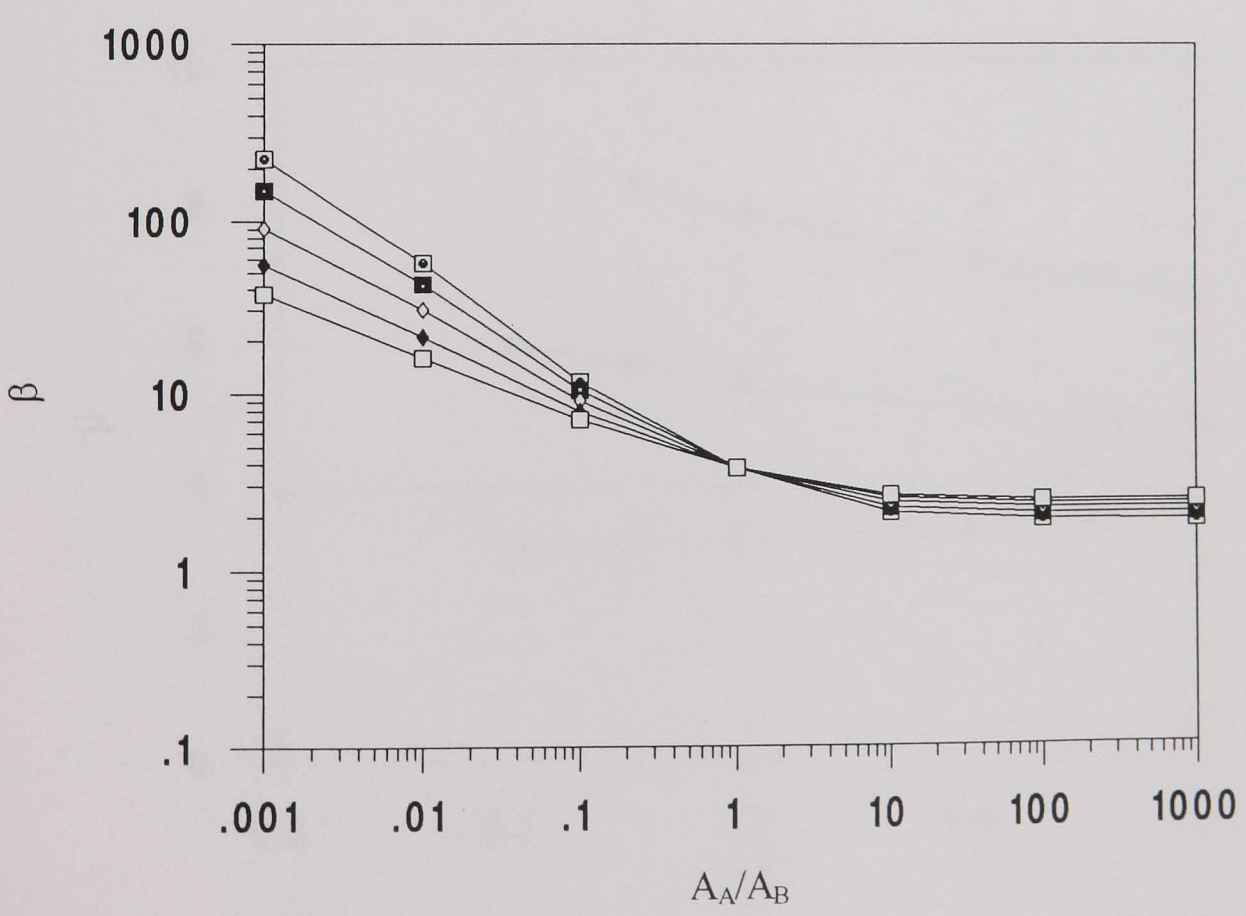

(b) β

Fig. 4.12 Variation of the reference parameters with A_A/A_B for the two materials (in series) case.

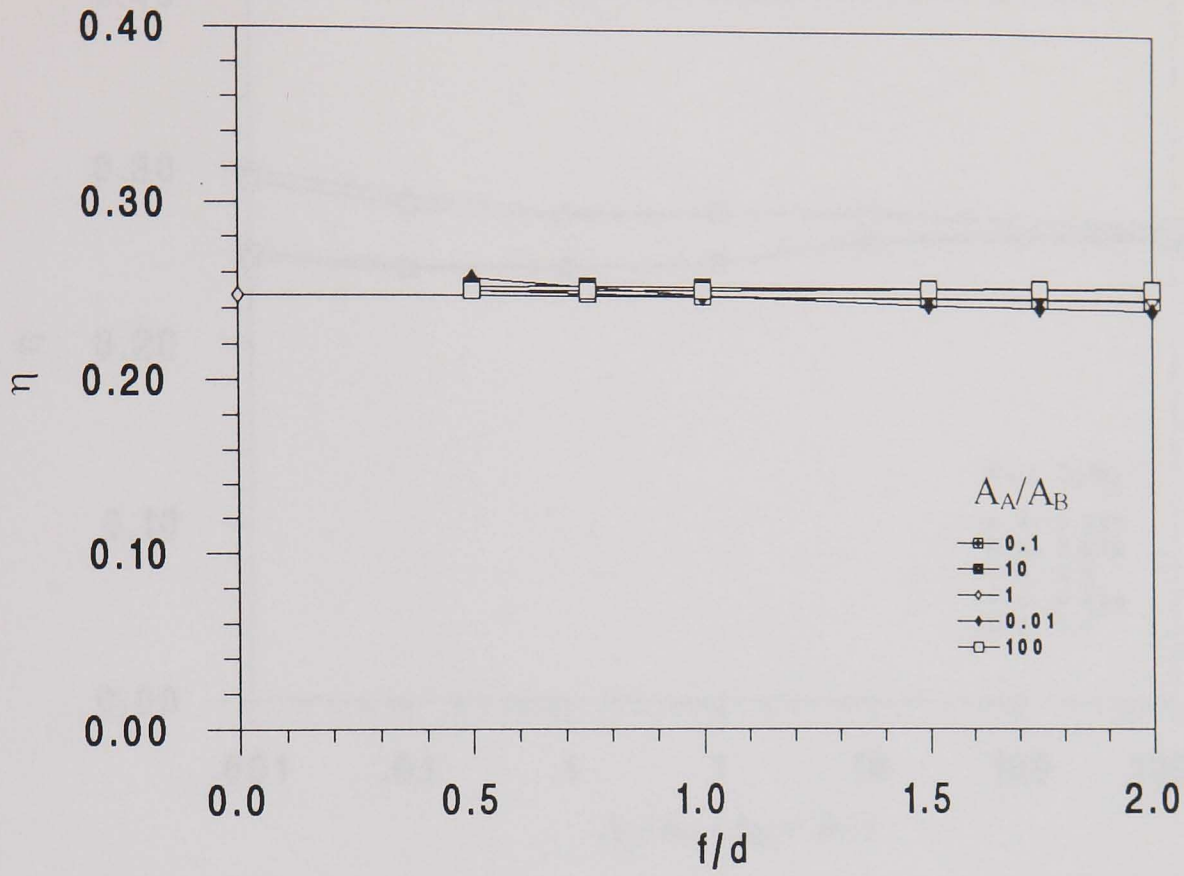

(a) η

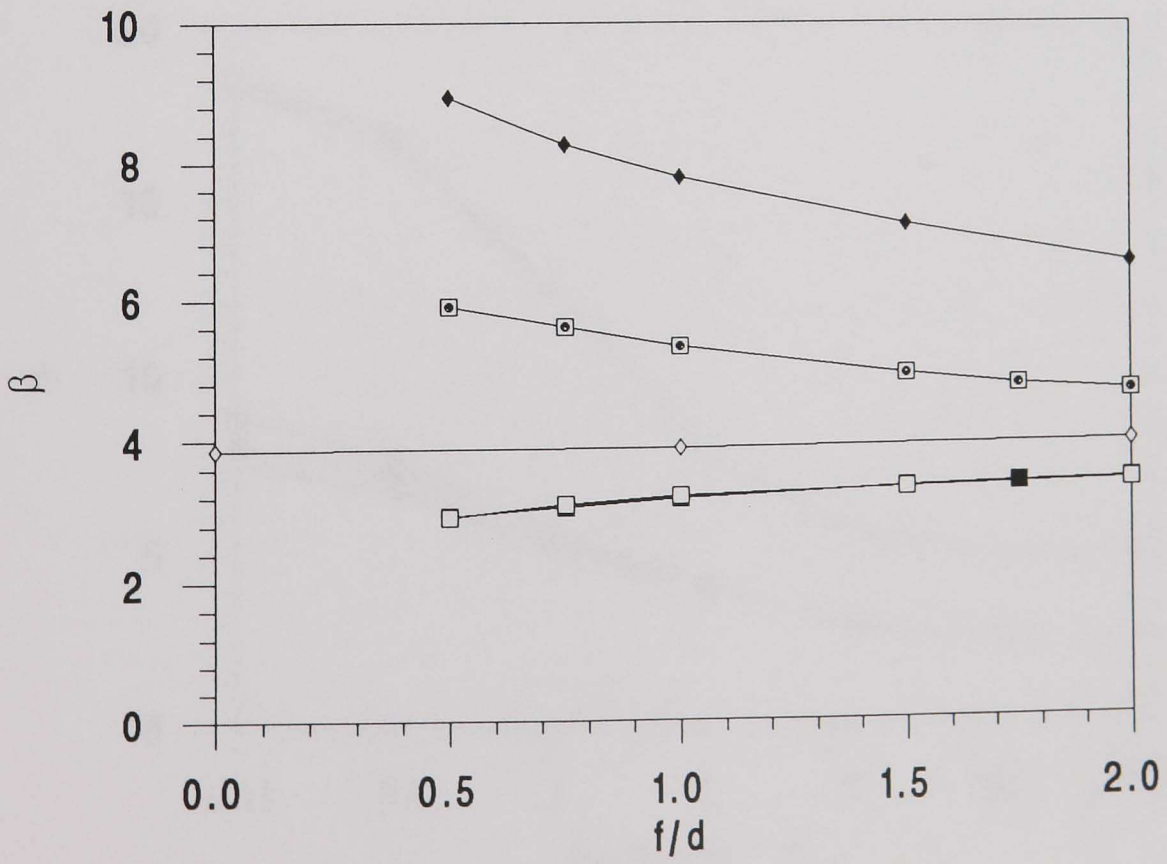

(b) β

Fig. 4.13 Variation of the reference parameters with f/d for the two materials (side by side) case.

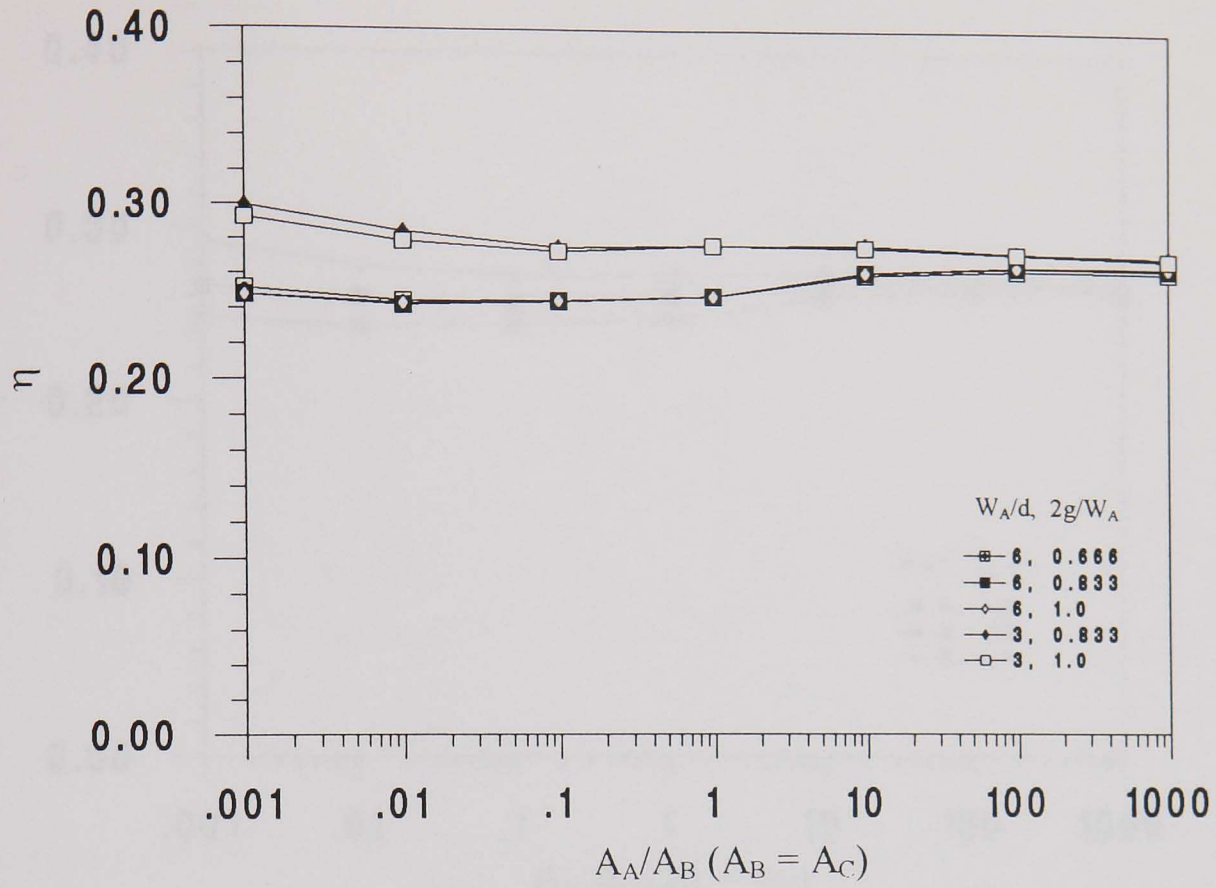

(a) η

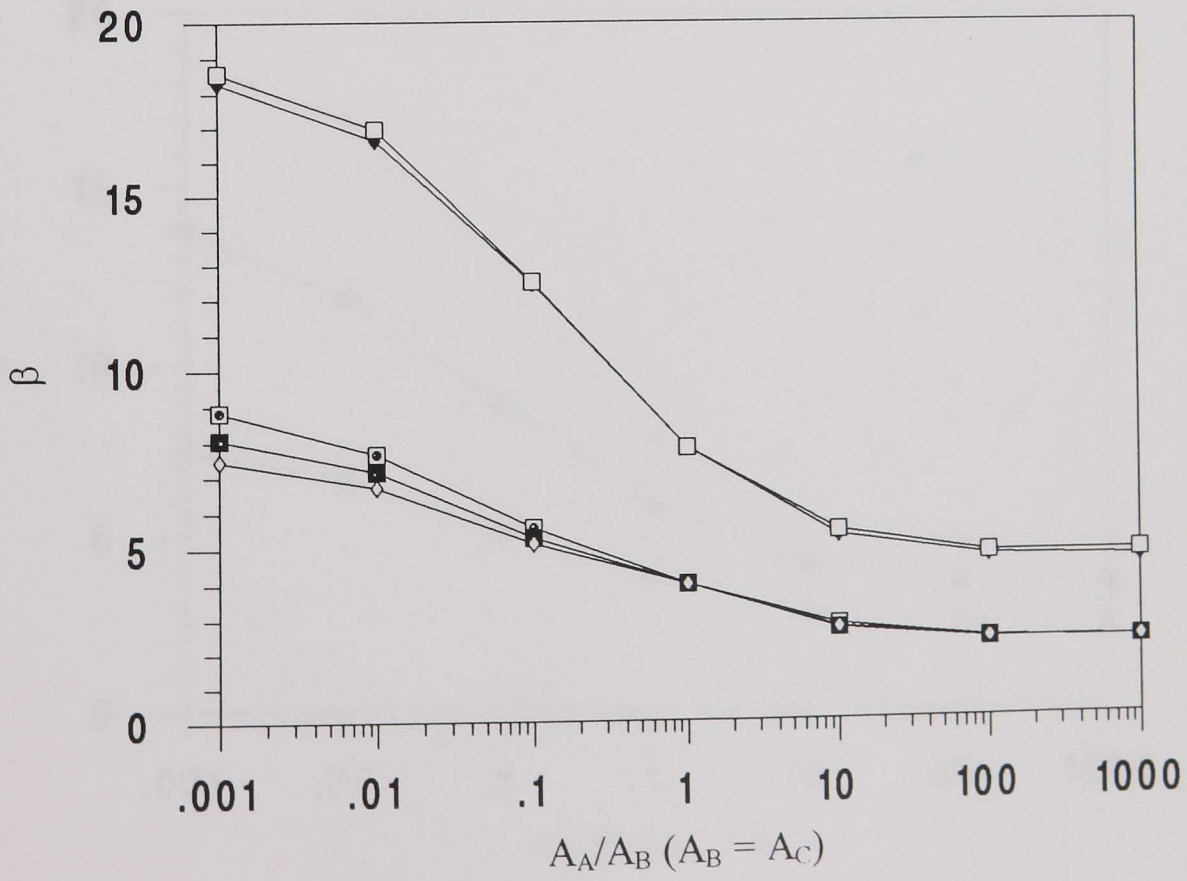

(b) β

Fig. 4.14 Variation of the reference parameters with A_A/A_B (with $2g/W_A = 1.0$ and 0.8333) for the three materials (side by side) case.

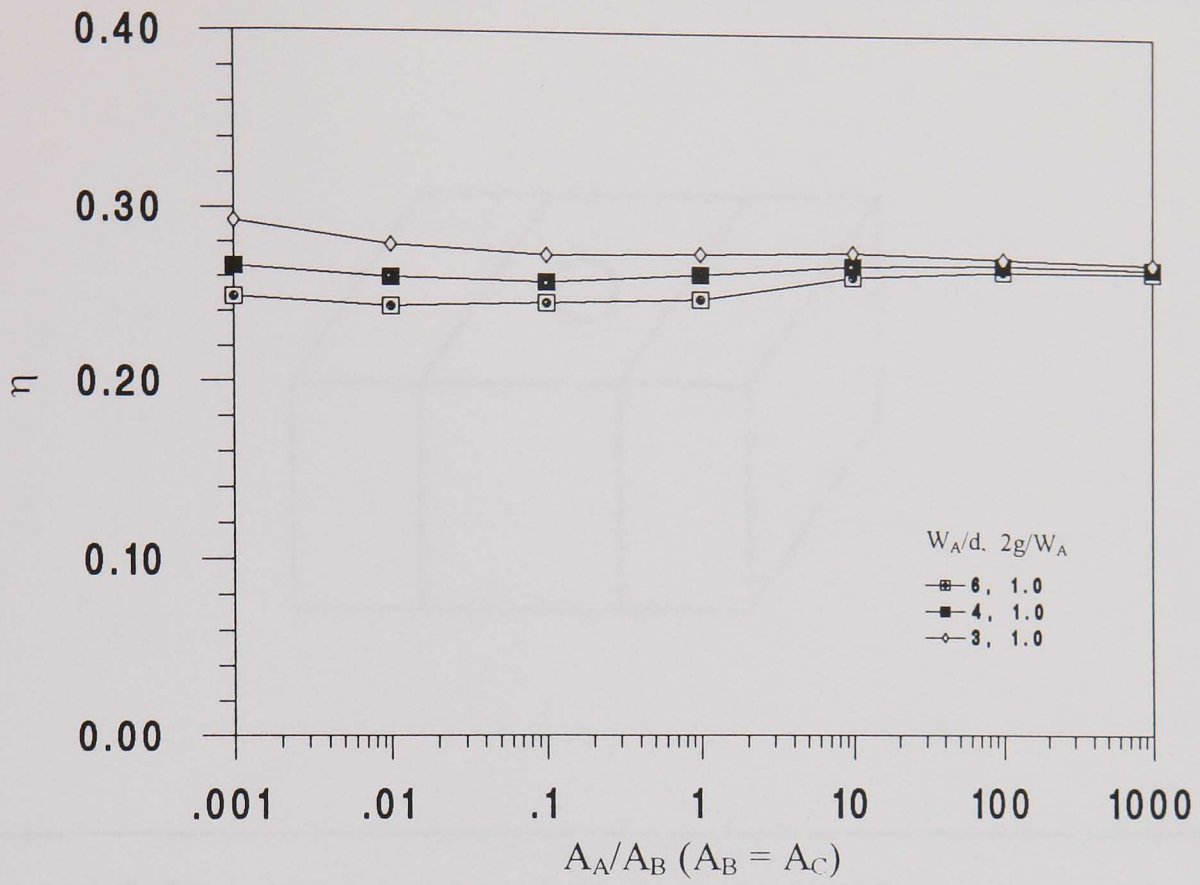

(a) η

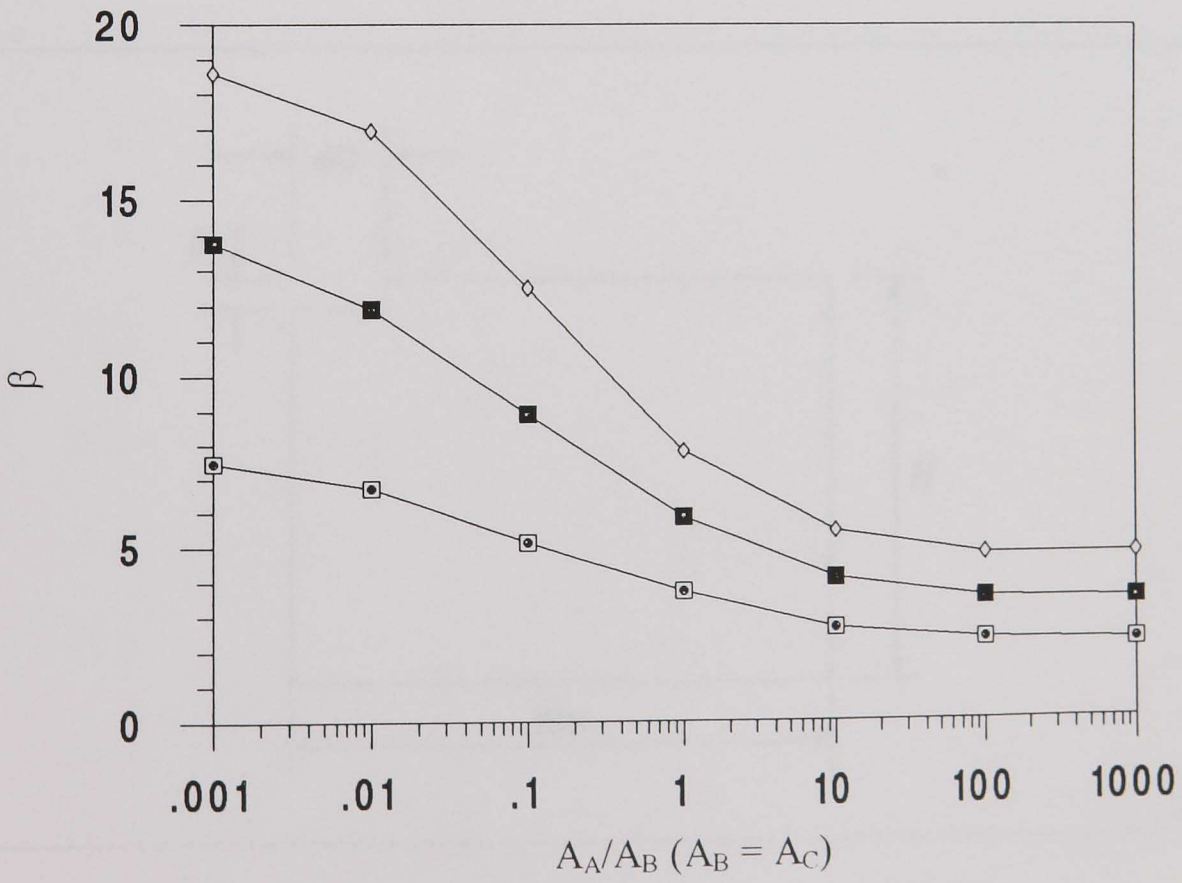

(b) β

Fig. 4.15 Variation of the reference parameters with A_A/A_B (with $2g/W_A = 1.0$) for the three materials (side by side) case.

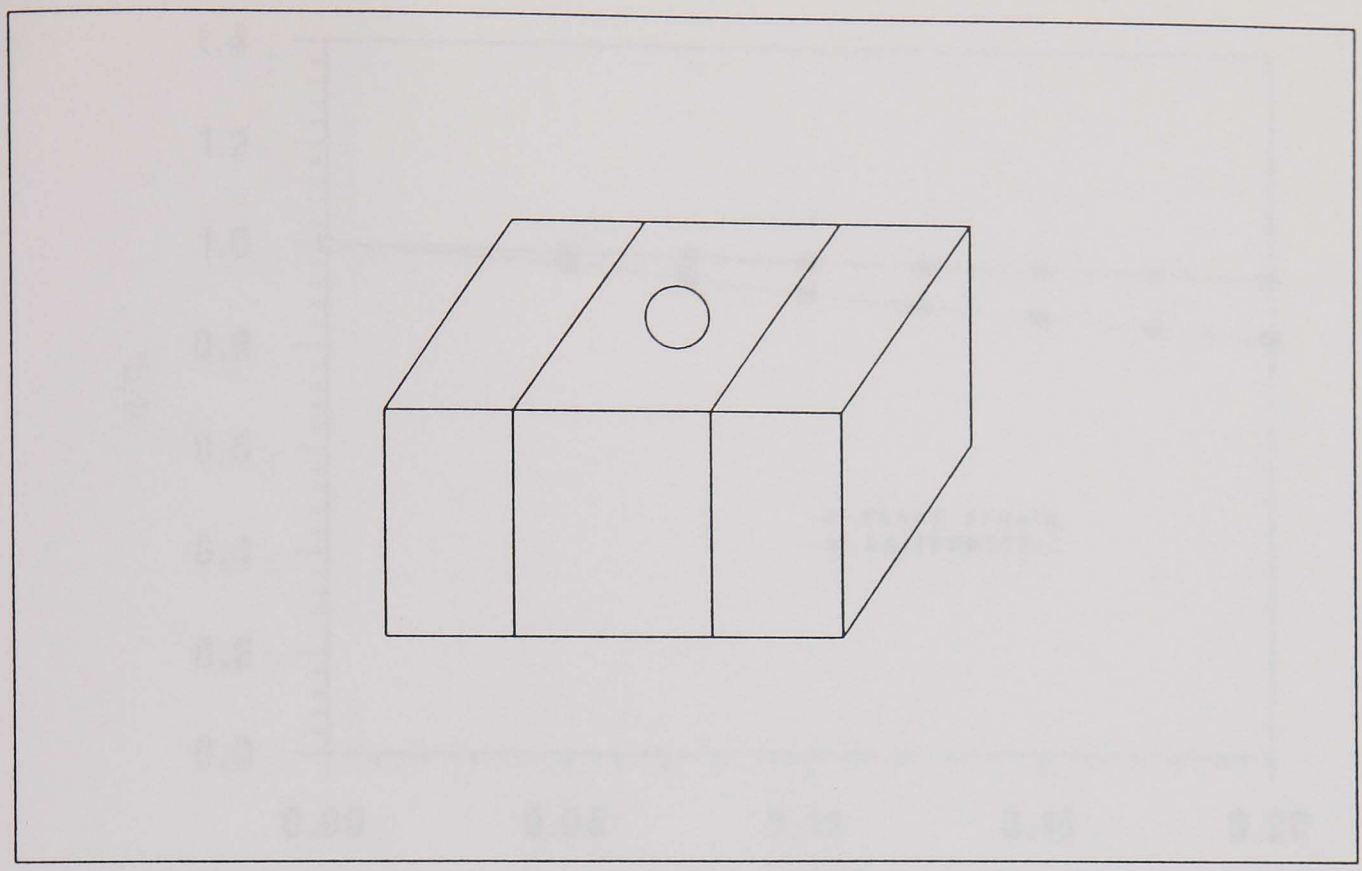

Fig. 4.16 3-D FE model for multi-zone indentation problem using cylindrical indenter.

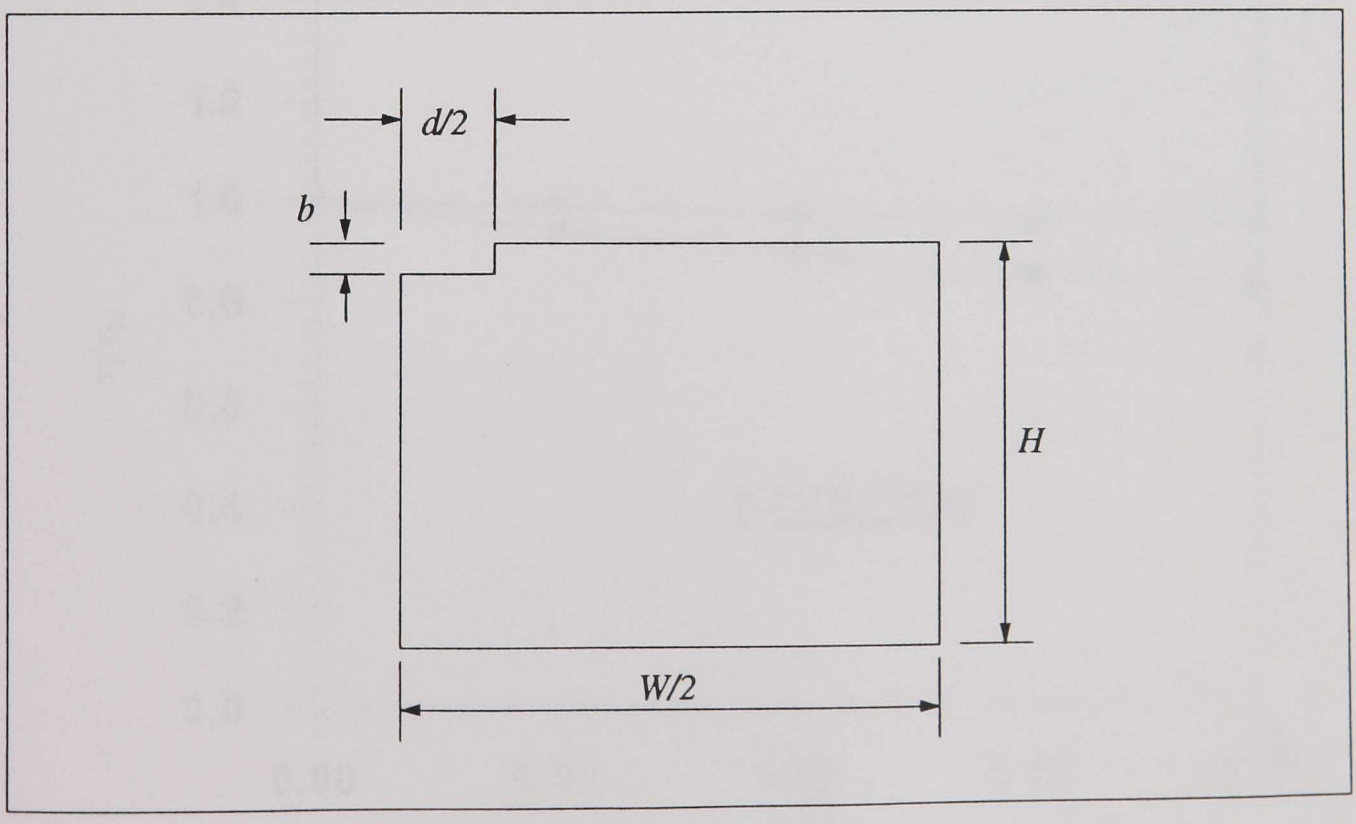

Fig. 4.17 FE model used to study the effect of indentation depth.

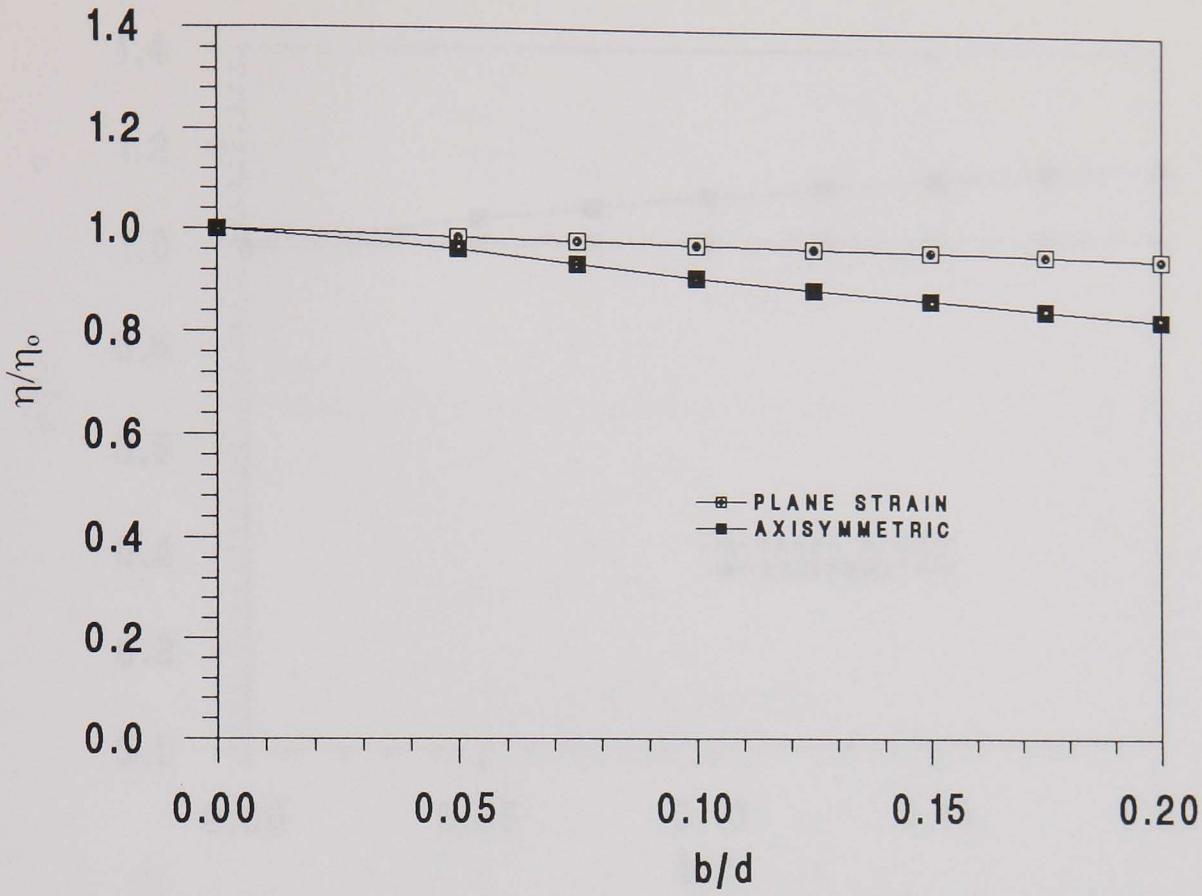

(a) from limit load solution

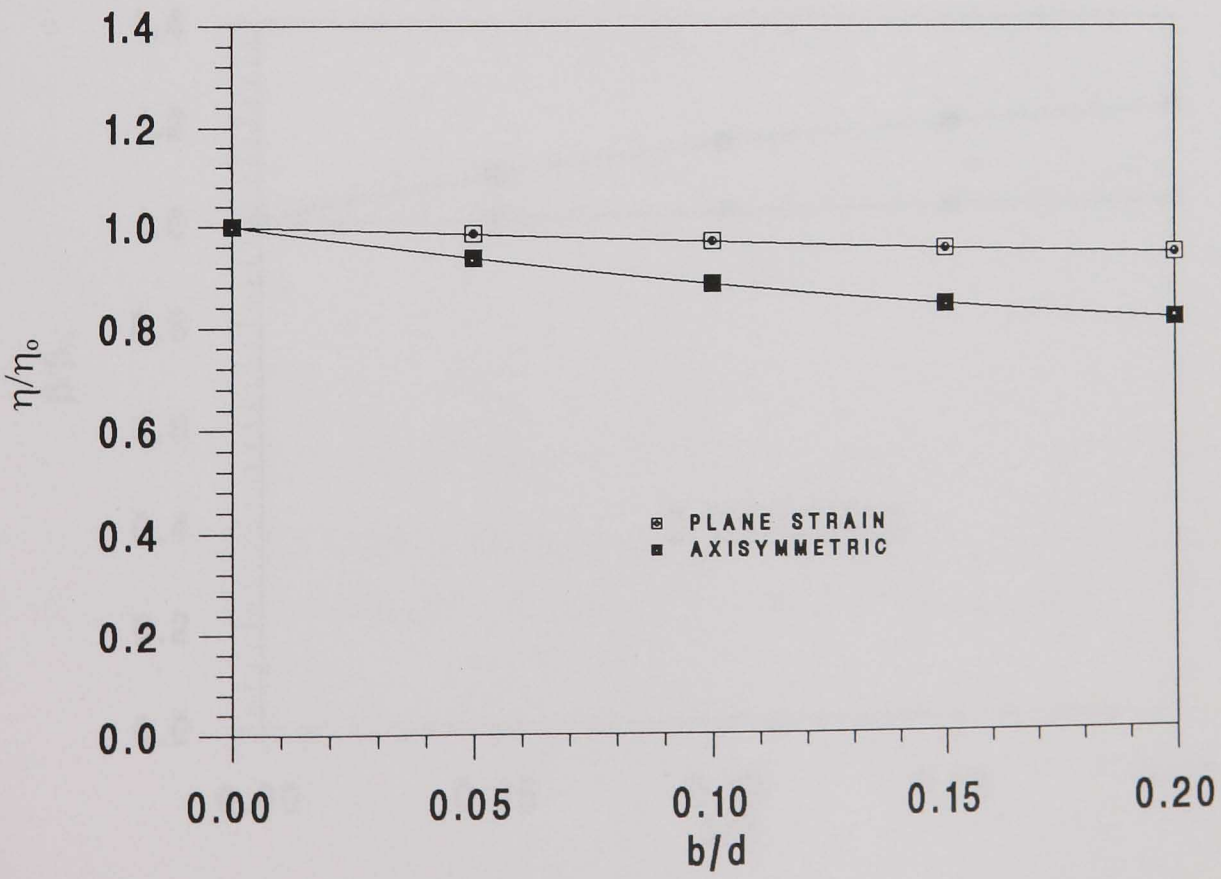

(b) from creep solution

Fig. 4.18 Variation of η/η_o with b/d (where η_o corresponds to b = 0) for single material case, W/d = 2H/d = 10.

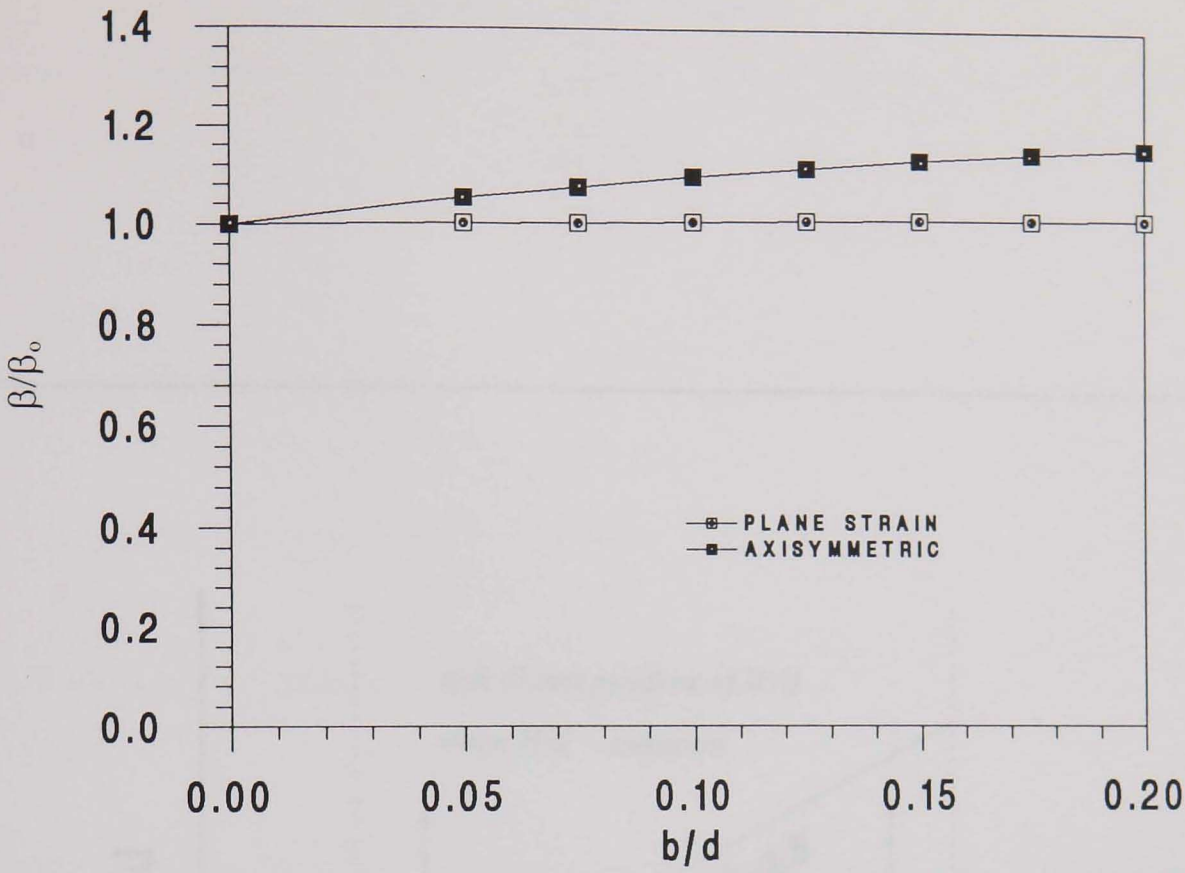

(a) from limit load solution

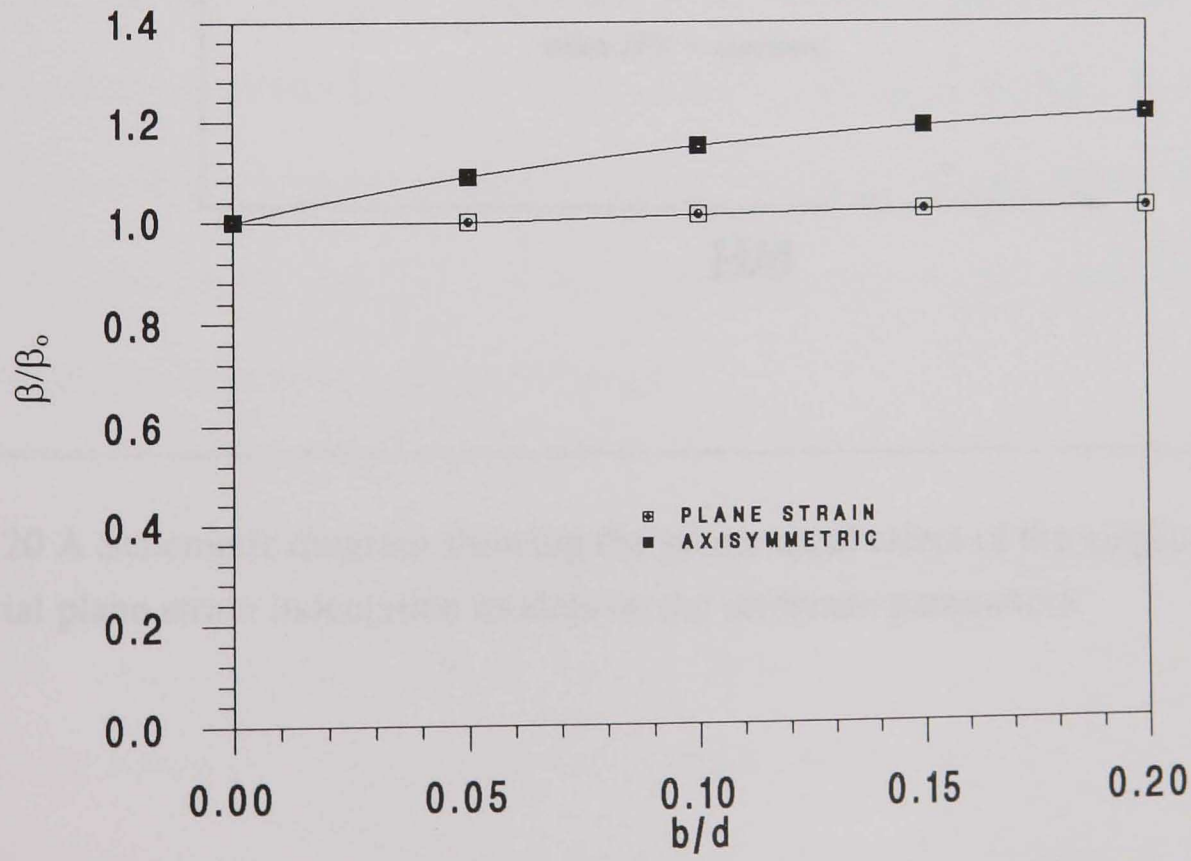

(b) from creep solution

Fig. 4.19 Variation of β/β_o with b/d (where β_o corresponds to b = 0) for single material case, W/d = 2H/d = 10.

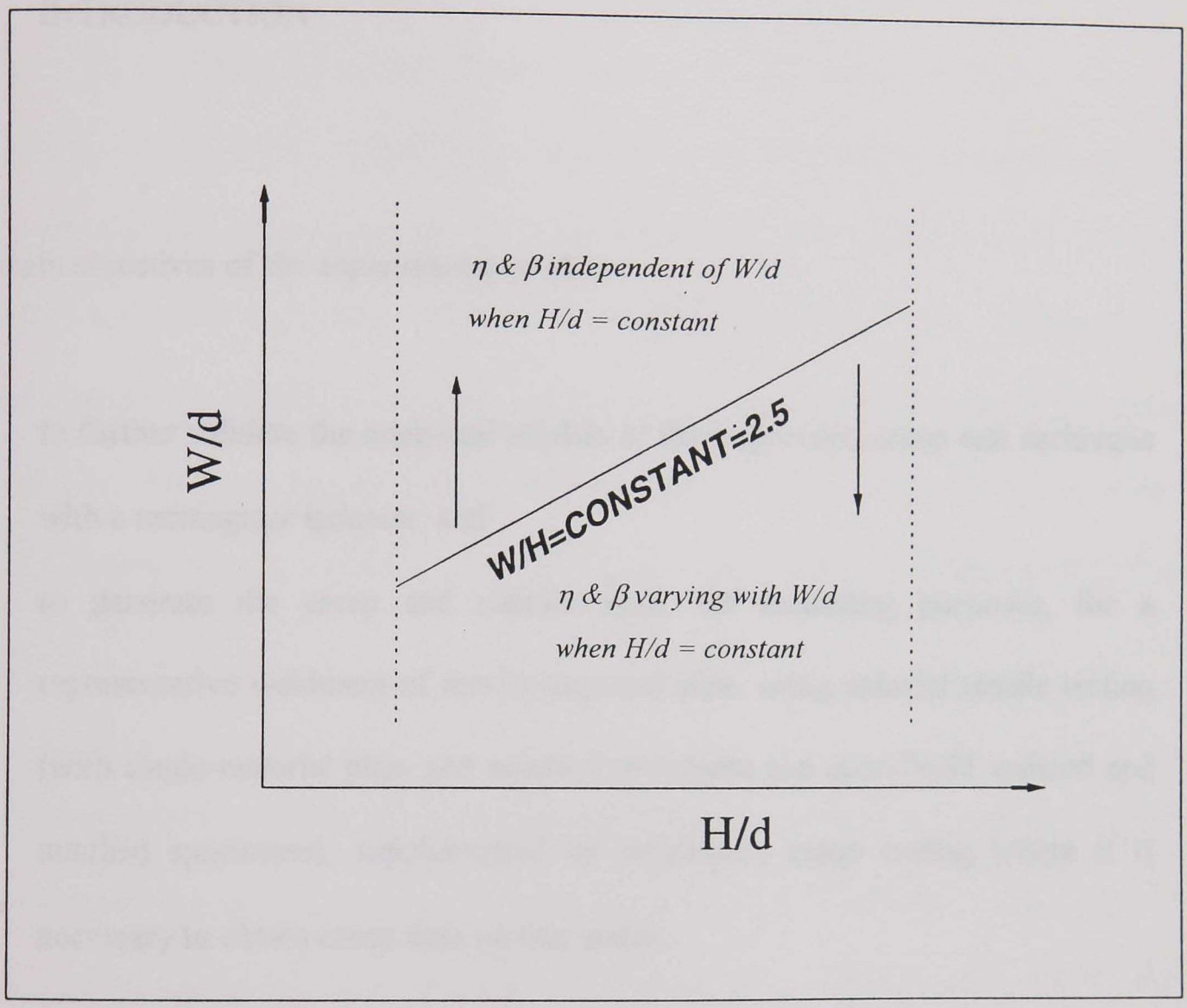

Fig.4.20 A Schematic diagram showing the geometrical effect of the single-material plane strain indentation models on the reference parameters.

CHAPTER V

EXPERIMENTAL WORK

5.1 INTRODUCTION

The main objectives of the experimental work are:

(a) to further validate the analytical models of the impression creep test technique with a rectangular indenter, and

(b) to generate the creep and rupture data, for modelling purposes, for a representative weldment of service-exposed pipe, using uniaxial tensile testing (with single-material plain and notched specimens and cross-weld waisted and notched specimens), supplemented by impression creep testing where it is necessary to obtain creep data on thin zones.

Hardness tests were used to assess the likely variations in creep properties of the cross-weld materials. Since it is believed that the creep constants (e.g. in Norton's law) may be related to the hardness of the material (Tu and Sandstrom [1994]), then hardness results can be used to quickly and directly estimate the variations of creep properties. However, it should be noted that the variation of hardness across a service-aged weld like that used for the present research will be different from the variation in its original

conditions, due to the long-term exposure to elevated temperature and stress. This introduces difficulties in the determination of the creep properties of service-aged weldments, for which the HAZ is very difficult or impossible to simulate, owing to the time-dependent changes of material properties.

A weld is an inhomogeneous structure. However, it is widely accepted that a weld can be assumed to consist of several different zones, each of which has constant creep properties. In this study, considering the difficulty in determining the variations of creep and damage properties within the HAZ of service-aged weldments and due to the fact that after long-term operation at elevated temperature the difference in material properties at different positions of the HAZ may become less significant due to diffusion, the service-aged weldments were divided into parent, HAZ and weld material zones, i.e. the material properties throughout the HAZ were assumed to be constant.

For the purpose of providing the creep and rupture data required for the generation of creep and damage constitutive equations of the exposed weldment materials, uniaxial tensile creep testing on both single-material (plain and notched) and cross-weld (waisted and notched) specimens is required. Single-material and cross-weld notched specimens, and cross-weld waisted specimens were specially designed and tested in order to supply the rupture data for the generation of the damage constants.

The impression creep testing technique described in Chapter IV was applied to perform indentation tests for obtaining the creep properties of the HAZ material. For

comparison reasons, impression creep tests of aged parent material, weld material and a thermally simulated HAZ material which corresponds to the material in the HAZ adjacent to the boundary between the HAZ and parent materials of a virgin weldment, were also conducted. A single material case was chosen for all of the impression creep tests and the conversion factors (reference parameters) described in Chapter IV were used to convert the impression creep test data to equivalent uniaxial creep data.

It should be noted that the thermally simulated material described above is termed "simulated HAZ material" in this work. In some publications it was referred to as "Type IV region" (e.g. Craine and Hawkes [1993]).

It should be mentioned that during the course of the creep testing, surface oxidation occurred for both the uniaxial and impression test specimens. Relatively speaking, the results from the indentation test specimens were probably more seriously affected by the oxidation damage than those from the uniaxial test specimens due to the smaller size of the specimens, the high localized indentation pressure and the relatively small indentations measured during the tests. In order to provide more reliable creep deformation information for the verification of the impression creep test technique, it was decided to perform some additional indentation tests, using 316 stainless steel specimens for which uniaxial creep data obtained without oxidation effects are available (Hyde [1988]).

5.2 EXPERIMENTAL PROGRAM

5.2.1 Tests Definition

Thermally simulated material and service exposed pipe material (1/2CrMoV parent with 2CrMo weld) were used for the tests. Three stress levels and one temperature level were defined for all the tests, except for the simulated material, for which three temperatures were used for the purpose of comparison with other data. For the impression creep test, single material specimens were used for all zones of material (parent, weld and HAZ) of the aged weldment and the simulated materials. The width chosen for the indenter was 1 mm. The uniaxial weld and base material specimens were standard specimens with a uniform gauge length and ridges from which the creep strains could be obtained. The notched bars were standard Bridgman notch specimens from which multi-axial stress damage data could be obtained. In order to provide information for the generation of the damage parameters of the aged HAZ material, cross-weld notched bar and waisted specimen tests were performed. Detailed information for the preparation of the specimens is given in Section 5.3.

5.2.2 Test Conditions

A total of 35 creep tests, as outlined above, were planned. For all of these tests, three uniaxial equivalent stress levels were used, i.e. 40, 54 and 70 MPa, except for the 316 stainless steel indentation creep tests in which the equivalent stress levels ranged between 200 and 300 MPa. The temperature chosen was 640° C for all the tests,

except for those performed on the simulated HAZ material, for which three temperatures, i.e. 640, 660 and 680° C, were used. The test types and the test conditions are shown in Table 5.1.

Table 5.1 Creep test types and conditions

Material type	Test type	Test code	Test conditions	
			T (° C)	σ (MPa)
Exposed parent	uniaxial plain	PBU-1	640	40
		PBU-2	640	54
		PBU-3	640	70
	uniaxial notched	PBN-1	640	54
		PBN-2	640	70
	indentation	PBI-1	640	40
		PBI-2	640	54
		PBI-3	640	70
Exposed weld	uniaxial plain	PWU-1	640	40
		PWU-2	640	54
		PWU-3	640	70
	uniaxial notched	PWN-1*	640	54
		PWN-2	640	70
	indentation	PWI-1	640	40
		PWI-2	640	54
		PWI-3	640	70
Exposed HAZ	indentation	PHAZ-1	640	40
		PHAZ-2	640	54
		PHAZ-3	640	70
Simulated HAZ	indentation	GIVI-1	640	40
		GIVI-2	640	54
		GIVI-3	640	70
		GIVI-4	660	54
		GIVI-5	680	54
Simulated base	indentation	GBI-1	680	54
Cross-weld	uniaxial waisted	PCWW-1	640	40
		PCWW-2	640	54
		PCWW-3	640	70
	uniaxial notched	PCWN-1	640	40
		PCWN-2	640	54
		PCWN-3	640	70
316 stainless steel	indentation	316I-1	640	200
		316I-2	640	260
		316I-3	640	280
		316I-4	640	300

* the test is still in progress

(i) Equivalent applied pressures for indentation tests

The small size of specimens used for the impression creep tests were chosen for the purpose of obtaining reliable material data, from specimens which were convenient to machine, and which made efficient use of the material available. Cylindrical, coin-shaped specimens were adopted for all test materials except for the HAZ material for which square specimens were used (see Fig. 5.3). Both types of specimens had the same W/d and W/H ratios, i.e. W/d = 10 and W/H = 4. The reference parameters for this case were obtained by FE-calculation, i.e. η (= α) = 0.4003 and β = 2.0790, see Figs. 4.9 and 4.10 in Chapter IV. From Figs. 4.10(a) and 4.10(b), it can be seen that, when W/H > 2, for a given ratio of W/d, the η and β values are practically constant. This is why it is possible to use the reference parameters from the plane strain analyses for the cylindrical indentation specimens.

Therefore, the applied indentation pressure can be converted to a corresponding uniaxial stress using the appropriate η value, i.e.

$$\sigma = \eta p \tag{5.1}$$

and the equivalent strains can be obtained using the appropriate β value, i.e.,

$$\varepsilon^c = \frac{\Delta^c}{\beta d} \tag{5.2}$$

Since the contact area is 10 mm^2, the corresponding converted loads, equivalent to the uniaxial stresses of 40, 54 and 70 MPa, are 1.0, 1.35 and 1.75 kN, respectively, see Table 5.2.

(ii) Applied loads for uniaxial tests

For the uniaxial ridged specimens, the specified equivalent stress levels were applied to the uniform cross-section in the gauge length, whereas for the notched bar specimens the equivalent stresses were applied to the smallest cross-section of the notch. For the waisted specimens the loads were determined on the basis of the stress in the waisted section where the HAZ was located. Table 5.2 shows the loading values for both the impression and uniaxial tests.

Table 5.2 Loading applied for the tests

Loading level	Converted applied loading to specimens			
σ (MPa)	Impression(kN)	Plain (kN)	Notched(kN)	Waisted(kN)
40	1.0	3.1416	1.7671	2.3561
54	1.35	4.2412	2.3856	3.1807
70	1.75	5.4978	3.0925	4.1231

5.3 TEST SPECIMEN PREPARATION

5.3.1 Materials

(i) Gleeble specimens

Six Gleeble specimens (thermally simulated specimens by Gleeble machines with the simulated HAZ material in the middle) were produced by PowerGen, the geometry of which is shown in Fig. 5.1. The material is Aberthaw cast (0.14%C, 0.44% Cr, 0.49% Mn, 0.58% Mo, 0.10% Ni, 0.023% Si, 0.025% S, 0.013% Sn, 0.25% V) CrMoV steam pipe material, as-manufactured, subjected to weld thermal simulation to a peak temperature of 860° C corresponding to the Type IV cracking position, at a simulated weld heat input of 16 kJ/cm. The ends of the specimens stay cool enough so that the thermal process is unlikely to have any effect in these regions of the specimens.

(ii) Service exposed pipe

Two sections of an exposed pipe, with weld, were supplied by PowerGen, the dimensions of which are shown in Fig. 5.2. The pipe sections were removed from the CrMoV main steam pipe of Ratcliffe Unit 4 after 174,800 hour service, at nominally 568° C and an internal pressure of 16.55 MPa; the OD (outer diameter) was 355.6 mm and the wall thickness was 63.5 mm. No previous repair was apparent and no cavitation damage was detected in the HAZ or parent material.

The welding process and conditions of the weldment are presented in Appendix V.

Since the amount of weld material was limited, the cutting and machining work for the specimens needed careful consideration. For the weld and cross-weld specimens, the material was just enough. Table 5.3 shows the numbers of the specimens removed from the service exposed pipe material.

Table 5.3 Numbers of the specimens removed from the exposed pipes

Material type	Test type			
	Uniaxial	Notched bar*	Impression**	Hardness
Parent	3	3	6	
Weld	3	3	6	
HAZ			6	
Cross-weld	3(waisted)	3		1

* two specimens were tested for parent and weld materials

** three specimens were tested for each material type

5.3.2 Machining of the Impression Creep Specimens

Since the thickness of the simulated HAZ in the Gleeble specimens was about 3 mm (see Fig. 5.1) the specimen was designed with a thickness of 2.5 mm and a diameter of 10 mm, in order to simplify the machining work and to suit the dimensions of the indenter and the loading bar. For the exposed pipe material, the specimens of base and weld materials have the same sizes as those obtained from the Gleeble specimens, but the HAZ specimens were made with a square cross-section instead of a circular one, with a width of 10 mm and the same thickness. For all of the indentation specimens,

W/D = 2.5 × W/H = 10. The geometries of the indentation specimens are shown in Fig. 5.3.

During the initial machining of specimens, an excess of 0.2 mm for each test contacted surface was left; then the two surfaces were slowly ground to the final thickness of 2.5 mm in order to remove the cutting marks and eliminate the residual stresses and surface damage which might have been caused by the initial machining process.

(i) Simulated HAZ and simulated parent material (virgin parent) specimens

Five simulated HAZ material impression creep specimens were removed from the Gleeble specimens and one impression creep specimen was removed from the end of a Gleeble specimen, which corresponds to the parent material for a new pipe, see Fig. 5.4(a).

(ii) Base material (exposed pipe) specimens

Base material indentation specimens were removed from the end of a bar which was used to machine the parent material uniaxial tensile specimens, see Fig. 5.6.

(iii) Weld material (exposed pipe) specimens

In order to save material and to make the machining work easier, weld material indentation specimens were removed from a slice containing weld metal (10 mm thick)

which was cut along the axial line of the pipe. A section of the weld was sawn out, taking care not to induce excessive heat or pressure during the process. From this slice of weld, a 10 mm diameter bar was removed from the centre of the weld (away from HAZ) by careful sawing and then by turning so that the maximum length was obtained. Finally, coin-shaped specimens were then removed from this cylinder taking care to note their positions (see Fig. 5.4(b)). A photograph of an etched weld is shown in Fig. 5.5.

(iv) HAZ material (exposed pipe) specimens

HAZ specimens were removed from the same slice from which the weld material specimens were machined. After the careful grinding and etching of the surfaces of the plate (see Fig. 5.4(b)), the different material zones could be clearly identified. From that, identification of the boundary lines was possible and rectangular cross-section bars on each side out of the adjoining material to the weld were cut. Care was taken to ensure that the surfaces of the bar next to the weld material were very close to the fusion line, because the HAZ was narrow and the specimens were designed to be indented in the direction from the base material (see Fig. 5.4(c)). The rectangular bars were obtained by carefully sawing and finish milling, using lots of coolant to reduce heat, and with a 0.3 mm excess on each side for subsequent grinding. When the final sizes 2.5 × 10 × length (mm) were reached, three 2.5 × 10 × 10 (mm) square specimens were carefully cut from the centre part of each bar, by an electric wire erosion machine. The specimens were then marked so that the positions of the specimens were recorded.

5.3.3 Machining of Uniaxial Specimens

Three types of uniaxial specimens were needed for this project, i.e. plain ridged specimens, Bridgman notched-bar specimens and waisted specimens, all of which were machined from the exposed pipe materials (see Table 5.3).

(i) Specimens from base material

Six round bars of 16 mm diameter were removed from block 1 (Fig. 5.2) in the section of the base material, and then were machined to produce three plain specimens and three notched bars. The specimens were cut longitudinally, parallel to the axial direction of the pipe. The longitudinal axes of each bar were located on the circle of the mean diameter of the cross-section (see Fig. 5.6). The dimensions of the plain, ridged and notched bar specimens are shown in Figs. 5.7(a) and 5.7(b).

(ii) Specimens from weld material

The weld material specimens were removed from the weld metal only. The machining procedure was as follows:

(1) A section of a toroid with the weld metal was cut first by a bandsaw parallel to the cross-section of the pipe (Fig. 5.8(a)), then the ends of the toroid were

finely ground, polished and etched. Therefore, the boundaries of the weld metal (fusion lines) could be clearly identified;

(2) Three round bars of 16 mm diameter were removed from the weld metal, as shown in Figs. 5.8(b) and 5.8(c). The gaps W1 and W2 in Fig. 5.8(c), which were the amounts of material removed during cutting, were kept as small as possible to ensure that the test sections (middle part of the bar) were close to the central area of the thickness of the pipe;

(3) The specimens (plain or notched bars) were then machined and marked. For the two specimens side-by-side on the top, the threaded sections were carefully machined because the fusion lines were very close to the blocks (see Fig. 5.8(c)). The axes of the specimens are perpendicular to the radial line in the symmetrical section A-A and the centres of the specimens (gauge length centre for plain, ridged specimens or notch centre for notched bars) are located on plane A-A.

(iii) Cross-weld specimens

Three cross-weld notched bars and three cross-weld waisted specimens were needed for the experimental work. A drawing of the waisted specimen is shown in Fig. 5.7(c). The cross-weld notched bars have the same geometry as that of the single-material notched specimens. The machining procedure for the cross-weld specimens was as follows:

(1) Six slices with weld were cut, using a bandsaw from a section of the pipe (see Fig. 5.9(a)). The cut surfaces were ground, polished and etched, so that the different zones of the weldment could be clearly identified;

(2) The required positions for the specimens were then marked on the etched surfaces and quadrangular prisms were machined from the slices, making sure that the position of the centre line of each bar was the same as that of the original quadrangular specimen, which was essential for the subsequent machining;

(3) The prisms were then machined to produce the round bars of 16 mm diameter which were then ground, polished and etched in the central regions of the bars, where HAZ was located;

(4) The specimens were then carefully machined. For the notched bars, the boundaries between HAZ and parent materials were positioned at the centre sections of the notches (see Fig. 5.9(c)). For the waisted specimens, the boundaries between HAZ and parent materials were positioned at the centre of the waisted sections (see Figs 5.7(c) and 5.9(d)).

Much care was taken during the cutting of those specimens to ensure that the axial lines of the specimens were on the radial sections of each of the slices of the weldment (see Fig. 5.9(b)). Before testing, the waisted specimens were checked using a Shadowed Graph Machine to ensure that there was no necking at the ends of the waisted sections.

5.4 EXPERIMENTAL PROCEDURES

5.4.1 Impression Creep Tests

(i) Impression creep test machine

(a) General description

A Mayes servo-electric machine was used to perform the tests (Max loading capacity is 100 kN) which had been used for the impression creep tests with cylindrical indenters at similar loading levels (Yehia [1994]). Because the contact area of the indenter was small, compared to that of a uniaxial specimen, the required loads were relatively small, and therefore care was taken to ensure that the sensitivity and stability of the machines were satisfactory at such low load levels. The performance of the machine during the tests indicated that the accuracy and stability of the load over long periods was satisfactory and that the accuracy of deformations obtained from low load levels was acceptable. This gave confidence in the load and measurement capability of the machine even at the smallest loading level (1 kN) used in the tests.

In order to indent the specimens, two adapters were made from a Ni-base superalloy and the indenter was machined on the lower end of the top adapter (see Fig. 5.10). The adapters, with the specimen, were attached to the Mayes machine and centralised after which two locating caps were tightened and the cross head of the machine was

raised until the indenter was in contact with the specimen. A thermocouple wire was soldered to each of the adapters and extensometers were attached, each having two legs (see Fig. 5.10) which were mounted on the knife edges of the adapters, such that the indentation movement was sensed by two transducers, each resting below one leg of each of the extensometers. Fig. 5.11 shows a photograph of the actual arrangement.

(b) Extensometer

The extensometers used were made of nimonic 80A, in order to withstand the high temperatures used for the tests. During the tests the extensometers were not subjected to any loads, except self-weight, and hence they were able to move rigidly and freely, following the movement of the indenter.

(c) Transducers

The transducers were inductive LVDT transducers from RDP Electronic Ltd, the plungers of which had a stroke of about 12 mm of which 5 mm was in the linear range where the measurements were most reliable. During the tests, the transducers were always set up so that they would be working in the linear range.

(d) Digital indicator

A displacement range was chosen using a switch on the machine, according to the expected total indentation. The full range, represented by a fixed voltage, in all cases was compared to the signal produced by the transducer which should correspond to the chosen range of displacement. A percentage of the full range voltage represented the percentage of the full range displacement chosen and was displayed on a digital indicator to show the total displacement as a percentage of the amount specified by the displacement range switch. Another digital scale was available which displayed, in the same manner, the percentage of the amount of load specified using a load range switch. For all impression creep experiments (except for the tests of 316 stainless steel), three load levels were used, i.e. 1.00 kN, 1.35 kN and 1.75 kN, which were converted from the corresponding equivalent uniaxial stresses of 40, 54 and 70 MPa by the reference loading conversion parameter, η (see Table 5.2).

(e) Chart recorder

The chart recorder has a chart of 250 mm width divided into 100 equal small divisions. Two pen plotters move horizontally along the chart width, according to the supply voltage, which is proportional to that supplied to the digital indicator. The chart speed adjustment is used to specify the time scale; several choices are available in steps which range from 120 mm/min to 7.5 mm/h. Magnification or reduction can be obtained such that the full scale of the chart can represent from 0.1% to 10 times the amount of displacement specified by the displacement range switch. This wide range of scale proportionality is satisfactory for choosing a reasonable scale to ensure that accurate readings can be obtained without electrical noise, which would occur if the

magnification was very high. A similar description applies to the case of the load, which can also be recorded on the chart. In the creep tests the load was kept constant throughout the test period, and hence it was not necessary to choose a scale range for the load.

(ii) Test procedure

When the adapters, specimen, thermocouple wire and extensometers are all set up properly, the furnace is then closed and switched on and the specimen is heated to the test temperature. The displacement range is chosen according to the expected deformation, the transducers are adjusted and the displacement digital scale is consequently set to the starting point relative to the position of the plungers of the transducers. Then a very small load is applied to the specimen. An appropriate range is chosen for the chart recorder and a suitable paper speed is set to represent the time scale specified. During the creep tests it is advisable to keep the paper speed relatively fast at the beginning of the test and slow it down later on when the displacement rate has slowed down significantly. The time scale is switched on and the chart recorder starting button is pressed at the same time as the load application potentiometer knob is turned to apply the load until the required load level is reached, as appears on the digital load indicator. The test is then left for the required time or until the required displacement or steady-state displacement rate has been achieved. To stop the test, the loading potentiometer knob is turned to remove the load, the furnace is switched off and the specimen is left to cool down so that it can be disassembled.

(iii) The indenter

As stated before, the indenter was machined on the end of the upper adapter. The two adapters were machined from an existing uniaxial tensile specimen. The material of the two adapters is a Nickel-based superalloy (Waspaloy) which has been studied extensively by Hyde et al [1996]. Since the creep speed of the indenter material is insignificant compared to that of the indented specimens, the two adapters may be assumed not to be creeping during the tests for such low loading levels and the durations of the tests. Uniaxial test results, at 700° C, show that when the applied stress $\sigma < 520$ MPa, the creep constants in Norton's equation are: $A = 9.226 \times 10^{-34}$ (σ in MPa, t in hour), n = 10.647 and Young's modulus is 178 GPa (Hyde et al [1996]). Typical values of A and n for the parent metal of a new pipe of similar material are 2.853×10^{-16} and 4.897 (Hall and Hayhurst [1991]), respectively. Using Norton's law and with a stress level of 54 MPa, it can be demonstrated that the secondary strain rate of Waspaloy is nearly 3.380×10^{7} times lower than that of the typical virgin parent material. In addition, the service-aged weldment materials are expected to creep faster than the corresponding virgin materials. Therefore, the creep deformations of the indenter material, compared with those of the test materials, can be ignored.

The dimensions of the indenter are given in Fig. 5.12.

5.4.2 Uniaxial Creep Tests

(i) Denison creep testing machine

(a) Mechanical system

The uniaxial creep tests were performed on the Denison Creep Testing Machine. The basic frame of the machine is a 2 m × 2 m 'L' shape, the vertical section having 4 × ϕ 50 mm columns and the horizontal section consisting of a lever system whereby the load is applied.

The graduated load lever is linked to the bottom lever which in turn connects, through knife edges, with the lower loading bar (within the afore-mentioned columns).

Since the lengthening of the specimens allows the load lever to gradually fall to its lower limit, a 'strain take-up' system comes into operation from time to time to prevent this happening. It is triggered by the end of the load lever pressing on a micro-switch which in turn causes a DC motor-drive screw system to draw the upper loading bar upwards. Since the upper loading bar is connected through the specimen to the lower loading bar, the load lever is gradually raised to its highest working position and as this occurs another micro-switch causes the strain take-up motor to be switched off. The whole of this operation is very slow, taking about half an hour and hence the load on the specimen remains steady.

(b) Strain Measurement

All of the specimens requiring strain monitoring have been machined with knife-edge flanges. Conventional extensometer 'legs' are fitted to these flanges and at the lower ends of the legs linear voltage displacement transducers produce, via a conditioning unit, a DC voltage which is proportional to strain. The voltage is then fed to a computer-based data-logging system.

(c) Temperature control

A 3-zone muff type furnace is lowered to surround the specimen which previously has had three thermocouples spot welded to it. Each of the three furnace zones, together with its thermocouples, forms an independent control loop via a Eurotherm electronic controller and its associated thyristor.

(ii) Test procedure

(a) Setting up a test

Both specimen 'caps' have their threads cleaned of debris by a M16 tap in order to avoid torsional effects when the specimen is fitted to the loading bars. The lower cap is screwed onto the lower bar and the specimen is then itself screwed into the M16 hole. Then the upper cap is screwed into the top of the specimen so that it almost goes beyond the lower end of the thread. This procedure allows the top cap to have full thread engagement on both the specimen and the upper loading bar, when fitting is completed.

Three thermocouples are then prepared by using three 1 m lengths of thermocouple wire. One end of each piece is connected to the controller input while the other is tightly twisted and spot welded to the appropriate position on the specimen (two outside the gauge length and one in the middle). Then the extensometer legs are fitted carefully, ensuring that the specimen knife edge flanges fully engage with the 'V' shaped grooves at the top of the assembly.

After a final inspection to ensure that everything is correctly positioned, the furnace is lowered so that its centre coincides with that of the specimen.

In order to avoid any damage to the specimen it is essential that whilst heating up to the test temperature, the strain take up system (S.T.S.) is operating. For this reason a minimum over balance is set on the load lever and the S.T.S. is switched on with the gear train pin engaged (a modification to the loading machine stops the furnace from being switched on whilst the S.T.S. is switched off).

(b) Preparing to start a test

In less than 2 hours the specimen should have reached the required temperature. When this is achieved the loading lever is temporarily supported by a prop close to its free end. The gear train pin is then removed and the manual S.T.S. wheel is turned anti-clockwise about 5 to 10 turns. This will ensure that the knife edges are at minimum disengagement so that when the load is manually wound on there is no jolting as

contact is re-established. With the loading lever firmly propped, the moveable weight is wound along the lever to the position where the scale indicates the appropriate force.

(c) Starting the test

The strain transducers are finally positioned so that their plungers are almost fully retracted and intercept values are keyed into the logger to ensure that zero strain is displayed. Then the manual S.T.S. wheel is steadily wound clockwise to bring the loading lever knife edges into contact and soon after this has occurred the load lever should rise from the prop and the latter is carefully removed.

After starting the test, it is only necessary to periodically check that progressive strain increase is displayed and that the load lever has not 'bottomed'. When the load lever reaches the bottom after a period of testing time, this will show that the specimen has failed.

5.5 EXPERIMENTAL RESULTS

Experimental work has been carried out, based on the test program described in Section 5.2. So far, all the creep tests have been completed except the uniaxial creep test of weld material notched bar at 54 MPa (PWN-1, see Table 5.1).

5.5.1 Hardness Test Results

Hardness tests were performed using a M400 Microhardness Tester which had a loading range of 10 - 1000 gf. Vicker hardness numbers (VHN) were obtained. The chosen loading was 500 gf for all of the indentations.

(i) Cross-weld hardness tests

A cross-weld hardness test specimen was removed from a piece of the pipe metal with the weld cut longitudinally across the weld (see Fig. 5.13(a)). The specimen was then finely ground, polished and etched to make sure that the detail microstructure could be observed by the microscope of the machine.

The indentations were performed along parallel lines which are roughly perpendicular to the fusion line. The indentation lines were spaced 1 mm apart. More than 30 points were tested on each line. The spacing of any two points near the interfaces was 0.25 mm, and it was 0.5 mm when the indentation positions were away from the interfaces (see Fig. 5.13(b)).

A high loading level (500 gf) was adopted in order to obtain relatively large indentations which would be easy to measure and give a good accuracy. The indentations between two points for the smaller distance of 0.25 mm were examined, to ensure that the distance was sufficiently large to satisfy the test requirements.

Fig. 5.14(a) and Fig. 5.14(b) show the hardness test results for the cross-weld specimen. Fig. 5.14(a) presents the results from 7 separate lines, and Fig. 5.14(b) shows the average values. It can be seen that the hardness of the weld metal is significantly higher than that of the base metal, and the HAZ and base materials nearly have the same hardness. It should be noted that, the origin of the x co-ordinates in Fig. 5.14(a) and Fig. 5.14(b) was defined on the fusion line, i.e. the hardness values of these indentation points were obtained from the points on each line which were closest to the fusion line observed by the microscope.

(ii) Simulated HAZ material hardness tests

A hardness test specimen for the thermally simulated HAZ material was machined from a Gleeble specimen. The specimen was 25 mm long with the simulated HAZ material in the middle (see Fig. 5.15). The surface of the specimen was flattened on one side along the axial direction and the flattened surface was then ground, polished and etched. The indentations were performed along three lines on the flattened surface with 1 mm line spacing. The distance between two indented points was 0.5 mm. More than 30 indentations were performed on each line.

The results obtained from the test are plotted in Fig. 5.16(a) and Fig. 5.16(b). It can be seen that there is only a slight increase in the hardness across the simulated HAZ material. Fig. 5.16 also shows that the hardness of the simulated HAZ material is

higher than that of the cross-weld specimen of the exposed pipe (see Fig. 5.14) at the same position.

5.5.2 Impression Creep Test Results

(i) Results from simulated HAZ material and simulated base material tests

In Fig. 5.17, the variations of creep displacements and the converted uniaxial strains with time are shown. The indentation strains in Fig. 5.17(b) were obtained from the displacements in Fig. 5.17(a) using the β value of 2.097. Systematic behaviour is shown, i.e. the displacement (or strain) rates increase with temperature or stress. All the tests exhibit smooth variations of strain with time, except for the test at the lowest temperature and loading. It can also be seen that the creep strain-rate of the simulated base material is slightly lower than that of the simulated HAZ material, at the same stress and temperature. However, the difference in the overall strain is small and the observed difference in the strain-rate may not be significant.

(ii) Results from the exposed material

The test results for the aged parent, weld and HAZ materials are shown in Figs. 5.18 - 5.20, respectively. From Fig. 5.18, it can be seen that the indentation deformation-rate of the parent material obtained in the 40 MPa test is close to that of the 54 MPa test. An additional test at 40 MPa was performed in order to assess the likely variability of the data, and was shown to produce similar results (see Fig. 5.18 and Table 5.9).

(iii) Results from 316 stainless steel

Significant surface oxidation damage occurred in both the uniaxial and indentation creep test specimens. In an attempt to obtain more reliable impression creep deformation data in order to experimentally verify the impression creep test technique, a group of additional indentation tests, using 316 stainless steel, were performed from which the uniaxial creep data at 600° C, for a range of stress levels, have been obtained by Hyde [1988]. No oxidation damage was observed in the uniaxial tests of the 316 stainless steel material.

The indentation tests were conducted at 600° C with pressures corresponding to uniaxial stresses of 200, 260, 280 and 300 MPa, using specimens with identical geometry to that shown in Fig. 5.3(a). The corresponding converted loading levels are 5.0, 6.5, 7.0 and 7.5 kN, respectively. The test results of the indentation deformations and the converted uniaxial stains are presented in Fig. 5.21.

5.5.3 Uniaxial Creep Test Results

The uniaxial creep strain data obtained from the base and weld material tests are shown in Fig. 5.22. The rupture data obtained from the aged parent and weld (plain and notched) and cross-weld (waisted and notched) specimen tests are presented in Table 5.4.

The weld material plain specimens tested at 54 MPa and 70 MPa failed outside the gauge length with final strains of about 6% and 8%, respectively, see Fig. 5.22(b). It was not possible to repeat these tests and therefore it was necessary to estimate the rupture data from these test results. Since the test of 40 MPa was expected to fail in a very long time, considering the limitation of the test machines, the test was stopped after 2000 hours. Therefore, no rupture data were obtained from this test.

The uniaxial creep test of weld material notched bar at 54 MPa is still in progress.

Table 5.4 Rupture times from the uniaxial creep tests (hour)

Material σ(MPa)	Parent		Weld		Cross-Weld	
	plain	notched	uniform	notched	waisted	notched
40	9560	——	(2000 +)$^{\oplus}$	——	2630	4240
54	1704	6430	3776	(8616→)*	1008	1854
70	381.5	1800	1026	4918	424	757

—— no test; * the test is still in progress; ⊕ the test was stopped at t = 2000 hours.

5.5.4 Examination of the Fracture Surfaces and Failure Positions of Cross-Weld Tested Specimens

The fracture surfaces of the cross-weld specimens were examined after testing in an attempt to check the microstructure appearance of the broken surfaces of the specimens after failure. The Examination was performed using a JEL6400 Secondary

Electron Microscope (SEM) on the tested specimens which were gold coated before the examination. Examples of photographs taken from the fracture surfaces of the cross-weld waisted specimen at 54 MPa are shown in Fig. 5.23. Microscopic examination indicated that the surface of the specimen was heavily oxidised and that surface emergent cracks appeared and whisker formation was merely a form of oxide growth.

Since the SEM examination could not clearly identify the fracture positions of the specimens, the broken parts of a notched bar and a waisted specimen, tested at 54 MPa, were sectioned along the centre line of the specimens. The sectioned specimens were then metallurgically polished, etched and microstructurally examined. The photographs of the sectioned surfaces are presented in Figs. 5.24 and 5.25. It can be clearly seen that failure occurred in the HAZ near the boundary between the HAZ and parent material for both the notched and waisted specimens.

5.6 DISCUSSION AND CONCLUSIONS

5.6.1 Hardness Tests

Hardness varies across the weld specimen in the exposed pipe. The values for the weld metal are about 20% higher than those for the base metal. The hardness of the parent material is practically the same as that of the HAZ. No sharp change occurs on or near

the boundary of the parent material and HAZ, which is the so called Type IV failure position. This indicates that the creep properties of the parent and HAZ materials are likely to be similar and that the creep properties for the weld material are likely to be significantly different from those of the parent and HAZ materials.

Hardness results for the simulated HAZ material (new material) were found to be about 20% higher than those of the base or HAZ material in the exposed pipe (old material). This suggests that the old materials of the cross-weld are likely to have become less creep resistant (softened) after long term service exposure.

It should be noted that the hardness results were obtained at room temperature and would be different from those obtained at elevated temperature. Also, since there is no direct link between the hardness and the creep properties, the magnitude of the hardness can only be regarded as indicative of the creep properties.

5.6.2 Steady-State Creep Properties

The steady-state strain-rates from the uniaxial tests and the equivalent strain-rates from the indentation tests, for the aged base, weld and HAZ materials and the simulated HAZ material, were obtained and are listed in Table 5.5.

By plotting $\log(\dot{\varepsilon}_{ss})$ versus $\log(\sigma)$, Norton's constants, A and n ($\ln \dot{\varepsilon}_{ss} = A\sigma^n$), can be obtained. Fig. 5.26 shows the plots for the exposed base and weld material from both indentation and uniaxial test results. Fig 5.27 presents the plots for the simulated HAZ

material and aged HAZ material from the indentation tests. The results of the Norton fits to the minimum creep strain-rate data are shown in Table 5.6.

Table 5.5 Steady-state strain-rates obtained from creep tests ($\dot{\varepsilon}_{ss}$ in h^{-1})

Material	Parent (aged)		Weld (aged)		HAZ (aged)	HAZ (simulated)
σ(MPa)	uniaxial	indentation	uniaxial	indentation	indentation	indentation
40	4.20×10^{-6}	2.20×10^{-5}	2.44×10^{-6}	2.60×10^{-5}	6.93×10^{-5}	1.61×10^{-5}
54	2.32×10^{-5}	4.21×10^{-5}	7.72×10^{-6}	3.62×10^{-5}	1.28×10^{-4}	3.32×10^{-5}
70	1.29×10^{-4}	1.26×10^{-4}	4.58×10^{-5}	1.27×10^{-4}	3.18×10^{-4}	4.45×10^{-5}

Table 5.6 Creep constants obtained from creep test (stress in MPa, time in hour)

Material	Parent		Weld		HAZ	HAZ (simulated)
	uniaxial	indentation	uniaxial	indentation	indentation	indentation
A	6.599×10^{-16}	2.220×10^{-10}	9.718×10^{-15}	1.513×10^{-13}	2.993×10^{-9}	1.836×10^{-8}
n	6.108	3.094	5.208	4.836	2.708	1.844

By using the Norton's constants, A and n, obtained from the uniaxial tests, secondary strain-rates can be calculated. The rupture time can be estimated from a uniaxial rupture equation (see Equ. (6.9) in Chapter VI). These results are shown in Table 5.7. It can be seen that the calculated data are close to the test results. This further demonstrates the close fit of the Norton's creep law to the steady-state material data.

Table 5.7 *Estimated minimum strain rates and rupture time for the uniaxial specimens (aged parent material)*

σ (MPa)	$\dot{\varepsilon}_{ss}$ (1 / hour) calculated	t_f (hour) calculated
40	4.0379×10^{-6}	9.6137×10^{3}
54	2.5250×10^{-5}	1.7032×10^{3}
70	1.2326×10^{-4}	3.1830×10^{2}

5.6.3 Verification of the Impression Technique

From the indentation creep test results of 316 stainless steel shown in Fig. 5.21, the minimum indentation creep deformation rates were converted to the corresponding uniaxial creep strain-rates. A plot of the strain-rates against the equivalent uniaxial stresses for the indentation pressure, together with the corresponding uniaxial creep results, obtained by Hyde [1988] is presented in Fig. 5.28. The comparison between the uniaxial creep data and impression creep data shows good agreement and confirms that the impression creep testing technique, using a rectangular indenter, can be used to obtain reliable equivalent uniaxial secondary creep properties.

Finite element, impression creep analyses were performed using the same geometries and loading conditions as those used in the experimental tests, and with the material properties (see Table 5.6) obtained from either the impression creep test experiments or the uniaxial creep test experiments. The predicted indentation displacements for the

base material specimens are shown in Fig. 5.29. The corresponding calculated strain-rates (converted) are listed in Table 5.8. By comparing these results with the test results shown in Table 5.5, it can be seen that the corresponding strain rates are very close to each other. This indicates that:

(a) The material properties, A and n, obtained by fitting the test data using the Norton's law are acceptable over the stress range 40 to 70 MPa.

(b) The indentation parameters, η and β give reliable results.

It should be noted that, since the material information which describes the primary creep of the material is not included in the calculations, the indentation FE-calculations using the Norton's law cannot simulate the primary creep deformation correctly (see Fig. 5.17 and Fig. 5.28) but the steady-state data can be accurately determined.

Table 5.8 Converted equivalent strain rates obtained by FE-calculation using the creep properties obtained by tests (base material)

σ (MPa)	A and n from uniaxial	A and n from indentation
40	4.2905×10^{-6}	2.0358×10^{-5}
54	2.5305×10^{-5}	5.1202×10^{-5}
70	1.2215×10^{-4}	1.1377×10^{-4}

5.6.4 Creep Strength of the Exposed Weldment Materials

Creep deformation parameters obtained from both indentation and uniaxial tests are summarised in Table 5.9 and Table 5.10. The 100 hours creep strains are plotted in Fig. 5.30.

Table 5.9 Creep deformation parameters from indentation tests

Material Type	Test conditions			Test results	
	T(° C)	σ(MPa)	t_T(hrs)	ε^c_{100}	$\dot{\varepsilon}^c_{ss}$(1 / hrs)
Simulated Type IV	640	40	478.7	6.97×10^{-3}	1.61×10^{-5}
	640	54	436.7	9.76×10^{-3}	3.32×10^{-5}
	640	70	199.7	1.59×10^{-2}	4.45×10^{-5}
	660	54	193.5	1.62×10^{-2}	7.21×10^{-5}
	680	54	161.9	2.49×10^{-2}	1.37×10^{-4}
Simu - base	680	54	162.9	1.49×10^{-2}	9.49×10^{-5}
Exposed parent	640	40	489.5	1.67×10^{-2}	2.20×10^{-5}
	640*	40*	797.4	1.45×10^{-2}	2.67×10^{-5}
	640	54	523.5	2.58×10^{-2}	4.21×10^{-5}
	640	70	433.3	3.36×10^{-2}	1.26×10^{-4}
Exposed weld	640	40	916.6	1.60×10^{-2}	2.60×10^{-5}
	640	54	463.6	2.16×10^{-2}	3.62×10^{-5}
	640	70	214.5	2.59×10^{-2}	1.27×10^{-4}
Exposed HAZ	640	40	836.5	1.33×10^{-2}	6.93×10^{-5}
	640	54	604.7	2.62×10^{-2}	1.28×10^{-4}
	640	70	236.8	4.30×10^{-2}	3.18×10^{-4}

* repeated test

Results show that the creep strain accumulated in 100 hours for the simulated HAZ material (virgin material) is slightly higher than that of the simulated parent material

(virgin parent), as shown in Fig. 5.30(a), but is much lower than that of the exposed parent material. This indicates that after long-term service exposure, the creep strength of the parent material may have been significantly reduced.

The aged parent material shows higher secondary strain-rates than the aged weld metal, see Tables 5.9 and 5.10. This suggests that the parent material is more substantially degraded by service aging, since for virgin parent material and weld metal, the weld metal strain rate is expected to be typically 4 times higher. Rupture data (see Table 5.4) also demonstrate that the aged parent material exhibits much poorer uniaxial rupture strength than that exhibited by the aged weld metal.

Table 5.10 Creep deformation parameters from uniaxial tests

Material Type	Test conditions			Test results	
	T(° C)	σ(MPa)	t_T(hrs)	ε^c_{100}	$\dot{\varepsilon}^c_{ss}$(1 / hrs)
Exposed parent	640	40	9560	4.90×10^{-2}	4.20×10^{-6}
	640	54	1704	2.15×10^{-1}	2.32×10^{-5}
	640	70	381.5	2.09×10^{-0}	1.29×10^{-4}
Exposed weld	640	40	(2000 +)	4.16×10^{-2}	2.44×10^{-6}
	640	54	3766	1.13×10^{-1}	7.72×10^{-6}
	640	70	1026	7.14×10^{-1}	4.58×10^{-5}

The impression creep test results in Table 5.9 show that the aged HAZ material has a higher secondary strain rate, at high stress level, than the aged parent material, but lower strain rate, at low stress level.

On the basis of secondary strain rates, the order of descending creep strength for parent material is: virgin parent (simulated parent), virgin HAZ (simulated HAZ) and aged parent; the order for the aged weldment material at high stress levels is: weld metal, parent material and HAZ material.

5.6.5 Surface Oxidation Damage of the Tested Materials

Oxidation damage has been found in both thermally simulated and aged materials creep tests. This is a result of the high temperature levels chosen for the tests. In general, oxidation effects always exist except when the creep tests are performed in a vacuum or in an inert gas such as helium. Oxidation damage may be ignored when the specimen dimensions are very large since the loss of surface material is insignificant in this case.

Material damage caused by oxidation is dependent upon the temperature, creep time, loading level, etc. At a given temperature, the creep time would contribute most to the oxidation damage.

Creep test strain curves are affected by surface oxidation. For a uniaxial test, the rupture time will be reduced due to the loss of cross-sectional area of the specimen. For an impression creep test, the loss of material around the indenter, caused by surface oxidation damage, will affect the local strength of the specimen and therefore will affect the accuracy of the indentation creep deformation.

It has been found that the oxidation damage is strongly dependent on the creep time, but the effect of the stress level is not obvious. However, it is expected that under the same temperature and at the same creep time, higher stress levels cause more serious oxidation damage.

Experimentally obtained uniaxial creep curves for the aged parent and weld material have clearly shown that the primary creep periods of these materials are very short under the specified test conditions, and that the secondary creep is achieved very quickly in comparison with the rupture lives of the tests, see Fig. 5.22. In the secondary creep periods of the uniaxial tests, since the stress in the specimens was uniform through the gauge length, then it can be assumed that the oxidation damage occurred uniformly on the surfaces of the specimens. Since surface oxidation damage is time-dependent and the serious oxidation damage was only observed after the failure of the specimens, it can be assumed that in the early stages of these creep tests (creep times are very short compared with the rupture times), the creep strains were not significantly affected by oxidation. This suggests that the secondary creep properties of the parent and weld material (see Table 5.6) obtained from such tests are reliable. However, the corresponding rupture data may not be very accurate. Two photographs of the tested uniaxial samples are shown in Fig. 5.31.

Based on the above analysis and compared with the uniaxial secondary creep data , see Table 5.5 and Fig. 5.26, the secondary strain-rates of the impression creep tests for the exposed materials (parent, weld and HAZ) are not very reliable except for the highest stress tests. This indicates that the secondary creep properties of the aged HAZ

material cannot be determined directly, at 640°C, from indentation tests due to oxidation effects. The indentation test specimens sustained more serious oxidation damage, probably due to the smaller size of the specimen and higher equivalent localized stress applied.

Cross-weld specimens also sustained oxidation damage which may have introduced some errors on the rupture life of the specimens. It should be noted that owing to the oxidation effect, the accuracy of the experimental creep data of the exposed weldment materials will be affected, hence reducing the accuracy of the creep and damage material properties generated from the creep test results of the exposed materials.

5.6.6 Fracture Surfaces and Failure Positions of Cross-Weld Test Specimens

The results of the SEM examination indicate that the fracture surfaces are intergranular with small "shear lips", but cannot be proven due to the oxide coating. The oxidation is very heavy, and the full metallurgical sections have to be used to properly define the failure positions and type of cracking of the specimens.

The failure positions of both the cross-weld notched and waisted specimens identified from the sectioned surfaces are located in the HAZ adjacent to the interface of the HAZ and parent material.. This was confirmed by detailed microstructure checks, i.e. the fracture surfaces were in the intercritical HAZ. This clearly demonstrates that the failure of the exposed material cross-weld specimens, under the specified test conditions, was caused by the so called "Type IV cracking".

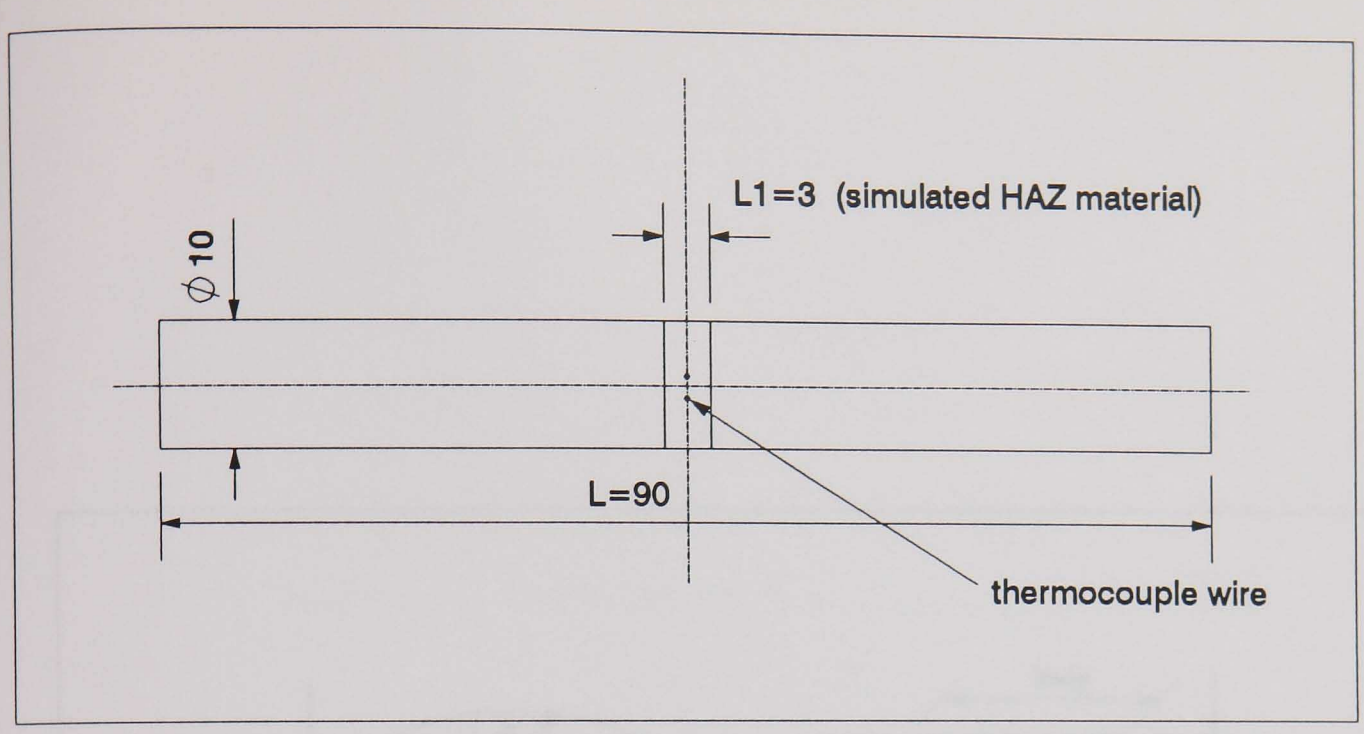

Fig. 5.1 Dimensions of Gleeble specimen (mm).

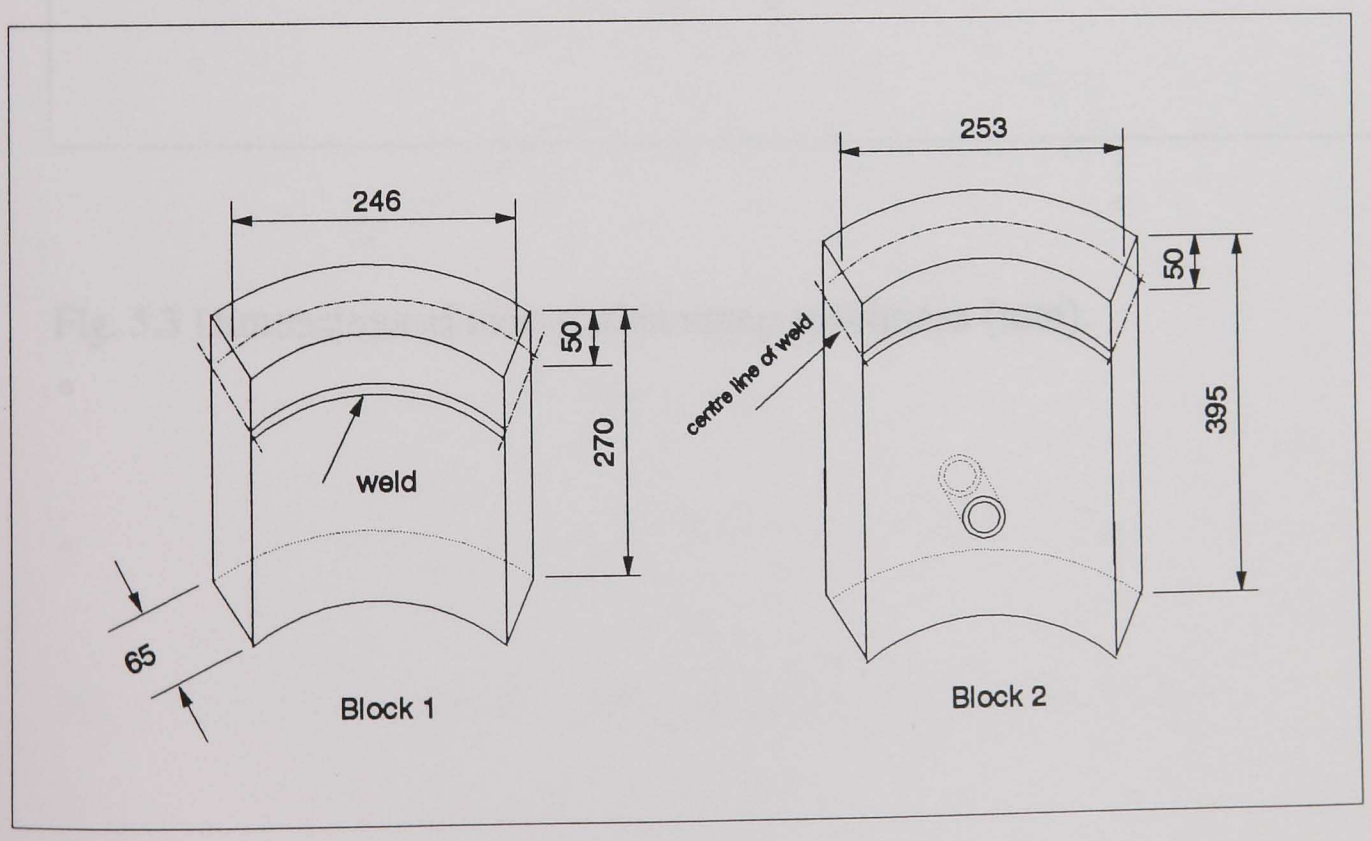

Fig. 5.2 Sections of exposed pipe with weld from which test specimens were machined (dimensions in mm).

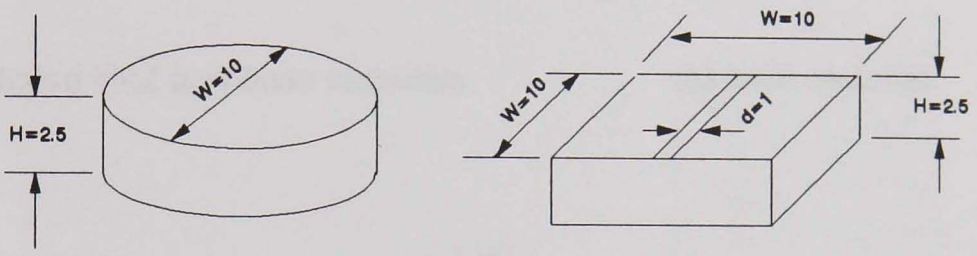

(a) for base and weld materials

(b) for HAZ material

Fig. 5.3 Dimensions of indentation creep specimens (mm).

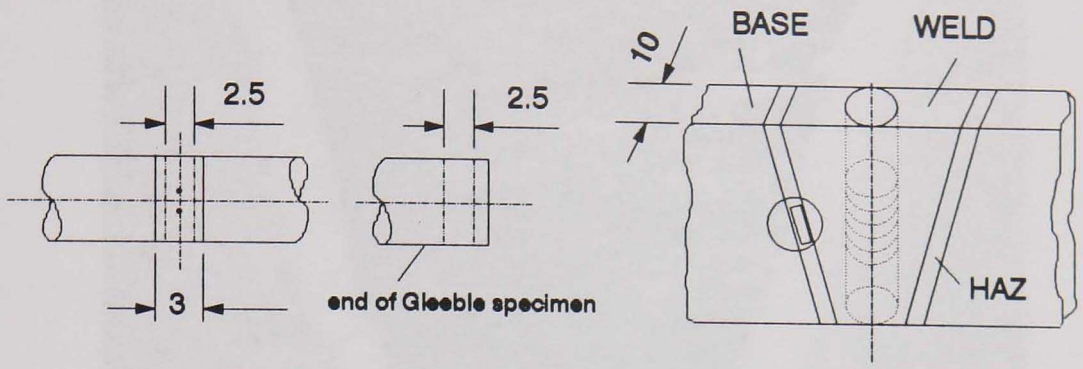

(a) simulated HAZ and base materials

(b) weld material

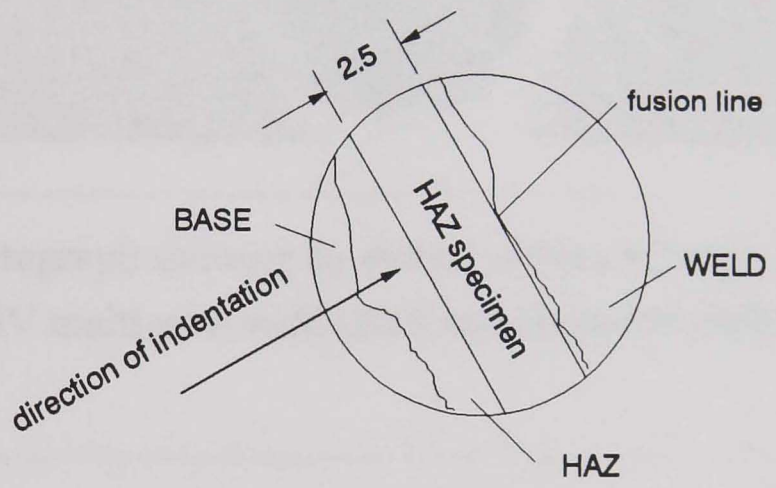

(c) HAZ material

Fig. 5.4 Machining of indentation specimens (dimensions in mm)

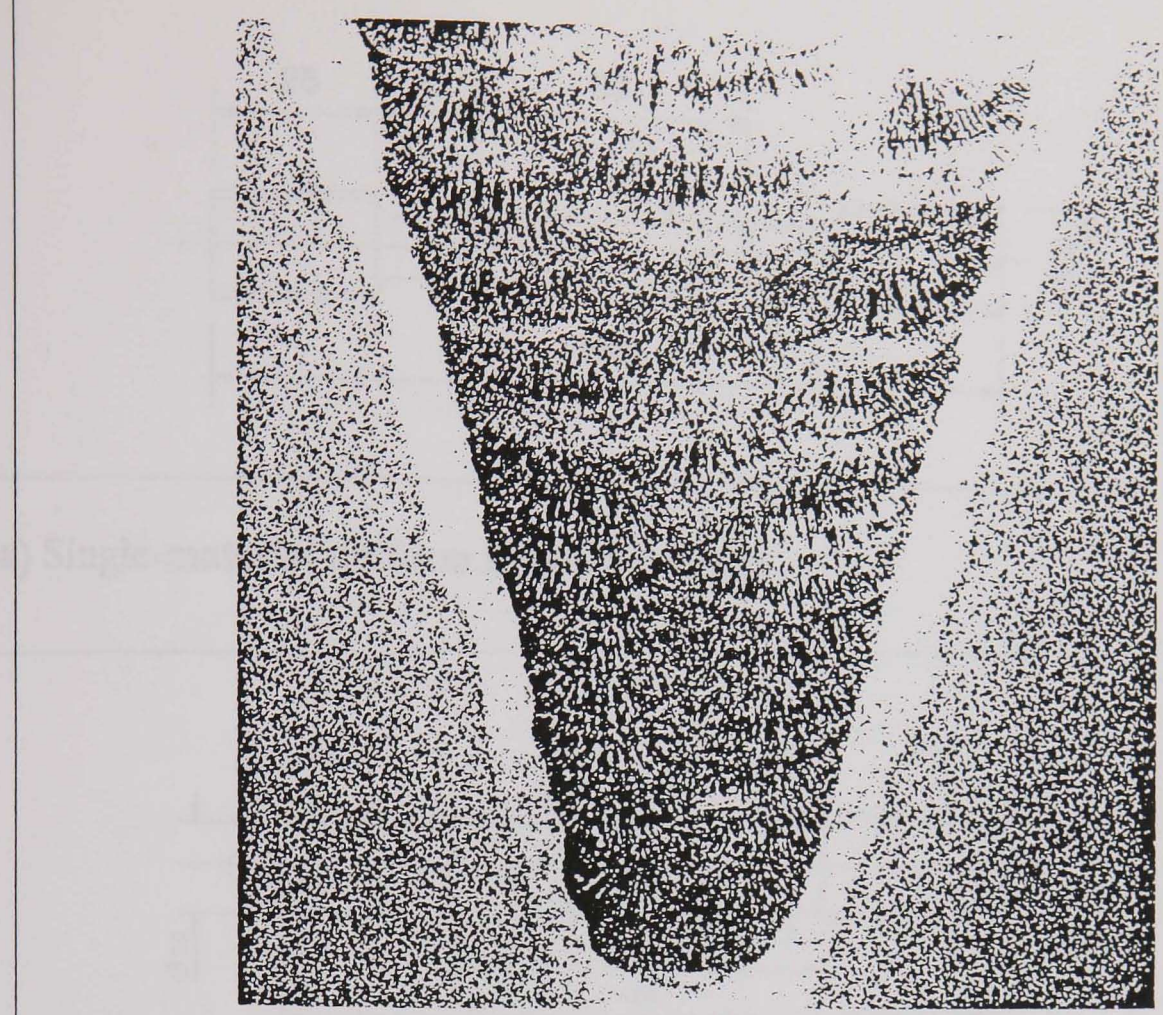

Fig. 5.5 A photograph showing an etched section through 2.25Cr1Mo: 1/2Cr1/2Mo1/4V multi-pass weld (Hall and Hayhurst [1991]).

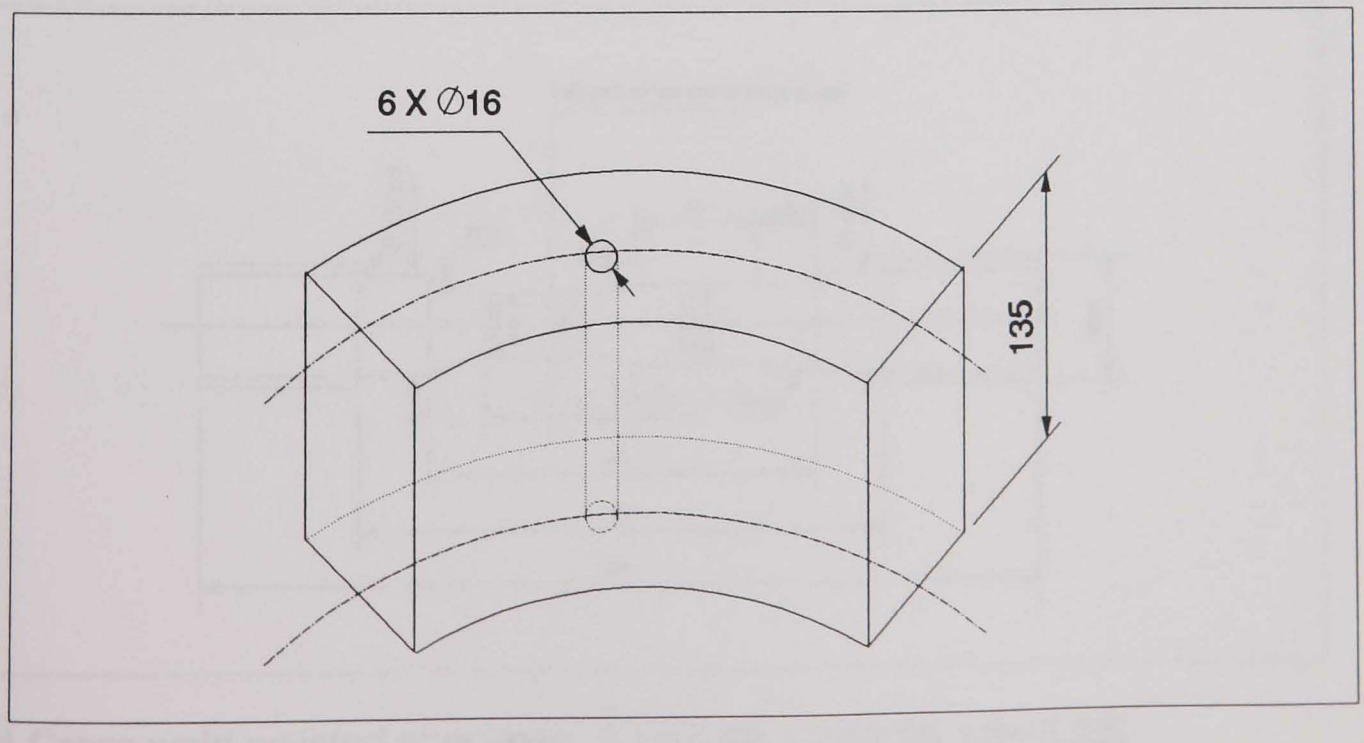

Fig. 5.6 Removal of base material specimens (dimensions in mm).

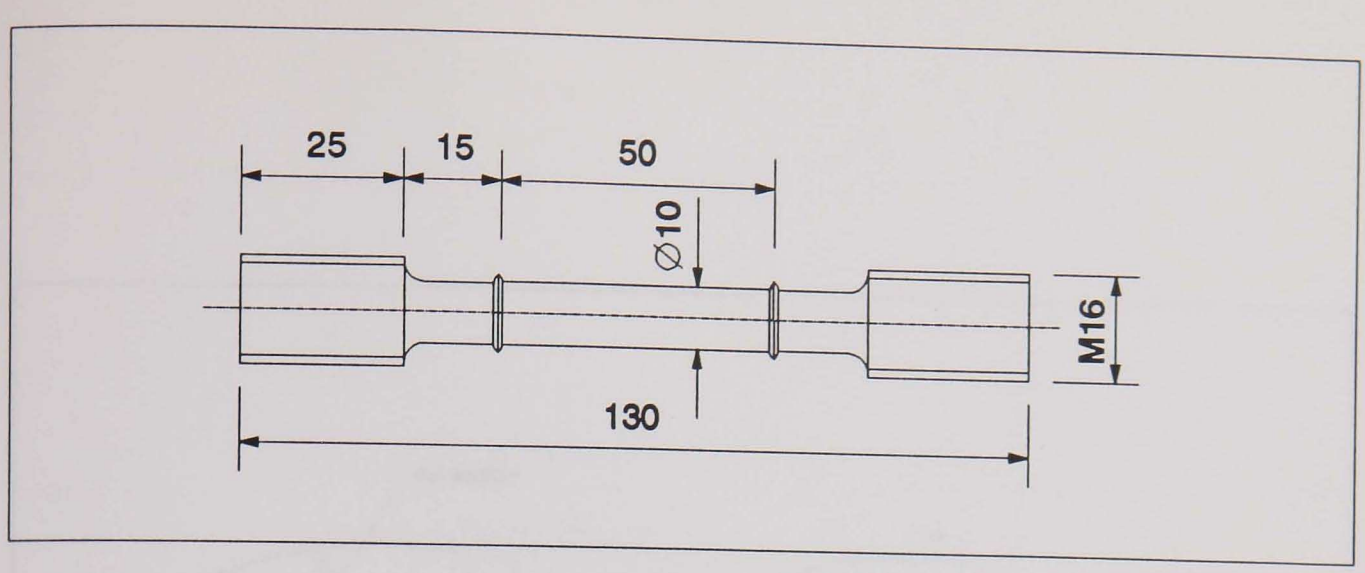

(a) Single-material uniform ridged specimen

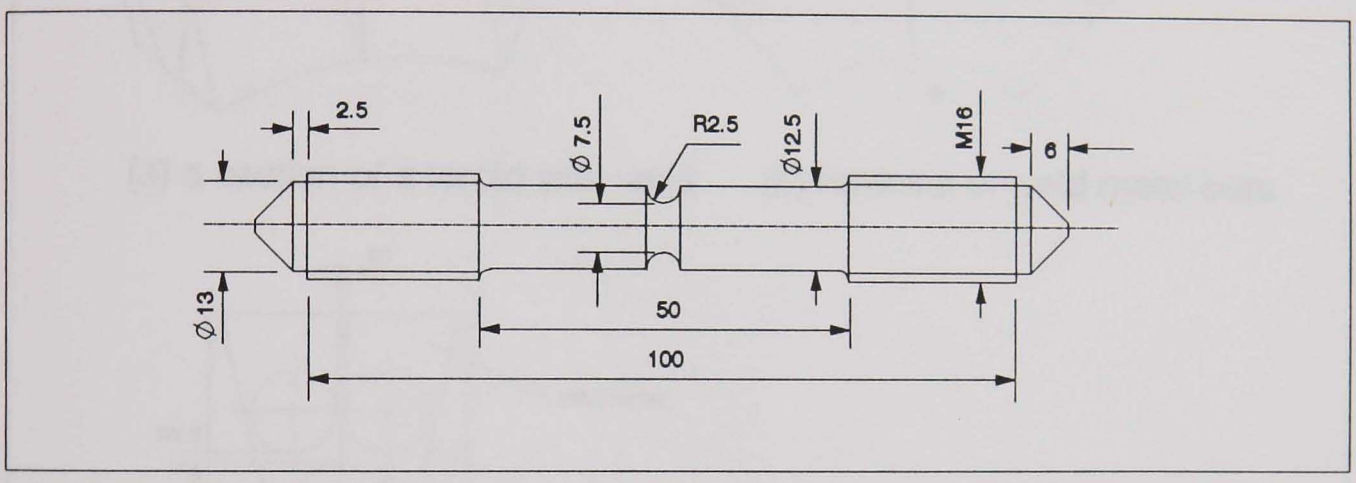

(b) Single-material or cross-weld Bridgman notch specimen

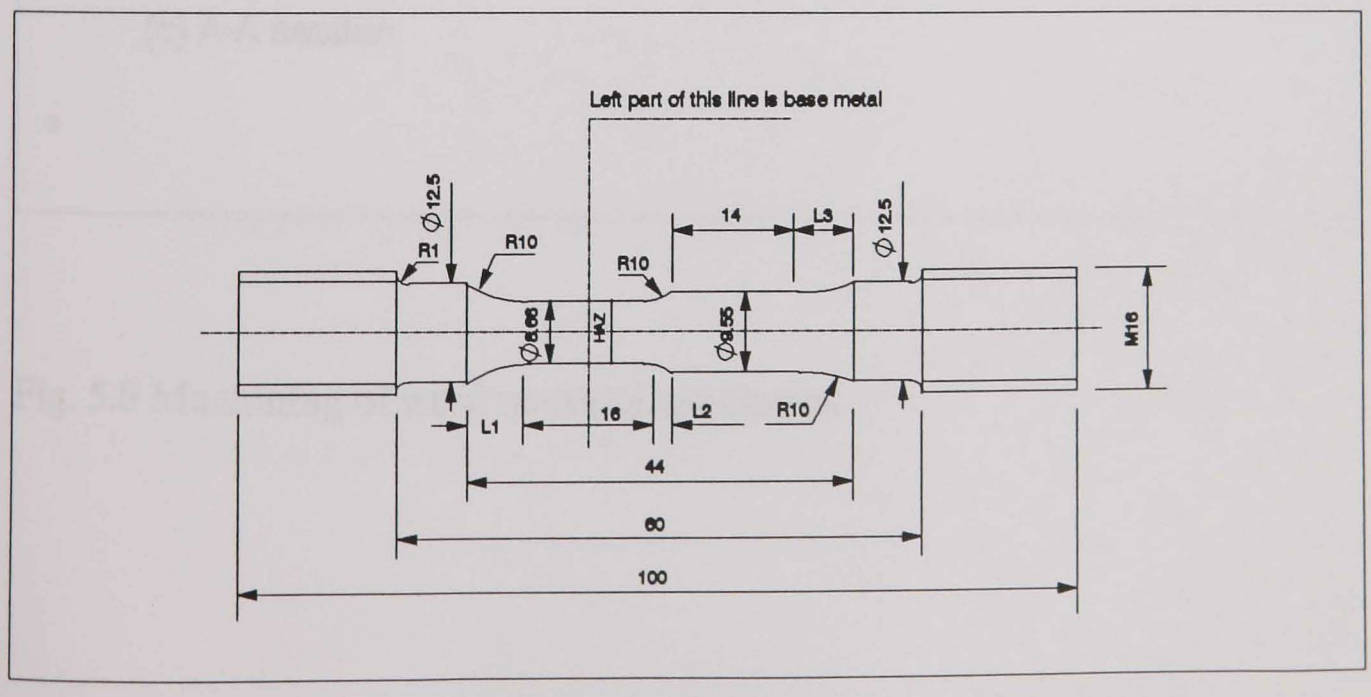

(c) Cross-weld waisted specimen (L1=5.89, L2=2.95, L3=5.23)

Fig. 5.7 Dimensions of uniaxial test specimens (mm).

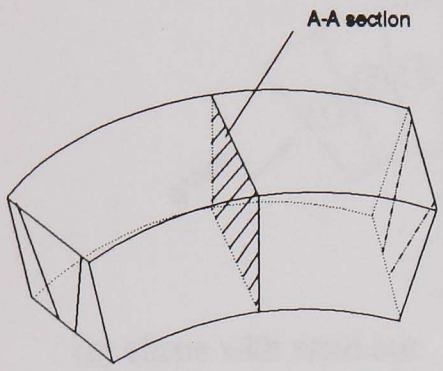

(a) a section of a toroid with weld

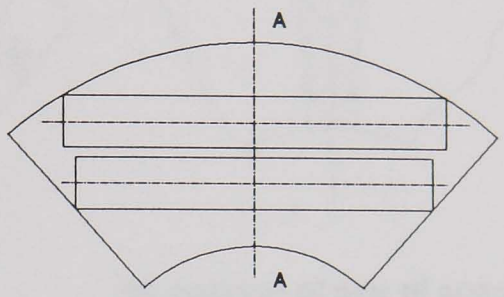

(b) removal of weld metal bars

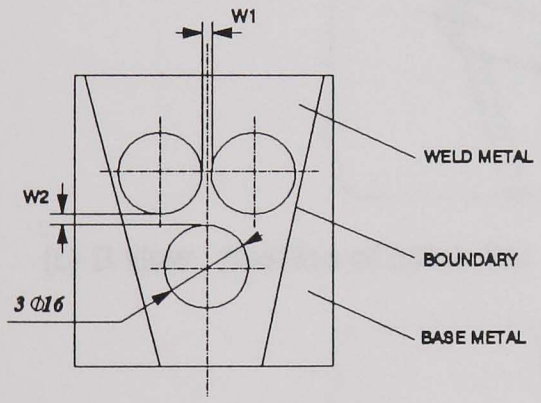

(c) A-A section

Fig. 5.8 Machining of weld material specimens.

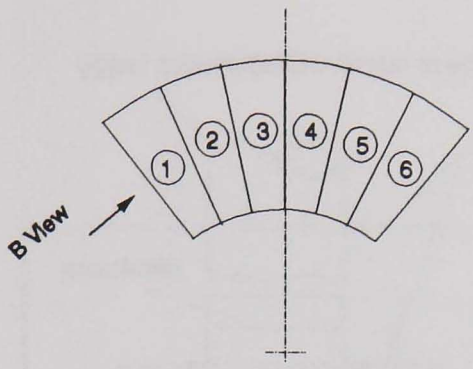

(a) slices with weld cut

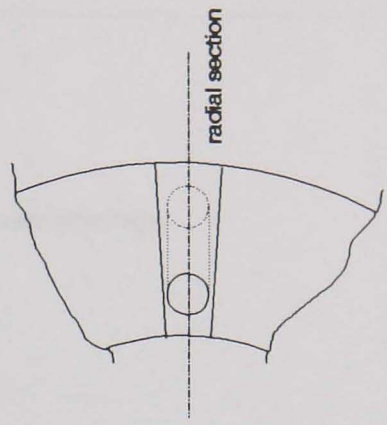

(b) position of axis of specimen

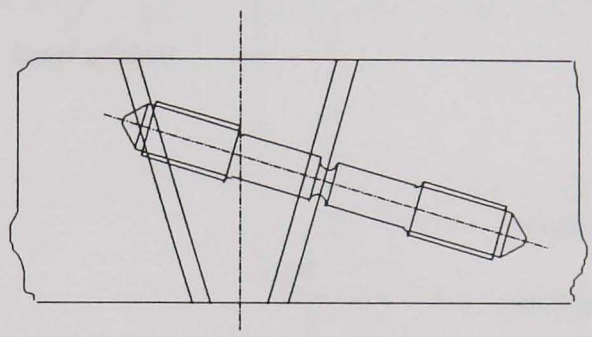

(c) B view : position of notch bar

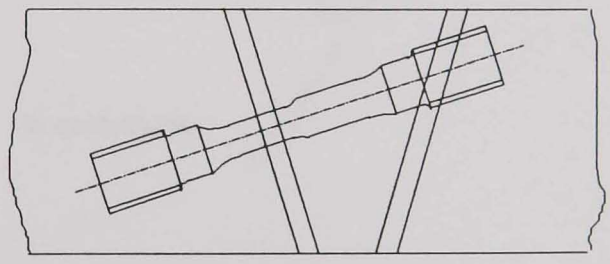

(d) B view : position of waisted specimen

Fig. 5.9 Machining of cross-weld specimens.

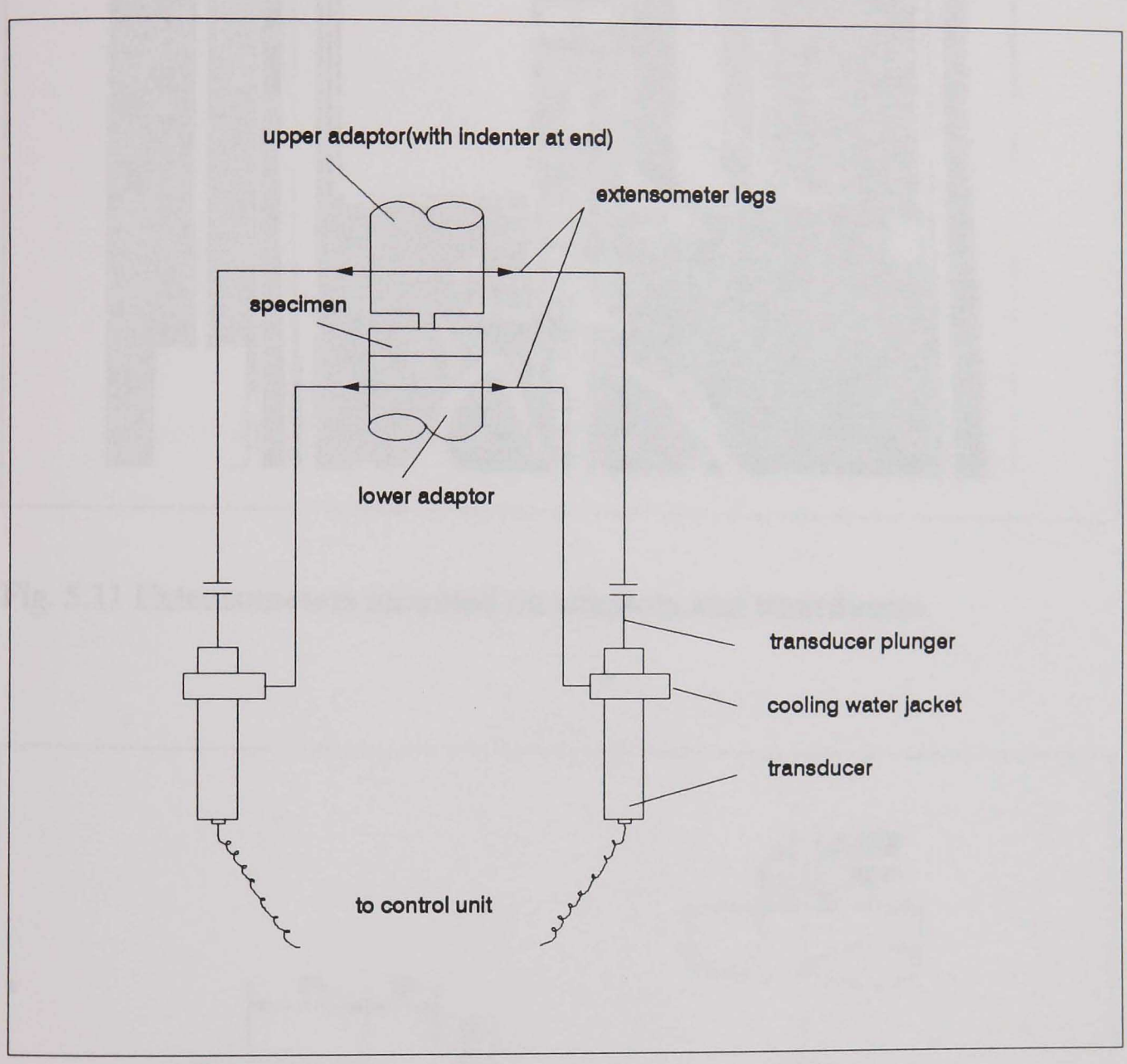

Fig. 5.10 Schematic diagram of the indentation displacement measuring system.

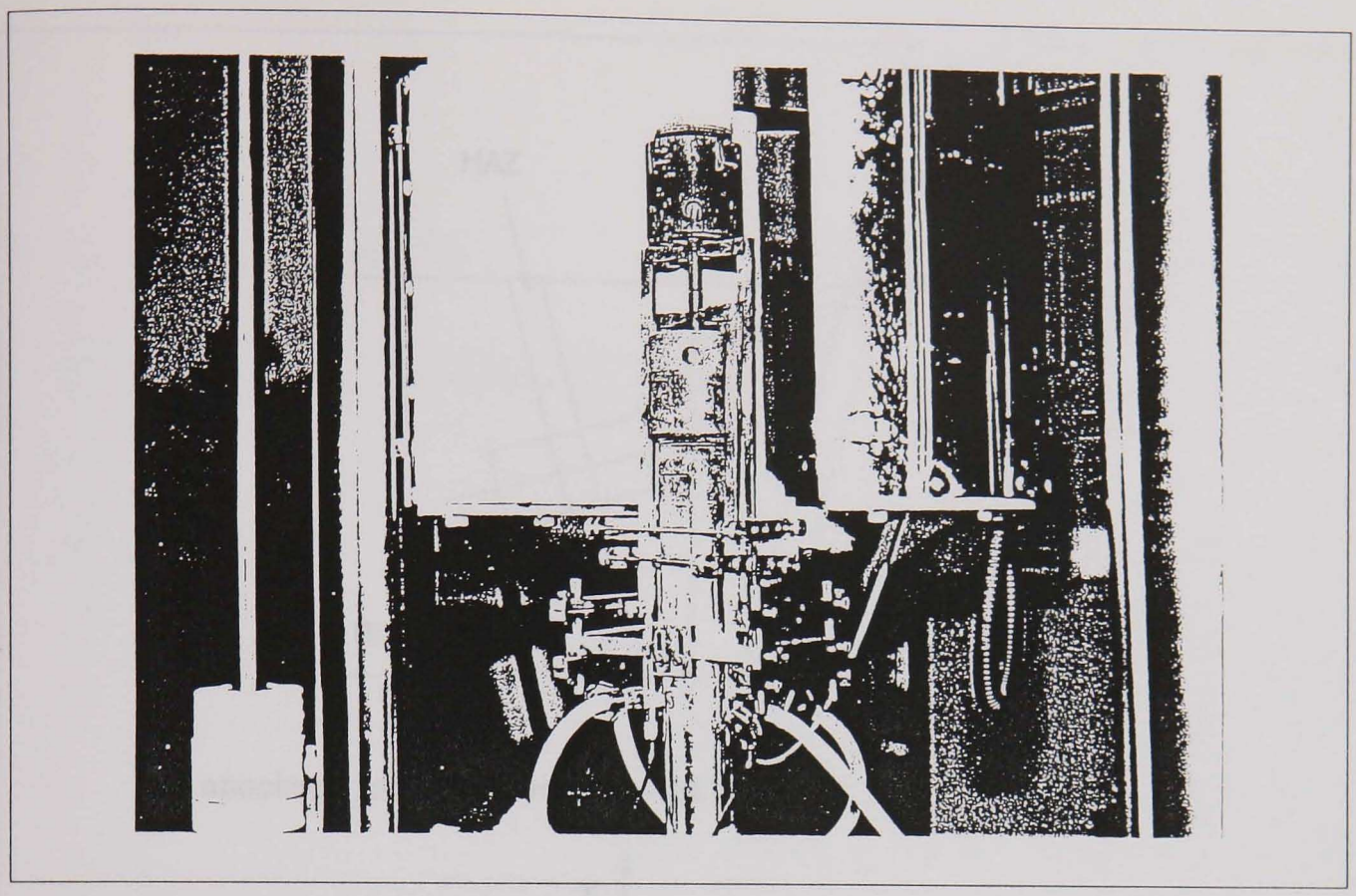

Fig. 5.11 Extensometers mounted on adaptors and transducers.

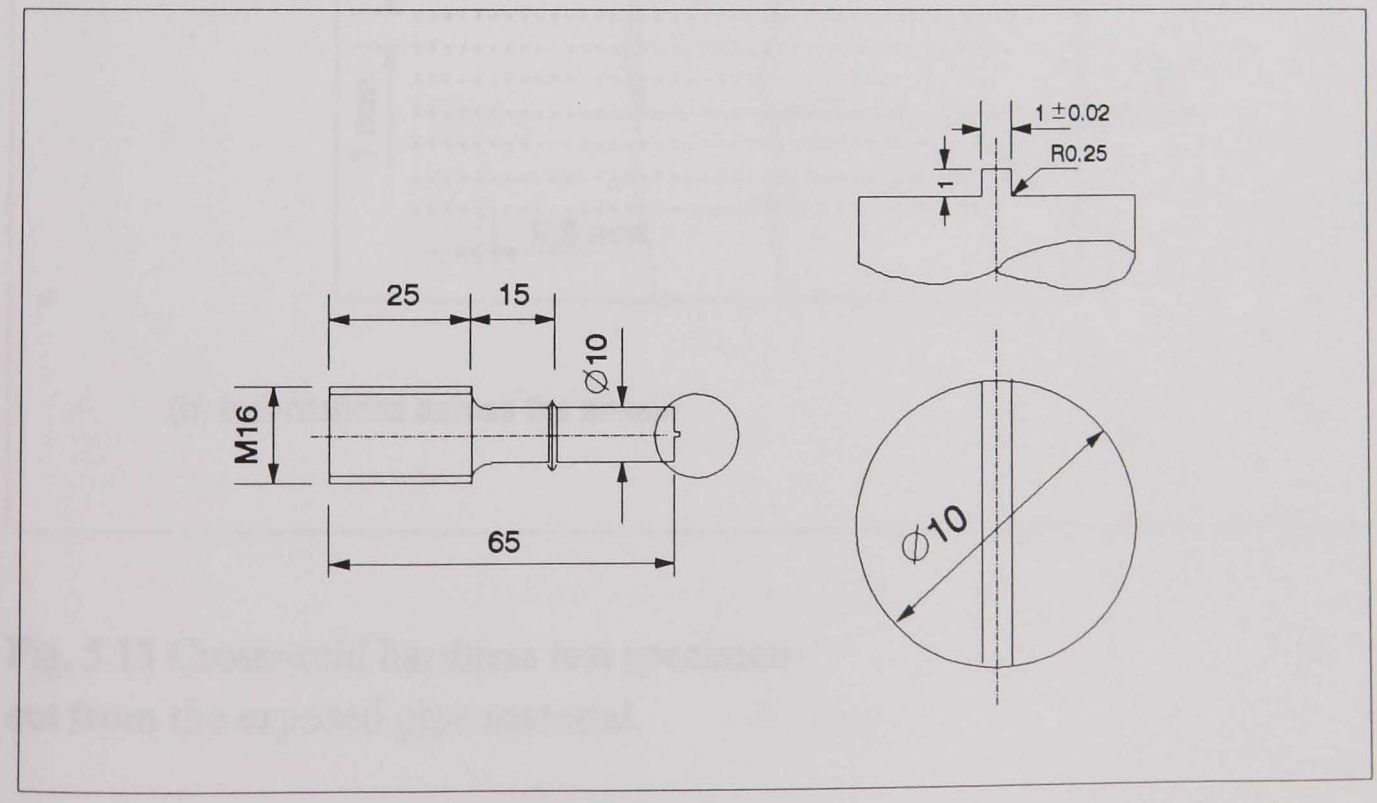

Fig. 5.12 Dimensions of the rectangular indenter (mm).

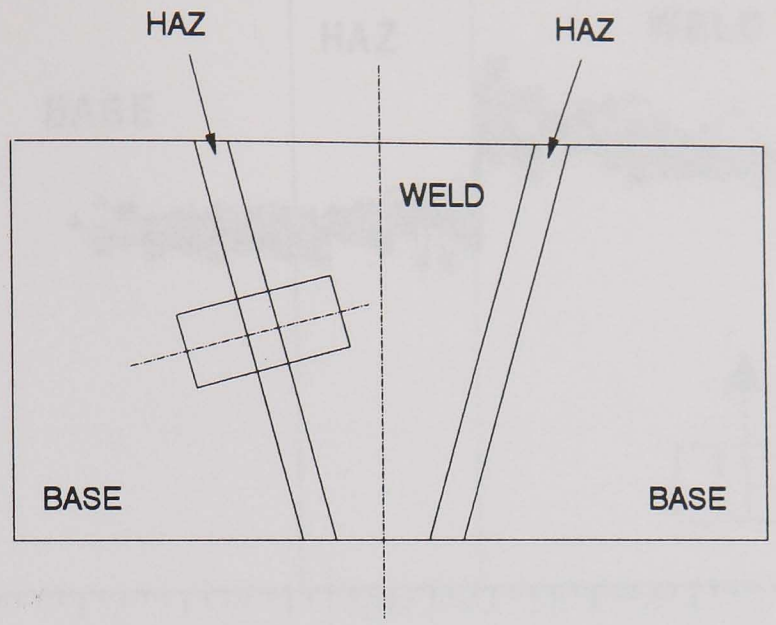

(a) specimen removed from the weld

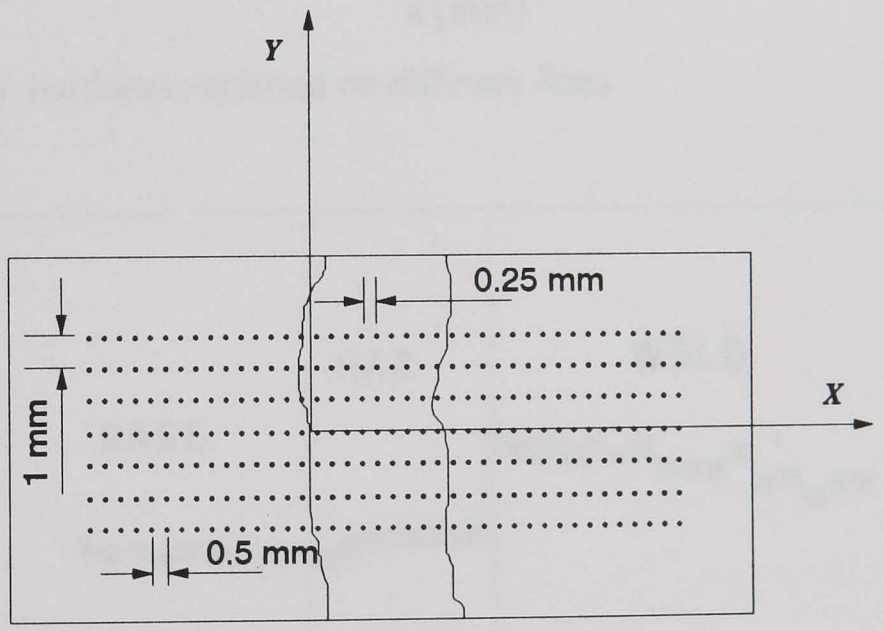

(b) indentations across the zones

Fig. 5.13 Cross-weld hardness test specimen cut from the exposed pipe material.

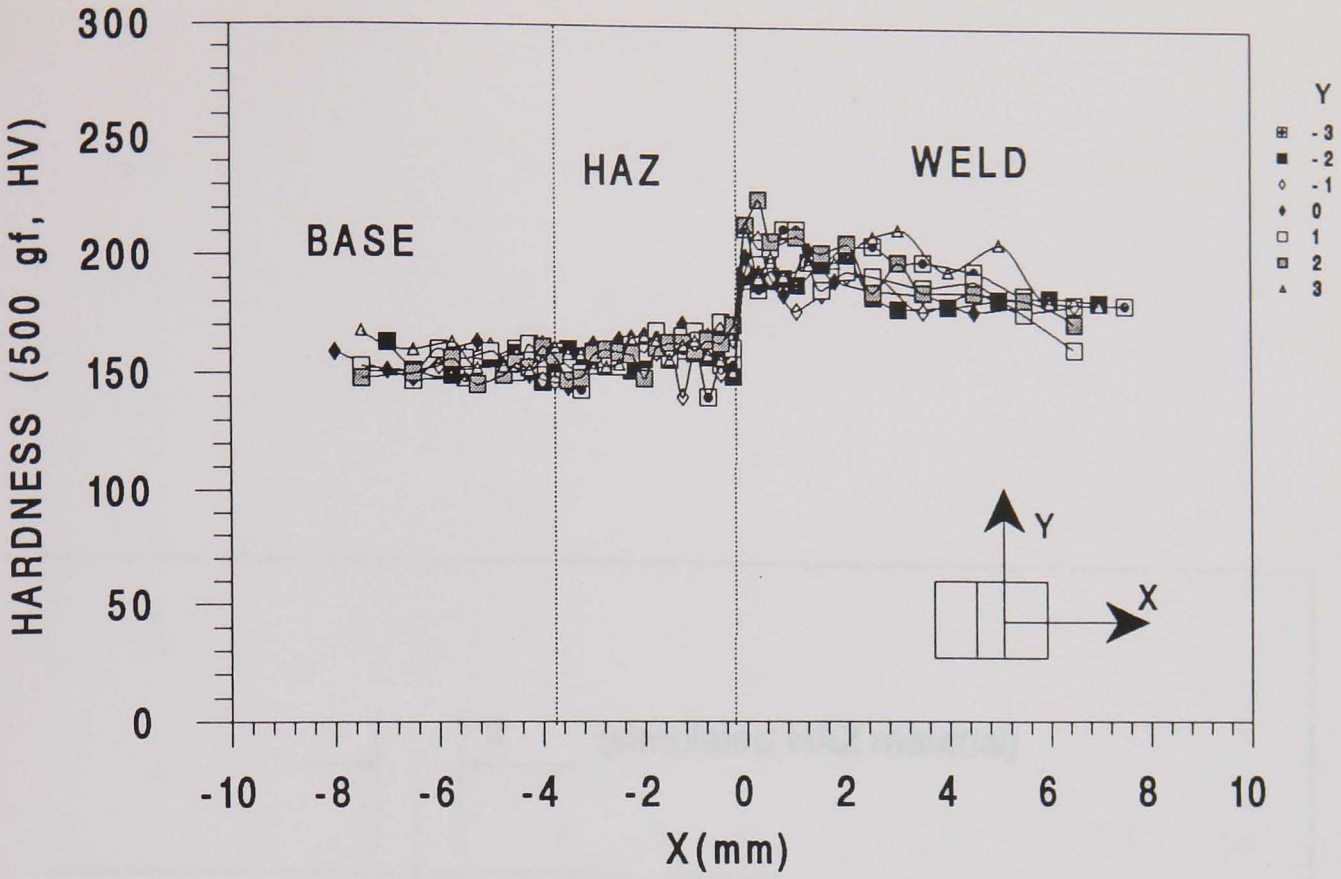

(a) hardness variation on different lines

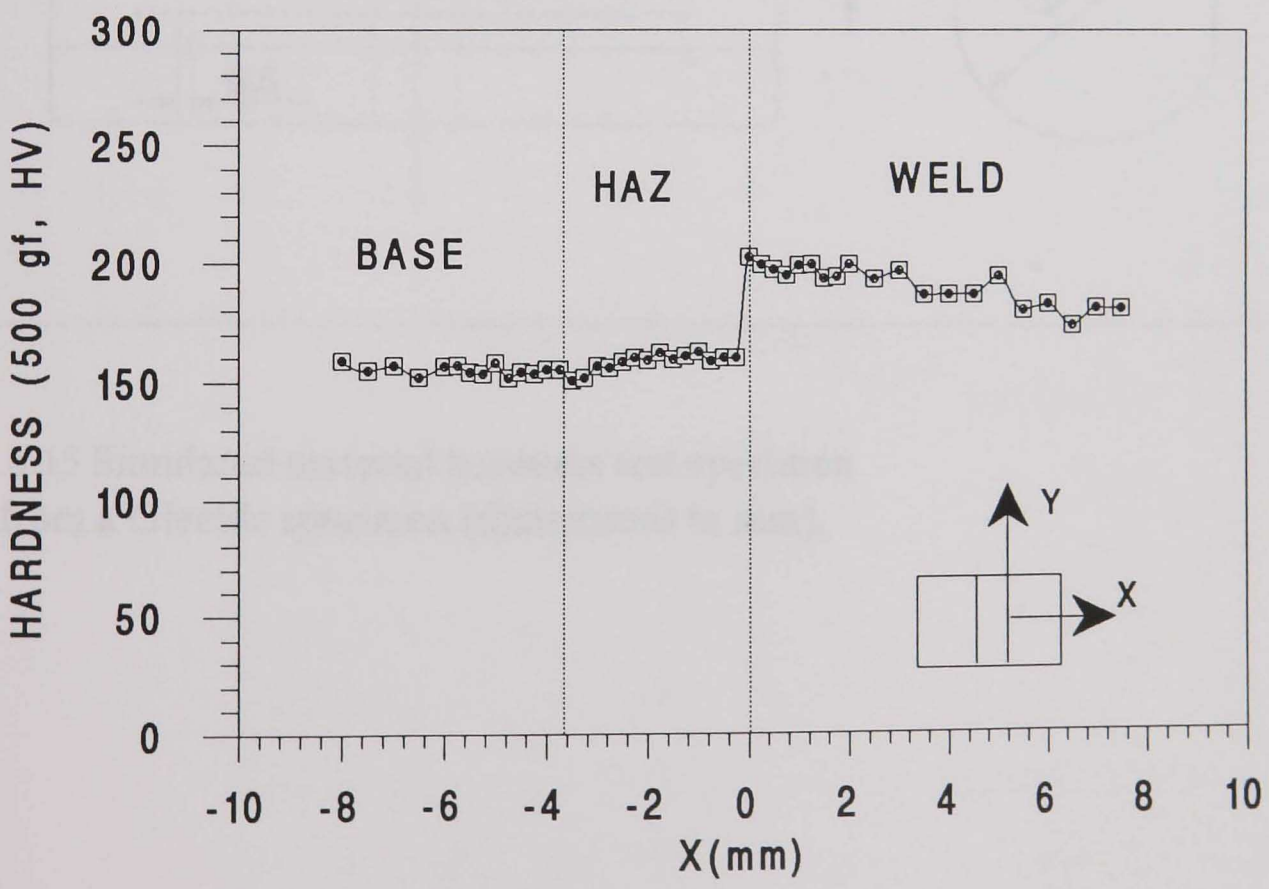

(b) averaged hardness

Fig. 5.14 Hardness variation across the material zones of the exposed weldment.

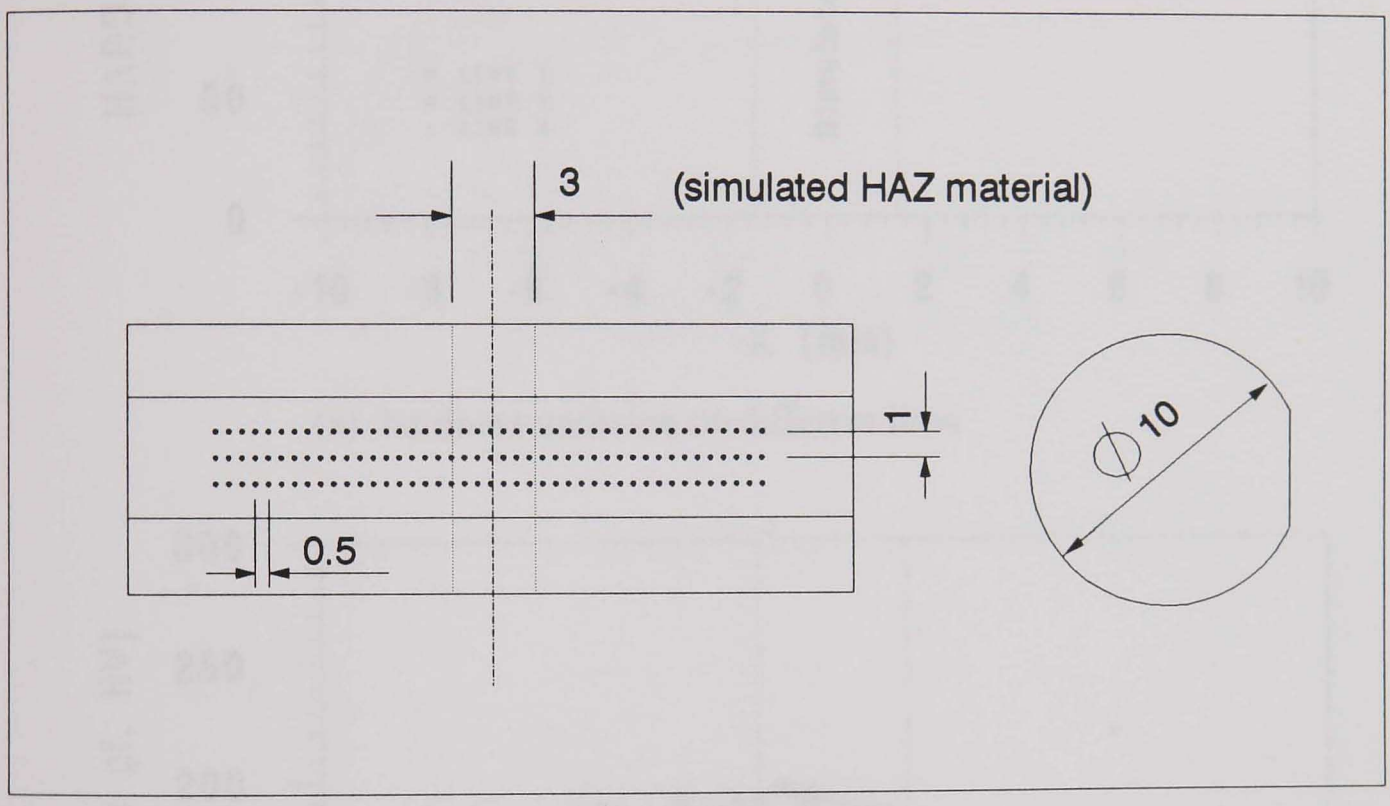

Fig. 5.15 Simulated material hardness test specimen cut from a Gleeble specimen (dimensions in mm).

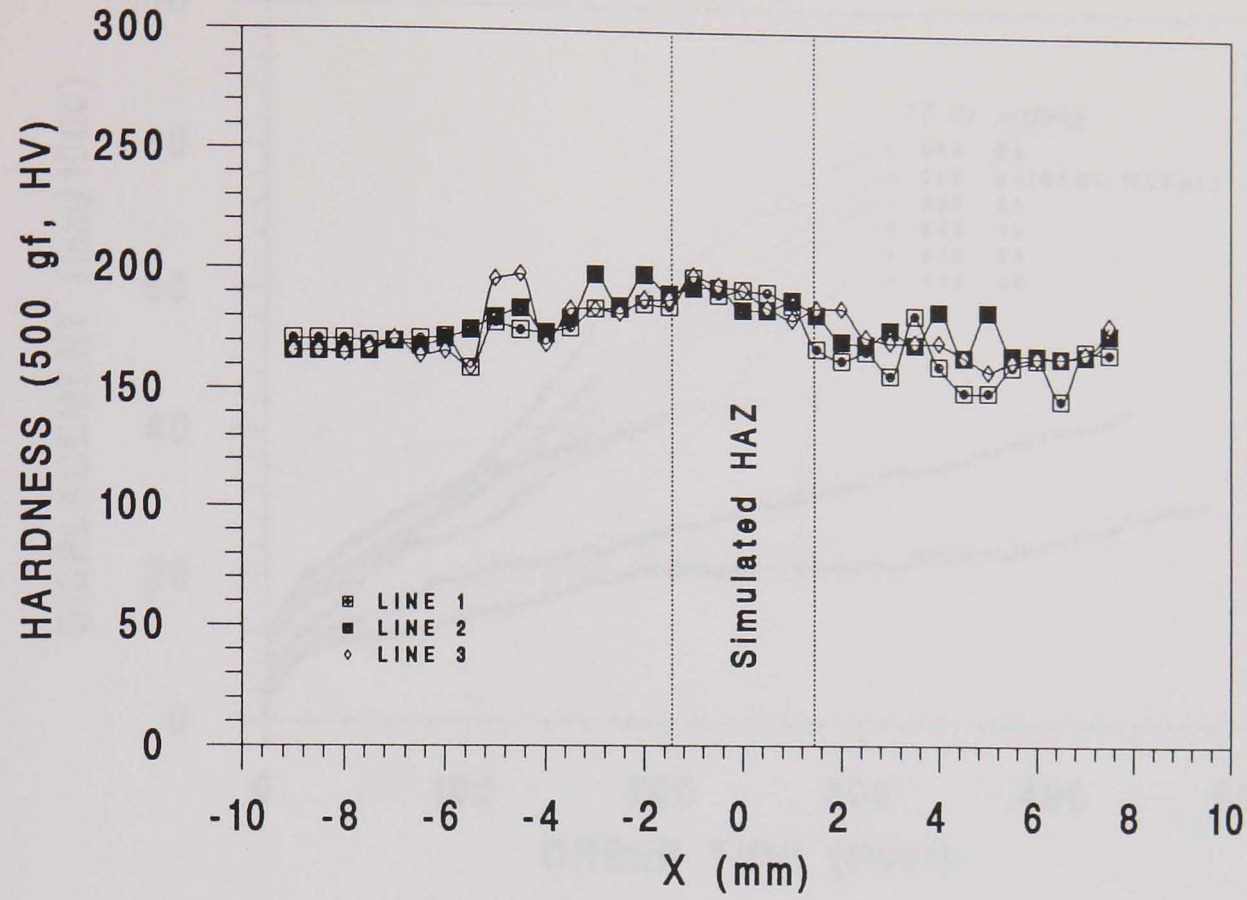

(a) hardness variation on different lines

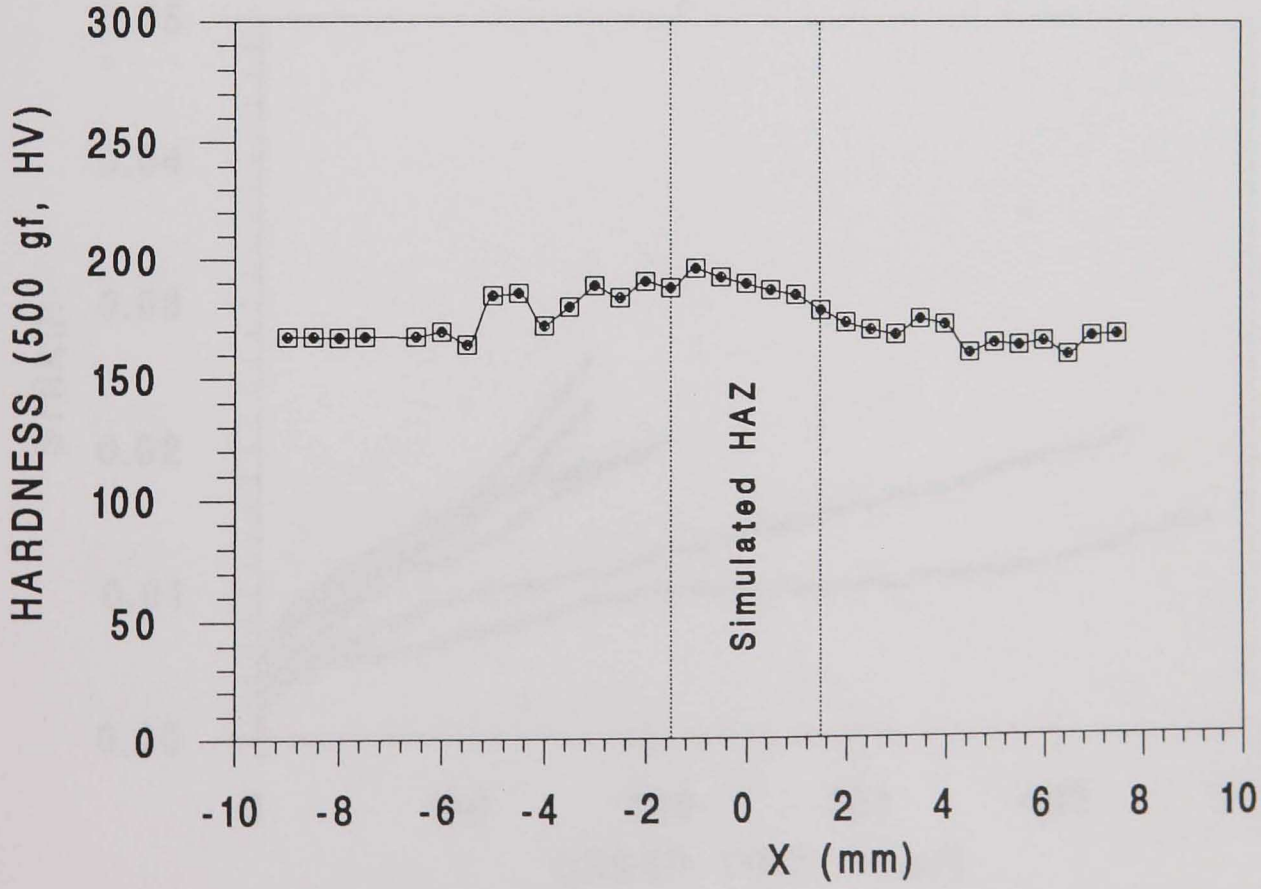

(b) averaged hardness

Fig. 5.16 Hardness variation across the simulated HAZ of a Gleeble specimen.

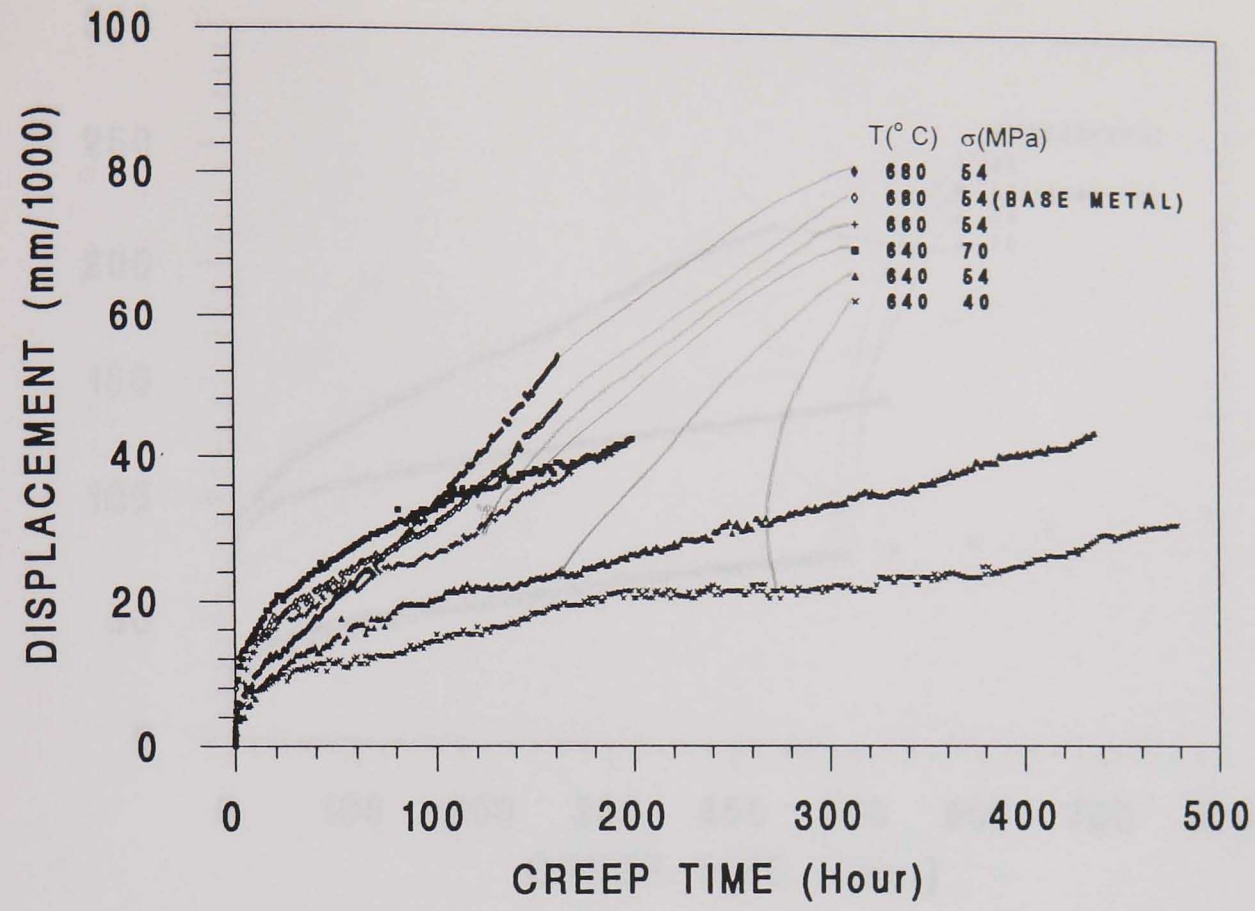

(a) displacement

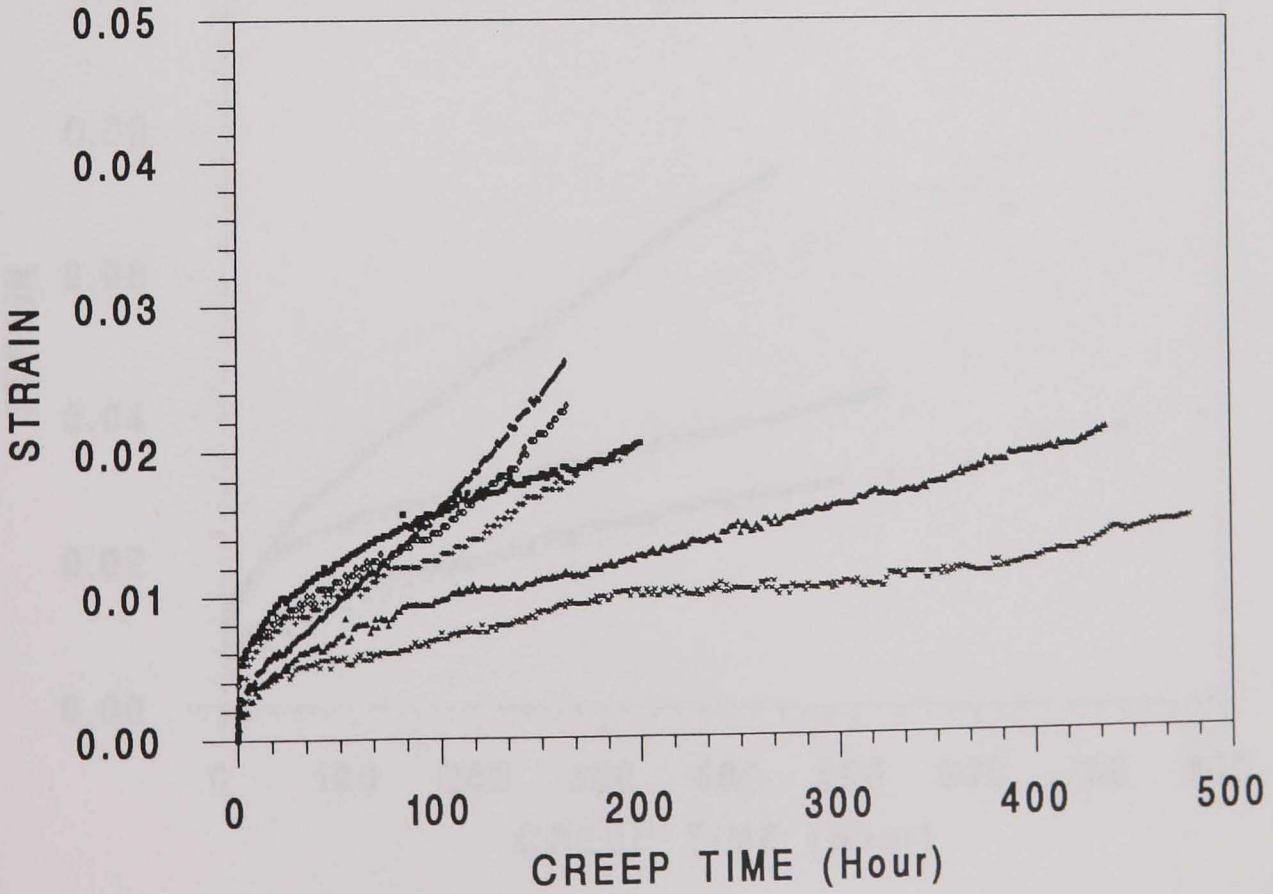

(b) strain

Fig. 5.17 Creep indentation displacement and converted strain of the simulated HAZ material.

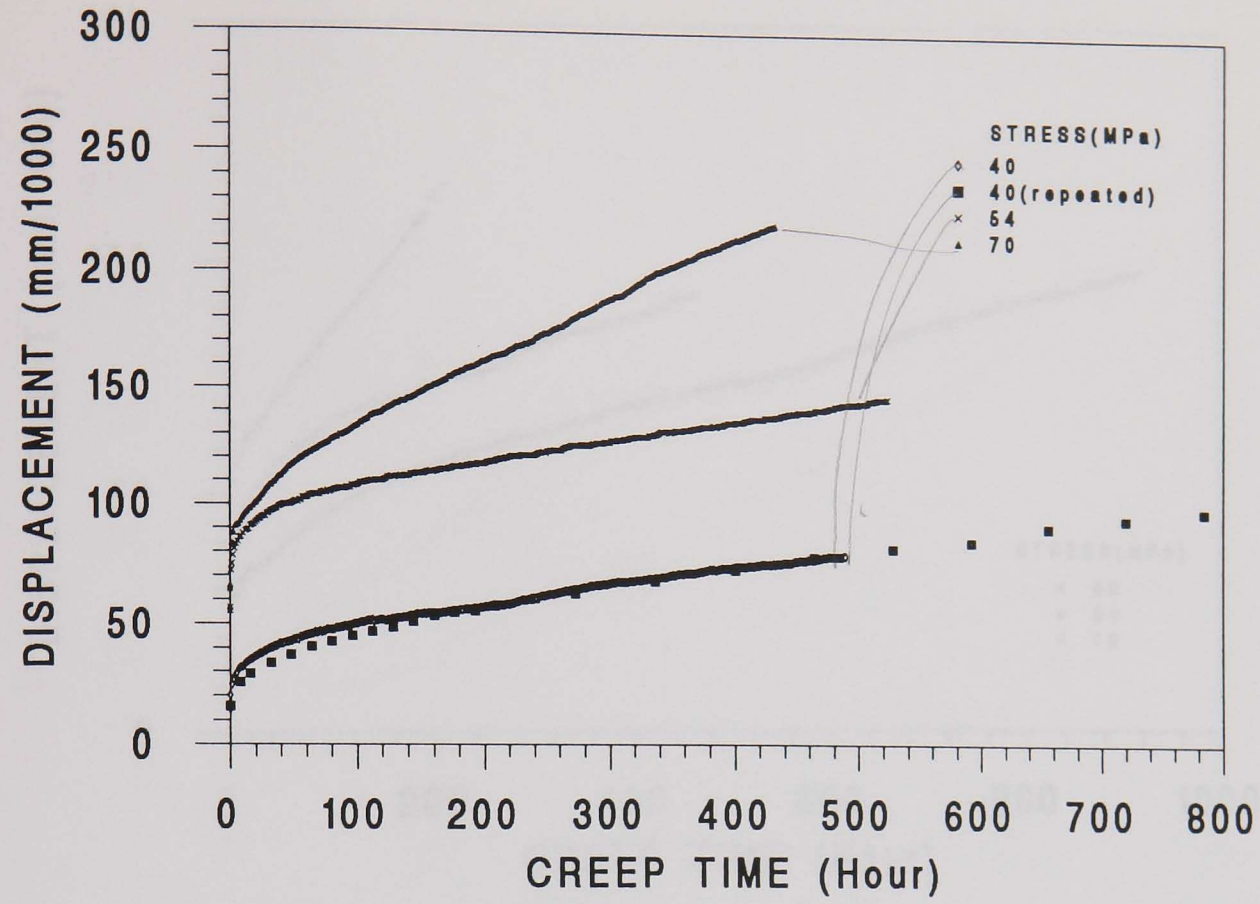

(a) displacement

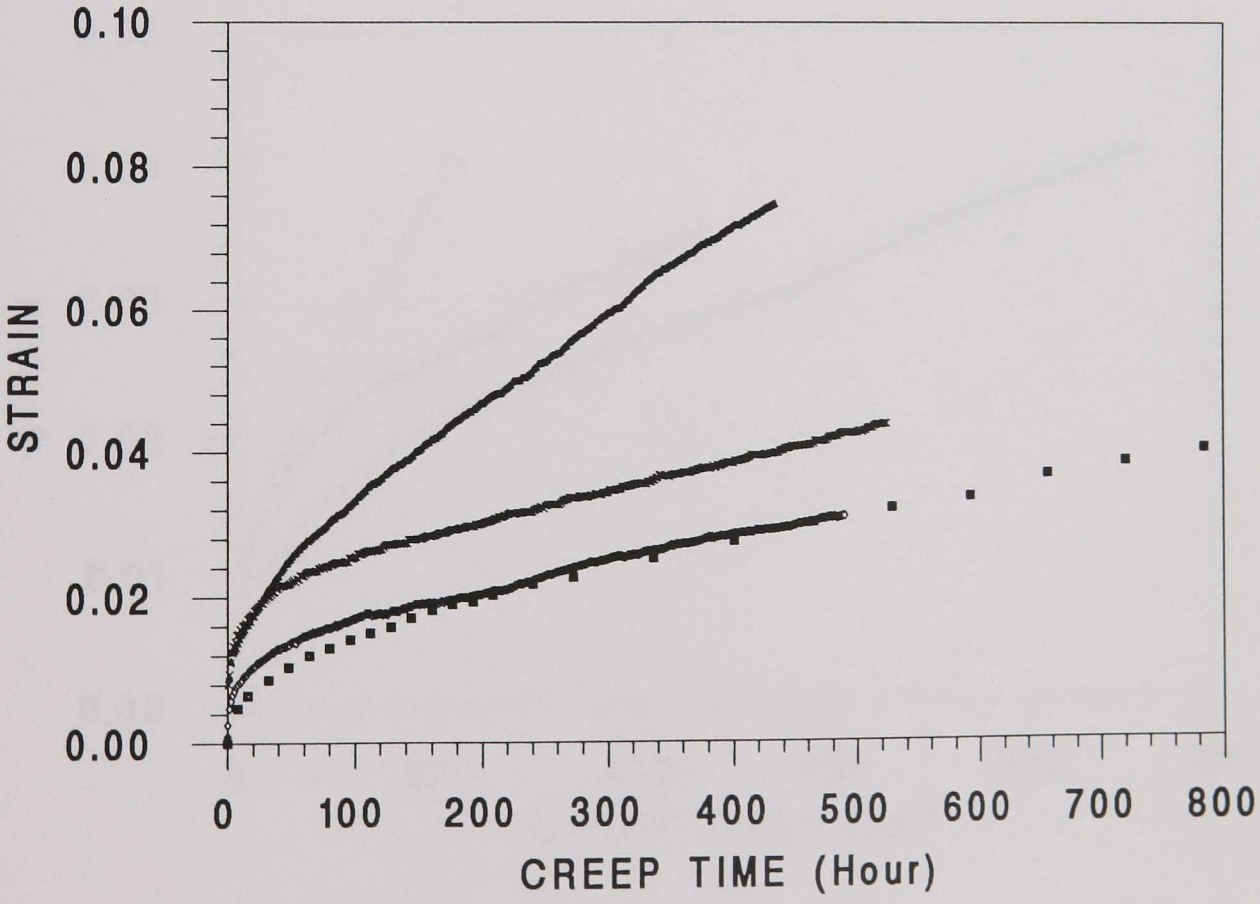

(b) strain

Fig. 5.18 Creep indentation displacement and converted strain of the aged parent material at 640° C.

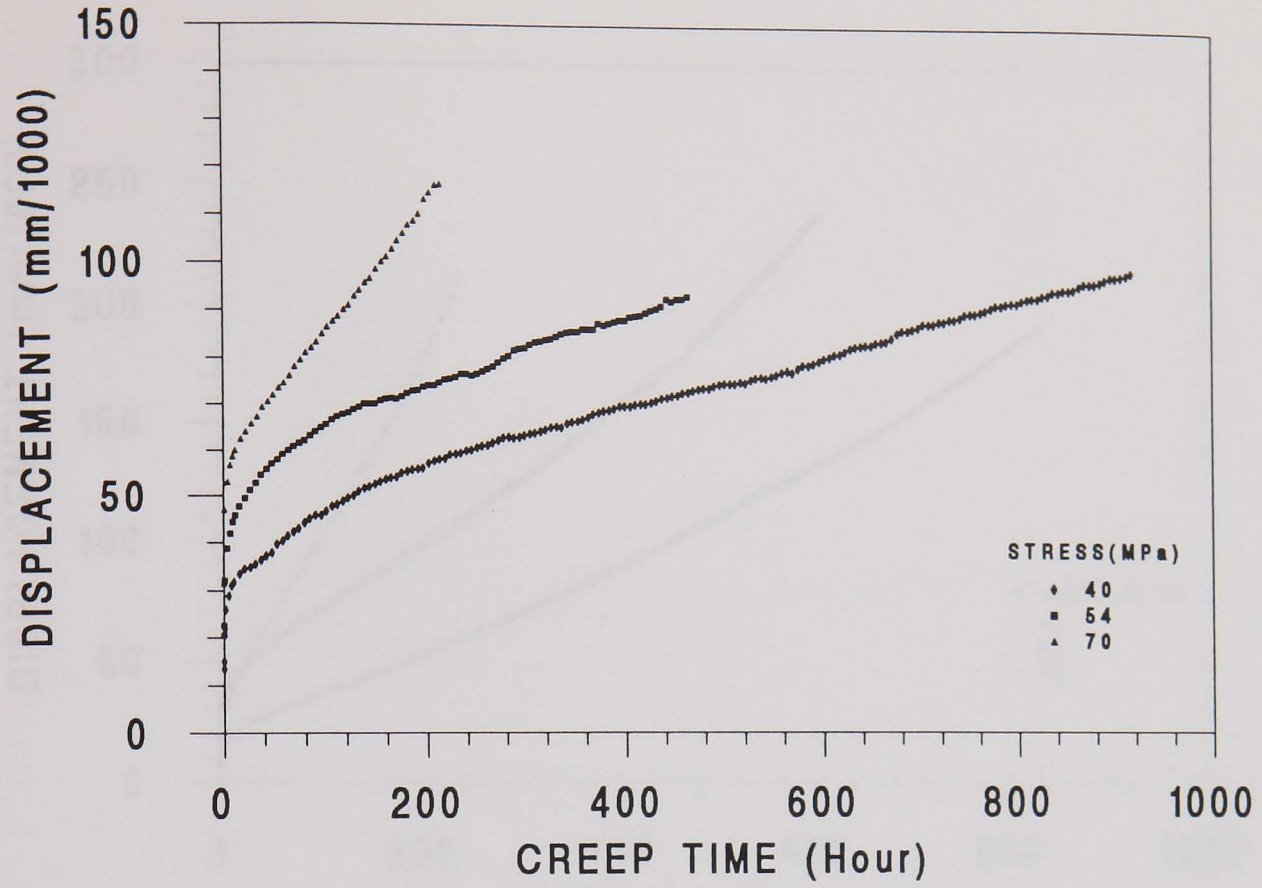

(a) displacement

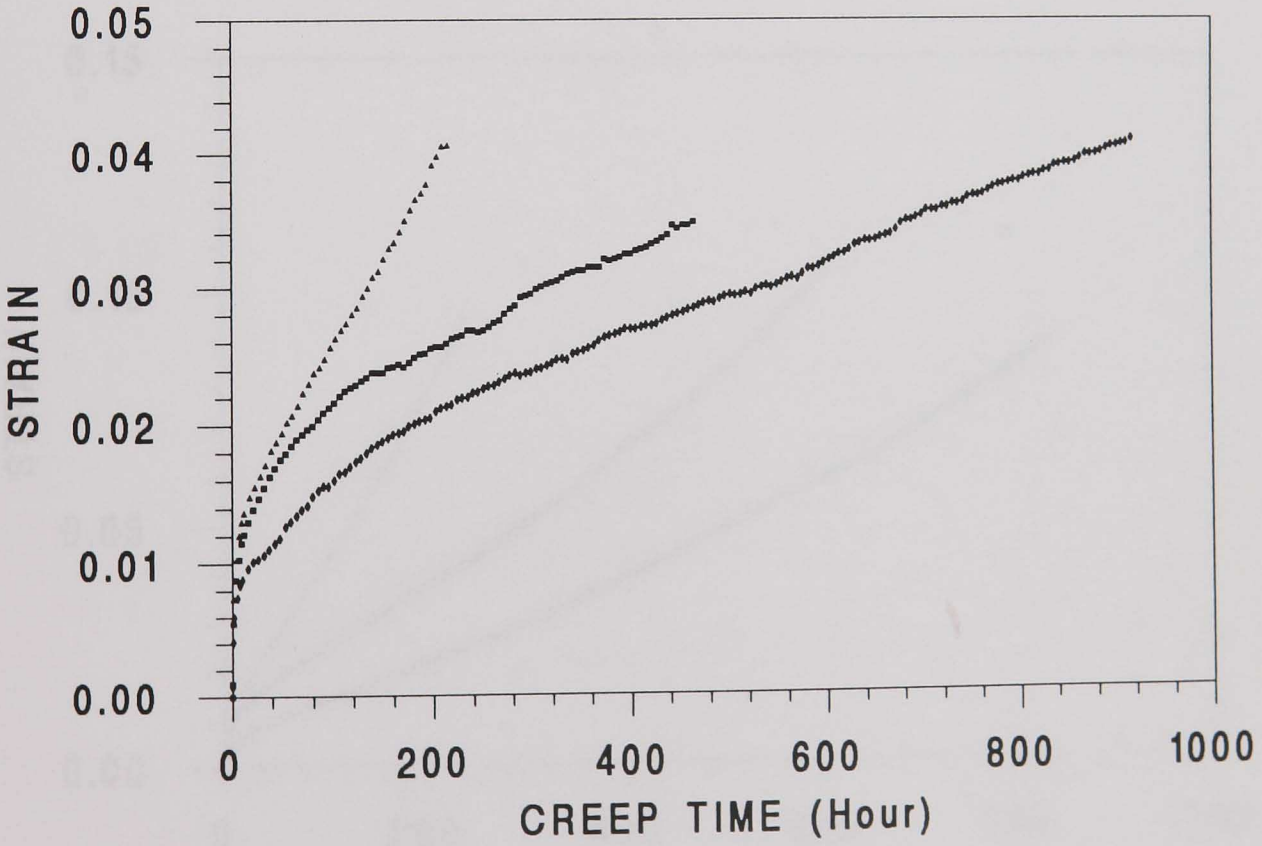

(b) strain

Fig. 5.19 Creep indentation displacement and converted strain of the aged weld material at 640° C.

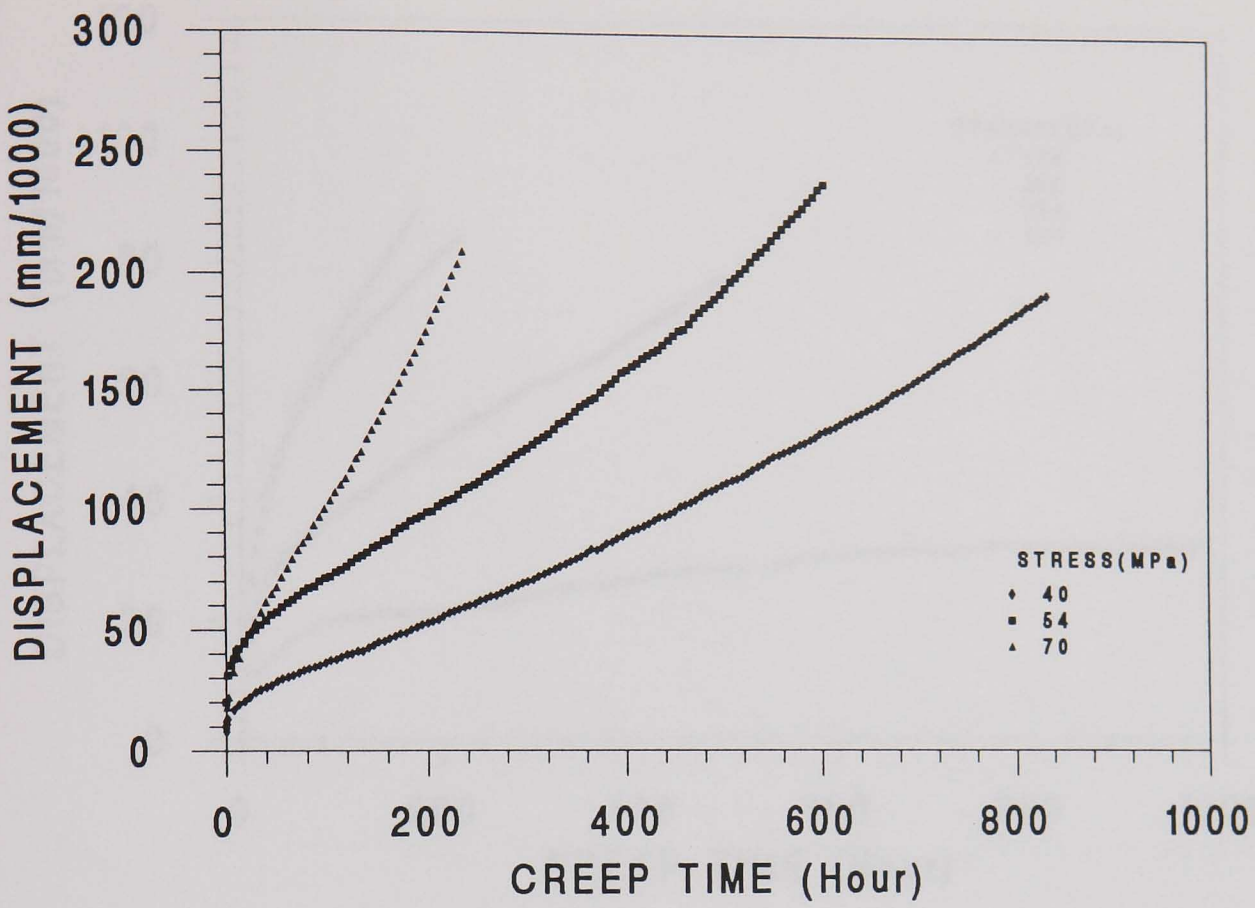

(a) displacement

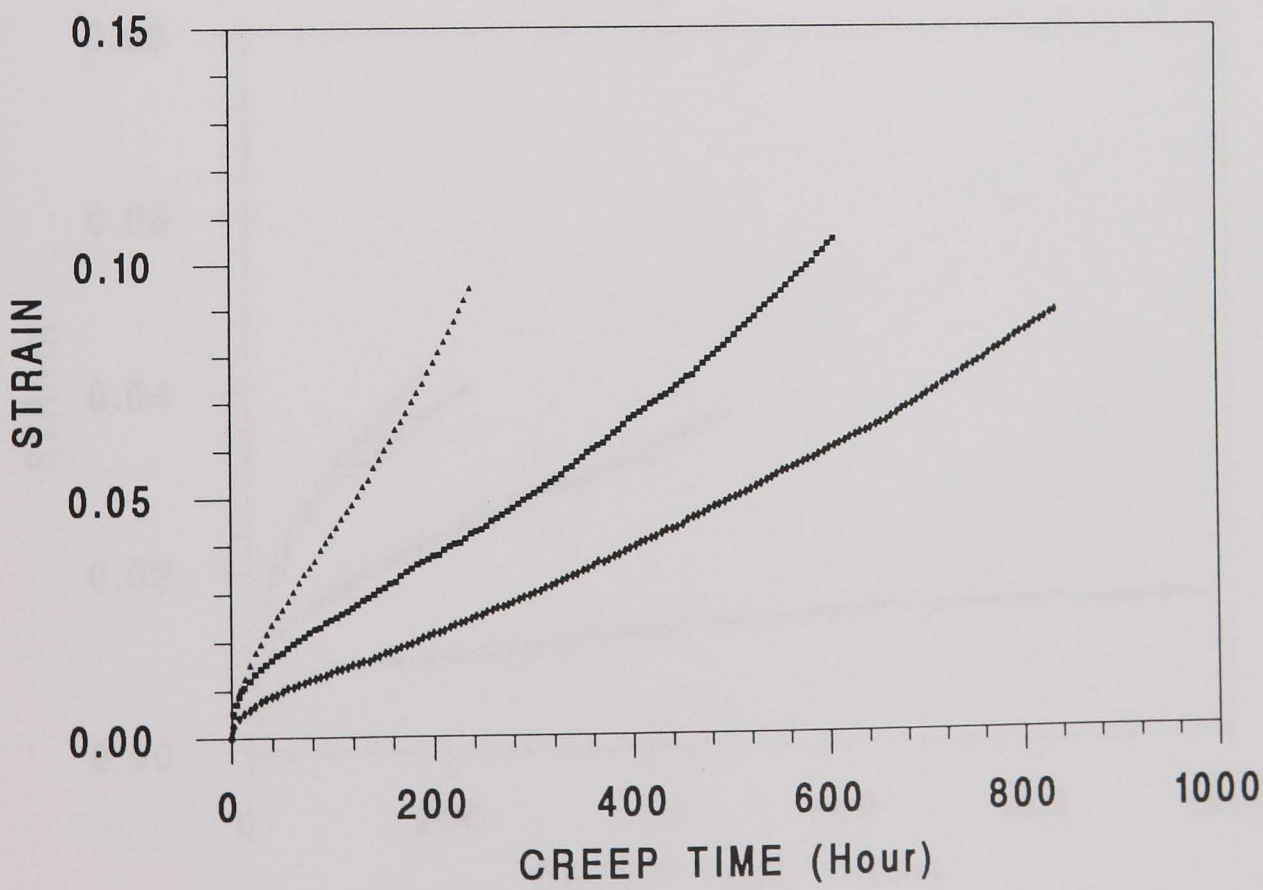

(b) strain

Fig. 5.20 Creep indentation displacement and converted strain of the aged HAZ material at 640° C.

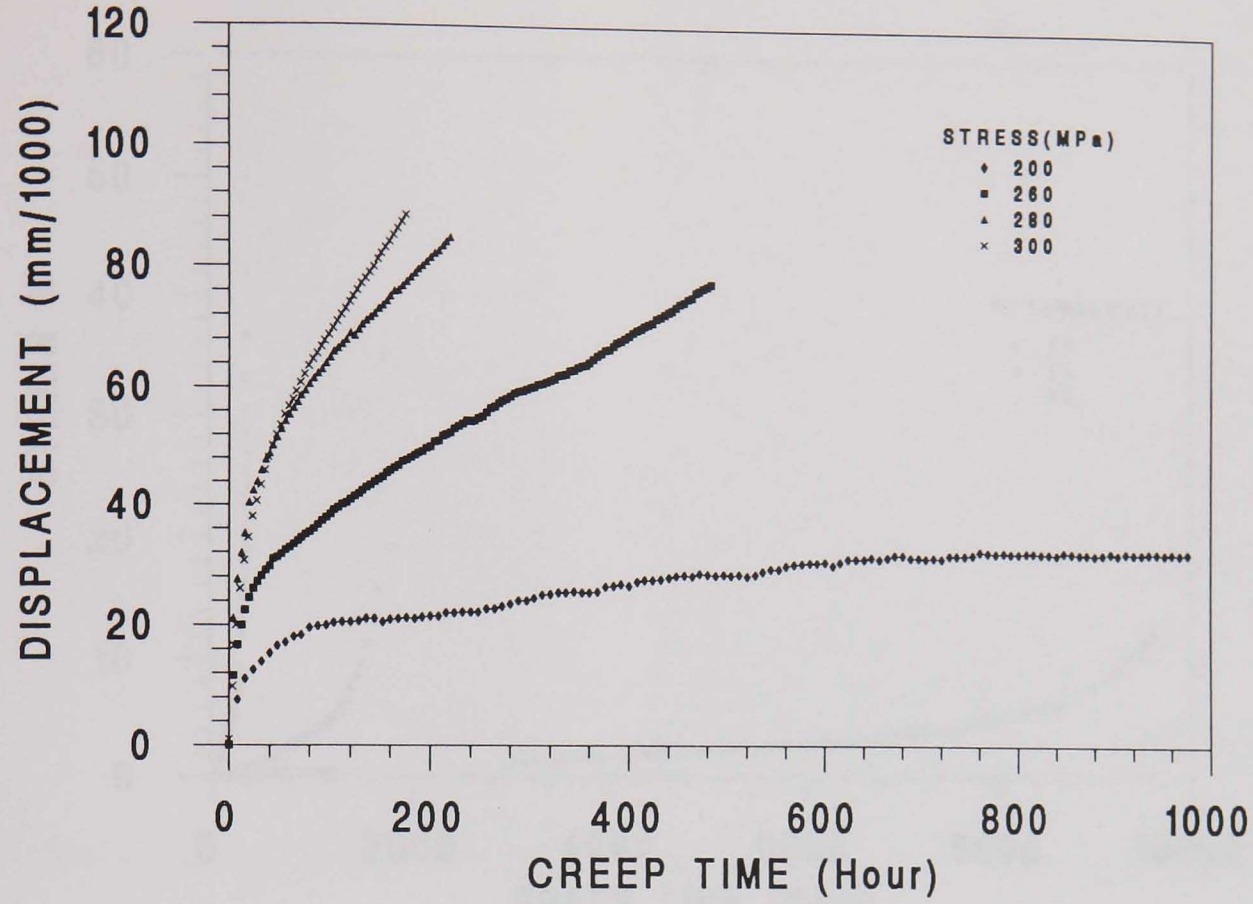

(a) displacement

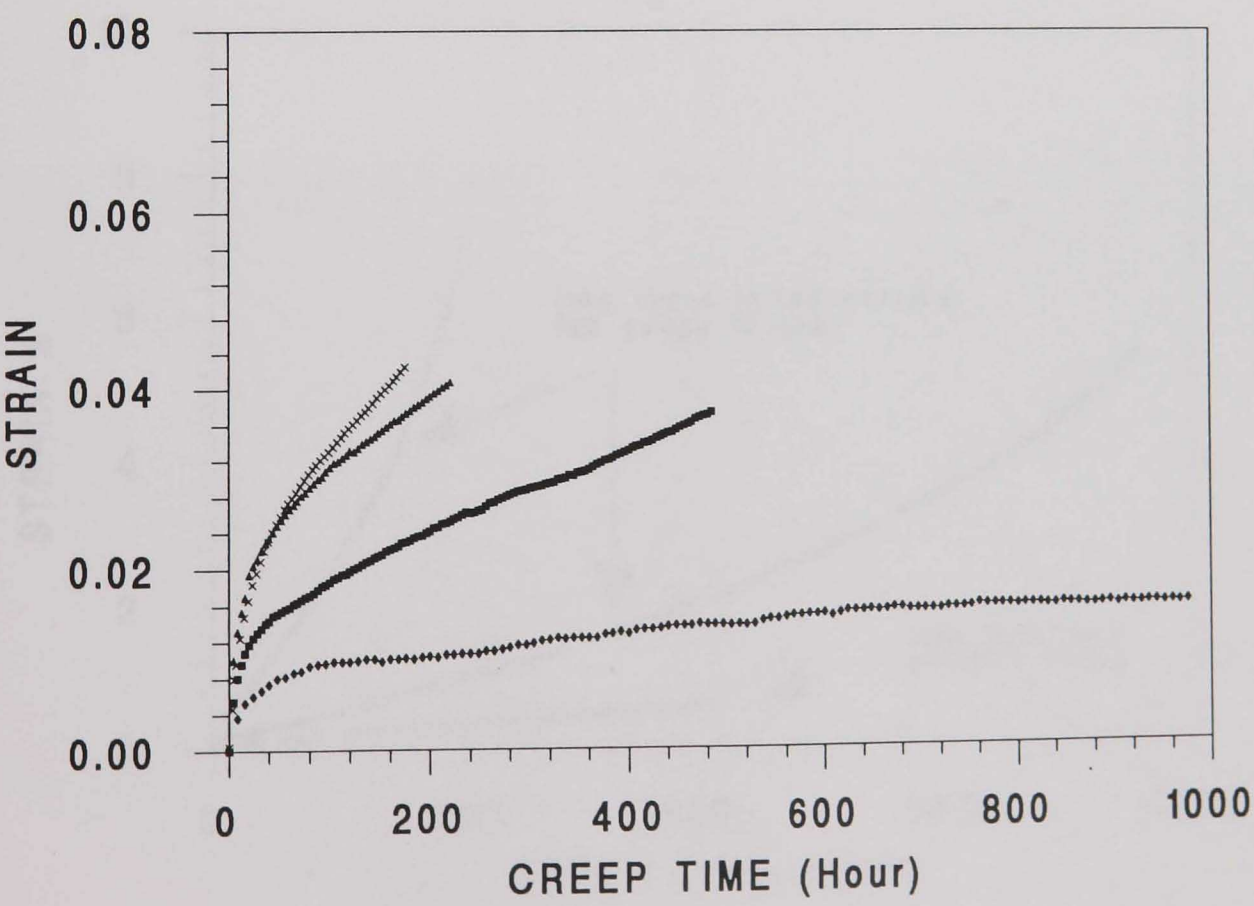

(b) strain

Fig. 5.21 Creep indentation displacement and converted strain of 316 stainless steel at 600° C.

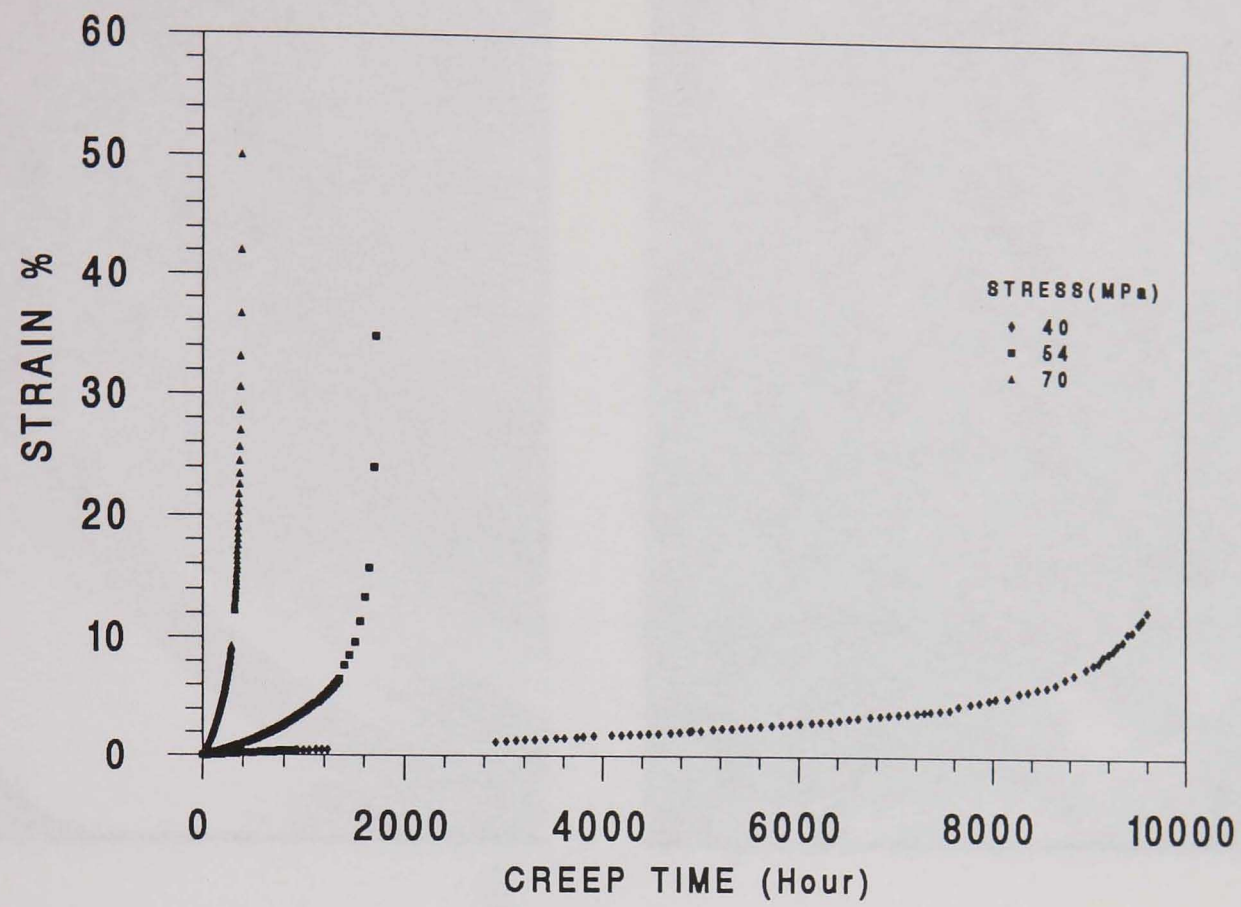

(a) parent material

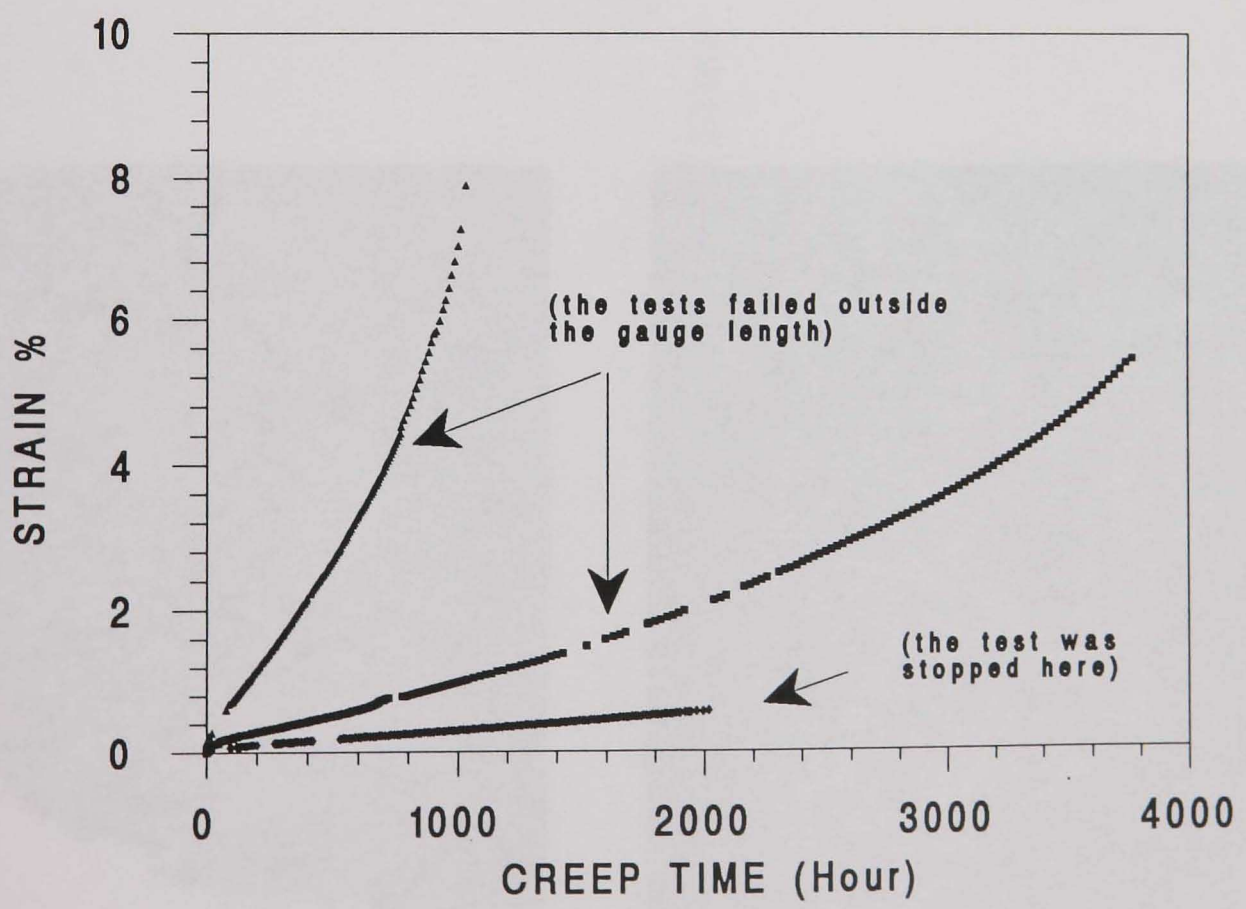

(b) weld material

Fig. 5.22 Creep strain of the aged parent and weld material uniaxial tests at 640° C.

5.23(a)

5.23(b)

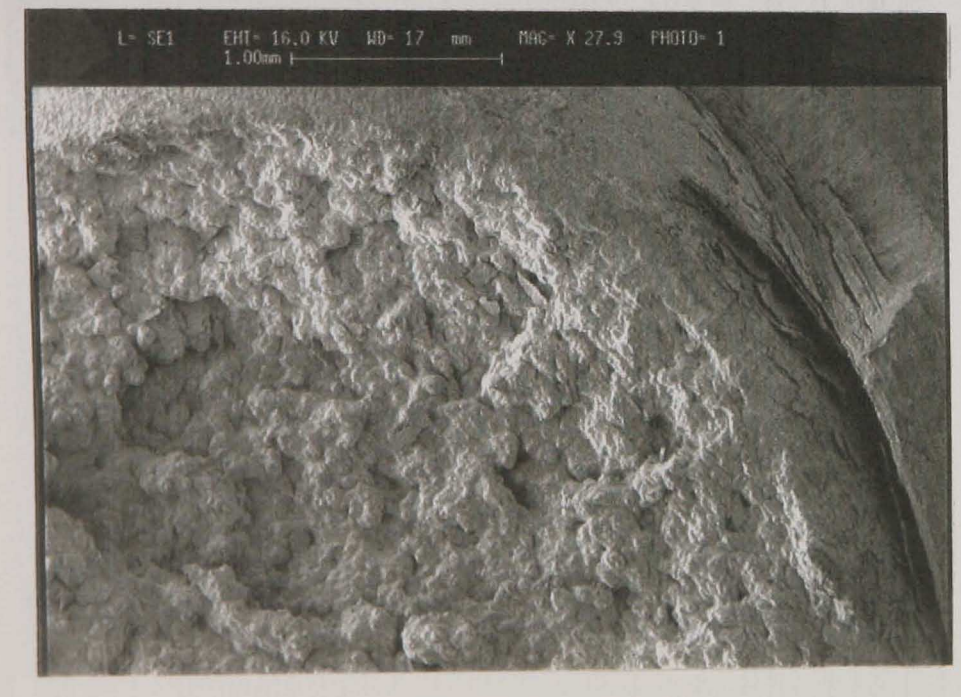

5.23(c)

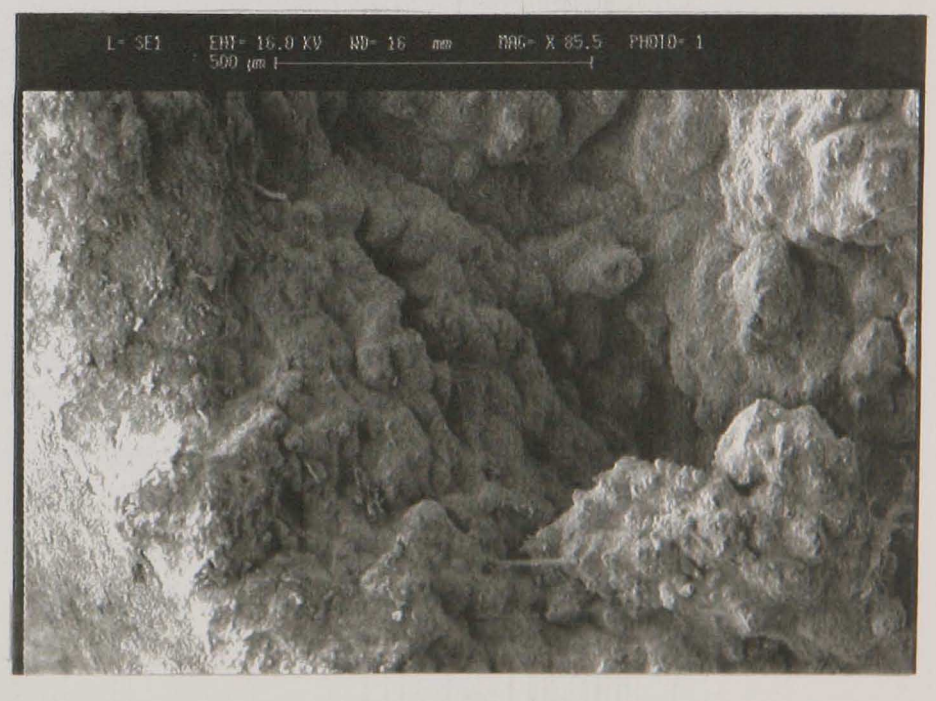

5.23(d)

5.23(e)

5.23(f)

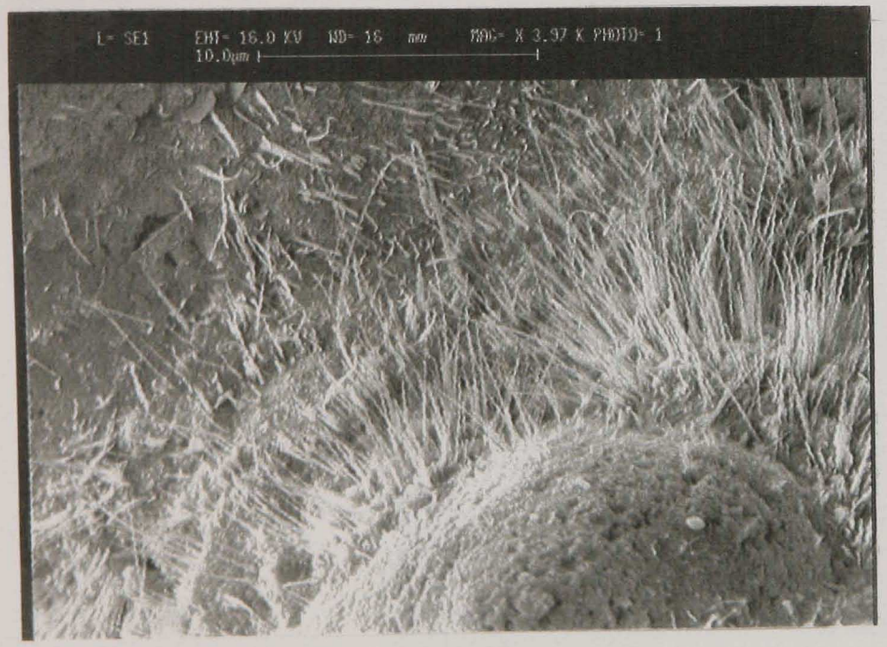

5.23(g)

Fig. 5.23 Photographs taken from the fracture surface of the cross-weld waisted specimen tested at 54MPa and 640° C.

(a) macrostructure of failure surface (× 10.8)
(b) oxide coating (× 19.9)
(c) detail of edge area (× 27.9)
(d) detail of central area (× 85.5)
(e) detail of central area (× 116)
(f) detail of one crack showing oxide whiskers (× 746)
(g) oxide growth whiskers (× 3970)

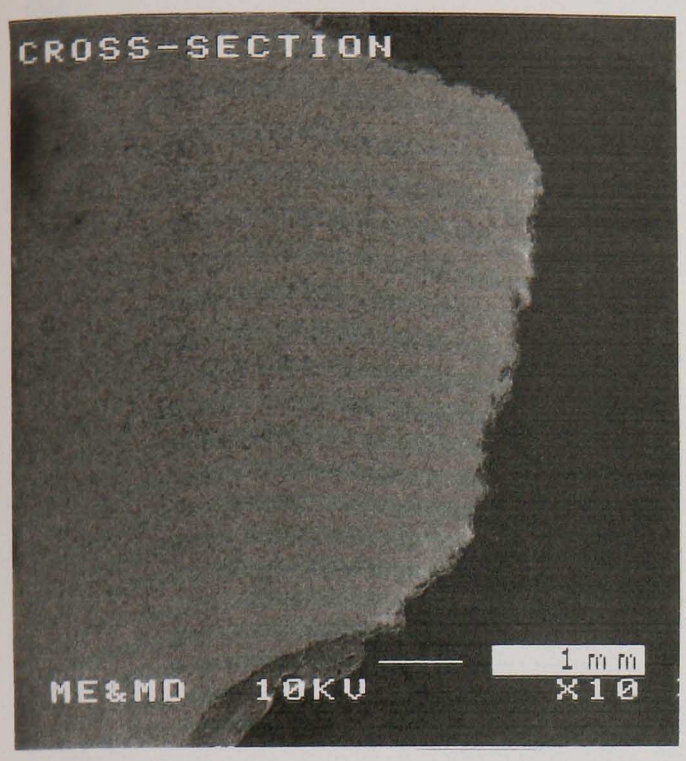

(a) notched bar, parent part

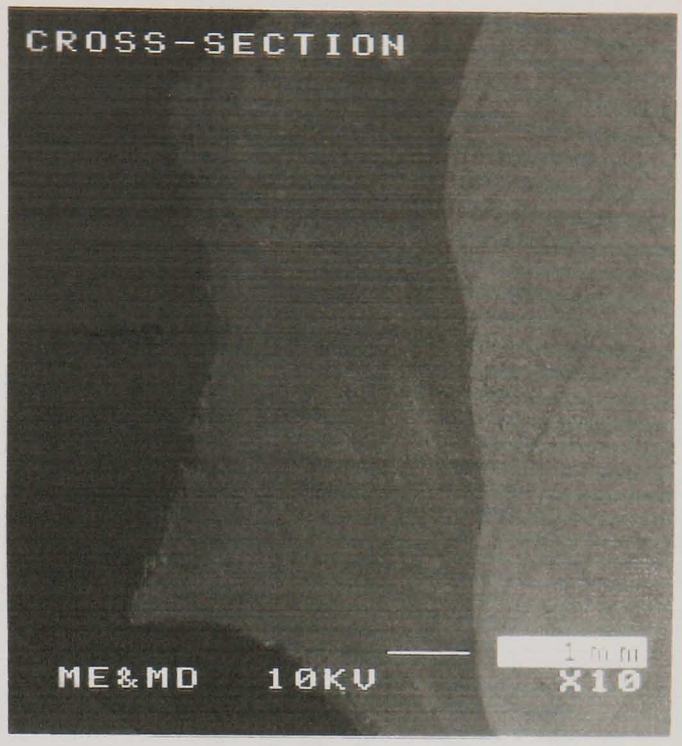

(b) notched bar, HAZ/weld part

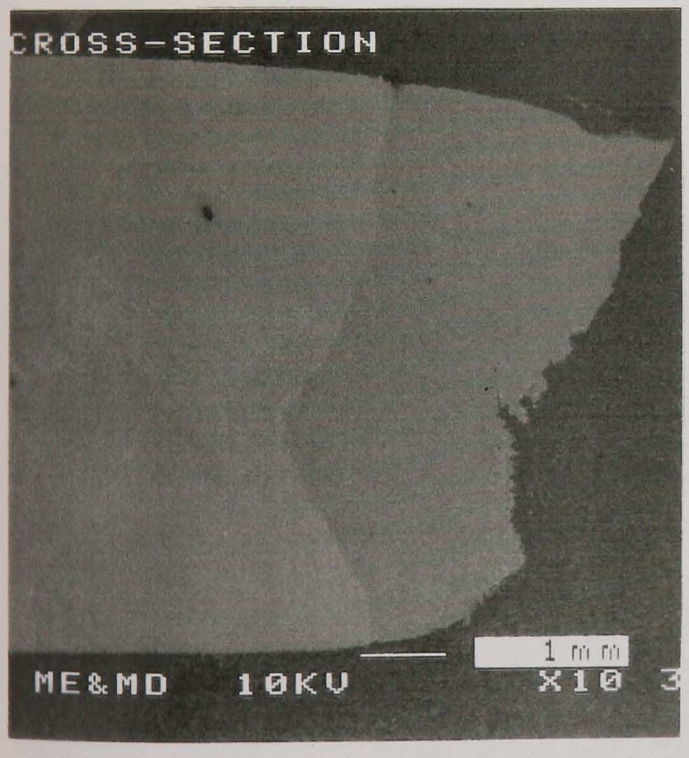

(c) waisted specimen, weld/HAZ part

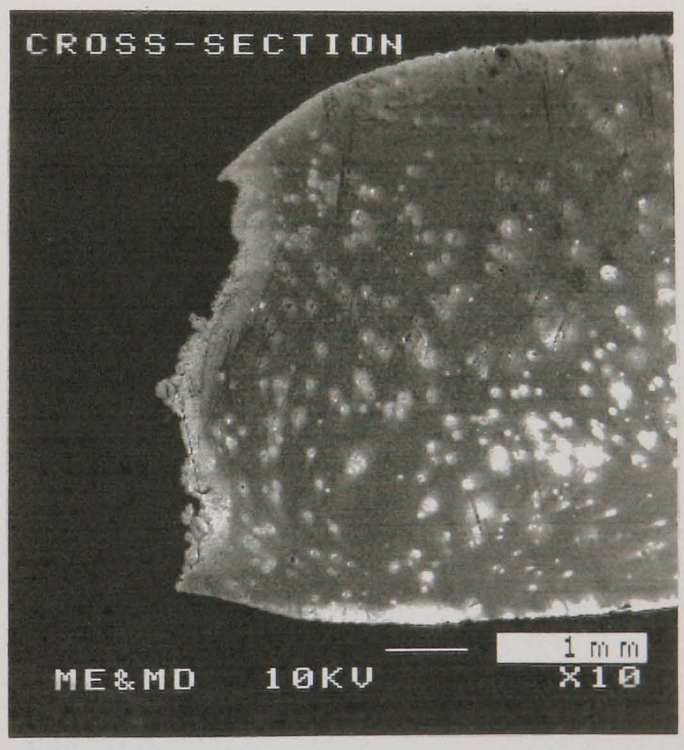

(d) waisted specimen, parent part

Fig. 5.24 Photographs (× 10) taken from the sectioned surfaces showing the failure position of the cross-weld notched and waisted specimens tested at 54MPa and 640° C.

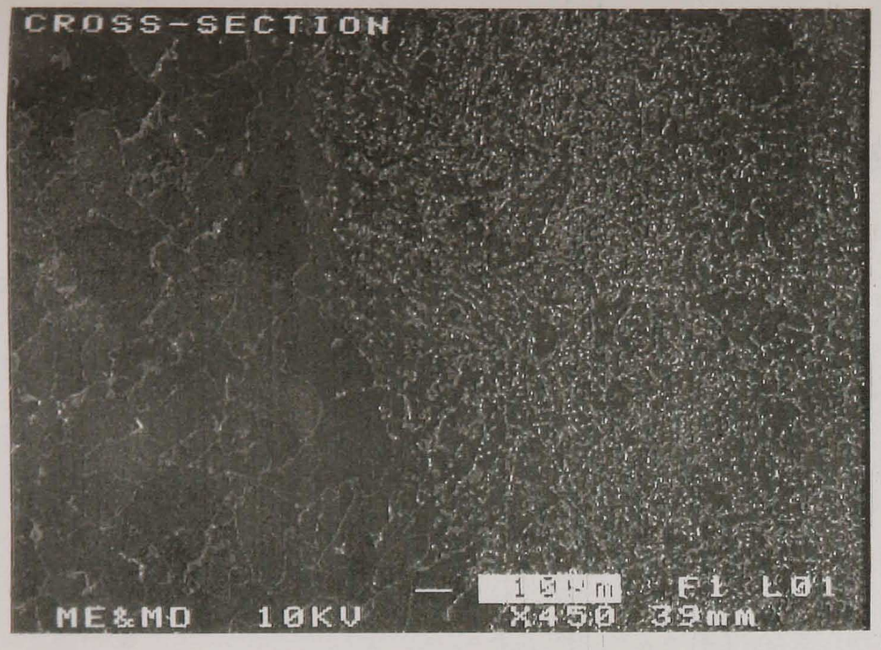

(a)

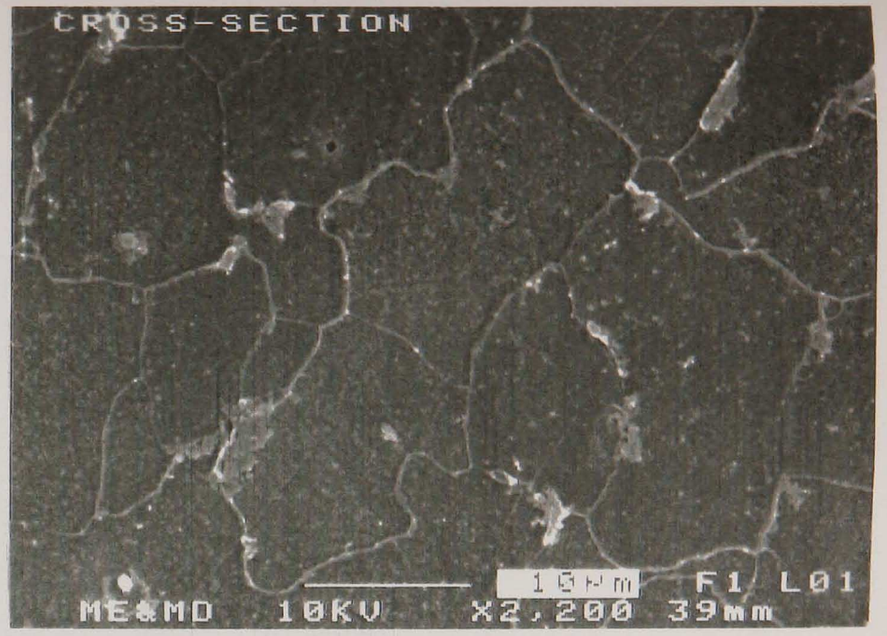

(b)

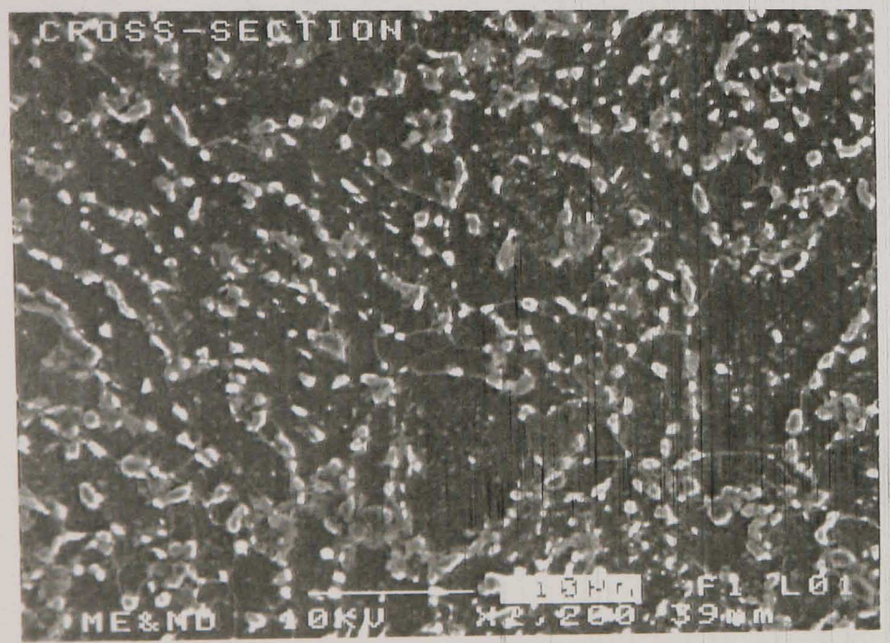

(c)

Fig. 5.25 Photographs showing the HAZ/weld material boundary (fusion line) and the microstructures of HAZ and weld materials, taken from the sectioned surface of the cross-weld notched bar tested at 54MPa and 640° C.

(a) HAZ/weld boundary (× 450)
(b) HAZ material (× 2200)
(c) weld metal (× 2200)

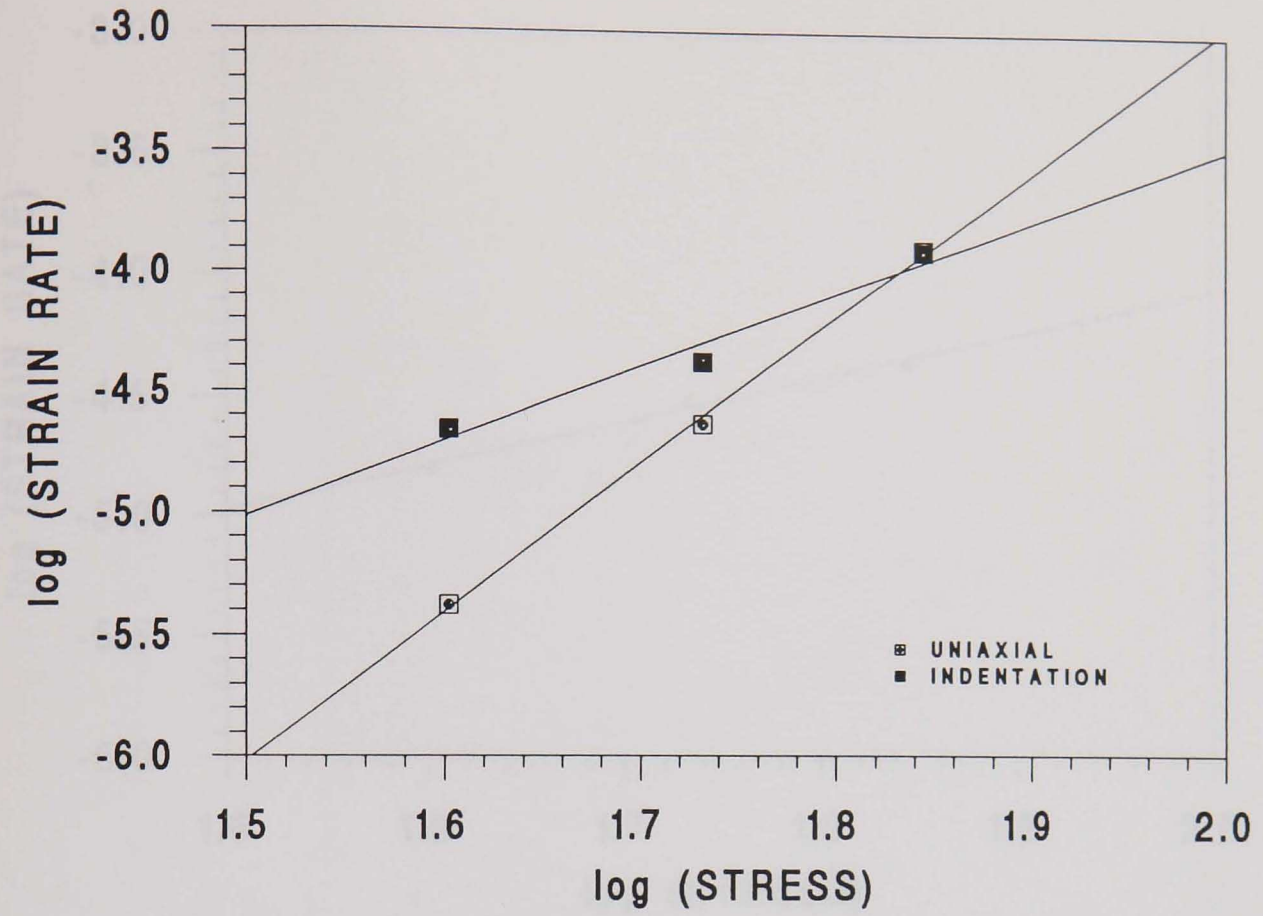

(a) parent material

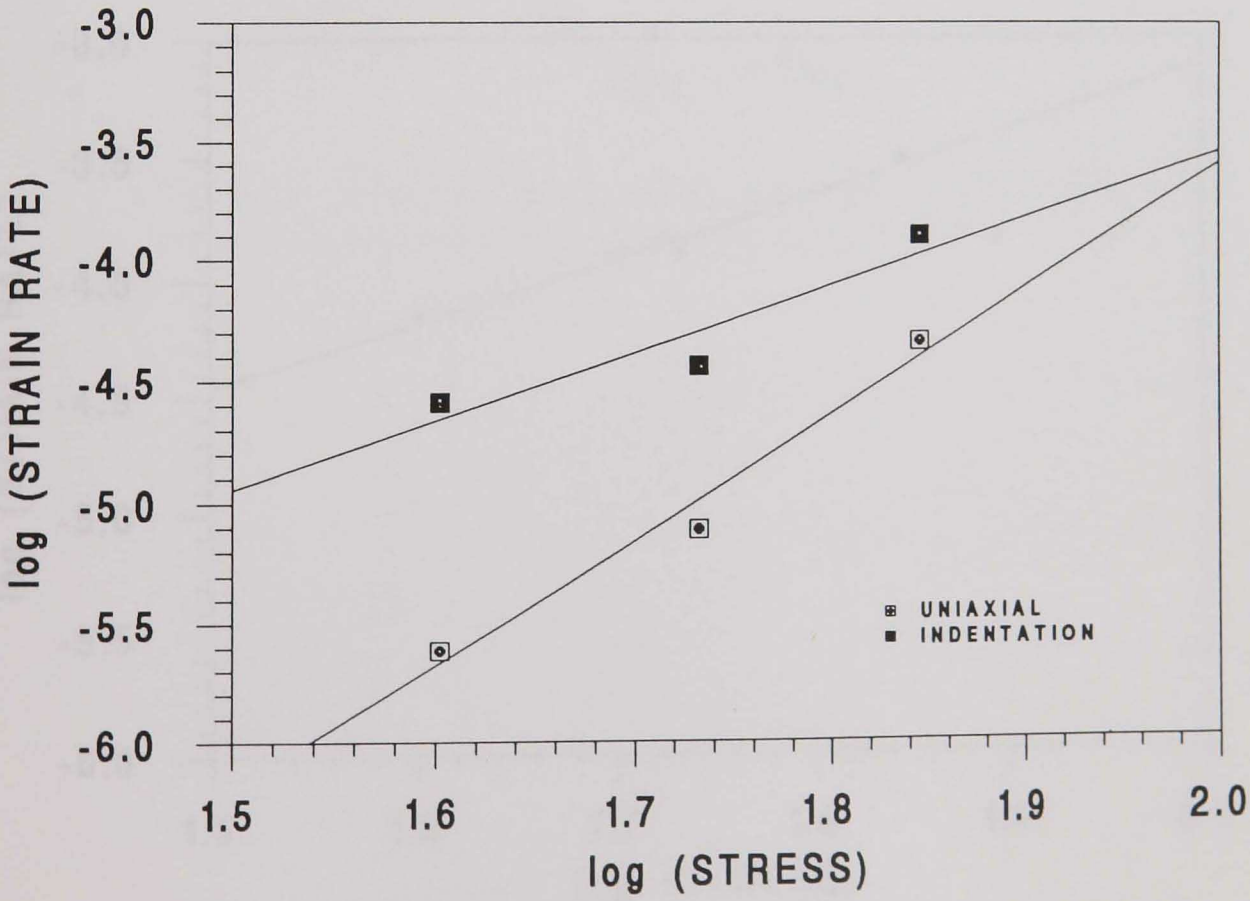

(b) weld material

Fig. 5.26 Plots of the secondary creep strain rates of the aged parent and weld materials obtained from uniaxial and indentation tests at 640° C.

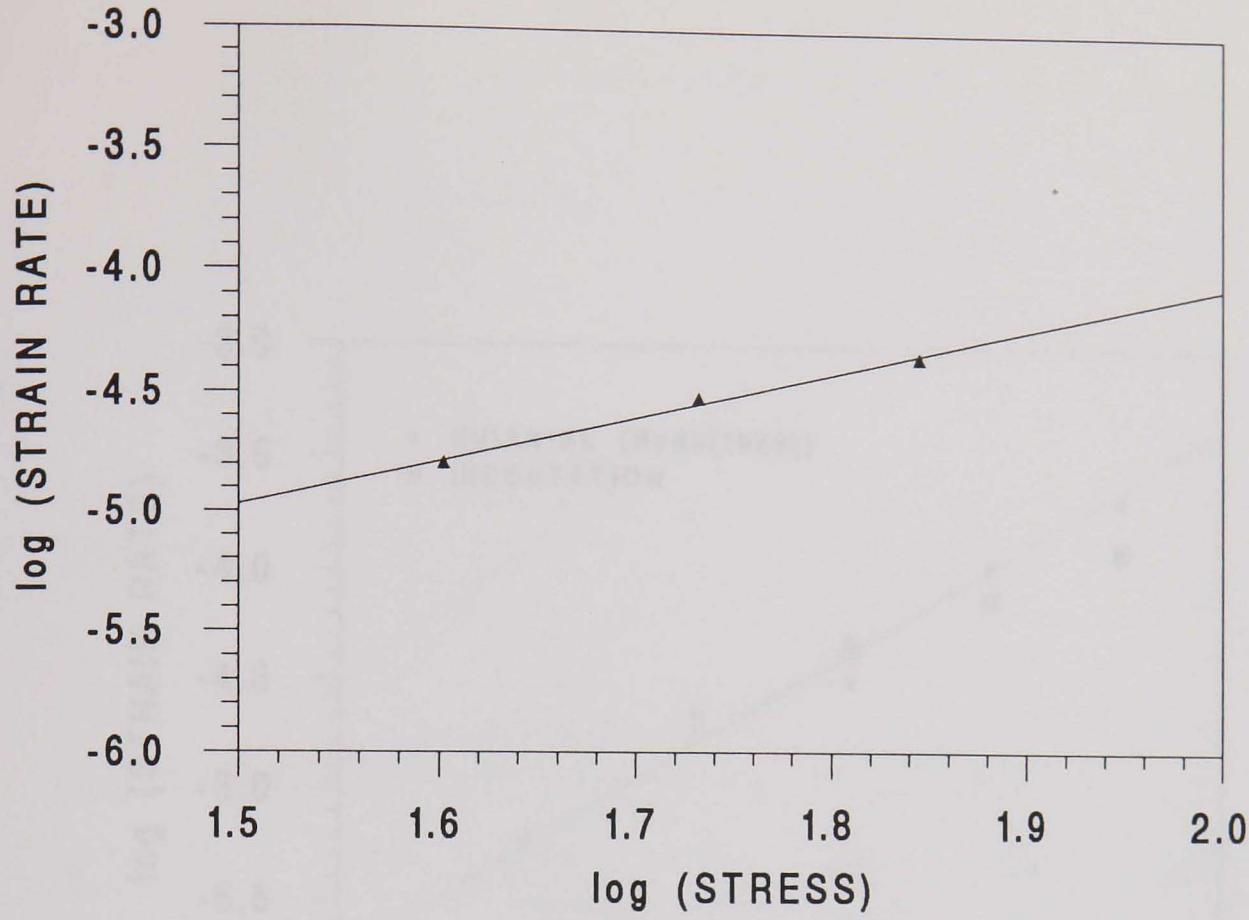

(a) simulated HAZ

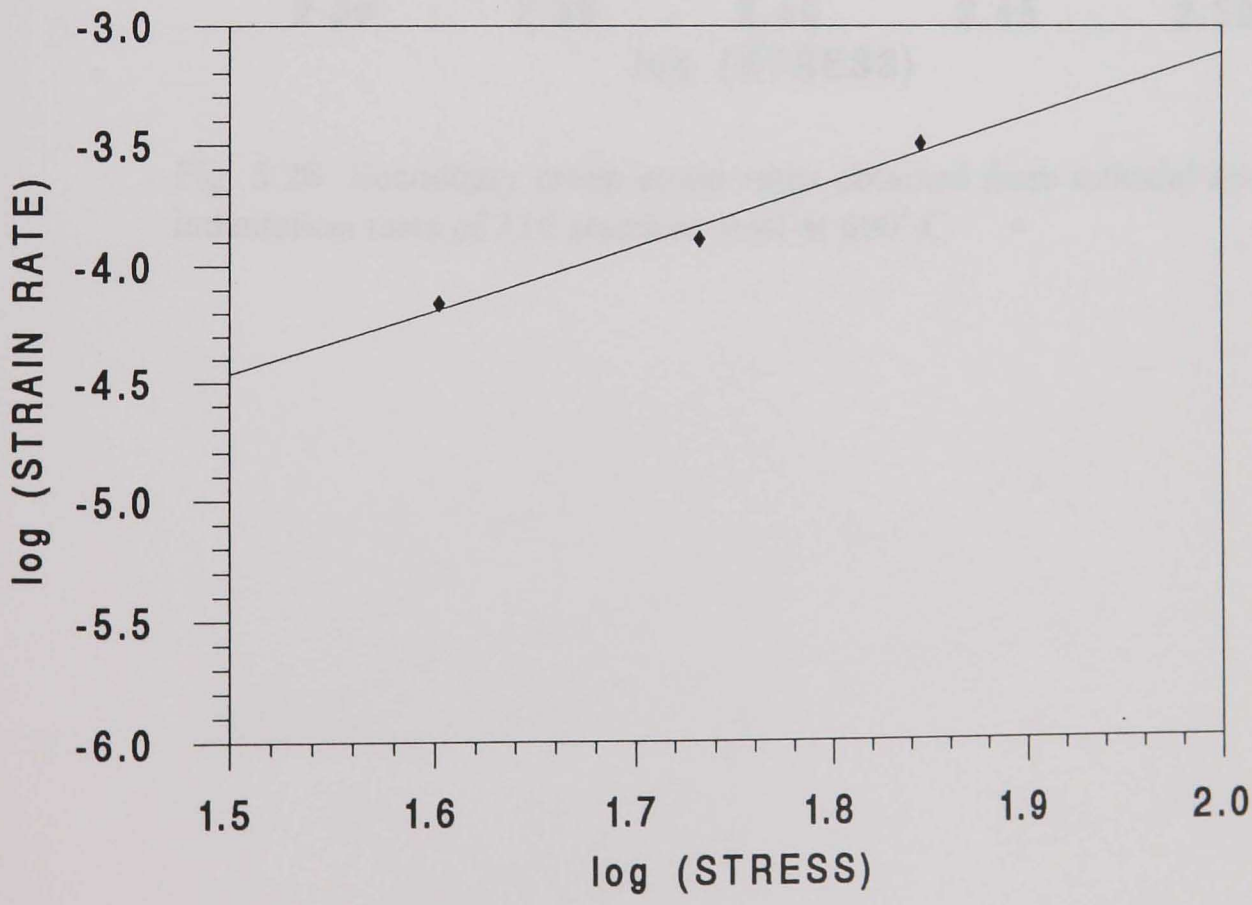

(b) aged HAZ

Fig. 5.27 Plots of the secondary creep strain rates of HAZ materials obtained from indentation tests at 640° C.

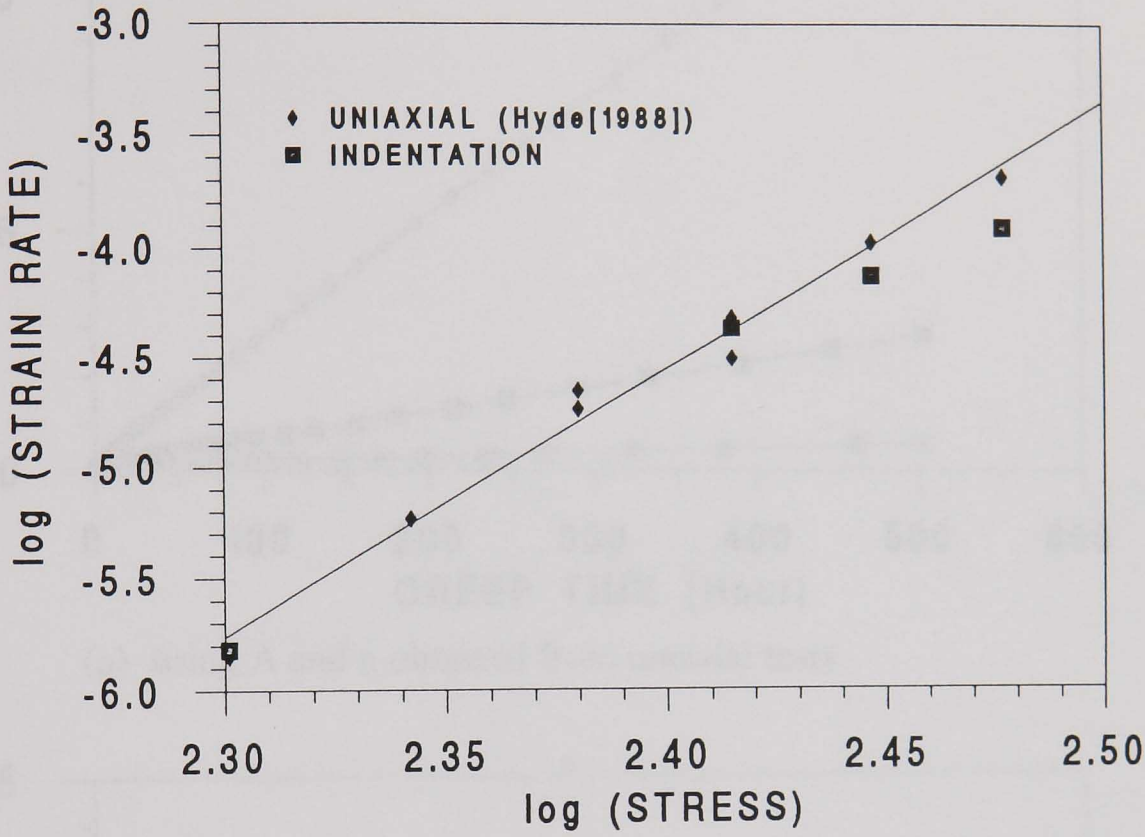

Fig. 5.28 Secondary creep strain rates obtained from uniaxial and indentation tests of 316 stainless steel at 600° C.

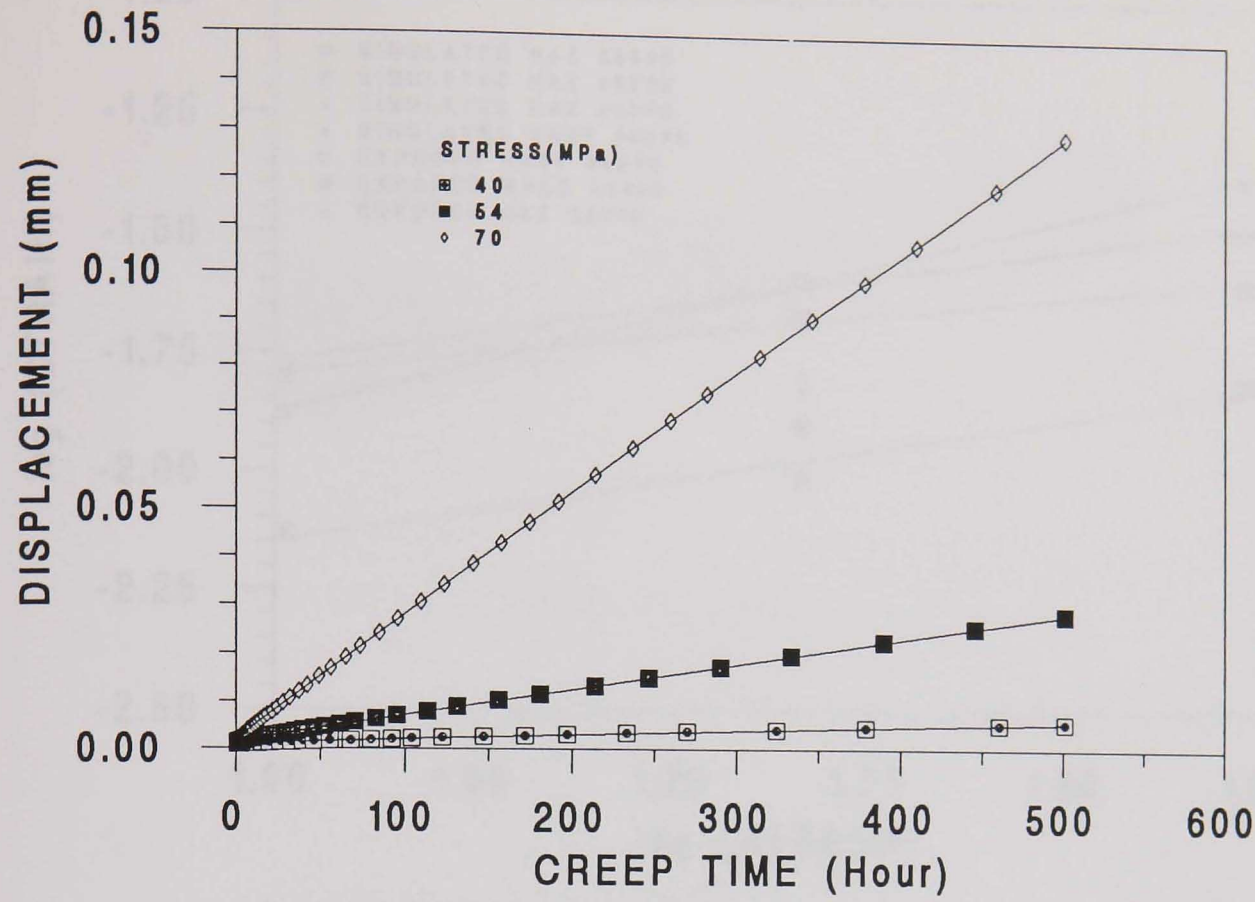

(a) using A and n obtained from uniaxial tests

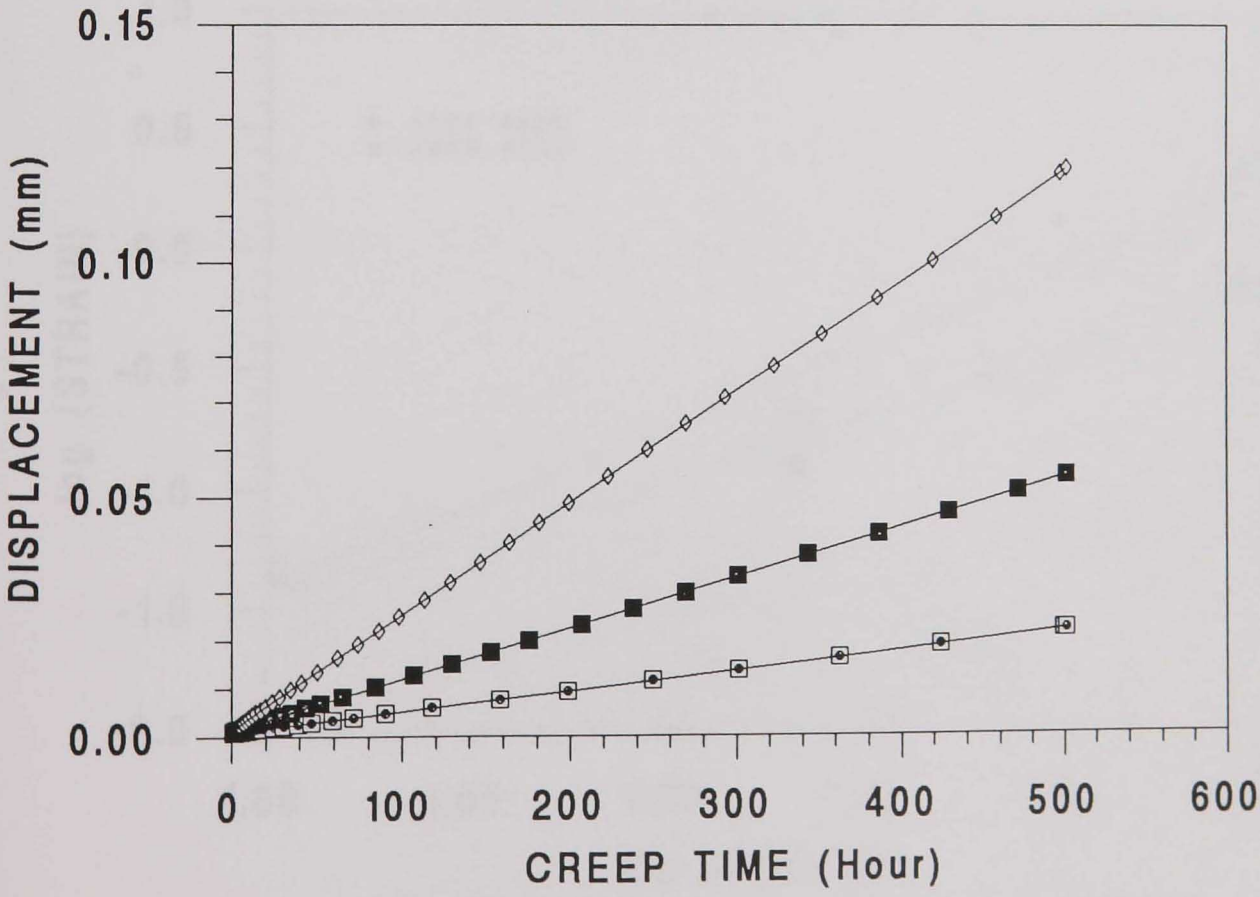

(b) using A and n obtained from indentation tests

Fig. 5.29 FE indentation simulation for the aged parent material indentation creep tests at 640° C.

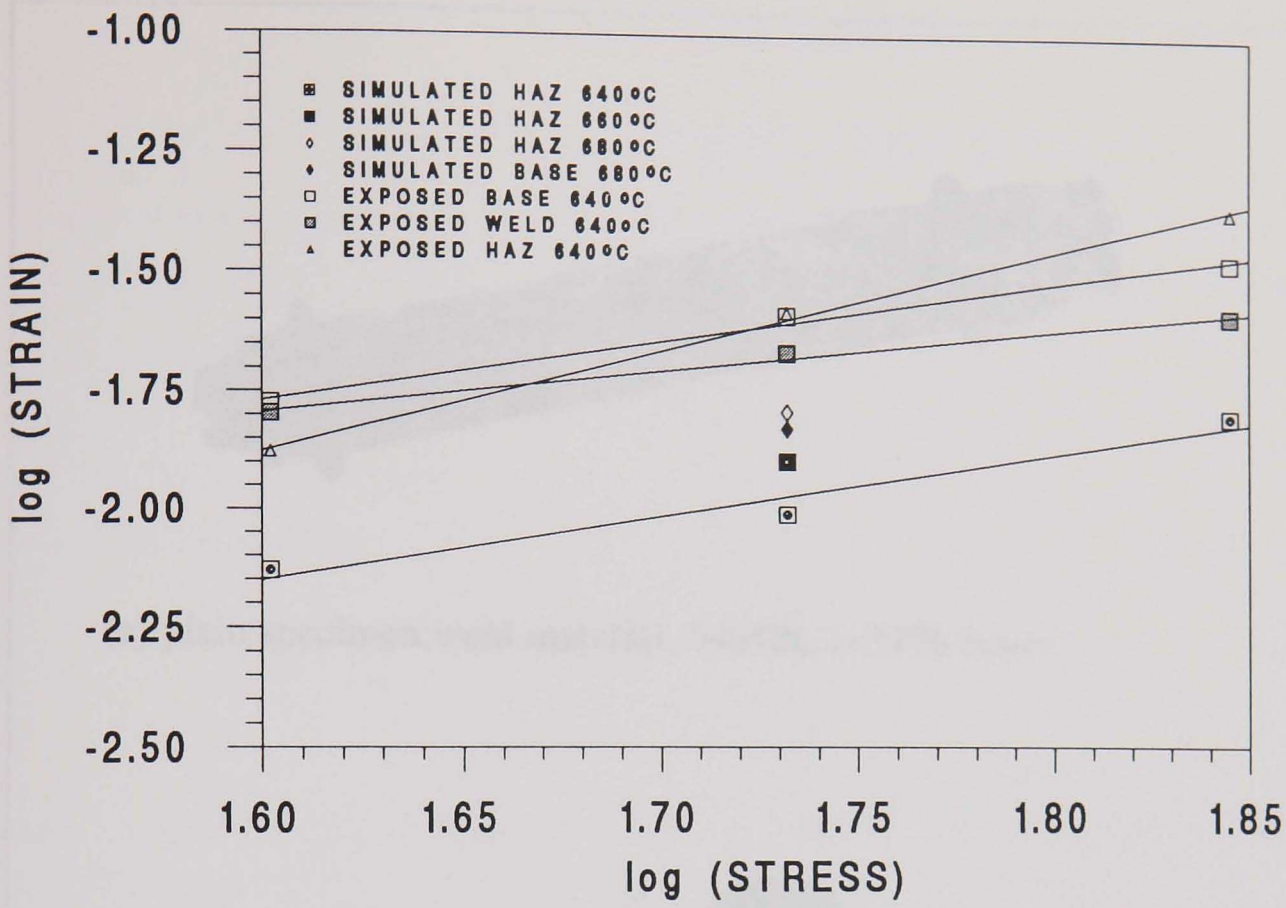

(a) indentation

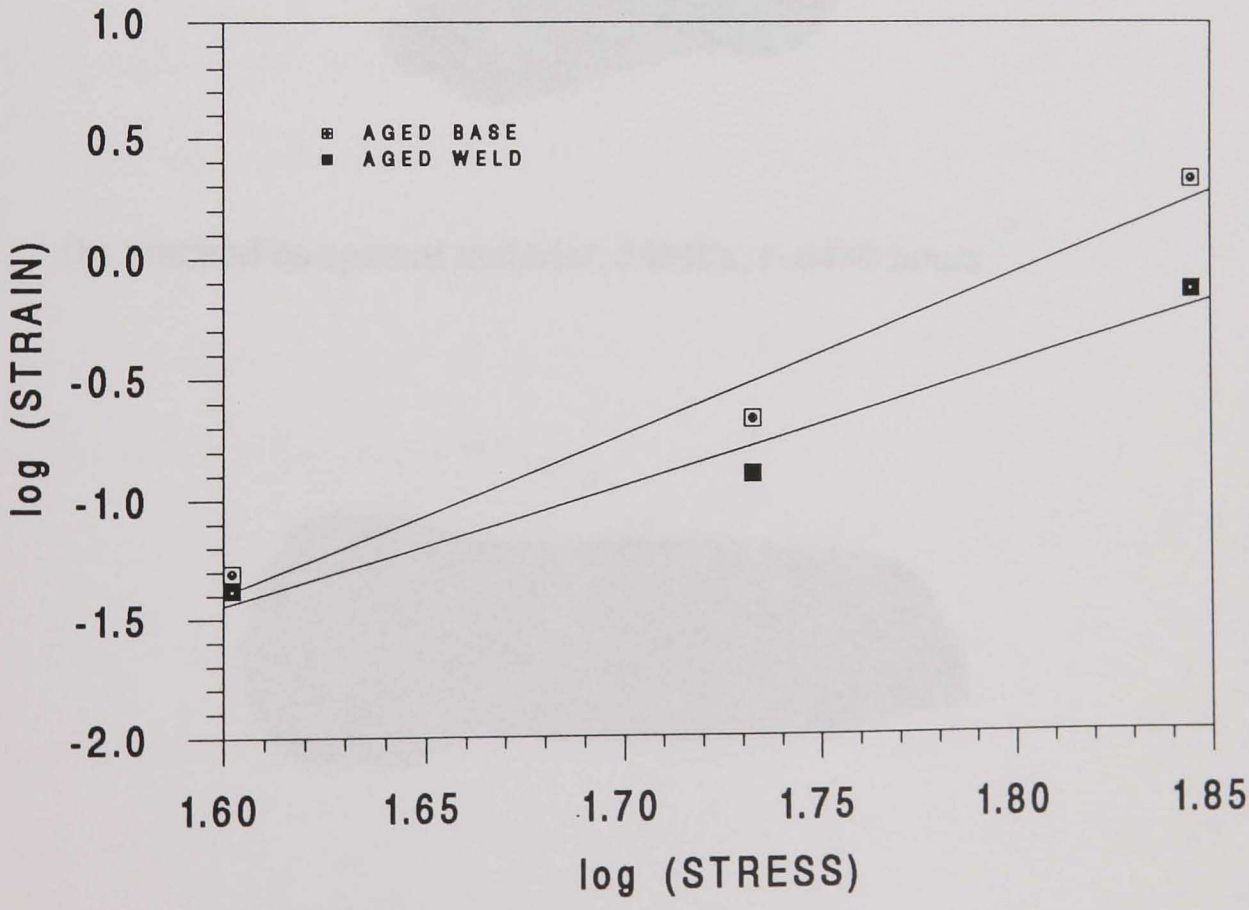

(b) uniaxial

Fig. 5.30 Creep strains at t = 100 hours obtained from the indentation and uniaxial tests at 640° C for the simulated and aged materials.

(a) plain specimen:weld material, 54MPa, t=3776 hours

(b) notched bar:parent material, 54MPa, t=6430 hours

(c) cross-weld specimen:70MPa, t=425 hours

Fig. 5.31 Photographs showing the surface oxidation damage in the aged material uniaxial specimens tested at 640°C.

CHAPTER VI

CONSTITUTIVE EQUATIONS

FOR SERVICE-AGED WELDMENT MATERIALS

6.1 INTRODUCTION

In order to perform failure analysis of the service-exposed weldments, damage parameters in the constitutive equations shown in Section 2.4 of Chapter II and Appendix IV are required for the exposed parent, weld and HAZ materials. Uniaxial creep test results have shown that, for the aged parent and weld materials, no significant primary creep stage was observed (see Figs 5.21(a) and 5.21(b)). This suggests that the constant m in Equ. (2.10) can be assumed to be zero. Therefore, from Equ. (2.10) and (A4.1) it can be seen that for each material, the full set of the material parameters to be determined are the steady-state creep constants A and n and the damage constants χ, ϕ, M and α. Steady-state constants can be determined from the secondary deformation rates of the uniaxial and indentation creep tests, whereas the damage parameters need to be generated using both experimental rupture data and FE damage modelling. The FE-damage calculations can be performed with the FE-DAMAGE code (Becker et al [1994]), in which the creep rupture is defined with a failure criterion of $\omega_{max} \rightarrow 1$.

The generation of damage constants for parent and weld materials involves uniaxial creep tests and FE damage modelling of single-material specimens. From the single material testing of uniaxial plain specimens and indentation specimens, the steady-state creep constants A and n (in Norton's law) for the parent, weld and HAZ materials can be obtained. Using uniaxial rupture data, damage constants χ and M for parent and weld materials can be determined. The ϕ values for the parent and weld materials can then be estimated by fitting the uniaxial ε - t curves with the uniaxial damage constitutive equations using the constants A, n, χ and M already determined. In order to find the α values for each material, notched specimen testing is used in conjunction with FE modelling of single-material notched bar rupture tests. It is found that for many materials the log (t_f) - α curves exhibit an approximately linear relationship, which makes the determination of a correct α value relatively simple.

The generation of the damage parameters χ, M, ϕ and α for the HAZ material is much more difficult, involving the creep testing and FE damage modelling of cross-weld specimens. Educated estimation and a trial-and-error approach are required in order to specify an initial value for some of these unknown parameters. If possible, an investigation to determine the influence of each parameter on the rupture time is required. By comparing the failure times calculated with those tested, the damage parameters can be reasonably estimated. Repeating this process, for both notched and waisted cross-weld specimen tests, until the calculated failure times are consistent with the corresponding experimental results at all stress levels, leads to accurate determination of the material parameters.

The procedure used for damage parameter generation is summarised in Table 6.1.

Table 6.1 Method used for damage parameter generation of the weldment

Specimen	Material Type	Test Data	Creep and Damage Parameters Obtained	
			By Creep Testing	By FE Modelling
Plain	Parent	$\dot{\varepsilon}_{ss}^{B}$, t_f^B	A^B, n^B, χ^B, M^B, ϕ^B	
	Weld	$\dot{\varepsilon}_{ss}^{W}$, t_f^W	A^W, n^W, χ^W, M^W, ϕ^W	
Notched	Parent	t_f^B		α^B
	Weld	t_f^W		α^W
Indentation	HAZ	$\dot{\varepsilon}_{ss}^{HAZ}$	A^{HAZ}, n^{HAZ}	
Waisted	Cross-Weld	t_f^C		χ^{HAZ}, M^{HAZ}, ϕ^{HAZ}, α^{HAZ}
Notched	Cross-Weld	t_f^C		

It should be noted that since the materials being tested in this project have been service-exposed for over 174,800 hours at 568° C with a steam pressure of 16.55 MPa, initial damage may have existed. In addition, significant oxidation damage has been observed in all of the aged material creep test specimens. Both the unknown initial damage and the oxidation damage may introduce some inaccuracies in the creep and damage parameters generated and hence in the modelling of the failure behaviour of the welded pipe of the service-aged material.

6.2 DAMAGE PARAMETER GENERATION FOR PARENT AND WELD MATERIALS

6.2.1 Extension of the Weld Material ε - t Curves of Uniaxial Tests

As mentioned in Chapter V, the weld material uniaxial specimens of 54 and 70 MPa failed at the positions outside the gauge length, see Fig. 5.21(b), with rupture strains of 5.4% and 7.3%, respectively. Since uniaxial rupture data were required in order to determine the damage parameters χ and M for the weld material, it was necessary to extend the strain - time curves up to failure, for the weld material.

It can be seen clearly from Fig. 5.21(b) that significant tertiary creep had occurred in both tests before failure. Therefore, an extension of the tests was performed by using a simple relationship suggested by Penny [1995]:

$$(t_f - t) \times \dot{\varepsilon} = \text{constant} = C \quad \text{(in tertiary stage)} \tag{6.1}$$

where t and $\dot{\varepsilon}$ are the current creep time and strain rate, respectively. This relationship allows the remaining part of a uniaxial test, which has reached the tertiary period, to be roughly estimated. Also, by integrating Equ. (6.1) the strain curve in t_f - t period can be approximated.

For a single test, if two data pairs of $(t - \dot{\varepsilon})$ in the tertiary period are available, the rupture time of the test can be obtained from Equ. (6.1):

$$t_f = \frac{t_i \dot{\varepsilon}_i - t_j \dot{\varepsilon}_j}{\dot{\varepsilon}_i - \dot{\varepsilon}_j} \tag{6.2}$$

and hence the constant C of the material in Equ. (6.1) can be determined:

$$C = (t_f - t_i) \times \dot{\varepsilon}_i = (t_f - t_j) \times \dot{\varepsilon}_j \tag{6.3}$$

Assuming that the test stops at $t = t_o$ with $\varepsilon = \varepsilon_o$ and $\dot{\varepsilon} = \dot{\varepsilon}_o$, and using Equ. (6.1), the strain against time relationship is given by:

$$\frac{d\varepsilon}{dt} = \frac{C}{t_f - t} \qquad (t_o \le t < t_f)$$

Integrating the above equation gives:

$$\varepsilon(t) = - C \ln (t_f - t) + \Delta \qquad (t_o \le t \le t_f - 1)$$

where Δ is a constant to be determined. Substituting the initial values of $t = t_o$ and $\varepsilon = \varepsilon_o$ gives:

$$\Delta = \varepsilon_o + C \ln (t_f - t_o) \qquad (6.4)$$

Therefore

$$\varepsilon(t) = - C \ln (t_f - t) + [\varepsilon_o + C \ln (t_f - t_o)] \qquad (6.5)$$

$$(t_o \le t \le t_f - 1)$$

The rupture strains, ε_f, can be obtained by

$$\int_{\varepsilon_o}^{\varepsilon_f} d\varepsilon = \int_{t_o}^{t_f - 1} \frac{C}{t_f - t} dt = \varepsilon_o + C \ln(t_f - t_o) = \Delta$$

Using the creep data for the weld material uniaxial tests, t_f and C in Equ. (6.1) were obtained (see Table 6.2) and the strain curves were extended using Equ. (6.5), as shown in Fig. 6.1.

Table 6.2 *Parameters used for strain curve extension of weld material uniaxial tests*

σ(MPa)	t_o(hour)	ε_o(%)	$\dot{\varepsilon}_o$(1/hour)	t_f(hour)	C	ε_f(%)
54	3742	5.3606	3.6708×10^{-5}	4907	0.0428	35.58
70	1007.66	7.2743	2.0275×10^{-4}	1391	0.0778	53.56

The validity of this technique has been confirmed by applying it to the case of parent material uniaxial tests, which is presented in Appendix VI.

6.2.2 Damage Parameters

(a) Uniaxial parameters χ and M

When m = 0, for the uniaxial case Equs. (2.10) and (2.11) reduce to the following:

$$\frac{d\varepsilon}{dt} = A\left(\frac{\sigma}{1-\omega}\right)^{n} \tag{6.6}$$

$$\frac{d\omega}{dt} = B\left(\frac{\sigma^{\chi}}{(1-\omega)^{\phi}}\right) \tag{6.7}$$

From the above equations the uniaxial creep strain under a constant uniaxial stress condition can be determined:

$$\varepsilon = \frac{A\sigma^{(n-\chi)}}{B(n-\phi-1)}\left(\left[1-B(1+\phi)\sigma^{\chi}t\right]^{\frac{\phi+1-n}{\phi+1}} - 1\right) \tag{6.8}$$

and the failure time, t_f, can be obtained by integrating Equ. (6.7) and substituting $\omega = 1$ at failure, as follows:

$$t_f = \frac{1}{B(1+\phi)\sigma^{\chi}} \tag{6.9}$$

Therefore χ and M (= $B(1+\phi)$), see Equs. (2.13) and (A4.1) can be obtained directly from Equ. (6.9) by plotting log (t_f) - log σ using the uniaxial creep rupture data of the tests. The plots for parent and weld material results are shown in Fig. 6.2. It should be noted that the rupture data, M and χ for the weld material were determined using the estimated rupture data obtained from the extended strain curves.

(b) Uniaxial parameter ϕ

Using Equ. (6.8) with the creep constants A and n and damage constants χ and M already determined from uniaxial tests of each material, for a given ϕ value the creep strain curve can be predicted. Fitting the experimental curves with the predicted curves using Equ. (6.8) allows the correct ϕ value to be determined. To do this, Equ. (6.8) can be rewritten:

$$\varepsilon(t) = B_o \frac{A\sigma^{(n-\chi)}(\phi+1)}{(n-\phi-1)}\left(\left[1-\frac{1}{B_o}\sigma^{\chi}t\right]^{\frac{\phi+1-n}{\phi+1}}-1\right) \qquad (6.10)$$

where $B_o = \dfrac{1}{B(1+\phi)} = \dfrac{1}{M}$.

Therefore, the damage parameter ϕ is the only unknown variable in Equ. (6.10) during the fitting procedure.

The constants χ, M and ϕ obtained for parent and weld materials are given in Table 6.3. The predicted curves of strain versus time for parent and weld materials are compared with the experimental data in Figs. 6.3(a) and 6.3(b), respectively.

Table 6.3 χ, M and ϕ for exposed parent and weld materials

Material	χ	M	ϕ
Parent	5.7670	5.9981×10^{-14}	4.50
Weld	4.8496	8.1202×10^{-13}	4.10

(c) Tri-axial parameter α

The material constant α is a tri-axial rupture parameter which is usually determined from bi-axial material testing (Hayhurst [1972]). The accurate determination of the α value ($0 \leq \alpha \leq 1$) plays an important role in the application of the multi-axial stress damage model. Rather than performing the usual pure shear and equi-biaxial experimental creep tests, which are time consuming and costly, the FE damage modelling technique can be used to obtain the α value (Hyde et al [1996]). In this case, the α value is determined when the calculated rupture times are consistent with the tested rupture times of the single-material notched specimens.

The values of α for the aged parent, weld and HAZ materials are assumed to be constant for the test stress range since the stress levels used in this research are lower than the break point stress observed in test results for similar materials (Cane [1981]).

(d) FE damage modelling of single-material notched specimens

A symmetrical quarter of the notched specimen was modelled by 26 axisymmetric eight-noded quadratic elements with 2×2 (reduced) integration points, as shown in Fig. 6.4. In order to demonstrate the accuracy of the FE model, initial calculations were conducted with a Titanium alloy at 650° C for which both the experimental rupture data and FE rupture results from a finer mesh (56 elements) were available (Hyde et al [1996]). By comparing the results from the model shown in Fig. 6.4 with

the experimental data and the FE data from the finer mesh, it was found that good accuracy was achieved. These results are given in Table 6.4.

Table 6.4 t_f (hour) calculated and tested for Titanium alloy at 650° C

σ(MPa)	68.4	85.0	136.8
Tested	2832	950	92.0
FE coarse mesh	2975	922	74.5
FE refined mesh	2960	920	74.0

(e) Determination of α values and the effects of damage parameters on the rupture time of notched bar specimens

FE damage calculations were performed using the notched bar models of parent and weld materials with A, n, χ, M and ϕ already determined and three selected α values of 0.0, 0.5 and 1.0. The calculated log (t_f) - α relationship for parent and weld materials are presented in Fig. 6.5. It can be seen that a reasonably linear relationship was exhibited. Also, for the same material, the curves are parallel to each other for different stress levels. With this relationship and the rupture times tested, α values for the two materials can be obtained. For a single α value obtained in this manner, the difference in t_f between the value taken from the linear equation and the accurate value from the FE calculation is very small, for example, in the case of parent material at 70 MPa, the error is only 1.66%. A typical variation of the maximum ω in the notched section with time t at 70 MPa is shown in Fig. 6.6 for different α values. It can be seen that the failure time , t_f, is very sensitive to α, i.e., in the case of the notched bar, the

rupture behaviour is strongly dependent on the tri-axial stress state within the notched area.

For the parent material, the α values obtained from the tests of 54 MPa and 70 MPa are 0.3470 and 0.2534, respectively. In order to have a α value which fitted the two tests better, the α value was finally adjusted to be 0.3. For the weld material, since only the rupture data of 70 MPa test was available when the α-value was determined, the α value had to be determined by that single test. The test rupture times and calculated rupture times for the α values obtained for both parent and weld materials are listed in Table 6.5. It can be seen that reasonably accurate data have been obtained although the tested specimens sustained serious oxidation.

Table 6.5 t_f and α values of exposed parent and weld materials (t_f in hour)

Material	σ(MPa)	54		70	
		α	t_f	α	t_f
Parent	Tested		6430		1800
	FE	0.3470	6430	0.2534	1800
	Modified	0.300	7191	0.300	1612
	Error %		11.8		10.4
Weld	Tested		*		4918
	FE			0.2639	4918
	Modified				
	Error %				

* the test is still in progress

The effects of ϕ, M and χ on the rupture life of the notched bars were also examined, as shown in Figs. 6.7 - 6.9, respectively, for the parent material at 70 MPa. It can be seen that the effect of ϕ is negligible, see Fig. 6.7; however, the influence of M and χ is significant, see Fig. 6.8 and Fig. 6.9. The linear relationship of t_f versus α still holds in the case of varying ϕ, M or χ with constant stress.

(f) Damage variation in the notched section

The damage values shown in Fig. 6.6 are obtained from the maximum damage position on the cross-section of the notch. It has been assumed that failure occurs when the damage level on the whole of the notched section has reached a specified maximum damage level ($\omega_{max} = 0.99$). At a given time, the damage variation along the radius of the notched section is dependent on the value of α. However, with the increase of time, the variation changes. In general, when $\alpha = 0$, the maximum damage occurs on the outer surface of the notch and then propagates inwards in a relatively short creep time; when $\alpha = 1$, the maximum damage appears first on the centre line and then grows outwards relatively slowly. This behaviour is mainly due to the fact that for the notched specimen, the maximum equivalent stress σ_e ($= \sigma_r$ when $\alpha = 0$) occurs on the outside surface whereas the maximum principal stress $\hat{\sigma}$ ($= \sigma_r$ when $\alpha = 1$) occurs on the centre line.

Figs. 6.10(a) - 6.10(c) present the damage history at various positions on the notched section, with $\alpha = 0.0$, 0.5 and 1.0, respectively, for the parent material at 70 MPa. The

corresponding variations of accumulated damage with radial position, at different creep times, are shown in Figs. 6.11(a) - 6.11(c).

6.3 DAMAGE PARAMETER GENERATION FOR HAZ MATERIAL

As mentioned in Section 6.1, the damage parameters for the aged HAZ material can be obtained by modelling the creep rupture tests of the cross-weld specimens, using the creep constants A and n of the three aged materials, the damage constants χ, M, ϕ and α of the parent and weld materials, obtained previously, and the assumed damage parameters χ, M, ϕ and α for the HAZ. Initially, the estimations using simple extrapolation techniques were used, and then a further investigation of the effects of the HAZ damage parameters on the rupture lives of the cross-weld specimens was performed, in order to eliminate the trial and error searching for the unknown damage constants and determine the correct values for the damage parameters with less computing effort. This is necessary because the modelling work in this case is much more time consuming than that in the single-material situation. It should be mentioned that since the failure times of the cross-weld specimens at the lowest stress level (40 MPa) are less reliable, due to the oxidation damage which is mainly dependent on the test duration, the rupture test modelling was only performed at the loading levels of 54 MPa and 70 MPa.

The secondary creep constants A and n of the HAZ material need to be modified due to the unreliability of the steady-state strain rate of the indentation tests, mainly caused by oxidation, as described in Chapter V.

6.3.1 Estimation of the Creep Constants A^{HAZ} and n^{HAZ}

By comparing the steady-state strain rates of the uniaxial tests for both parent and weld materials with the corresponding results of indentation tests, it was found that due to oxidation the results from the two kinds of tests were only consistent for the highest stress situation, i.e. 70 MPa.

Assuming that the stress exponent n of the HAZ is the same as that of the parent material, i.e.

$$n^{HAZ} = n^{B} = 6.108$$

then A^{HAZ} can be obtained by using the steady-state strain rate from the indentation test of 70 MPa,

$$A^{HAZ} = \log^{-1}\left[\log\left(\dot{\varepsilon}_{ss}^{HAZ}(70)\right) - n^{B}\log(70)\right] = 1.7083 \times 10^{-15}$$

and the strain rates of the HAZ material for the lower loading cases can be estimated as

$$\dot{\varepsilon}_{ss}^{HAZ}(54) = 6.5167 \times 10^{-5}$$

$$\dot{\varepsilon}_{ss}^{HAZ}(40) = 1.0422 \times 10^{-5}$$

The procedure used is illustrated in Fig. 6.12 and the corresponding strain rates and the creep constants are given in Table 6.6.

Table 6.6 Secondary strain rates and creep constants of parent and HAZ materials

Material and Test		$\dot{\varepsilon}_{ss}$(40MPA)	$\dot{\varepsilon}_{ss}$(54MPA)	$\dot{\varepsilon}_{ss}$(70MPA)	A	n
Parent	Uniaxial	4.20×10^{-6}	2.32×10^{-5}	1.29×10^{-4}	6.599×10^{-16}	6.108
HAZ	Indentation	6.93×10^{-5}	1.28×10^{-4}	3.18×10^{-4}	2.933×10^{-9}	2.709
	**	1.04×10^{-5}	6.52×10^{-5}	3.18×10^{-4}	1.708×10^{-15}	6.108

** using the indentation strain rate $\dot{\varepsilon}_{ss}^{HAZ}$ at 70 MPa and $n^{HAZ} = n^{B}$

6.3.2 FE-Damage Models of the Cross-Weld Specimens

(a) FE meshes

FE damage analyses of the cross-weld notched and waisted specimens were performed using parent, weld and HAZ material zones, as shown in Fig. 6.13, with 132 and 128 elements, respectively. As described in Chapter V, the position of a Type IV crack is located at the notch centre of the notched bar and at the centre of the uniform smaller diameter part of the waisted specimen.

In order to perform the damage calculations for the cross-weld specimens, the FE-DAMAGE code (Becker et al [1994]) was modified to incorporate the multi-material situation. The creep and damage constants were specified for the elements in the different material zones. The elastic and plastic properties were assumed to be the same for all of the specimen materials.

(b) Specification of the damage areas of the FE models

Under uniaxial loading, both the notched and waisted specimens exhibit multi-axial stress/strain behaviour which appears in both single and multi-material cases. Obviously, in the case of single-material waisted specimens, the tri-axiality is relatively weak, whereas for the notched bar, the multi-axiality is considerably strong in the notched area. Generally speaking, the stress/strain multi-axiality causes localised damage concentration within a specimen; damage concentration is usually due to changes in geometry and the relative creep and damage constants in different zones.

Due to the feature of the shape (notched and waisted) of the specimens and the fact that the HAZ material creeps significantly faster than the weld metal and faster than the parent material at high stress levels, the maximum damage is expected to occur in or near the HAZ of the cross-weld specimens. In the notched bar, the damage concentration is localised near the notched sections, away from which (in both parent or weld material) the damage values are very much smaller. In the cross-weld waisted specimens the maximum damage is expected to appear in the HAZ or in the parent material near the HAZ, whereas the damage level in the weld material and the other parts of the specimens will be significantly lower.

In order to reduce the calculation time , an "effective" damaged area for each specimen can be specified, see Fig. 6.14 (shaded area). It has been demonstrated that this can significantly reduce the computing time with negligible errors. For instance, in Fig. 6.14(b), if the damaged area is defined by l or l_o, the difference in the damage value, ω, is about 2% when t/t_f is small and is even smaller when t/t_f increases. The results from

the model (Fig. 6.14(b)) for parent material at 70 MPa with $\alpha = 0$ show that the rupture times obtained by specifying the damaged area with l and l_o are 377.6 hours and 378.3 hours, respectively, with an error less than 0.2%.

6.3.3 Damage Parameter Generation

(a) Estimation of χ^{HAZ}, M^{HAZ} and ϕ^{HAZ}

By using the Monkman and Grant equation (Monkman and Grant [1956]),

$$\dot{\varepsilon}_{ss}^{k} t_f = \text{constant} = c \tag{6.11}$$

where $\dot{\varepsilon}_{ss}$ is the uniaxial secondary strain rate and k is a material constant which is near 1 for many materials (Nicol and Williams [1985]). The k values for aged parent and weld materials can be obtained from uniaxial test data, using Equ. (6.11):

$$k^B \approx 0.8722 \text{ and}$$

$$k^W \approx 0.7080$$

Assuming the k value for HAZ to be the average value, then

$$k^{HAZ} \approx \frac{k^B + k^W}{2} = 0.7883$$

From Equ. (6.11) for the HAZ material "equivalent" uniaxial tests, we have

$$\frac{t_{fi}^{HAZ}}{t_{fj}^{HAZ}} = \left[\frac{\dot{\varepsilon}_{ssj}^{HAZ}}{\dot{\varepsilon}_{ssi}^{HAZ}}\right]^{k^{HAZ}} = R_{ij}^{HAZ} \tag{6.12}$$

This equation indicates that if the steady-state strain rates of two tests are available for a material, the ratio of the corresponding rupture times can be estimated. Using the data shown in Table 6.6, we have

$$\frac{t_f(54)}{t_f(70)} = R_{ij}^{HAZ} = 3.4887$$

From this ratio, the χ^{HAZ} value can be estimated (see Equ. (6.9)):

$$\chi^{HAZ} = \frac{\log\left(R_{ij}^{HAZ}\right)}{\log\left(\frac{\sigma_j}{\sigma_i}\right)} = 4.8149$$

Using the Monkman and Grant equation again and with two uniaxial test data, the c value in Equ. (6.11) for the parent material can be obtained as follows:

$$c^B = 0.1546$$

Assuming that $c^{HAZ} = c^B$, from Equ. (6.11) we have

$$t_{fi}^{HAZ} = \frac{c^{HAZ}}{\dot{\varepsilon}_{ssi}^{k^{HAZ}}}$$

Substituting the above equation into Equ. (6.9), gives

$$M^{HAZ} = \frac{\dot{\varepsilon}_{ssi}^{k^{HAZ}}}{c^{HAZ}} \sigma_i^{-\chi}$$

Since χ^{HAZ} has been estimated, M^{HAZ} can be calculated as follows

$$M^{HAZ} = 1.4779 \times 10^{-11}$$

Using χ^{HAZ} and M^{HAZ} the rupture times of the "equivalent" HAZ uniaxial tests can also be approximated, see Fig. 6.15.

From fitting the uniaxial creep curves with the uniaxial strain equation (6.8) and the results from the single-material notched bar FE damage calculations (see Fig. 6.7), it was found that ϕ values are not sensitive to the rupture time and only change the

magnitudes of the creep strain. However, the effect of ϕ^{HAZ} on the rupture time of the cross-weld specimen was unknown and therefore needed to be examined. Initially, the ϕ^{HAZ} could be assumed to be the same as that of the parent material.

It should be noted that the χ^{HAZ}, M^{HAZ} and ϕ^{HAZ} values estimated in this manner are only rough approximations. They were modified during the process of the FE damage modelling for the HAZ damage data generation in order to obtain the best consistency of the calculated failure times with the test failure times of the cross-weld specimens.

(b) Effect of damage constants of the HAZ material on the rupture lives of the cross-weld specimens

In order to understand the influence of the damage constants of the HAZ material on the rupture times of the cross-weld specimens, t_f^C, FE damage computations were performed to determine the variation of the failure life with changes in each of the damage parameters of HAZ. It should be mentioned that since the calculation work is very time consuming, a full parametric investigation has not been conducted; only results for some specific situations have been obtained which are presented here.

An understanding of the effect of the damage parameters on the rupture time in a single-material case is essential, certain aspects of which have been described in Section 6.2. Fig. 6.16 and Fig. 6.17 present the variations of the failure times t_f with α for different stress levels. It can be clearly seen that the rupture times of waisted

specimens weakly depend on the tri-axial parameter α. When α is less than 0.5 the rupture time is practically independent of α.

Cross-weld specimen FE damage calculations show that the t_f^C of both notched and waisted specimens is nearly independent of ϕ^{HAZ}, see Fig. 6.18, and the effect of α^{HAZ} on the t_f^C of the waisted specimens is not significant, see Fig. 6.19. This is very similar to the single-material case.

The variation of t_f^C of notched and waisted specimens with χ^{HAZ} for $\phi^{HAZ} = 4.3$, $M^{HAZ} = 1.478 \times 10^{-11}$ and $\alpha^{HAZ} = 0.3$ is shown in Fig. 6.20. It can be seen that by increasing χ^{HAZ}, the t_f^C of both notched and waisted specimens reduces significantly, following an approximately linear relationship. Fig. 21 shows the variation of the ratio of the failure times, t_f^C(54 MPa)/t_f^C(70 MPa) with χ^{HAZ} for $\phi^{HAZ} = 4.3$, $M^{HAZ} = 2.5 \times 10^{-9}$ and $\alpha^{HAZ} = 0.49$. The results clearly show that the ratio is controlled by the χ^{HAZ} values for the given conditions and reduces significantly when χ^{HAZ} decreases.

The relationships of t_f^C against α^{HAZ} and M^{HAZ} under given conditions are presented in Fig. 6.22 and Fig. 6.23, respectively. Similar to the single-material case, linear relationships between t_f^C and α^{HAZ} are exhibited for the notched specimens (see Fig. 6.22), and t_f^C has been found to be approximately proportional to M^{HAZ}. For the waisted specimens, t_f^C reduces with the increase of M^{HAZ}.

(c) Determination of the damage constants

From the above analysis it can be seen that for both waisted and notched cross-weld specimens, in general, the rupture times depend on χ^{HAZ}, M^{HAZ} and α^{HAZ} and are nearly independent of ϕ^{HAZ}. For both waisted and notched specimens, the rupture life is approximately proportional to $1/M^{HAZ}$, and reduces with increasing χ^{HAZ} value. Also, the ratio of the rupture times for different stress level tests is controlled by the χ^{HAZ} values. These observations were found to be very useful for determining a group of HAZ damage constants which can roughly satisfy the failure lives of all the test data. The predicted rupture times of the notched specimens are greatly affected by the α^{HAZ} values, and the linear relationship of $\log (t_f)$ - α^{HAZ} is still exhibited in the calculated cases. The effect of α^{HAZ} on the rupture life of waisted specimens is less significant; when $\alpha^{HAZ} \leq 0.5$ the rupture time is nearly independent of α. Therefore, based on the study of the influence of the HAZ damage parameters on the cross-weld specimen rupture life, a procedure to generate the HAZ damage constants, from the cross-weld specimen rupture tests, was established which is described as follows:

1) Choose the value of ϕ^{HAZ}; this can be assumed to be similar to the value for the parent material.

2) Calculate the rupture times of both waisted and notched specimens for two stress levels (e.g. 54 MPa and 70 MPa), with the ϕ^{HAZ} chosen, $\alpha^{HAZ} \leq 0.5$ and the M^{HAZ} value estimated using the Monkman and Grant relationship. Adjust the value of χ^{HAZ} by a trial-and-error method to make the calculated ratio of $t_f^C(\sigma_i)/t_f^C(\sigma_j)$ close to the experimentally determined ratio.

3) Modify the value of M^{HAZ}, using the approximate relationship $t_f^C \propto 1/M^{HAZ}$, to make the calculated rupture times of the waisted specimens close to the corresponding experimental test results.

4) Modify the value of α^{HAZ} ($0 \leq \alpha^{HAZ} \leq 0.5$) to make the calculated rupture times of the notched specimens close to the corresponding experimental test results (note that the rupture times of the waisted specimens are practically independent of α^{HAZ} when $0 \leq \alpha^{HAZ} \leq 0.5$).

5) Perform calculations to obtain predictions of the rupture times for all the tested specimens (waisted and notched at different stress levels) using the constants χ, ϕ, M and α of the HAZ material already determined in the above procedure and, if required, further adjust the relevant parameters in order to obtain more accurate results.

The HAZ damage parameters finally generated and the experimental and calculated rupture times are presented in Table 6.7.

Table 6.7 Rupture times of cross-weld specimens tested and calculated using the generated creep and damage parameters of aged materials

Specimen	σ(MPa)	Tested(h)	Calculated(h)	Error (%)
Notched	54	1854	2079	12.14
	70	757	861	13.74
Waisted	54	1008	1043	3.47
	70	424	361	14.86
HAZ damage parameters: $\chi^{HAZ} = 3.20$, $\phi^{HAZ} = 4.30$, $M^{HAZ} = 2.5 \times 10^{-9}$, $\alpha^{HAZ} = 0.49$				

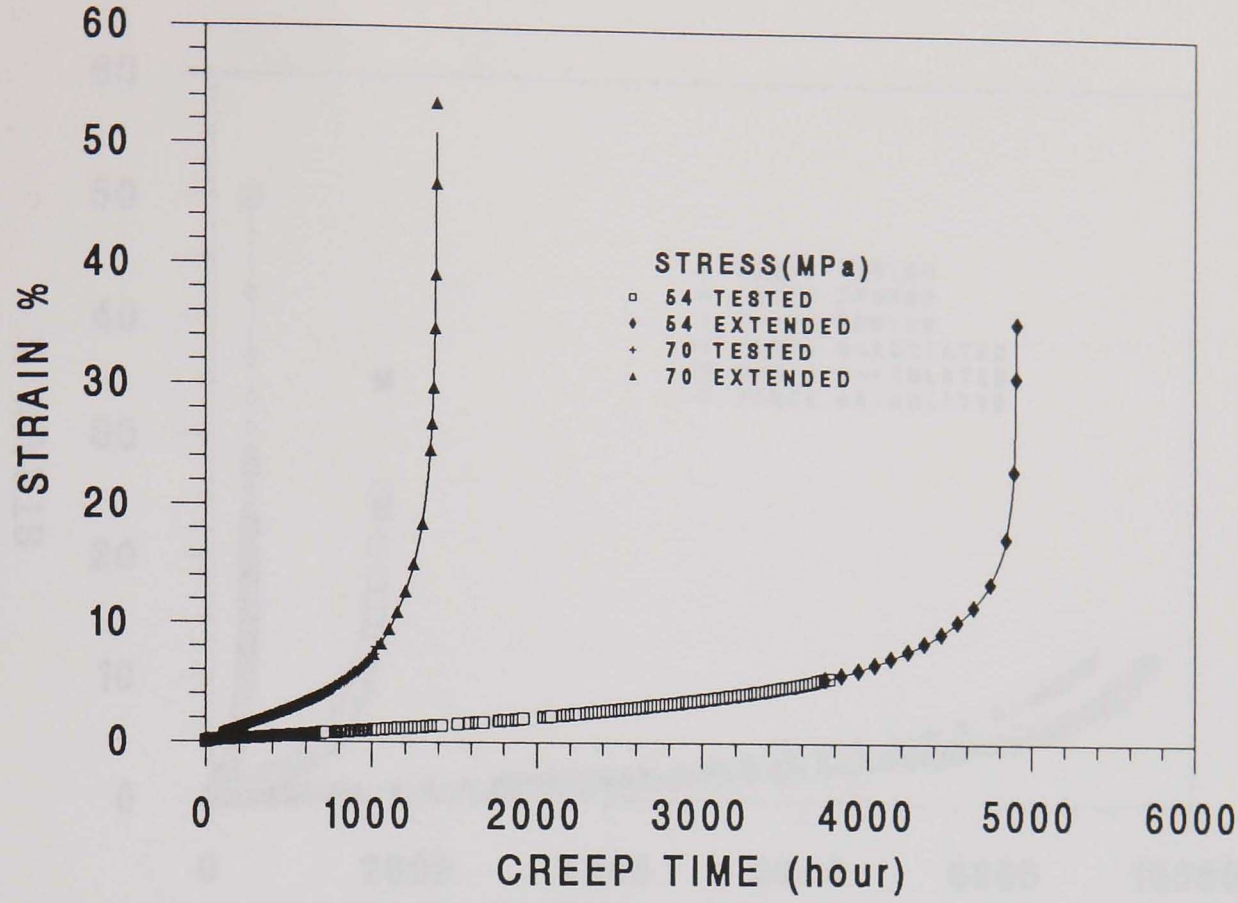

Fig. 6.1 Extension of the creep strain curves for aged weld material uniaxial tests at 640° C.

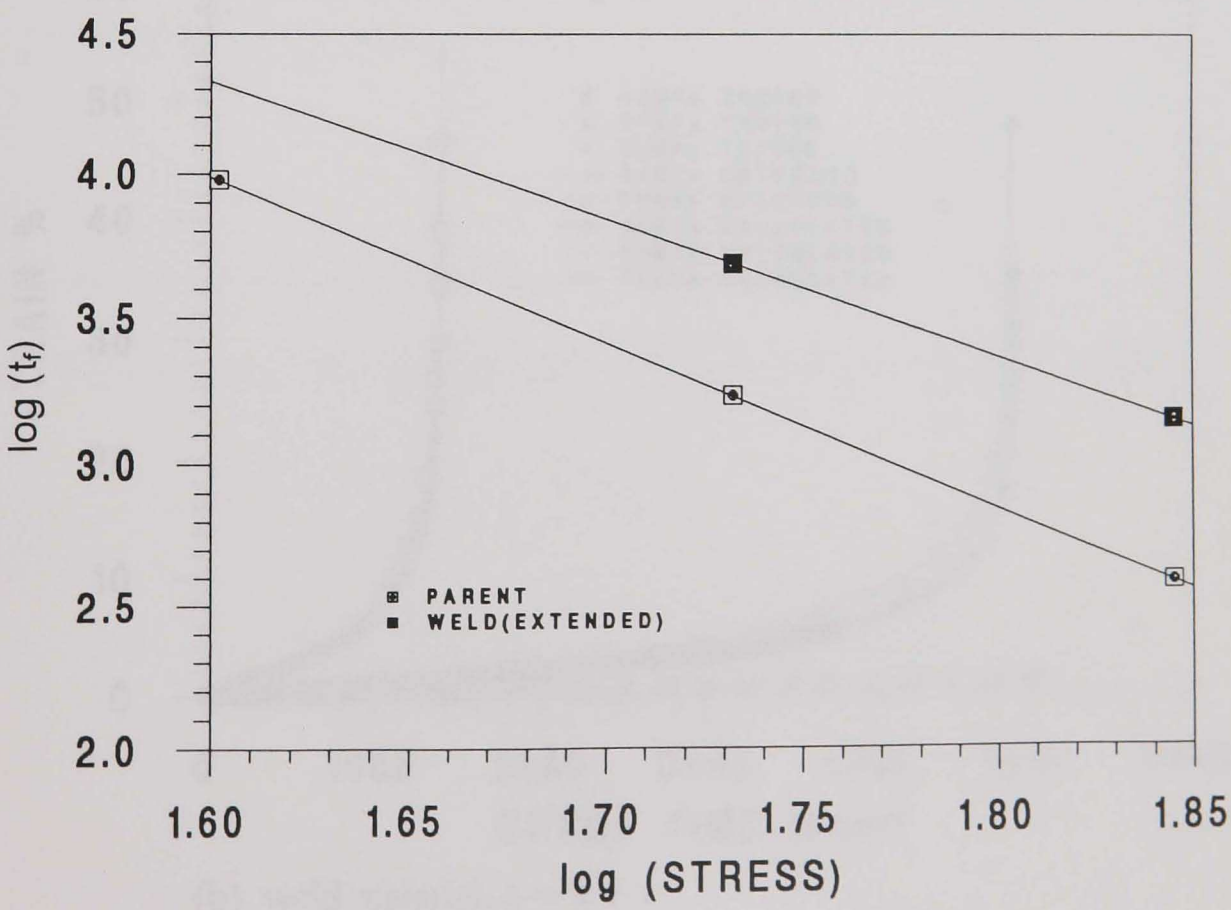

Fig. 6.2 Uniaxial creep rupture times against stress for aged parent and weld materials at 640° C.

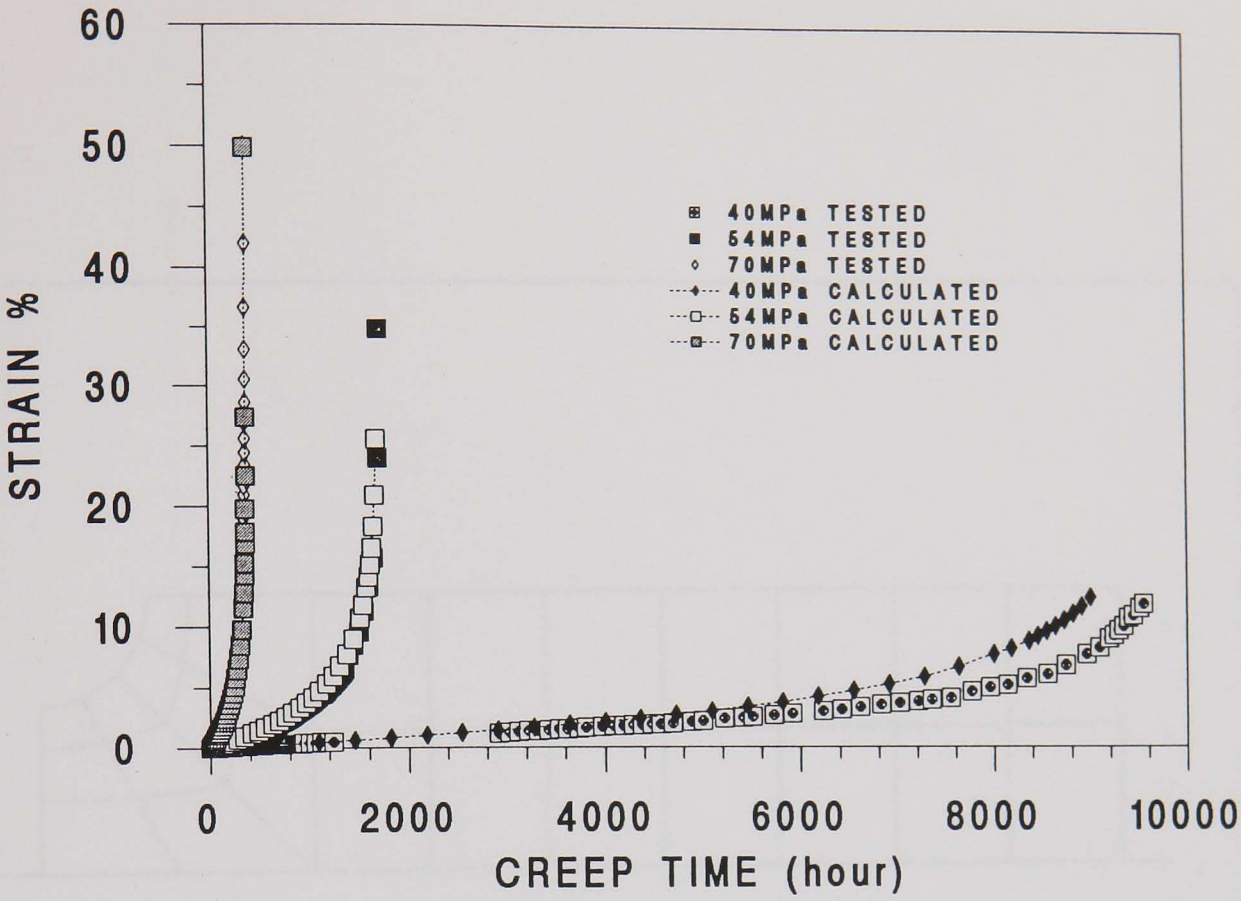

(a) parent material, $\phi = 4.5$

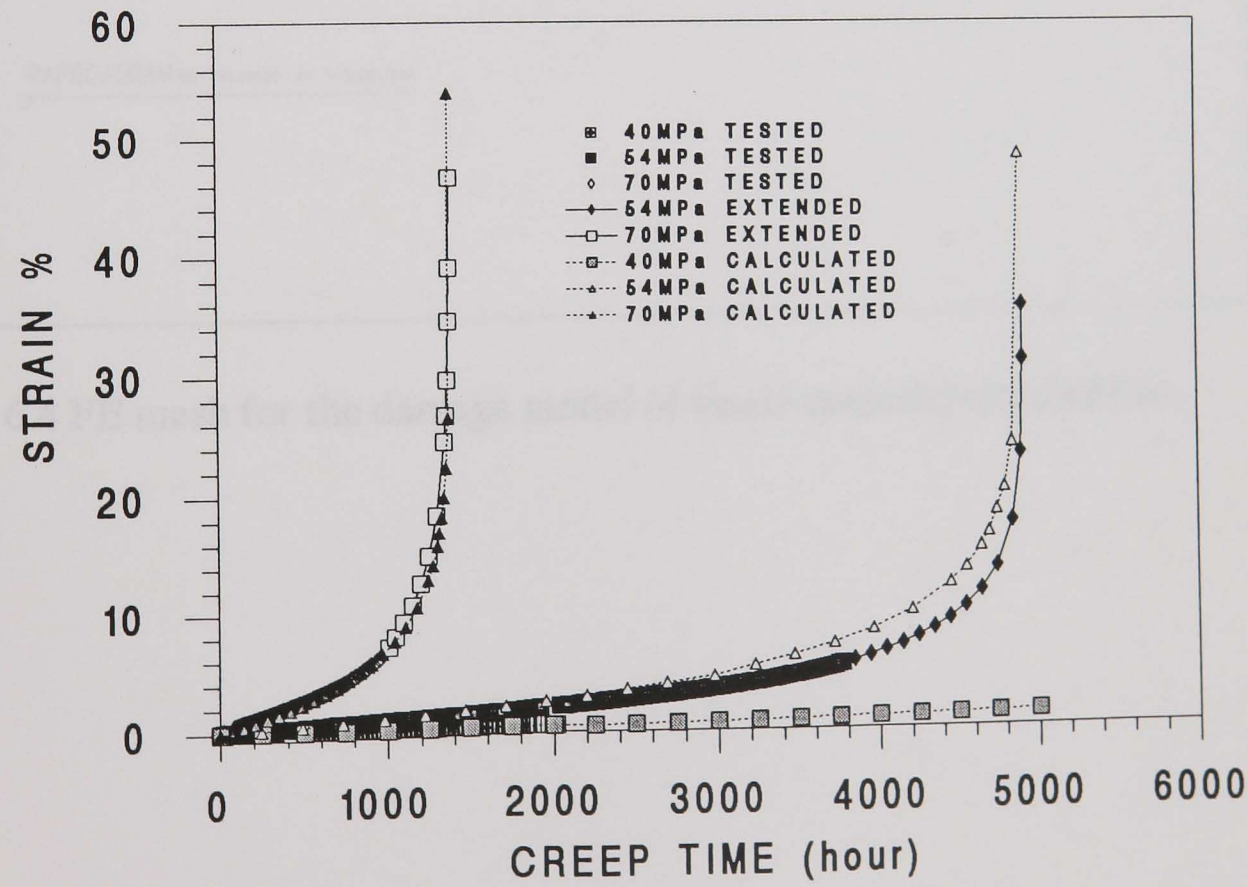

(b) weld material, $\phi = 4.1$

Fig. 6.3 Uniaxial creep strain curves tested and fitted for aged parent and weld materials at 640° C.

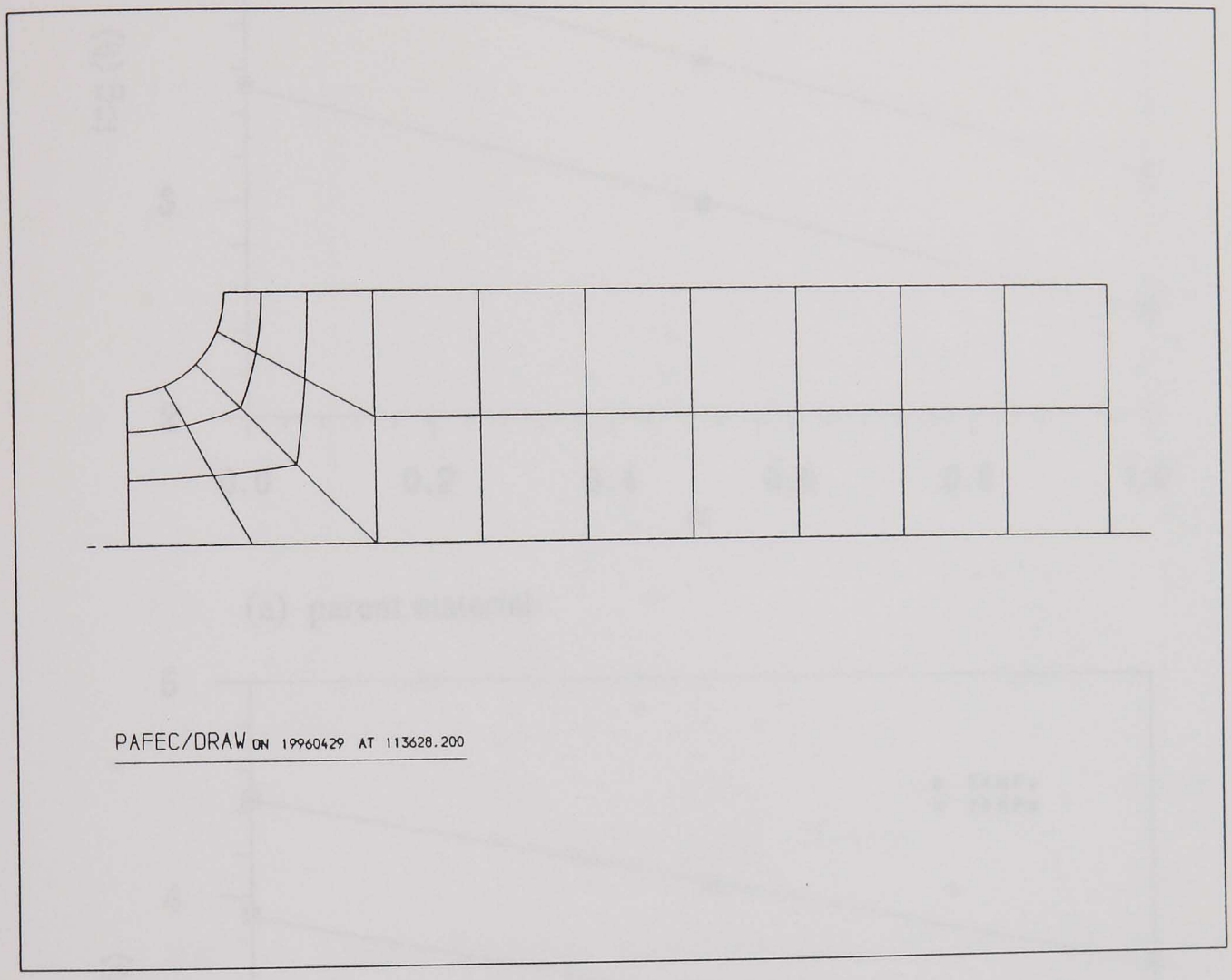

Fig. 6.4 FE mesh for the damage model of single-material notched bar.

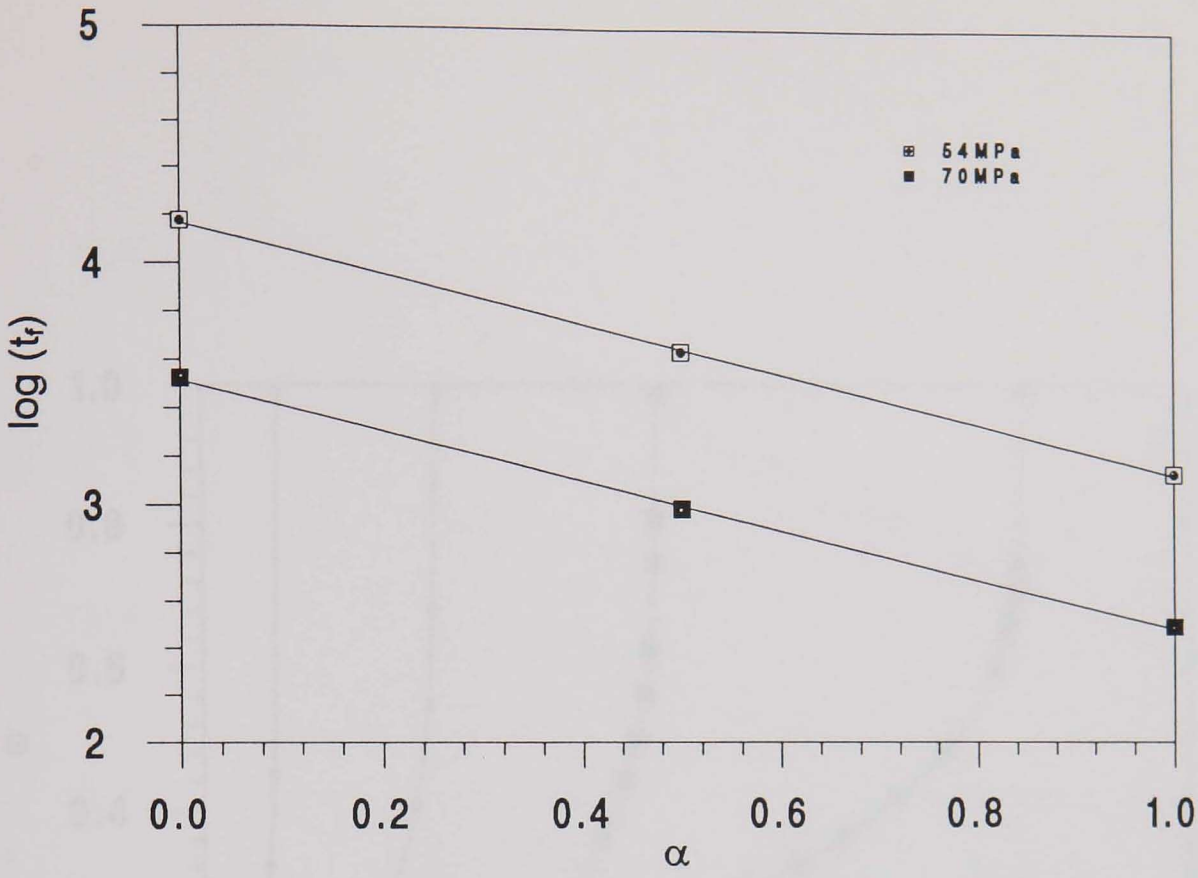

(a) parent material

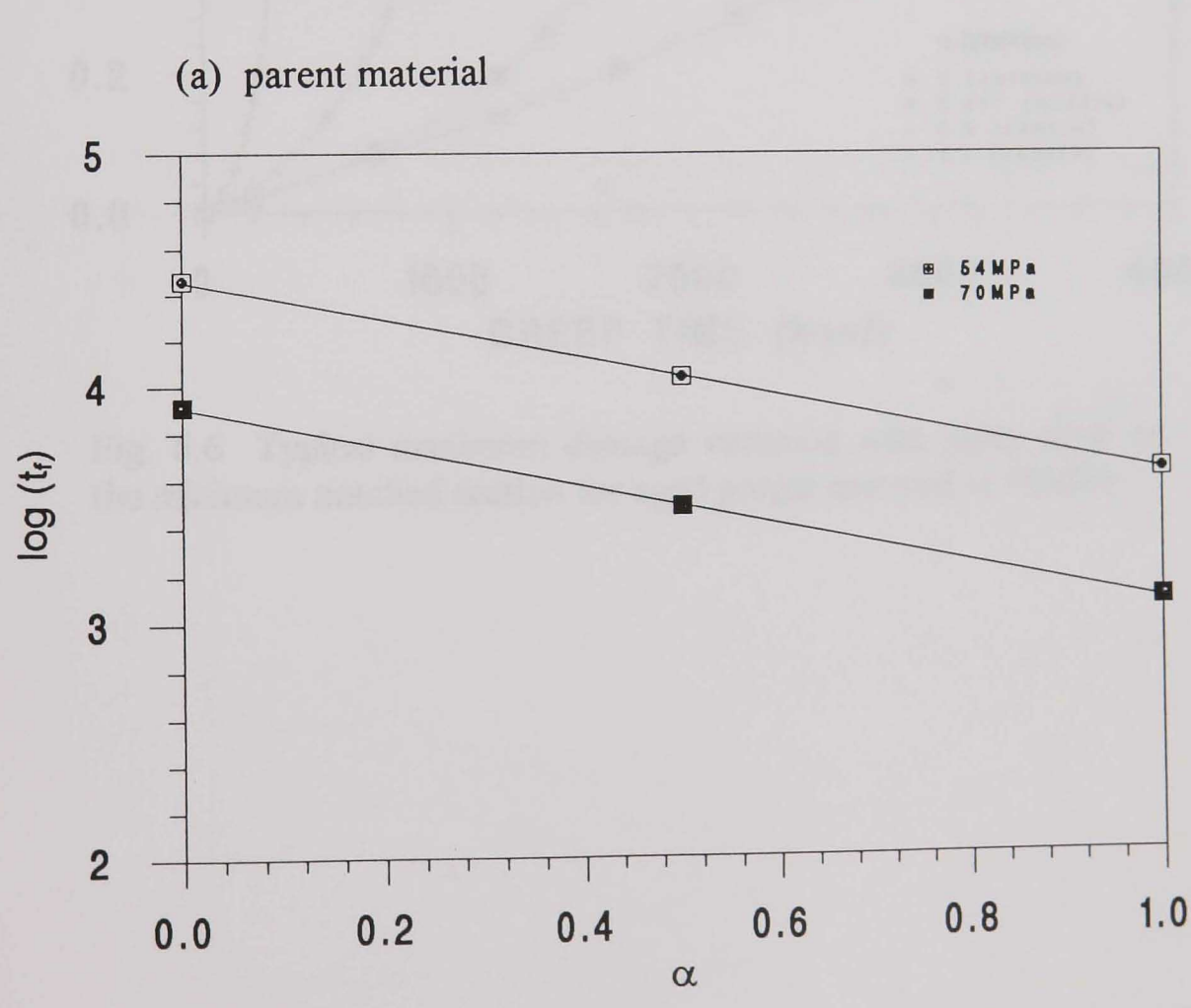

(b) weld material

Fig. 6.5 Relationship between t_f and α obtained from single-material notched bar damage model for aged parent and weld materials at 640° C.

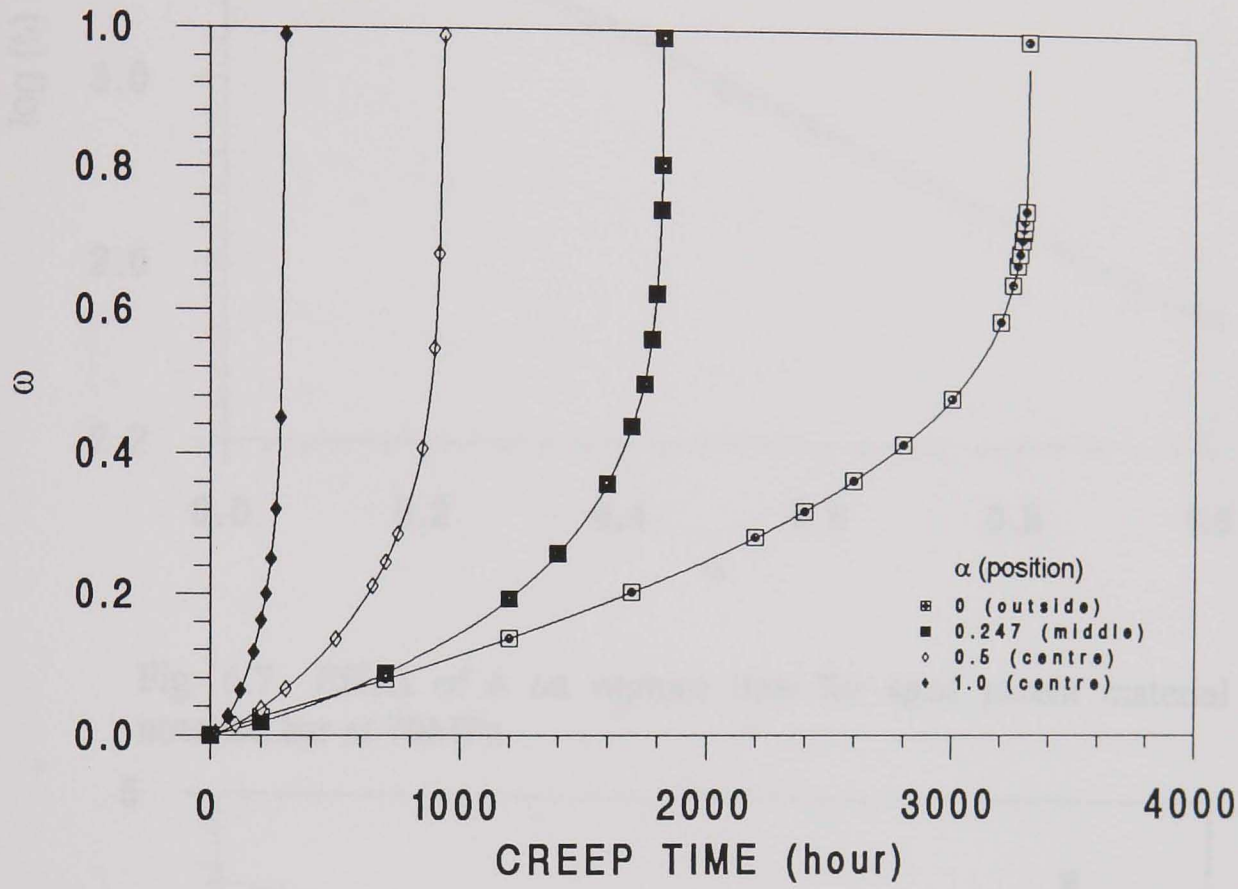

Fig. 6.6 Typical maximum damage variation with creep time on the minimum notched section for aged parent material at 70MPa.

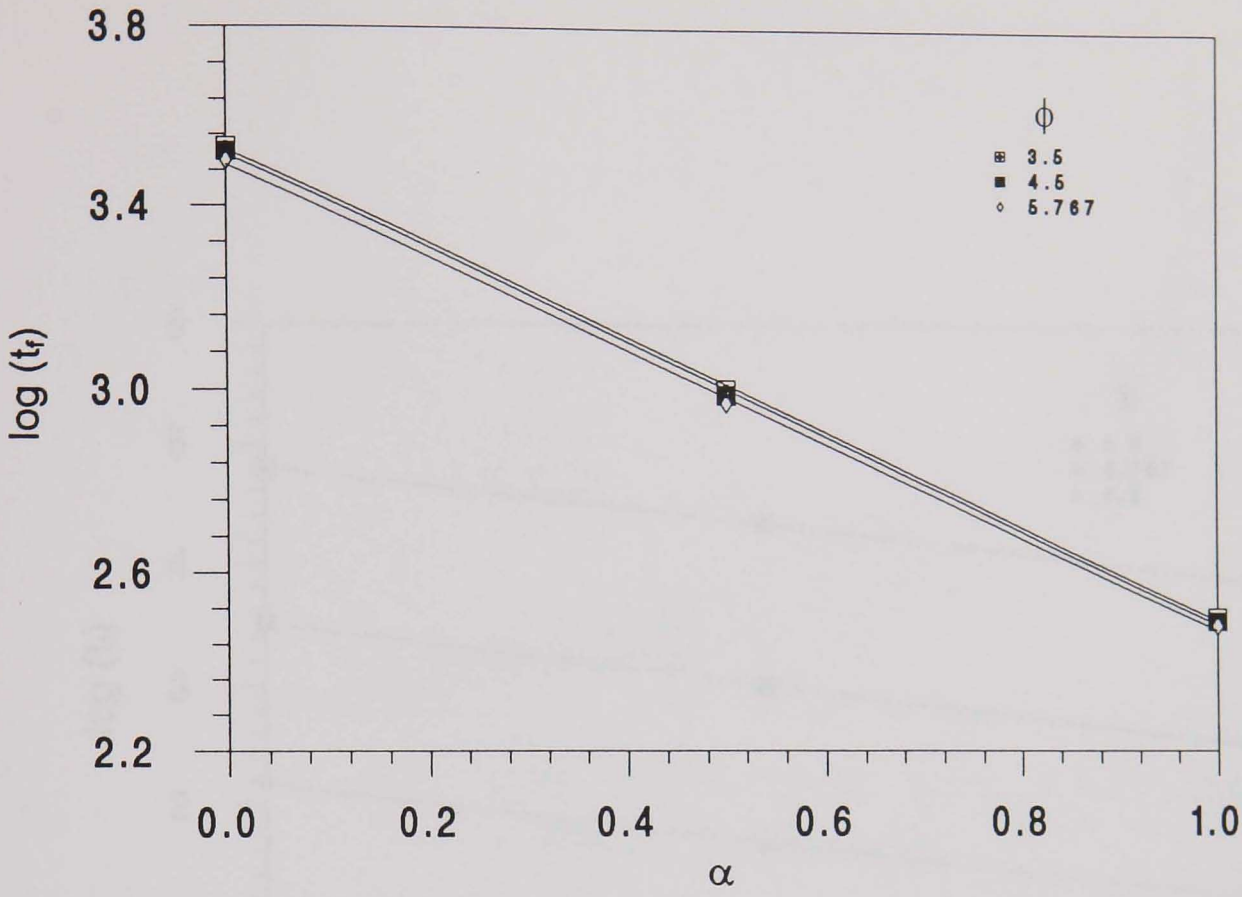

Fig. 6.7 Effect of ϕ on rupture time for aged parent material notched bar at 70MPa

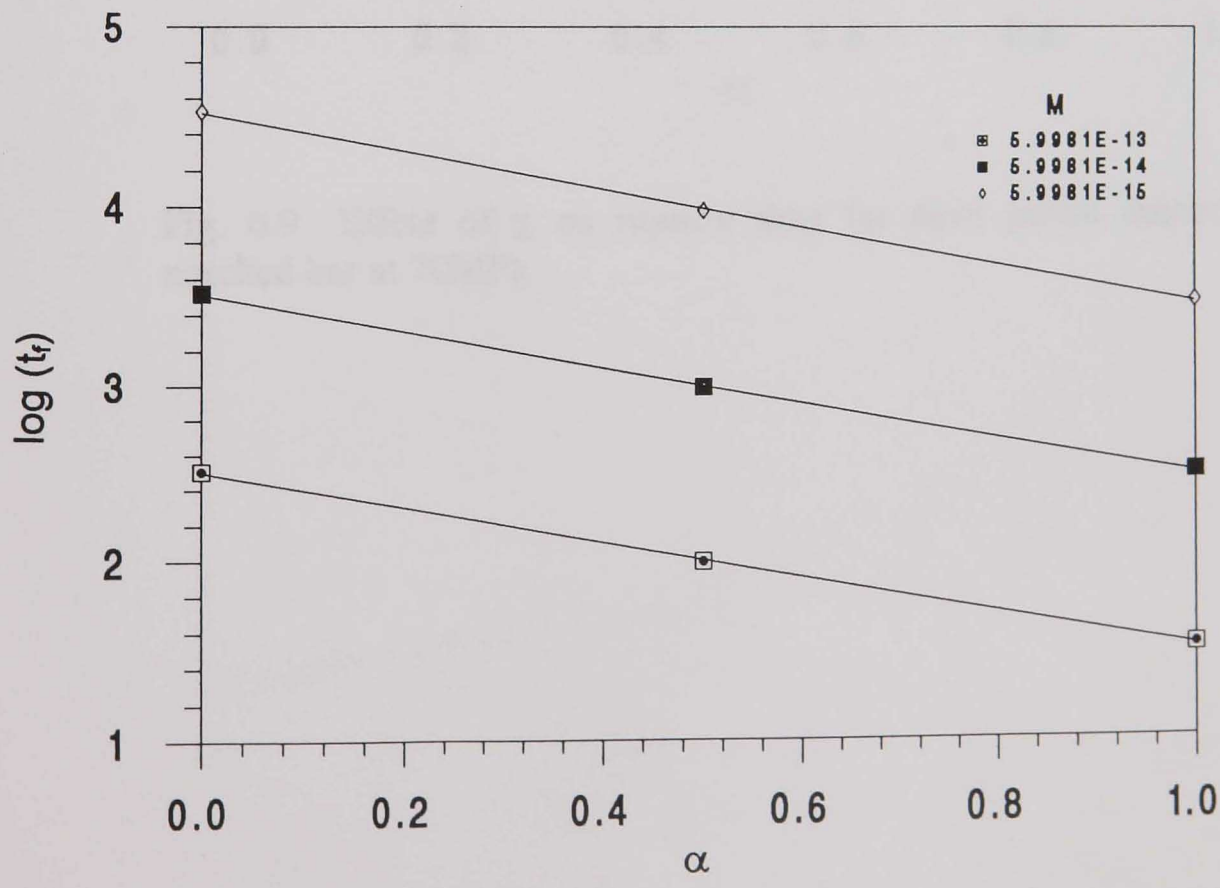

Fig. 6.8 Effect of M on rupture time for aged parent material notched bar at 70MPa

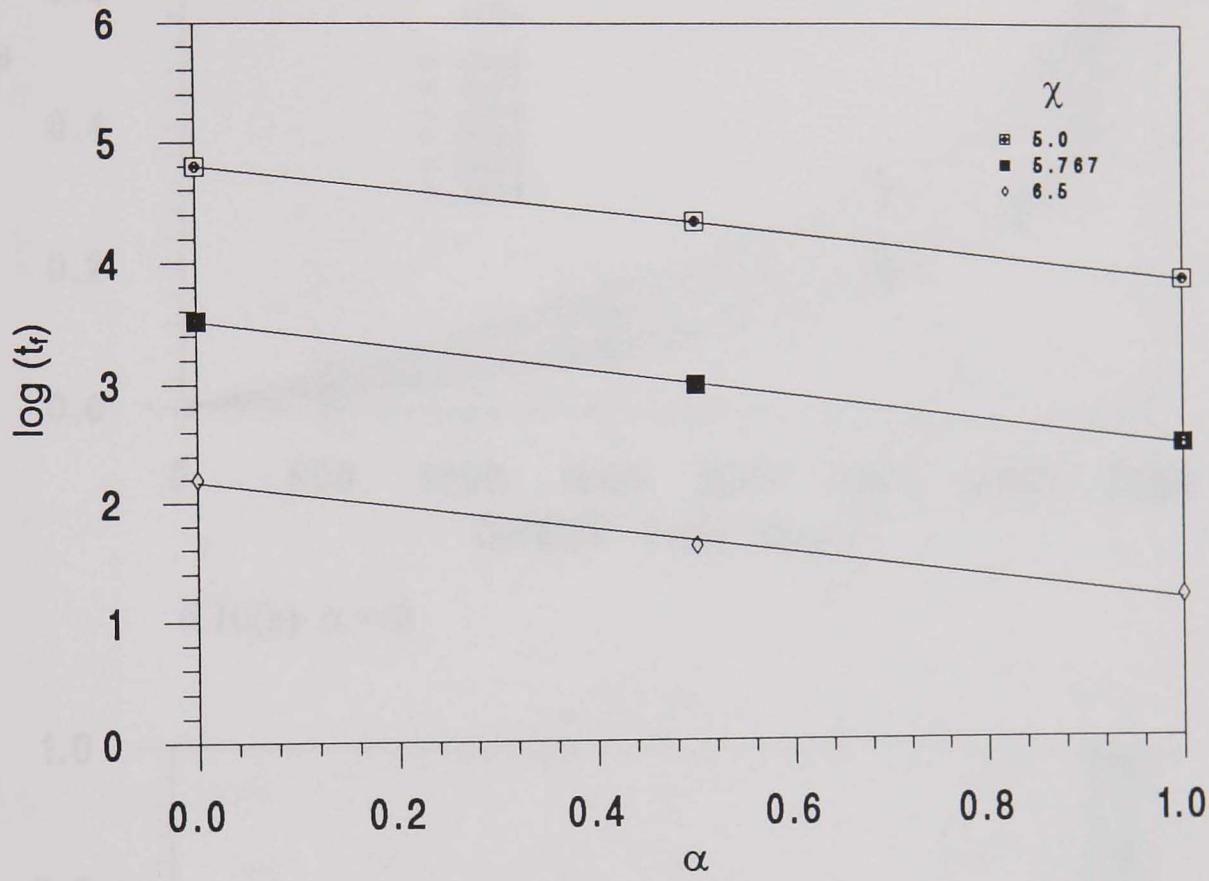

Fig. 6.9 Effect of χ on rupture time for aged parent material notched bar at 70MPa

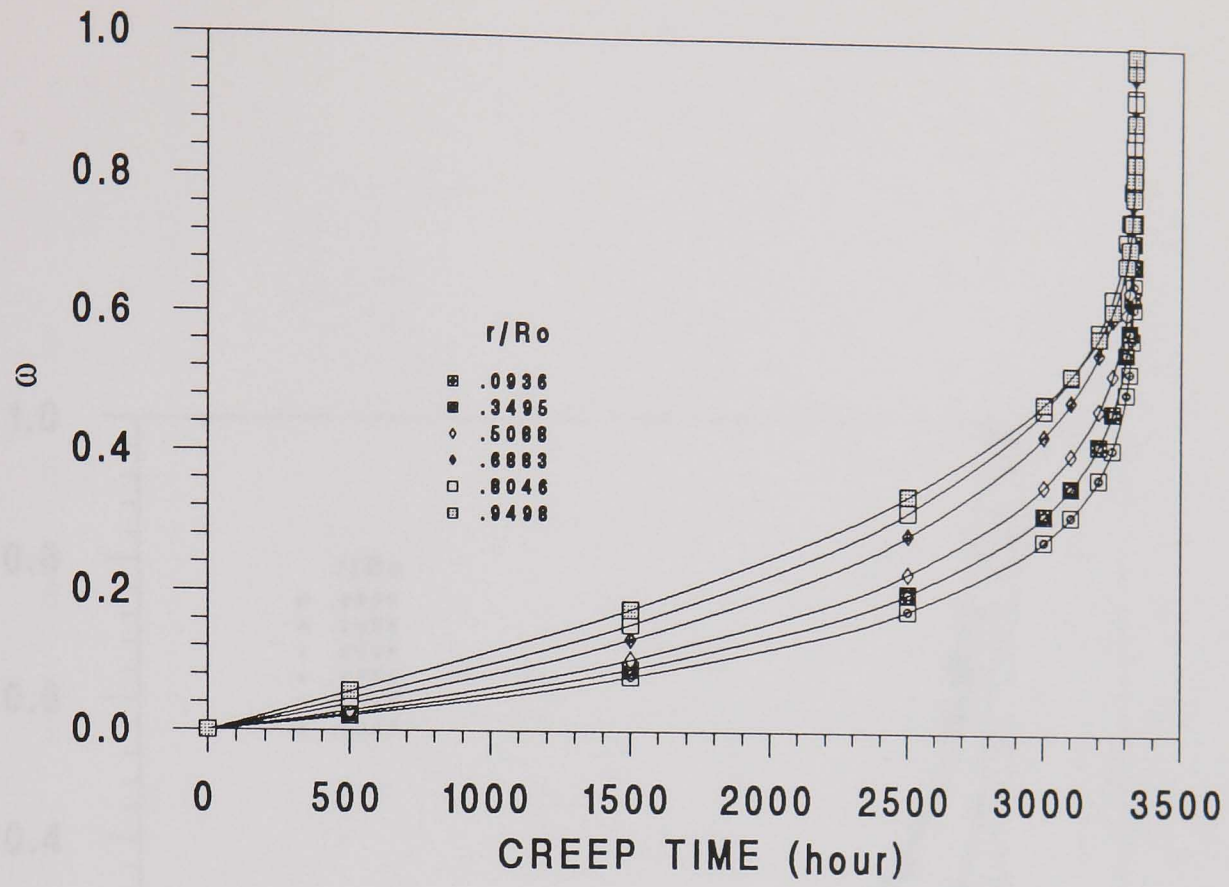

6.10(a) $\alpha = 0$

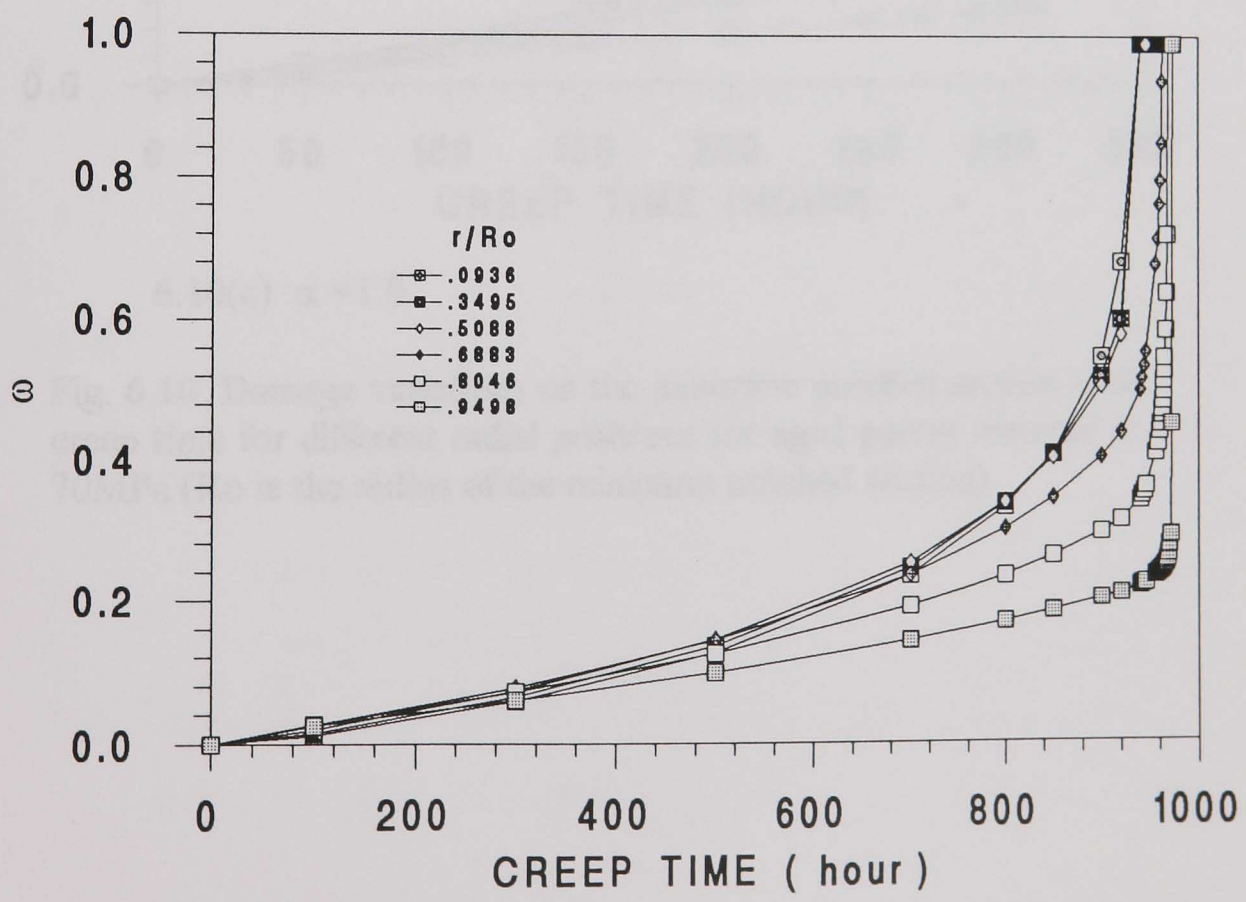

6.10(b) $\alpha = 0.5$

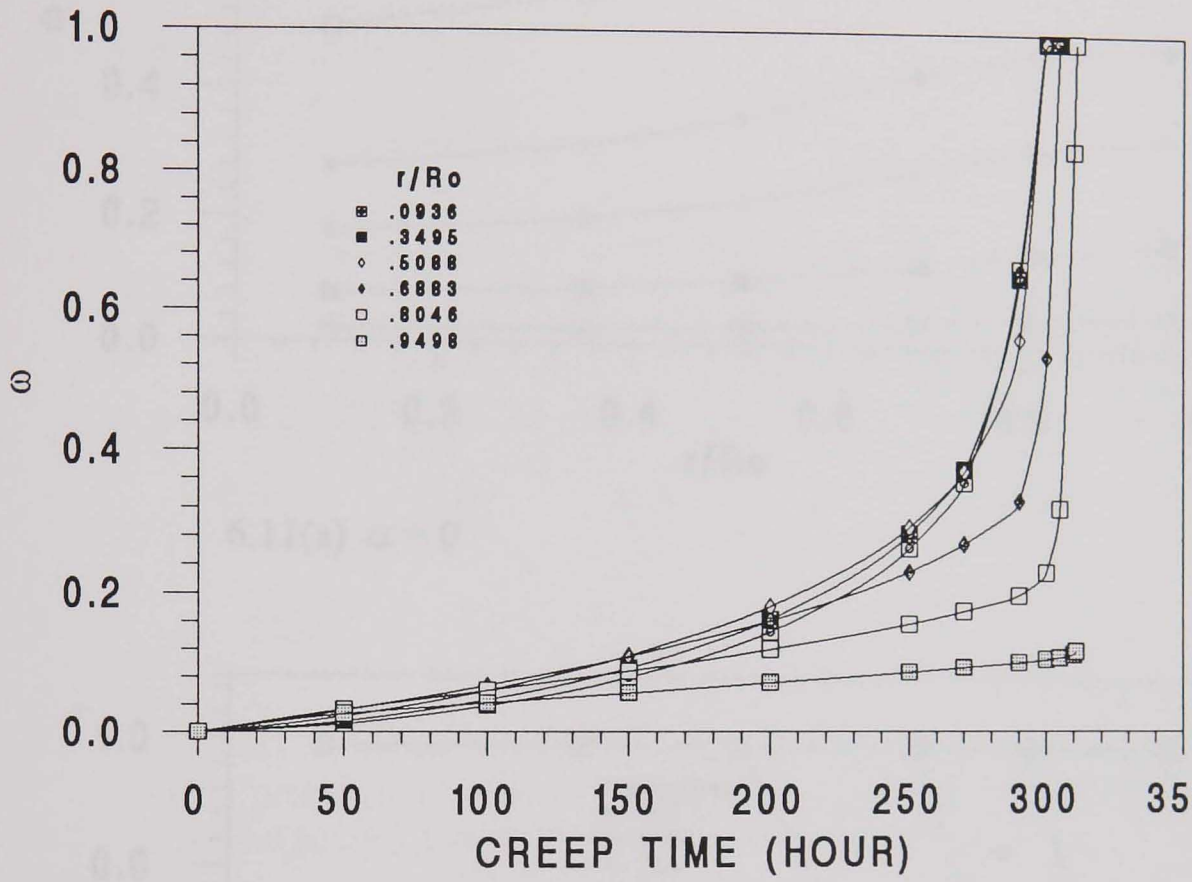

6.10(c) $\alpha = 1.0$

Fig. 6.10 Damage variations on the minimum notched section with creep time for different radial positions for aged parent material at 70MPa (Ro is the radius of the minimum notched section).

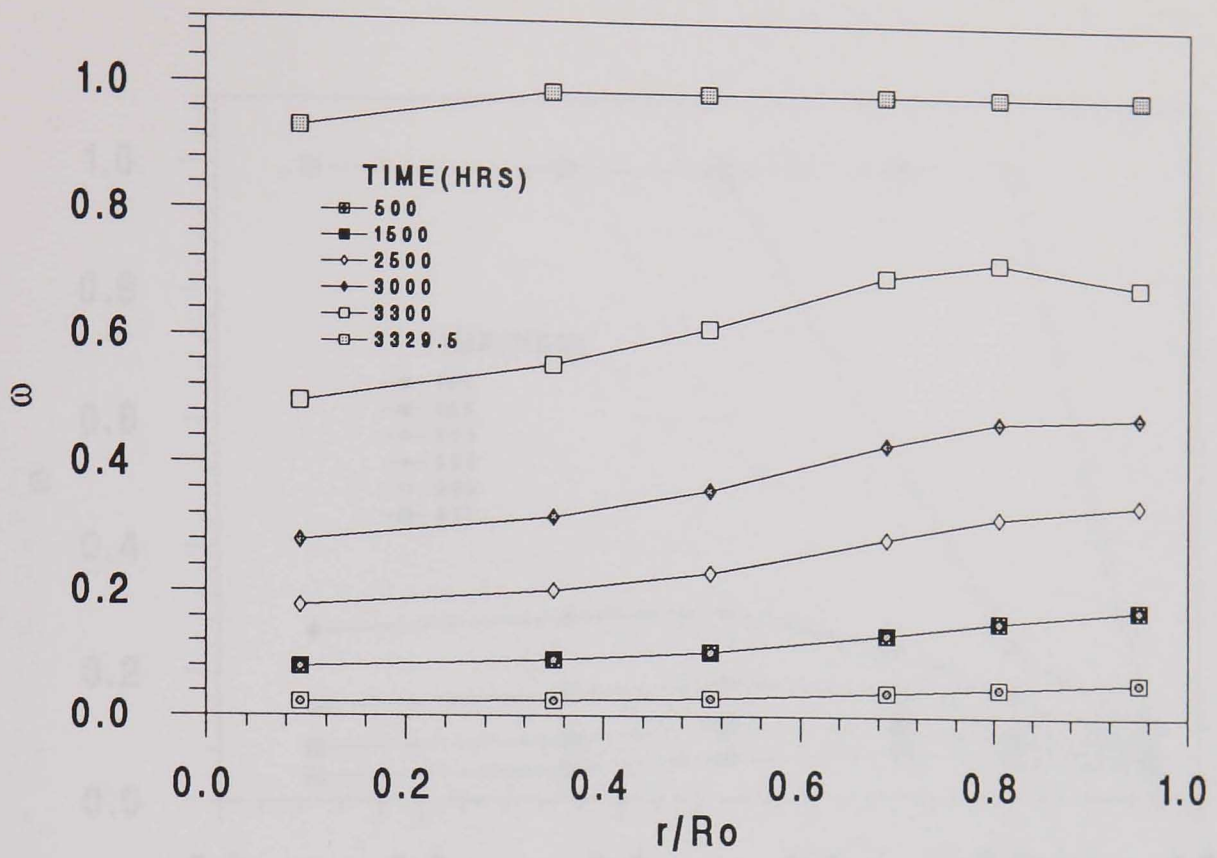

6.11(a) $\alpha = 0$

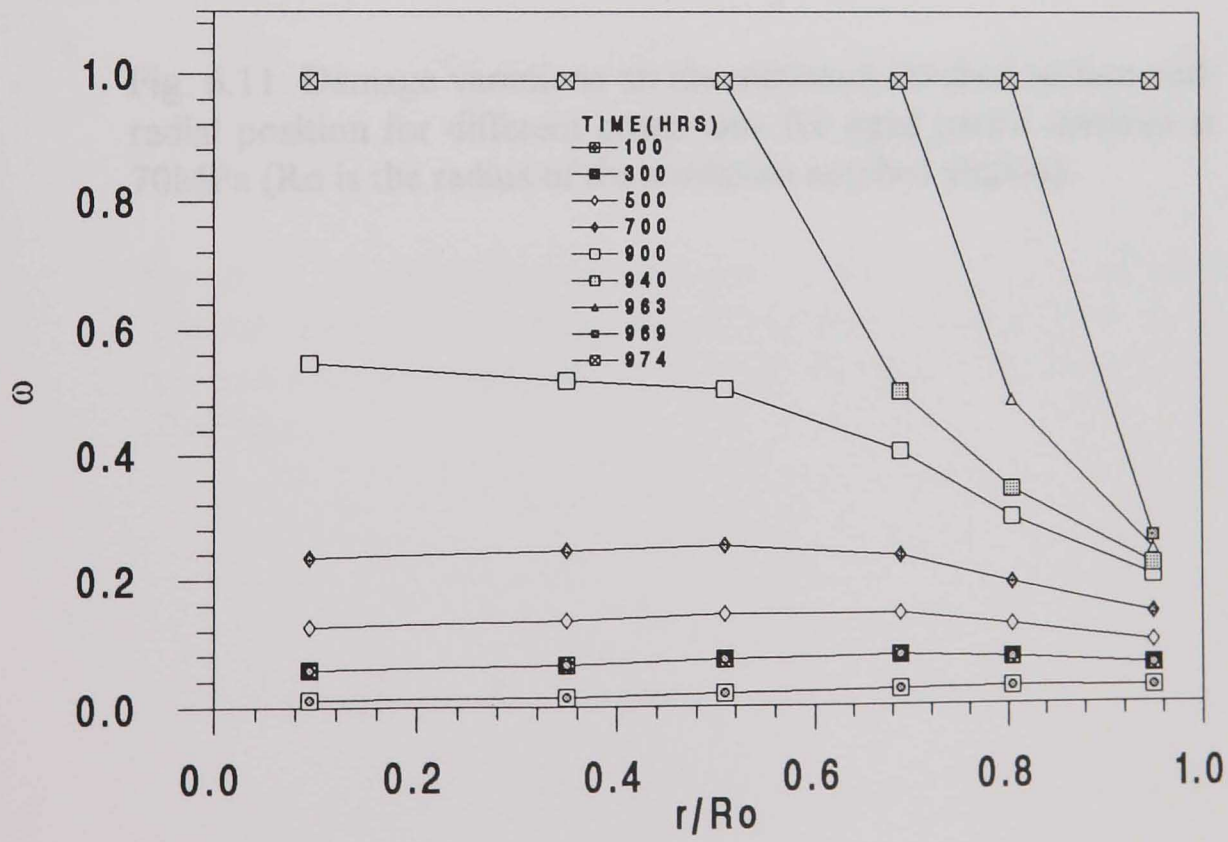

6.11(b) $\alpha = 0.5$

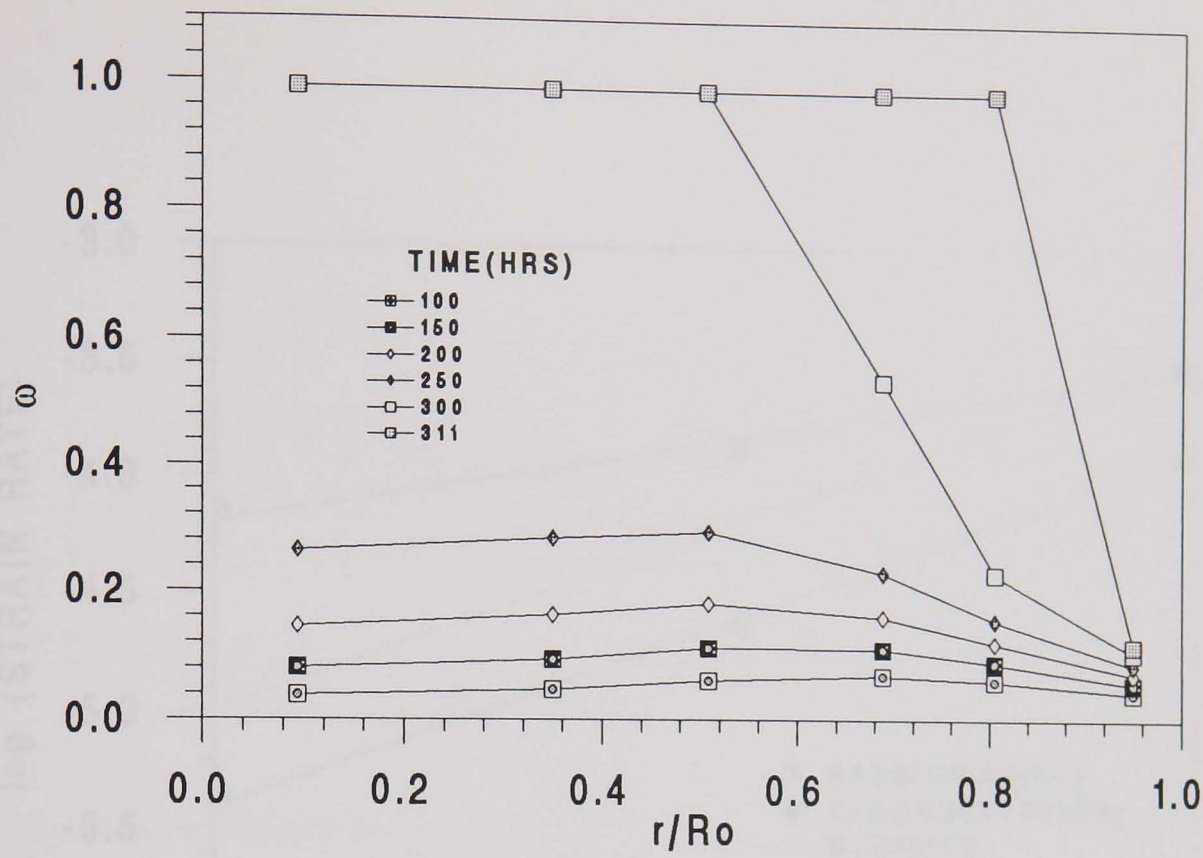

6.11(c) $\alpha = 1.0$

Fig. 6.11 Damage variations on the minimum notched section with radial position for different creep time for aged parent material at 70MPa (Ro is the radius of the minimum notched section).

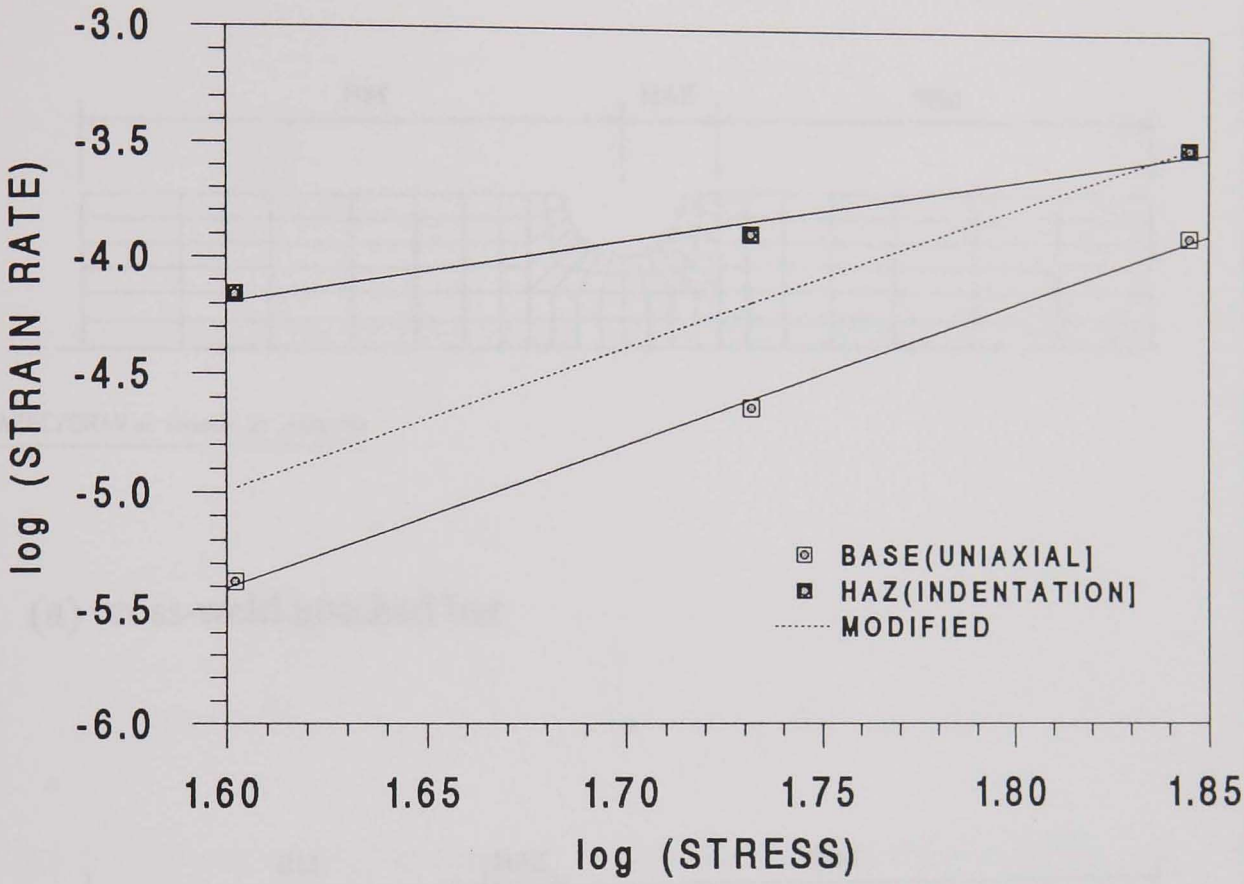

Fig. 6.12 Modification of steady-state strain rate of aged HAZ material (using the n value of aged parent material and the strain rate value obtained from the aged HAZ material indentation test at 70MPa).

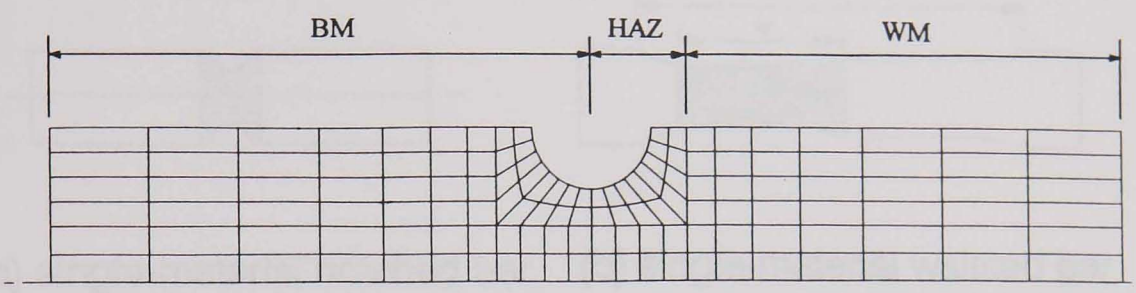

(a) cross-weld notched bar

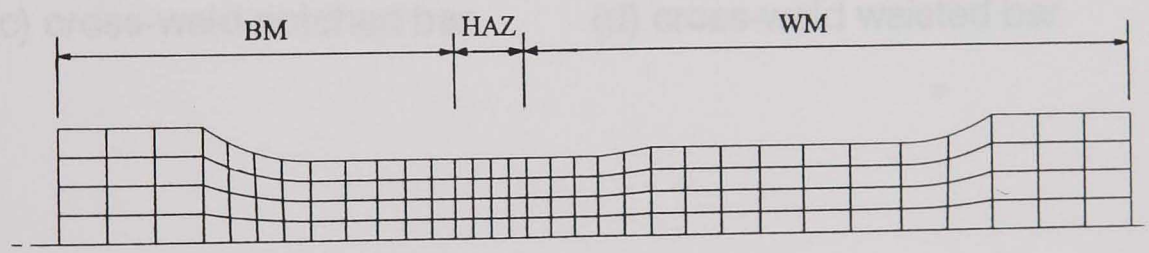

(b) cross-weld waisted bar

Fig. 6.13 FE meshes for the damage models of cross-weld specimens.

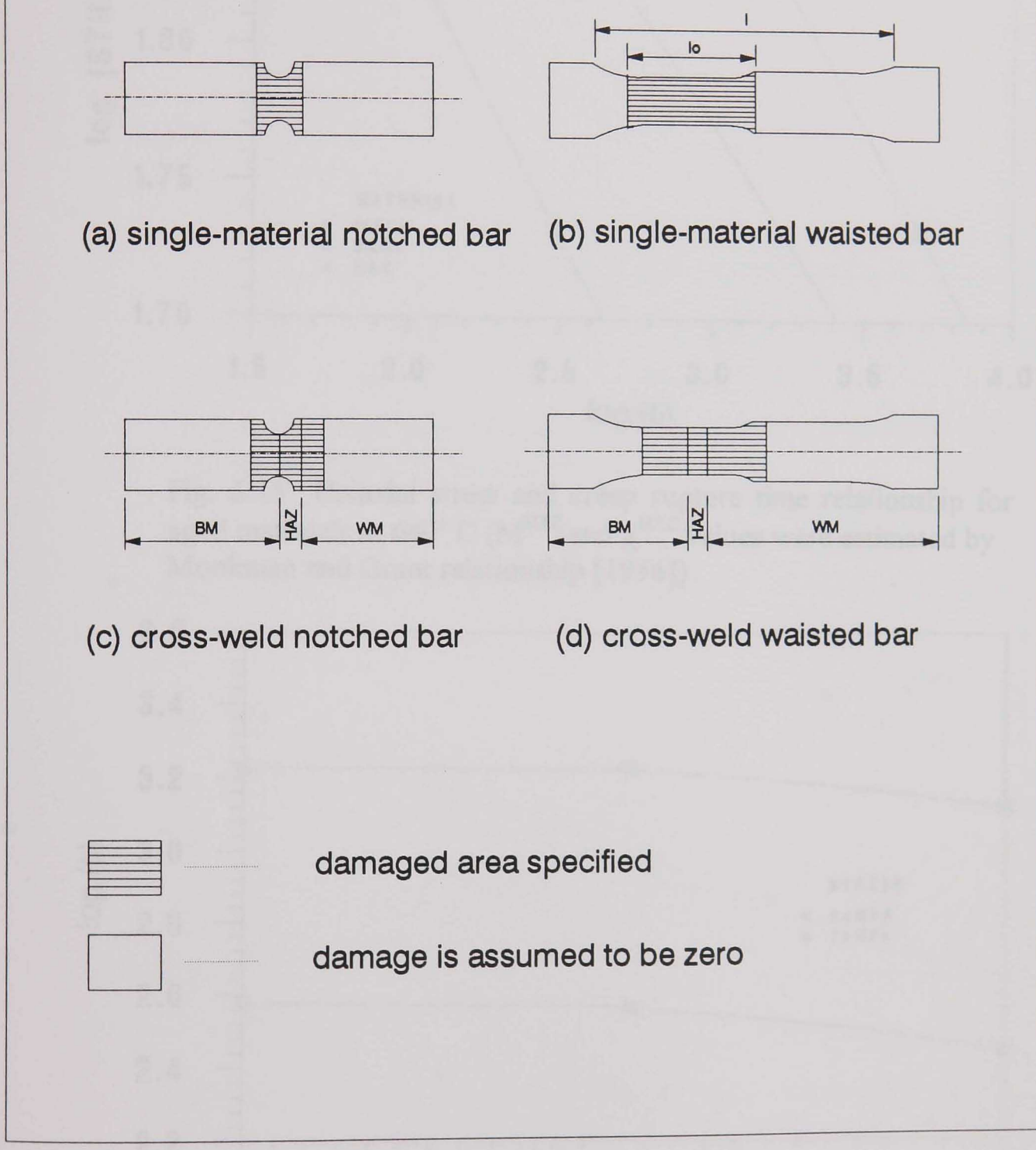

(a) single-material notched bar (b) single-material waisted bar

(c) cross-weld notched bar (d) cross-weld waisted bar

Fig. 6.14 Specification of the damage areas of FE models.

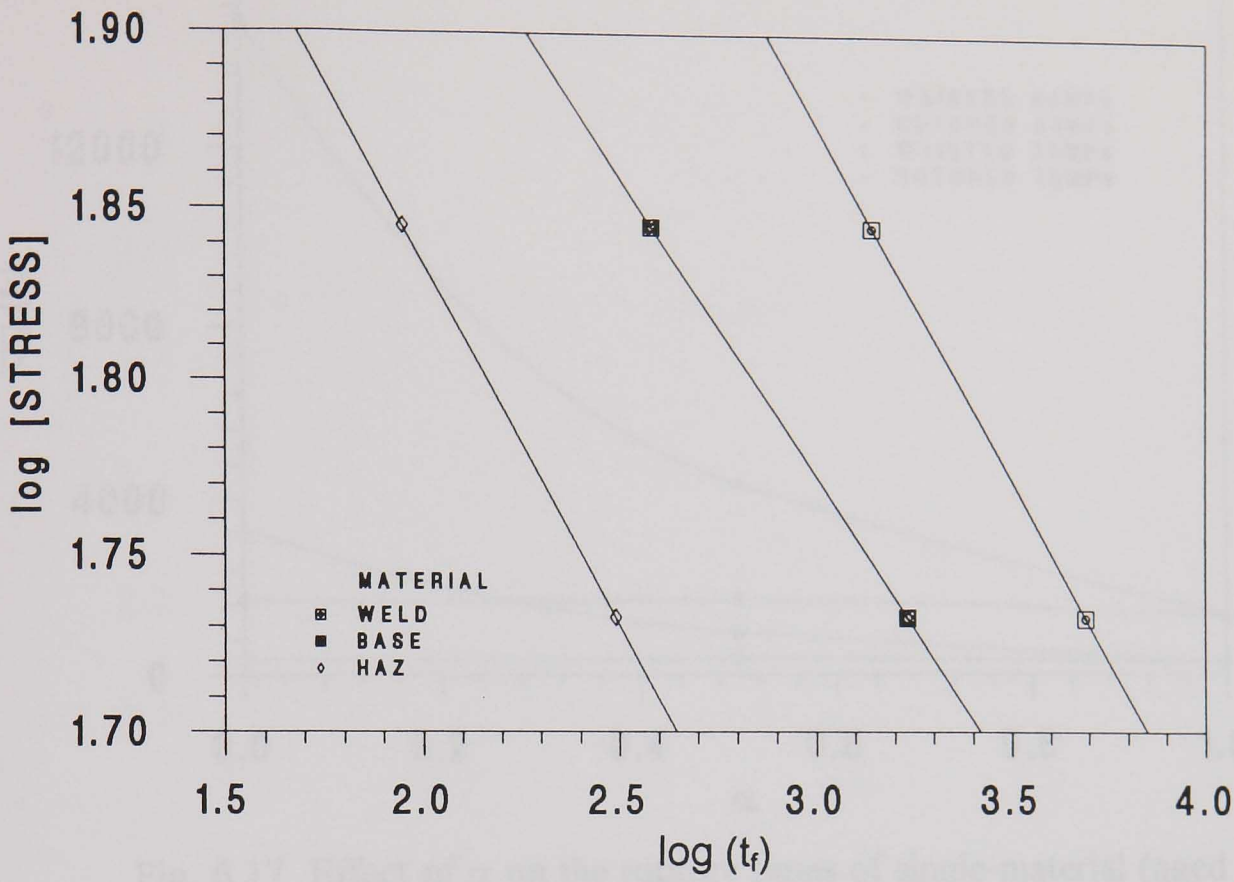

Fig. 6.15 Uniaxial stress and creep rupture time relationship for aged materials at 640° C (M^{HAZ} and χ^{HAZ} values were estimated by Monkman and Grant relationship [1956]).

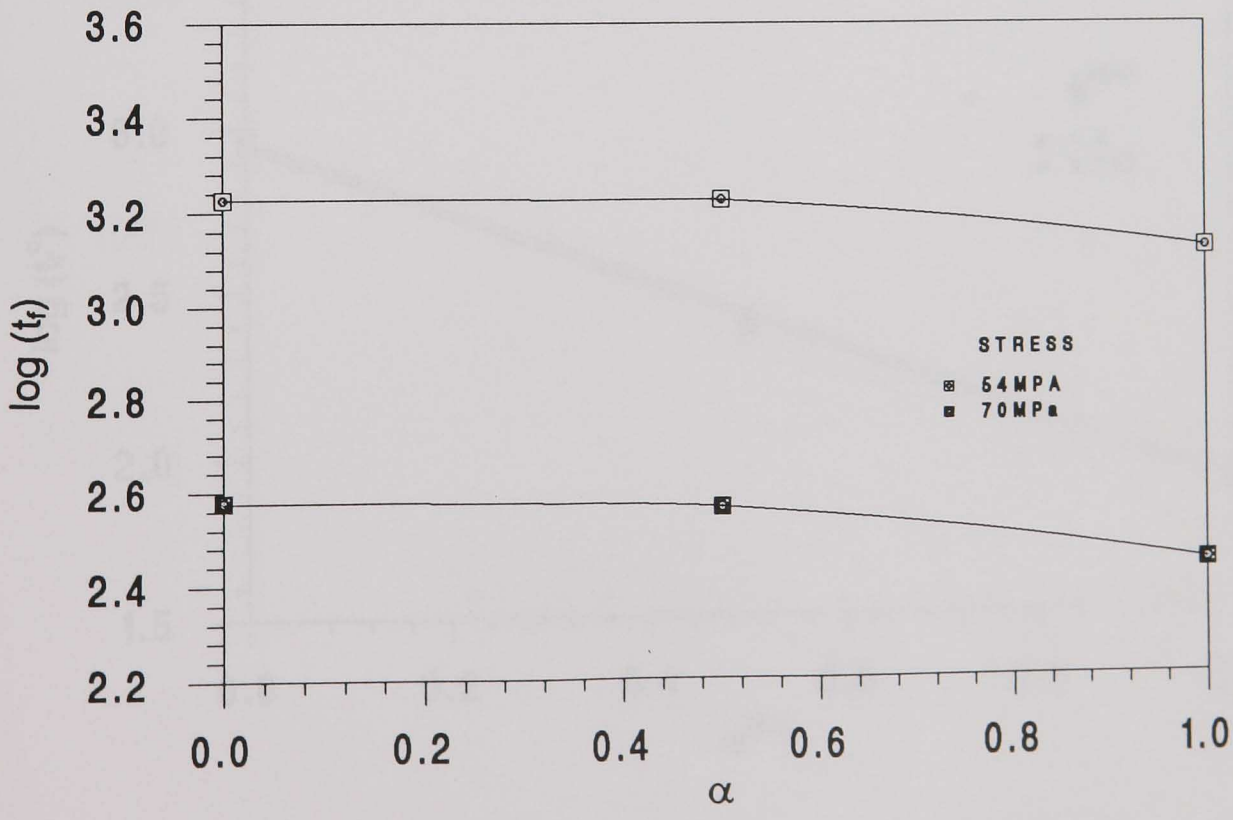

Fig. 6.16 Effect of α on the rupture time of single-material (aged parent) waisted specimen.

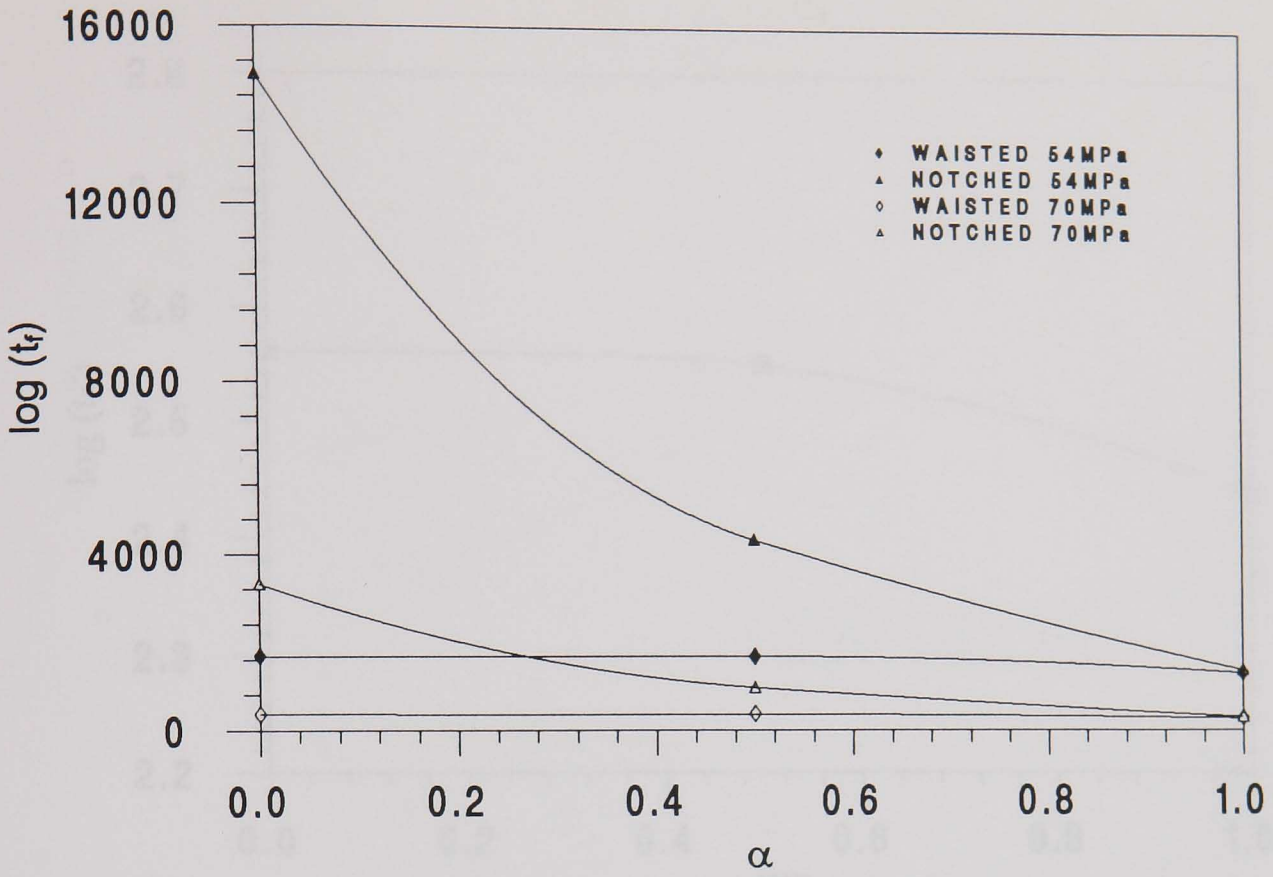

Fig. 6.17 Effect of α on the rupture times of single-material (aged parent) waisted and notched specimens.

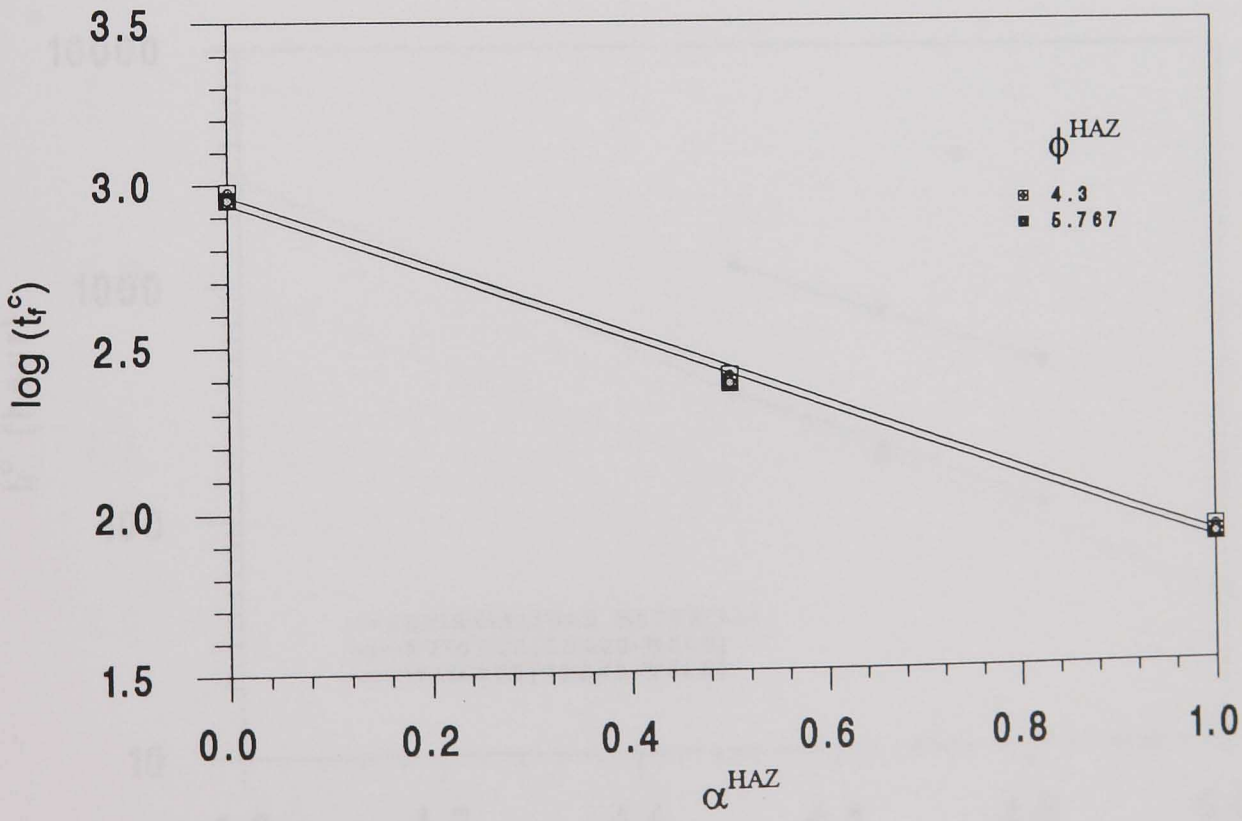

Fig. 6.18 Effect of α^{HAZ} and ϕ^{HAZ} on the rupture time of cross-weld notched bar at 70MPa ($M^{HAZ} = 1.478 \times 10^{-11}$ and $\chi^{HAZ} = 4.1849$).

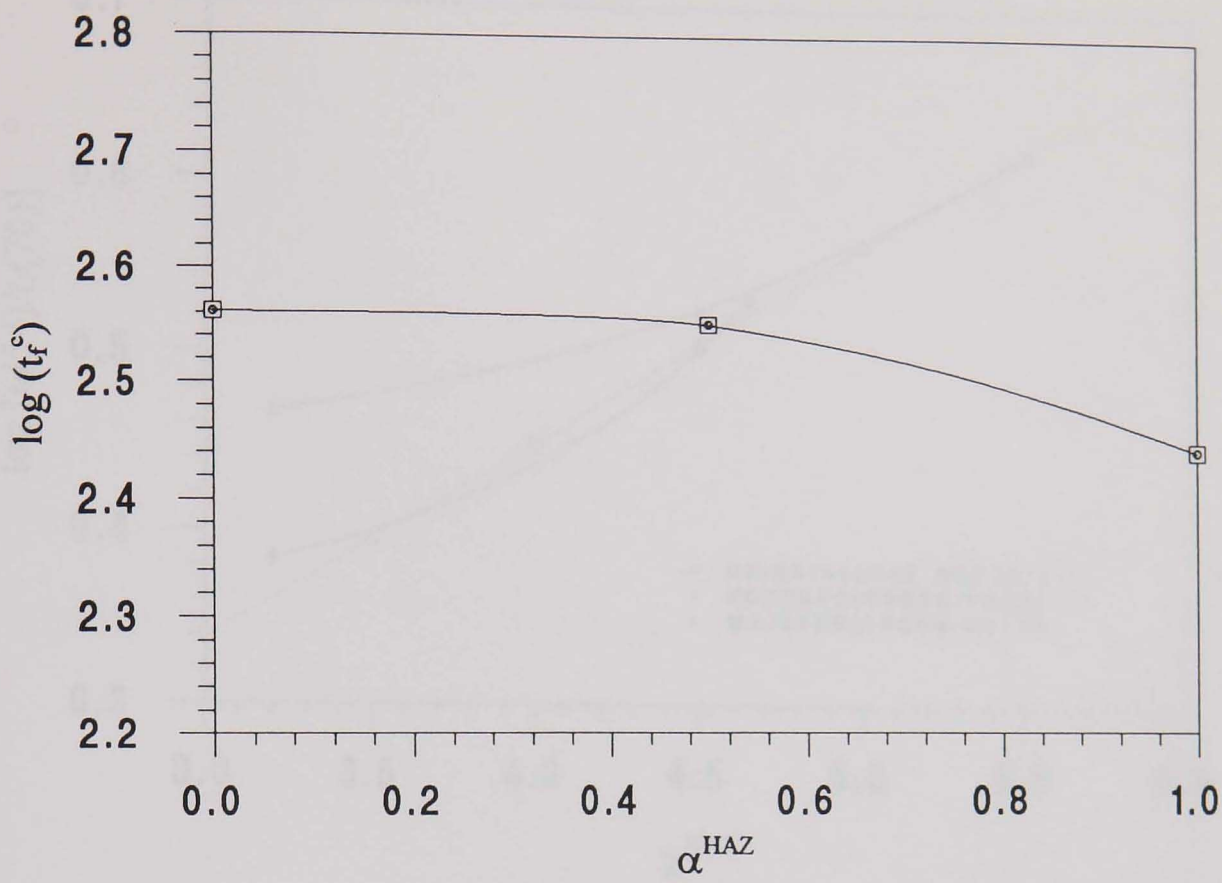

Fig. 6.19 Effect of α^{HAZ} on the rupture time of cross-weld waisted specimen at 70MPa ($\phi^{HAZ} = 4.3$, $M^{HAZ} = 2.5 \times 10^{-9}$ and $\chi^{HAZ} = 3.2$).

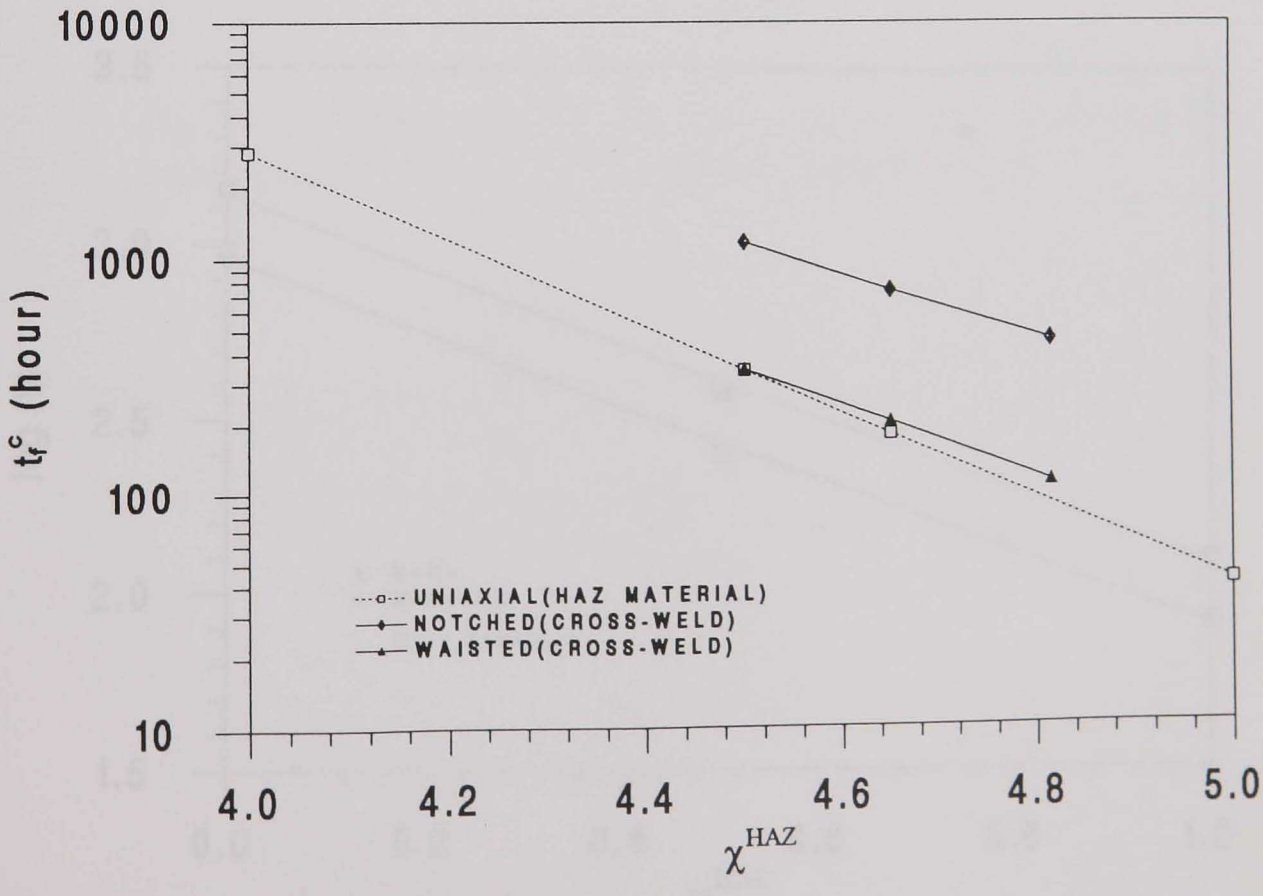

Fig. 6.20 Effect of χ^{HAZ} on the rupture time of cross-weld specimens at 70MPa ($\phi^{HAZ} = 4.3$, $M^{HAZ} = 1.478 \times 10^{-11}$ and $\alpha^{HAZ} = 0.3$).

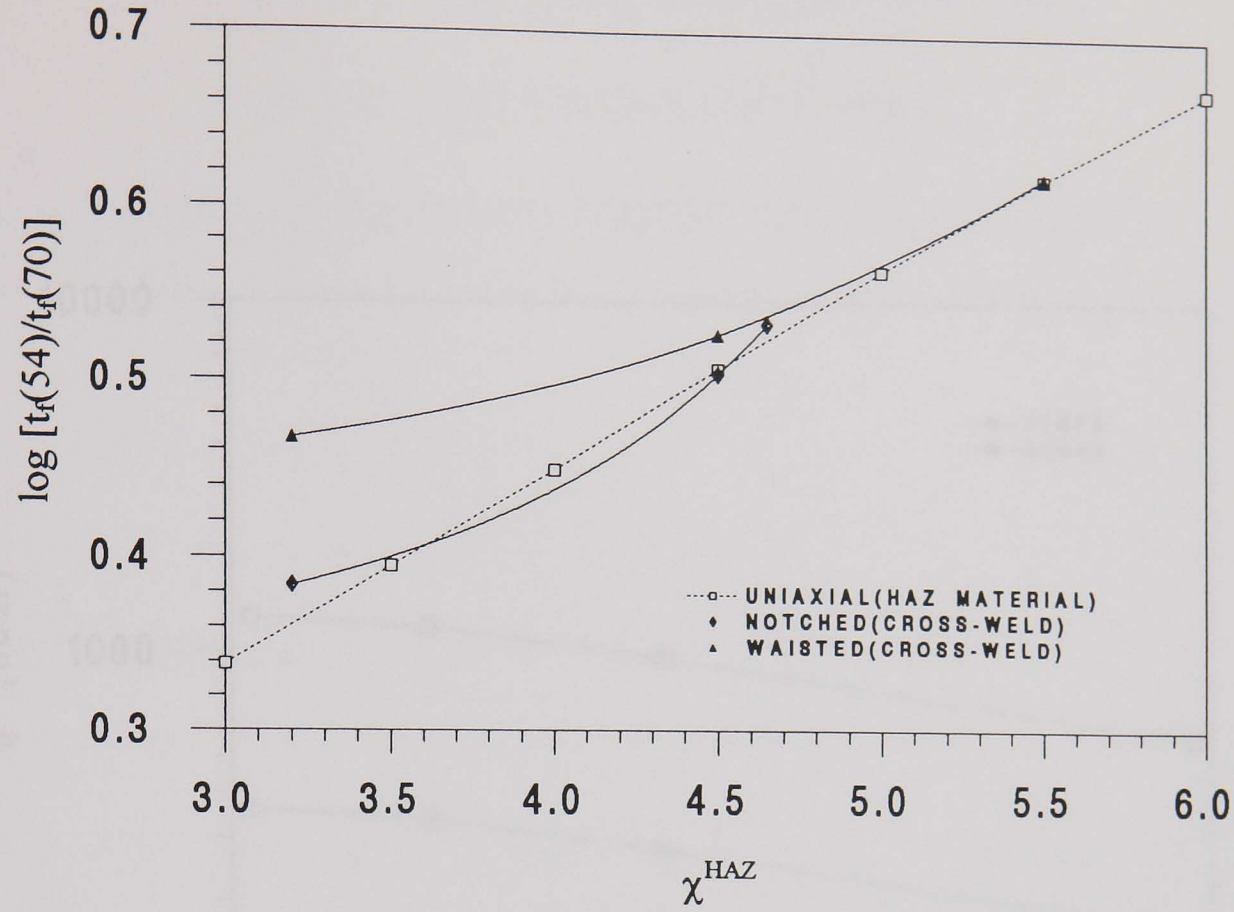

Fig. 6.21 Effect of χ^{HAZ} on the rupture time ratios of 54MPa to 70MPa of cross-weld specimens ($\phi^{HAZ} = 4.3$, $M^{HAZ} = 1.478 \times 10^{-11}$ and $\alpha^{HAZ} = 0.3$).

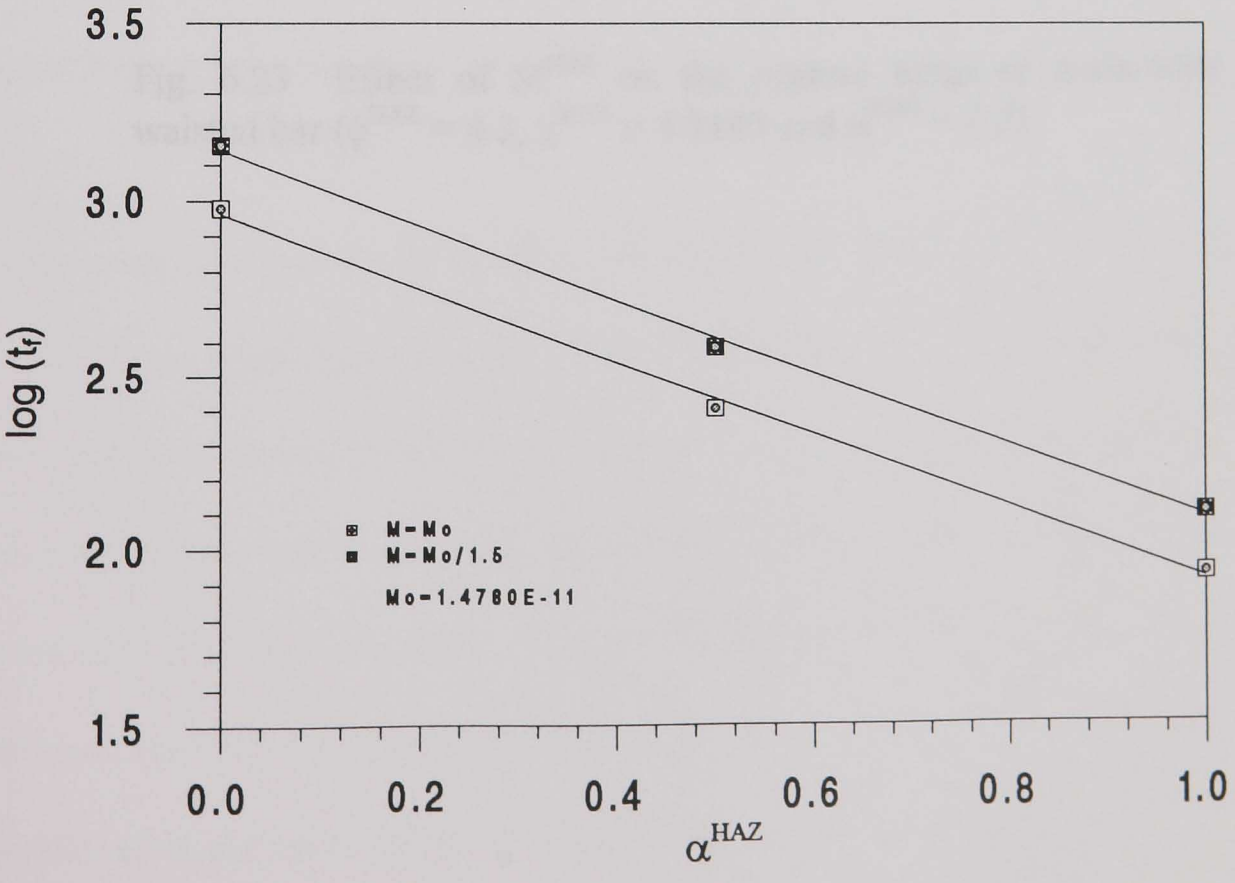

Fig. 6.22 Effect of M^{HAZ} on the rupture times of cross-weld notched bar at 70MPa ($\phi^{HAZ} = 4.3$ and $\chi^{HAZ} = 4.8149$).

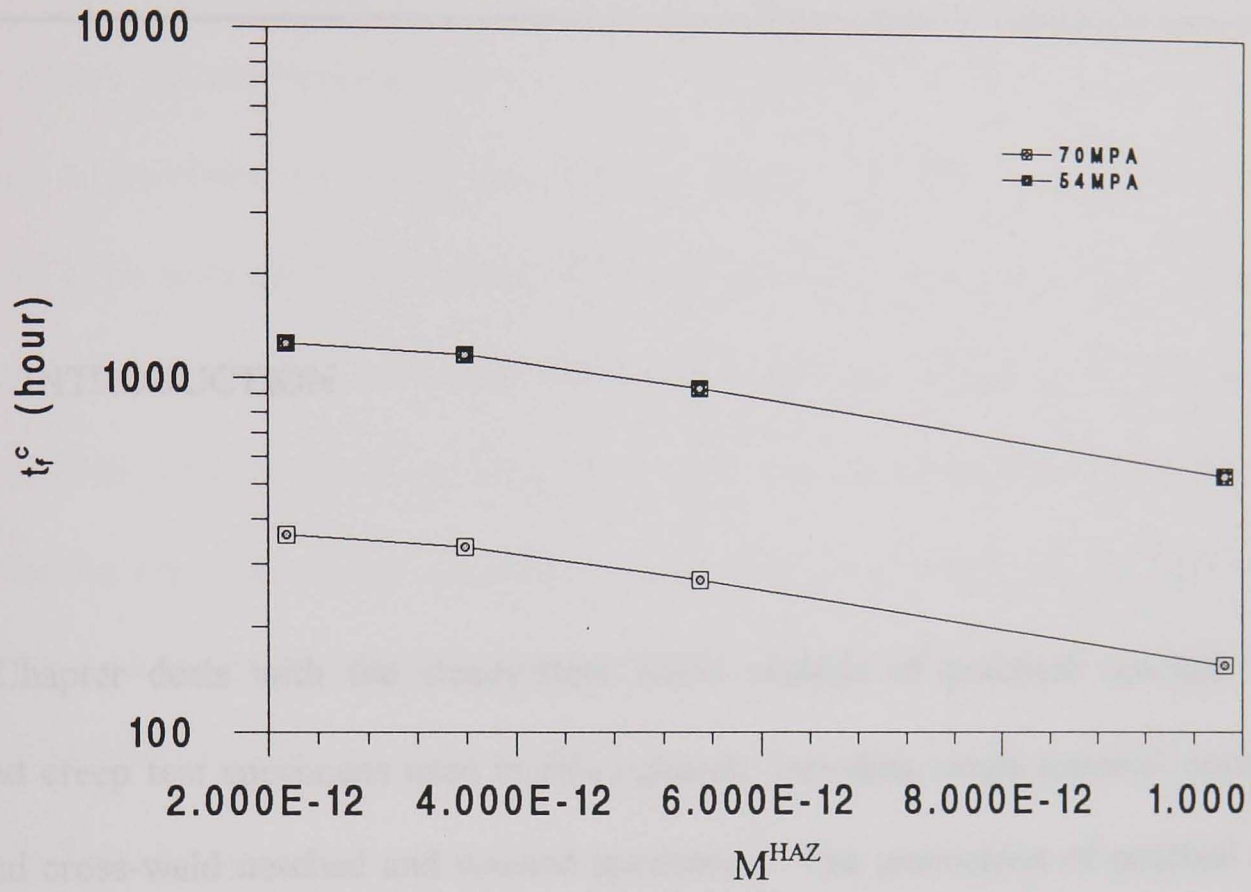

Fig. 6.23 Effect of M^{HAZ} on the rupture times of cross-weld waisted bar ($\phi^{HAZ} = 4.3$, $\chi^{HAZ} = 4.8149$ and $\alpha^{HAZ} = 0.3$).

CHAPTER VII

STEADY-STATE RUPTURE STRESS ANALYSIS AND FAILURE PREDICTION FOR NOTCHED AND WAISTED CREEP TEST SPECIMENS

7.1 INTRODUCTION

This Chapter deals with the steady-state stress analysis of practical notched and waisted creep test specimens used in this research, including single-material notched bar and cross-weld notched and waisted specimens. The geometries of notched and waisted specimens have been shown in Fig. 5.7.

Steady-state creep analyses of the notched and waisted specimens were performed for the purpose of investigating the detailed stress distributions and examining the multi-axial stress states of notched and waisted specimens. As in damage modelling, the cross-weld specimens were assumed to consist of three materials, i.e. parent material, HAZ (4 mm in width) and weld metal. In cross-weld specimens, the boundary of HAZ and parent material is positioned in the centre section of the notch for notched bars, and is positioned at the centre of the waisted section for waisted specimens. The creep properties used (see Table 7.1) are the realistic material properties of the service-aged

weldment which have been obtained at 640° C (see Chapters V and VI). Therefore, the results of this investigation can be used directly to present the steady-state creep behaviour of these test specimens.

The notched and waisted specimens were modelled using axisymmetric, 8-node, isoparametric, quadratic elements. Typical FE meshes of symmetric halves of the notched and waisted specimens are shown in Figs. 7.1(a) and 7.1(b), respectively. Uniaxial loads were applied to the ends of the specimens to give a nominal stress, σ_{nom}, on the minimum notched section of the notched bars and on the uniformly waisted section of the waisted specimens (σ_{nom} = 70 MPa was used in the investigation). As used for the experimental test specimens, the dimensions of single-material and cross-weld notched specimens were identical. Both the single and multi-material (exposed parent, HAZ and weld materials) notched and waisted specimens were analysed, in order to examine the multi-axial stress states and compare steady-state data with the damage modelling results which have been introduced in Chapter VI. The steady-state creep analysis was performed by ABAQUS [1994].

Table 7.1 Material constants A, n, M, χ and α of the aged weldment

	PARENT	HAZ	WELD
A	6.5991×10^{-16}	1.7083×10^{-15}	9.7181×10^{-15}
n	6.1080	6.1080	5.2082
M	5.9981×10^{-14}	2.5×10^{-9}	8.1202×10^{-13}
χ	5.767	3.2	4.8496
α	0.30	0.49	0.2639

The steady-state stresses of the single-material and cross-weld notched and waisted specimens were investigated. A steady-state rupture stress, σ_r, has been defined, i.e. $\sigma_r = \alpha\hat{\sigma} + (1-\alpha)\sigma_{eq}$, which has the same form as that of Equ. (2.14), where α is a tri-axial parameter. In addition, for the purpose of examining the shape effect of the notched bars, single-material notched specimens with varied geometry were also modelled. A geometry ratio, Φ/Φ_o, was used to represent the size of the notched bars, where Φ is the diameter of the uniform sections of the notched bars and Φ_o is the diameter of the minimum notched section. The ratio of Φ/Φ_o used for the practical test specimens of the notched bars in this research is 1.6667, see Fig. 5.7.

Using an "effective steady-state rupture stress", an approximate method for specimen failure prediction was employed. By comparing the failure results of the cross-weld test specimens predicted by steady-state analysis with the results from damage modelling, the applicability of the technique can be established.

7.2 STRESS ANALYSIS OF THE NOTCHED AND WAISTED SPECIMENS

7.2.1 Stress Distributions

(a) Single-material specimens

Examples of stress contours (only parts of the models are shown) of σ_a, $\hat{\sigma}$, σ_{eq} and σ_r in notched and waisted specimens for the aged parent material ($\alpha^B = 0.3$) are presented in Fig. 7.2 - Fig. 7.5, where σ_a, $\hat{\sigma}$, σ_{eq} are the axial stress, maximum principal stress and von-Mises equivalent stress, respectively. It can be seen that on the centreline of both the notched and waisted specimens, $\hat{\sigma} = \sigma_a$, see Figs. 7.2 and 7.3, due to the assumption of axisymmetry. For the notched bar, as expected, significant stress concentration is exhibited in the notched area. The peak value of $\hat{\sigma}$ occurs at the centreline on the notched section, see Fig. 7.3(a), with a normalised value of $\hat{\sigma}_{max}/\sigma_{nom}$ = 1.090, whereas the peak value of σ_{eq} occurs at the outer surface of the notched section, as shown in Fig. 7.4(a), with a normalised value of $\sigma_{eqmax}/\sigma_{nom}$ = 0.7686. The rupture stress, σ_r, has no significant variation across the notched section, with a peak value of $\sigma_{rmax}/\sigma_{nom}$ = 0.8114, see Fig. 7.5(a) at the outer surface. In the case of the waisted specimen, no significant stress concentration was identified. The peak values of $\hat{\sigma}$, σ_{eq} and σ_r all occur on the centre line in the waisted section and near the corner towards the end of the specimen, having normalised values of 1.0728, 1.0157 and 1.0271, respectively, see Figs. 7.2(b) - 7.5(b). The distributions of σ_{eq} and σ_r are similar, see Figs. 7.4(b) and 7.5(b).

Table 7.2 presents the normalised peak rupture stress $\sigma_{rmax}/\sigma_{nom}$ from which the stress reduction of the notched specimen can be clearly seen, especially in the cases of small α values. When $\alpha = 0$ ($\sigma_r = \sigma_{eq}$) the peak rupture stress is 23.14% lower than the nominal stress. However, with the increase of α, the stress reduction becomes less significant. When $\alpha = 1$ ($\sigma_r = \hat{\sigma}$) the peak rupture stress is 9.0% higher than the

nominal stress. The variations of the peak rupture stresses against α for the notched and waisted specimens are also shown in Fig. 7.6.

The tri-axiality caused by the waisted shape is very weak, i.e. the creep behaviour of the uniformly waisted part of the specimen will be similar to that of a uniaxial specimen under the same nominal stress. The behaviour can also be seen in Table 7.2 and Fig. 7.6 from which it can be found that the rupture stress is very weakly dependent on α and an approximately linear relationship between the peak rupture stress and α was obtained.

Table 7.2 *Normalised peak rupture stresses of single-material (aged parent material) notched* (Φ/Φ_o =1.6667) *and waisted specimens*

	$\sigma_r(\alpha = 0)$	$\sigma_r(\alpha = 0.2)$	$\sigma_r(\alpha^B = 0.3)$	$\sigma_r(\alpha = 0.5)$	$\sigma_r(\alpha = 1)$
Notched	0.7686	0.7857	0.8114	0.8828	1.0900
Waisted	1.0157	1.0228	1.0271	1.0371	1.0728

(b) Cross-weld specimens

Examples of stress contours (only parts of the models are shown) of σ_a, $\hat{\sigma}$, σ_{eq} and σ_r ($\alpha^{HAZ} = 0.49$) of cross-weld notched and waisted specimens are presented in Figs. 7.7 - 7.10. Again, on the centreline of both the notched and waisted specimens, $\hat{\sigma} = \sigma_a$, see Fig. 7.7 and Fig. 7.8. Also, for the notched bar, the peak value of $\hat{\sigma}$ in the HAZ

occurs at the centreline on the notched section, with a normalised value of 1.1286. The normalised peak value of σ_{eq} in the HAZ is 0.8243 occurring at the outer surface of the notched section, whereas the peak value of the rupture stress, σ_r, in the HAZ appears near the centreline on the notched section with a value of $\sigma_{r\,max}^{HAZ}/\sigma_{nom} = 0.88$. In the case of the waisted specimen, stress concentration appears around the material interfaces. The peak $\hat{\sigma}$, σ_{eq} and σ_r in the HAZ all occur at the centreline, having the normalised values of 1.1814, 0.9657 and 1.0714, respectively. Fig. 7.11 shows the normalised peak rupture stress variations against α for the notched and waisted specimens. An approximately linear relationship was found between the peak rupture stress in the HAZ and α of the waisted specimen.

It should be noted that since the meshes for the cross-weld specimens at the stress singularity areas are not sufficiently fine, the stresses near the singular points are not accurate.

7.2.2 Shape Effect of Single-Material Notched Bars

It can be seen from the above analysis that stress reduction occurs in the notched section of the notched bar in the case of Φ/Φ_o =1.6667, for both single-material and cross-weld specimens, when $\alpha \leq 0.8$ and $\alpha \leq 0.75$, respectively. In order to study the shape effect of the notched specimens, single-material (aged parent) notched bars with different Φ/Φ_o ratios were analysed (without changing the shape of the semi-circle), using the parent material creep properties. The normalised peak rupture stress and the rupture stresses at the centre line and outer surface of the notched section, against α,

for a range of Φ/Φ_o values, are presented in Figs. 7.12(a) - 7.12(c), respectively, where it can be seen that the centre line and outer surface rupture stresses vary linearly with α. When $\alpha \leq 0.5$, stress reduction occurs for all values of Φ/Φ_o. In addition, it can be seen that the highest values of the peak rupture stresses occur at $\Phi/\Phi_o = 1.3333$, when $\alpha \leq 0.35$, and at $\Phi/\Phi_o = 2.0$, when $\alpha > 0.35$.

7.3 APPLICATION OF THE STEADY-STATE STRESS ANALYSIS RESULTS

7.3.1 Steady-State Failure Predictions

As described in Section 7.2, the positions where the steady-state peak rupture stresses occur, in single-material specimens or in the different zones of cross-weld specimens, can be identified. Since in creep damage rupture equations (see Equs. (2.11) and (2.13)) the failure behaviour of a structure or a component is governed by the rupture stress, it can be assumed that the failure will occur at the positions where the maximum rupture stress appears. Also, by assuming that the peak values of the steady-state rupture stresses remain constant throughout the creep process, it is possible to make an approximate prediction of the failure times, t_{fss}, from the steady-state creep solutions. Based on these assumptions, Equ. (2.13) can be integrated to give

$$t_{fss} = \frac{1}{M\sigma_r^{\chi}} \tag{7.1}$$

where M and χ are material constants shown in Table 7.1.

The rupture stress in Equ. (7.1) can be referred to as an effective failure stress. In multi-material cases, each material zone has a steady-state peak rupture stress (obtained with the corresponding α value of the material). The peak rupture stress throughout the zones which gives the minimum rupture life is taken to be the effective failure stress of the component.

Using the above equation, with the peak rupture stresses obtained from the steady-state analysis and the damage constants M and χ already generated (see Table 7.1), the corresponding rupture times of the notched and waisted specimens can be estimated. Table 7.3 presents the failure times of single-material specimens at σ_{nom} = 70 MPa predicted using the steady-state peak rupture stress, σ_{rmax}. For comparison purposes, the failure times predicted using both the centreline rupture stress, σ_{rc}, and the rupture stress at the outer surface, σ_{ro}, are also presented. Obviously, the rupture times predicted by the peak rupture stress, σ_{rmax}, are generally consistent with the corresponding FE damage data, but are significantly conservative.

Referring to the steady-state results for the peak rupture stresses in the different material zones and using Equ. (7.1), the failure times of the cross-weld notched and waisted specimens at 70 MPa have been predicted and presented in Table 7.4, which also shows the results of the damage analyses. The failure times and the failure positions of the cross-weld specimens, predicted by both the steady-state and damage analyses, are presented in Table 7.5. The failure times of the specimens are determined by the minimum rupture times of the three zones. It can be seen from Table 7.4 and

Table 7.5 that the rupture time of the notched bar is controlled by the peak rupture stress in the HAZ at the interface between the HAZ and parent material whereas the rupture time of the waisted specimen is controlled by the peak rupture stress in the parent material at the same boundary. Again, the steady-state predictions are conservative, compared with the damage predictions, with an error of 12.4% for the notched bar and 40% for the waisted specimen.

Table 7.3 Steady-state rupture times of the single-material notched bar (exposed parent material at 70 MPa) for different α values

α	Damage t_f(hour)	Steady-State (stress in MPa and time in hour)					
		σ_{rmax}	t_{fss}	σ_{rc}	t_{fss}	σ_{ro}	t_{fss}
0.0	3330.0	53.8	1740.0	45.9	4348	53.8	1740.0
0.5	974.0	61.8	782.2	61.0	843.3	56.0	1381.0
1.0	312.5	76.3	232.0	76.1	235.5	58.3	1094.9

Table 7.4 Failure times of the different zones of the cross-weld specimens predicted by the steady-state analysis at 70 MPa

	Steady-State Prediction				Damage Prediction	
	Notched		Waisted		t_{fss}(hour)	
	σ_{rmax}(MPa)	t_{fss}(hour)	σ_{rmax}(MPa)	t_{fss}(hour)	Notched	Waisted
PARENT	58.7	1052.6	77.2	216.8	861	361
HAZ	61.5	754.5	75.0	399.8		
WELD	45.3	11455.6	89.4	423.9		

Table 7.5 *Comparison between the steady-state and damage failure predictions for the cross-weld specimens at 70 MPa*

	Steady-State		Damage		$(t_f-t_{fss}) / t_f$
	t_{fss}(hour)	Position	t_f(hour)	Position	(%)
Notched	754.5	At Boundary* (HAZ) and on the centreline	861	At Boundary* (HAZ) and on the centreline	12.37
Waisted	216.8	At Boundary* (Base) and on the centreline	361	At Boundary* (Base) and on the centreline	39.94

* Boundary of parent material and HAZ.

From the above analyses it is concluded that in addition to providing detailed stress distributions, the steady-state creep analyses can also be used to give a rough estimation of the failure time and position for creep components. On this basis, it can be assumed that the steady-state analysis can be used instead of damage modelling where an approximate, but quick estimation of the rupture data is required.

7.3.2 Other Applications

(a) Damage parameter generation

Based on the previous results, it has been demonstrated that steady-state rupture predictions can be used as an approximate method of predicting the failure behaviour of a uniaxial notched or waisted specimen, with acceptable accuracy. Therefore, it is reasonable to expect that the technique can also be used, as an approximate method, for damage constants generation. As mentioned before, the damage modelling is very time consuming, especially in the multi-material cases, such as those of cross-weld

specimens where relatively finer meshes are required. Although the steady-state predictions are not as accurate as the damage predictions, they can give quick estimations of the damage constants to be determined. An example is shown in Fig. 7.13 which presents the log (t_f) - α^{HAZ} relationships for the cross-weld notched specimens, predicted by both the steady-state and damage analyses. It can be seen that the approximate linear relationship still holds in the case of steady-state analysis and the gradients of the straight lines obtained from the steady-state results are nearly the same as those obtained from the damage modelling. This indicates that the errors of the steady-state predictions of the rupture time are practically independent of the α values.

(b) Determining the size of notched bars

In the steady-state failure prediction, the rupture life is only dependent upon the peak rupture stress, see Equ. (7.1). This implies that for a given material and under the given test conditions (nominal stress level, temperature, etc.), the rupture life of a notched specimen can be directly linked to the steady-state peak rupture stress. It can be seen that since the notched specimens used in this work possess a feature of stress reduction on the notched section, the rupture times of the notched bars, obtained experimentally and numerically, are significantly higher than those of the corresponding uniaxial plain specimens with the same nominal stress. Fig. 7.14 illustrates the rupture time ratios of the notched and waisted specimens against α, obtained from the steady-state solutions. It can be seen that the ratios are greater than unity for most of the α values and reduce when α increases. In addition, the ratios for the single-material case

are higher than those for the multi-material situation when $\alpha < 0.8$. Since in many practical cases, the α values for the ferritic weldment materials are generally less than 0.5, the increase of the test duration of the notched specimens will be significant.

From the results shown in Fig. 7.12(a), it seems possible that the experimental rupture times of the notched bars can be reduced by choosing a suitable notch geometry (Φ/Φ_o ratio) which gives a relatively higher peak rupture stress than other geometries at the same nominal stress. Fig. 7.12(a) shows that the optimum geometry ratios of the notched bar (Φ/Φ_o) can be determined if the α value of the material is known. For example, if $\alpha \approx 0$, then $\Phi/\Phi_o = 1.3333$ can be chosen. However, a further study needs to be carried out using damage modelling to confirm the behaviour established by the steady-state analysis.

7.4 DISCUSSION AND CONCLUSIONS

Generally, in the case of single-material notched bars, the notched shape introduces a strong stress concentration and causes a significant stress reduction in the notched section, i.e. $\sigma_r/\sigma_{nom} < 1$, when $\alpha \leq 0.8$, and the stress reduction is strongly dependent upon the tri-axial parameter, α, see Fig. 7.6. Obviously, if the failure time of the specimen is related to the steady-state rupture stress (based on the assumptions made earlier), the reduction of the rupture stress may introduce a life strengthening of the notched specimen, i.e., the failure life of a uniaxial notched specimen with a nominal

stress, σ_{nom}, should be greater than that of a uniaxial plain specimen, at the same nominal stress. However, the single-material waisted specimen does not exhibit stress reduction and the stress distribution is weakly dependent on α.

For the cross-weld specimens, the stress concentration in the notched bars is caused by both the shape and the multi-material properties, whereas the stress concentration in the waisted specimens is mainly caused by the difference in material properties. Again, similar to the single-material case, the notched shape causes a significant stress reduction in the HAZ of the notched area when $\alpha < 0.75$, and the rupture stress in the HAZ of the waisted specimens does not exhibit stress reduction, see Fig. 7.11. However, the rupture stress is more strongly dependent upon α than that of the single-material case.

Results of the steady-state analyses of both the single-material and cross-weld specimens have shown that the steady-state failure predictions can be used as an approximate, but quick method to estimate the possible failure life and failure position of single-material and multi-material components in creep conditions. On this basis, it is suggested that the steady-state analysis can also be used as an approximate technique for damage parameter generation, and the linear relationship between log (t_f) and α obtained from the steady-state solution still holds. It should be mentioned that although the steady-state rupture time prediction may not be completely accurate, the correct failure position can be obtained. In general, the rupture life predicted by the steady-state analysis is conservative, compared to the corresponding failure life predicted by damage modelling.

The principle the steady-state failure prediction is that the rupture life of a specimen or component can be related to the steady-state peak rupture stress. This indicates that in order to shorten the durations of the uniaxial rupture tests of the specimens such as the notched bars or other types of specimen, the steady-state analysis can be used to determine the suitable sizes or shapes of the specimens, which give relatively high peak rupture stresses at the possible failure positions. For instance, in the single-material case, it is evident that the rupture stresses of the notched specimens depend significantly on the Φ/Φ_o ratio. The relationship between the peak rupture stress and Φ/Φ_o is complex, see Fig. 7.12(a). For practical applications, the determination of Φ/Φ_o should be carefully considered, taking into account the possible α value of the specimen materials.

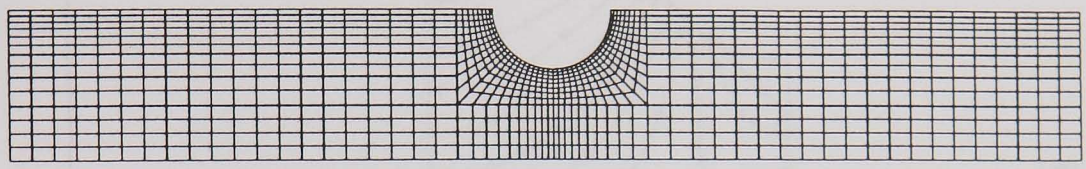

(a) notched bar

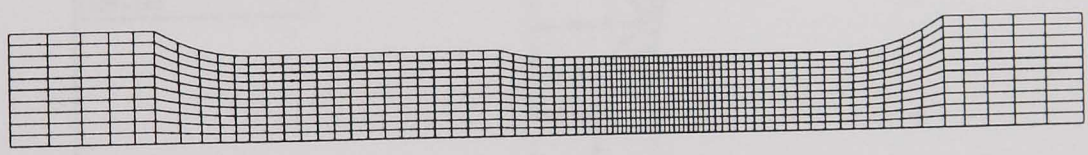

(b) waisted specimen

Fig. 7.1 Axisymmetric FE meshes of the cross-weld specimens used for steady-state creep analysis (positions of the HAZ have been shown in Fig. 6.13).

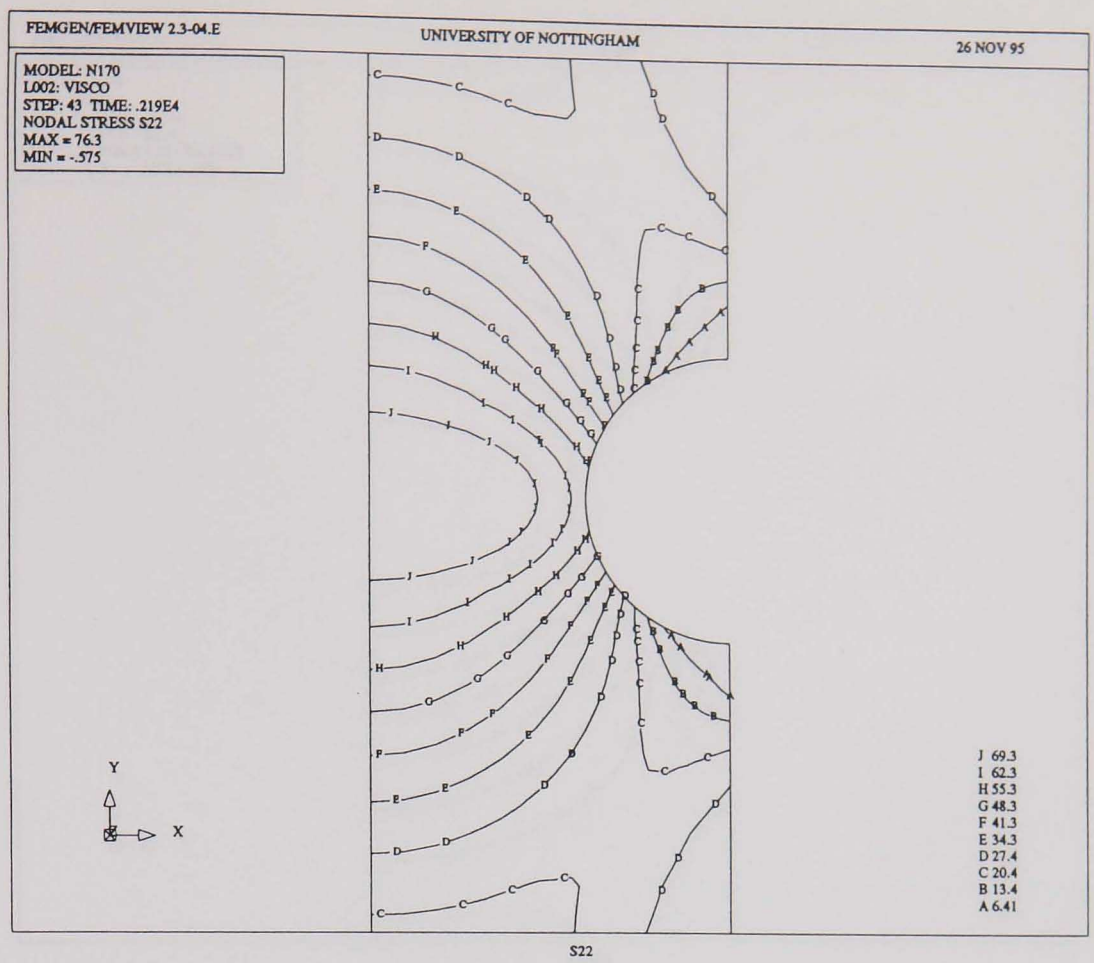

(a) notched bar

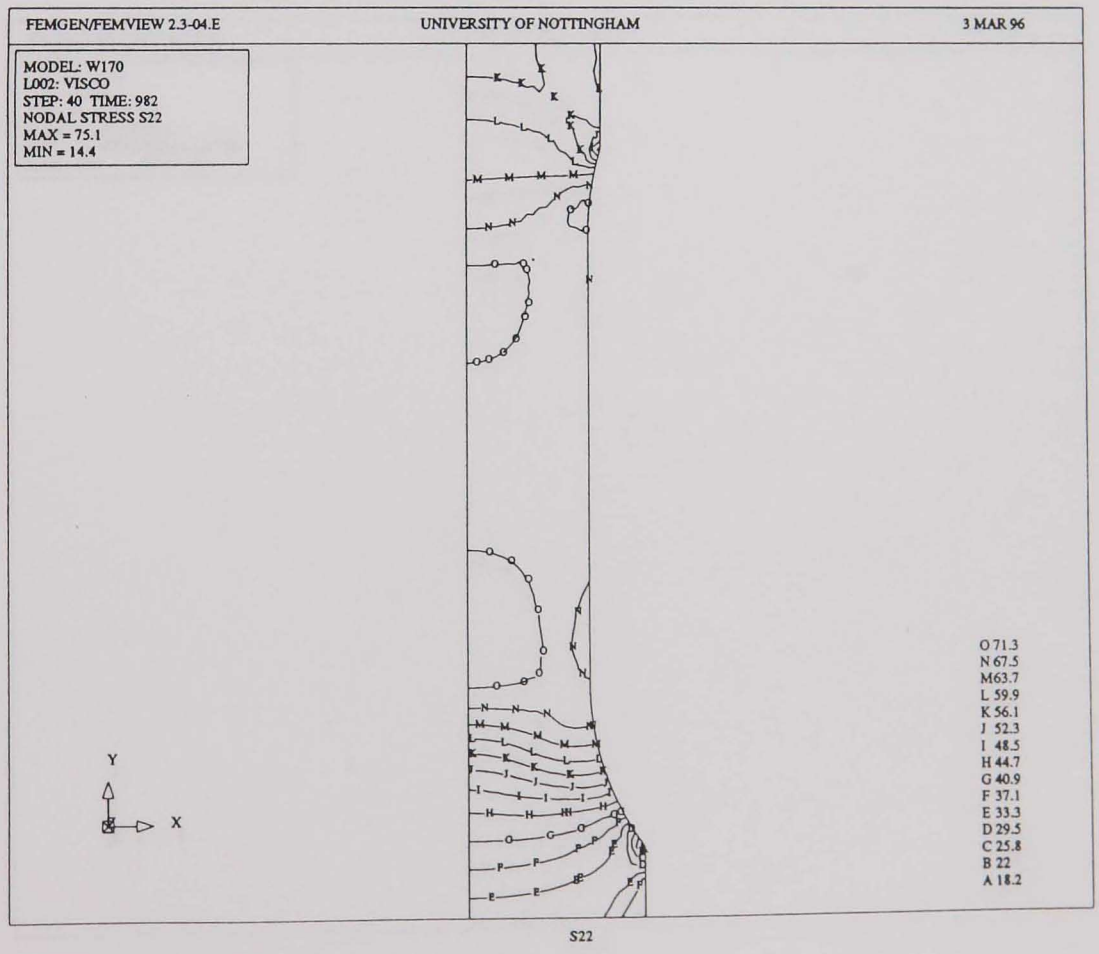

(b) waisted specimen

Fig. 7.2 Steady-state axial stress distributions of the single-material notched and waisted specimens (aged parent material, σ_{nom} = 70 MPa).

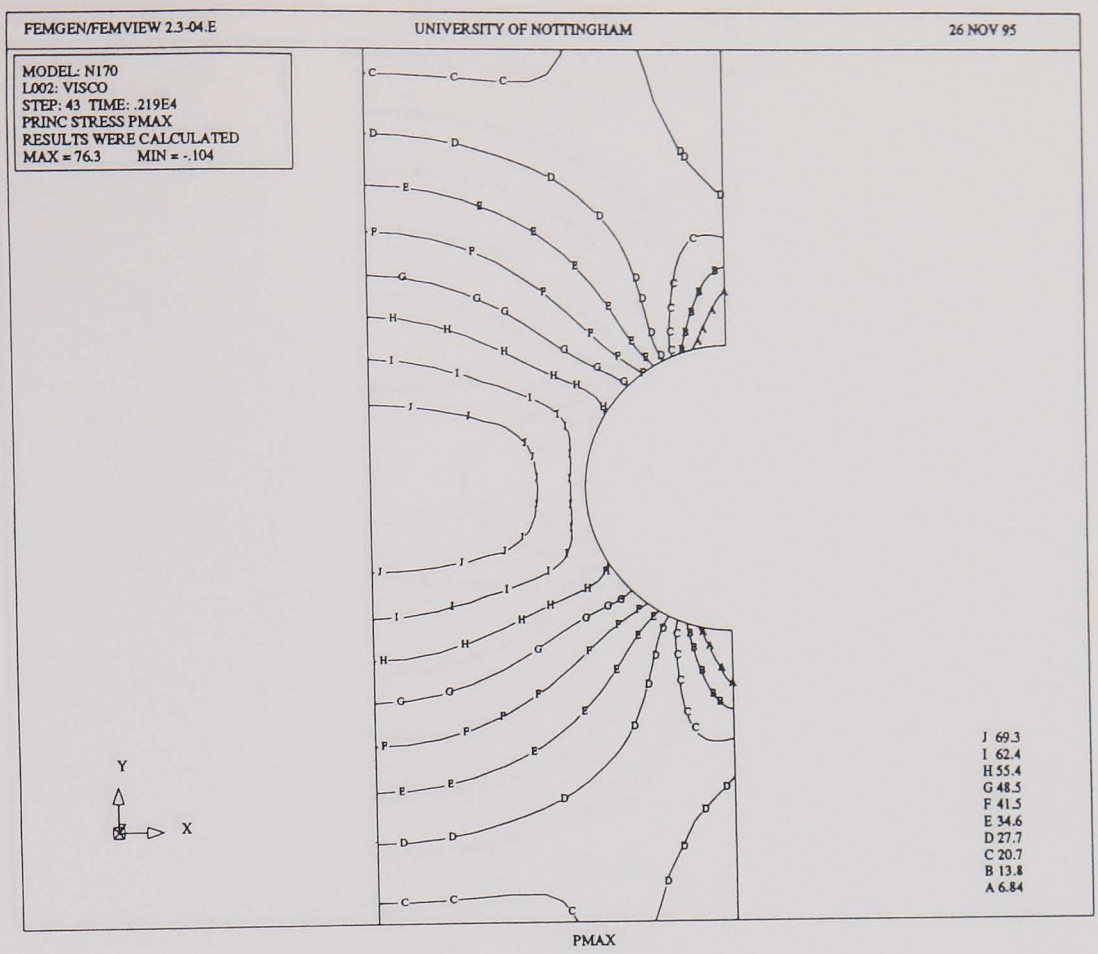

(a) notched bar

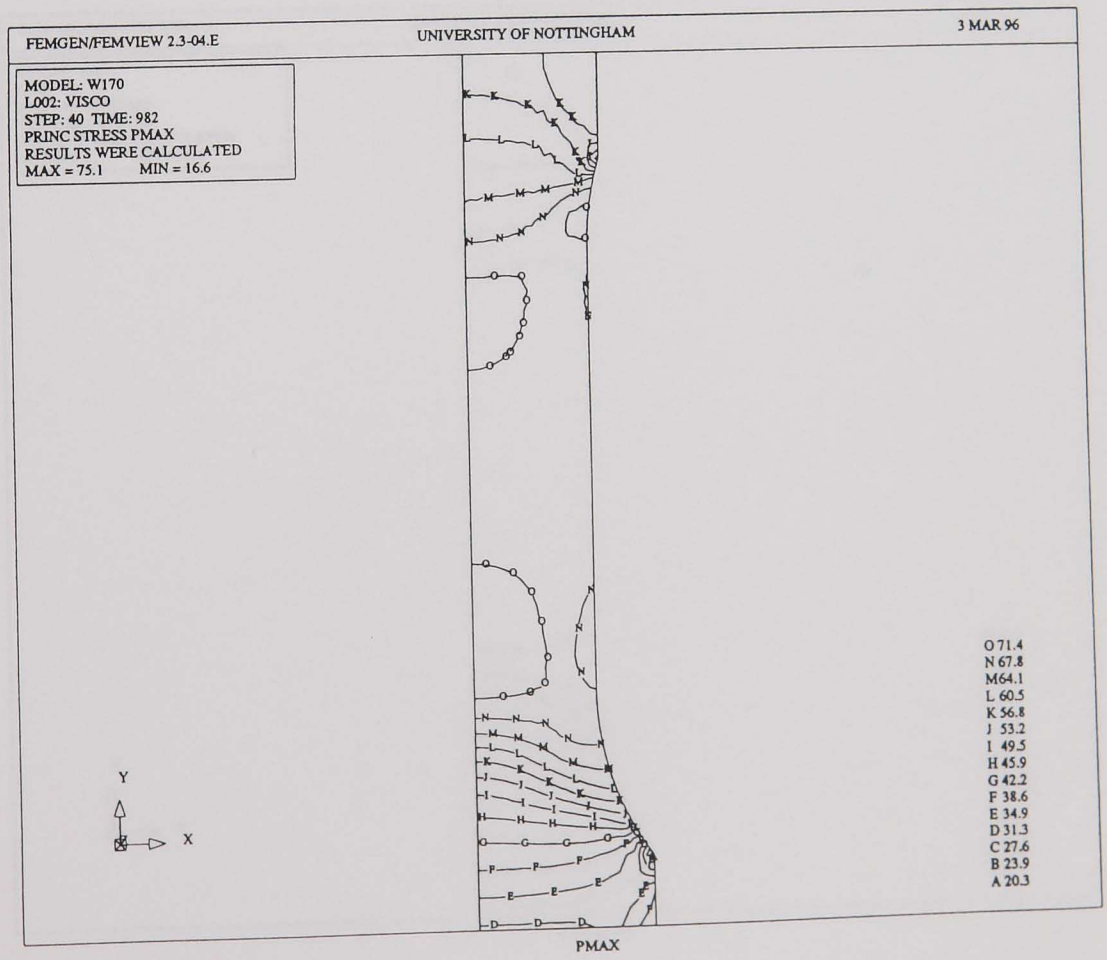

(b) waisted specimen

Fig. 7.3 Steady-state maximum principal stress distributions of the single-material notched and waisted specimens (aged parent material, σ_{nom} = 70 MPa).

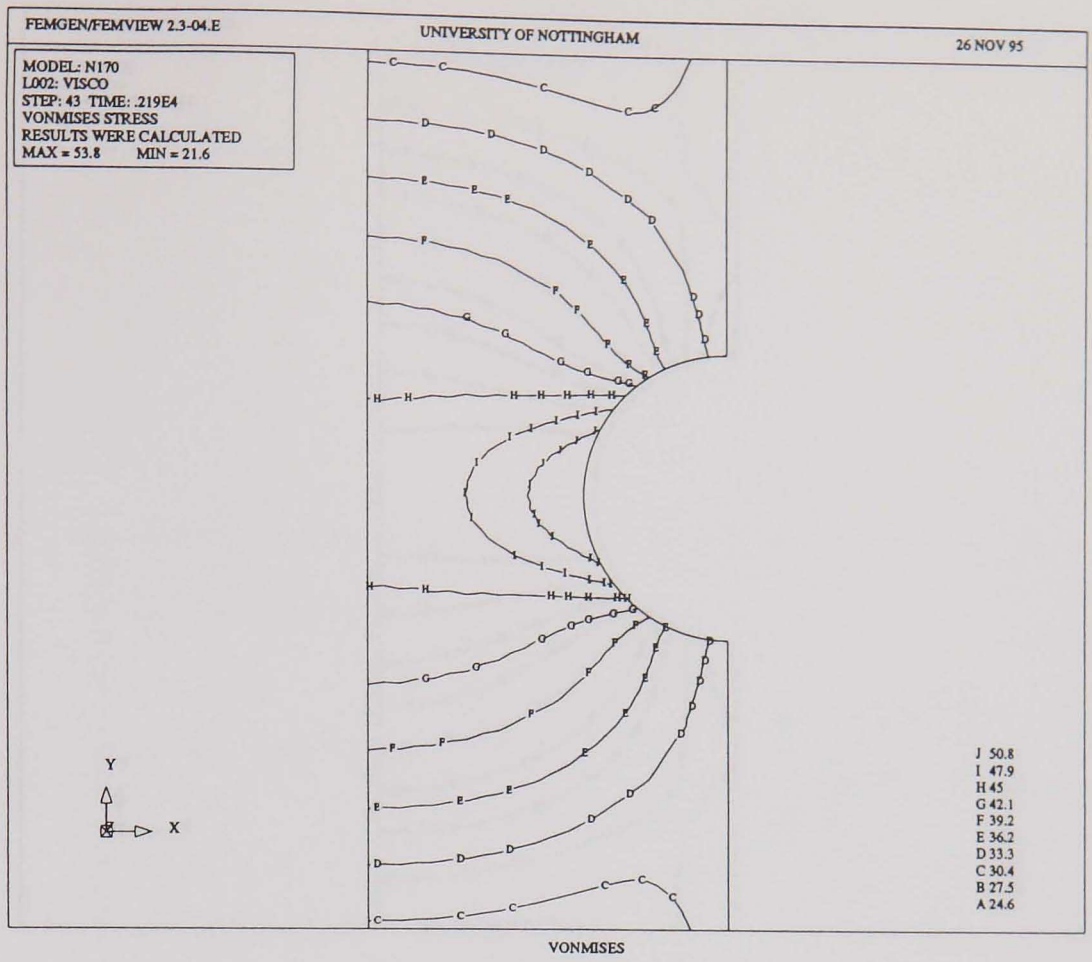

(a) notched bar

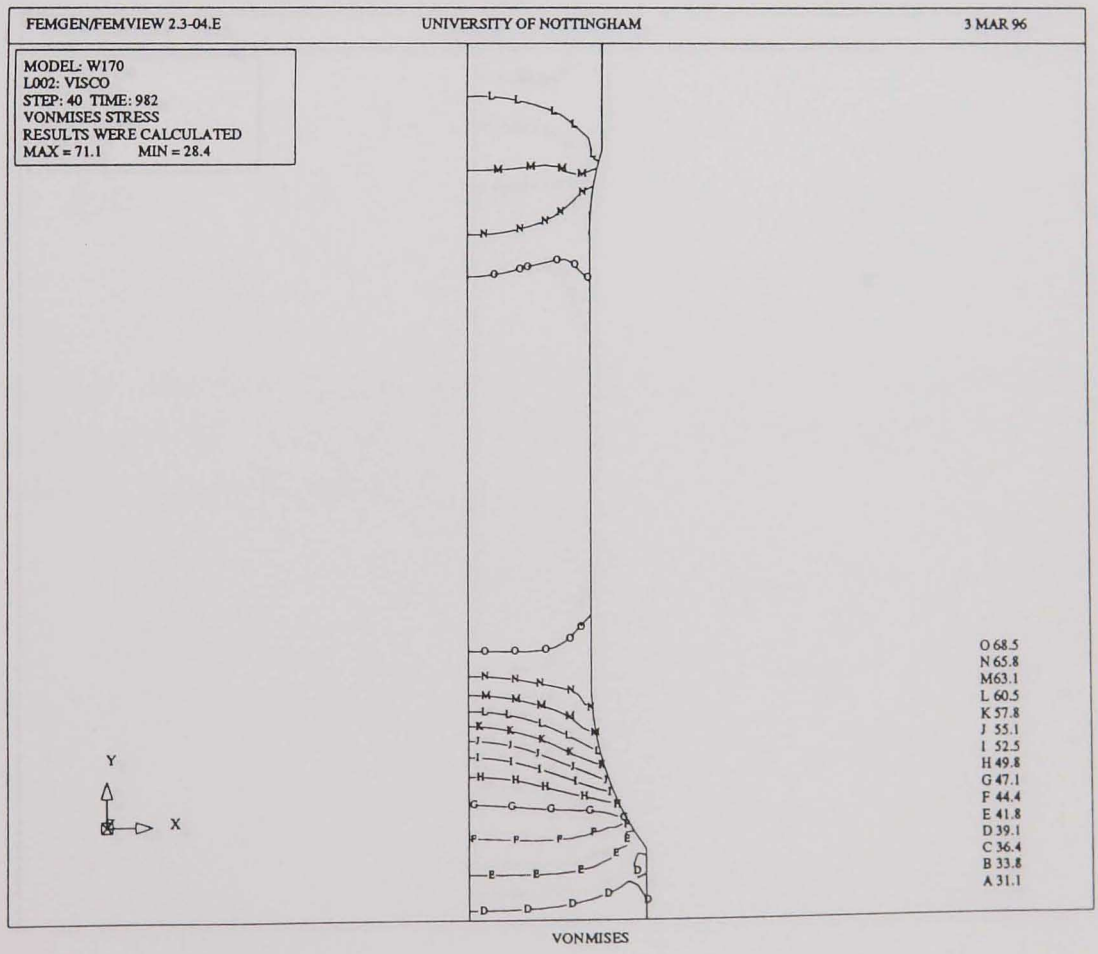

(b) waisted specimen

Fig. 7.4 Steady-state von-Mises equivalent stress distributions of the single-material notched and waisted specimens (aged parent material, σ_{nom} = 70 MPa).

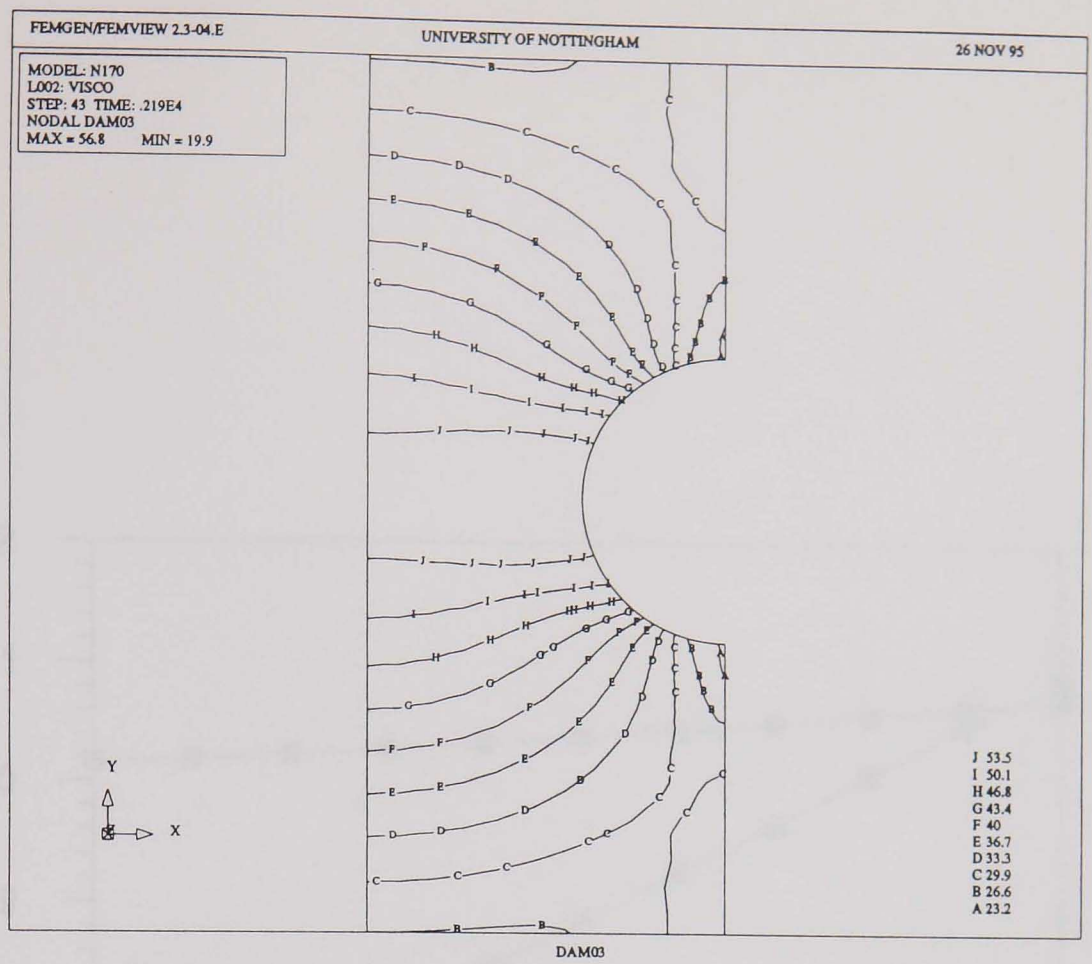

(a) notched bar

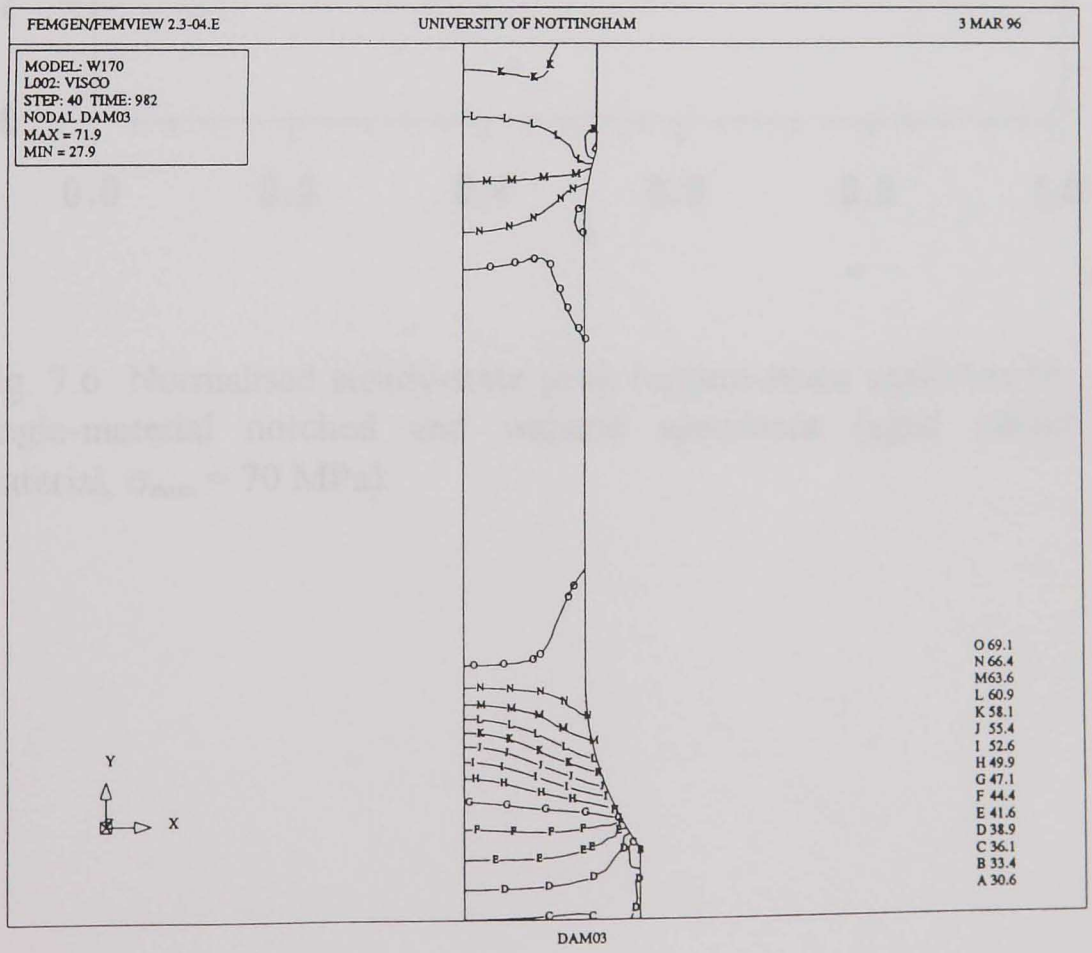

(b) waisted specimen

Fig. 7.5 Steady-state rupture stress distributions of the single-material notched and waisted specimens (aged parent material, σ_{nom} = 70 MPa, α = 0.3).

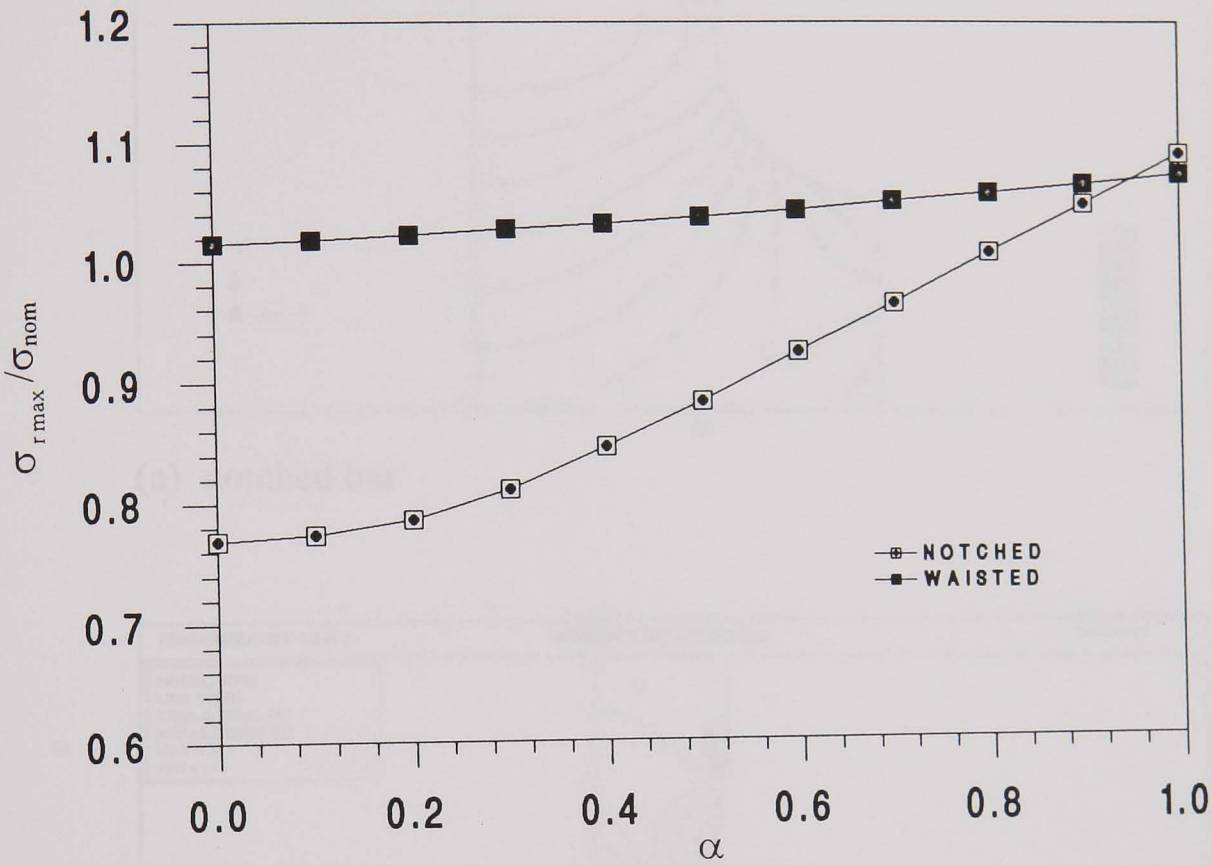

Fig. 7.6 Normalised steady-state peak rupture stress against α for single-material notched and waisted specimens (aged parent material, σ_{nom} = 70 MPa).

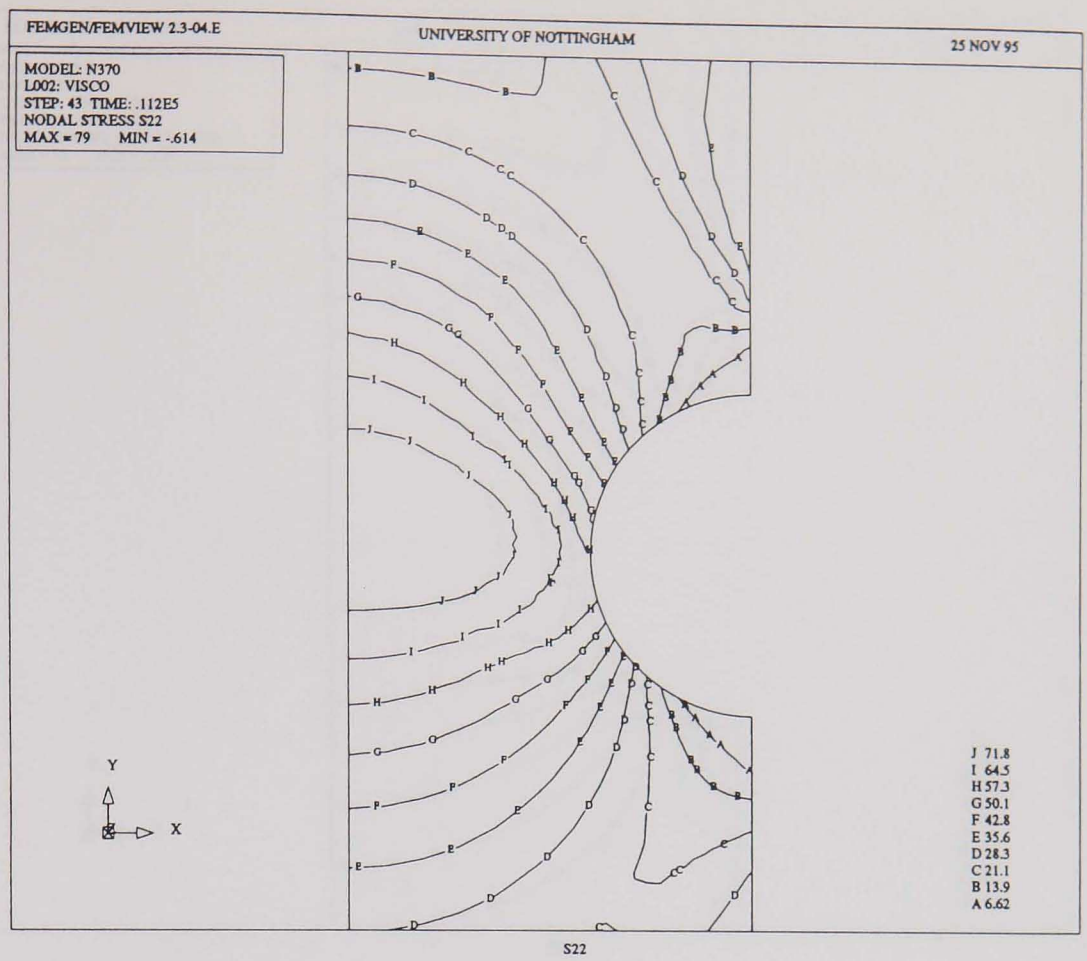

(a) notched bar

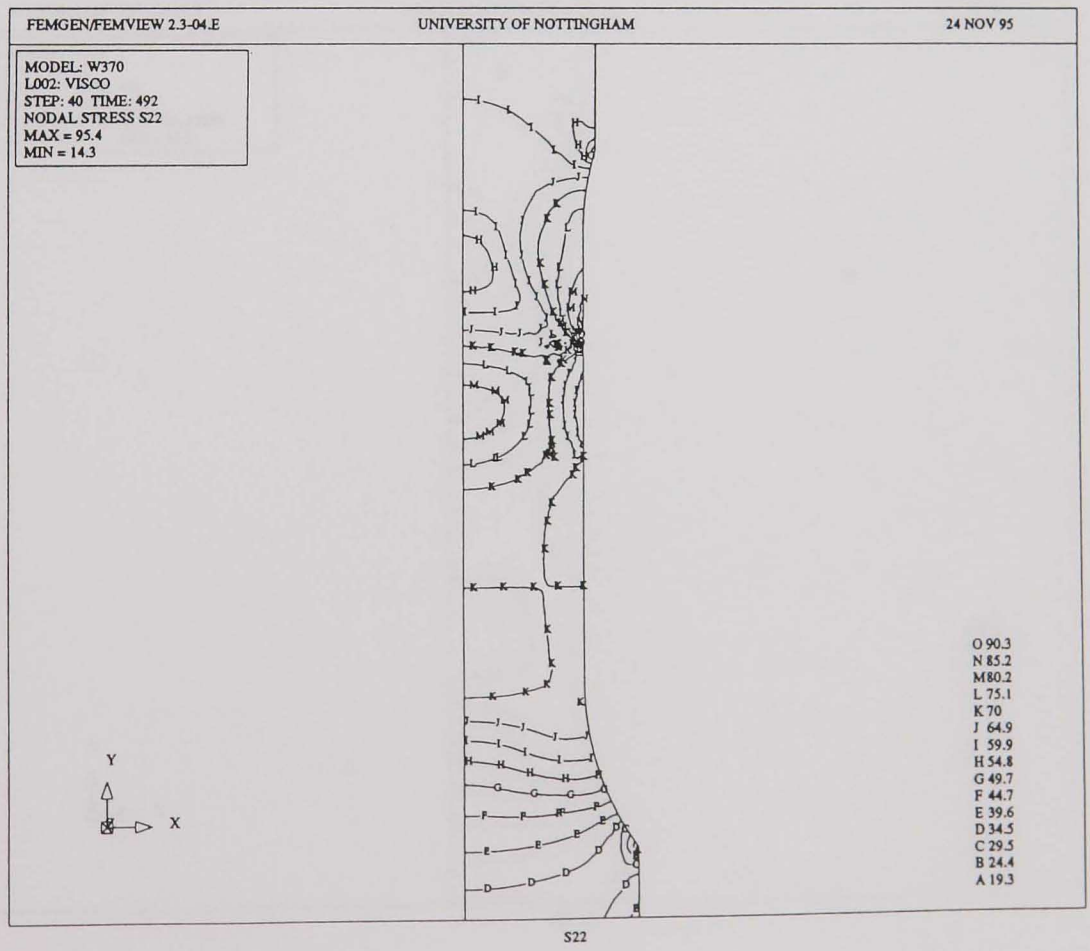

(b) waisted specimen

Fig. 7.7 Steady-state axial stress distributions of the aged material cross-weld notched and waisted specimens (σ_{nom} = 70 MPa).

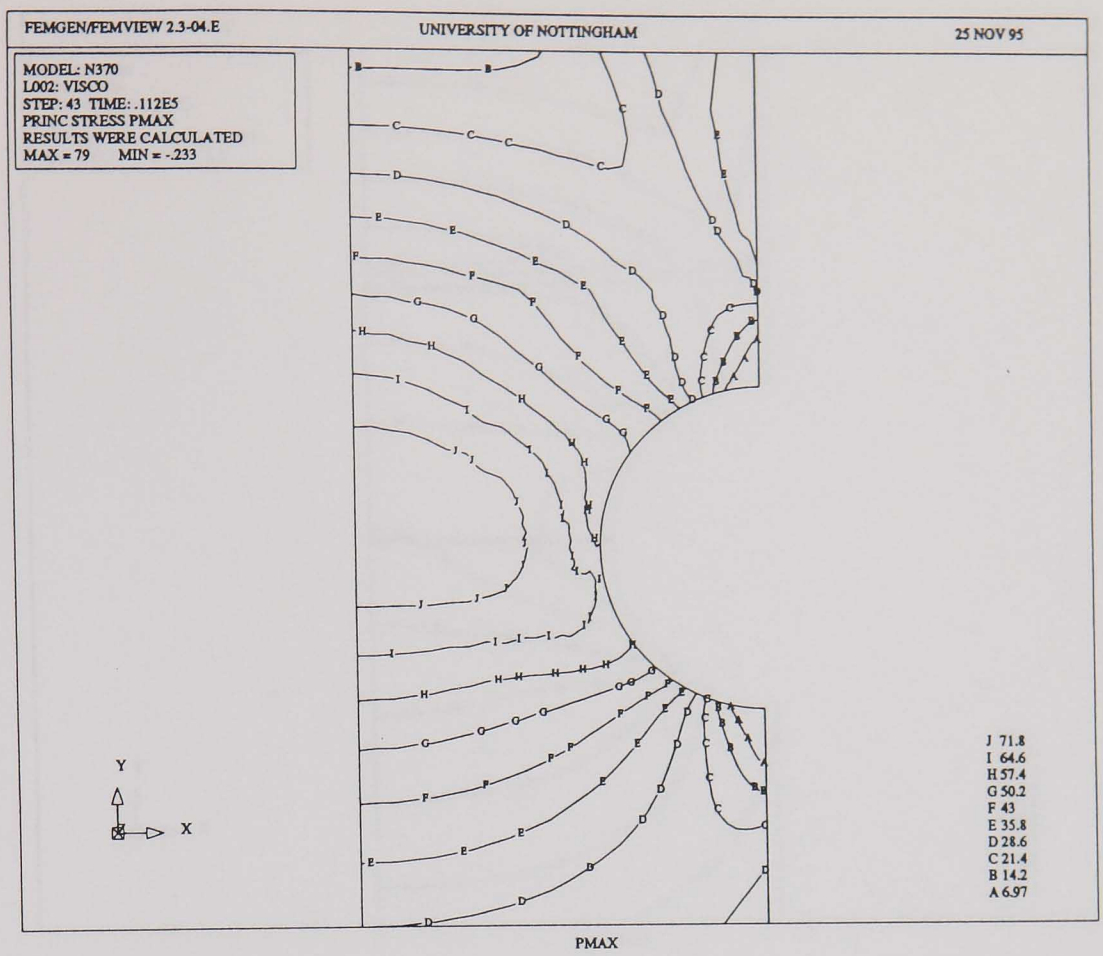

(a) notched bar

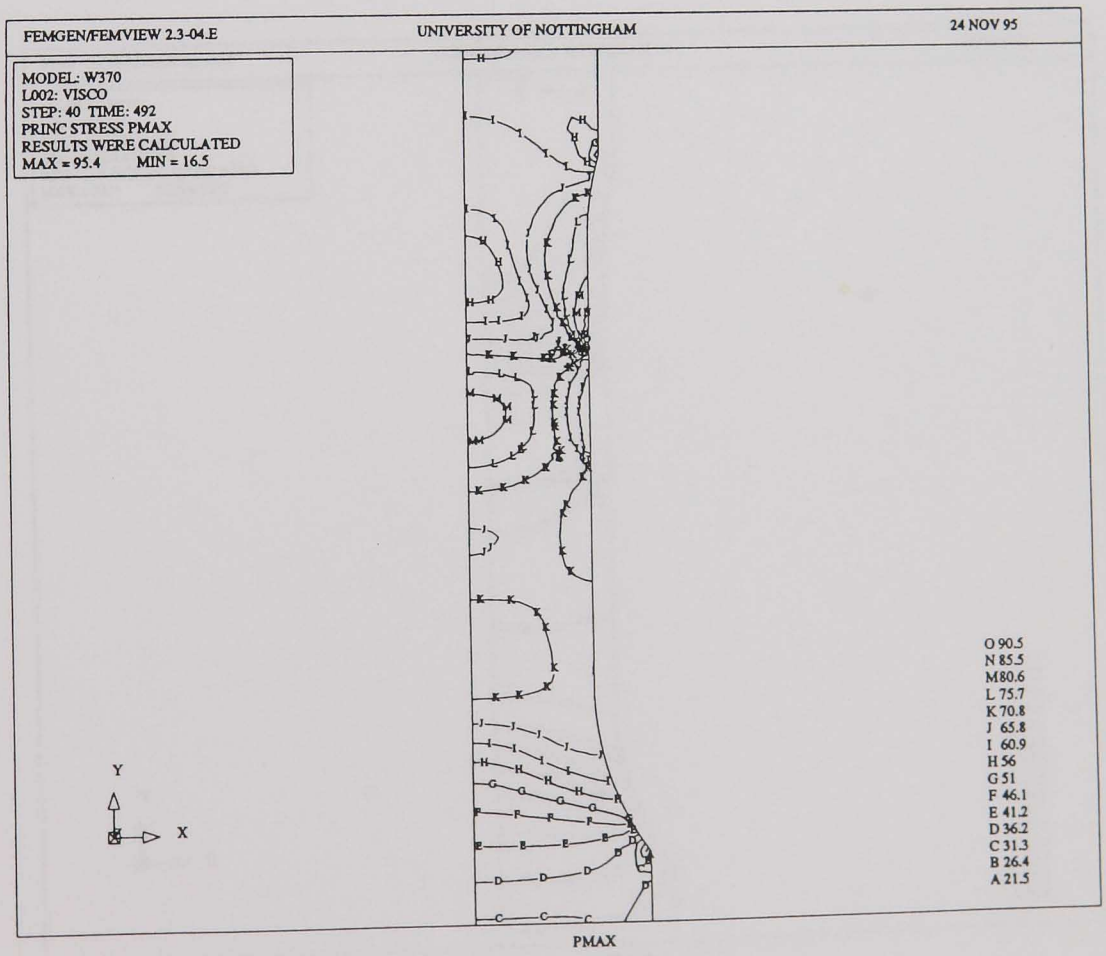

(b) waisted specimen

Fig. 7.8 Steady-state maximum principal stress distributions of the aged material cross-weld notched and waisted specimens (σ_{nom} = 70 MPa).

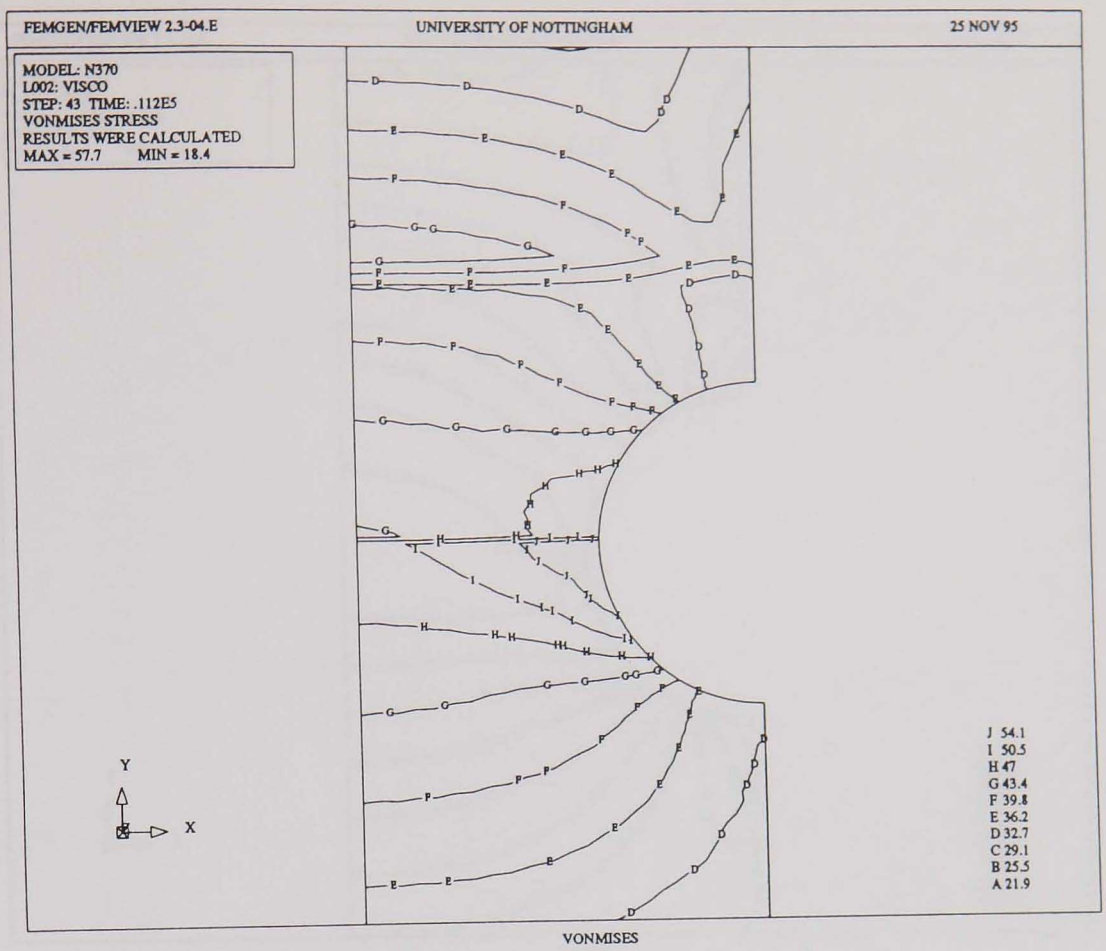

(a) notched bar

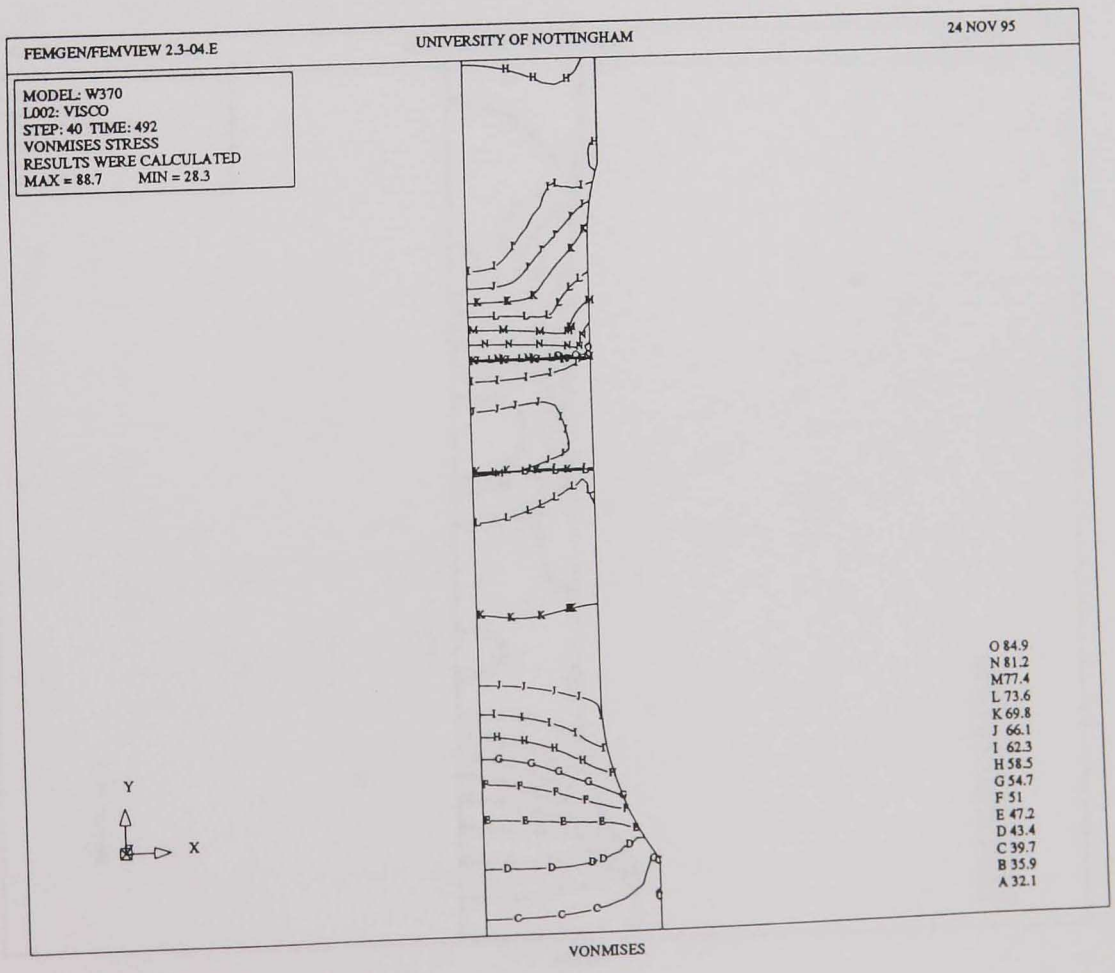

(b) waisted specimen

Fig. 7.9 Steady-state von-Mises equivalent stress distributions of the aged material cross-weld notched and waisted specimens (σ_{nom} = 70 MPa).

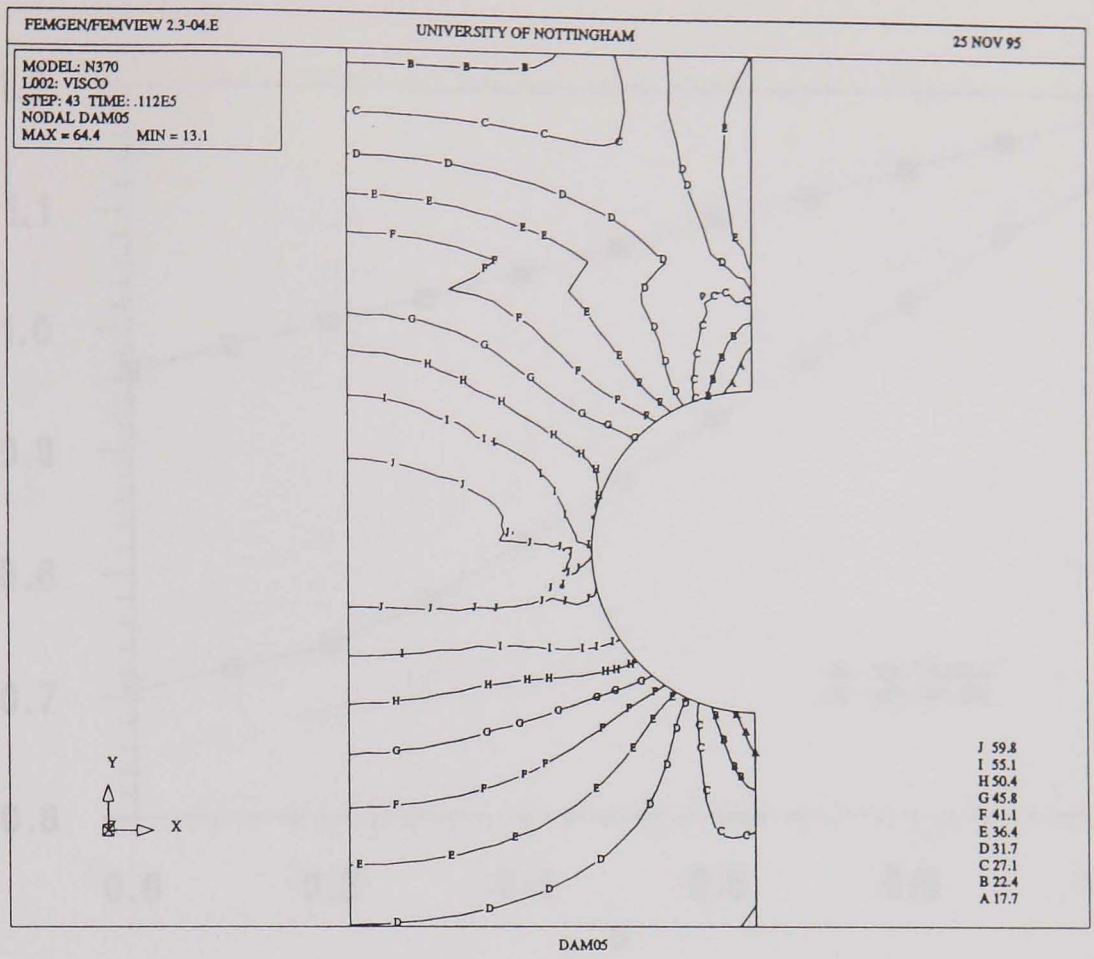

(a) notched bar

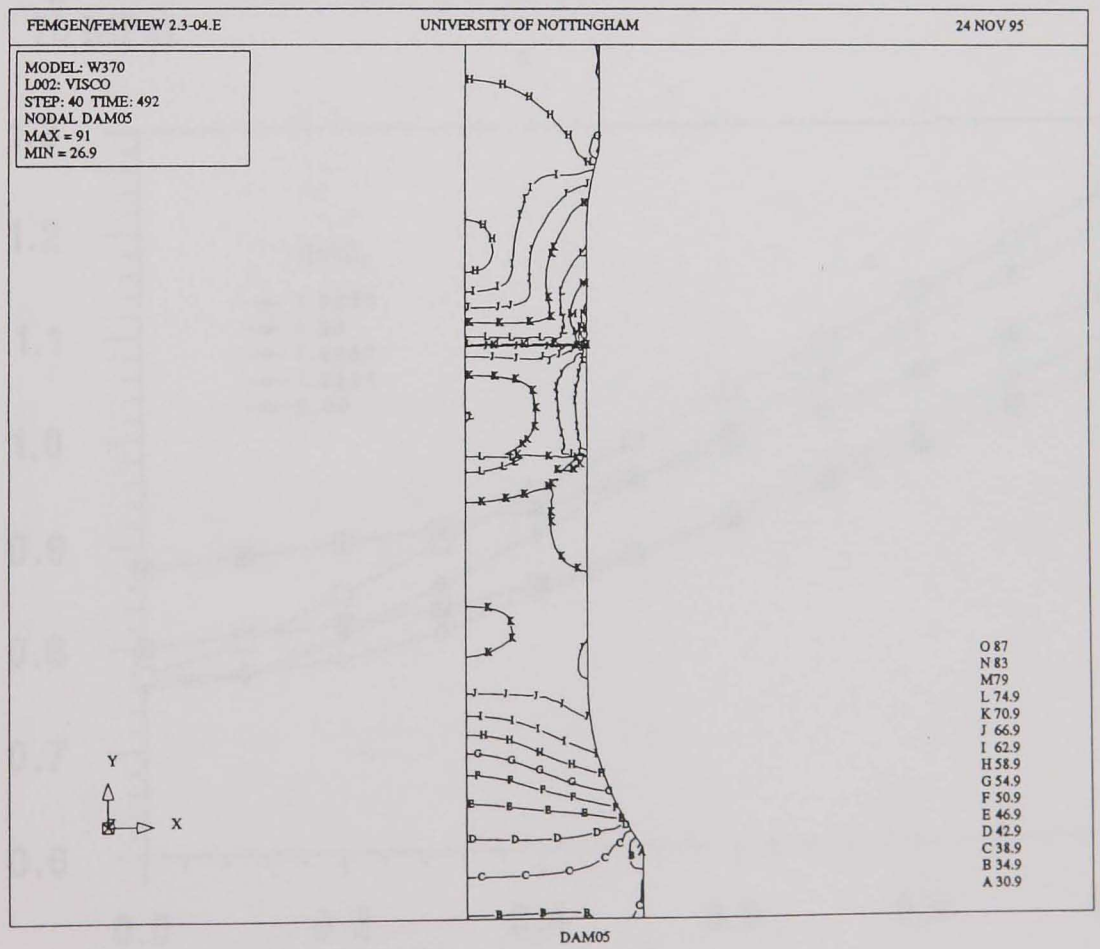

(b) waisted specimen

Fig. 7.10 Steady-state rupture stress distributions of the aged material cross-weld notched and waisted specimens (σ_{nom} = 70 MPa, α = 0.49).

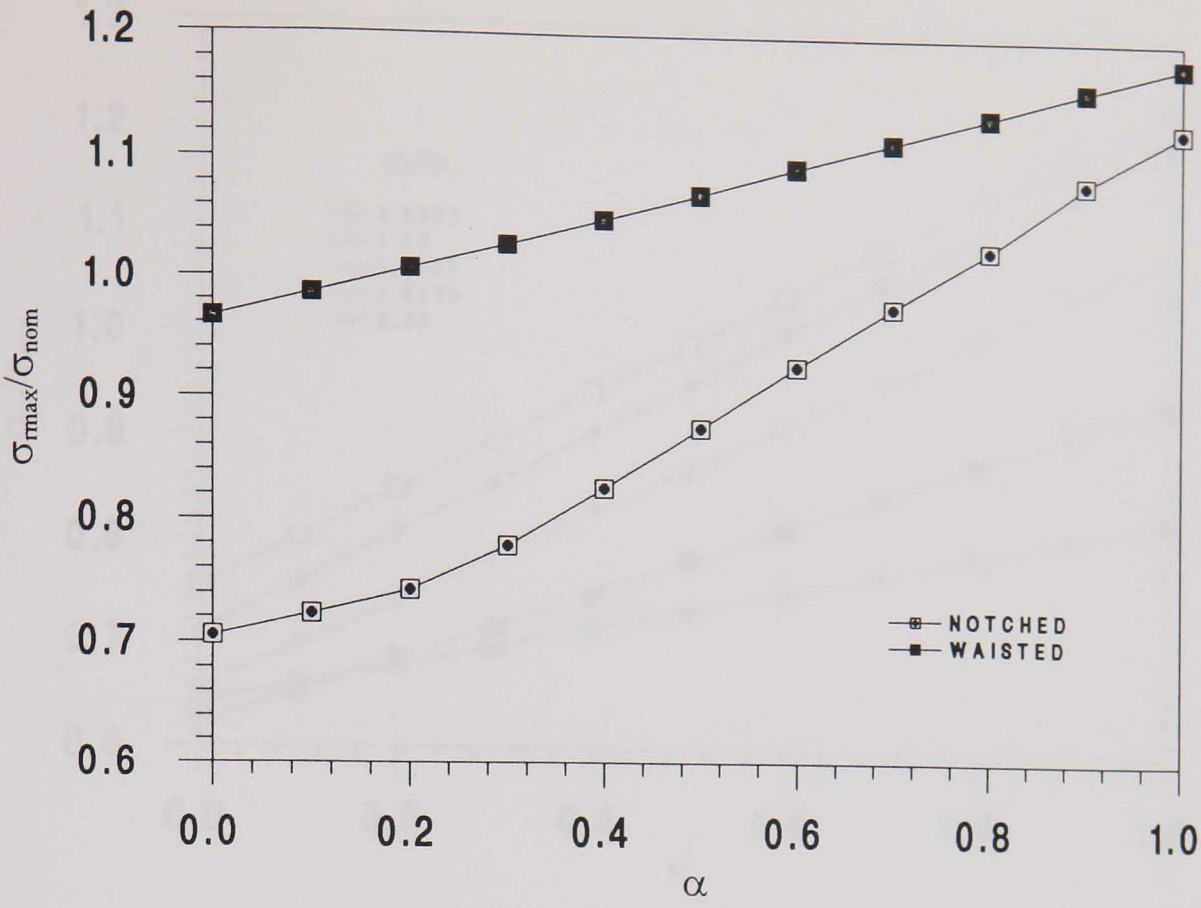

Fig. 7.11 Normalised steady-state peak rupture stress against α for aged material cross-weld notched and waisted specimens (σ_{nom} = 70 MPa).

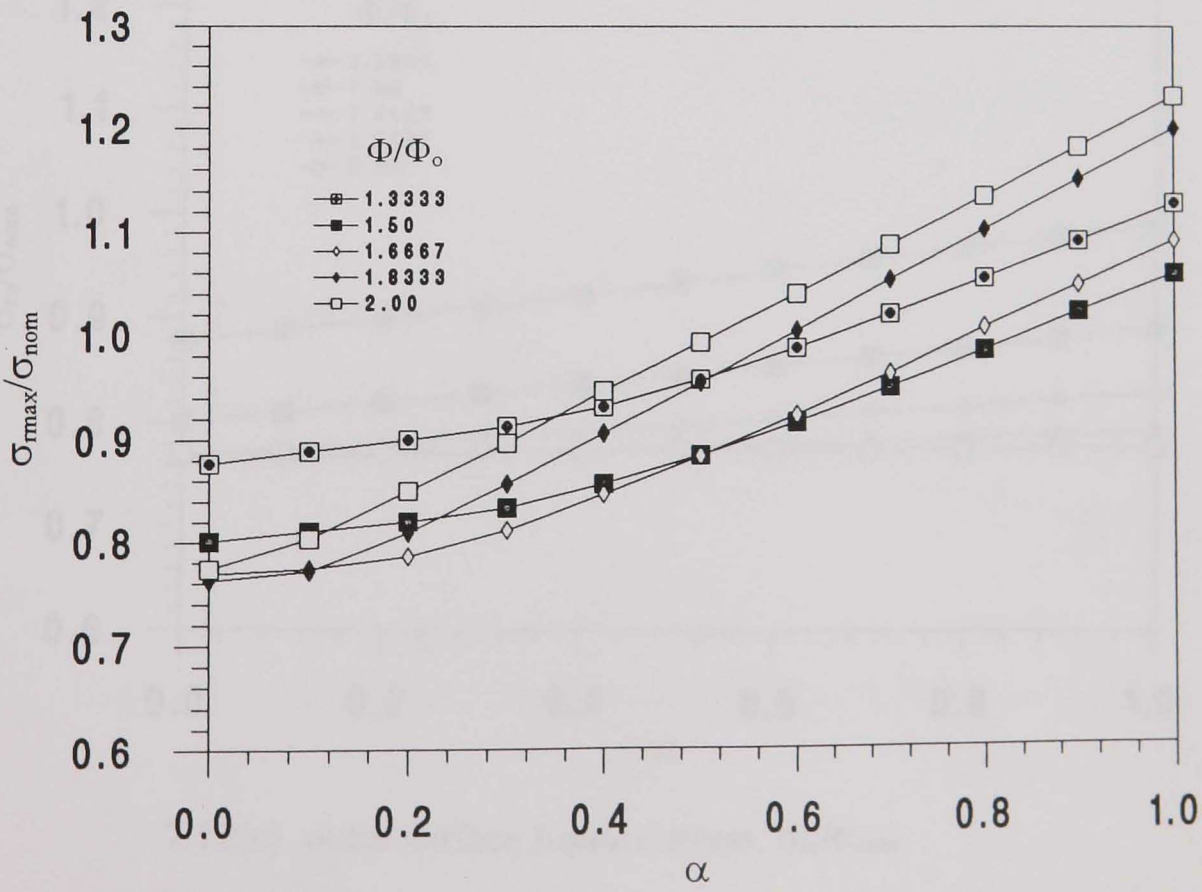

7.12(a) peak rupture stress, $\sigma_{rmax}/\sigma_{nom}$

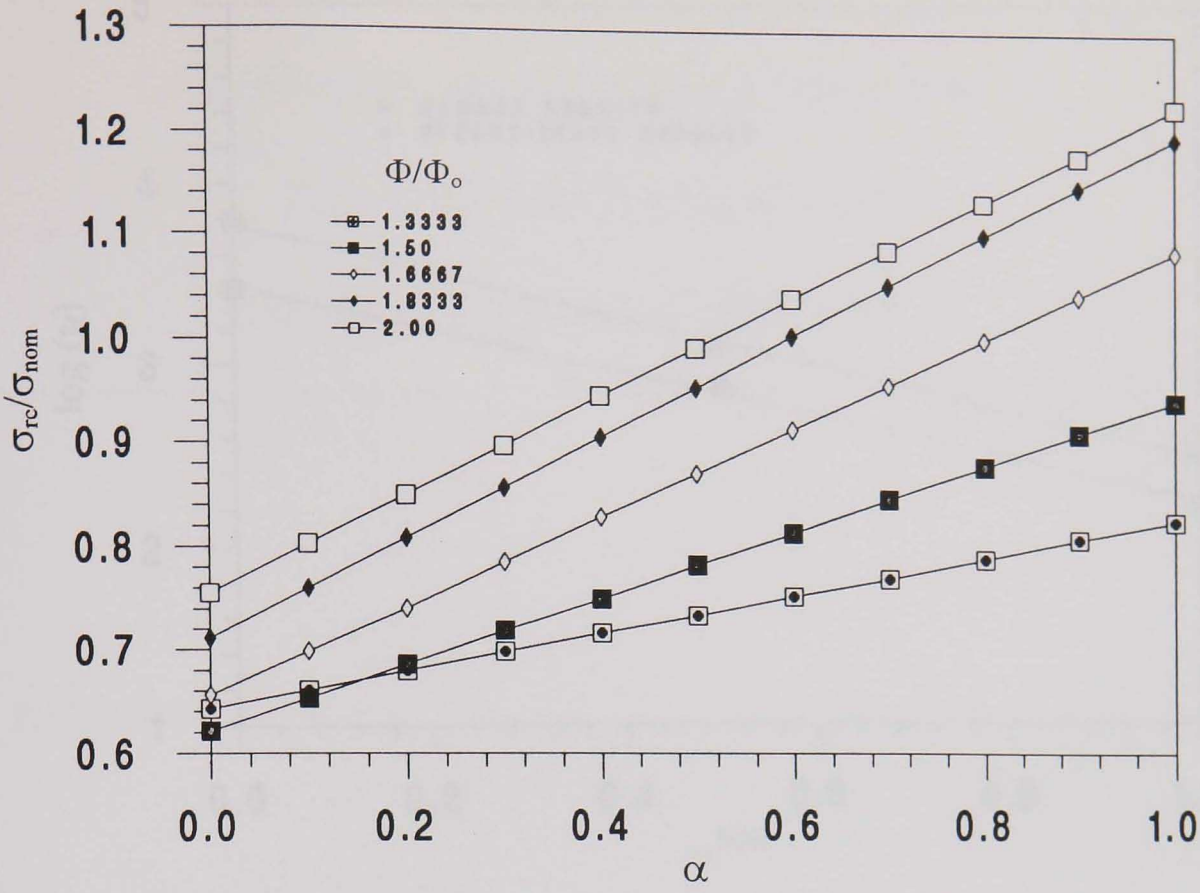

7.12(b) centre line rupture stress, σ_{rc}/σ_{nom}

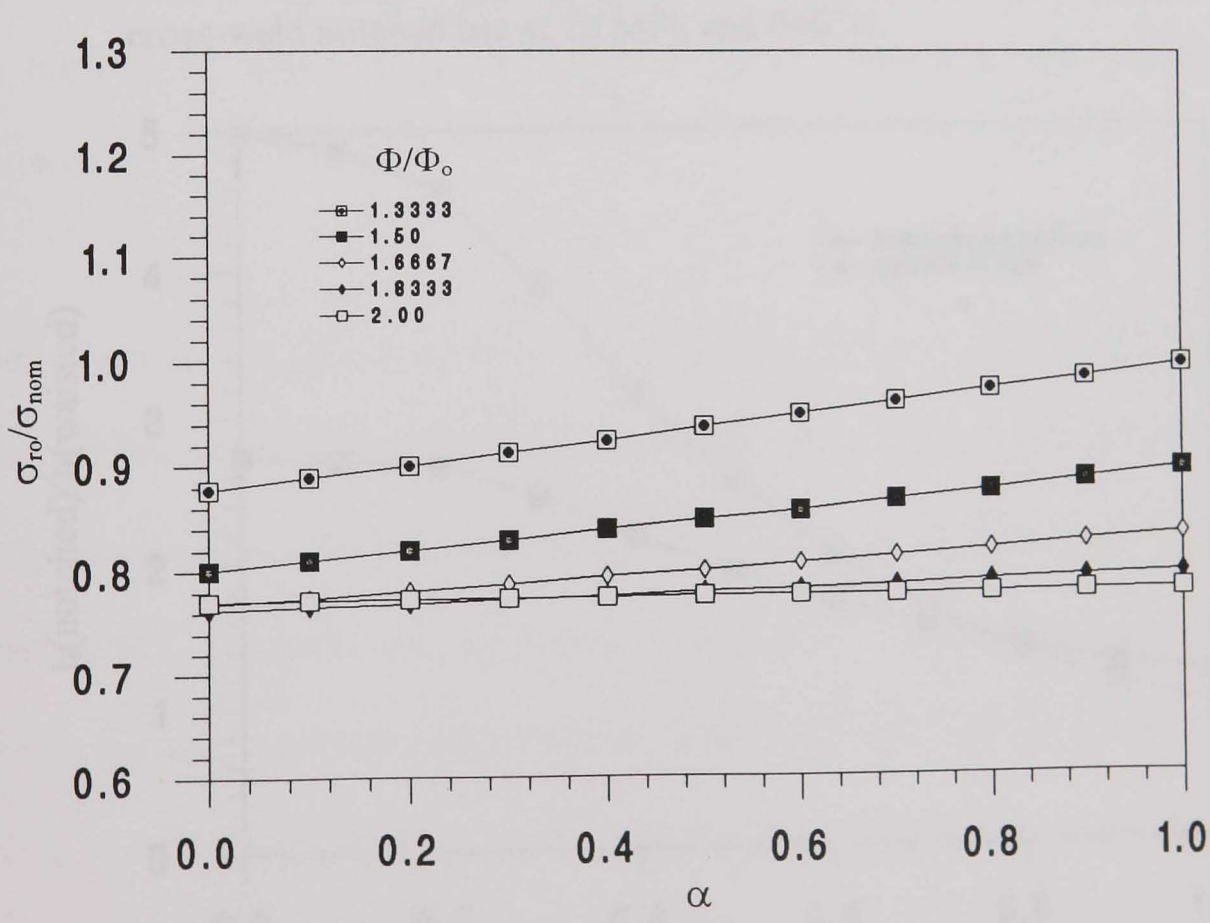

7.12(c) outer surface rupture stress, σ_{ro}/σ_{nom}

Fig. 7.12 Normalised steady-state rupture stresses against α for single-material notched with different Φ/Φ_o (aged parent material, σ_{nom} = 70 MPa).

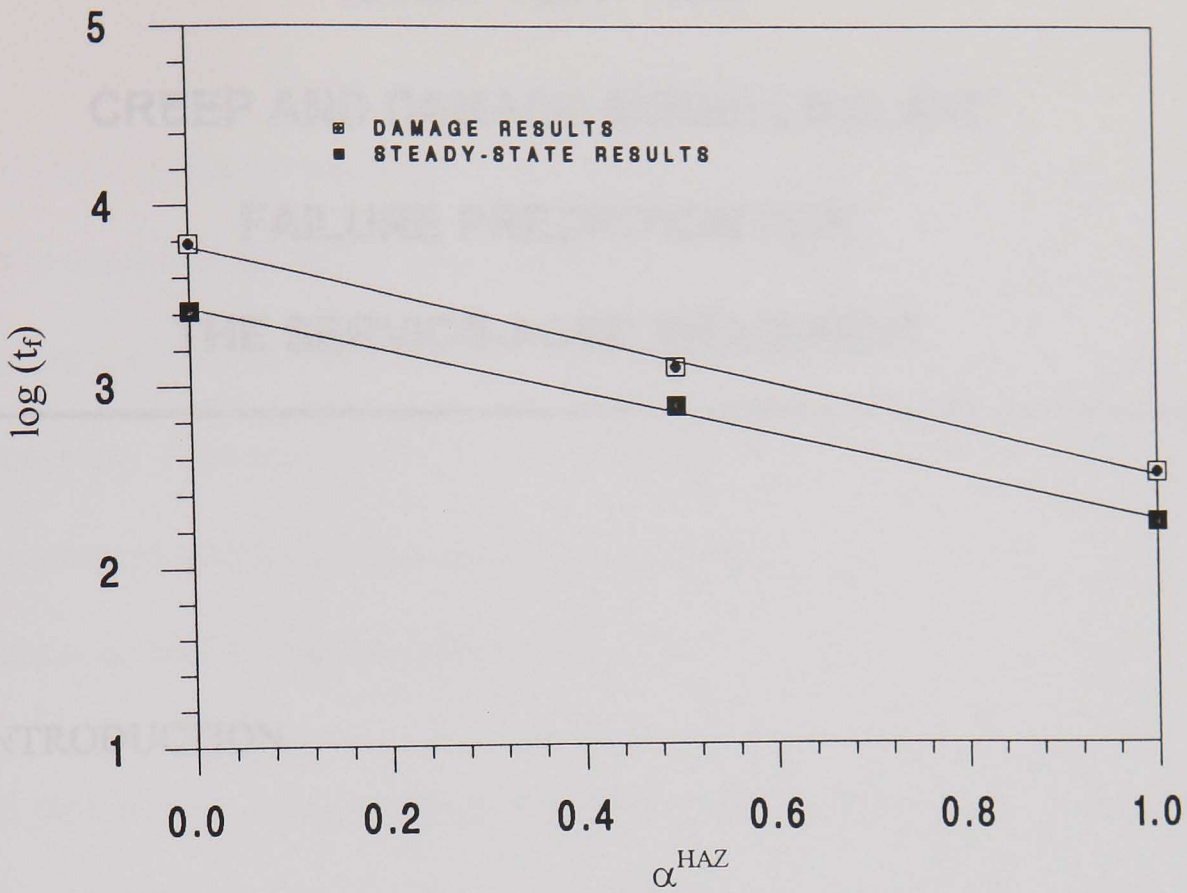

Fig. 7.13 Relationships between failure times and α^{HAZ} obtained from steady-state analysis and damage modelling for aged material cross-weld notched bar at 70 MPa and 640° C.

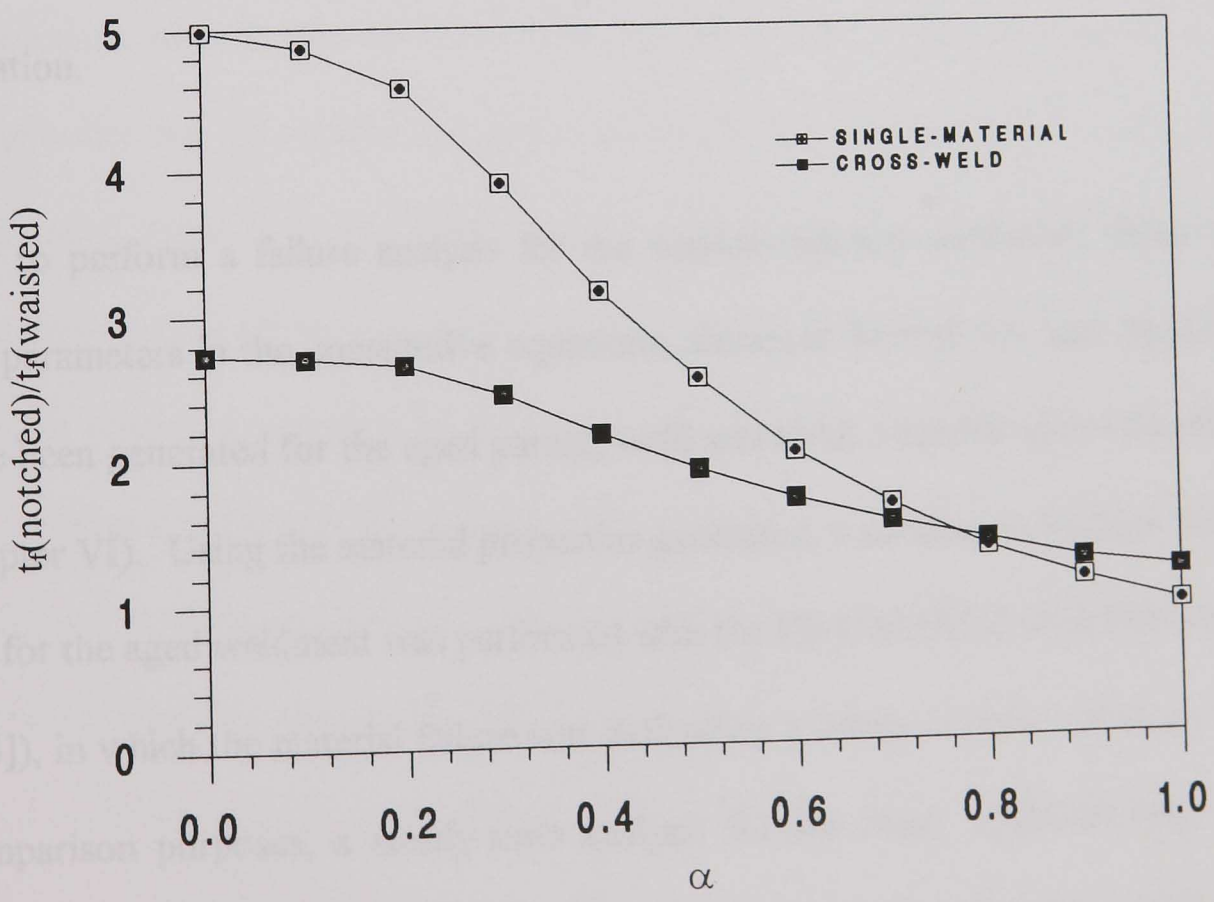

Fig. 7.14 Rupture life ratios t_f(notched)/t_f(waisted) against α obtained from steady-state solutions for single-material (aged parent) and cross-weld (aged materials) specimens at 70 MPa and 640° C.

CHAPTER VIII

CREEP AND DAMAGE MODELLING AND FAILURE PREDICTION FOR THE SERVICE-AGED WELDMENT

8.1 INTRODUCTION

This Chapter contains the failure prediction of the service-exposed weldment, which mainly consists of two parts: FE numerical failure modelling and rupture life extrapolation.

In order to perform a failure analysis for the service-exposed weldment, creep and damage parameters in the constitutive equations, shown in Section 2.4 and Appendix IV, have been generated for the aged parent, weld and HAZ materials (see Chapter V and Chapter VI). Using the material properties generated, a continuum damage failure analysis for the aged weldment was performed with the FE-DAMAGE code (Becker et al [1994]), in which the material failure was defined by a failure criterion of $\omega_{max} \rightarrow 1$. For comparison purposes, a steady-state analysis for the same weldment was also conducted using the ABAQUS [1994] package. The approximate failure prediction method using steady-state analysis (see Chapter VII) was also used in this case.

As mentioned in Chapter VI, the creep and damage constants of the aged weldment materials in the constitutive equations were generated from the creep tests at 640° C. Therefore, the results of the failure analysis, at 640° C, of the exposed weldment had to be carefully extrapolated in order to predict the behaviour of the weldment under the practical operating temperature of 568° C. To do this, a simplified extrapolation method was adopted which could be used to provide a rough estimate of the failure life of the weldment at 568° C from the data at 640° C.

The welded pipe was modelled by three material zones, i.e., parent material, HAZ and weld metal. Fig. 5.5 presents a photograph of the cross-weld section and Fig. 8.1 shows the dimensions of the weldment used in the FE modelling.

The pipe sections used in the study were removed from the main steam pipework between the boiler and the turbine. Normally, this could be treated as being equivalent to a closed-ended vessel in terms of end loading, the value of which can be determined by the magnitude of the internal pressure and the cross-section dimensions of the pipe. Usually steam pipework can also be subjected to bending loads and system stresses whose magnitudes are not generally known. However, since the weldment studied was removed from a straight vertical pipe run, it was unlikely to have been affected by system stresses. For this reason, the bending loads and system stresses were ignored. The internal pressure, p_i, used in the analysis is 16.55 MPa, i.e. the operating pressure sustained by the exposed pipe in service. The axial end tensile pressure, p_a, can be therefore calculated as:

$$p_a = p_i R_i^2/(R_o^2 - R_i^2)$$

where R_i and R_o are the inside and outside diameters of the pipe, respectively.

It should be noted that since the tested materials have been in service for over 174,800 hours at 568° C, with a steam pressure of 16.55 MPa, initial damage may have existed. In addition, surface oxidation damage was observed in all the aged material creep tested specimens. Both the unknown initial damage and the oxidation damage may introduce some inaccuracies in the creep and damage parameter generation and hence in the modelling of the failure behaviour of the practical welded pipe of the service-aged material.

8.2 CREEP AND DAMAGE FAILURE MODELLING FOR THE SERVICE-AGED WELDMENT

8.2.1 Steady-State Analysis

For comparison purposes, the steady-state creep finite element analysis was carried out for the exposed weldment for which the secondary creep material properties A and n had been generated (see Tables 5.6 and 6.6).

(a) Model definition

A symmetrical half of the exposed welded pipe was modelled by a two-dimensional axisymmetric, three-material section with 4473 nodes and 1994 elements (8-node isoparametric, quadratic rectangular elements and 6-node isoparametric, quadratic triangular elements), loaded by an internal pressure of 16.55 MPa and an end tensile pressure of 11.6569 MPa. A uniform axial displacement (r direction, see Fig. 8.1) condition was applied to the end of the pipe. The HAZ was modelled by 5 rows of 8-node elements, each row consisting of 35 elements. A mesh of the modelled weldment is shown in Fig. 8.2. The analysis was conducted by ABAQUS using a time hardening power law (i.e., $\dot{\varepsilon}^c = A\sigma^n$).

(b) Results

Results of the steady-state creep stress distributions within the weldment are presented by colour contours. Figs 8.3(a) - 8.3(e) show the contours of maximum principal stress, $\hat{\sigma}$, equivalent stress, σ_{eq} (von-Mises), and three "rupture stresses", $\sigma_r = \alpha\hat{\sigma} + (1-\alpha)\sigma_{eq}$, where $\hat{\sigma}$ and σ_{eq} take the steady-state values, which correspond to the α values of the exposed parent, HAZ and weld materials, i.e. $\alpha^B = 0.3$, $\alpha^{HAZ} = 0.49$ and $\alpha^W = 0.2639$, respectively (see Table 6.5 and Table 6.7). For this model, the maximum principal stress is equal to the hoop stress. Uniform stress distribution along the axial direction of the pipe has been achieved when the axial distance from the weld centre is over about 2.5 times of the wall thickness, which indicates that the stress distribution in the weldment is virtually unaffected by the end conditions. Therefore,

the pipe model used for the FE damage calculation can be significantly shortened in order to reduce the element numbers and therefore save computation time. The variations of the stresses with the normalised wall thickness in the uniformly distributed area were checked and compared with the results obtained from the theoretical plane strain creep solutions (see Equs. (3.2.9) and (3.2.10)), as illustrated in Fig. 8.4, which clearly shows that the axial and radial loadings had been correctly applied.

Steady-state results show that the peak maximum principal stress (= hoop stress) occurs on the outer surface in the weld material near the HAZ, with a value of 36.9 MPa, see Fig. 8.3(a). The peak equivalent stress also occurs in the weld material but on the inside surface near the HAZ, with a value of 38.3 MPa, see Fig. 8.3(b).

The rupture stress for the parent material, σ_r^B (α^B =0.3), exhibits a practically uniform distribution within the material zone with a value of 31.5 MPa, see Fig. 8.3(c). The peak rupture stress for the HAZ material, σ_r^{HAZ} (α^{HAZ} = 0.49), occurs at the position near the outer surface and adjacent to the parent material, with a value of 28.2 MPa, see Fig. 8.3(d). In fact, the magnitude of the rupture stress in the HAZ adjacent to the parent material does not vary significantly. The maximum rupture stress for the weld metal, σ_r^W (α^W = 0.2639), occurs on the inside surface adjacent to the HAZ, with a value of 35.5 MPa, see Fig. 8.3(e).

8.2.2 Creep Damage Failure Modelling

(a) FE-damage model

The damage model of the exposed welded pipe was generated with 1159 nodes and 360 axisymmetric, 8-node isoparametric quadratic elements, as shown in Fig. 8.5, each of which contains four Gauss points (2 × 2 reduced). There are two elements through the thickness of the HAZ. A time hardening creep law has been assumed. The calculation was performed with the FE-DAMAGE Code (Becker et al [1994]). The dimensions of the model and the loading applied are identical to those used for the steady-state model except that the length of the pipe was shortened to reduce the model size.

The limiting damage level in the FE damage calculation has been specified as ω_{max} = 0.99. In other words, the material is assumed to sustain up to a maximum creep damage of 99%, at any Gauss point in the model. Due to the complexity of the constitutive equations when damage has reached 99% at several Gauss points, the computational analysis, when significant damage has been achieved, is extremely time consuming, especially when the model has a large number of elements. In general, the time increments become very small as high damage level zones propagate through the material, but the actual creep time is relatively short. Therefore, the time to failure can be accurately predicted when a 99% damage zone has been reached across a complete section of the model or across only part of the section.

The FE damage analyses have produced results in the form of rupture time and accumulated damage contours at several time steps during the creeping life of the

weldment modelled. These can be compared with, or related to, other computational results such as the existing steady-state results of this work.

(b) Damage results: rupture life and failure position

The creep failure results of the exposed weldment were presented with damage contours. Rupture life, t_f, of the weldment under the given loading and temperature (640° C) was found to be 15,640 hours. The maximum damage values were found to be in the HAZ at all time periods during the analysis. Figs. 8.6(a) - 8.6(d) present damage history contours for the creep time from 5,000 hours to the failure time of 15,640 hours. It has been found that the damage levels in the parent and weld materials are significantly lower than those in the HAZ, and are nearly constant ($\omega \approx$ 0.06 to 0.08) for $t > 12{,}000$ hours. The material failure ($\omega_{max} = 0.99$) first occurs near the outer surface of the pipe in the HAZ adjacent to the parent material, at about $t_s =$ 14,000 hours. The outer surface then fails quickly, and the failed material area expands and grows inside into the HAZ. The value of $(t_f - t_s)/t_f$ is 10.49 %. The maximum damage history obtained from the elements next to the parent material, against normalised distance starting from the outer surface along the HAZ, is presented in Fig. 8.7.

Therefore, it can be concluded that the rupture is caused by the HAZ failure, initially starting from the position near the outer surface of the pipe adjacent to the parent material. The rupture life predicted is 15,640 hours, under the internal pressure of 16.55 MPa and the axial tensile pressure of 11.6569 MPa at 640° C.

8.2.3 Steady-State Failure Prediction

As shown in Section 8.2.1, the positions in the different material zones, where the steady-state peak rupture stresses occur, can be identified by steady-state modelling. Since in the rupture equations (see Equ (2.11) or (2.13)) the failure behaviour is dominated by the rupture stress, it can be reasonably assumed that failure will occur at the positions where the maximum rupture stress appears. The peak steady-state rupture stresses in the parent, HAZ and weld material zones were found to be 31.5, 28.2 and 35.5 MPa, respectively, see Table 8.1.

Table 8.1 Steady-state failure time prediction.

Material Zone	Steady-State Rupture Data		t_f (hour) predicted by damage
	σ_r (MPa)	t_{fss} (hour)	
PARENT	31.5	38,127	15,640
HAZ	28.2	9,147	
WELD	35.5	37,363	
$(t_f - t_{fss}^{HAZ}) / t_f$ (%) = 41.51			

Using the steady-state peak rupture stresses of the parent, HAZ and weld material zones (from the corresponding α value of each material), the rupture times of the different zones can be estimated by using Equ. (7.1), the minimum value of which can be referred to as the rupture time of the weldment, predicted by the steady-state

analysis. Table 8.1 presents the steady-state rupture results in which it can be seen that the error of the rupture time predicted by the steady-state analysis, compared to the damage prediction, is 41.5 %.

The failure position of the weldment, predicted by the steady-state analysis, is exactly the same as that predicted by damage modelling when the first failure damage level appears (see Figs. 8.3 and 8.6).

8.3 EXTRAPOLATION ESTIMATE OF THE RUPTURE LIFE OF THE SERVICE-AGED WELDMENT AT 568° C

The rupture life of 15,640 hours obtained from damage modelling of the exposed weldment is valid for a temperature of 640° C at which the present test programme was carried out. This rupture time is much shorter than the remnant life of the in-service weldment which was operating at a temperature of 568° C. Therefore, the rupture life of the weldment obtained from damage modelling will need to be extrapolated to provide an estimate of the practical residual life at the operating temperature. It must be emphasised that the testing within this project was only carried out at 640° C and hence numerous assumptions have to be made to provide an estimate for the life at 586° C. In practice, further limited test data would need to be generated at $T < 640°$ C in order to provide more accurate values for the constitutive laws.

8.3.1 Simplified Extrapolation Method

The extrapolation was performed on the basis of the following assumptions:

1. The aged materials obey Norton's law over the relevant stress and temperature range, i.e.

$$\dot{\varepsilon} = A\sigma^n \tag{8.1}$$

2. No mechanism change occurs in the temperature range of 568° C to 640° C, i.e. the material constants n and χ at 568° C are the same as those at 640° C and the materials are in the low stress range over the required σ - T regime.

3. The aged materials possess the same temperature-dependent behaviour, i.e. the uniaxial rupture life ratios at 568° C to 640° C (for tests performed at the same stress levels) for the aged materials are identical, i.e.

$$\frac{t_f^B(568)}{t_f^B(640)} = \frac{t_f^{HAZ}(568)}{t_f^{HAZ}(640)} = \frac{t_f^W(568)}{t_f^W(640)}$$

The secondary creep strain rate in Equ. (8.1) can then be expressed as a function of temperature as follows:

$$\dot{\varepsilon} = [A' e^{-Q/RT}]\sigma^n \tag{8.2}$$

where Q is the activation energy, T is the temperature in Kelvin, and R is the gas constant. Assuming that A' in equation 8.2 is independent of temperature, i.e. $[A' e^{-Q/RT}] = A$, and using the measured creep data of the aged materials at 640° C, with given Q and R values, A' can be calculated and hence, knowing T, the strain rates of the materials can be estimated at any temperature.

A typical value of Q in the low stress regime would be that for the vacancy diffusion in a ferritic matrix. Typically, this would be around 60,000 cals/mole with a gas constant, R, of 2 cals/mole/ K (Dorn and Mote [1963]).

Assuming that the uniaxial rupture life is a function of temperature and stress, equation (8.3), which is obtained by polynomial fitting to the rupture data of virgin 1/2Cr1/2Mo1/4V parent material up to 600° C, can be used (Hickin et al [1972]), i.e.,

$$\left(\frac{\log_{10}(t_f)-8.659}{(T-650)^{0.95}}\right)(-10^2)=5.6419-13.4707\log_{10}(\sigma)+16.3115[\log_{10}(\sigma)]^2-$$

$$8.2217[\log_{10}(\sigma)]^3+1.5473[\log_{10}(\sigma)]^4 \qquad (8.3)$$

where T is in K, t_f is in hour and σ is in MPa. This relationship can be used to generate the ISO materials data but is only strictly valid for $T \leq 600°$ C. It is assumed that equation (8.3) can be extrapolated to 640° C. This approach is applied to the parent material.

Following the definition of a uniaxial-equivalent failure stress level, the rupture life of the weldment at 568° C can be estimated as follows:

$$t_f^{\text{weldment}}(568°\,C)=t_f^{\text{weldment}}(640°\,C)R_{MS}R_{TS} \qquad (8.4)$$

where $t_f^{\text{weldment}}(640°\,C)$ is the failure time of the exposed weldment predicted by FE damage modelling or by steady-state modelling at 640° C, see Section 8.2; R_{MS} (> 1) is the uniaxial rupture time ratio of the virgin parent material to the aged parent at 568°

C, which takes into account the material difference (virgin and aged) and is stress-dependent; R_{TS} (> 1) is the rupture time ratio for the virgin parent material at a temperature range of 568° C to 640° C, which again depends on the stress level.

Assuming that, for the aged material, the steady-state material property ratios $A^B:A^W:A^{HAZ}$ and $n^A:n^W:n^{HAZ}$ at 568° C are equal to the same ratios at 640° C and that the rupture parameter α at 568° C is equal to that at 640° C, then the stress distributions of the weldment at the two temperatures are the same, and therefore, the steady-state peak rupture stresses in the three zones of the weldment at 568° C and 640° C are identical.

The following extrapolation procedure was used:

i) Calculate the secondary strain rates at 568°C for the aged material, using Equ. (8.2) and the experimental data at 640° C.

ii) Calculate the rupture time ratios of the virgin parent (from Equ. (8.3)) to aged parent (from tests) materials at 640° C.

iii) Calculate the rupture time ratios of the virgin parent (from Equ. (8.3)) of 568° C to 640° C.

iv) Choose the steady-state peak rupture stress to be the uniaxial-equivalent, and calculate the extrapolated rupture life of the weldment at 568° C with Equ. (8.4).

8.3.2 Extrapolation Results

Using the extrapolation technique described in Section 8.3.1 the estimated steady-state uniaxial strain rates of the aged materials at 568° C using Equ. (8.2) can be obtained and the uniaxial rupture life of the aged parent material can be estimated using Equ. (8.4).

(a) Steady-state strain rates of the aged materials at 568° C

The calculated uniaxial strain rates obtained using Equ. (8.2) with the creep data for the aged parent, HAZ and weld materials at 640° C, at the nominal stress (30 to 70 MPa), for a range of temperatures (500 to 640° C) are shown in Figs. 8.8(a) - 8.8(c), respectively. Since the n values in Equ. (8.1) are assumed to be temperature-independent, then the ratios of $\dot{\varepsilon}(640°)/\dot{\varepsilon}(568°)$ should be constant for all the materials and stress levels. This ratio was found to be 16.66, i.e. at 568° C the secondary creep rate of the aged materials is about 17 times lower than that at 640° C.

(b) Rupture life extrapolation

Using Equ. (8.3) the uniaxial rupture times at 640°C can be calculated, which are referred to as the rupture times of the virgin parent material at 640° C. The rupture time ratios of the virgin parent material (calculated by Equ. (8.3)) to the aged parent material (tested) at 640° C against the nominal stress are illustrated in Fig. 8.9. It can be seen that the ratio increases rapidly with increasing stress and when the stress is lower, the ratio is closer to unity. The results in Fig. 8.9 indicate that at very low

stresses the virgin parent and the aged parent may have similar rupture times at 640° C. Once the stress level for the rupture extrapolation is determined, the difference in rupture times between virgin and exposed materials can be estimated, by assuming that the rupture time ratio at 568° C is similar to that at 640° C.

The calculated virgin parent material failure times against stress and the reciprocal of temperature, calculated using Equ. (8.3), are presented in Fig. 8.10 and Fig. 8.11, respectively. The rupture time ratio at 568° C to 640° C against stress in the given range is shown in Fig. 8.12. It was found that the ratios increase with the increase of stress, having an averaged value of 18 which is close to the corresponding calculated secondary strain rate ratio of 17.

As shown in Section 8.2, the steady-state peak rupture stress in the parent material of the exposed weldment at 640° C is 31.5 MPa. Using this stress value, the ratio R_{TS} in Equ. (8.4) can be determined by Fig. 8.12, i.e. $R_{TS} = 14.28$. The value of R_{MS} in the low stress case can be taken to be unity. Thus the failure time of the weldment at 568° C can be finally estimated by using equation (8.4), i.e.,

$$t_f = 15640 \times 1.0 \times 14.28 = 2.2339 \times 10^5 \text{ (hours)}$$

where 15640 (hours) is the failure time of the weldment predicted by damage modelling at 640° C.

It should be mentioned that the failure time of 2.2339×10^5 hours estimated for the exposed weldment at 568° C was obtained based on several assumptions stated earlier and hence may not be accurate if some of these assumptions are not realistic.

8.4 DISCUSSION AND CONCLUSIONS

The rupture life of 15,640 hours was obtained for the exposed weldment by damage modelling at 640° C. The maximum damage first occurred near the outer surface in the HAZ adjacent to the parent material and grew inwards. The failure life of the weldment at 640° C predicted by the steady-state analysis is conservative, compared with the damage prediction, i.e. $t_{ss}/t_f = 0.5848$.

The steady-state peak rupture stresses can be used to represent the rupture behaviour of welded components. At this point, the peak rupture stresses can be referred to as "effective failure stresses" or "equivalent uniaxial stresses". The failure positions predicted by both damage and steady-state modelling are virtually identical and are located in the HAZ.

An estimated failure life of 2.2339×10^5 hours was obtained for the exposed weldment at 568° C using a simplified extrapolation technique. This estimated failure life can only be used as a rough guide since the extrapolation was carried out based on several assumptions and limited test data at 640° C.

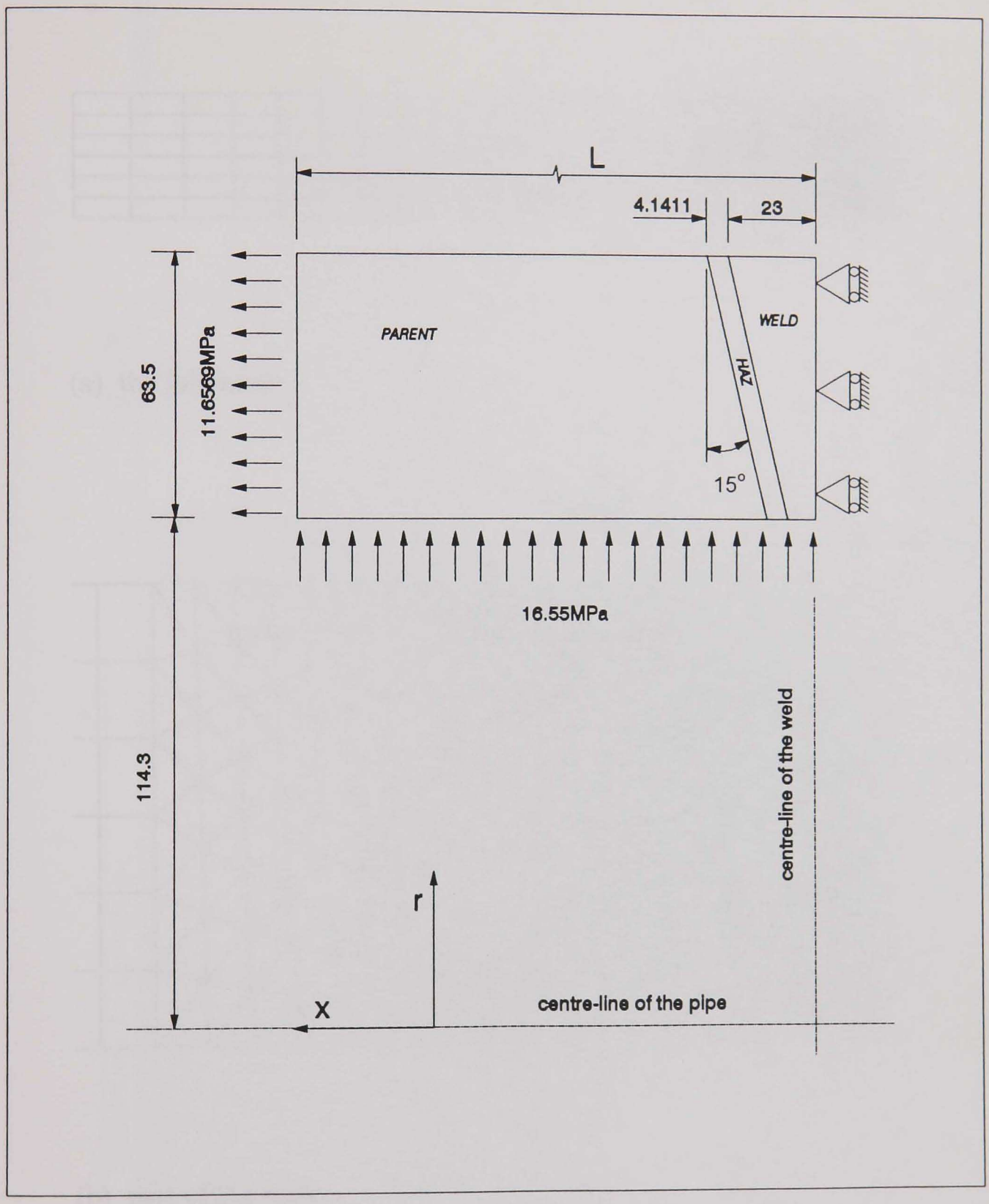

Fig. 8.1 Axisymmetric finite element model of the service-aged weldment (dimensions in mm).

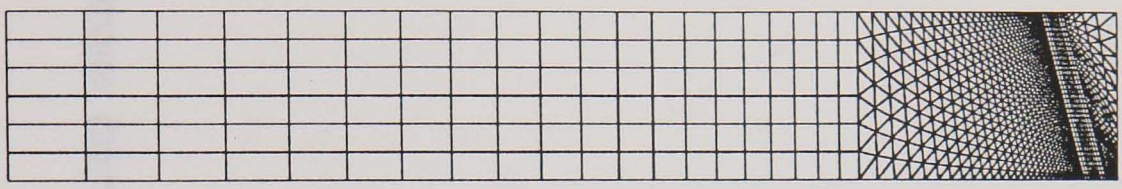

(a) the full mesh

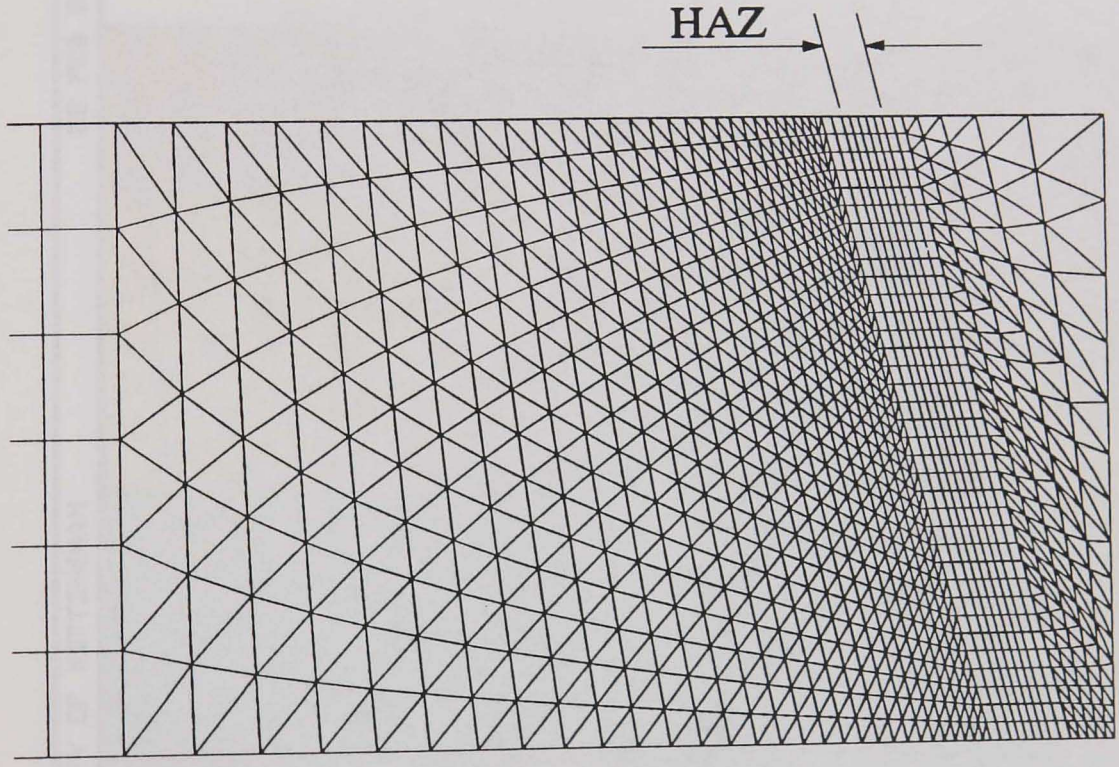

(b) part of the mesh

Fig. 8.2 Axisymmetric finite element mesh of the service-aged weldment for steady-state creep analysis.

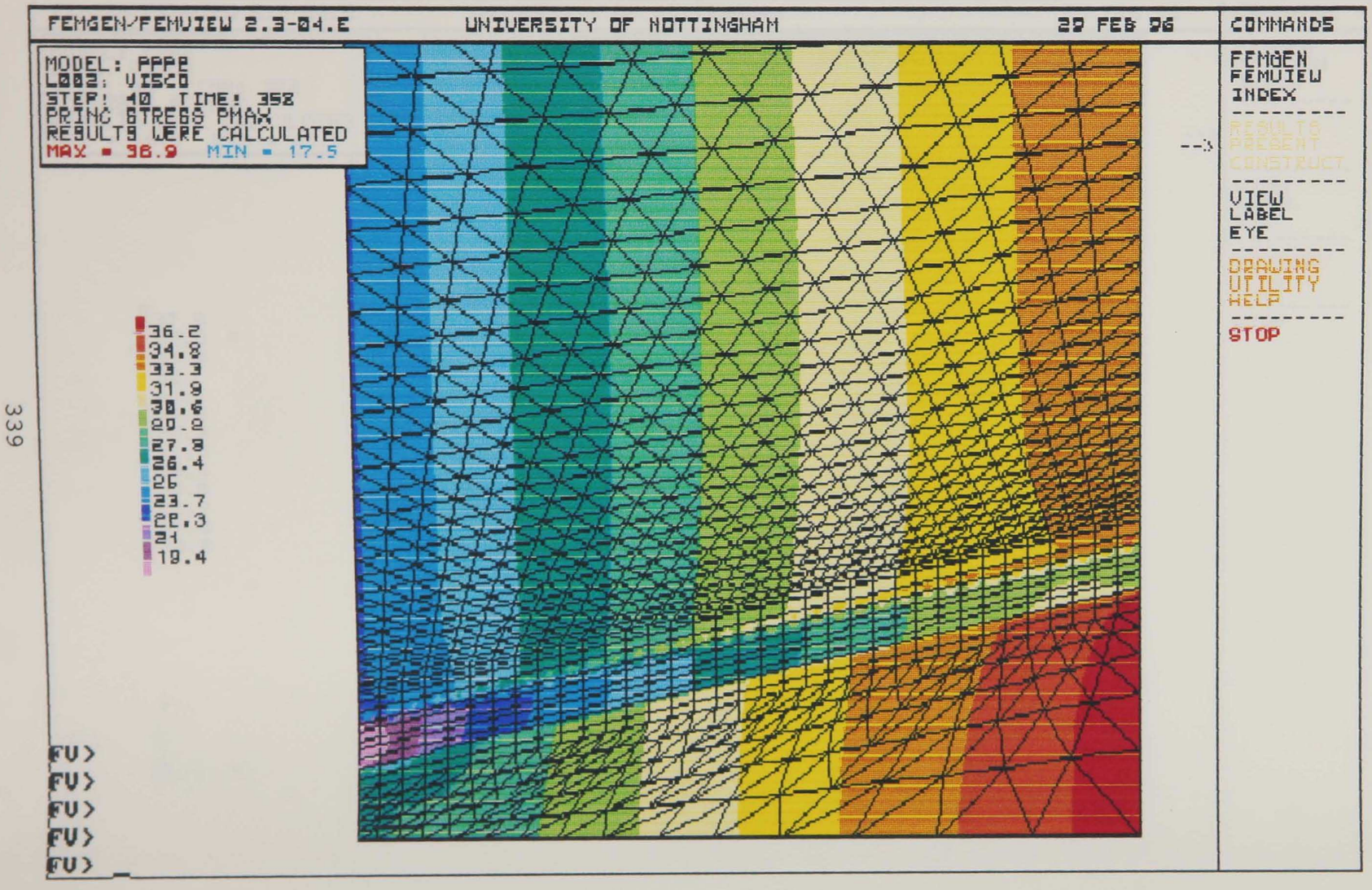

8.3(a) maximum principal stress, $\hat{\sigma}$

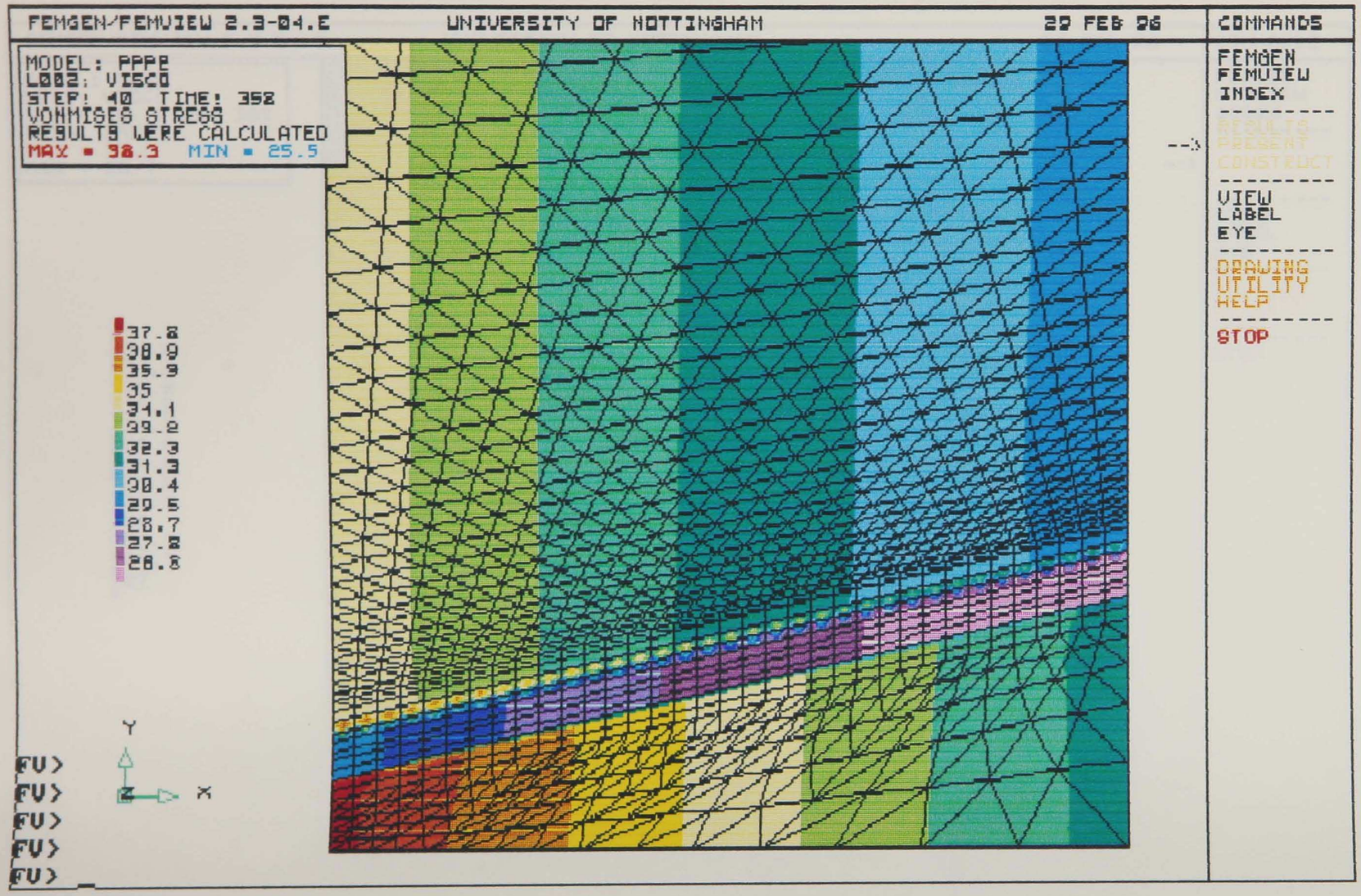

8.3(b) von-Mises equivalent stress, σ_{eq}

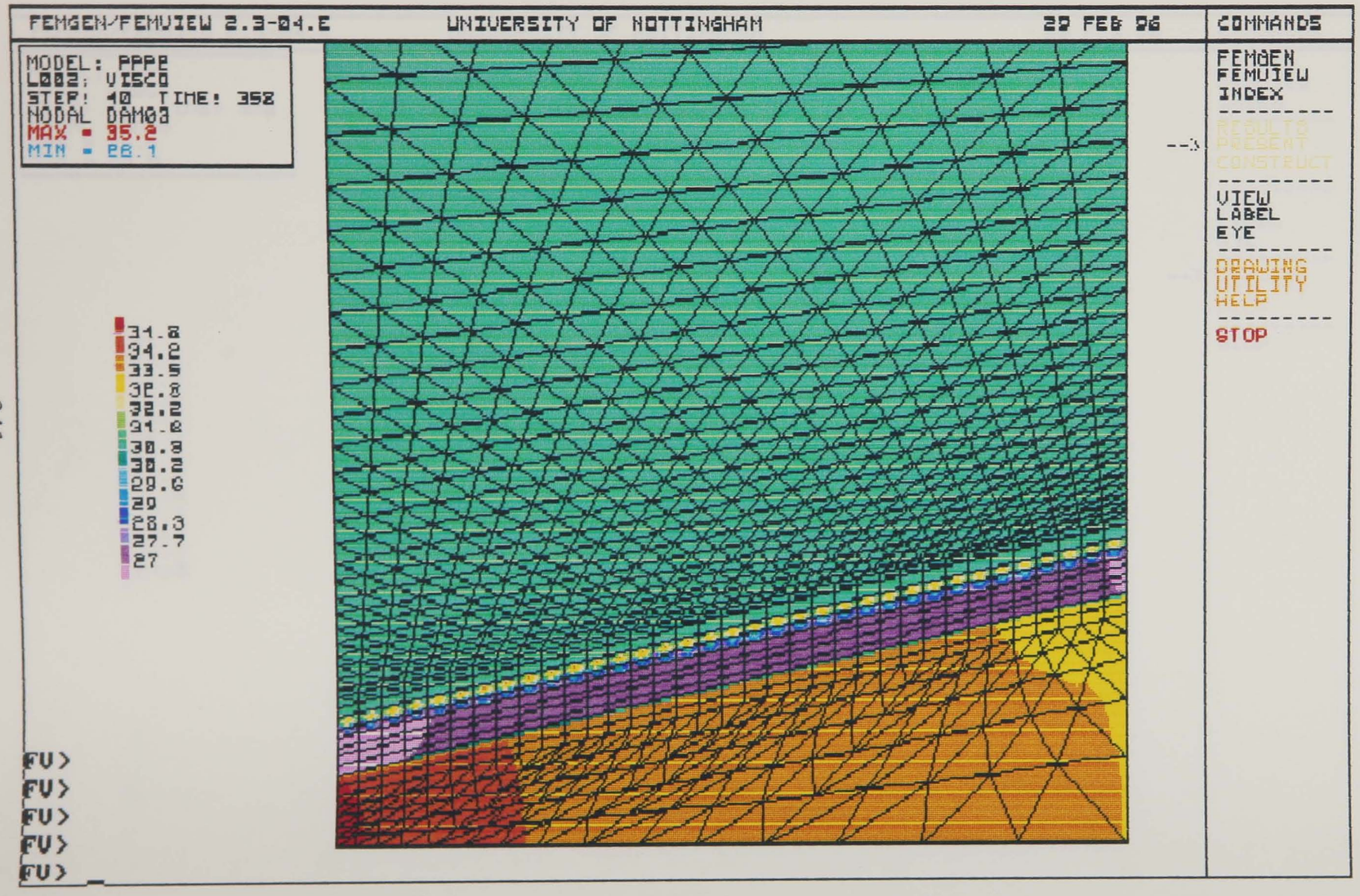

8.3(c) rupture stress, σ_r (α=0.3)

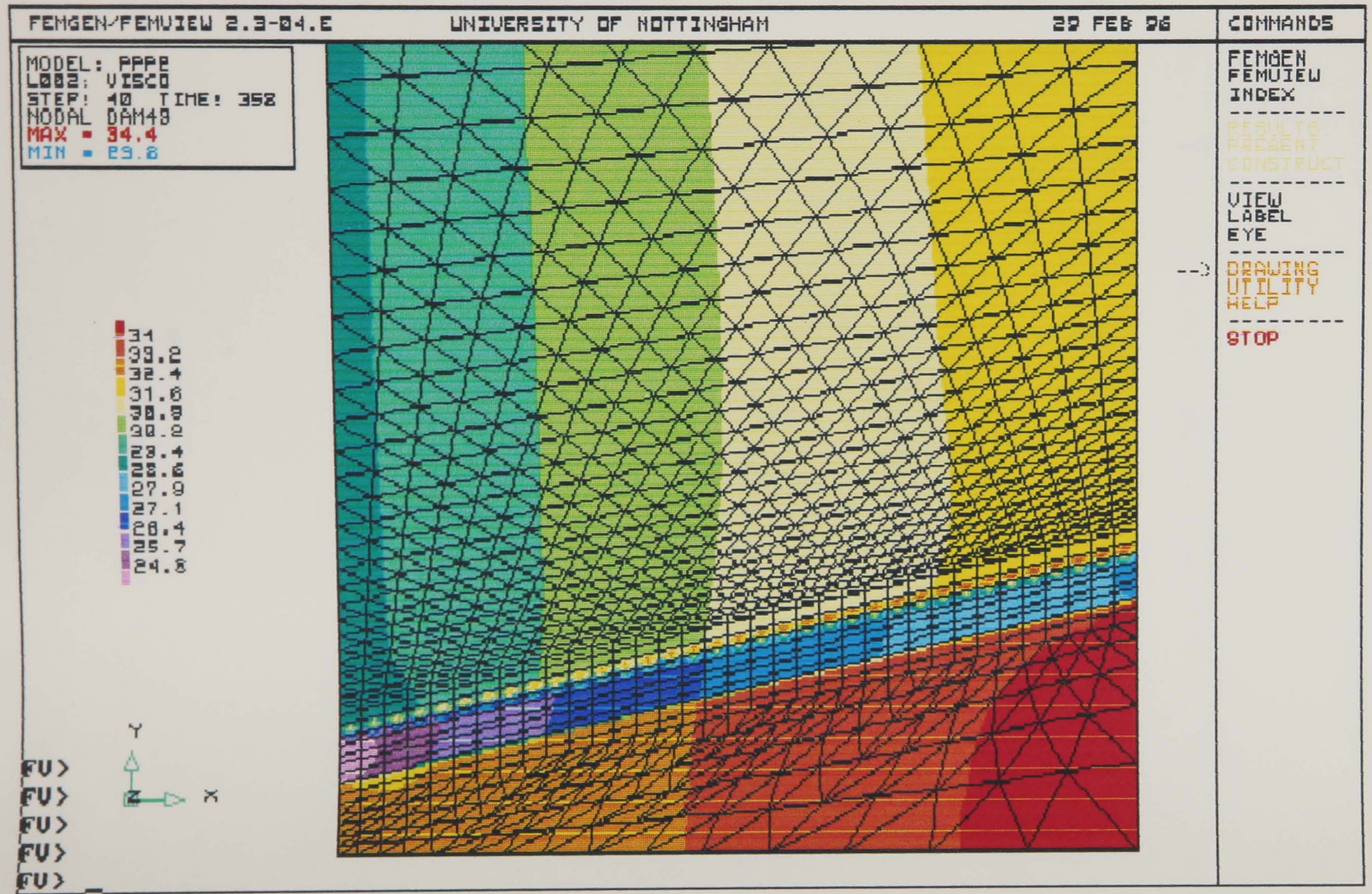

8.3(d) rupture stress, σ_r (α=0.49)

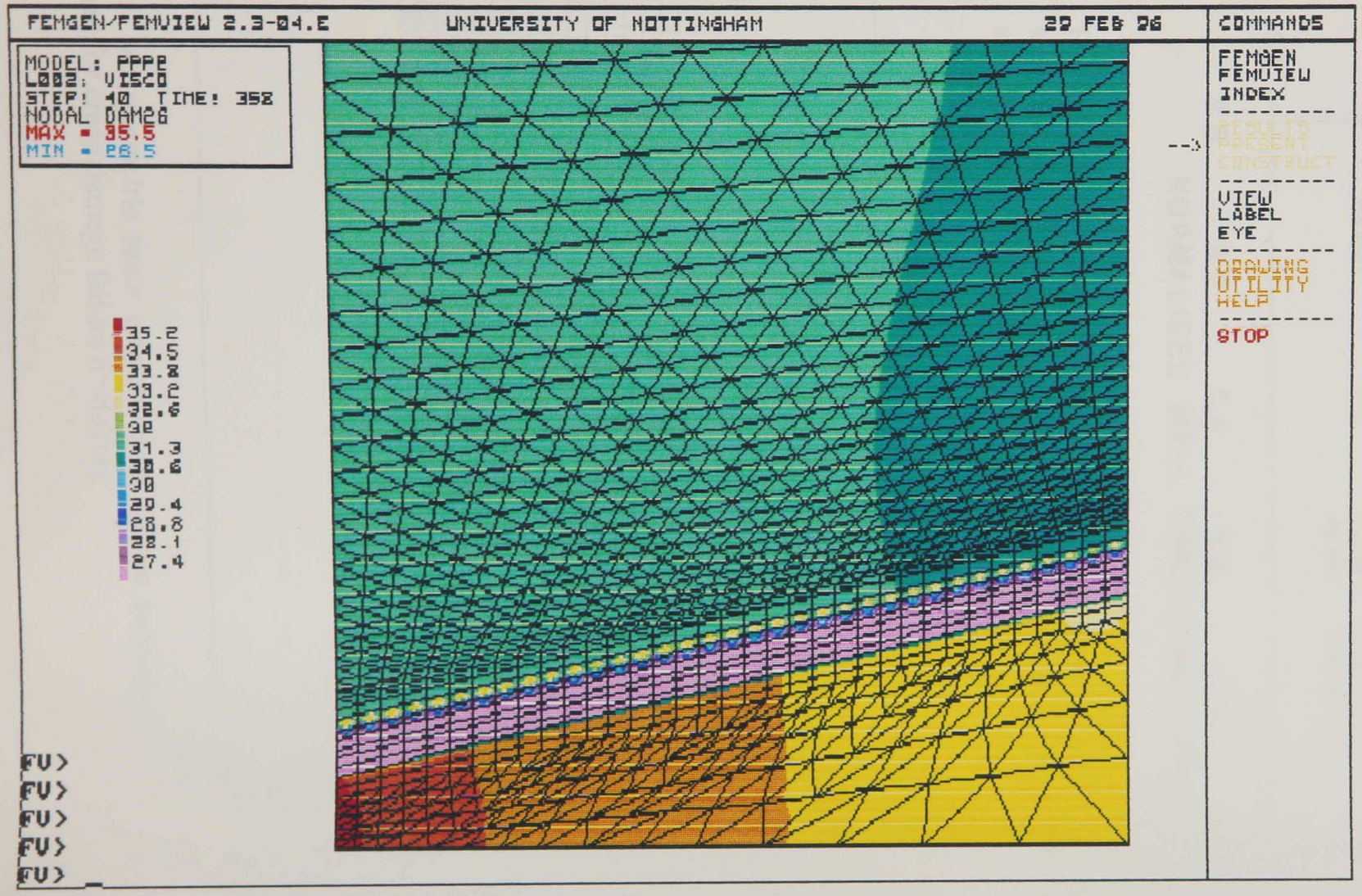

8.3(e) rupture stress, σ_r (α=0.2639)

Fig. 8.3 Steady-state stress distributions of the service-aged weldment using material properties generated at 640° C.

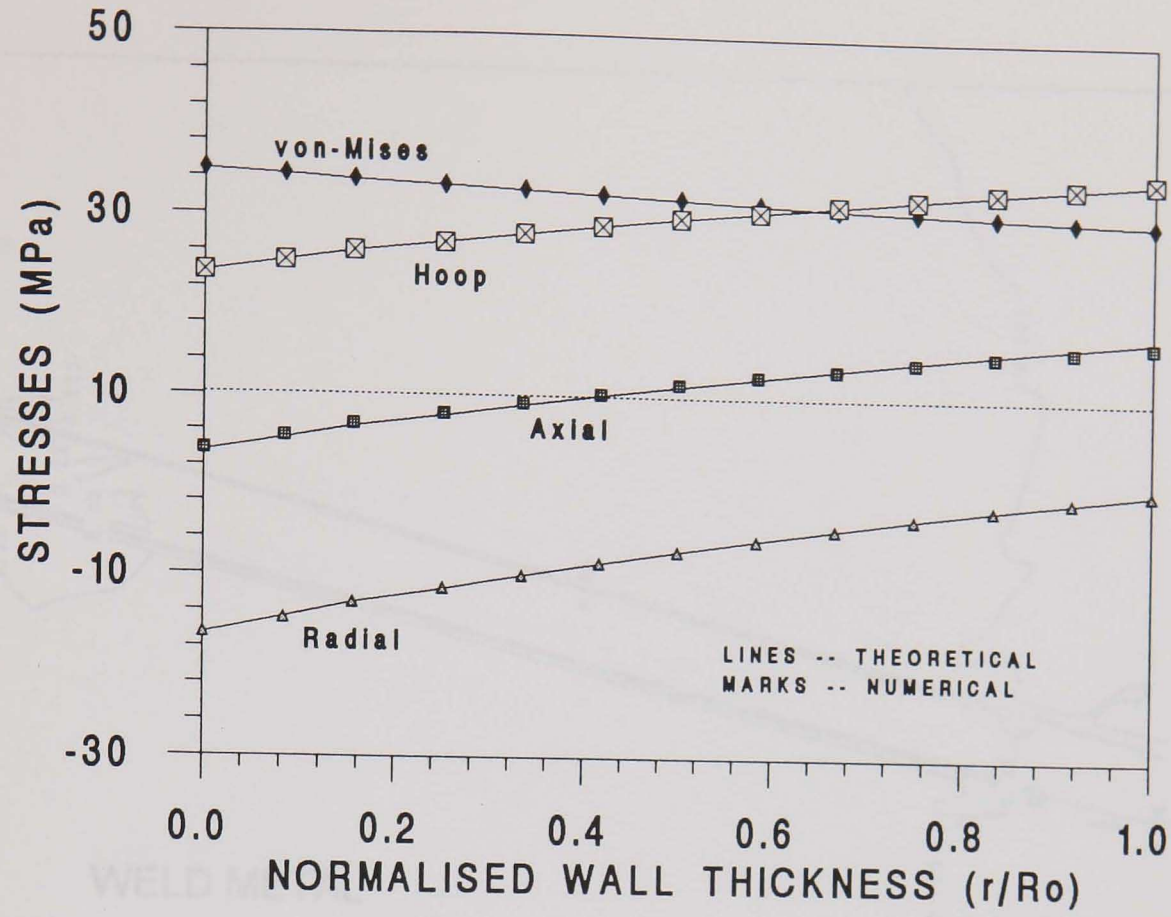

Fig. 8.4 Steady-state creep stresses at the remote area of the welded pipe obtained from finite element analysis and plane strain analytical solutions (Equs. (3.2.9) and (3.2.10)).

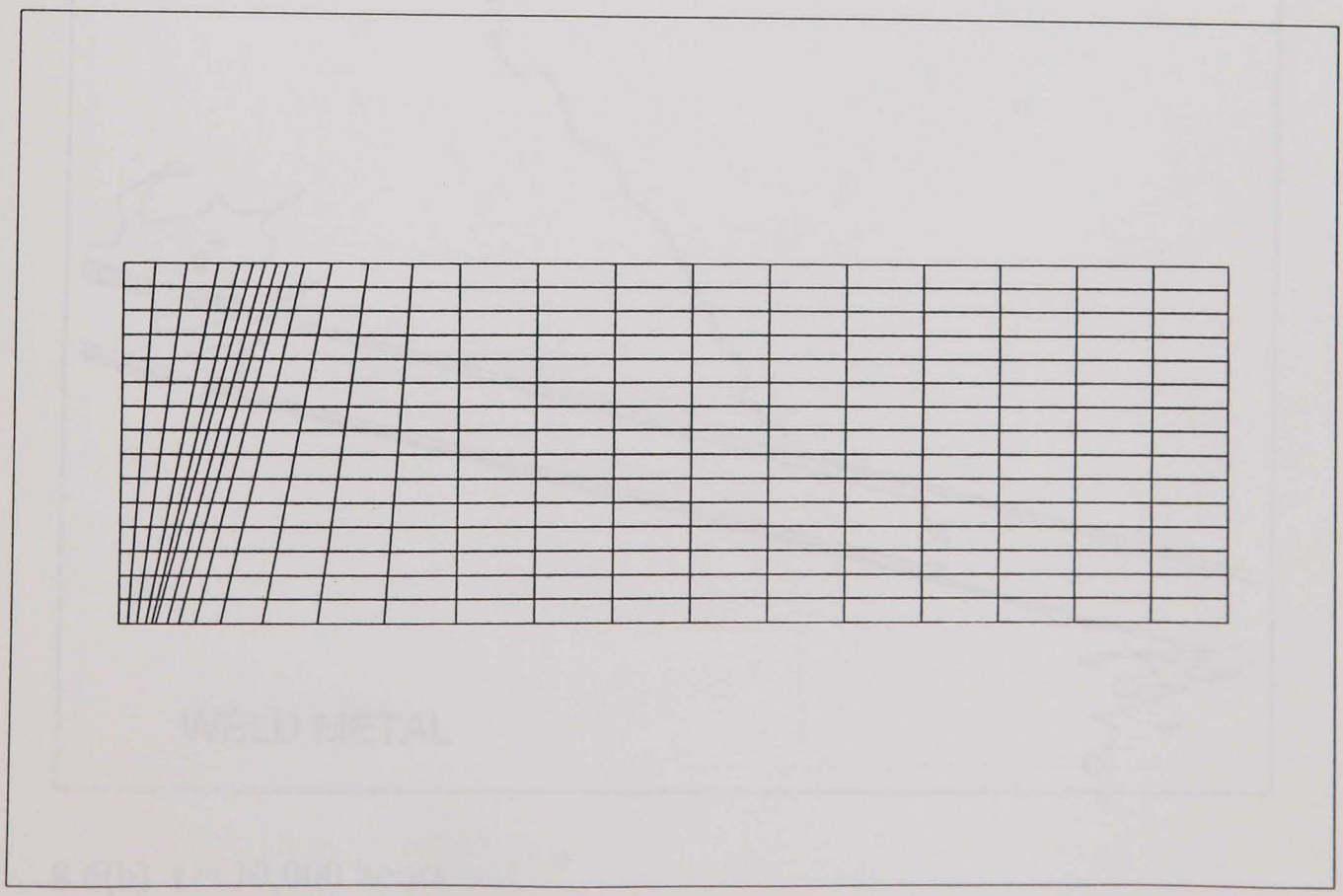

Fig. 8.5 Axisymmetric finite element mesh of the service-aged weldment for creep damage failure modelling.

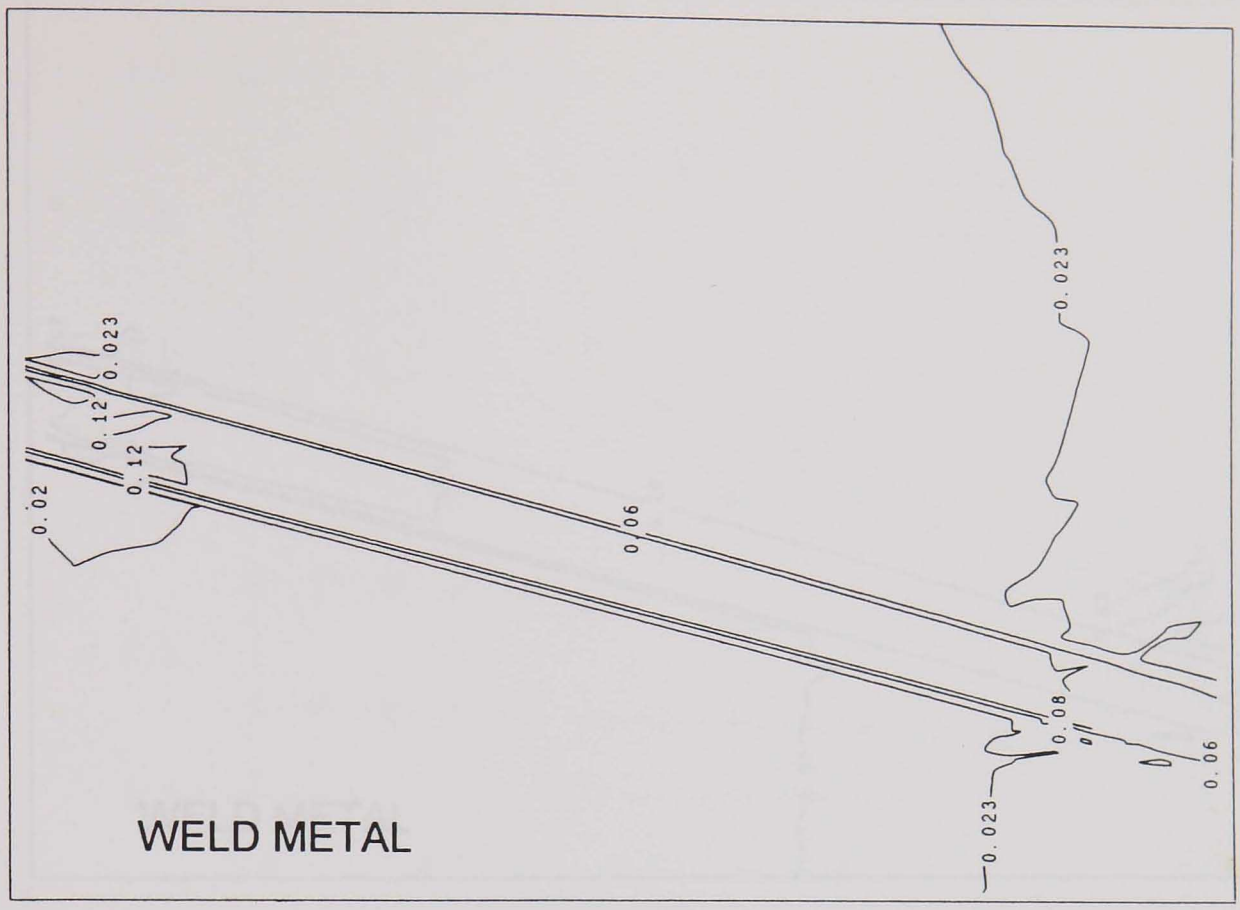

8.6(a) t = 5,000 hours

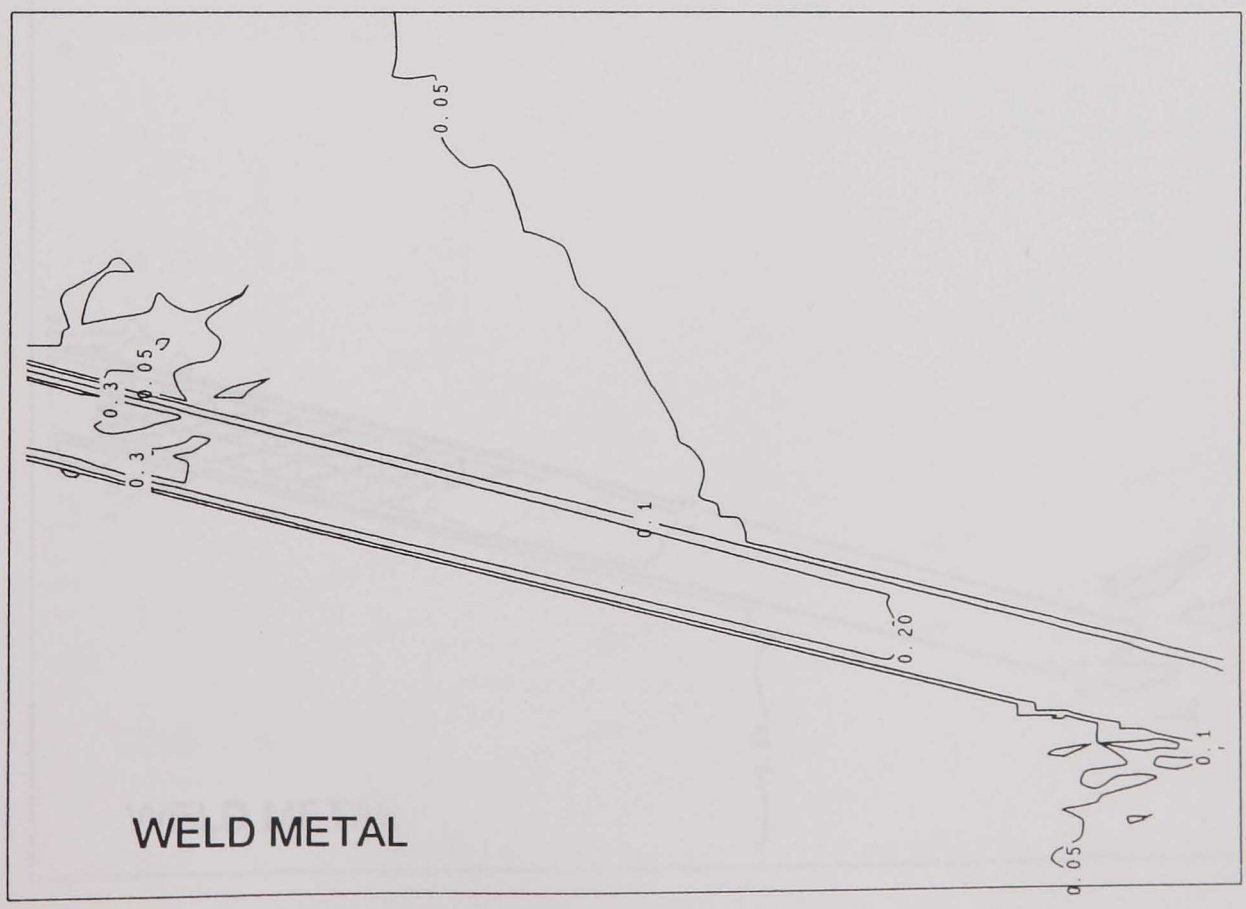

8.6(b) t = 10,000 hours

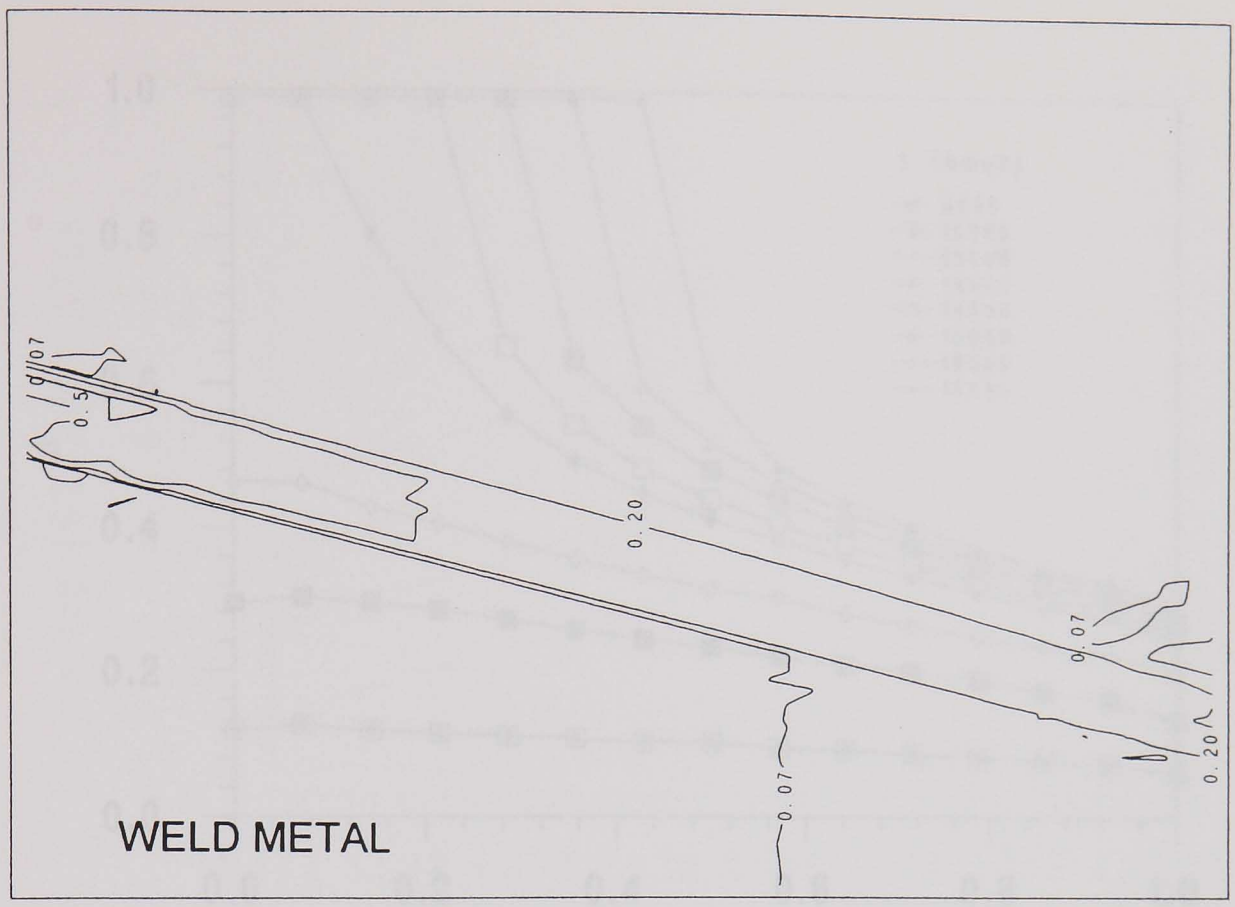

8.6(c) t = 14,000 hours

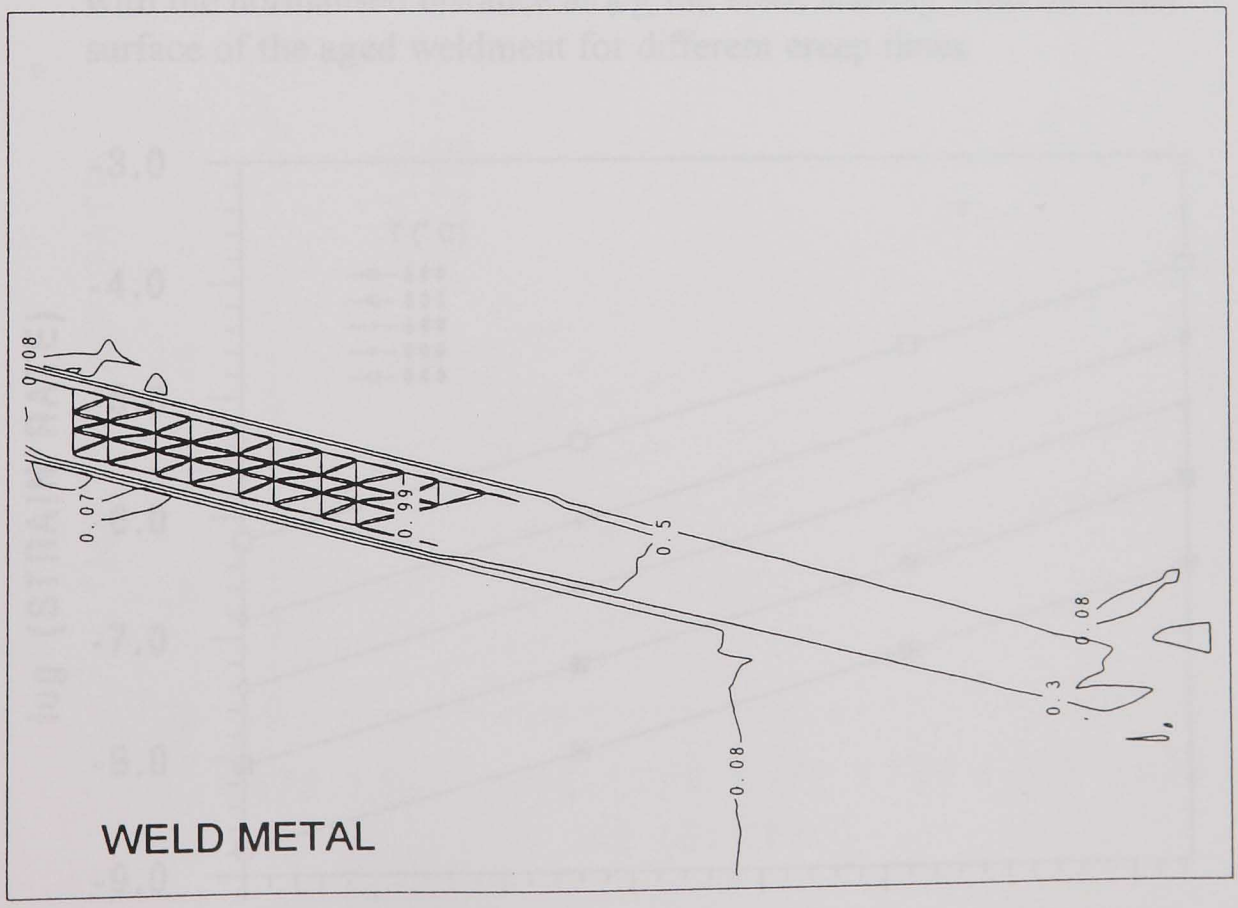

8.6(d) t = 15,640 hours = t_f

Fig. 8.6 Damage distributions of the service-aged weldment at different creep times (using material properties generated at 640° C).

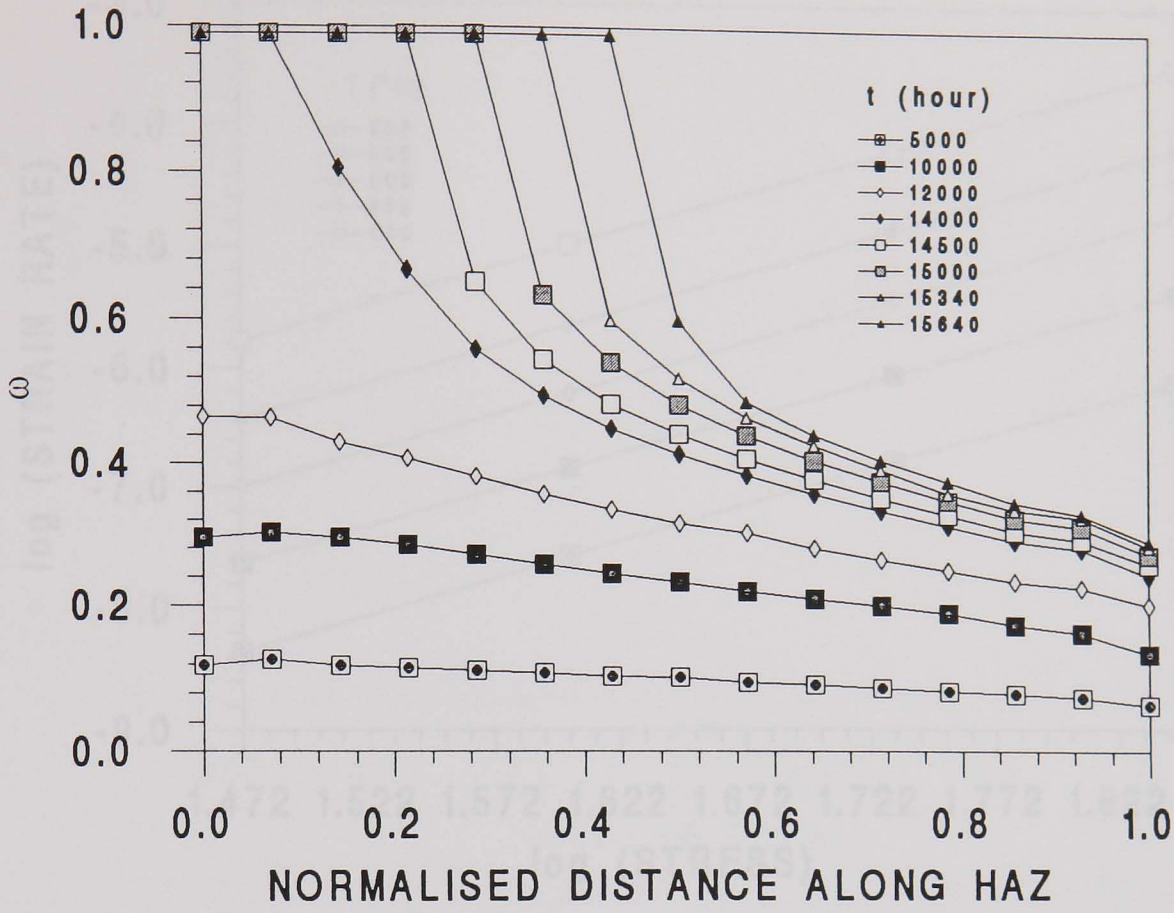

Fig. 8.7 Damage variations in the HAZ adjacent to parent material with the normalised distance along the HAZ starting from the outer surface of the aged weldment for different creep times.

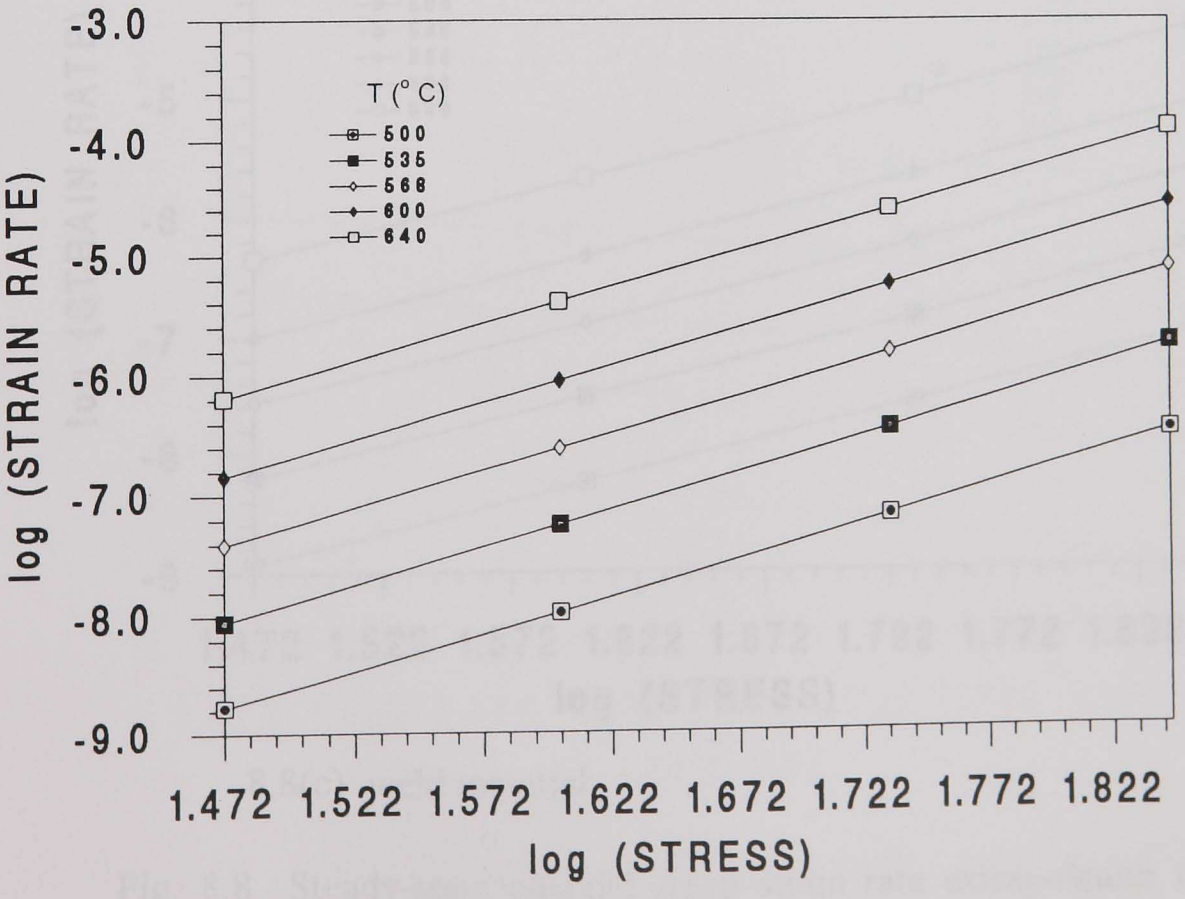

8.8(a) parent material

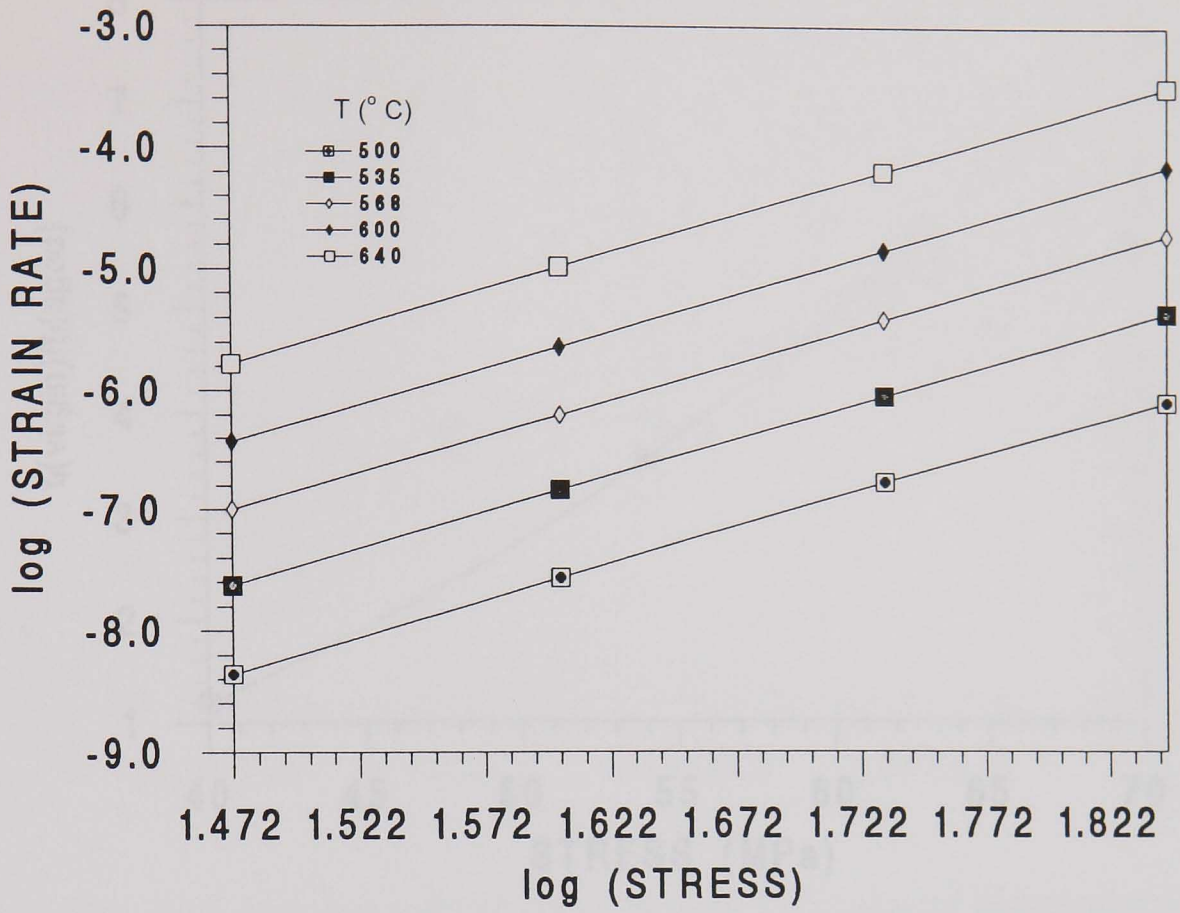

8.8(b) HAZ material

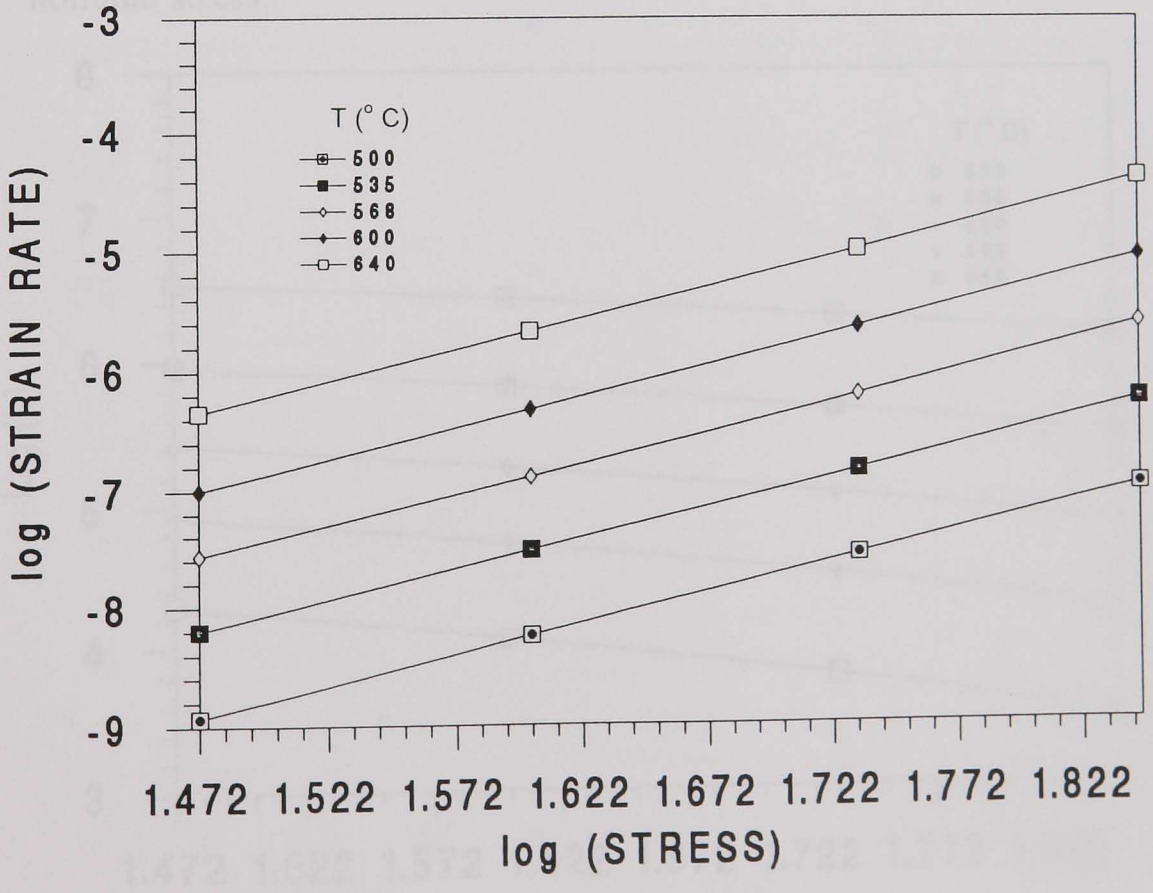

8.8(c) weld material

Fig. 8.8 Steady-state uniaxial creep strain rate extrapolation for the aged weldment materials for a range of temperature, using the tested data at 640° C.

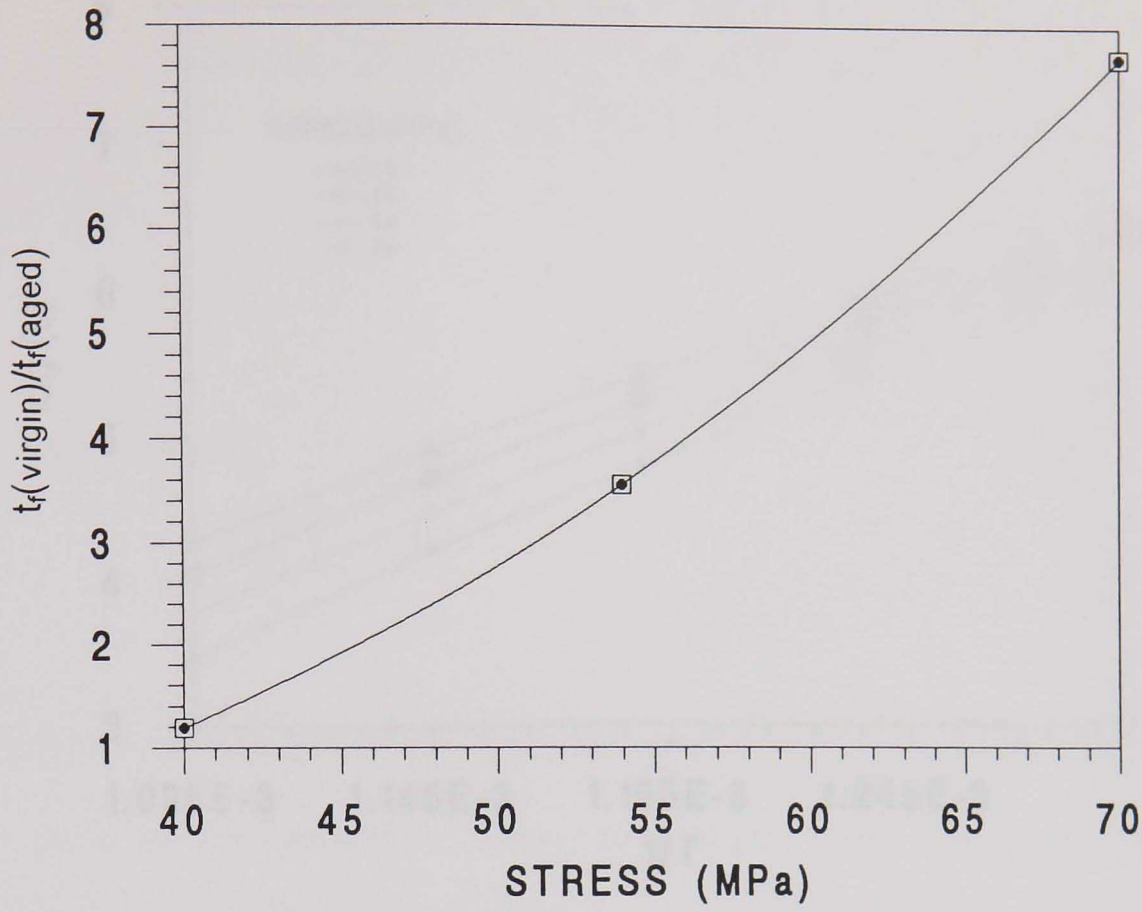

Fig. 8.9 Uniaxial rupture time ratio of the virgin parent material (1/2Cr1/2Mo1/4V) to the aged parent material at 640° C against nominal stress.

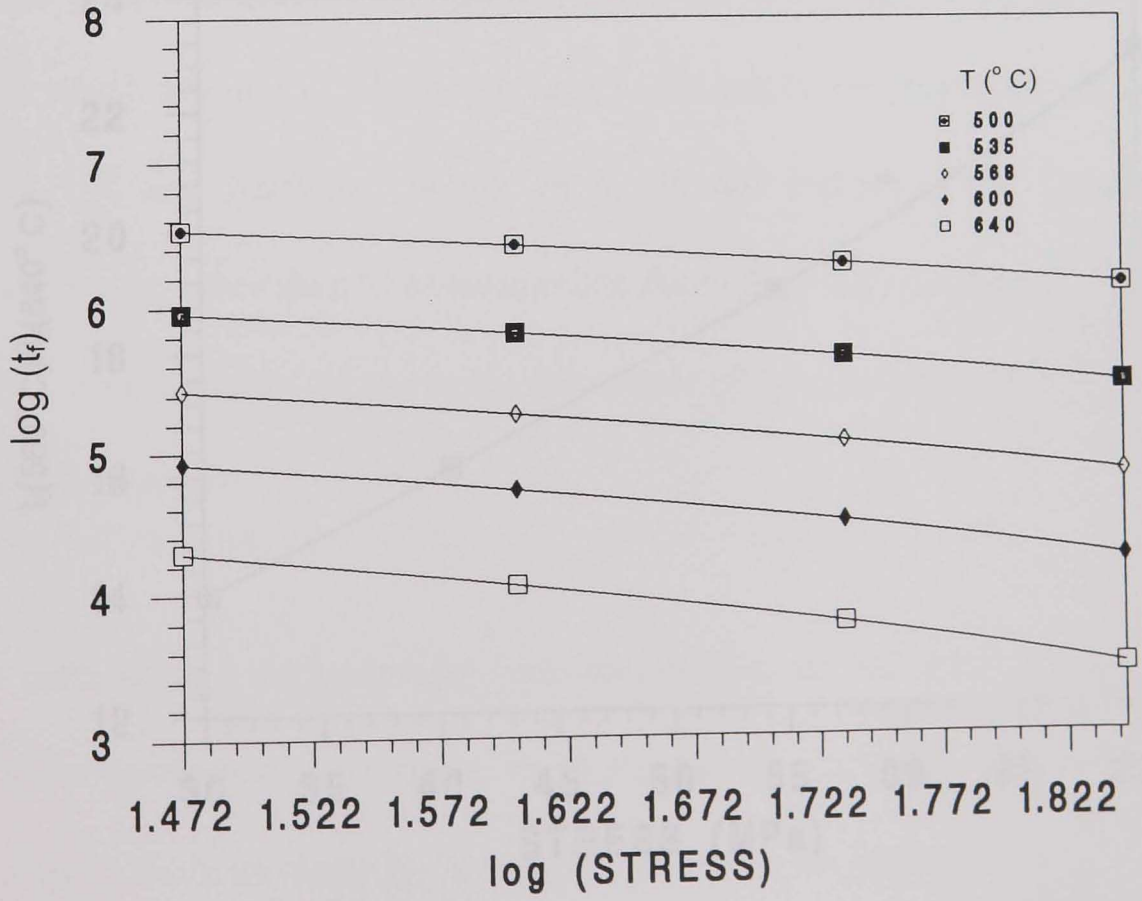

Fig. 8.10 Uniaxial rupture time against stress with different temperatures for 1/2Cr1/2Mo1/4V steel.

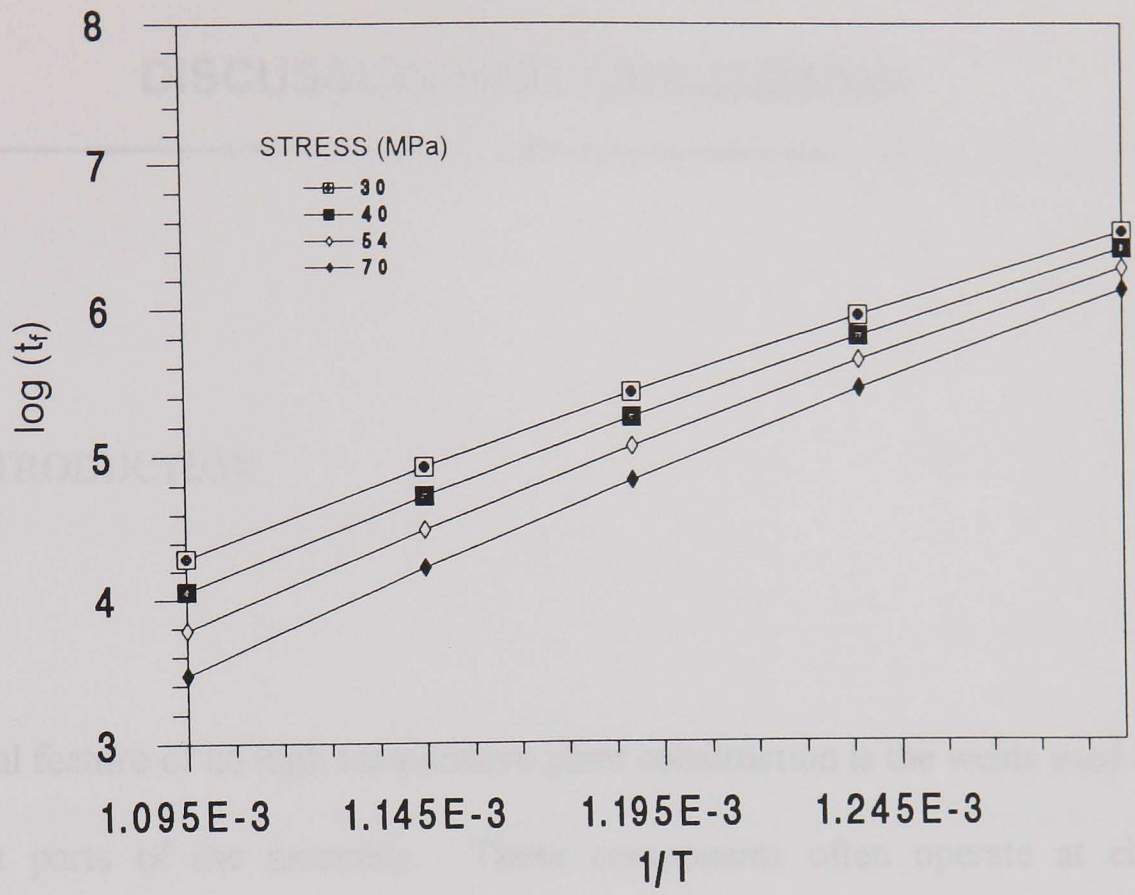

Fig. 8.11 Uniaxial rupture times against reciprocal of temperature with different stresses for 1/2Cr1/2Mo1/4V steel.

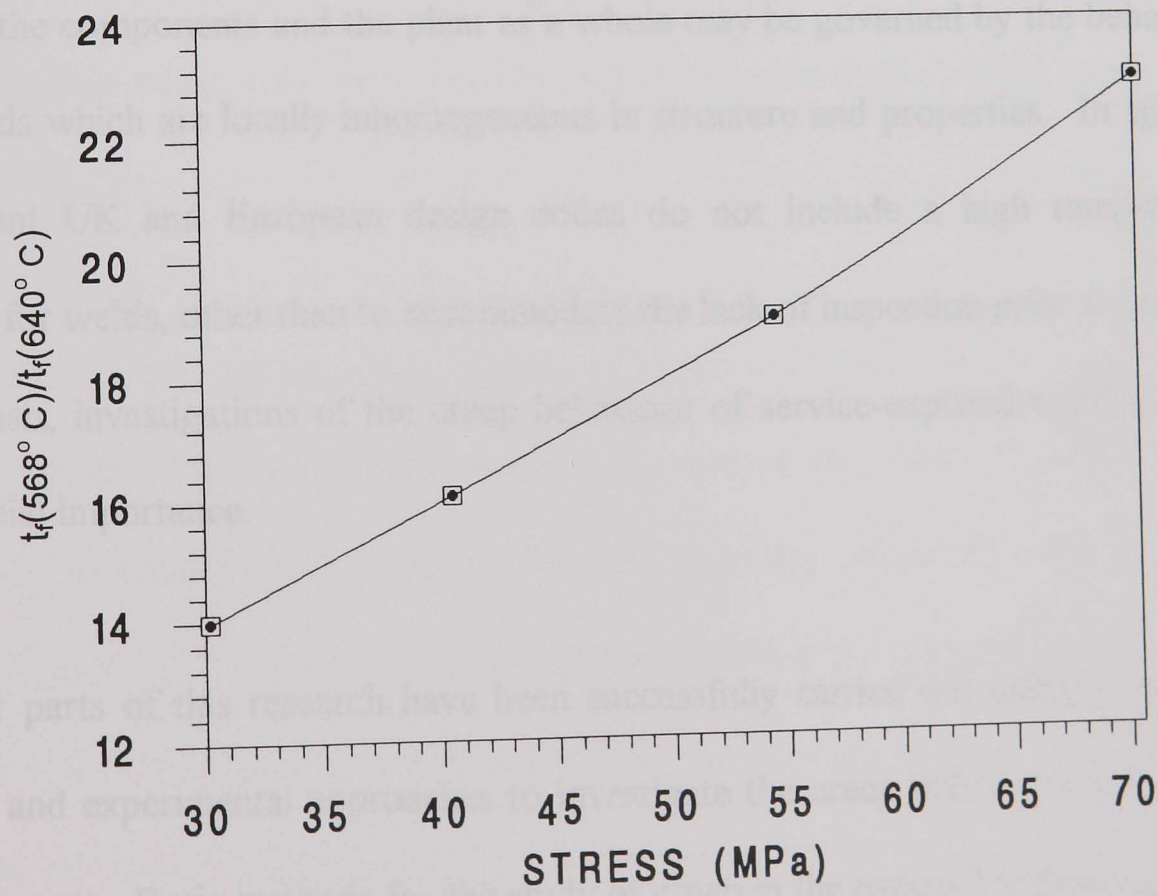

Fig. 8.12 Uniaxial rupture time ratio at 568° C to 640° C against stress for virgin parent material (1/2Cr1/2Mo1/4V).

CHAPTER IX

DISCUSSION AND CONCLUSIONS

9.1 INTRODUCTION

An essential feature of all high temperature plant construction is the welds used to join component parts of the assembly. These components often operate at elevated temperatures and are subjected to relatively steady loads (pressure) for long period of time, i.e. they operate under predominantly creep conditions. Experience suggests that the life of the components and the plant as a whole may be governed by the behaviour of the welds which are locally inhomogeneous in structure and properties. In spite of this, present UK and European design codes do not include a high temperature allowance for welds, other than to accommodate the lack of inspection prior to service. On this basis, investigations of the creep behaviour of service-exposed welded joints are of crucial importance.

The major parts of this research have been successfully carried out using analytical, numerical and experimental approaches to investigate the creep behaviour in service-aged weldments. Basic methods for the study of creep in the exposed weldments have been established. Some metallurgical studies have been involved in this research, but most of the work involved in this study has been focused on mechanical behaviour.

The main contents of this research have been presented in Chapters III to VIII. This Chapter contains a general discussion and the conclusions drawn from the main features of the work.

9.2 GENERAL DISCUSSION

9.2.1 Parametric Study of the Creep Behaviour of Two-Material Structures and Test Specimens

The steady-state creep behaviour of typical two-material structures and test specimens has been studied using a theoretical approach and FE numerical analysis, as described in Chapter III.

General observations on the creep stress variations were made using the analytical solutions derived from four typical simple two-material structures for which closed form exist. For comparison purposes, the corresponding single-material cases were also investigated. The steady-state stress distributions in a two-bar structure, beams in bending and a thick cylinder subjected to internal pressure have been fully investigated. In general, the stress variations greatly depend on the relative creep properties of the two materials and the dimensions or volume which each material occupies, i.e. the interaction effect on the creep behaviour is controlled by both the material properties

and the geometries of the structures. Results obtained have also demonstrated the applicability of simple design rules, for example, the linear relationship between σ_{ij} and 1/n, established for single-material structures, to two-material structures.

A parametric investigation of the stress or strain-rate distributions on the centre-line and of the singularity region of idealised, axisymmetric, two-material creep test specimens has been performed, using FE numerical analysis. The results show that the stress or strain-rate variations are strongly dependent on the specimen geometry and the relative creep properties, similar to those in the typical two-material structures investigated. It has also been shown that the simple linear approximation for σ_{ij} versus 1/n can also be employed, which allows interpolation of the results to be used to obtain reasonable predictions for the centre-line stress or strain-rate distributions for any relative material properties and geometries. The results of the stress singularity analysis suggest that the stress variations in the singularity zones strongly depend on the relative creep properties. If the "singularity zone" is small compared with metallurgical features such as the grain size etc., then the singularity will have no physical significance. For practical purposes, the singularity is unlikely to be important for an n-value greater than about 4, unless the ratio of the creep resistance of the two materials is very large ($>>100$) or very small ($<<0.01$).

In general, the results of the parametric study can be used to describe the essential features of the multi-axial stress state of the cross-weld specimens, i.e. the effects of zone size ratio and relative material creep properties on the tri-axial state of stress or strain-rate can be identified. However, since practical cross-weld specimens usually

consist of more than two material zones, the results obtained from the two-material models cannot be directly applied to real cases. In order to obtain results which are more directly applicable to cross-weld specimens, further analyses using FE models, consisting of three or more material zones, would need to be performed. In addition, in the cases where the weld angle needs to be considered, three-dimensional FE analyses would be required.

9.2.2 Impression Creep Test Technique with Rectangular Indenters

An impression creep test method using a rectangular indenter, under plane strain conditions, instead of the traditional cylindrical indenter, has been developed as a practical technique to determine the creep properties in welded structures, as described in Chapter IV. The technique has been successfully applied to perform practical indentation creep tests for this research. Experimental results obtained from indentation creep tests of 316 stainless steel have shown good agreement in secondary strain-rate values by comparing the indentation data with the corresponding uniaxial data. This further validates the conversion factors, η and β (reference parameters), obtained from plane strain finite element analyses and confirms the applicability of the technique, which can be used to obtain reliable creep properties of conventional uniaxial creep tests. Compared to the conventional impression creep test method with cylindrical indenters, the impression creep test method, using rectangular indenters, possesses some attractive advantages, especially in the determination of the creep properties in welds, where the significant variations in material properties only occur in one direction, i.e. perpendicular to the fusion line.

As has been shown in Chapter IV, three possible loading directions and four possible specimen configurations have been defined. Although only three distinct material zones have been included in the impression models, the method established can be applied to the cases of more than three distinct metallurgical zones. In general, the conversion factors, η and β, are functions of material and geometric ratios of the three zones. However, in many cases (for instance, two materials in series, see Fig. 4.4(b)), if the creep resistance ratio is known and the creep stress index, n, can be assumed to be the same for the two materials, the η and β values can be directly obtained from the available results for the given geometries, see Fig. 4.11. For the simplest case of single material situation, η and β values only depend on the dimensions of the specimens. Since the single-material case can provide the most accurate results and is easiest in specimen manufacturing and testing, it is suggested that whenever this type of test is possible, it is preferable to use single-material specimens for the impression creep tests.

The impression creep test can only be used to determine the primary and secondary creep deformation behaviour. It should be noted that, for practical impression tests, the creep data are only effective in the small deformation situation. This indicates that the highest loading level for an indented material (specimen) should be carefully determined to ensure that realistic test results are obtained.

9.2.3 Experimental Creep Tests

Experimental work has been performed for the purpose of verifying the impression creep test technique and providing creep and rupture information for the generation of the constitutive equations for the exposed weldment materials, as discussed in Chapter V. For the indentation creep test, small size single-material specimens were chosen. For the uniaxial creep test, single-material plain and notched specimens and cross-weld notched and waisted specimens were used.

The experimental data show that after long-term service ageing, the weldment materials have been significantly softened and therefore the creep strength of the welded joint may have been considerably reduced. On the basis of secondary strain rates, the order of descending creep strength for parent material is: virgin parent (simulated parent), virgin HAZ (simulated HAZ) and aged parent; the order for the aged weldment materials at high stress level is: weld metal, parent material and HAZ.

Surface oxidation damage was observed in the creep tests of the exposed material specimens at 640° C. The effect of oxidation damage was found to be strongly dependent upon creep time. Due to oxidation, for the exposed materials, the indentation creep test data were considered to be reliable only at the highest stress level used, i.e. 70 MPa.

Fracture surfaces and failure positions of both the cross-weld notched and waisted specimens were examined after test. SEM examinations showed that the fracture

surfaces were heavily oxidised but appeared to be intergranular in nature. Microstructure examinations on sectioned surfaces of the tested cross-weld specimens confirmed that the fracture surfaces were located in the HAZ and adjacent to the parent material, i.e. the failure of the cross-weld specimens was confirmed to be Type IV cracking. This also implies that the design of the size and shape of the cross-weld waisted specimens is reasonable.

It should be mentioned that the temperature of 640° C chosen for the creep tests of the service-aged materials is very high compared with the likely service temperatures. If lower temperature levels were used, for instance, if $T \leq 600°$ C, the surface oxidation damage would not be significant, and failure life predictions or extrapolations for the weldment would be significantly more reliable.

9.2.4 Creep Damage Study – Damage Constitutive Equation Generation and Failure Modelling for the Exposed Weldment

The creep continuum damage approach has been used as the basis for generating creep and damage constitutive equations of the aged weldment materials, see Chapter VI, and for performing failure analyses of practical exposed welded joints using the creep and damage material parameters already generated for the aged materials, as shown in Chapter VIII.

Methods used for the determination of damage parameters for the exposed materials, based on FE-damage modelling, have been established. By comparing the calculated

rupture times with those tested, it was demonstrated that the damage parameters generated for the exposed materials accurately represent their mechanical behaviour, although the accuracy of the data generation may have been affected by oxidation.

Results of damage modelling of the exposed welded pipe suggests that the failure of the weldment will occur in the HAZ, starting from a position near the outer surface and adjacent to the parent material. The rupture life predicted is 1.564×10^4 hours at 640° C. This rupture life has been extrapolated to that at the practical temperature of 568° C, giving an estimate for the rupture time of 2.234×10^5 hours for the exposed weldment.

For the purpose of comparison, a steady-state creep analysis of the weldment was also performed. The failure position was also found to be in the HAZ and the rupture life obtained was found to be about 40% shorter than that predicted by damage modelling.

9.2.5 Steady-State Failure Prediction

In order to demonstrate the applicability of the failure prediction using steady-state analysis, an investigation of the multi-axial stress distributions and rupture stress variations of cross-weld specimens was conducted, as discussed in Chapter VII, in which the single-material case was also investigated.

Results of both the cross-weld specimens and welded pipe have shown that the steady-state prediction can be used to obtain an approximate, but reasonably accurate

prediction of the failure life and failure position of single-material and multi-material components in creep conditions. On this basis, it is also suggested that a steady-state analysis can be used as an approximate technique for damage parameter generation. In general, the rupture life predicted by steady-state analysis is conservative, compared to the failure life predicted by damage modelling.

The principle of the steady-state failure prediction is that the rupture life of a specimen or component can be related to the steady-state peak rupture stress. This indicates that in order to shorten the durations of the uniaxial rupture tests of the specimens such as notched bars or waisted specimens, a steady-state analysis can be used to determine the optimum sizes or shapes of the specimens, which give relatively high peak rupture stresses at the possible failure positions.

9.2.6 HAZ Material Properties of the Exposed Weldment and the Type IV Failure

As mentioned in Chapter V, the creep and damage material properties within the HAZ of the service-exposed weldment were assumed to be constant, i.e. the cross-weld models were assumed to consist of parent material, weld metal and a single heat affected zone. The reason for making this assumption is that when welds have been exposed for long periods at service conditions, say $\geq$ 150,000 hours at 500-600° C, the HAZ region can be generally tempered and softened, and due to diffusion, the difference in material properties at different positions within the HAZ of the weldment will become less significant after long-term service, which makes the identification of the individual zones more difficult. Microstructure examination on the cross-weld

materials, before and after test, has shown that there is no significant difference in microstructure compositions of the HAZ, i.e. no distinct sub-zones could be clearly identified. Cross-weld hardness tests also indicate that the hardness values across the HAZ were practically the same and no sharp change was observed on or near the boundary between the parent and HAZ which is the so called Type IV cracking position.

Over the years, cracks have been described by their length, width, form and position within the structures. This can be complicated, and hence the German designations (Schuller et al [1974]) have provided a useful framework by which the positions and orientations of cracks may be simply and clearly defined. The various coded crack forms are shown (see Fig. 2.2) for completeness. The Type IV cracking can be seen to be a form of crack, which in a circumferential pipe weld, will be in the circumferential direction. The crack will appear and run near the edge of the HAZ of the weldment on the parent material side, as opposed to the Type III crack which occurs near the weld metal side of the HAZ. It is important to note that the code merely defines the type of crack position; it says nothing about the metallurgical structure and the mechanisms by which the crack forms and the cavity link up process occurs. However, it would appear that all of the Type IV cracks recorded in the literature follow similar growth patterns and seem to occur in the same relative microstructure zone of ferritic weldments, namely, within the HAZ but close to the parent material side of the zone.

For a virgin ferritic weldment, the variations in metallurgical and mechanical properties across the HAZ can be clearly described (e.g. Storesund and Tu [1995]) and the

position in the HAZ where the Type IV crack occurs usually has a relatively low creep strength and high ductility. However, this does not mean that the Type IV failure is only associated with the material properties in the region where the crack forms. Since Type IV cracks only appear after service times of about 50,000 to 80,000 hours (Williams [1982-2]), the creep properties within the HAZ may have been significantly changed. In fact, it may be more precise to assume that the Type IV cracking is a result of the comprehensive interaction effect of the welded joints of this kind, due to long-term service exposure, subjected to loading and high temperature. In other words, the failure modes of a weldment are dominated by metallurgical properties, geometrical features and the mechanical loading. Mechanically speaking, the damage accumulation in a multi-material structure is strongly dependent upon the tri-axial state of stress and strain. In a narrow zone, such as the HAZ, the local deformation usually sustains additional constraints and therefore subsequent stress concentration will occur near the boundary of the zone. The final outcome is that the localised maximum damage is most likely to be accumulated near the boundary of the narrow zone.

The Type IV cracking has been predicted for the cross-weld test specimens of the aged weldment in this research. The FE damage modelling for the cross-weld specimens and for the welded pipe of the exposed material also shows that the maximum damage first occurs in or near the Type IV cracking position. In addition, the steady-state analyses for both cross-weld specimens and the welded pipe demonstrate that the peak rupture stresses occur at the HAZ boundary on the parent material side. This indicates that although the material properties within the HAZ were assumed to be constant, the three-material-zone models can also exhibit this failure mode. This phenomenon

confirms that the detailed material properties in the Type IV cracking position are not the only important factors which result in Type IV failure.

It should be noted that in order to understand the mechanism of Type IV failure of exposed weldments, an extensive microstructure investigation including creep cavitation examination (Walker et al [1996]) would need to be carried out .

9.2.7 Creep Test Temperature and Failure Life Extrapolation

In this research, the experimental creep tests of the service-aged weldment materials were performed at 640° C. Based on the test data, creep and damage constitutive equations of the aged materials have been generated and the failure behaviour of a service exposed weldment has been modelled using the material properties generated at 640° C.

Two problems have arisen from choosing the test temperature level to be 640° C. Firstly, the test specimens have sustained serious surface oxidation damage, which will inevitably have affected the accuracy of the test data. Secondly, the predicted failure life of the weldment, at 640° C, has had to be extrapolated to that at the practical operating temperature of 568° C. Difficulties have been encountered in failure life extrapolation, mainly due to the lack of the creep data for exposed materials and the differences in the failure behaviour between a weldment and a uniaxial specimen. Therefore, the prediction for the rupture life of the aged weldment was performed

based on numerous assumptions, and consequently, it can only provide a very approximate estimation of the failure life of the weldment at 568° C.

9.3 GENERAL CONCLUSIONS

Based on the above discussion, the main conclusions of this work can be summarised as follows.

(1) Investigations of two-material structures and test specimens can be used to demonstrate the applicability of simple design rules, developed for single-material cases, to two-material situations. The parametric investigation of the two-material cross-weld specimens can be used to identify the essential features of the multi-axial state of stress or strain-rate and the stress singularity behaviour at the free surface, caused by the material dissimilarity. The stresses or strain-rates on the centre-line are strongly dependent on the relative material and geometric ratios. The stress singularity behaviour is mainly affected by the relative creep resistance ratio, A/B, and stress index, n. When $n > 4$ and $0.01 < A/B < 100$, the existence of the singular points is unlikely to be significant.

(2) The impression creep test technique, using a rectangular indenter, has been verified and shown to be an effective creep test method; it has some attractive advantages, compared with the conventional technique, using cylindrical

indenters, in determining the creep properties in welds. For a specific test, the conversion factors, η and β (reference parameters), can be obtained using plane strain FE analysis. In general, the η and β values are geometry and material dependent.

(3) The creep strength of the weldment investigated has been reduced due to long-term service exposure. The aged parent material shows higher secondary strain-rates than the aged weld metal. Since for the virgin parent material and weld metal, the weld metal strain-rate is expected to be typically 4 times higher than that of the parent metal, it is suggested that the parent material is more substantially degraded by service ageing. Significant surface oxidation has been observed in the specimens of aged materials tested at 640° C.

(4) FE damage modelling of the single-material notched specimens and cross-weld notched and waisted specimens can be used as an accurate method to generate the required damage parameters. The method developed can be applied, in general, to other multi-material cases.

(5) The failures of both the notched and waisted cross-weld test specimens were found to be caused by Type IV cracking. The failure of the exposed weldment, predicted by damage modelling, occurs in the HAZ and starts from a position near the outer surface, adjacent to the parent material. The failure time predicted is 1.564×10^4 hours at 640° C and the failure time estimated at 568° C is 2.234×10^5 hours for the weldment.

(6) Steady-state creep analysis can be used with reasonable accuracy as an approximate technique for the failure prediction of welded pipe and specimens. The failure life prediction, in general, is conservative, compared with creep damage prediction. In principle, steady-state creep analysis can also be used as an alternative, approximate method for damage parameter generation.

CHAPTER X

FUTURE WORK

10.1 PARAMETRIC ANALYSIS OF THE CREEP BEHAVIOUR OF THE CROSS-WELD SPECIMENS WITH THREE OR MORE CONSTITUENT MATERIAL ZONES

In the current work, the steady-state parametric study of the creep behaviour of cross-weld specimens was performed using two-material, axisymmetric models, as introduced in Chapter III. Stress analysis and the failure modelling of cross-weld specimens were only conducted for the situation of realistic dimensions and material properties (see Chapter VIII). However, since practical cross-weld specimens usually consist of three or more distinct material zones, the results obtained from the two-material models cannot necessarily be directly applied to the real-life cases. Therefore, in order to further understand the practical interaction effects of the multi-zone cross-weld specimens and to provide more realistic stress and deformation information, further investigations using models consisting of three or more material zones are necessary. Also, the influence of the weld angles needs to be understood. In this case, three dimensional analysis is required.

10.2 CREEP TESTING OF SERVICE-EXPOSED MATERIALS AT LOWER TEMPERATURE

As described in Chapter IX, problems have resulted by choosing the relatively high test temperature (T = 640° C) for the exposed material creep tests. Firstly, during the testing, surface oxidation damage was found in all of the uniaxial and indentation test specimens. Secondly, the failure life of the weldment predicted using material properties at 640° C has to be extrapolated to that at the practical operating temperature, i.e. T = 568° C. Precise data extrapolation is very difficult; one of the reasons for this is that an accurate temperature-dependent relation for the exposed weldment materials in the range of 568° C < T < 600° C does not exist, owing to the lack of relevant creep data. Obviously, both the oxidation damage and data extrapolation will affect the accuracy of the failure prediction of the exposed weldment.

Therefore, in an attempt to provide more reliable creep data for assessing the performance of the service-aged weldments, it is suggested that future creep tests for the exposed parent, HAZ and weld materials should be performed at lower temperature, e.g. T ≤ 600° C.

10.3 INVESTIGATION OF THE CREEP BEHAVIOUR OF REPAIRED WELDS

A procedure for studying the creep behaviour of the service-aged weldments have been introduced and established in this thesis. It would be possible to extend the techniques employed by the current research to study the behaviour of repaired weldments.

Experience shows that many welded components will be repaired within the design life of the plants in which they are used. It is essential, for any safety and economic approval, that the performance of such repairs can be realistically and consistently underwritten. It is therefore useful that current understanding of damage mechanics, finite element analysis, welding technology and methods of determining material properties should be incorporated in a comprehensive investigation of this problem.

To date, no attempts have been made to establish the creep properties of zones within a repaired weld; the impression creep testing technique could be used for this purpose. By determining the creep properties within the various zones of a repaired weld and the geometry of the repair excavation, it would be possible to identify the circumstances under which a weld repair would improve the life of a structure and to quantify the improvement, thereby maximising the use of high temperature materials and plant. An investigation of the creep behaviour of repaired weldments would provide essential information for the performance assessment of the weldments.

REFERENCES

ABAQUS Version 5.4 [1994], Hibbitt, Karlsson and Sorenson, Inc.

ANDERSON, R. G., GARDENER, L. R. T. and HODGKINS, W. R. [1963], Deformation of uniformly loaded beams obeying complex creep laws, *J. Mech. Engng. Sci.*, Vol. **5**, pp. 238-244.

BECKER, A. A., HYDE, T. H. and SUN, W. [1994], FE-Damage Users Manual, University of Nottingham.

BECKER, A. A., HYDE, T. H. and XIA, L. [1994], Numerical analysis of creep in components, *J. Strain Analysis*, Vol. **29**, No. 3, pp. 185-191.

BOGY, D. B. [1968], Edge-bonded dissimilar orthogonal elastic wedges under normal and shear loading, *J. of Applied Mechanics*, Vol. **35**, pp. 460-466, Transactions of ASME.

BOGY, D. B. [1971], Two edge-bonded elastic wedges of different materials and wedge angles under surface tractions, *J. of Applied Mechanics*, Vol. **38**, pp. 377-386, Transactions of ASME.

BOODALL, I. W. (Editor) [1990], Assessment Procedure R5, Issue 1, An assessment Procedure for the High Temperature Response of Structures, published by Nuclear Electric plc.

BOYLE, J. T. [1983], The reference stress and its role in high temperature design, in Engineering Approach to High Temperature Design, Vol. **2** of Recent Advances in Creep and Fracture of Engineering Materials and Structures, Series Edited by B. Wilshire and D. R. J. Owen, Pineridge Press, Swansea.

BOYLE, J. T. and SPENCE, J. [1983], Stress analysis for creep, Butterworths, London.

CANE, B. J. [1981], Collaborative programme on the correction of test data for high temperature design of welded steam pipes, CEGB Report, RD/L/2101N81.

CHILTON, I. J., PRICE, A. T. and WILSHIRE, B. [1984], Creep deformation and local strain distributions in dissimilar metal welds between AISI type 316 and 2.25Cr-1Mo steels made with 17Cr-8Ni-2Mo weld metal, *Metals Technology*, Vol. **11**, pp. 383-391.

CHU, S. N. G. and LI, J. C. M. [1977], Impression creep; a new creep test, *J. Mat. Sci.*, Vol. **12**, pp. 2200-2208.

CHU, S. N. G. and LI, J. C. M. [1979], Impression creep of β-Tin single crystals, *Material Science and Engineering*, Vol. **39**, pp. 1-10.

CHU, S. N. G. and LI, J. C. M. [1980], Localised stress relaxation by impression testing, *Material Science and Engineering*, Vol. **45**, pp. 167-171.

COLEMAN, M. C., PARKER, J. D. and WALTERS, D. J. [1985], The behaviour of ferritic weldments in thick section 1/2Cr1/2Mo1/4V pipe at elevated temperature, *J. Pres. Ves. & Piping*, V**18**, pp. 277-310.

COLEMAN, M. C. and MILLER, D. A. [1994], Inspection, assessment and repair strategies for Type IV cracking in power plant companies, AWS/EPRI Conf., Orlando, Floride, pp. 5-15.

CORUM, J. M. [1990], Evaluation of weldment creep and fatigue strength-reduction factors for elevated-temperature design, *J. Pres. Ves. Technology*, V**112**, pp. 333-339, Transactions of ASME.

CRAINE, R. E. and HAWKES, T. D. [1993], On the creep of ferritic weldments containing multiple zones in plates under uniaxial loading, *J. Strain Analysis*, Vol. **28**, No. 4, pp. 303-309.

CRAINE, R. E. and NEWMAN, M. G. [1992], Modelling Type IV cracking in thin plates under uniaxial loading, Proc. 13th Riso Int. Symp. on Mat. Sci., Ed. S. I. Andersen et al, Riso Nat. Lab., Roshilde, Denmark.

CRAINE, R. E. and NEWMAN, M. G. [1996], Modelling creep failure in welded plates under uniaxial loading, *J. Strain Analysis*, Vol. **31**, No. 2, pp. 117-124.

CRISFIELD, M. A. [1981], A fast incremental/iteration procedure that handles Snapthrough, *Computers & Structures*, **13**, pp. 55.

DOLE, A. K. [1991], Influence of weld factors on creep-rupture cracking at elevated temperature, *J. Pres. Ves. Technology*, V**113**, pp. 194-209, Transactions of ASME.

DORN, J. E. and MOTE, J. D. [1964], Physical aspects of creep, Office of Naval Research Structural Mechanics Series, High Temperature Structures and Materials, Proceedings of the Third Symposium on Naval Structural Mechanics, Edited by A. M. Freudenthal, B. A. Boley and H. Liebowitz, Pergamon Press Ltd.

DUNDURS, J. [1969], Discussion on: Edge-bonded dissimilar elastic wedges under normal and shear loading, *J. of Applied Mechanics*, Vol. **36**, pp. 650-652, Transactions of ASME.

ELLIS, F. V. and BROSCHE, D. J. [1993], Creep-rupture properties of low carbon virgin 2-1/4Cr-1Mo saw longitudinal seam weldments and effect of specimen size, ASME Pressure Vessels & Piping Division (Publications), PVP-Vol. **262**, High-Temperature Service and Time-Dependent Failure, pp. 147-156.

ENGLAND, A. H. [1971], On stress singularities in linear elasticity, *Int. J. Eng. Sci.*, Vol. **9**, pp. 571-585.

ETIENNE, C. F. and HEERINGS, J. H. [1993], Evaluation of the influence of welding on creep resistance (strength reduction factor and lifetime reduction factor), IIW doc. IX-1725-93, presented at meeting IIW Cie IX Working Croup Creep, Copenhagen.

EVANS, R. W. and WILSHIRE, B. [1985], An analysis of the creep fracture characteristics of austenitic steel transition welds, *Mechanics of Materials* **4**, pp. 51-65.

FEMGEN/FEMVIEW [1992], Femsys Ltd.

GIBBS, W. S. [1983], High temperature impression creep of weldments, Master of Science Thesis, T-2723, Colorado School of Mines, Golden, Colorado.

GIBBS, W. S., WANG, S. H. MATLOCK, D. K. and OSLON, D. L. [1985], High temperature impression creep testing of weldments, *Welding Journal*, Vol. **64** (6), pp. 153(s)-158(s).

GIBBS, W. S., AIKIN, R. M., MARTIN, P. L. and PATTERSON, R. A. [1990], Impression creep characterisation of Ti Al weldments, Proc. 4th Int. Conf. on Creep and Fracture of Engineering Materials and Structures, Swansea, pp. 227-286.

GOOCH, D. J. and KIMMINS, S. T. [1987], Type IV cracking in 1/2Cr1/2Mo1/4V-1/4Cr1Mo weldments, in Proc. 3rd Int. Conf. on Creep and Fracture of Engineering Materials and Structures, Edited by R. W. Evans and B. Wilshire, pp. 689-703, The Institute of Metals, London.

GREEN, A. E., NAGHDI, P. M. and OSBORN, R. B. [1968], Theory of an elastic-plastic Cosserat surface, *Int. J. Solids and Structures*, **4**, pp. 907.

HALL, F. R. and HAYHURST, D. R. [1991], Continuum damage mechanics modelling of high temperature deformation and failure in a pipe weldment, *Proc. R. Soc. London,* A **443**, pp. 383-403.

HAWKES, T. D. [1989], Mathematical modelling of the creep of weldments using the Cosserat theory of plates and shells, PhD Thesis, University of Southampton.

HAYHURST, D. R [1972], Creep rupture under multi-axial states of stress, *J. Mech. Phys. Solids.*, Vol. **20**, pp. 381-390.

HAYHURST, D. R [1983], The role of creep damage in structural mechanics, in Engineering Approach to High Temperature, edited by B. wilshire and D. R. Owen, Pineridge Press, Swansea.

HAYHURST, D. R., DIMME, P. R. and CHERNUKA, M. W. [1975], Estimates of the creep rupture lifetime of structure using the finite element method, *J. Mech. Phys. Solids* , Vol. **23,** pp. 335-355.

HAYHURST, D. R., DIMME, P. R. and MORRISON, C. J. [1984], Development of continuum damage in the creep rupture of notched bars, *Phil. Trans R. Soc. London*, A **311**, pp. 103-129.

HENRY, J. F. and ELLIS, F. V. [1990], The effect of SA weld metal inclusions and specimen size on rupture life, ASME Pressure Vessels & Piping Division (Publications), PVP-Vol. **193**, pp. 47-55.

HICKIN, W. D., PLASTOW, B. and DAVISON, J. K. [1972], A graphical presentation of the I. S. O. stress rupture data for tube and pipe steels, CEGB Report, SSD. MID. /M. 3/72.

HINTON, E. (editor) [1992], NAFEMS Introduction to Non-linear Finite Element Analysis, NAFEMS.

HORTON, C. A. P. and LAI, J. K. [1980], Effect of specimen size on reproducibility of creep rupture test results on type 316 stainless steel weldments, *Metal Science*, Vol. **14**, No. 10, pp. 502-505.

HYDE, T. H. [1988], Creep crack growth in 316 stainless steel at 600°C, *High Temperature Technology*, Vol. **6**, No. 2, pp. 51-61.

HYDE, T. H., YEHIA, K. A. and BECKER. A. A. [1993], Interpretation of impression creep data using a reference stress approach, *Int. J. Mech. Sci.*, Vol. **35**, No. 6, pp. 451-462.

HYDE, T. H., XIA, L. and BECKER, A. A. [1996], Prediction of creep failure in aeroengine materials under multi-axial stress states, *Int. J. Mech. Sci.*, Vol. **38**, No. 4, pp. 385-403.

HYDE, T. H., YEHIA, K. A. and SUN, W. [1996], Observations on the creep of two-material structures, *J. Strain Analysis* (to be published).

IVARSSON, B. and SANDSTROM, R. [1980], Creep deformation and rupture of butt-welded tubes of cold-worked AISI 316 steel, *Metals Technology*, Vol. **7**, No. pt 11, pp. 440-448.

JOHNSON, W. and MELLOR, P. B. [1962], Plasticity for Mechanical Engineers, D. Van Nostrand Company Ltd, London.

JOHNSSON, A. [1973], An alternative definition of reference stress for creep, IMechE. Conf. Pub. **13**, pp. 205.1-205.7.

KACHANOV, L. M. [1960], Theory of Creep (English translation edited by A. J. Kennedy), National Lending Library, Boston Spa.

KELLY, P. A., HILLS, D. A. and NOWELL, D. [1992], The design of joints between elasticity dissimilar components, *J. Eng. Mat. & Tech.*, Vol. **110**, pp. 41-47.

KRAUS, H. [1980], Creep Analysis, John Wiley, New York.

KUSSMAUL, K., MAILE, K. and ECKERT, W. [1993], Influence of stress state and specimen size on creep rupture of similar and dissimilar welds, ASTM Special Technical Publication, No. 1171, pp. 341-360.

LAU, C. W. and DELALE, F. [1988], Interfacial stress singularities at free edge of Hybrid matrix composite, *J. of Eng. Mat. & Tech.*, Vol. **110**, pp. 41-47.

LEE, Y. J. and MUDDLE, B. C. [1986], Assessment of creep damage in weldments of 1Cr-0.5Mo pressure vessel steels operating at 480-540°C — AWRA document No. P1-16-86, Australian Welding Research.

LISIN, M. A. [1989], Impression creep testing within a microstructural gradient, Colorado School of Mines, T-3687, Golden, Colorado.

MACKENZIE, A. C. [1968], On the use of a single uniaxial test to estimate deformation rates in some structures undergoing creep, *Int. J. Mech. Sci.*, Vol. **10**, pp. 441-453.

MASUBUCHI, K. [1981], Models of stresses and deformation due to welding — a review, *J. Metals*, pp. 19-23.

MONKMAN, F. C. and GRANT, N. J. [1956], An empirical relationship between rupture life and minimum creep rate, *Proc. ASTM*, **56**, pp. 593-596.

MURAMATSU, Y., YAMAZAKI, M., HONGO, H. and MONMA, Y. [1992], Size and shape effects of welded joint specimen on creep behaviour, Proc. 7th Conf. on Pressure Vessel Technology I, VdTuV, Dusseldorf. Verband der Technischen Uberwachungs-Vereine e.V.(VdTuV), Essen, Vol. **1**, pp. 737-753.

NEWMAN, M. G. [1993], Mathematical modelling of creep in weldments using the Cosserat theory of plates and shells, PhD Thesis, University of Southampton.

NEWMAN, M. G. and CRAINE, R. E. [1991], Creep failure of weldments in thin plates, in Mechanics of Creep Brittle Material-2, ED. A. C. F. Cocks & A. R. S. Ponter, Elsevier Applied Science, London, pp. 296-307.

NICOL, D. A. C. [1985], Creep behaviour of butt-weld joints, *Int. J. Engng. Sci.*, Vol. **23**, No. 5, pp. 541-553.

NICOL, D. A. C. and WILLIAMS, J. A. [1985], The creep behaviour of cross-weld specimens under uniaxial loading, *Res. Mechanics*, Vol. **14**, pp. 197-223.

PAFEC [1974], PAFEC-70+ with Extensions, University of Nottingham.

PAFEC [1984], Users Manual, PAFEC Ltd.

PARKER, J. D. [1988], The high temperature creep behaviour of 2-1/4Cr1Mo manual metal arc weldments in a 1/2Cr1/2Mo1/4V pressure vessel, in Understanding Variability in Creep and Rupture Behaviour, ASME Pressure Vessel and Piping Conf., Pittsburgh, Pennsylvania, pp. 63-73.

PARKER, J. D. and Parsons, A. W. J. [1995], High temperature deformation and fracture processes in 2-1/4Cr1Mo-1/2Cr1/2Mo1/4V weldments, *Int. J. Pres. Ves. & Piping* **63**, pp. 45-54.

PARKER, J. D. [1995], Creep behaviour of low alloy steel weldments, *Int. J. Pres. Ves. & Piping* **63**, pp. 55-62.

PARKER, J. D. and STRATFORD, G. C. [1996], Strain localisation in creep testing of samples with heterogeneous microstructures, *Int. J. Pres. Ves. & Piping* **65**, in press.

PENNY, R. K. and MARRIOTT, D. L. [1971], Design for Creep, McGraw-Hill, New York.

PENNY, R. K. and MARRIOTT, D. L. [1992], Design for Creep, second Edn, Chapman & Hall.

PENNY, R. K. [1995], The use of damage concepts in component life assessment, Proc. CAPE '95 Colloquium, Ageing of Materials and Component Life Assessment, South Africa.

POWELL, G. W. [1986], Metals Handbook, Vol. **11**, 9th Edn, Ohio: Amer. Soc. Metals.

POWELL, G. and SIMONS, J. [1981], Improved iterative strategy for non-linear structures, *Int. J. Num. Meth. Eng.*, **17**, pp. 1455.

PRAGER, M. and LEYDA, W. E. [1988], Effects of heat treatment variables on the creep and rupture behaviour of 2-1/4Cr1Mo steel, in Understanding Variability in Creep and Rupture Behaviour, ASME Pressure Vessel and Piping Conf., Pittsburgh, Pennsylvania, pp. 23-55.

PRICE, A. T. and WILLIAMS, J. A. [1982], The influence of welding on the creep properties of steels, in Recent Advances in Creep and Fracture of Engineering Materials and Structures, Edited by B. Wilshire and D. R. J. Owen, Pineridge Press Ltd, Swansea, pp. 265.

RABOTNOV, Y. N. [1969], Creep problems in structural members, North Holland, Amsterdam.

ROODE, F., ETIENNE, C. F. and ROSSUM, O. van [1980], Stress and strain analyses for creep and plasticity of welded joints in AISI 316, IMechE International Conference on Engineering Aspects of Creep (Volume 2), Sheffield.

RUDGE, M. R. H. [1993], Interfacial stress singularities in a bi-material wedge, *Int. J. Frac.*, Vol. **62**, pp. 21-26.

RYDER, R. H. [1990], Design criteria for dissimilar welds, in Life of Welds at High Temperature, IMechE Seminar Papers, London.

SAMUELSON, L. A., SEGLE, P. and TU, S.-T. [1992], Design of weld joints subjected to high temperature creep, ASME PVP-Vol. **230**, Stress Classification, Robust Methods and Elevated Temperature Design.

SCHULLER, H. J., HAGN, L. and WOITSCHECK, A. [1974], Cracking in the weld region of shaped components in hot steam pipelines — materials investigations, *Der Maschinenschaden* **47**, pp. 1-13.

SENIOR, B. A. [1990], Effect of phase transformation on the creep rupture properties of two type 316 weld metals, *J. Mat. Sci.*, Vol. **25**, pp. 45-53.

SIM, R. G. [1968], Creep of Structures, PhD Thesis, University of Cambridge.

SIM, R. G. [1970], Reference stress concepts in the analysis of the structures during creep, *Int. J. Mech. Sci.*, Vol. **12**, pp. 561-573.

SIM, R. G. [1971], Evaluation of reference stress for structures subjected to creep, *Int. J. Mech. Sci.*, Vol. **13**, pp. 47-50.

SIM, R. G. and PENNY, R. K. [1971], Plane strain creep behaviour of thick-walled cylinders, *Int. J. Mech. Sci.*, Vol. **13**,. pp. 987-1009.

STORESUND, J., TU, S.-T. and WU, R. [1992], A study of the stress distribution in uniaxial cross weld creep test specimens, Int. Symp. Life & Performance of High Temperature Materials & Structures, Tallinn, Estonia.

STORESUND, J. and TU, S.-T. [1995], Geometrical effect on creep in cross weld specimens, *Int. J. Pres. Ves. & Piping* **62**, pp. 179-193.

TASNADI, P., JUHASZ, A, CHINH, N. Q. and KOVACS, I. [1988], Theoretical description of the deformation taking place in an impression test, *Res. Mechanics*, Vol. **24**, pp. 335-347.

TOFT, L. H. and YELDMAN, D. E. [1972], Weld performance in high pressure steam generating plant in the Midlands region CEGB, in Proc. Int. Conf. Welding Research Related to Power Plants, Southampton.

TU, S.-T., SEGLE, P. M. and SAMUELSON, L. A. [1993], Some aspects of the design of welded structures subjected to high temperature creep, ASME PVP-Vol. **262**, High-Temperature Service and Time-Dependent Failure, pp. 27-34.

TU, S.-T. and SANDSTROM, R. [1994], The evaluation of weldment creep strength reduction factors by experimental and numerical simulations, *Int. J. Pres. Ves. & Piping* **57**, pp. 335-344.

TU, S.-T., WU, R. and SANDSTROM, R. [1994], Design against creep failure for weldments in 1/2Cr1/2Mo1/4V pipe, *Int. J. Pres. Ves. & Piping* **58**, pp. 345-354.

WALTERS, D. J. and COCKCROFT, R. D. M. [1972], A stress analysis and failure criteria for high temperature butt welds, Colloquium on Creep Behaviour of Welds in Boilers, Pressure Vessels and Piping, IIW, Toronto.

WALKER, N. S., KIMMING, S. T. and SMITH, D. J. [1996], Type IV creep cavitation in ferritic steel welds, 6th Int. Conf. on Creep and Fatigue, IMechE Conference Transaction 1996-2, pp. 341-350.

WESTWOOD, H. J., CLARK, M. A. and SIDEY, D. [1990], Creep failure and damage in main steam line weldments, Proc. 4th Int. Conf. on Creep and Fracture of Engineering Materials and Structures, Edited by B. Wilshire and R. W. Evans, pp. 621-634, The Institute of Metals, London.

WILLIAMS, J. A. [1982-1], A simple approach to the effect of specimen size on the creep rupture of cross weld samples, *J. Eng. Mat. & Tech.*, Vol. **104**, pp. 36-40, Transactions of the ASME.

WILLIAMS, J. A. [1982-2], Methodology for high temperature failure analysis, Proc. of the European Symposium, Petten (N.H), Netherlands, "Behaviour of Joints in High Temperature Materials", Edited by T. G. Gooch, R. Hurst and M. Merz.

WU, R., STORESUND, J., SANDSTROM, R. and von WALDEN, E. [1992], Creep properties of 1Cr1/2Mo steel welded joints with controlled microstructures, *Weld. World*, **30**, pp. 239-336.

YEHIA, K. A. [1994], Reference stresses for impression creep and two material components, PhD Thesis, University of Nottingham.

YU, E. C. and LI, J. C. M. [1977], Impression creep of LiF single crystal, *Phil. Mag.*, **36**, pp. 811-825.

YU, H. Y., IMAM, M. A. and RATH, B. B. [1985], Study of the deformation behaviour of homogeneous materials by impression tests, *J. Mater. Sci.*, Vol. **20**, pp. 636-642.

YU, H. Y., IMAM, M. A. and RATH, B. B. [1986], An impression test method for characterisation of superplastic material, *Material Science and Engineering*, Vol. **79**, pp. 125-132.

APPENDIX I RELATIONSHIPS BETWEEN STRESSES AND STRAIN RATES ON THE CENTRE-LINE OF AN AXISYMMETRIC COMPONENT

The following solutions were derived for the two-material model shown in Section 3.2 of Chapter III.

(i) Anywhere on the Centre-Line

$$\sigma_x = f(2x/w, n, A/B, w/d) \tag{A1.1}$$

$$\sigma_r = \sigma_\theta \tag{A1.2}$$

$$\sigma_{eq} = \sigma_x - \sigma_r \tag{A1.3}$$

$$\dot{\varepsilon}_x = \dot{\varepsilon}_{eq} \tag{A1.4}$$

$$\dot{\varepsilon}_r = \dot{\varepsilon}_\theta = -\dot{\varepsilon}_x / 2 = -\dot{\varepsilon}_{eq} / 2 \tag{A1.5}$$

(ii) On the Centre-Line, at the Interface between Two Materials (A and B)

$$\sigma_x^A = f_A (n, A/B, w/d) \tag{A1.6}$$

$$\sigma_x^B = f_B (n, A/B, w/d) \tag{A1.7}$$

$$\sigma_x^A = \sigma_x^B \tag{A1.8}$$

$$\sigma_r^A = \sigma_\theta^A = \left(\frac{B}{A}\right)^{\frac{1}{n}} \sigma_\theta^B + \left(1 - \left(\frac{B}{A}\right)^{\frac{1}{n}}\right) \sigma_x^A = \left(\frac{B}{A}\right)^{\frac{1}{n}} \sigma_r^B + \left(1 - \left(\frac{B}{A}\right)^{\frac{1}{n}}\right) \sigma_x^B$$

(A1.9)

$$\sigma_r^B = \sigma_\theta^B = \left(\frac{A}{B}\right)^{\frac{1}{n}} \sigma_\theta^A + \left(1 - \left(\frac{A}{B}\right)^{\frac{1}{n}}\right) \sigma_x^A = \left(\frac{A}{B}\right)^{\frac{1}{n}} \sigma_r^A + \left(1 - \left(\frac{B}{A}\right)^{\frac{1}{n}}\right) \sigma_x^A$$

(A1.10)

$$\sigma_{eq}^A = \sigma_x^A - \sigma_r^A = \left(\frac{B}{A}\right)^{\frac{1}{n}} \sigma_{eq}^B \qquad \text{(A1.11)}$$

$$\sigma_{eq}^B = \sigma_x^B - \sigma_r^B = \left(\frac{A}{B}\right)^{\frac{1}{n}} \sigma_{eq}^A \qquad \text{(A1.12)}$$

$$\dot{\varepsilon}_{eq}^A = A\,(\sigma_{eq}^A)^n \qquad \text{(A1.13)}$$

$$\dot{\varepsilon}_{eq}^B = B\,(\sigma_{eq}^B)^n \qquad \text{(A1.14)}$$

$$\dot{\varepsilon}_x^A = \dot{\varepsilon}_{eq}^A = \dot{\varepsilon}_x^B = \dot{\varepsilon}_{eq}^B \qquad \text{(A1.15)}$$

$$\dot{\varepsilon}_r^A = \dot{\varepsilon}_\theta^A = \dot{\varepsilon}_r^B = \dot{\varepsilon}_\theta^B = -\dot{\varepsilon}_x^A/2 = -\dot{\varepsilon}_{eq}^A/2 = -\dot{\varepsilon}_x^B/2 = -\dot{\varepsilon}_{eq}^B/2$$

(A1.16)

APPENDIX II DETERMINATION OF K_{ij} AND N_{ij} IN STRESS SINGULARITY ANALYSIS

Using the co-ordinates defined in Section 3.4 of Chapter III, the stress components investigated can be given as the following:

$$\sigma_{rr} = \cos^2\theta\ \sigma_{xx} + \sin^2\theta\ \sigma_{yy} + \sin 2\theta\ \tau_{xy}$$

$$\sigma_{\theta\theta} = \sin^2\theta\ \sigma_{xx} + \cos^2\theta\ \sigma_{yy} - \sin 2\theta\ \tau_{xy} \qquad \text{(A2.1)}$$

$$\tau_{r\theta} = -\sin 2\theta/2(\sigma_{xx} - \sigma_{yy}) + \cos 2\theta\ \tau_{xy}$$

The general forms of the stresses near the singularity points for a given geometry and creep properties can be expressed by

$$\sigma_{ij}(r, \theta) = K_{ij}(\theta)\, r^{Nij(\theta)}$$

$$\sigma_{eq}(r, \theta) = K_{eq}(\theta)\, r^{Neq(\theta)} \qquad \text{(A2.2)}$$

where $r > 0$ and N ($= N_{ij}$ or N_{eq}) < 0. Since $r^N > 0$, Equation A2.2 can be rewritten:

$$|\sigma| = |K|\, r^N \qquad \text{(A2.3)}$$

From A2.3 we know that

if $\sigma > 0$, then $K > 0$,

if $\sigma < 0$, then $K < 0$, and

if $\sigma = 0$, K and N indeterminate.

Therefore, if $\sigma \neq 0$, from equation A2.3 we have:

$$\log |\sigma| = \log |K| + N \log (r)$$

Then K and N can be obtained by fitting the σ- r curves. Note that

if $\sigma > 0$, $K = \log^{-1} [\log |K|]$;

if $\sigma < 0$, $K = -\log^{-1} [\log |K|]$.

APPENDIX III CFS (CONVERSION FACTOR SEARCHING) PROGRAM

This Appendix describes the method used to find the impression creep test conversion factors η and β (reference parameters) in Chapter IV.

A3.1 Method

Using MecKenzie's method the normalised impression deformation rate can be defined by

$$D \approx \dot{\Delta}_{ss}(n) / [d \times \dot{\varepsilon}^{c}(\sigma_R, t)] = \dot{\Delta}_{ss} / [d \times A \times (\alpha\sigma_{nom})^{n}] \qquad \text{(A3.1(a))}$$

or

$$\log(D) \approx \log[\dot{\Delta}_{ss} / (d \times A)] - n \log(\alpha\sigma_{nom}) \qquad \text{(A3.1(b))}$$

which shows that a straight line is obtained when plotting log (D) against n for different α values. The intercepts of these lines are independent of α and are equal to $\log[\dot{\Delta}_{ss} / (d \times A)]$ at n = 0, from which the value of normalised reference multiplier, D_R (= β), can be obtained. The α value which makes log (D) independent of n gives the value of the reference stress parameter, α_R (= η).

From equation A3.1 we know that due to the power relationship, when n is large the effect of α on log (D) is very sensitive. This indicates that the determination of an accurate α_R value is necessary.

A trial-and-error approach could be adopted to obtain the α_R and D_R values (Hyde et al [1993]). However, this is found to be time consuming and may lead to the determination of inaccurate values. In an attempt to make the results more accurate, a simple optimisation technique was used.

A3.2 CFS Algorithm

A Fortran program CFS was developed to obtain the conversion factors (reference parameters), using the data obtained from impression creep finite element analysis. Data pairs were established with respect to the different α values which are defined in a given range of $\alpha^L < \alpha < \alpha^U$. For each α value the data pairs are fitted by a straight line, using a simple linear regression technique based on the least square method. The algorithm is described below.

If the calculated data pairs x_i (= n), y_i $(= \log[\dot{\Delta}_{ss}(n)/(d \times A \times (\alpha\sigma_{nom})^n)])$ for a given α are available, i.e.

$$x_1, x_2, \ldots\ldots, x_m,$$

$$y_1, y_2, \ldots\ldots, y_m,$$

then define a linear equation

$$\hat{y} = a + kx$$

and make

$$\sum_{i=1}^{m}[y_i - \hat{y}_i]^2 = \sum_{i=1}^{m}[y_i - (a + kx_i)]^2 \rightarrow \min$$

Then the regression factors a and k can be obtained by

$$k = L_{xy} / L_{xx} \text{ and}$$

$$a = \bar{y} - k\bar{x},$$

in which

$$\bar{x} = 1/m\sum_{i=1}^{m}x_i, \bar{y} = 1/m\sum_{i=1}^{m}y_i,$$

$$L_{xx} = \sum_{i=1}^{m}(x_i - \bar{x})^2 \text{ and}$$

$$L_{yy} = \sum_{i=1}^{m}(x_i - \bar{x})(y_i - \bar{y})$$

For each straight line fitted, when the value of the gradient k is gained, the optimum value of α (= α_R) and D (= D_R) can be found by a simple trial method which satisfies

$$k(\alpha_R) = \min|k(\alpha)| \rightarrow 0, \alpha_R \in [\alpha^L, \alpha^U]$$

The corresponding D_R value can be determined by

$$D_R = \log^{-1}[a]$$

A flow chart for the CFS program is shown in Fig. A3.1.

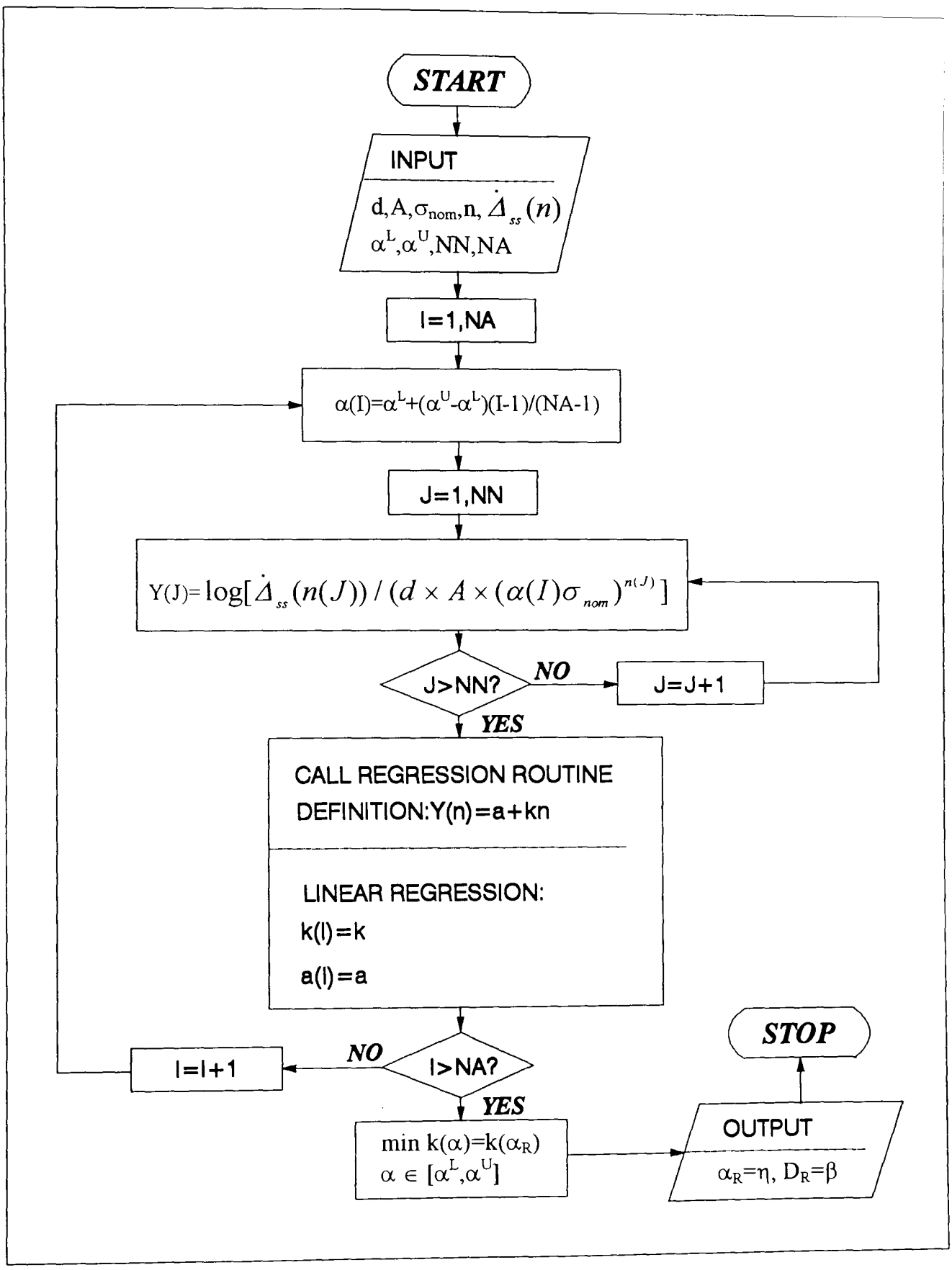

Fig. A3.1 Flowchart of CFS (conversion factor searching) program.

APPENDIX IV PAFEC-70 FE-DAMAGE CODE

A4.1 INTRODUCTION

The FE-DAMAGE Code is used to perform continuum damage analysis of creeping components. The creep damage routines were designed, to be used with the PAFEC-70 package. Several sub-programs were specially written to provide creep damage input into PAFEC-70 and call the damage routines. Damage analysis is executed by running these independent sub-programs in order. In order to perform the damage analysis for welded structures, a multi-material model has been incorporated in the damage code and a self-contained manual has been written (Becker et al [1994]).

It should be noted that PAFEC-70 is an older version of the standard PAFEC package, and is not a commercial FE package. The current commercial FE packages do not include the capability of damage analysis.

This Appendix contains only a summary of the creep continuum damage code, mainly involving the structure of the code and the execution procedure of the damage analysis. Further details concerning information such as the damage work programs, mesh generation and data input preparation can be found in the program users manual (Becker et al [1994]).

A4.2 CREEP CONTINUUM DAMAGE (CCD) FE MODEL

The model used in the FE-DAMAGE program to describe the rate of damage accumulation is based on the Hayhurst damage law (Hayhurst [1983]), as follows:

$$\frac{d\omega}{dt} = \frac{M[\alpha\hat{\sigma} + (1-\alpha)\sigma_{eq}]^{\chi}}{(1+\phi)(1-\omega)^{\phi}} t^{m} \qquad (A4.1)$$

Creep strains and stresses, at the end of a specified period, are computed by utilising a time stepping procedure which involves successive solutions to reach the final time. The user first specifies the initial time step. The time increment is subsequently doubled provided that the change in stress due to redistribution, and any increment of damage, is limited to an acceptable tolerance. If either criterion fails, then the time step is reduced and the solution repeated. For creep problems, the user has the option of using either a time hardening or a strain hardening formulation. However, if continuum damage is incorporated then damage hardening is used.

For each Gauss point, an effective time, t_{eff}, can be calculated for the current value of damage, ω, and stress level, by integrating equation (A4.1) with initial $\omega = 0$ and initial $t = 0$ to get

$$t_{eff} = \left[\frac{[1-(1-\omega)^{\phi+1}](m+1)}{M[\alpha\hat{\sigma} + (1-\alpha)\sigma_{eq}]^{\chi}}\right]^{\frac{1}{m+1}} \qquad (A4.2)$$

The effective time, t_{eff}, is then used to calculate the damage rate $d\omega/dt$ and strain rate, $d\varepsilon/dt$, appropriate to the current stress level and state of damage at the Gauss point, with $t = t_{eff}$.

By assuming the damage rate to be constant over the time step, Δt, the damage increment, $\Delta\omega$, is given by

$$\Delta\omega = \frac{d\omega}{dt}\Delta t \qquad \text{(A4.3)}$$

Similarly, provided that the damage increment is less than some maximum value (typically $\Delta\omega < 0.5\%$), $\Delta\varepsilon$ is obtained as follows:

$$\Delta\varepsilon = \frac{d\varepsilon}{dt}\Delta t \qquad \text{(A4.4)}$$

For the special case of the $t_{eff} = 0$, which occurs on the very first time increment (i.e. $\omega = 0$), the damage increment is obtained from:

$$\Delta\omega = \frac{M[\alpha\hat{\sigma} + (1-\alpha)\sigma_{eq}]^{\chi}}{(1+\phi)(m+1)}(\Delta t)^{m+1} \qquad \text{(A4.5)}$$

and the creep strain increment is obtained from:

$$\Delta\varepsilon = \frac{A}{m+1}(\sigma_{eq})^{n}(\Delta t)^{m+1} \qquad \text{(A4.6)}$$

Components of creep strain increments, $\Delta\varepsilon_{ij}$, are obtained from equivalent creep strain increment, $\Delta\varepsilon$, through the associated Prandtl-Reuss flow rules (Hinton [1992]). Elastic displacements for the current time are then calculated and the stress components, σ_{ij}, and the equivalent stress, σ_{eq}, obtained. Provided that the change in effective stress at each Gauss point satisfies the stress change criterion, the solution is accepted and the current value of damage is updated to include the damage increment. Using the updated stress levels and value of accumulated damage, the method is repeated to obtain the solution at the end of the remaining time increment.

A4.3 THE PAFEC-70 PROGRAM

PAFEC-70 is a general purpose Finite Element package developed by the CDI group of the Department of Mechanical Engineering at the University of Nottingham. The data input to this code is different to the data input required for the commercial code PAFEC-FE supplied by PAFEC Limited.

To define a problem, a data file containing all relevant information must be constructed and saved. This involves using the editor on the VME operating system to create and save a data input file.

The order of the PAFEC-70 input data is shown below.

1. Title identifying the job
2. Control Parameters
3. CRDDC array information
4. Element information, possibly with data for the semi-automatic front solver
5. Pressure at nodal points information
6. Point load information
7. Displacement boundary conditions
8. Stress information

The PAFEC-70 package contains built-in mesh generation based on grouping elements together in "blocks" which are referred to as "PAFBLOCKS". The elements covered in the CCD code are isoparametric quadratic quadrilateral (8-noded) elements (Type 36210).

Detailed information on the preparation and description of the PAFEC-70 data input can be found in the PAFEC manuals (e.g. PAFEC [1974][1984] and Becker et al [1994]).

A4.4 THE FE-DAMAGE PROGRAM

Creep damage analyses are performed by running several main work programs in turn, as follows:

1. PB program : a program for the evaluation of PAFBLOCKS data.
2. MTP program : a program for mesh data input, manipulation and storage.
3. CCD program : a program for the calculation of creep damage solutions.

In most problems, PAFBLOCKS are used in mesh generation. If PAFBLOCKS are not used, the running of the PB program is not required. The corresponding PAFEC-70 input data is then manipulated by the MTP program directly. All the nodal information must be included in a PAFBLOCKS data file for this case.

A flowchart of the FE-damage program is shown in Figure A4.1.

A4.5 EXECUTION PROCEDURE

A complete FE analysis of a creep damage problem involves the sequential running of several separate main work programs as mentioned above. For any specific problem, the main work programs need to be informed by a data input file and may be modified according to the type of analysis required. To do this, the user should have a reasonable knowledge of the VME FORTRAN 2900 command language and the preparation of FORTRAN programs.

Usually a main work program needs to be modified to cater for a specific problem. The modifications mainly include the following:

1. Use job control commands to define output files.
2. Insert job dependent parameters in the FORTRAN text.
3. Insert the data file and/or the file generated by a previous run.
4. Delete any unused line.
5. Insert calls to the specific routines required.
6. Delete all INFO, OPTIONAL and OPT/INFO in the lines which have been modified.

A4.5.1 The PB Program

This program is required when the user specifies part or all of the mesh in the form of PAFBLOCKS. To run this program, the PAFEC-70 data file should be constructed (see Becker et al [1994]). The PB program performs the following tasks:

(i) Read in the PAFBLOCKS/element data, evaluate the PAFBLOCKS and subsequently store the element data in a file.

(ii) Read in the file containing the newly generated element data and produce mesh drawings.

It is considered essential to produce mesh drawings at this stage to ensure that the PAFBLOCKS have been correctly described and evaluated. The drawings are not necessary for the subsequent running of the program.

To run the PB program, the following steps should be followed:

1. Input the PAFEC-70 data file (see Becker et al [1994]) into the PB program using:

   < Library name.file name >

2. Use job control commands to specify the job required.

3. Specify the values of six array parameters in the FORTRAN program, as follows:

   IX width of the CPDDC array

IEG number of elements in the final structure (set IEG = 50 if default value is being used in the data input file)

INEMAX maximum number of nodes in any element (INEMAX = 8 for FE damage analysis)

IPG overestimate of the number of nodes in the final structure after PAFBLOCKS have been expanded to element form (set IPG = 200 if default value is being used)

IP number of chassis nodes

ICA the length of the array BLIST. BLIST is the PAFBLOCKS equivalent of DLIST and its default value if ICA = 0 is 500.

These values may need to be modified after the first run.

4. Submit the program to PAFEC job queue.

A file named *<JOBNAME> + NEWDATA* will be generated after a successful run of the PB program. This file automatically becomes an input file for the MTP program which generates the DLIST and CPDDC arrays data file required for all problems.

A4.5.2 The MTP Program

Once the mesh input data is in element form, the MTP program can be run. It performs the following tasks:

(i) Read in the data from PB output file:

<JOBNAME> + NEWDATA

(ii) Generate the DLIST and CPDDC arrays.

(iii) Modify these arrays for the frontal solution calculations.

(iv) Store the modified DLIST and CPDDC arrays on a file called:

M + <*JOBNAME*> + *T*

(v) Plot any mesh drawings requested in the data.

PAFEC-70 data input file should be prepared before running this program and fed into the program if there is no PAFBLOCKS job required. The MTP program is the first program to be run in this case. If PAFBLOCKS are used, the PB program will generate the element data, i.e. the input data to this problem are already stored in a file. This file can be automatically used by the MTP program as input information.

To run the MTP program, the following steps should be followed:

1. Create a data file if necessary.
2. Specify the values of the array parameters IP and IX, where IP is the number of nodes and IX is the width of the CPDDC array.
3. Modify the job dependent commands.
4. Submit the MTP program to the PAFEC job queue.

A4.5.3 The CCD Program

The CCD program is the solution program that performs creep continuum damage analysis. The program can also be used for creep analysis only. The CCD program requires the following files:

(a) Creep damage data file (see Becker et al [1994]).

(b) Special damage subroutines DAMPLEEP, DAMSUB and JCALCSUB must be available that will be compiled when the CCD program is run. If only the creep solution is required, these subroutines are not necessary, and the command for the compilation of these subroutines in the CCD program should be deleted. The damage parameters in the creep damage data file must be omitted.

The CCD Program performs the following tasks:

(i) Compile the damage subroutines.

(ii) Read in the creep damage data file.

(iii) Calculate node displacements, creep stresses and strains, and creep damage accumulations. The computed results are stored in a file.

To run the CCD program, the following steps should be followed:

1. Feed the creep damage data file into the main program.

2. Specify the values of parameters LD, LS, IP, IX, IDT and ILD which can be found in the output of MTP program, where :

LD = size of DLIST

LS = size of stiffness matrix

I = number of nodes

IX = width of CPDDC array

IDT = number of degrees of freedom

ILO = number of loading cases

3. Feed the file *M <JOBNAME> T* from the previous run of the MTP program into the CCD program.

4. For a restart problem, read in the restart file.

5. Submit the program to PAFEC job queue.

A4.5.4 The ELAS Program

ELAS executes the elastic analysis of PAFEC-70 as an independent main work program. In a creep analysis, the running of ELAS is not necessary because elastic calculation is included in the analysis. However, for the purpose of reducing the difficulties a user may encounter in creep damage calculations, it is recommended that ELAS is used to spot any errors (in loading conditions and prescribed boundary conditions, etc.) in the model, after the mesh generation stage or before the final damage analysis. It is also advisable that the user should run the creep analysis before the final stage of damage analysis.

To run the ELAS program, the following steps should be followed:

1. Specify the values of parameters LS, IP, IX, IDT and ILO which can be found in the output of program MTP (journal file).

2. Read in the file named:

   M + *<JOBNAME>* + *T*

   from the previous run of the MTP program into the current program.

3. Submit the program to PAFEC job queue.

A4.5.5 Journal File and Error Information

After each run of a work program, a journal file named *<JOBNAME>*+*Journal* is automatically created. If the run is successful, this file usually lists all the job commands in order. If a run is unsuccessful, the journal file will list error messages specifying the type and location of the errors. However, in many cases the error location may be difficult to spot. Some error messages may be generated in another file called <filename + OP> after running the PB or the MTP programs, if the file has been specified by the program.

Unsuccessful runs are usually caused by mistakes in the data preparation or the use of the job commands. Some of the commonly encountered errors may be caused by the following:

- Mistakes in data file format
- Mistakes in files read in
- Mistakes in job command arrangement
- Wrong values used for array parameters

- Storage space full

- Run time exceeded

- FORTRAN errors

Useful information can be obtained from the VME manuals.

A4.6 MESH GENERATION AND DATA INPUT

A4.6.1 Mesh Generation with PAFBLOCKS

The purpose of adopting PAFBLOCKS in PAFEC-70 data preparation is to simplify the specification of the nodal co-ordinates and the element topologies.

Constructing the mesh for a particular geometry using PAFBLOCKS involves the following stages (see Becker et al [1994] for details):

1. Divide the domain into convenient PAFBLOCKS.
2. Define the coordinates of the nodes that are needed to define each PAFBLOCK.
3. Decide which type of element to use in each PAFBLOCK.
4. Define the total number of elements and their relative lengths (using the MESH module).

In the PAFBLOCKS scheme each block of elements can be thought of as a large finite element. The user has to describe these blocks in PAFEC-70 input data to the scheme. As in the normal scheme for PAFEC data, this consists of

(a) control integers

(b) coordinate data of chassis nodes

(c) topological or connection information

The control integers give general information about the blocks of the elements.

The co-ordinate data required by the PAFBLOCKS scheme consist of an array known as the CHASSIS CPDDC in which the x and y coordinates are stored respectively in columns 1 and 2. The array is closely analogous to the standard CPDDC array. Only the co-ordinates of vertices of the PAFBLOCKS need to be given. If a PAFBLOCK has a curved side, the co-ordinates of a mid-side node on that curve have to be specified.

The topological information describes in turn the way in which each PAFBLOCK is fitted into the CHASSIS structure and gives details about the numbers of the elements along each of the sides of the blocks and the orientation of elements within the blocks.

The PAFBLOCKS scheme reads in this data and prepares the data automatically for a normal PAFEC job.

A4.6.2 PAFEC-70 Data Input

A complete PAFEC-70 input file requires the following data (see Becker et al [1994] for details):

1. Title identifying the job
2. Control parameters
3. CRDDC array information
4. Element information, possibly with data for the semi-automatic front solver
5. Pressure at nodal points information
6. Point load information
7. Displacement boundary conditions
8. Stress information

A4.6.3 FE-Damage Data Input

The input data file is composed of data cards. Each data card follows a specified format (see Becker et al [1994] for details). A FE-damage input file mainly contains the following information:

1. Loading and time information
2. Plastic and creep properties
3. Damage properties
4. Control integers

In the damage analysis, the structure is assumed to be initially unloaded. Hence, one or more load cards must appear before the first creep load step. However, this does not apply to a restart analysis.

A4.7 DAMAGE CONTOUR DRAWING

A DAMAGE-Post program named DCD was developed to perform the damage contour drawing. The program is written in Fortran and calls SIMPLEPLOT routines which are set in CCC VME Libraries. Two specialised routines should be modified by a user in order to satisfy his specific problems. Damage results including the co-ordinates of Gauss points and damage values should have been available in file which is an output of a damage analysis by defining a special output file in CCD program. This data file can be read automatically by running the FORTRAN job.

The flowchart of the DCD program is shown in Figure A4.2.

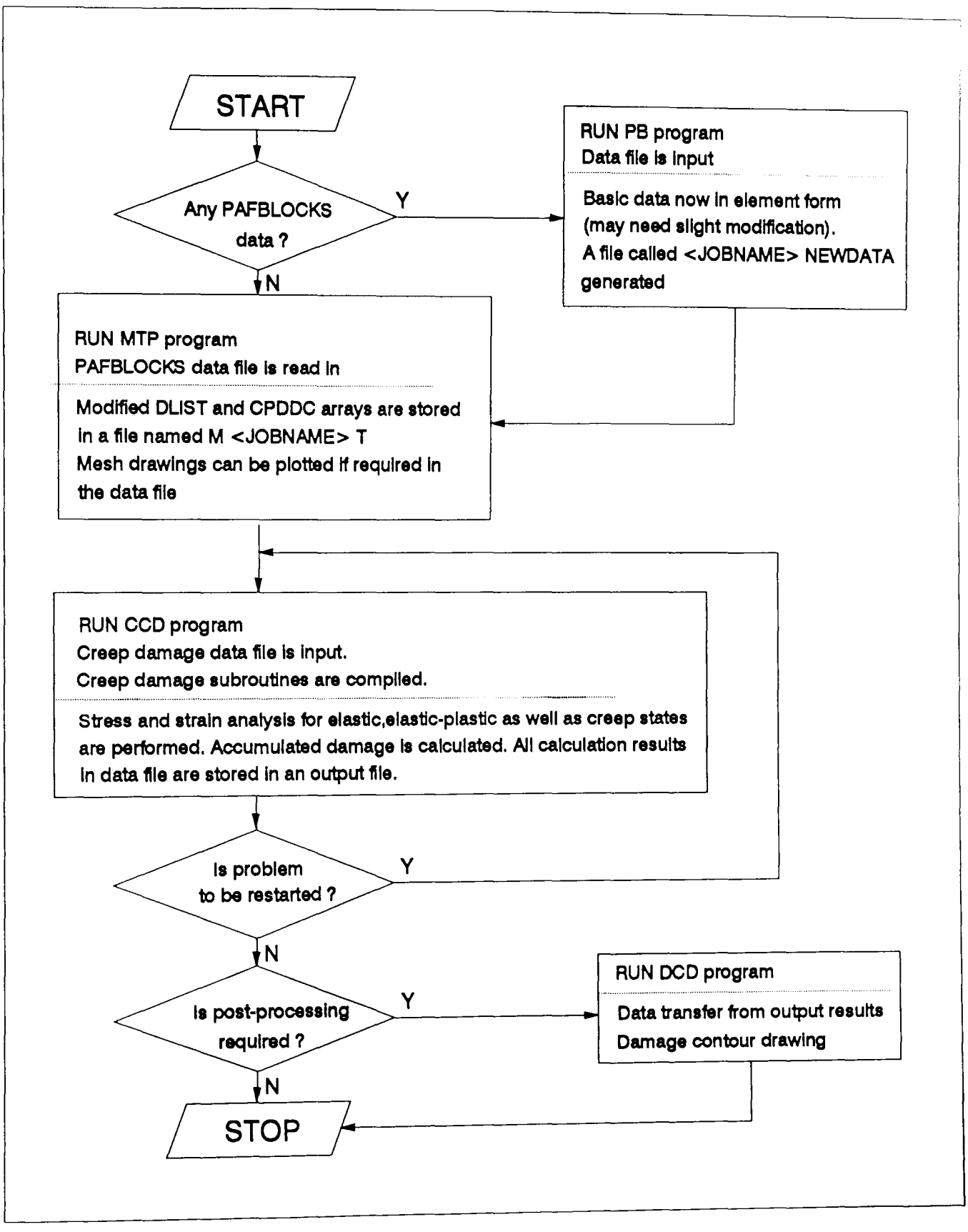

Fig. A4.1 Flowchart of CCD-FE Code.

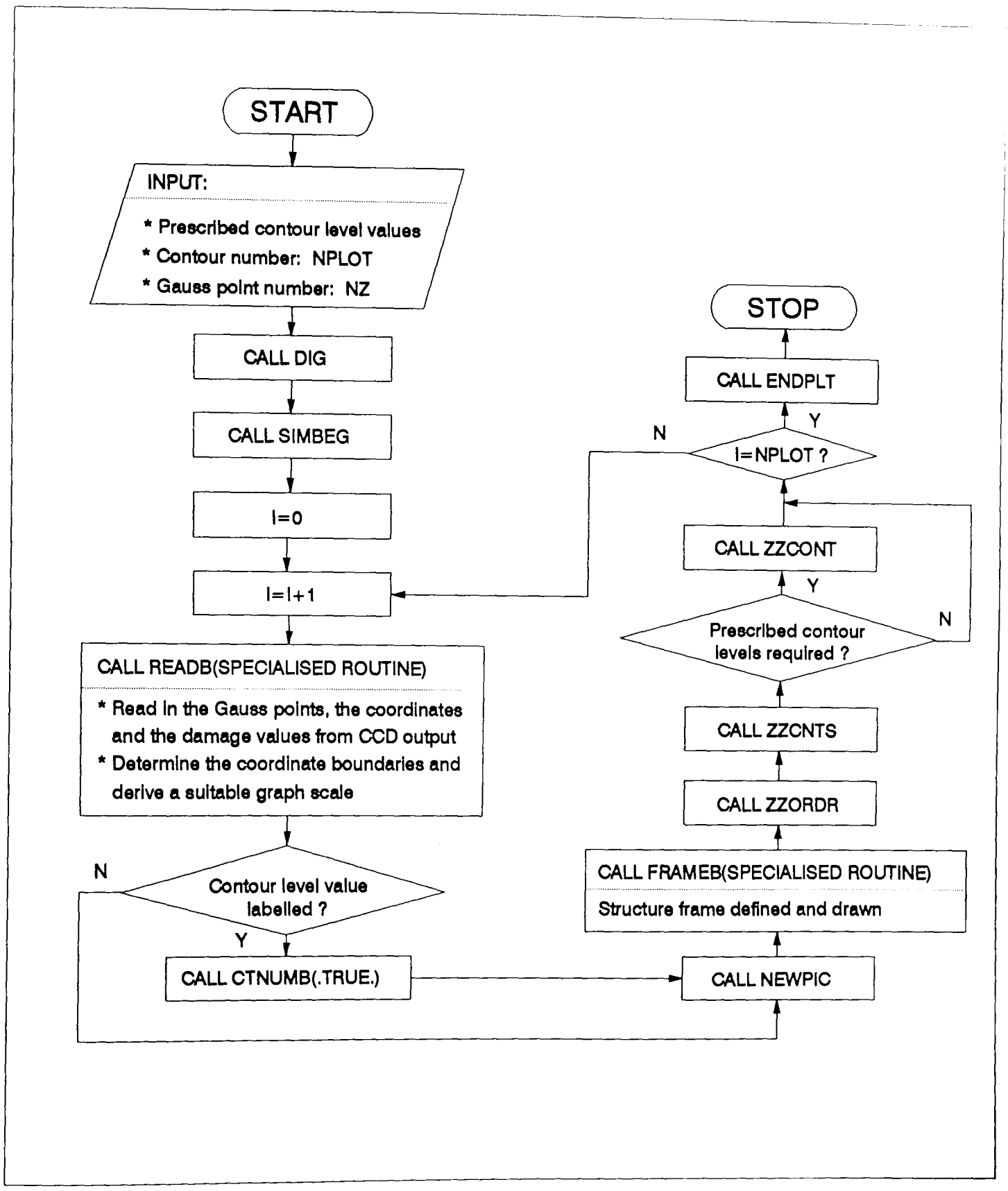

Fig. A4.2 Flowchart of damage contour drawing (DCD) program.

APPENDIX V WELDING PROCEDURE AND CONDITIONS OF CrMoV JOINTS

The welding procedure and conditions of the aged CrMoV welded joints investigated by this research are shown in Table A5.1. The dimensions of the joints and the thermocouple arrangement are presented in Figs. A5.1 and A5.2, respectively.

Table A5.1 Welding process of CrMoV joints

MATERIAL: 1/2 %Cr, 1/2 %Mo, 1/4 %V Steel 660 to 1/2 %Cr, 1/2 %Mo, 1/4 %V Steel 660				
WELD TYPE: tube & pipe butt weld			POSITION: all	
SIZE RANGE: > 88.9mm OD > 15 mm thick			JOINT PREPARATION: see Fig. A5.1 for dimensions	
PREHEAT (see Fig. A5.2 for thermocouple arrangement)	ROOT 100° C for 2 hrs before welding			FILL 250° C for 2 hrs before welding
	METHOD: gas heating or electric resistance coils			INDICATION: tempilstick thermocouples
WELDING PROCEDURE		PROCESS	CONSUMABLE	REMARKS
	ROOT	TIG Electrode -ive	BS2901, Pt 1 Type A33 1.6-2.4mm dia	Electrode: 2% thoriated tungsten, 2.4mm diameter Shielding: Argon, 8-10 l/min
	FILL	MMA Electrode +ive	BS2493 type 2Cr Mo B 2.5 -4.0mm dia	Welding current to be in accordance with manufacture's recommendation
POST WELD HEAT REATMENT (see Fig. A5.2 for thermocouple arrangement)	HEATING RATE: 100° C/hr maximum			
	SOAKING TIME: 2.5 min/mm thickness (minimum 180 min) at 690-720° C			
	COOLING RATE: 50° C/hr down to 350° C, then cool in still air			
	NOTES: For pipes of thickness t > 62.5mm, heating rate = 250×25/t° C/hr. Weld profile to be hot ground before stress relief and polished after stress relief Electric resistance coils or furnace methods only to be used			
WELD FINISH AND QUALITY ASSURANCE	Weld profile, root penetration, pipe alignment and radiographic or ultrasonic and magnetic particle assessment to BS 2633			
CONSUMABLE PREPARATION	Low hydrogen electrodes to be baked for 2 hrs at 250o C and stored at 120o C prior to use			

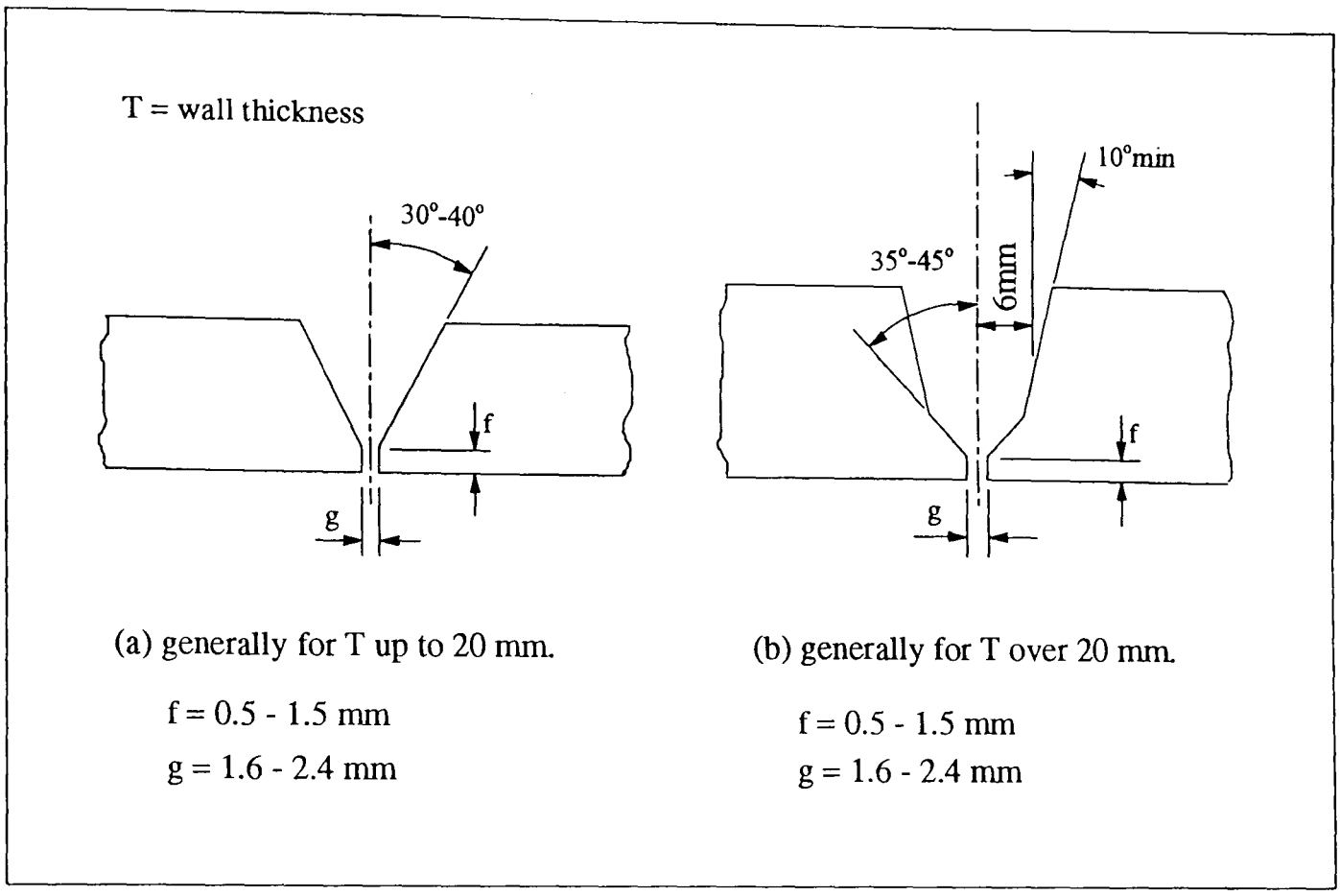

Fig. A5.1 End preparation.

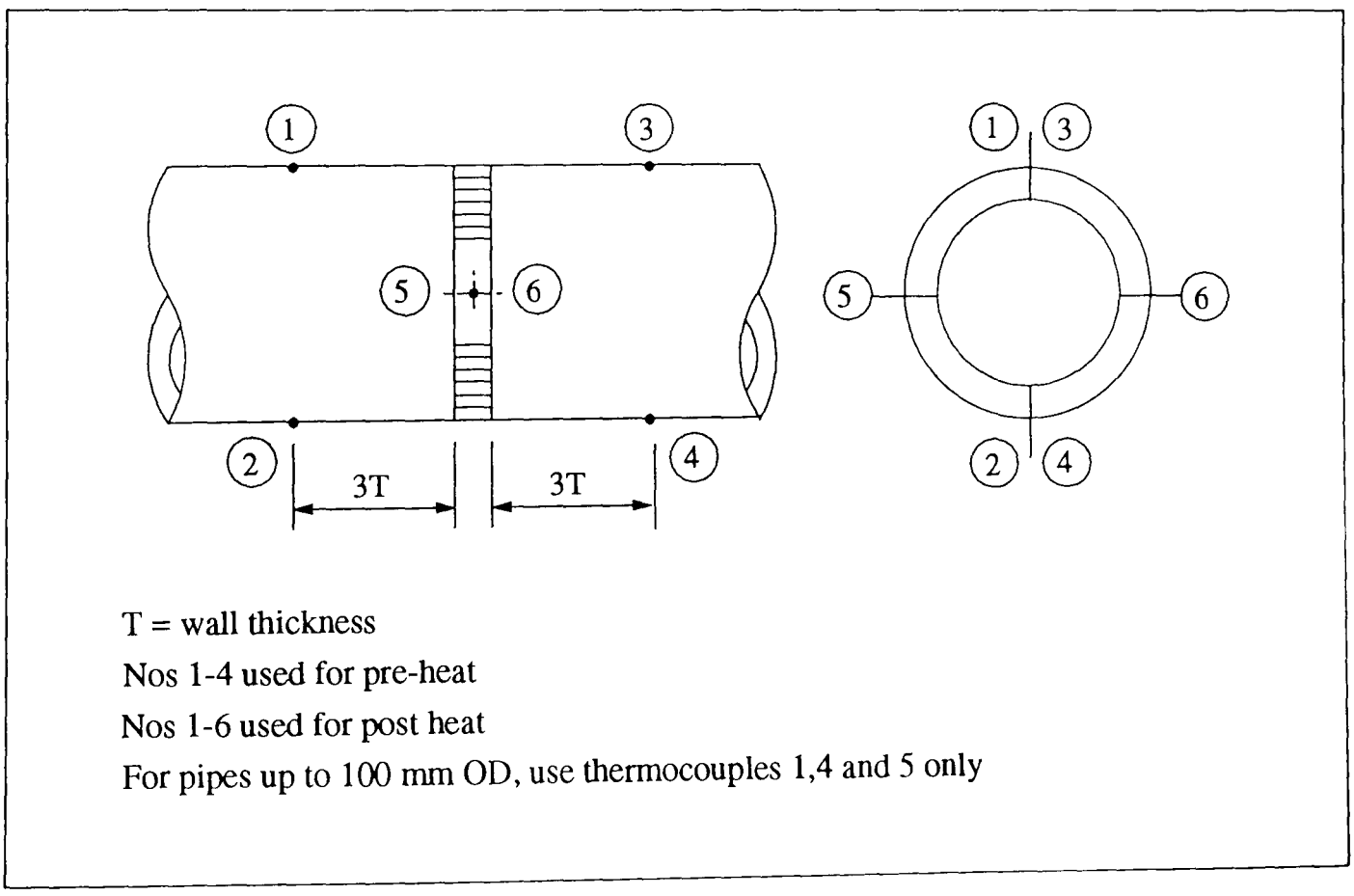

Fig. A5.2 Thermocouple arrangement.

APPENDIX VI VALIDITY OF THE RELATIONSHIP BETWEEN REMNANT LIFE AND STRAIN RATE FOR UNIAXIAL CREEP TESTS

The equation used to extend the creep curves of the exposed weld material uniaxial tests (see Chapter VI) was suggested by Penny [1995]:

$$(t_f - t) \times \dot{\varepsilon} = \text{constant} = C \quad \text{(in tertiary stage)} \qquad \text{(A6.1)}$$

where t_f is the rupture life, t and $\dot{\varepsilon}$ are the current creep time and strain rate, respectively, of a uniaxial creep test.

The applicability of the above relationship was examined by applying it to the exposed parent material uniaxial tests. Table A6.1 presents the results predicted by using this technique, in which it can be seen that the validity of Equ. (A6.1) as an approximate method to extend the uniaxial creep curves is confirmed. The failure strains in Table A6.1 were calculated by Equ. (6.4).

Table A6.1 Uniaxial creep test data and predicted data for the exposed parent material at 640° C.

σ(MPa)	C	Test Data					Predicted Rupture Strain
		t (h)	ε	$\dot{\varepsilon}$ (1/h)	t_f (h)	ε_f	
54	0.0541	1555	0.1130	3.628×10^{-4}	1704	0.348	0.3837
70	0.0828	339.5	0.1628	1.971×10^{-3}	381.5	0.501	0.4723

The C values in Equ. (A6.1) obtained from the tertiary creep data of a single uniaxial test have been demonstrated to vary slightly. Table A6.2 presents examples of C values obtained from the exposed parent material uniaxial test at 70 MPa.

Table A6.2 The C values obtained from the exposed parent material uniaxial test at 640° C and 70 MPa.

t (hour)	319.5	329.5	339.5	349.5	359.5
$\dot{\varepsilon}$(1/h)	1.305×10^{-3}	1.540×10^{-3}	1.971×10^{-3}	2.825×10^{-3}	4.115×10^{-3}
C	0.08091	0.08008	0.08277	0.09040	0.09053